Micromechanical experimental investigation and modelling of strain and damage of argillaceous rocks under combined hydric and mechanical loads

Linlin Wang

THESE présenté pour l'obtention du grade de

Docteur de l'Ecole Polytechnique

Spécialité : Mécanique

par

Linlin WANG

Laboratoire de Mécanique des Solides

Micromechanical experimental investigation and modelling of strain and damage of argillaceous rocks under combined hydric and mechanical loads

---

Soutenue publiquement le 7 décembre 2012, devant le jury composé de:

M. Jacques DESRUES	Université Joseph Fourier de Grenoble	Président
M. Philippe COSENZA	Université de Poitiers	Rapporteur
M. Jianfu SHAO	Université de Lille 1	Rapporteur
M. Georg DRESEN	Deutsches GeoForschungsZentrum	Examinateur
M. Jean-Charles ROBINET	ANDRA	Examinateur
M. Bernard HALPHEN	SETRA	Directeur
M. Michel BORNERT	Ecole des Ponts Paristech	Co-Directeur
M. Ahmad POUYA	Ecole des Ponts Paristech	Co-Directeur
M. Serge CHANCHOLE	Ecole Polytechnique	Invité

Remerciements

Ce travail de thèse a été effectué à l'Ecole Polytechnique, dans le Laboratoire de Mécanique des Solides (LMS).

Je voudrais exprimer toute ma reconnaissance à Monsieur Philippe Cosenza, Professeur à l'Université de Poitiers, et à Monsieur Jianfu Shao, professeur à l'Université de Lille 1, qui ont bien voulu accepter les charges de rapporteurs de ma thèse. Je les remercie pour le temps qu'ils ont bien voulu y consacrer et les commentaires qu'ils m'ont adressés. J'adresse également mes remerciements à Monsieur Jacques Desrues, Directeur de recherche CNRS à l'Université Joseph Fourier de Grenoble, qui m'a fait l'honneur d'accepter d'être le président de mon jury de thèse. Mes remerciements vont également à Monsieur Georg Dresen, directeur du Deutsches GeoForschungsZentrum (GFZ) et à Monsieur Jean-Charles Robinet, Docteur ingénieur à l'Agence Nationale pour la Gestion des Déchets Radioactifs (ANDRA) pour l'intérêt qu'ils ont porté à ce travail en acceptant de participer au jury.

Je tiens à exprimer toute ma gratitude à Bernard Halphen de m'avoir accueilli au sein du Laboratoire de Mécanique des Solides (LMS) et d'avoir dirigé mon travail. Il a su me transmettre les bases des raisonnements indispensables pour le travail de recherche scientifique ainsi que l'esprit de synthèse nécessaire. Je tiens plus particulièrement à remercier Michel Bornert, mon co-directeur avec qui j'ai passé beaucoup de temps sur ma thèse. Ce fut un privilège de travailler avec lui car, bien plus qu'un responsable de thèse, il m'a communiqué son enthousiasme pour la recherche ainsi que sa persévérance. Je remercie aussi Ahmad Pouya, qui m'accompagne depuis mon master et devient mon co-directeur, s'occupant de la partie modélisation. Je le remercie aussi pour ces longues heures de discussions scientifiques ainsi que pour m'avoir fait profiter de son savoir, de ses compétences et de son enthousiasme pour la science.

Je n'oublie pas non plus Serge Chanchole et je ne le remercierai jamais assez pour son soutien indéfectible tout au long de mes trois années de thèse. Je remercie vivement Diansen Yang pour son accompagnement aussi que pour ses conseils avisés. Je remercie également Duc Nguyen-Minh pour son soutien, sa gentillesse et son humour.

Une reconnaissance particulière va à notre excellente plateforme MIMECA : Daniel Caldemaison, Eva Héripré et Alexandre Tanguy. Sans leurs développements et leurs soutiens techniques, les essais de chargement mécanique et hydric combinés dans le microscope électronique à balayage, L'une des parties majeures de ma thèse n'aurait pas existé. J'ai garde dans mon cœur leur soutien, leur disponibilité et leur aide. Je remercie également Frédéric Valès et Hakim Gharbi pour leur soutien et leur aide scientifique.

Je remercie vivement les Géomechaniciens du LMS, Pierre Bérest, Alexandre Dimanov et Jean Raphanel pour leur soutien et les nombreux échanges que nous avons eu aussi bien du point de vue professionnel que personnel. Je remercie particulièrement Benoît Brouard pour les

nombreux conseils qu'il m'a donnés. Je remercie également Mathieu Bourcier et David Picard avec qui j'ai partagé le même bureau pendant ma thèse. Merci pour leur amitié et leur bonne humeur.

Merci au Laboratoire Navier à l'Ecole des Ponts Paristech où mes deux co-directeurs s'installent maintenant et où j'ai travaillé partiellement pour ma thèse. Un grand merci à Yujun Cui pour son soutien indéfectible. Je remercie également Matthieu Vandamme et Benoît Carrier avec qui j'ai testé le gonflement des films des argiles qui fut vraiment intéressant.

Je tiens à remercier tous les membres du LMS pour les trois années que j'ai passées auprès d'eux. Au cours de mon travail, j'ai pu bénéficier d'un environnement scientifique et humain de grande qualité. Je remercie vivement Patrick Le Tallec pour m'avoir accueilli au sein de son laboratoire si chaleureusement.

Enfin je remercie les "jeunes" du LMS, stagiaires, thésards et post-doc, pour la bonne humeur qu'ils font régner et leurs amitiés.

Et, un dernier mot pour les amis, les membres de ma famille, et en particulier mon amie Ying qui m'a toujours soutenu.

Contents

List of Figures

List of Tables

Chapter 1

Hydromechanical behavior of Callovo-Oxforian argillaceous rocks

Contents

1.1 Industrial context: underground storage of radioactive waste

Nuclear energy plays an important role in modern era: it produces 17% electricity of the world, while this value reaches more than 75% in France. Like other industries, nuclear produces wastes, moreover, their radioactive nature make the waste management much more delicate. According to the radioactive period, the activity level and the radiation type, three types of nuclear wastes can be distinguished: 1) category A (short life, weak or intermediate activity) 2) category B (weak or intermediate activity, but some tens of thousands of years life) 3) category C (high radioactivity). The management of the nuclear waste of short life is relatively simple, whereas, the wastes of high activity or long life lead to crucial issues since they would be radioactive during thousands or even millions of years (Aublive-Conil, 2003).

One solution for the long-term management of high-level radioactive waste consists in storing them deeply (500 - 1000 m) in an impermeable geological formation. In France, the national radioactive waste management agency (ANDRA), being in charge of the research on geological disposal, has chosen the Bure site (on the Meuse/Haute-Marne border) to construct an underground research laboratory (illustrated in Fig.1.1) where the studies on the reliability of long-term underground storage is performed. One geological layer of Callovo-Oxfordian argillaceous rocks is chosen to be the potential host rock, as it satisfies the main properties required by the long-term storage: 1) weak permeability (to avoid water movement as well as eventual transport of radioactive elements by convection); 2) geological stability (the site should tectonically inactive and aseismic); 3) favorable hydrogeological condition (the surrounding geological layers should be also weakly permeable); 4) a depth of at least 200 m (to ensure the containment).

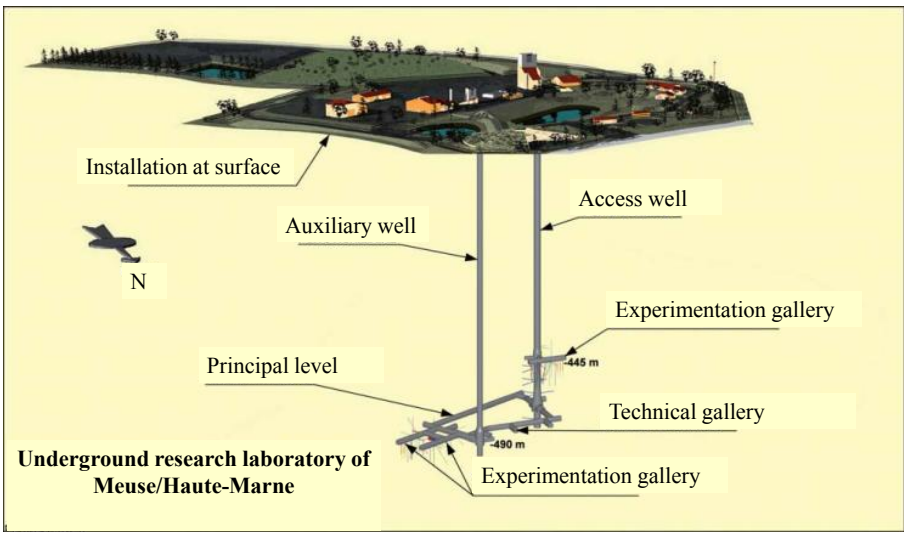

Figure 1.1: Underground research laboratory of Meuse/Haute-Marne (ANDRA, 2005).

Argillaceous rocks may undergo various types of aggressions during its service life, which subsequently alters its mechanical properties and permeability. This involves in a complex Thermal-Hydraulic-Chemical-Mechanical (T-H-C-M) coupled problem, which encourages great scientific attention and has been investigated extensively in the last decades. Among these environmental loads, one important term is linked to the change of surrounding humidity, such as the desiccation due to the ventilation during tunnel excavation. This thesis is focused on the hydromechanical behavior of argillaceous rocks, of which a good understanding is of critical importance for the safety and reliability of long-term storage. The evolution of such rocks under combined hydric and mechanical loads will be investigated experimentally and numerically.

After introducing the industrial context and main objective, chapter 1 also focuses on a detailed bibliography associated to the subject of this thesis. Firstly, the mineralogy and petrology of argillaceous rocks are discussed, as well as their microstructure which is crucial important for their hydromechanical behavior. Secondly, the swelling property of clay minerals (the predominant constituent of the studied material), is detailed. As the hydric load involves in always involves in a fluid transport process, the mechanisms of humidification/desiccation are discussed and a simplified transport model is introduced for the weakly permeable porous media (as the studied material). Finally, the existing experimental investigations and models of the hydromechanical behavior are summarized.

1.2 Callovo-Oxfordian argillaceous rocks

1.2.1 Mineralogy and petrology

The material investigated in the present work is Callovo-Oxfordian argillaceous rock taken from the French underground research laboratory at Bure, which dates about 155 million years. This argillaceous sedimentary layer is 130 m thick and is located at 400 - 600 m depth. The mineralogy analysis (Gaucher et al., 2004) reports three principal components of such rocks: clay minerals (40% - 45% in weight), mostly illite and interstratifies of illite-smectite), carbonate (22% - 37%), and quartz (25% - 30%). Other secondary minerals such as feldspar, iron sulphur and organic material are also present in the material.

1.2.2 Clay minerals

The clay minerals (fine grains smaller than 2 μm), principal component in argillaceous rocks, play a key role for the hydromechanical behavior of such material, due to its relatively low stiffness as well as its special sensitivity to water. The properties of argillaceous rocks, such as Young's modulus, compressive strength and hydraulic conductivity, are strongly dependent on their water content (Bornert et al., 2010; Chiarelli et al., 2003; Valès et al., 2004; Zhang

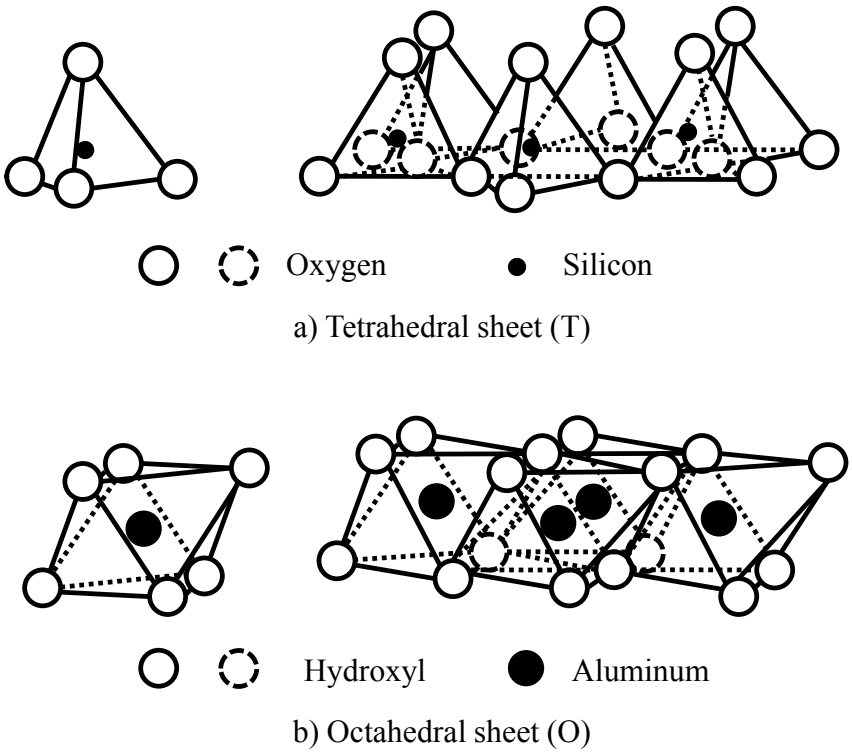

Figure 1.2: Basic unities of clay minerals: a) Tetrahedral sheet, b) Octahedral sheet (Mitchell, 1993)

et al., 2004). The properties of clay minerals (for example the swelling feature) are strongly associated with their plate-like microstructure, which will be described in following.

1.2.2.1 Structure of clay minerals

Clay minerals are hydrous aluminum phyllosilicates, sometimes with variable amounts of iron, magnesium, and other cations. Several organization levels exist for the clay minerals, ranging from elementary atom up to clay aggregate. Three structural unities among them, playing a role of crucial importance for the macroscopic behavior of clay minerals, are described in this section with increasing order.

Sheet

As all the phyllosilicates, clay minerals are characterized by two-dimensional sheets. Two types of sheets can be distinguished: SiO_4 tetrahedral sheet (T) and Al_2O_3 octahedral sheet (O). In a T-type sheet, one silicon atom is enclosed by four oxygen atoms at the vertex of one tetrahedron (see Fig.1.2a). In a O-type sheet, one aluminum or magnesium atom is surrounded by six hydroxyls at six vertex of one octahedron (see Fig.1.2b). Within the sheet, the bonds are electrovalent nature (electrostatic attraction between ions with opposite charge and share of two electrons): the strong bonds between Si and O, or between Al and O.

Layer

Due to the analogical symmetry and the sub-identical dimensions, the fourth oxygen atom of the tetrahedral sheet can be shared by the octahedral sheet. This combination of one octahedral sheet with one or two tetrahedral ones, of which the bond nature is covalent, constitutes one layer. Two principal types of layer can be characterized for clay minerals: TO type (or 1:1) and TOT type (or 2:1).

Within the tetrahedral sheet, the tetravalent Si is sometimes replaced by the trivalent Al. For the octahedral sheet, the replacement of Al by bivalent Ma, or by Fe, Cr, Zn, and Li is also possible. This replacement of cations is often referred as **isomorphic substitution** since the dimension of the layers varies hardly.

This isomorphic substitution, in which one atom with high valence is replaced by one with low valence, leads to the excess of negative charge. Hence, the positive ions or cations are adsorbed on the layer surfaces ensuring the electroneutrality of the layers. With the presence of water, these compensator cations are partially exchangeable with the cations in the solution. The amount of these **exchangeable cations**, expressed as milliequivalent of hydrogen per 100 g of dry clay, is called cation exchange capacity (CEC).

The layer and cation natures confer on clay minerals their specific properties (for example swelling capacity) and great diversity.

Particle

The TO and TOT layers are never present independently inside clay minerals. They exist generally in the form of an assembly, called particle. Such stacking of elementary layers, ordered or not, is controlled by certain attraction forces with different natures: 1) Electrostatic attraction comes generally from Coulomb force between the layer surfaces with negative charge due to isomorphic substitution and the compensator cations among the layers. 2) Van de Waals force is also responsible for attraction. Note that these inter-layer bonds are much weaker than the intra-layer ones (ionic or covalent).

The distance between one prescribed plane in one layer and the corresponding one in the adjacent layer, is called for **001** or **c spacing**. Such spacing is commonly used, notably to quantify the crystalline swelling of clay, which will be described in detail later.

One single particle contains several to hundreds layers. The number of elementary layers per particle depends on several factors: layer charge, nature of compensator cation, hygrometry etc. In general, the number of layers per particle tends to increase with: 1) layer charge increasing; 2) passing from monovalent cation to divalent one; 3) augmenting saline concentration; and 4) the decrease of RH. In other words, the enhancement of cohesion between the basal surfaces, tends to augment not only the number of layers but also their extension (Tessier, 1984). Van Olphen (1963) argued that the particle dimension is probably limited by the tension created in it. There are several origins of such structural tension. Firstly, crystal imperfection due to

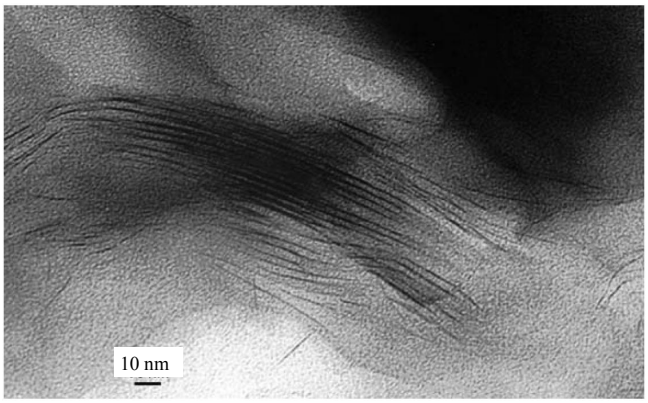

Figure 1.3: Arrangement of individual layers in one smectite particle, observed by TEM (Laird, 2006).

the isomorphic substitution introduces faults in the crystal. The second cause of this tension comes from the unfitting between the octahedral sheets superposed on the tetrahedral sheets by sharing of oxygen atom.

The observation by TEM (Transmission electron microscopy) can reveal the stacking of individual layers in the particle (Al-Mukhtar et al., 1996; Laird, 2006; Segad et al., 2012). One example is shown in Fig.1.3. The sub-parallel orientation of the elementary layers is obvious. Most of the layers are slightly curved and also the particle, indicating that the smectic layers are flexible. Some layers terminate inside the particle, whereas some others exceed the principal part. This random stacking of elementary layers implies one important conclusion: the particle is dynamic. This means that the particle can disintegrate, forming several smaller particles. Inversely, some small particle can assemble into one large particle. It is worth noting that such breakup and formation of quasicrystal is one important mechanism of the swelling/shrinking of the smectite.

Due to their plate-like microstructure, adsorption phenomenon is considerable for the clay particles. One parameter, called **specific surface** (m^2/g), characterizes the adsorption capacity of the material. Considering the case in which the water molecules are adsorbed on the particle surface, the adsorbate quantity depends on hygrometry. This variation of absorbed water molecules results in the evolution of the macroscopic volume, which is another mechanism of the swelling for clay minerals.

The particle is a well-defined structural unity for clay minerals, which manifests its crucial importance for studying the swelling property (discussed in the following section) and mechanical behavior of such minerals. However, the term “aggregate” is also often used, in particular when argillaceous rocks are described as an inclusion-matrix composite: the mineral grains is wrapped clay aggregates which totally constitute a continuous clay matrix. A precise definition of “aggregate” doesn’t exist. Normally, it represents an assembly of the crystals and fragments of clay minerals and some calcites scattered in them, with size of dozens or hundreds

of micrometers.

1.2.2.2 Main groups of clay minerals

Due to the great variety (layer nature, compensator cations, etc.), there are numerous groups of clay minerals of which the properties are dissimilar. We discuss here 5 principal groups, of which the structures and swelling properties are summarized in Fig.1.4, and also in Tab.1.1.

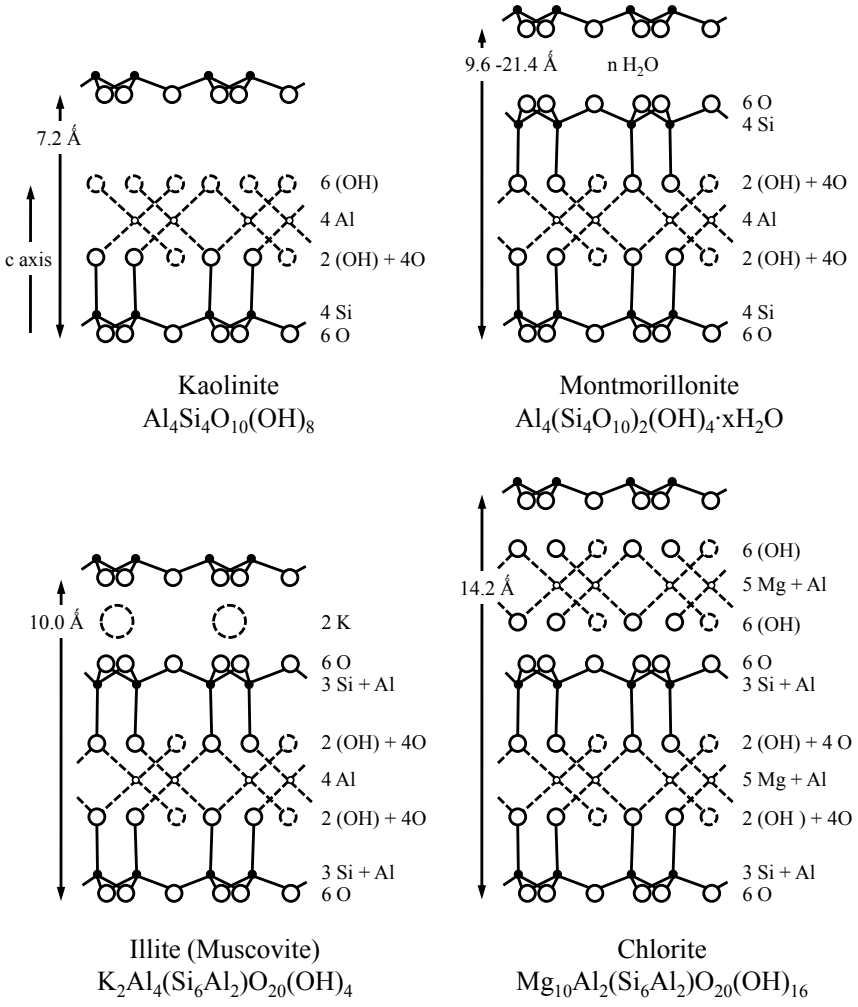

Figure 1.4: Structure of different groups of clay minerals (Karl, 1968).

Kaolinite

Kaolinite is a TO type clay mineral without substitution. The arrangement of elementary layers is stable, of crystal type, with the chemical composition $Al_2[(OH)_4Si_2O_5]$ (for no hydration case). The cohesion inside kaolinite is principally attributable to electrostatic force, accompanied by van der Waals force and certain hydrogen bonds. Due to the absence of compensator cation at inter-layer space, there is merely surface hydration for the repulsion part,

Table 1.1: Some main properties of three groups of clay minerals.

Groups of clay minerals	Kaolinite	Illite	Smectite
Layer	1 :1 (TO)	2 :1 (TOT)	2 :1 (TOT)
Exchangeable cation	-	K^+	Ca^{2+}, Na^+
CEC (meq/100g)	3 - 15	10 -40	70 - 100
Arrangement of particles	Isolated crystal	Mecaceosus aggregate	Quasi-crystal
Swelling property	Hardly swelling	Moderate swelling	Great swelling

which is not sufficient to exceed the great attraction. Hence, the size of kaolinite can't be modified and it has a low swelling capacity.

Illite

Illite is a TOT type clay mineral for which the substitutions take place principally in tetrahedral sheets. The negative charge is compensated by K^+ ions at inter-layer space. Due to the suitable size of K^+ ions, the interlocking in the hexagonal cavity forbids neither sliding nor separation of layers. Such special arrangement of layers by K^+ ions in illite is ordered and stable. The presence of inter-layer water is forbidden.

Smectites group

The smectites group is similar with illite (2:1), but with a lesser organization in the arrangement of layers. Such disorder and the small charge of layers facilities their separation. Diverse cations, water and organic molecules can exist in the inter-layer space, and this is why the inter-layer spacing can vary for different cases. There is a wide variety of smectite according to different exchangeable cations. The nature of the various compensator cations directly effects the interpolation of water molecules. For example, the Na-smectite swells greatly, whereas the swelling capacity of Ca-smectite is much weaker.

Chlorite

Chlorite owns also a TOT structure. Unlike other 2:1 clay minerals, a chlorites's interlayer space is composed of $(Mg^{2+}, Fe^{3+})(OH)_6$. This $(Mg^{2+}, Fe^{3+})(OH)_6$ unit is more commonly referred to as brucite-like layer, due to its closer resemblance to the mineral brucite ($Mg(OH)_2$). Therefore, chlorite's structure appears as TOT - brucite - TOT.

Mixed layer clay variations

Mixed layer clays are intimate associations of two (or more than two) types of clay minerals. For Callovo-Oxfordian argillaceous rocks, they are principally the interstratified illite/smectites, which are the consequence of the incomplete transformation from smectite to illite under certain conditions (burying, temperature and pressure).

The clay minerals in the argillaceous rocks of the Bure site are principally interstratified

illite/smectite (I/S), illite, mica, chlorite and kaolinite. Interstratified illite/smectite (< 0.2 μm) is the most abundant, stacked up with layers in generally two ways: type R0 (disordered) which contains more smectite (50 - 70%), and type R1 (ordered) with less smectite content (20 - 40%). For the samples tested in this study, which are taken from the EST28031 borehole at 550m depth, interstratified illite/smectite principally belong to type R1 (ANDRA, 2005), and smectites are essentially dioctahedral (dominant aluminum or ferric octahedrons).

1.2.3 Microstructure and porous space

1.2.3.1 Anisotropic texture

Besides the petrologic analysis, the observation by scanning electron microscopy (SEM) can be used to perform a 2D characterization of the microstructure of argillaceous rocks: phase distribution and typical sizes of different constituents (Sammartino et al., 2003; Robinet, 2008). FigB.3. presents a typical SEM micrograph of argillaceous rocks in backscattered electron (BSE) mode. At this scale, such rocks can be described as a composite with some mineral inclusions (mostly carbonate and quartz) fairly homogeneously scattered in a continuous clay matrix. The clay minerals form the matrix where the crystals and fragments are distributed. They assemble the aggregates with size of dozens or hundreds of micrometers. Note that the clay matrix itself exhibits a complex heterogeneity reflecting the particle structure of clay with typical size below or near a few micrometers and some calcites scattered in them (Robinet, 2008).

The grain size of quartz varies from 10 to 100 μm, while the carbonate grains exhibit a more variable size and can reach 200 μm. The GSDs (grain size distribution) of carbonate and quartz grains in Callovo-Oxfordian argillaceous rocks have been estimated (shown in Fig.1.6), which can be described by a power law:

$$N_i\left(S_i\right) = a \cdot {S_i}^{-D} \tag{1.1}$$

where S_i is grain surface and $N_i(S_i)$ is grain number density. For Callovo-Oxfordian argillaceous rocks, $D = 0.8$ for carbonate grains, and $D = 0.7$ for quartz grains.

The shapes and orientations of carbonate and quartz grains in Callovo-Oxfordian argillaceous rocks have been investigated by Robinet (2012), based on a statistical analysis on a representative population of grains in two planes: 1) plane 1 parallel to the bedding plane, and 2) plane 2 perpendicular to the bedding plane. Carbonate grains exhibit an elongated shape, and the distribution of their elongation index (ratio between minimum and maximum length of grain) shows a peak at 0.6. Moreover, these carbonate grains present a preferred orientation parallel to the bedding plane in plane 2, while their orientations are somewhat random in plane 1 (Fig.1.7). For quartz grains, they are less elongated than carbonate grains, with a most frequent elongation index of 0.7. Similar to the carbonate grains, the quartz grains exhibit

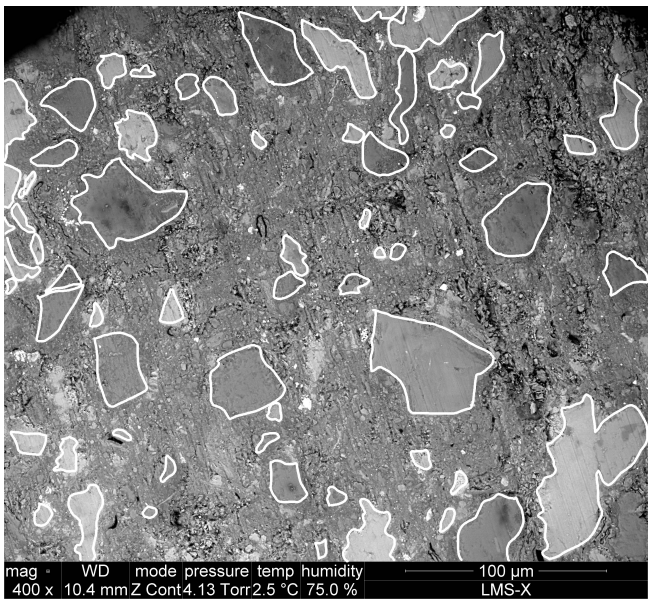

Figure 1.5: Microstructure of argillaceous rocks by ESEM observation: backscattered electron imaging, environmental mode. Argillaceous rocks can be described as a composite structure made of continuous clay matrix scattered by some mineral inclusions (mostly carbonate and quartz). The contours of some big inclusions, appearing in relatively homogeneous grey, are marked in white lines. Besides the three principal components, some pyrites (the brightest domains in the ESEM image) can also be found, as well as some pores principally around big grains or in clay matrix.

a moderate preferred orientation that is sub-parallel to the bedding plan in plane 2, whereas randomly orientated in plane 1 (Fig.1.8). Geometric characterization reveals that Callovo-Oxfordian argillaceous rocks exhibit an anisotropic texture at the scale of inclusion-matrix composite.

The orientation of clay particles is essentially related to mechanical compaction. By reason of sedimentation and diagenesis during geological formation, clay particles are settled preferentially in the direction parallel to the bedding plane. It is noted that this particle orientation depends on the humidity state of material: a more saturated state in general results in a lager extent of chaos for the orientation of clay particles.

Wenk et al. (2008) has used a method based on hard synchrotron X-rays to obtain diffraction images of Callovo-Oxfordian argillaceous rocks and applied the crystallographic Rietveld method to deconvolute the images and extract quantitative information about about the preferred orientation of clay minerals. The results are shown in Fig.1.9. The (100) pole figures of illite (major clay mineral in the studied material) show a moderate texture (3.2 - 3.6 m.r.d.) with a substantial proportion of randomly oriented crystallites (the minimum is 0.2 m.r.d.). The distribution is more or less axially symmetric about the normal to the bedding plane. (010) pole figures of illite show a uniform girdle with poles concentrated in the bedding plane.

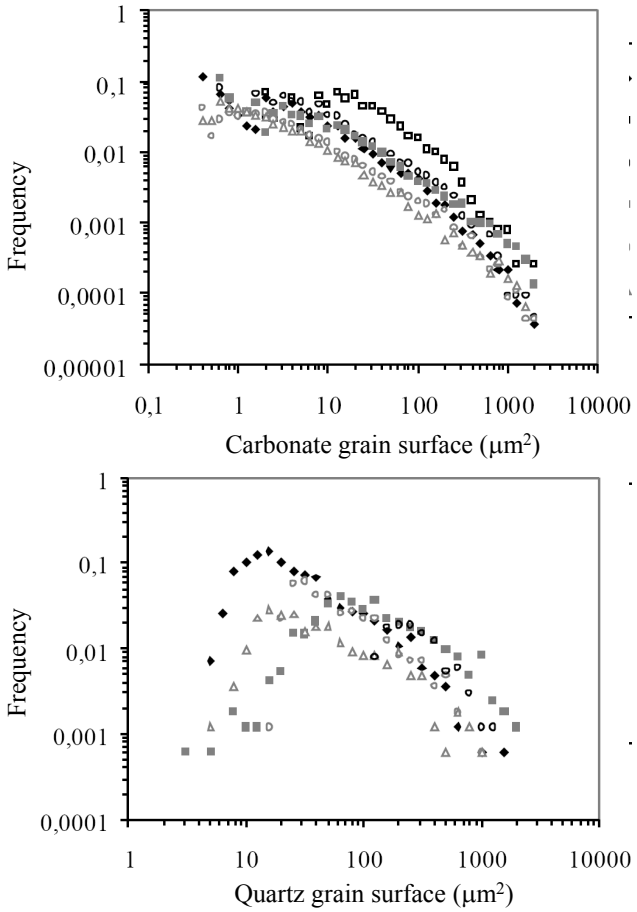

Figure 1.6: Frequency distribution of the carbonate and quartz grain numbers as a function of grain surface (Robinet, 2008).

Similar to illite, Kaolinite also displays a weak preferred orientation in such rocks.

Such an anisotropic texture of the Callovo-Oxfordian argillaceous rocks introduces a strong anisotropy for their hydromechanical behaviors. For example, the deformation due to humidification or desiccation is more significant in the direction normal to the bedding plane than parallel to it. Note that the anisotropic properties of the component (in particular clay particle) are another origin of the anisotropy.

1.2.3.2 Porous space

The initial water content of Callovo-Oxfordian argillaceous rocks is about 7%. Their reference porosity is 18%, with a distribution shown in Fig.B.2. Such a pore size distribution leads to an extremely low permeability (10^{-19} - 10^{-23} m^2) for such materials. In general, three types of porosities can be distinguished according to their sizes and locations (Sammartino et al., 2003):

- Macroporosity (about 10% of the total connected porosity) corresponds to inter-aggregate pores which principally develop around grains of quartz and with a lesser extent around

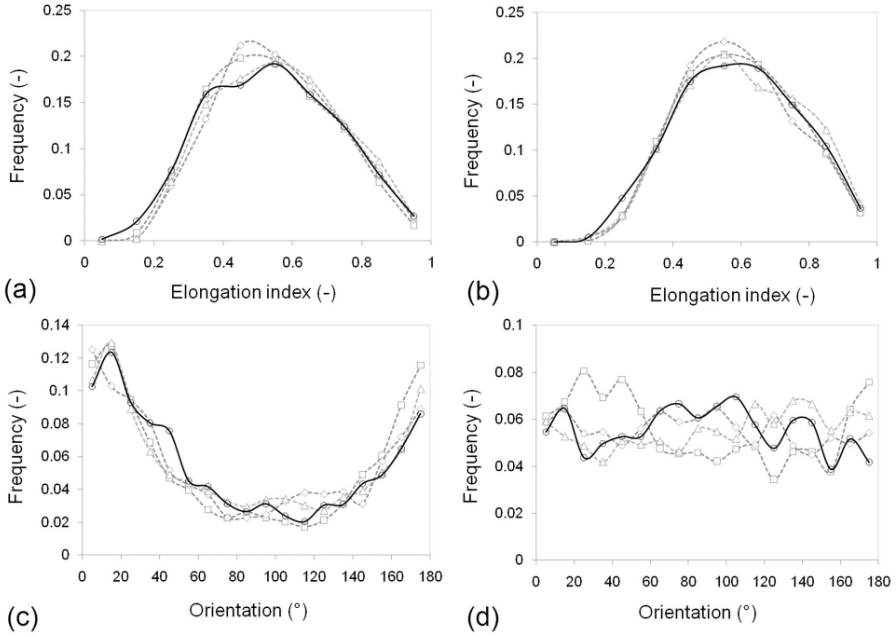

Figure 1.7: Frequency distributions of the elongation indexes (top) and the orientation of carbonate grains in the planes perpendicular (left) and parallel (right) to the bedding plane (Robinet, 2012).

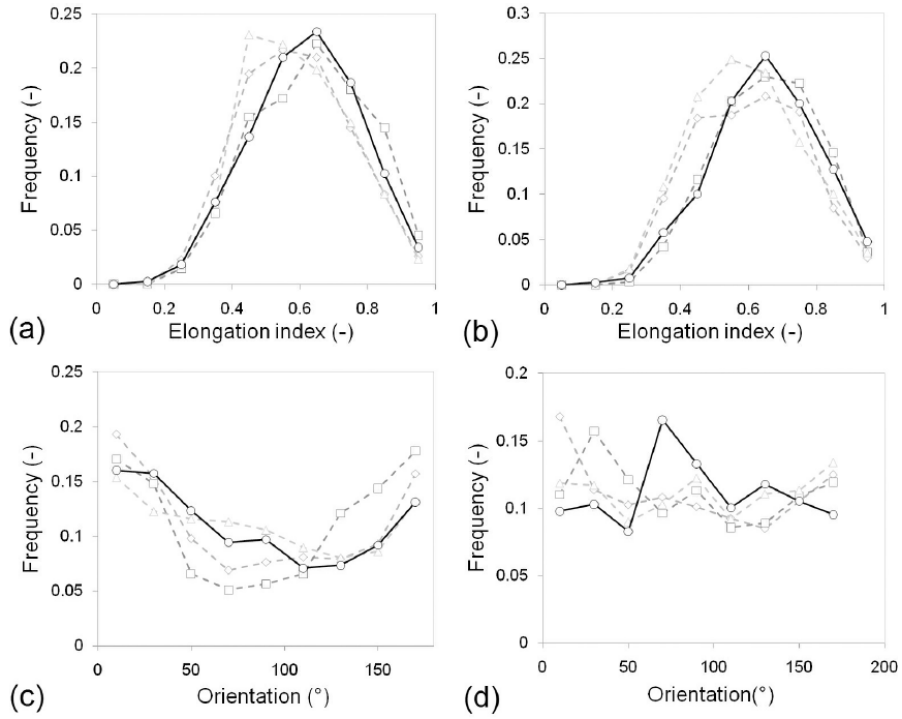

Figure 1.8: Frequency distributions of the elongation indexes (top) and the orientation of quartz grains in the planes perpendicular (left) and parallel (right) to the bedding plane (Robinet, 2012).

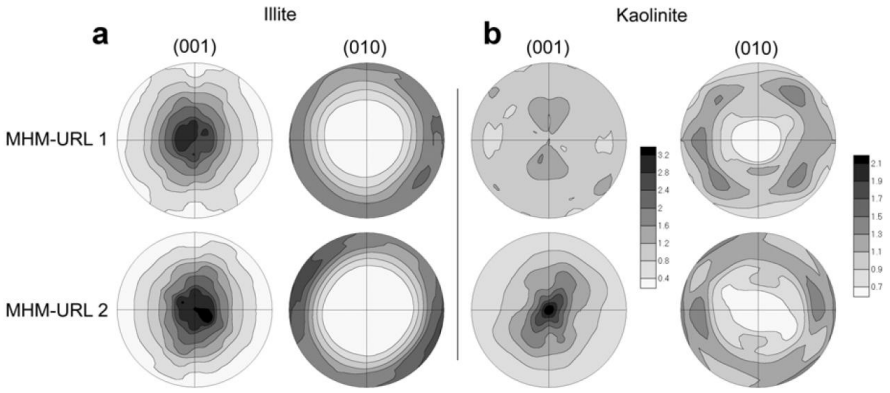

Figure 1.9: (001) and (010) pole figures of illite and kaolinite of the Bure (MHM-URL) shales. Equal area projection. Different pole density scales are used for (001) and (010) pole figures (values in m.r.d.) (Wenk et al., 2008).

carbonate. The minimum size of such inter-aggregate pore is 1 to 2 μm. Besides, the size of these pores increases with the grain size.

- Mesoporosity corresponds to intra-aggregate (inter-particle) pores predominantly located between clay particles and surrounding secondary minerals. Such intra-aggregate pores own typical size ranging from nanometer to submicrometer. They strongly depend on the humidity state of the rocks. The inter-particle pores, occupying 86% of the total connected porosity, are of crucial importance for the fluid transport in argillaceous rocks.

- Microporosity corresponds to intra-particle pores (i.e. inter-layer space of clay particle). It occupies 4% of the total connected porosity.

1.3 Swelling property of argillaceous rocks

Under humidification, argillaceous rocks would undergo a considerable volume change. This swelling property is essentially linked to the presence of the water-sensitive clay minerals. Note that all porous solid would deform mechanically, when relative humidity changes, due to the variation of capillary pressure, which can be described by standard poromechanics. However, the swelling of clay minerals include not only this effect of capillary pressure, but also some other physic-chemical effects.

The swelling of clay minerals is variable, depending on certain factors: group of clay mineral, layer charge, exchangeable cation (see Fig.1.11) and so on (Arifin, 2008; Delage et al., 1998). For kaolinite and illite, the inter-layer space can't be hydrated and the particles of these clay are rigid (or quasi rigid). The moderate swelling of the two groups is predominantly attributable to the arrangement of particles. However, for smectite, its 001 space can be hydrated, and not

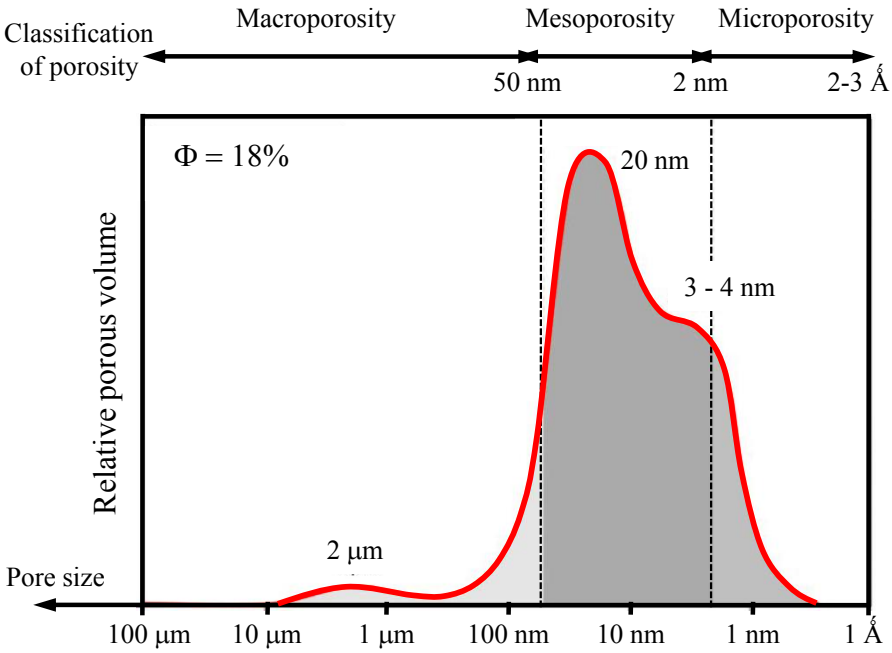

Figure 1.10: Pore size distribution of the argillaceous rocks at Bure (ANDRA, 2005).

only the arrangement of the clay particles but also their internal structure could evolve. Hence, the swelling capacity of smectite is significant.

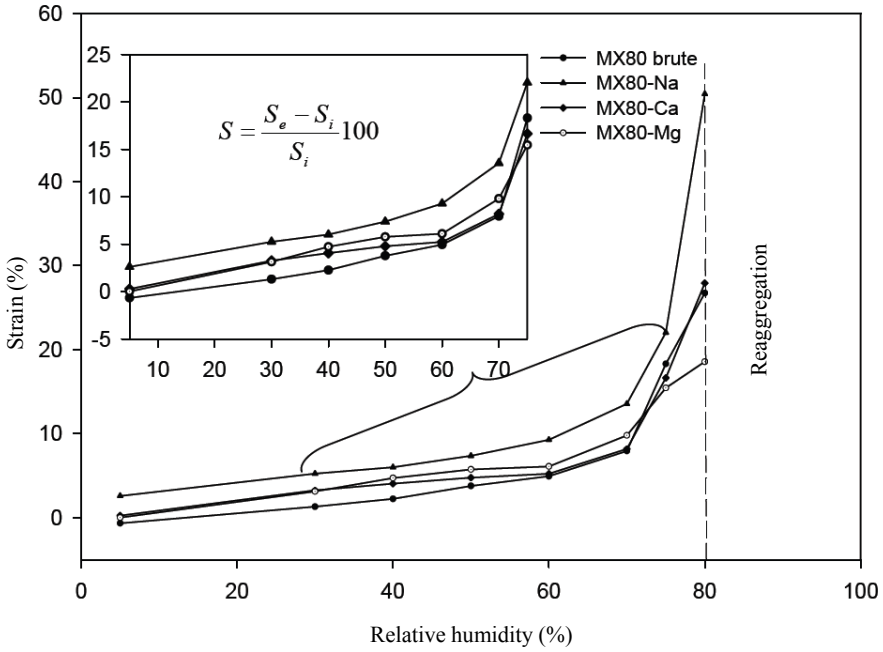

Figure 1.11: Swelling-shrinking of clay aggregate (Montes-H, 2002).

1.3.1 Water and associated bonds in argillaceous rocks

As discussed in the previous section, different types of pores are present in argillaceous rocks. It should be noted that there is somewhat a corresponding between the three types of porosity and their locations. The swelling-shrinking property of argillaceous rocks with RH change is essentially associated with the volume variation of the porous spaces in argillaceous rocks governed by their interaction with water present in them. Actually, the water in these pores is governed by different types of bonds, strongly depending on the pore size (Kowalski, 2003). For argillaceous rocks, three types of governing bonds can be distinguished for the three porosities:

- The water of microporosity (inter-layer space) is predominantly governed by chemical bonds (hydration of interlayer cation, electrostatic force).
- The water of mesoporosity is principally controlled by physic-chemical bonds (osmosis effect, adsorption);
- The water present in macropore is generally governed by physic-mechanical bonds (capillary pressure, inertial force).

Note that the energy magnitude of these bonds generally decreases with the pore size. When water activity (relative humidity) changes, these bonds varies, leading to the evolution of the pores spaces. And this would manifest at macro-scale a "swelling" of the porous solid.

For standard porous solid which can be investigated in the context of standard poromechanics, the governing forces generally consist of physic-mechanical bonds. This is quite different from argillaceous rocks (particular the component of clay minerals) which involves also in chemical bonds and physic-chemical bonds. That is the main origin of the specific swelling property of argillaceous rocks (clay minerals).

1.3.2 Swelling mechanisms of clay minerals

The swelling of argillaceous rocks is predominately attributable to the specific physic-chemical chemical properties of clay minerals present in them. Referring to the governing bond classification, four swelling mechanisms of clay minerals can be distinguished:

- Crystalline swelling is associated with a change of inter-layer spacing due to the hydration of discrete 0, 1, 2, 3, 4 water layers by interlayer cations between the elementary layers of clay particles (Laird et al., 1995; Karaborni et al., 1996). The layer hydrated with 0, 1, 2, 3, and 4 layers of water molecules are distinguished by 001 spacing approximately of 10.0, 12.5, 15.0, 17.5 and 20.0 Å, respectively. Crystalline swelling is governed by the combining effects of repulsion, which is attributable to hydration energy of interlayer cation, and attraction which is essentially associated with van der Waals forces and Coulomb force

between negatively charged layers and positively charged inter-layer cation. A example of such crystalline swelling investigated by X-Ray diffraction is presented in Fig.1.12. Crystalline swelling is extensively studied in the last decades, particularly with the help of X-rayon diffraction (XRD). In general, the extent of crystalline swelling is strongly controlled by the type of interlayer cation. For a Mg saturated SPV bentonite (a Wyoming bentonite), XRD pattern indicates that the sample is dominated by 2-layer hydrates at both 55%RH and 75%RH, while, it is dominated by 2-layer hydrates but has a considerable portion of randomly interstratified 3-layers hydrates (Reynolds and Reynolds, 1996). Transitions from 0 to 1 and from 1 to 2 layers for Na^{+}-smectite occur within RH regimes ranging from 10 - 40%RH and 50 - 90%RH respectively (Likos et Lu, 2006). Ca^{2+}-smectite has been shown to retain one water layer even at 0%RH. Transition to 2 layers occurs at approximate 25%RH, and this two-layer state remains stable until 90%RH. In general, 95%RH can be considered as the upper limit of the two-layer hydration state for both clays. This is confirmed by the results of Laird et al. (1995) in which a transition from 2 to 3 layers starts from 95%RH for both 5 reference smectites.

- 2) Double-layer swelling (or osmotic swelling) involves in a separation of inter-particle space by a diffuse double-layer effect (Barbour and Fredlund, 1989; Bolt, 1956; Delville and Laszlo, 1998; Dormieux et al., 2003; Wersina et al., 2004). The negative charge on the external surface of the clay particle forms one half of the electric double layers. And this negative charge would be equilibrated by the exchangeable cation in the solution, forming the other half of the electric double layers (Fig.1.13). This results in a more important concentration of the exchangeable cation in the region adjacent to the external surface than in the bulk solution. Hence, the water molecules tend to diffuse toward the surface in attempt to equalize the ion concentration and produce a separation of the clay particles. Double-layer swelling depends on the exchangeable cation type and the bulk solution concentration. Bolt (1956) applied the theory of electronic double layers to investigate the compressibility of pure clays (Fig.1.14). Saiyour et al. (2000) investigated the swelling of FoCa7 (Fourges-Cahaignes clay) and revealed that the inter-particle space can reach 150 Å(Fig.1.15).

- When RH increases, water pressure in the porous solids varies accordingly. This would lead to a mechanical deformation of material, which can be investigated by standard poromechanics. Note that surface tension plays a crucial role in unsaturated case. The observations have revealed that the pore shapes in the clay are somewhat like cages or lentils, moreover, their sizes are very regular for the given humidity condition (Murray and Quirk, 1980; Tessier, 1984). This suggests one mechanism of this form: surface energy between the solution and particle's wall. If the clay particle is sufficiently soft (Young's modulus is extremely small), the pore size can be predicted by Laplace's law, as shown

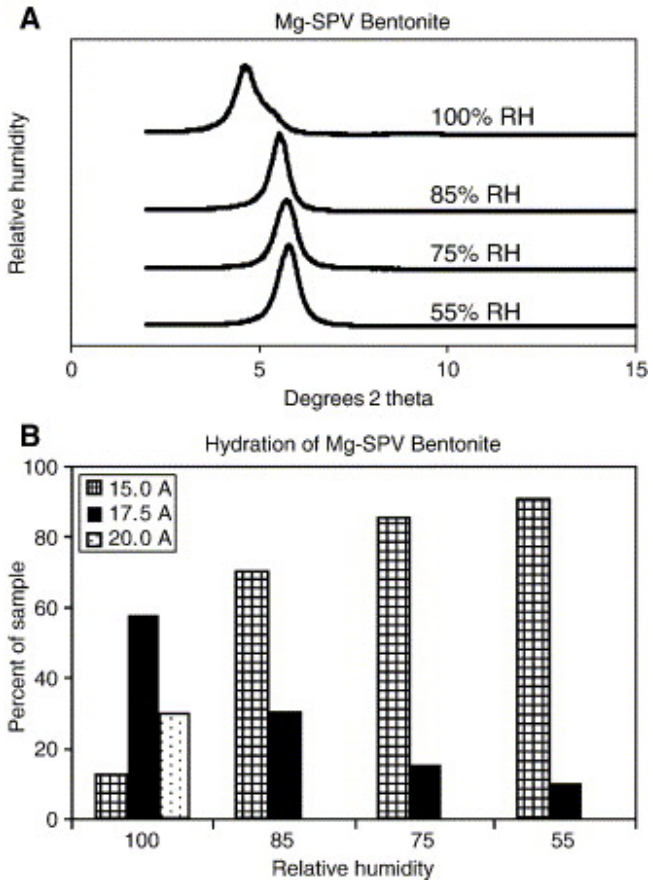

Figure 1.12: A) X-ray diffraction patterns of Mg saturated SPV bentonite (a Wyoming bentonite) equilibrated with atmospheres at 55, 75, 85, and 100% RH. B) Histogram depicting the proportions of various hydrated layes in Mg-SPV bentonite as a function of RH (Reynolds and Reynolds, 1996).

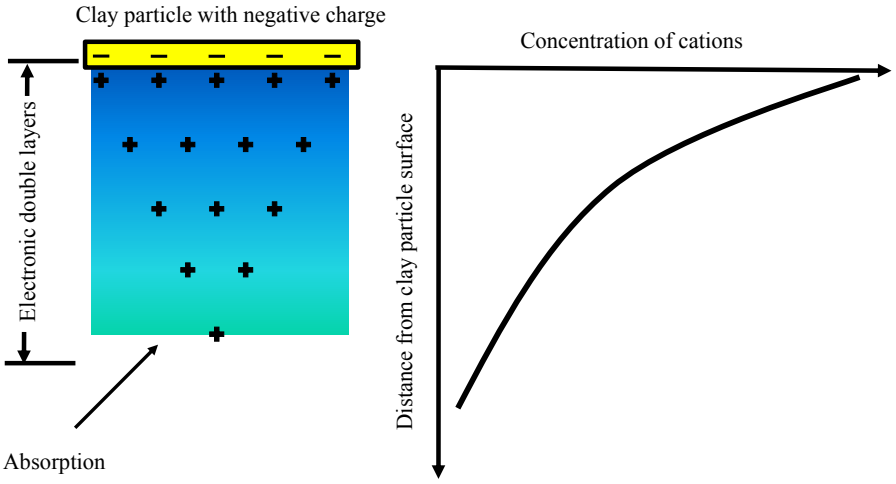

Figure 1.13: The electronic double layers created at the surface of a clay particle (Cernica, 1995).

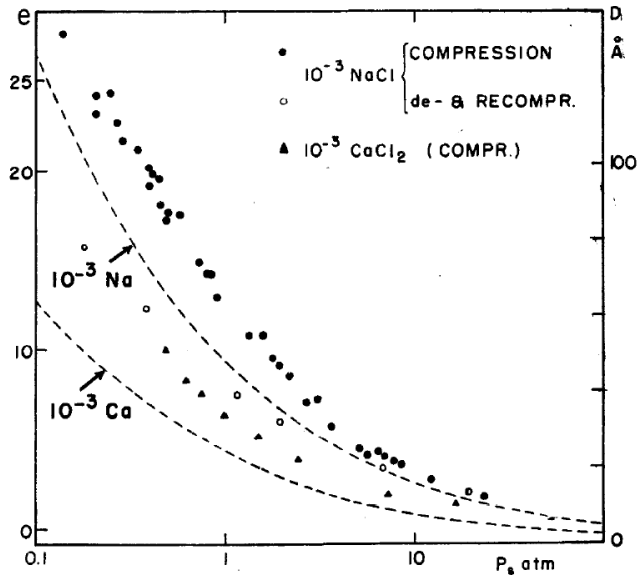

Figure 1.14: Osmose swelling curve of Na-montmorillonite and Ca-montmorillonite, in equilibrium with 10^{-3} molar NaCl and CaCl respectively, (Bolt, 1956).

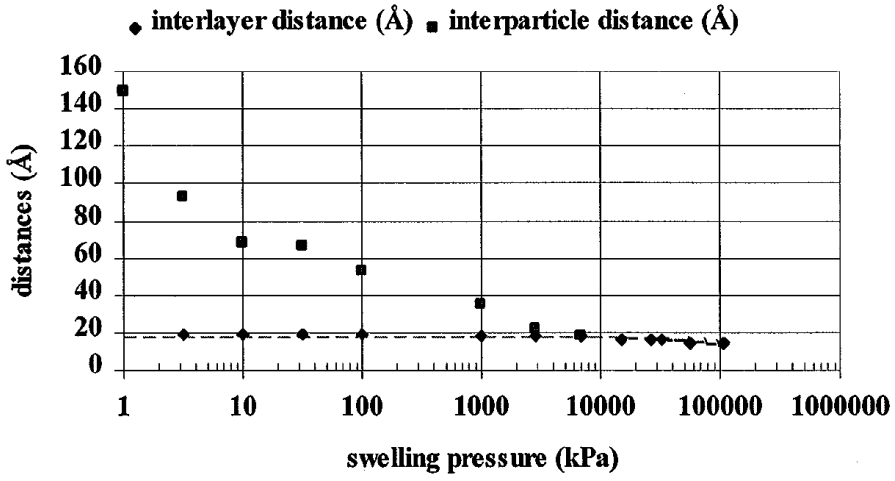

Figure 1.15: Interlayer and inter-particle separation versus suction (Saiyour et al., 2000).

by Tessier (in Fig.1.16).

- 4) Besides the quantitative spacing changes of different types of pores, transition can take place as well, leading to the swelling of clay mienrals: the breakup of clay particles, which is a dynamic process whereby the inter-layer space turns into the inter-particle space. In fact, many researchers have shown there is a dependence of the layer number per clay particle with water activity (Tessier et al., 1998; Saiyour et al., 2004; Laird, 2006): it decreases with RH (in Fig.1.17). This phenomenon is related to the breakup of particles during hydration. The 001 spacing between layers of particle grows up with increasing water activity. If the layers are sufficiently separated (with inter-layer distances similar

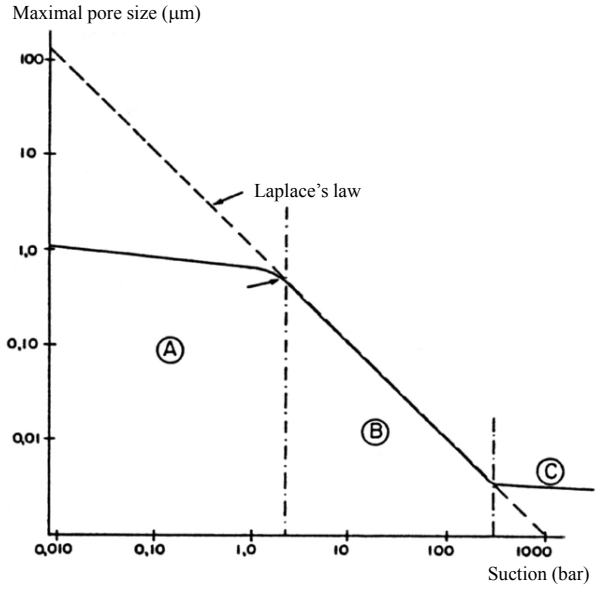

Figure 1.16: Maximal size of pores filled by water predicted by Laplace's law and the maximal size of pores of one water-clay system (Tessier, 1984).

to those at the end of the crystalline swelling process with four layers of water molecules), the electrostatic forces would undergo a complete reversal from being attractive as in the crystalline swelling stage, to being repulsive as in the double layer region. The consequence is that a large particle may decompose into two or several separate but smaller particles, manifesting as a swelling at macro-scale.

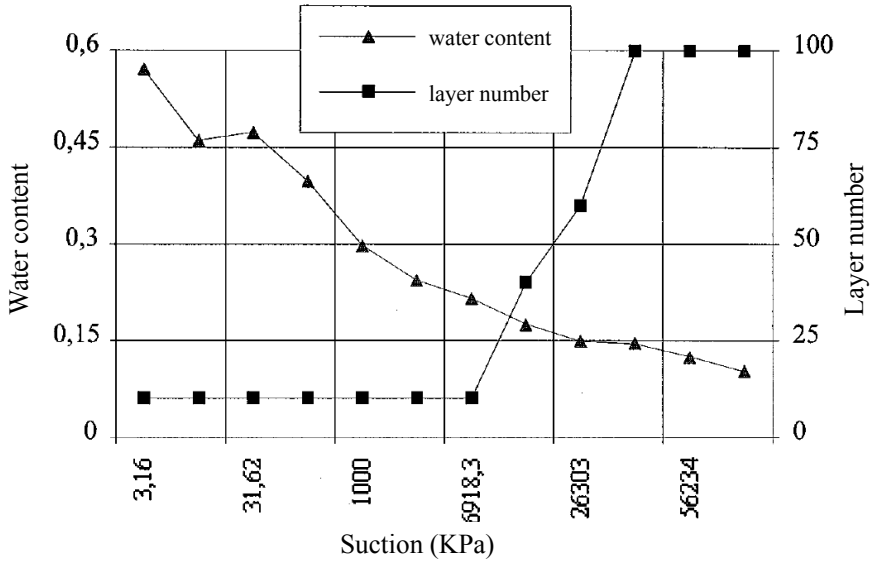

Figure 1.17: Number of layers per particle and water content versus suction (Saiyour et al., 2000).

Saiyour et al. (2000) investigated the swelling mechanisms for a highly compacted smectite clay (one dimensionally compacted up to 60 MPa) by means of a microstructural approach in which the inter-layer spacing could be measured by X-rays diffraction: a transition of one water layer to two water layers (crystal swelling) arises when suction changes from 50 MPa (corresponding to about 70%RH) to 7 MPa (95% RH), while the average layer number per clay particle decreases in the same time from 100 to 10 (a ratio of 10). This shows the dependence of the fourth swelling mechanism (breakup of particle) on the first (crystalline swelling).

In summary, the swelling property of clay minerals is essentially linked to an evolution of its microstructure, in particular a change of pore spaces inside. The above discussion suggests that the unity of clay particle is an interesting scale for studying the swelling phenomenon. From the viewpoint of clay particle, the swelling can be described as two levels: 1) arrangement of clay particles (separation between each other and the evolution of the inter-particle pore due to the flexion of the clay particles); 2) evolution of internal structure of clay particles (extension, number of layers per particle, and 001 spacing). An illustration of the main swelling mechanisms is given in Fig.1.18.

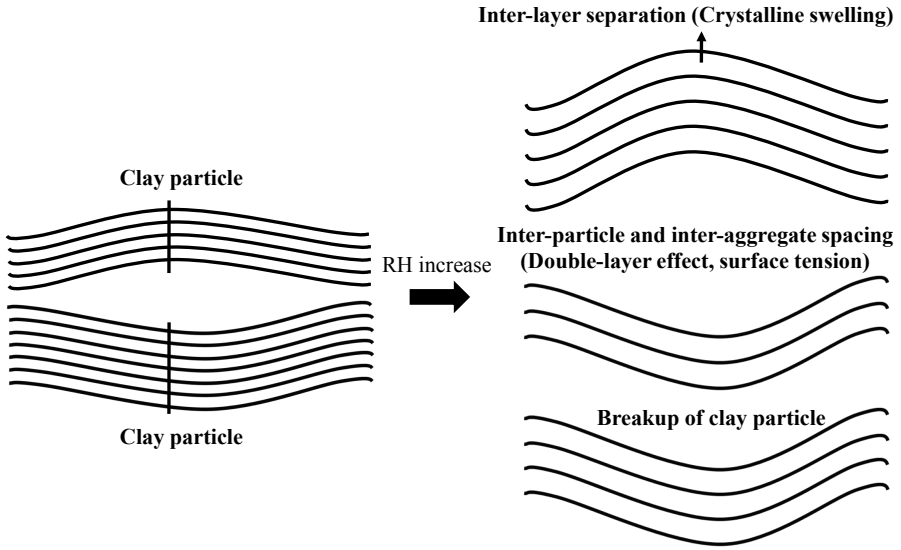

Figure 1.18: Illustration of different swelling mechanisms of clay minerals.

1.3.3 Interaction between multi-scale swellings: double structure concept

Based on the above discussion, the swelling mechanisms of clay minerals, developed at various scales, are all functions of water activity. Hence, it should be reversible for a humidification-desiccation cycle although exists a hysteresis (Laird et al., 1995). However, the experimental investigations on expansive soils have revealed that either residual contraction or expansion

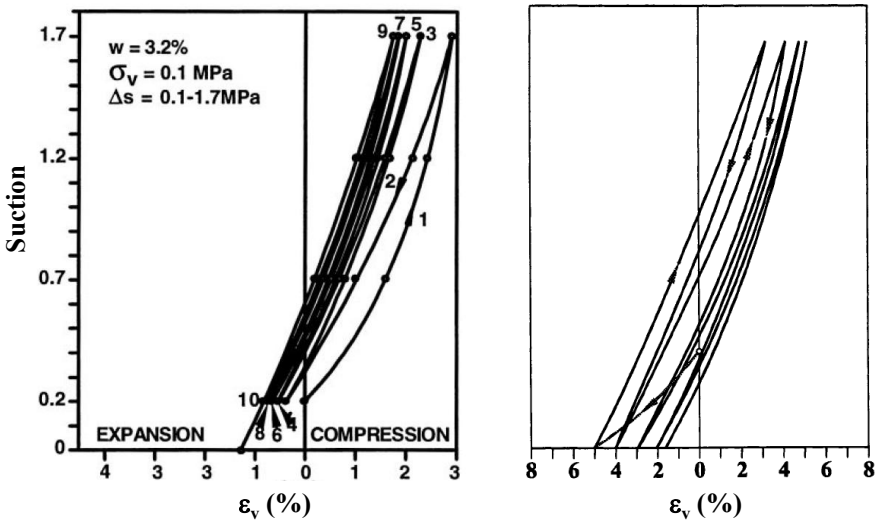

Figure 1.19: Accumulation of expansion (left) and compaction (right) strains during suction cycles (Gens, 1992).

(Fig.1.19) can develop after a humidification-desiccation cycle, depending on stress level and initial fabric of material (essentially void ratio) (Tripathy et al., 2002). Moreover, this residual strain is accumulated when subsequent cycles continue and its amount tends to a stationary value after a large number of hydric cycles.

To explain these experimental observations, Gens (1992) proposed the double structure concept which takes into account the interaction between the multi-scale swellings for expansive soils. In this framework, two scales of swelling are distinguished: the swelling of active clay minerals (ε_m) being fairly reversible and volumetric at microscopic level, and structural rearrangement (ε_M) caused by the microstructural swelling, being elastoplastic and irreversible, at macroscopic level. Since the macrostructural strain is essentially associated with the microstructural strain, they introduced a coupling function linking the two scales of swelling:

$$f(p/p_0) = \frac{\varepsilon^M}{\varepsilon^m} \tag{1.2}$$

where p/p_0 is a measure of the distance from the current stress state to the yield locus of the macrostructure LC and has the same meaning as the overconsolidation ratio for an isotropically consolidated saturated soil. A different coupling function should be specified for humidification (suction decrease, f_D) or desiccation (suction increase, f_I) path due to the different mechanisms of rearrangement for the two hydration paths. These functions depend on stress state and compaction state on the basis of experimental data: the lower void ratio (higher density) leads to a bigger swelling during humidification while it may inhibit the shrinkage during desiccation. In addition, the higher confinement would prevent swelling whereas it promotes shrinkage. The typical forms of these coupling functions are presented in Fig.1.20.

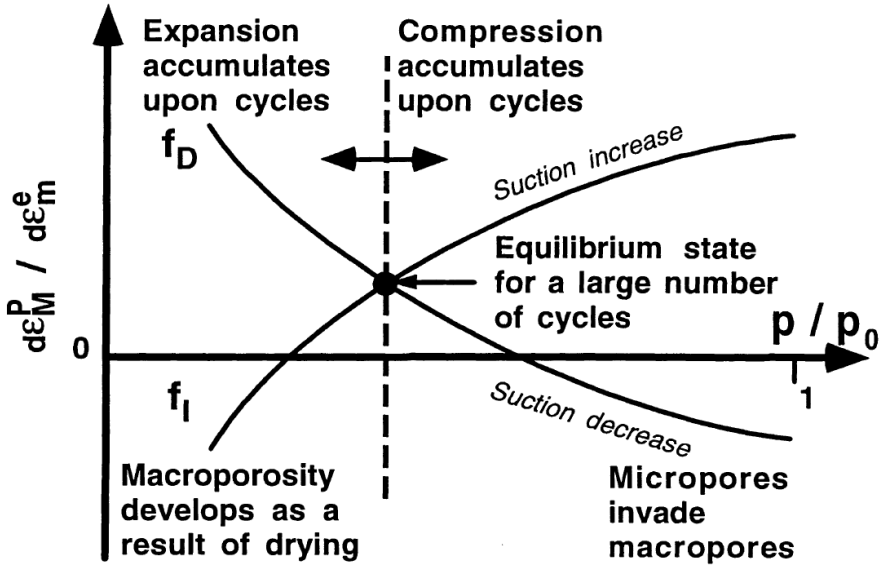

Figure 1.20: Coupling functions between microporosity and macroporosity deformations (Alonso et al., 1999).

By means of these coupling functions, residual strain under cyclic hydric loads, expansion or contraction, can be phenomenally explained: when $f_D > f_I$, humidification-desiccation cycle would result in a residual expansion as the absolute value of irreversible macroscopic strain during humidification is larger than that during desiccation. Analogically, a residual contraction may develop after a hydric cycle when $f_D < f_I$. The condition $f_D = f_I$ results in a hysteretic but stable suction-deformation loop. If $f_D = f_I = 0$ only reversible (micro) deformations will be generated under suction cycles. It should be noted that the coupling functions are not always positive as considered usually, and some additional mechanisms should be incorporated. For wetting case, a microstructural expansion could invade the macropores and leads to a reduction of macroporosity in soft highly active clays (Komine, 1994). In addition, there is some experimental evidence which may be interpreted in the sense that macroporosity develops during drying. For example, Shear et al. (1992) has reported an increase of the hydraulic conductivity when a clay is subjected to a desiccation.

Similar to the double structure concept, Likos et Lu (2006) proposed a bi-modal pore fabric model to investigate the bulk volume change due to the crystalline inter-layer swelling. In the context of crystalline swelling (without considering osmotic swelling), the changing of inter-layer spacing is indeed the motor of swelling, nevertheless, the macroscopic swelling is associated with not only crystalline swelling, but also a rearrangement of inter-particle space activated by the former. A parameter descrbing the fabric, the ratio between inter-layer void and inter-particle void is introduced to characterize the efficiency of the upscaling of crystalline swelling to macroscopic volume change: bulk volume change increases with this ratio for the same total void ratio. The residual bulk volume change is essentially related to the irreversible

alteration of inter-particle pores.

Finally, it is noted that water activity alone (chemical potential) is absolutely insufficient to determine the swelling magnitude of the clay minerals. It strongly depends on the hydric loading history (in particular the maximal subjected desiccation). Besides, the sharp and gentle humidifications lead to absolutely different swelling magnitudes (Tessier, 1984).

1.4 Fluid transport in porous solid

The humidification or desiccation process takes place when a porous medium is put in an environment of which the relative humidity is different from that inside the sample. They involve be means of different phenomena: transport of liquid and gas, as well as phase transition between the two formers (condensation, evaporation) (Fig.1.21).

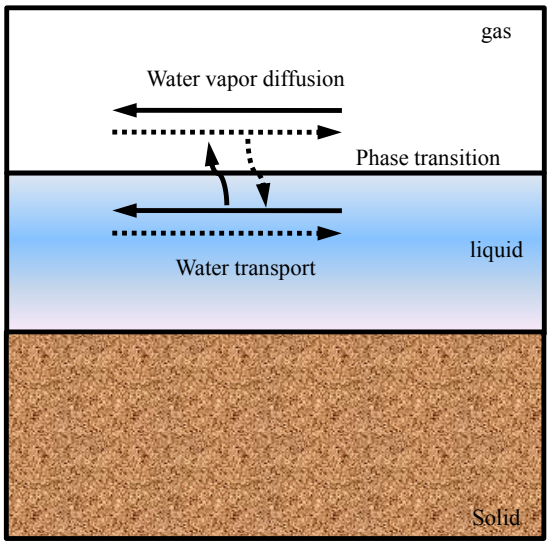

Figure 1.21: Schema of humidification (dashed lines) and desiccation (solid lines) processes in porous medium.

1.4.1 Liquid transport

The liquid transport in a porous medium obeys Darcy' law:

$$w_l = -\rho_l k_l \nabla P_l \tag{1.3}$$

with

$$k_l = \frac{K k_{rl}\left(S_l\right)}{\eta_l}$$

where k_l is water permeability. w_l ,P_l and ρ_l denote respectively water flux, water pressure and water density. Note that Darcy's law describes the liquid movement in saturated porous

medium, nevertheless, it is often extended to the unsaturated case. K is the intrinsic permeability of porous media independent of saturating phases and saturation, while relative permeability k_{rl} depends on degree of saturation. The parameter η_l denotes the viscosity of water.

1.4.2 Gas diffusion

Gas diffusion is a phenomenon related to the displacement of one constituent of the gas mixture from high concentration region to low concentration region. When the speeds of the constituents are different, the total pressure of the gas mixture would vary and advection takes place. Hence, gas diffusion involves in two different movements: the diffusion of each constituent through the gas mixture, and the global advection activated by the total pressure variation, due to the difference of diffusion speeds.

Considering the problem of humidification (desiccation), the gas can be described as a bi-phase mixture: water vapor and dry air. The bi-phase gas diffusion obeys Fick's law. Note that there are different expressions of this law depending on the choice of reference speed, among which the most used is molar concentration:

$$C_i = \frac{c_i}{c_g} \tag{1.4}$$

where c_i, c_g are molar per volume of constituent i and of the whole gas mixture. Then, Fick's law can be written as:

$$J_i^c = -D_i c_g \nabla C_i \tag{1.5}$$

where D_i is the diffusion coefficient, J_i^c is the diffusion speed of constituant i :

$$J_i^c = c_i \left(v_i - v_g^c\right) \tag{1.6}$$

where v_i, v_g^c are the absolute speed of constituent i and the reference speed of gas mixture defined by :

$$v_g^c = \sum_{i=1}^{n} C_i v_i \tag{1.7}$$

It can be proved that the diffusion coefficients of the constituents are identical. For a mixture composed of water vapor and dry air, de Vries and Kruger has proposed an expression of the diffusion coefficient, based on both kinetics theory and experimental results:

$$D_0 = \frac{D_{va}}{P_g} = 2.17 \times 10^{-5} \frac{P_{atm}}{P_g} \left(\frac{T}{T_0}\right)^{1.88} \tag{1.8}$$

where T is the temperature (K), and T_0 is some reference temperature. P_g is the total pressure of the gas mixture (Pa), and P_{atm} is the atmospheric pressure (101325 Pa).

It is assumed that the two constituents are ideal gas and are ideally mixed, so the total gas flux of each constituent i can be expressed as a function of pressure gradient:

$$w_i = -K_g \frac{P_i M_i}{RT} \nabla P_g - D \frac{P_{atm} M_i}{RT} f\left(S_l\right) \nabla \left(\frac{P_i}{P_g}\right) \tag{1.9}$$

The first term in right side describes the advection of the gas mixture, which is analogic to liquid transport. K_g represents the gas permeability of the porous medium. Regarding diffusion coefficient, certain modifications have to be considered for porous medium: reduction of pore space and tortuosity effect. These two effects are taken into account by one parameter, nominated as diffusion resistance $f(S_l)$.

1.4.3 Phase transition

Besides the movements of water vapor and water liquid, phase transition takes places, which can be described by thermodynamics.

Free enthalpy G is defined as:

$$G = H - TS \tag{1.10}$$

where H and S are enthalpy and entropy respectively.

The chemical potential of the constituent i is defined by the partial derivative of free enthalpy to its quantity (number of particle) n_i:

$$\mu_i = \left(\frac{\partial G}{\partial n_i}\right)_{T,P,n_j(j \neq i)} \tag{1.11}$$

The differential of free enthalpy is (Coussy, 2010):

$$dG = VdP - SdT + \mu_i dn_i \tag{1.12}$$

The vapor-water equilibrium requires the equality of the chemical potentials of the two phases:

$$\mu_v = \mu_l \tag{1.13}$$

For isothermal conditions, one obtains:

$$\frac{\partial P_v}{\rho_v} = \frac{\partial P_l}{\rho_l} \tag{1.14}$$

Assuming invariance of water density, the integral form of the above equation can be derived from the ideal gas law:

$$\rho_l \frac{RT}{M_v} lnh_r = P_l - P_{atm} \tag{1.15}$$

where h_r is the relative humidity, defined as the ratio between water pressure P_v and saturated water pressure P_{vs}:

$$h_r = \frac{P_v}{P_{vs}} \tag{1.16}$$

1.4.4 Capillary effect

Surface tension

The molecules of a condensate are subjected to cohesive forces from their neighbors. Creating an interface leads to removing one portion of these cohesion forces, and the cost energy is the surface energy Es. It is proportional to interface area A and a coefficient referred to surface tension γ (N/m). In other words, surface tension measures the work quantity required to create one unity of interface.

This surface tension due to cohesion force is the origin of capillary pressure which develops at the interface between two fluids (water and air for example), since the molecules are subjected to no equilibrated cohesive force. A water molecule in the water massif undergoes the same type of actions, while that on it is subjected to different actions on the interface: the action from water and the action from air.

Laplace 's law

When the interface between two fluids is curved, the surface tension needs to be equilibrated by a pressure difference between the two media (Fig.1.22). The equilibrium condition in the direction normal to the interface is written as:

$$(P_2 - P_1)\, R_1 d\theta_1 R_2 d\theta_2 = 2R_1 d\theta_1 \gamma \times \sin\frac{d\theta_2}{2} + 2R_2 d\theta_2 \gamma \times \sin\frac{d\theta_1}{2} \tag{1.17}$$

where R_1, R_2 are the radius of curvature in each of the axes that are parallel to the surface.

Then one obtain the famous Laplace law:

$$P_2 - P_1 = \gamma\left(\frac{1}{R_1} + \frac{1}{R_2}\right) \tag{1.18}$$

where P_1 is the pressure of the convex side and P_2 is the pressure of the concave side.

Contact angle

When three phases (liquid, air and solid) meet, three interfaces (water-air, water-solid, air-solid) are formed, as shown in Fig.1.23. The minimum surface energy condition requires the arrangement of the three interfaces, which can be described by contact angle. Contact angle is the angle that the tangent to the water-air interface makes with the solid surface. Considering the balance of the three surface tensions, one obtains Young's relation:

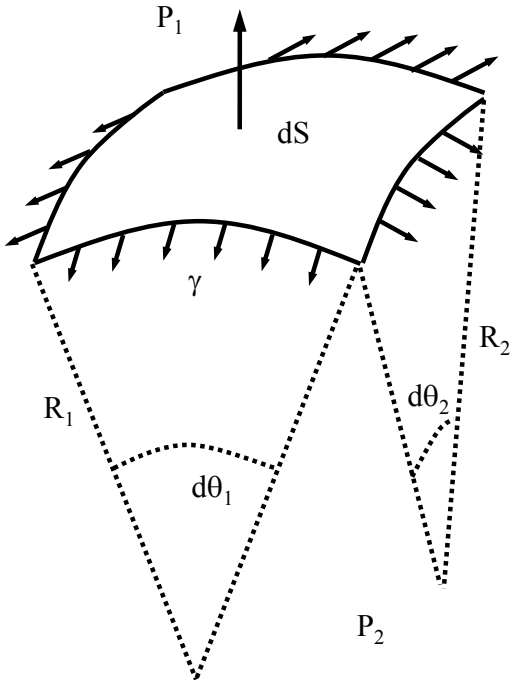

Figure 1.22: Schema of Laplace's law.

$$\cos\theta = \frac{\gamma_{AS} - \gamma_{LS}}{\gamma} \tag{1.19}$$

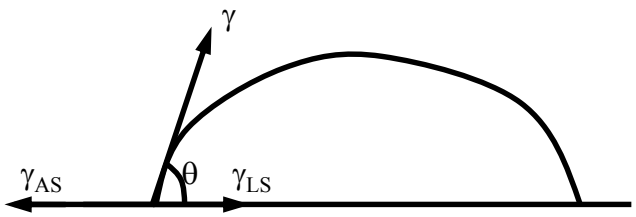

Figure 1.23: Schema of Young's law.

Capillary pressure

Capillary pressure is the difference in pressure across the interface between two immiscible fluids:

$$P_c = P_g - P_l \tag{1.20}$$

Combining the equations 1.15 and 1.20, one obtains:

$$\rho_l \frac{RT}{M_v} lnh_r = -P_c + P_g - P_{atm} \tag{1.21}$$

Substituting Laplace's law into equation 1.21, the famous Kelvin-Laplace's law is finally derived:

$$\rho_l \frac{RT}{M_v} ln h_r = \frac{2\gamma}{R} \tag{1.22}$$

Assuming hemispherical meniscus (for perfect wetting liquid so that contact angle θ is null) and indeformability of pore's wall, the maximal radius of the pore filled with water in function of RH can be estimated, shown in Fig.1.24.

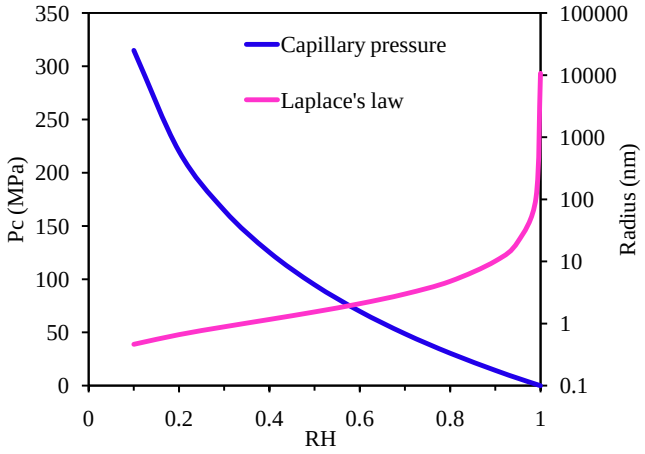

Figure 1.24: Maximal radius of the pore filled with water versus RH (from Kelvin-Laplace's law).

Capillary pressure is one inherent parameter describing like a "force" controlling the multi-fluids distribution (saturation) in the porous medium. From the viewpoint of thermodynamics, capillary pressure can be considered as a thermodynamic parameter comparable to hydraulic charge for the saturated case. Such pressure equals to the negative quantity of the work necessary for the transport of a unit volume of pure water from the outside of an unsaturated porous medium towards the inside.

The detailed determination of fluids distribution in the porous medium is extremely delicate, since it involves in complex phenomena: network of porous space, surface tension, contact angle, fluid viscosity etc. The isothermal sorption curve is commonly applied for characterizing the fluids distribution in the porous medium. A principal interest of this curve is that all these complex phenomena are integrated in it. The isothermal sorption for Callovo-Oxfordian argillaceous rocks is illustrated in Fig.1.25.

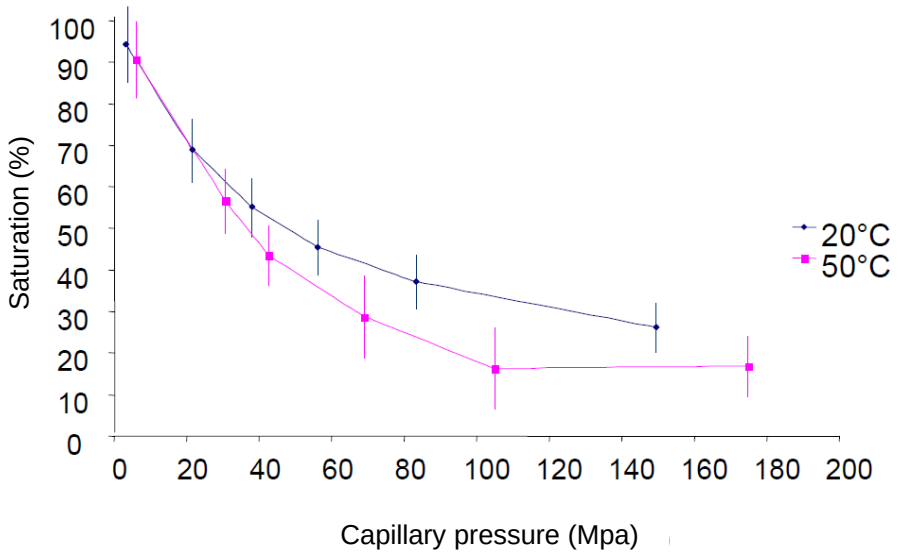

Figure 1.25: Isothermal sorption curve for Callovo-Oxfordian argillaceous rocks (ANDRA, 2005).

1.4.5 Isothermal humidification/desiccation process in weakly permeable porous medium

The isothermal humidification/desiccation process involves in the movements of three constituents: liquid water liquid (l), dry air (a), and water vapor (v). In the following part, the isothermal desiccation case is considered. Note that isothermal humidification is just the inverse process of desiccation in most of the existing models.

The mass conservation of these constituents can be written as:

$$\frac{\partial m_l}{\partial t} = -\nabla \cdot w_l - \dot{m}_{l\to g}^{H_2o} \tag{1.23a}$$

$$\frac{\partial m_v}{\partial t} = -\nabla \cdot w_v + \dot{m}_{l\to g}^{H_2o} \tag{1.23b}$$

$$\frac{\partial m_a}{\partial t} = -\nabla \cdot w_a \tag{1.23c}$$

where m_i and w_i are mass per unit volume and flux of the constituent i. $\dot{m}_{l\to g}^{H_2o}$ is the mass rate of phase transition from water liquid to vapor. The terms m_i can be expressed by porosity (ϕ) and liquid saturation (S_l):

$$m_l = \phi S_l \rho_l \tag{1.24a}$$

$$m_v = \phi \left(1 - S_l\right) \rho_v \tag{1.24b}$$

$$m_a = \phi \left(1 - S_l\right) \rho_a \tag{1.24c}$$

The fluxes of these constituents can be calculated by Darcy's law and Fick's law:

$$w_v = -\frac{K}{\eta_g} k_{rg}(S_l) \frac{P_v M_v}{RT} \nabla P_g - D_0 \frac{P_{atm} M_v}{RT} f\left(S_l\right) \nabla \left(\frac{P_v}{P_g}\right) \tag{1.25a}$$

$$w_a = -\frac{K}{\eta_g} k_{rg}(S_l) \frac{P_v M_a}{RT} \nabla P_g - D_0 \frac{P_{atm} M_a}{RT} f\left(S_l\right) \nabla \left(\frac{P_a}{P_g}\right) \tag{1.25b}$$

$$w_l = -\rho_l \frac{K}{\eta_l} k_{rl}(S_l) \nabla P_l \tag{1.25c}$$

1.4.5.1 The role of gas advection and Peclet number

As discussed above, Fick's law consists of two terms: 1) global advection of gas mixture, 2) diffusion of each constituent. The relative importance of each transport mode can be analyzed by a dimensionless quantity (Peclet number), defined as the ratio between the advection flux and the diffusion one. A small Peclet number indicates the gas movement is predominated by the diffusion term, while the advection is dominant for a large Peclet number.

$$P_e^v = \frac{p_v}{p_a} P_e^a \tag{1.26}$$

For 20°C conditions, the ratio between water vapor pressure and dry air pressure is small, implying a big Peclet number for dry air and a low number for water vapor. The Peclet number for dry air is indeterminable a priori. Coussy (2004) suggested one quantity easily determinable to investigate the condition where the advection term is negligible:

$$\frac{K}{\eta_g} \times \frac{P_g}{\tau D_0} \ll 1 \tag{1.27}$$

Letting $\eta_g = 1.8 \times 10^{-15}$ kg/(m/s), $P_g \leq 10^6$ Pa, $\tau D_0 \sim 10^{-8}$ m^2/s, one threshold of intrinsic permeability is derived:

$$K \ll 10^{-19} m^2 \tag{1.28}$$

For weakly permeable material which satisfies the above condition (for example Callovo-Oxfordian argillaceous rocks), the advection of the gas mixture can be neglected and the flux equations are rewritten as:

$$w_v = -D_0 \frac{P_{atm} M_v}{RT} f\left(S_l\right) \nabla \left(\frac{P_v}{P_g}\right) \tag{1.29a}$$

$$w_a = -D_0 \frac{P_{atm} M_a}{RT} f\left(S_l\right) \nabla \left(\frac{P_a}{P_g}\right) \tag{1.29b}$$

Moreover, the capillary pressure quickly reaches large value that is much larger than atmosphere pressure for weakly permeable material. Hence, one obtains:

$$dP_c \approx -dP_l \tag{1.30}$$

Combining the equations 1.23,1.24 and 1.29, the governing equation for the humidification/desiccation process is:

$$\phi\frac{\partial S_l}{\partial t}+\phi\frac{M_v}{\rho_l RT}\frac{\partial\left[\left(1-S_l\right)P_v\right]}{\partial t}-\frac{P_{atm}M_a}{\rho_l RT}D_0\nabla\cdot\left[f\left(S_l\right)\nabla\left(\frac{P_v}{P_g}\right)\right]-\nabla\cdot\left[D_l\left(S_l\right)\nabla S_l\right]=0 \tag{1.31a}$$

$$\phi\frac{\partial\left[\left(1-S_l\right)\left(P_g-P_v\right)\right]}{\partial t}+P_{atm}D_0\nabla\cdot\left[f\left(S_l\right)\nabla\left(\frac{P_v}{P_g}\right)\right]=0 \tag{1.31b}$$

Equation 1.31a describes the moisture transport, not only in liquid form but also in gas form. Equation 1.31b describes the transport of dry air. Moreover, the thermodynamic liquid-vapor equilibrium is given by equation 1.21.

1.4.5.2 The role of water vapor diffusion and bi-step desiccation process

The Darcean transports of water liquid and gas mixture are related to the same intrinsic permeability, however, water liquid is more viscous than gas. One can prove that the transport speed of liquid water liquid is much smaller than the diffusion speed of water vapor (or dry air) for weakly permeable material. Hence, the condition (equation 1.28) also leads to a bi-step isothermal desiccation process: 1) the first step, the water vapor tends to be uniform within the sample by diffusion effect; 2) the second step, the gas diffusion terminates and the desiccation process is predominated by the transport of water liquid towards outside.

In addition, Coussy (2004) has proved that the contribution of gas diffusion for drying the weakly permeable material is extremely samll. Considering one desiccation case ($S_0 = 0.892975$ to $S_1 = 0.4243$), the simulation carried out by him revealed the saturation at the end of the first desiccation step merely descends to 0.892915.

1.4.5.3 Simplified model for weakly permeable material

According to the above discussions, the desiccation process in the weakly permeable material is predominately attributable to the transport of moisture in its liquid form. Neglecting the effect of gas phase and the evaporation inside the sample, one simplified model can be derived (Mainguy et al., 2001):

$$\phi\frac{\partial S_l}{\partial t}+\nabla\cdot\left(D_l\nabla S_l\right)=0 \tag{1.32}$$

with,

$$D_l=P_c'\left(S_l\right)K_l=P_c'\left(S_l\right)\frac{Kk_{rl}\left(S_l\right)}{\eta_l}$$

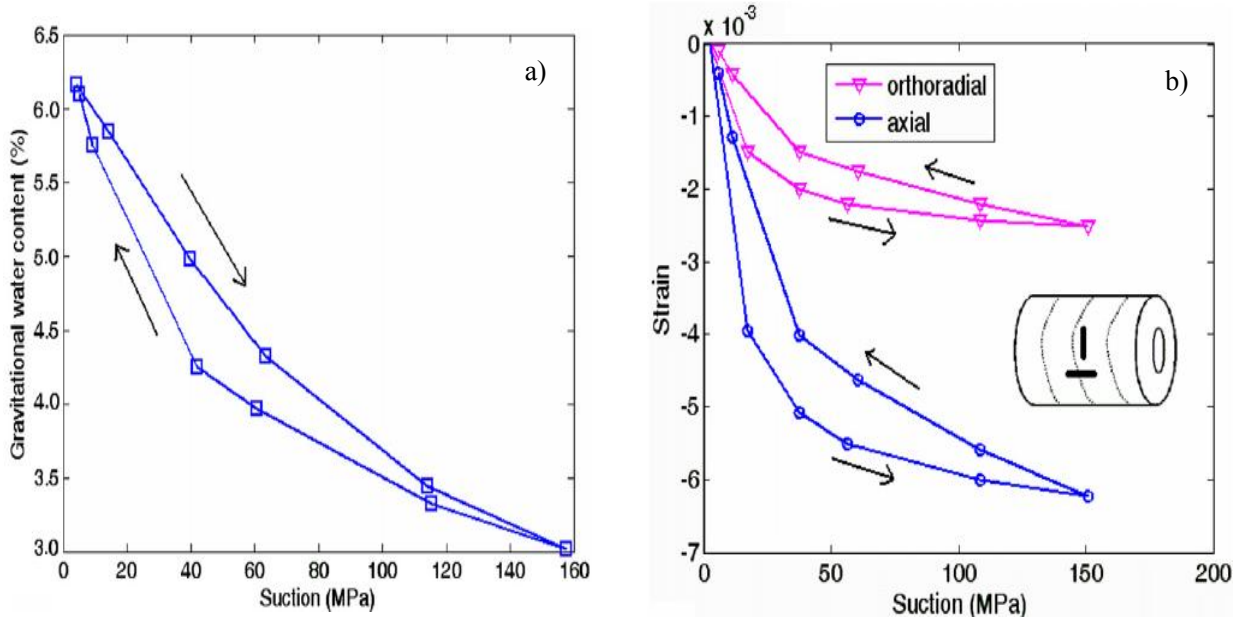

Figure 1.26: Water retention curve (a) and strain evolution (b) during humidification-desiccation (Pham et al., 2007).

1.5 Hydromechanical behaviors and motivation of this work

1.5.1 Experimental investigation

1.5.1.1 Behavior under humidification/desiccation

The behavior of argillaceous rocks under humidification/desiccation has been investigated by numerous researchers, mostly at the macro-scale (Pham, 2006; Valès et al., 2004). However, the recent application of DIC techniques on such rocks, typically using optical microscopy, yields the possibility of a study at micro-scale (Valès, 2008). In addition, humidification/desiccation tests under certain mechanical load is also performed by Yang et al. (2012).

Swelling/shrinking under humidification/desiccation

A typical result of humidification/desiccation is shown in Fig.B.1. For the water retention curve, a hysteresis is normally observed: the free water content during desiccation is generally more important than that during humidification. Such hysteresis is one typical characteristic of a porous solid containing various sizes of pores with capillary condensation, and its mechanisms have been well recognized: neck effect and different interface geometries for condensation and evaporation (Donohue et al., 1998; Hassanizadeh and Gray, 1993). Moreover, this hysteresis is also related to the inherent swelling hysteresis of clay minerals, in particular the hysteresis of crystalline swelling (Laird et al., 1995; Likos et Lu, 2006).

Concerning the deformation due to humidification/desiccation, three main features for such rocks can generally be summarized: nonlinearity, anisotropy and hysteresis.

- During humidification, the swelling of argillaceous rocks is firstly moderate at low RH (high suction) while it becomes more significant at high RH (low suction). This phenomenon, which is likely to related to a change of deformation mechanism, has been observed in several macroscopic studies (Pham et al., 2007; Valès et al., 2004). In addition, such nonlinearity still exit when strain is plotted versus suction (Fig.1.27b). This means that it can't be described by the standard linear poroelasticity. Valès (2008) has demonstrated that the dependence of strain with normalized water content is nonlinear as well (Fig.1.27c). Based on this observation, he attributed this nonlinearity to the microcracking due to humidification, and some meso-cracks have indeed been observed (Fig.1.28). Although this phenomenon has been evidenced by numerous experimental results, the real mechanisms of this nonlinearity are not yet well recognized.

- Besides the nonlinearity, the deformation under hydric loading exhibits anisotropy: it is more significant along the direction perpendicular to the bedding plane than along the direction parallel to it. Such anisotropy is believed to be related to clay particles. In fact, the clay particle shows an anisotropic swelling (it is predominant along the direction normal to its orientation), and there is a preferred orientation (sub-parallel to the bedding plane) of the clay particle in Callovo-Oxfordian argillaceous rocks due to sedimentation. In addition, Robinet (2008) has revealed a moderate texture anisotropy of the inclusions in such rocks, which can also be contributable to the anisotropic swelling. However, all these interpretations require experimental demonstration and furthermore quantitative studies (for example, the relative contribution of these sources of anisotropy).

- The experimental data at macro-scale showed that the deformation of argillaceous rocks is fairly reversible under a humidification/desiccation cycle in the absence of external stress, nevertheless, a hysteresis is manifested: the desiccation leads to a contraction while additional expansion develops for the same relative humidity during the humidification stage. It is noted that such hysteresis is opposite to the hysteresis manifested in the water retention curve, so it can't be explained by the latter. The interpretation of this inconsistency is still a waited for.

It should be emphasized some recent advances on the observation at micro-scale, principally based on the combination of optical microscopy and DIC techniques (Valès, 2008; Yang et al., 2011, 2012). By means of these microscopic observations, some local phenomena during humidification/desiccation can be investigated. For example, some local hydric deformations, related to some pre-existing cracks and big carbonate grains, has been evidenced. In addition,

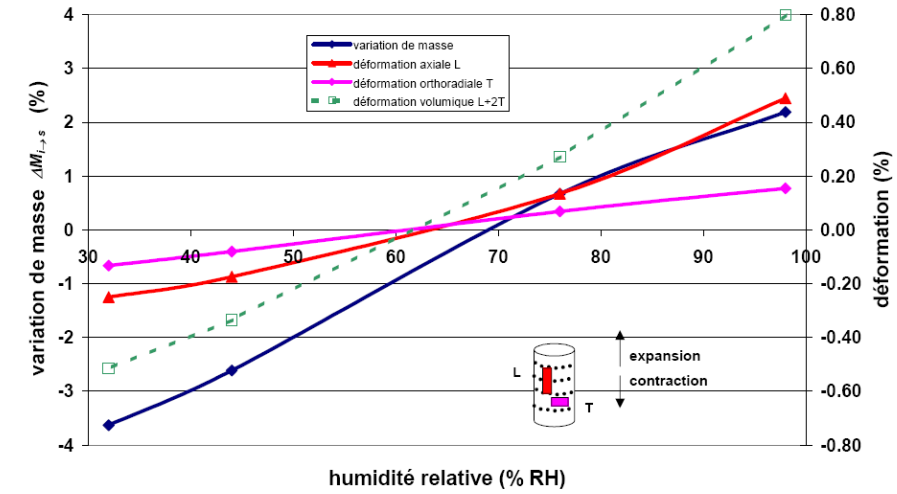

(a) variations de masse et déformation en fonction de l'humidité relative.

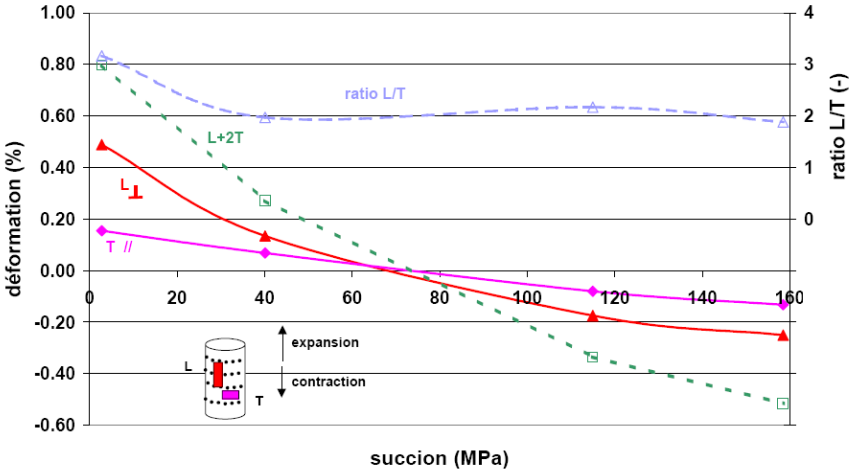

(b) déformation en fonction de la succion.

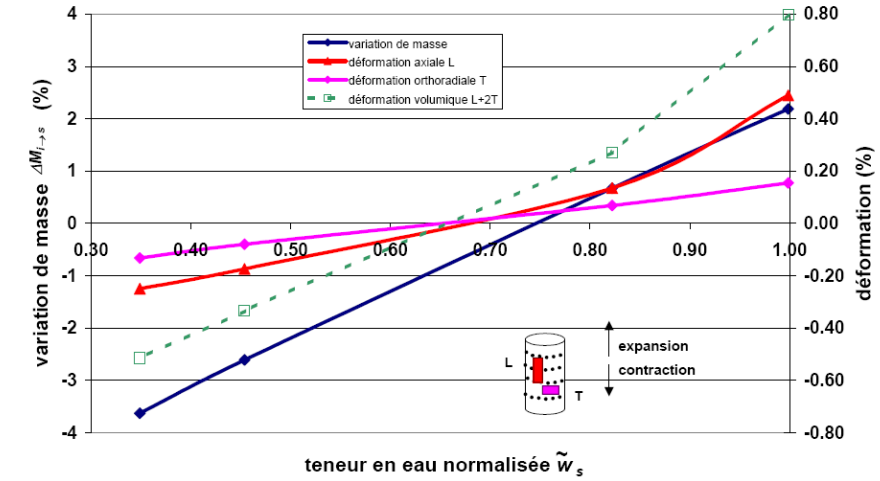

Figure 1.27: Evolution of water mass and strain when RH changes (Valès, 2008).

some meso-cracks due to humidification, with the length at the order of dozens of micrometers, have also been observed.

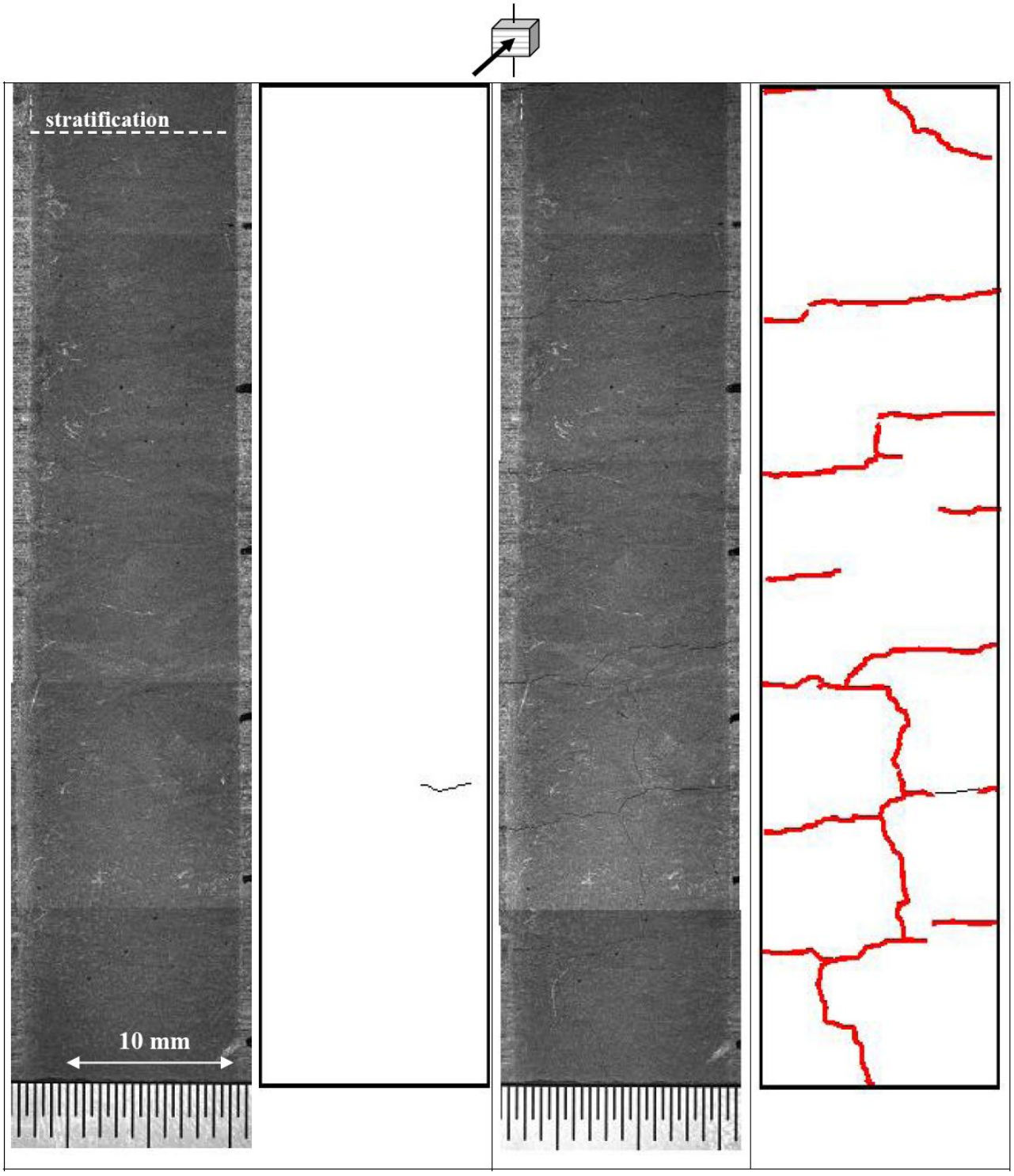

Figure 1.28: Cracks developped due to humidification (Valès, 2008).

Besides the free humidification/desiccation tests, Yang et al. (2012) conducted humidification/desiccation tests under some mechanical loads (uniaxial compression at 0.3, 2, and 8.5 MPa). A linear relation between the strain and RH is found when the later is less than 75%. It is reversible during hydration and dehydration at low stresses (0.3 MPa, 2 MPa) and is irreversible at 8.5 MPa (shown in Fig.1.29). The high applied axial stress limits the swelling of the material during rehydration but has much less effect on shrinkage. This observed behavior does not have a simple interpretation and is probably the signature of complex nonlinear hydromechanical couplings.

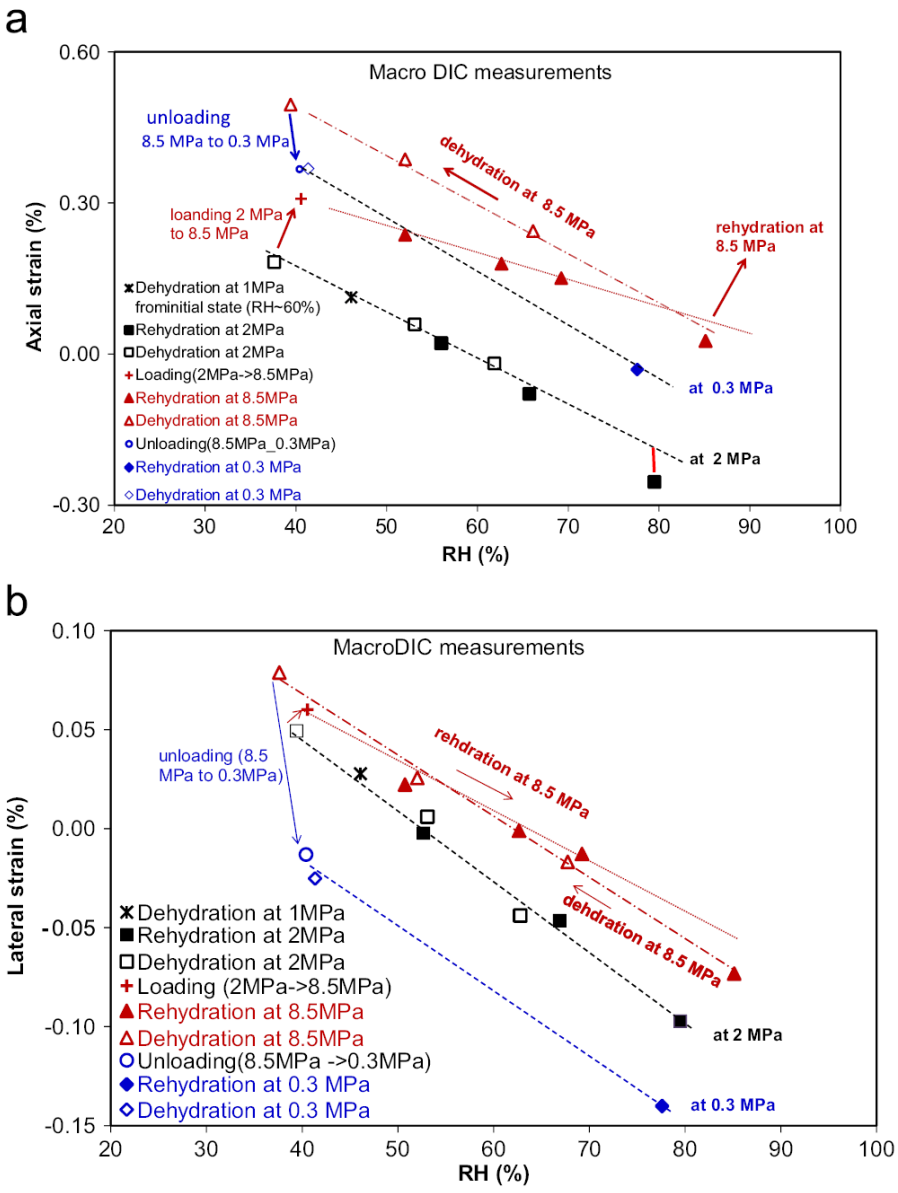

Figure 1.29: (a) axial strain,(b)lateral strain, versus relative humidity at each moisture equilibrium state during three cycles of rehydration and dehydration at the different applied uniaxial stress (2 MPa,8.5 MPa,0.3 MPa) (Yang et al., 2012).

It should be noted that the exiting observation at micro-scale is still too big for argillaceous rocks. For the observation mentioned above, the size of the observation zone can't be smaller than 1.5×1.5 mm^2 (with a physic length represented by a pixel being 0.75 mum). Such a resolution is still too great to distinguish the composite microstructure of the investigated material. An improvement of the observation resolution, relevant to the scale of the microstructure of such rocks, is always a waited for.

Damage phenomena due to humidification/desiccation

Under humidification/desiccation, some damage phenomena have been observed. Some meso-cracks developed at high RH, with the length at the order of dozens of micrometers (Fig.1.28), have been evidenced by (Valès, 2008; Yang et al., 2012). Montes-H et al. (2004) showed some damage phenomena during hydric cycles by means of environmental electron scanning microscopy: microcracking, aggregation/deaggregation, opening/closing of certain pores and cracks. In addition, the extension of these cracks is principally parallel to the stratification. Despite these observations, the physical origins of these crackings under hydric load are still uncertain.

The desiccation of argillaceous rocks could lead to a cracking. In fact, this can belong to the ubiquitous phenomenon of shrinkage cracking, commonly observed on paints, cement-based materials (Bazant and Raftshol, 1982), mud (Weinberger, 1999) and soils (Peron et al., 2009). This phenomenon principally depends on the type of restraint against shrinkage and the dimension of the shrinking specimen. The shrinkage cracking is essentially due to tensile stress caused by various restraints which can be generally classified into two types: external restraint (such as restraining substrate) and internal restraint (essentially the non-uniform shrinkage of the specimen) (Bisschop and van Mier, 2002).

Contraction gradient induced microcracking has been intensively studied in the last few years (Augier, 2002; Goltermann, 1995; Jenkins, 2009), and the main features of such type of microcracking are summarized here: 1) The moisture/contraction gradient, which is the motor of microcracking, is actually related to specimen's thickness and desiccation rate, therefore it exists a critical specimen's thickness and a critical desiccation rate below which contraction gradient is too small to generate significant tensile stress causing microcracking. 2) In view of desiccation surface, the network of microcracks forms generally polygonal patterns: they typically intersect at right angles forming T- junctions. The explanation of such pattern is well recognized: tension microcrack propagates in the direction perpendicular to local maximum tensile stress and the first microcrack releases the normal stress in its vicinity and so the second tends to approach the first orthogonally (Weinberger, 1999). 3) Concerning the propagation of microcracking due to desiccation, the half-plane model predicts a crack spacing and depth doubling process for unconfined specimen (Jagla, 2002; Jenkins, 2005). At the beginning, a range of parallel cracks with a specific spacing is nucleated on the drying surface and then

propagates equally. Until the depth of these microcracks reaches a threshold where the stress field of adjacent cracks begins to strongly interact, every two crack continues to propagate as the middle one becomes shielded by their neighbors. This process can be repeated several times depending on specimen's thickness. Besides, warping (global curving of specimen in the case of one-side desiccation, as our case) may reduce the contraction gradient induced stress and so can impede the microcracking (Bisschop, 2011).

1.5.1.2 Behavior under mechanical load

Stress-strain curve

The behavior of Callovo-Oxfordian argillaceous rocks under mechanical is normally investigated by two types of tests: 1) uniaxial compression tests, 2) triaxial compression tests. Concerning triaxial compression tests, the range of confining pressure is from 0 to 20 MPa, which correspond to the estimation of in situ stresses (Chiarelli et al., 2003). An example of these results in shown in Fig.1.30.

Several characteristics can be summarized:

- The stress-strain relationship is linear when the deviator stress remains below 40 - 50% of the compressive resistance. However, this linearity doesn't imply at all a linear elasticity: unloading reveals that irreversible strain in both two directions already emerges at this region (at small stress limit), indicating an extremely small elastic limit. This co-existence of linearity and irreversibility has been explained by a slip between mineral grains with elastic deformation (Aublive-Conil, 2003). However, its real mechanisms are still unknown. Note that such beginning linear part corresponds to the specimens without pre-existing cracks. If there are some cracks pre-existing at initial state, there closing would manifest a nonlinear part at the beginning, as observed for a lot of rocks.

- When stress exceeds certain value (linear limit), the stress-strain curve becomes nonlinear, accompanied by more significant irreversible strain and a deterioration of elastic modulus (in particular the lateral ones) (Chiarelli et al., 2003).

- The rupture of such rocks manifests rather fragile and localized for small confining pressure, while it is ductile for big confinement. Zhang et al. (2004) has given the peak strength as a function of confining pressure for the Callovo-Oxfordian argillite, shown in Fig.1.31.

- After the rupture (the post-peak region), a residual strength exists for argillaceous rocks. Such residual strength also depends on the confinement: it increase from 0 to 30 MPa when the confining stress varies from 0 to 20 MPa (Zhang et al., 2004).

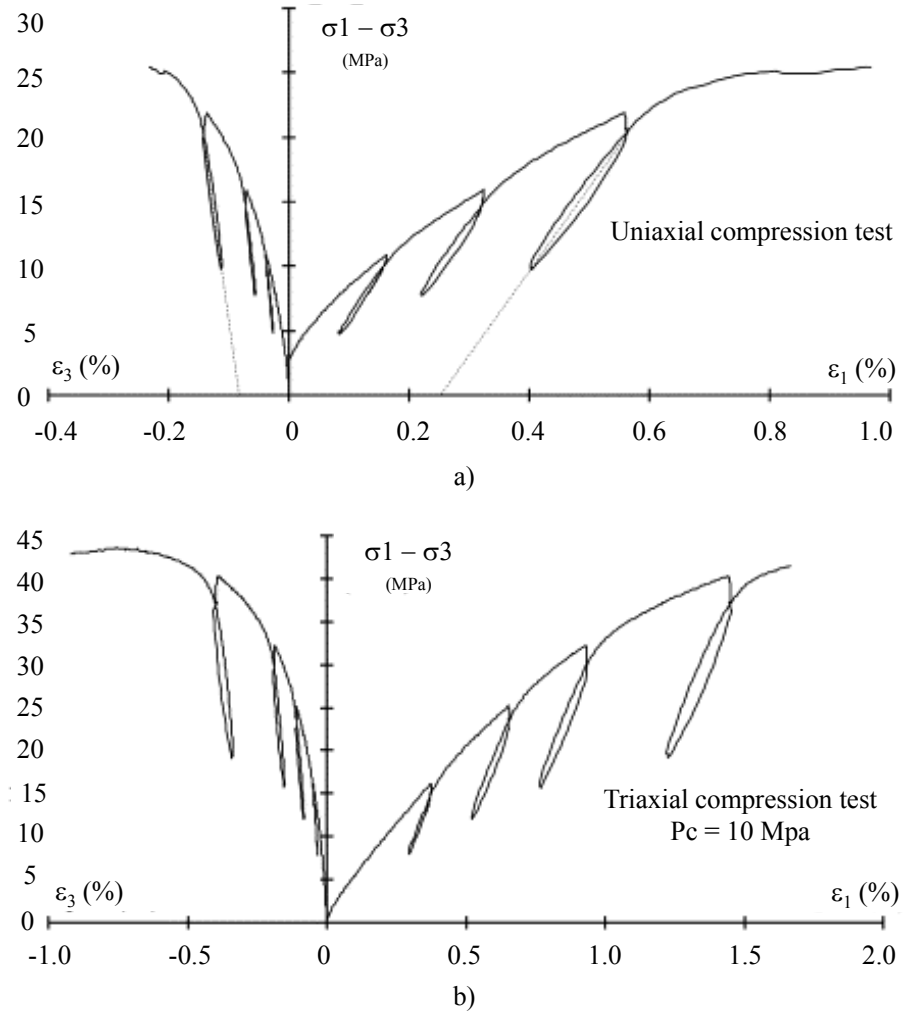

Figure 1.30: Typical stress-strain curves for a) uniaxial compression test, b) triaxial compression test with a confining pressure of 10 MPa (Chiarelli et al., 2003).

- The behavior of Callovo-Oxfordian argillaceous rocks can be considered to be quasi-isotropic from most of the results (ANDRA, 2005). However, Zhang et al. (2004) has shown that the stiffness in the direction parallel to the bedding plane is up to 1.5 times larger than that perpendicular to the bedding.

Effect of water content(humidity state)

The water content (humidity state) has a significant influence on the mechanical behavior of argillaceous rocks (Bornert et al., 2010; Erguler et al., 2009). One example is shown in Fig.1.32. In general, when the water content increases, the material become more deformable and the strength stress decreases.

The effect of humidity state on the elastic stiffness has been investigated by numerous researchers (Cariou, 2010; Chiarelli et al., 2003; Ibrahim, 2008; Pham et al., 2007; Yang et al., 2012). In general, the Young's modulus decreases with RH (or water content) in both

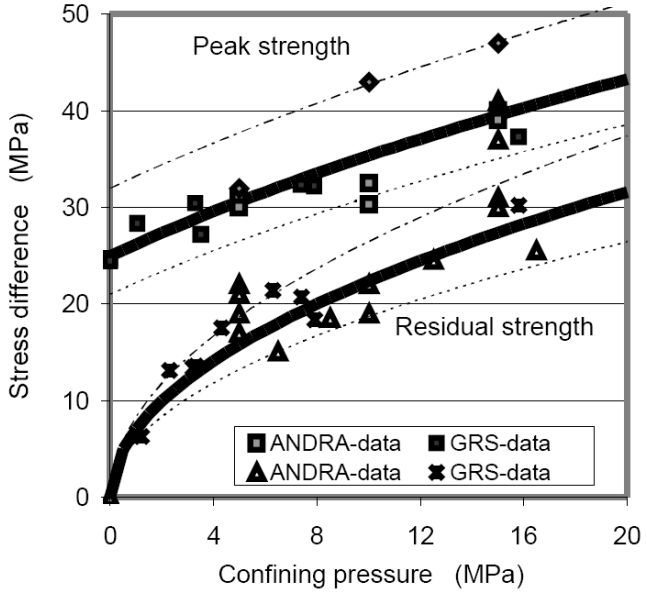

Figure 1.31: Peak and residual strength of the Callovo-Oxfordian argillite (Zhang et al., 2004).

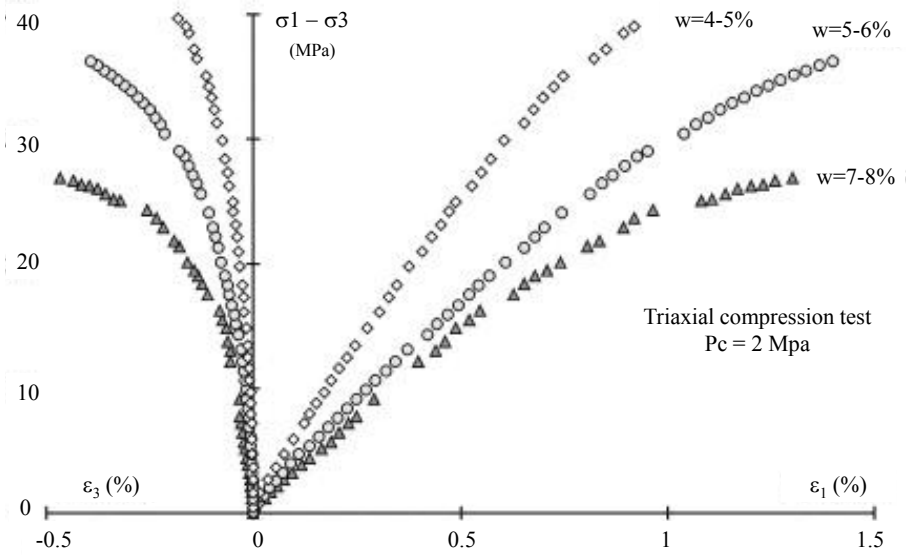

Figure 1.32: Stress-strain curves for three samples with different moisture contents (confining pressure of 2 MPa) (Chiarelli et al., 2003).

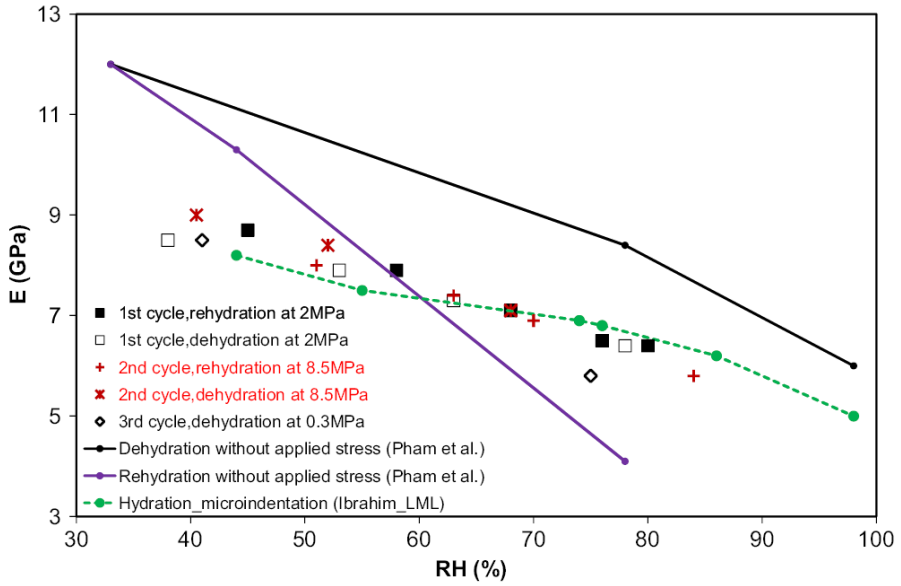

Figure 1.33: Young's modulus versus relative humidity (Yang et al., 2012).

the directions (perpendicular and parallel to the bedding plane). Yang et al. (2012) showed that this relationship of axial Young's modulus (normal to the bedding plane) is rather linear (Fig.1.33). However, Cariou et al. (2012) observed that the Young's modulus in both directions don't depend on water content when the latter is greater than 1.56%. There is no evidence that the Poisson's ratio depends on water content (Fig.1.34). Concerning the effect of water content on rupture, Zhang et al. (2004) revealed that the compressive strength and the failure strain of the air-dried specimens are about two times higher than those of the saturated ones.

All the existing experimental results demonstrate a strong effect of water content on the mechanical behavior. Nevertheless, a convincing, generally received explanation of this dependence hasn't been attained. For example, concerning the softer response of wet samples, Cariou et al. (2012) explained by the solid phase having interactions with the fluid in the porous network and becoming softer when the porous network is filled by water from being fully dried. However, Bornert et al. (2010) suggested that this is essentially governed by the presence and the motion of cracks induced by the preliminary swelling, and the intrinsic behavior of the sound rock being almost unchanged with respect to dry materials (Fig.1.35). These arguments imply that the real mechanisms are still uncertain.

Effect of mineralogy and microstructure

The mechanical behavior of argillaceous rocks depends on mineralogy. When calcite content increases, Young's module increases accordingly, however, Poisson's coefficient is nearly constant. For plastic deformation, it is found that plastic strains decrease when calcite content increases, but become more important when quartz or clay content increases. Consequently, it seems that the behavior is more brittle when calcite content increases, and inversely becomes

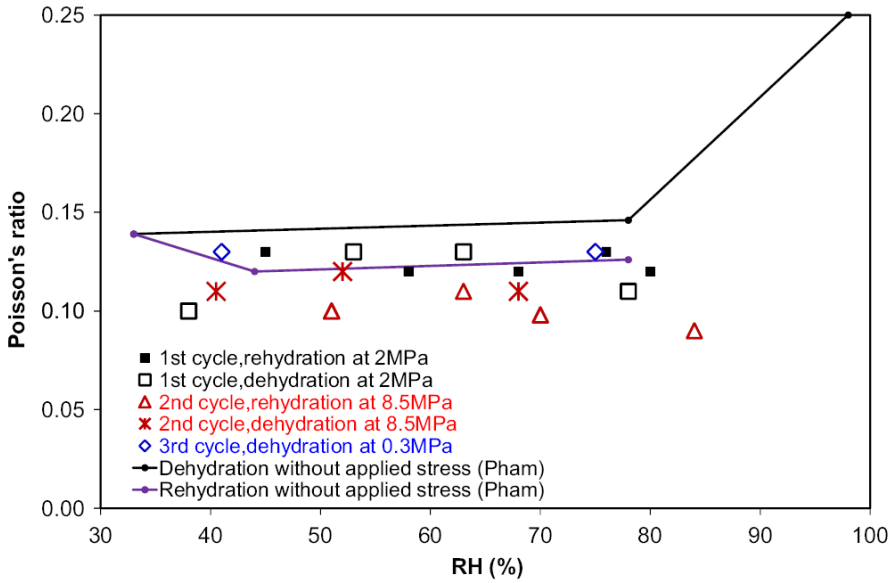

Figure 1.34: Poisson's ratio versus relative humidity (Yang et al., 2012).

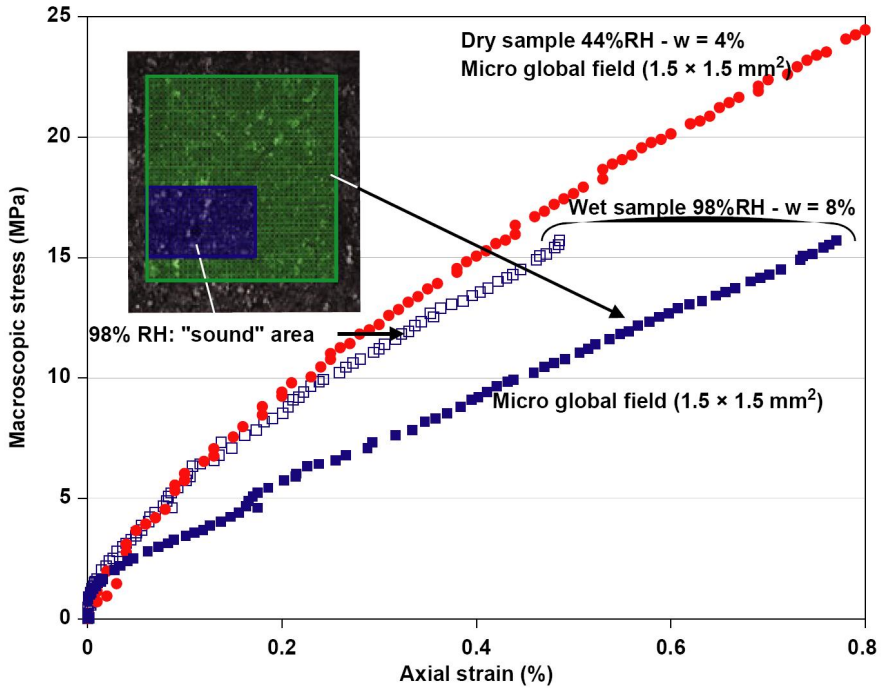

Figure 1.35: Comparison between 44% RH (left) and 98% RH (right) samples (Bornert et al., 2010).

more ductile when clay content increases (Chiarelli et al., 2003).

In fact, this depending on mineralogy is essentially related to the composite microstructure (clay matrix with grains of carbonate and quartz) and the contrasting behaviors of these constituents. A summary of the physical, hydric and mechanical behaviors properties of these components are presented in Tab.1.2.

Table 1.2: Some physical and mechanical properties of main phases in argillaceous rocks (Valès, 2008).

Phase	**Mass density** (kg/m^3)	**Young's modulus** (GPa)	**Poisson's ratio**	**Thermal conductivity** (W/m/°C at 20°C)	**Specific heat** (J/kg/°C at 20°C)
Clay minerals	2000 - 2400	4 - 20	0.2 - 0.4	2.0 - 3.5	800
Quartz	2650	96	0.08	6.8 - 12	712
Calcite	2710	84	0.27	4.6 - 5.5	808

Inside argillaceous rocks, clay minerals would swell significantly under humidification, due to their specific physic-chemical properties. Nevertheless, other mineral inclusions (mostly carbonate and quartz) are insensitive to water. Besides, the swelling properties for the different groups of clay minerals are also variable, as discussed in section 1.2. The elastic modulus of quartz and carbonate are in order of 100 GPa, whereas the elastic modulus of clay matrix is an order of magnitude smaller than the former. Therefore, clay matrix plays a predominant role for both hydric and mechanical behaviors of argillaceous rocks.

Clay particle is composted of dozens or hundreds of elementary layers. Such plate-like microstructure yields its anisotropic properties. As discussed in section 1.3, clay particle tends to swell much more significantly in the direction normal to its orientation that in the direction parallel to it. The mechanical behavior of clay particle is usually described by a transverse isotropy (Sayers, 1994), defined by five independent components. The transverse isotropic stiffness tensor for clay particle is:

$$\begin{pmatrix} C_{11} & C_{12} & C_{13} & & & \\ C_{12} & C_{11} & C_{13} & & & \\ C_{13} & C_{13} & C_{33} & & & \\ & & & C_{44} & & \\ & & & & C_{44} & \\ & & & & & C_{66} \end{pmatrix} \tag{1.33}$$

Note that plane $[\underline{e}_1, \underline{e}_2]$ is bedding plane, and $\underline{e}_3$ is the direction normal to the bedding plane (symmetry axis). One example based on nanoindentation results (Ortega et al., 2007) can be found in Tab.1.3.

Besides mineralogy, the porosity (or clay packing density η) is a crucial parameter effecting both hydric and mechanical behaviors of such rocks. The nanoindentation results (Bobko and Ulm, 2008) have revealed the nanogranular nature of shale (Bobko and Ulm, 2008; Ulm and Abousleiman, 2006): 1) A mechanical percolation threshold (roughly $\eta_0 = 0.5$) exists for shale

Table 1.3: Transverse isotropic stiffness properties of clay particle (Ortega et al., 2007).

Elastic constant	C_{11}	C_{12}	C_{13}	C_{33}	C_{44}	C_{66}
(GPa)	44.9	21.7	18.1	24.2	3.7	11.6
Elastic constant	E_1	E_3	ν_{12}	ν_{13}	G_{13}	G_{12}
(GPa)	39.3	14.4	0.69	0.27	3.7	11.6

below which the material has no appreciable stiffness (nor strength). 2) Beyond this percolation threshold, the elastic and anisotropy scale linearly with clay packing density (as shown in Fig.1.36). Moreover, such nanogranular behavior of shale has some important consequences on their poromechanical properties, which will be discussed in the following.

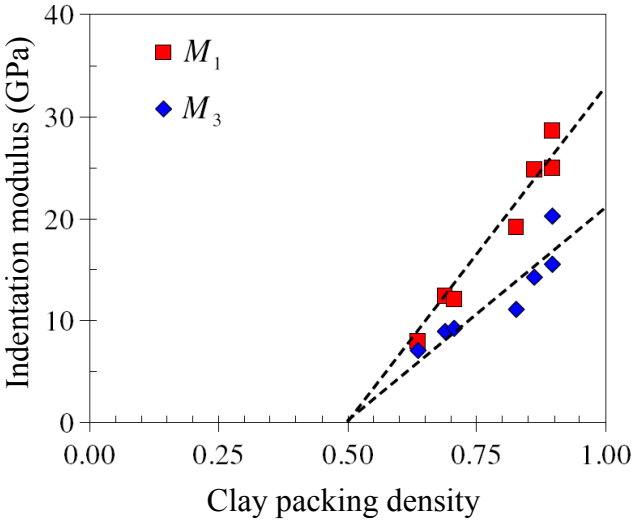

Figure 1.36: Influence of clay density packing density on elastic modulus of shale from nanoindentation tests (Bobko and Ulm, 2008).

1.5.1.3 Hydromechanical behavior and poromechanics

Poroelasticity

Argillaceous rocks are indeed a porous solid, of which the behavior is affected by the presence of fluids and the pore pressure evolution. Poromechanics is developed to describe the hydromechanical behavior of such materials (Coussy, 2010; Dormieux et al., 2006). For a saturated elastic porous solid, the constitutive equation is written as:

$$\underline{\underline{\sigma}} = \underline{\underline{\underline{\underline{C}}}} : \underline{\underline{\varepsilon}} - \underline{\underline{B}} P_l \tag{1.34a}$$

$$\varphi - \varphi_0 = \underline{\underline{B}} : \underline{\underline{\varepsilon}} + \frac{P_l}{M} \tag{1.34b}$$

where $\underline{\underline{\sigma}}$ and $\underline{\underline{\varepsilon}}$ are respectively the stress and strain tensors. P_l is the interstitial pore fluid pressure. C is the elastic stiffness tensor, and M is Biot's modulus. $\underline{\underline{B}}$ the Biot's tensor and is equal to $b\underline{\underline{I}}$ in the case of isotropy, where b is so-called Biot's coefficient.

For unsaturated case, Bishop (1959) has generalized the above equation by replacing fluid pressure by the average of air P_g and water pressures weighted by the saturation degree S_l:

$$\underline{\underline{\sigma}} = \underline{\underline{\underline{\underline{C}}}} : \underline{\underline{\varepsilon}} - \underline{\underline{B}} \left(S_l P_l + (1 - S_l) P_g \right) \tag{1.35}$$

Biot's coefficient

The Biot's coefficient is a key parameter in poromechanics. It quantifies the compressibility of the skeleton of the porous solid with respect to its solid phase. In drained condition (without variation of the pore pressure), it indicates the contribution of the variation of porous spaces on the total strain (see the second formula in equation). In general, one has an expression for isotropic case:

$$\varphi_0 \leq b = 1 - \frac{K}{k_s} \leq 1 \tag{1.36}$$

where K is the drained bulk modulus of the porous material, and k_s is the bulk modulus of the solid phase.

The lower bound of b is the porosity of porous solid, corresponding to the Voight-bound. The upper bound (as Terzaghi's soil mechanics) corresponds to the case of imcompressible solid phase, indicating the total deformation of the porous material is totally attributable to the changing of its porous space. It should be noted that Biot's coefficient is also a function of porosity, and one theoretical prediction is shown in Fig.1.37. It is always equal to 1 below the solid percolation threshold (due to nanogranular nature of such material), and would decreases when the packing density increases (porosity decreases).

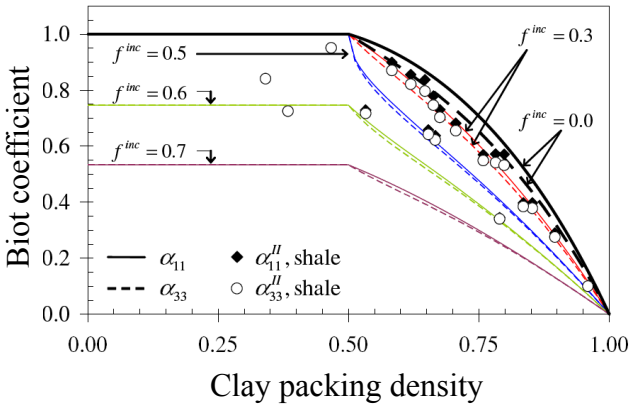

Figure 1.37: Model predictions of Biot's coefficient as a funciton of clay packing density (Ortega et al., 2007).

Poroelastic parameters for Callovo-Oxfordian argillaceous rocks

Numerous studies have been conducted to identify the poroelastic parameters by different methods (Bemer et al., 2004; Cariou et al., 2012), however, the results are usually so variable and are difficult to be explained. Cariou et al. (2012) carried out a triaxial "change in pore pressure" poromechanical measurement and observed that Collovo-Oxfordian argillaceous rocks behave like a Terzaghi's material (Biot's coefficient equal to 1). However, Bemer et al. (2004) identified this parameter, after a careful water resaturation procedure, by using an oedometric cell: they obtained an average value equal to 0.52. Assuming Poisson's ratio equal to 0.3, Homand et al. (2006) deduced (also by oedometric cell) the value of b decreasing from 0.95 to 0.55 when the axial load varies from 8 to 24 MPa. In order to explain such variations, both Bemer et al. (2004) and Homand et al. (2006) emphasized how difficult to re-saturate such rocks: their specimens may be still unsaturated during the tests. Homand et al. (2004) applied a completely different method: using pulse-test monitoring and mass variation during drying, and identified b equal to 0.75.

It should be noted that, the values of poroelastic parameters depend on stress states (Bemer et al., 2004). It is shown that Biot's coefficient decreases with an increase of Terzaghi's effective axial stress (Fig.1.38). Concerning Biot's modulus, it appears to depend on both Terzaghi's effective axial stress (Fig.1.39) and the pore stress (Fig.1.40): it increases with the effective stress and the pore pressure. A significant increase of M with the pore pressure can be explained by the unsaturated state of the tested samples. Indeed, M is a function the pore fluid(s) compressibility and so depends on saturation and pore pressure through the gas compressibility.

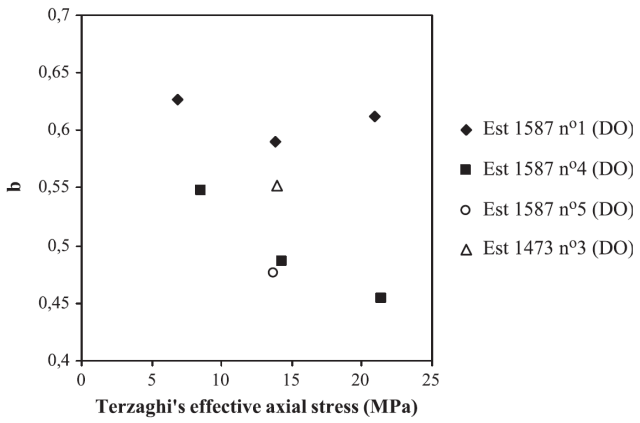

Figure 1.38: Biot's coefficient as a function of Terzaghi's effective axial stress (Bemer et al., 2004).

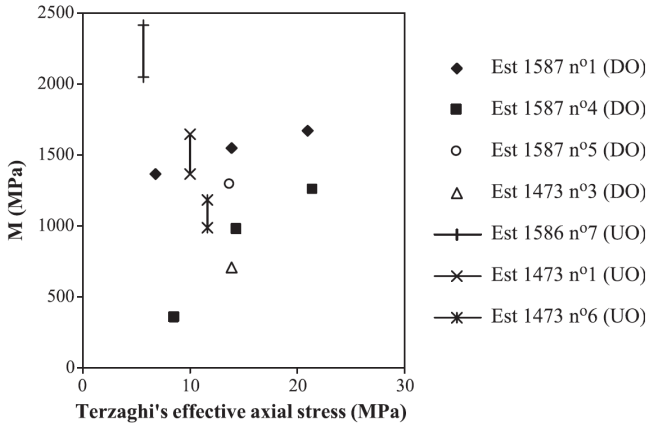

Figure 1.39: Biot's modulus as a function of Terzaghi's effective axial stress (Bemer et al., 2004).

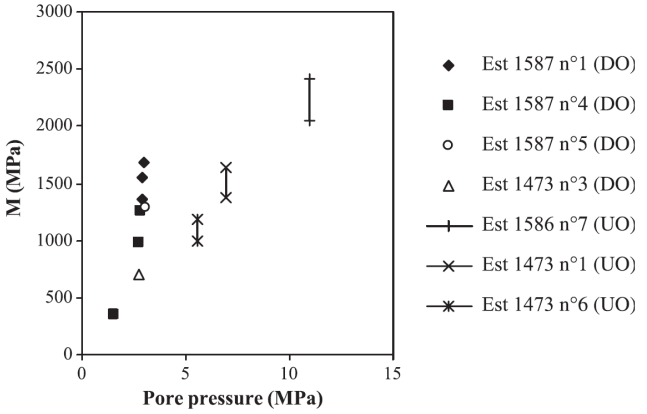

Figure 1.40: Biot's modulus as a function of pore pressure (Bemer et al., 2004).

1.5.2 Modeling investigation

Numerous constitutive models have been developed to predict the hydromechanical behavior of Callovo-Oxfordian argillaceous rocks. In general, these models can be classified under two types: 1) macroscopic (phenomenological) models, and 2) micromechanical (physical) models. For phenomenological models, argillaceous rocks are considered as a homogenous material, and the constitutive models are established to describe the main features observed from the standard rocks mechanics tests.

Macrosocpic modelings

An elastoplastic damage model has been proposed by Chiarelli et al. (2003) to describe plastic deformation and induced damage. The plastic behavior is considered as a typical cohesive-frictional model, and a non-associated type of plastic flow is chosen to incorporate the plastic dilatancy (positive volumetric strains). The material damage is represented by a second rank symmetric tensor, and its evolution rate is linked to both elastic and plastic strains. The

damage component of the model allows to describe the deterioration of elastic properties and induced anisotropy of such material. The coupled elastoplastic-damage approach incorporates the fact that the two mechanisms, the plastic shearing and the damage due to microcracking, are usually coupled and affect each other. Moreover, this model has been extended to partially saturated conditions in order to study the coupled hydromechanical behaviors, such as pressure sensitivity, capillary effects during drying and wetting processes (Shao et al., 2006).

In the other hand, argillaceous rocks are a porous media, of which the behavior is affected by the presence of fluids and the evolution of pore pressure. Hence, the mechanics of porous solid should be applied to the modeling of the hydromechanical behavior of such material. Conil et al. (2004) has established a poroplastic damage model for the same rocks. The reproduction of the plastic behavior is based on the Drucker-Prager criterion that takes into account the stress path followed, an isotropic hardening and a non-associated law. The damage is represented by a second-order tensor to describe the induced anisotropy. An original point of this model consists in a powerful setting to study the fluid-skeleton interactions in such a porous material and to reproduce the anisotropic evolution of the hydromechanical coupling tensor (Biot coefficients tensor) due to an orientated microcracking: an increase of the Biot coefficient along the radial direction and a remaining constant of that along the axial direction. However, this model is elaborated for the saturated poromechanical behavior without considering unsaturated state.

To deal with unsaturated behavior of argillaceous rocks, Hoxha et al. (2007) proposed a unified model for both saturated and unsaturated behaviors, by using the effective stress concept and the equivalent stress principle. Different from the previous models, the particular forms of the yield criterion and the plastic flow potential is proposed to better describe the behavior in tension-stress path. The evolution of the poroelastic parameters due to microcracking is also considered. In addition, an extension of the saturated elastic-plastic model in unsaturated condition is proposed. The main hypothesis of this extension is the evolution of Biot coefficient as a function of the suction, justified by laboratory results and micromechanical analysis.

Physically based modelings

The phenomenological models are not able to take into account deformation mechanisms related to material heterogeneities. Hence, it is useful to develop more physical modeling approaches for such rocks.

Abou-Chakra Guéry et al. (2008) proposed a micromechanical model of elastoplastic and damage. The material is modeled as a three-phase composite: an elastocplastic clay matrix, linear elastic quartz grains, and damaged elastic calcite grains. A nonlinear homogenization, based on the incremental method proposed by Hill, is adapted to obtain the macroscopic constitutive law. A Mori-Tanaka scheme is used for the localization step, considering the matrix-inclusion morphology. For the damage modeling, only the transgranular fractures in the calcite is taken into account, but decohesion at inclusion-matrix boundaries (evidenced by

experimental observations) is neglected.

1.6 Outline of this thesis

As discussed in the preceding section, the hydromechanical behavior of argillaceous rocks is extensively investigated in recent years, not only in the experimental part, but also in the modeling and simulation part. However, the experimental study until now is principally conducted at macro-scale, hence it is rather phenomena characterizations. Some real physical mechanisms are still sigma, and numerous phenomena can't be explained.

The Callovo-Oxfordian argillaceous rocks exhibits a multi-scale heterogeneity, ranging from the nanometric scale of clay elementary layer to the kilometric scale of geological formation. One interesting characteristic heterogeneity scale of such rocks is related to its composite structure: the complex interactions between clay matrix and mineral inclusions owning quite contrasting hydromechanical properties would lead to potential damage of the material, which is very important for the stability assessment of long-term storage.

This thesis is focused on the scale of composite microstructure of argillaceous rocks, aiming at a micromechanical experimental investigation and modeling of the deformation and damage of such rocks under hydric and mechanical loadings. The structure of this thesis is as following:

The second chapter concerns the experimental method. The experimental investigation is achieved by means of the combination of environmental scanning electron microscope (ESEM) and digital image correlation (DIC) techniques. Their principles are presented and discussed. In particular, the different errors associated to the strain measurement, are discussed in detail.

In the third chapter, the behavior of argillaceous rocks under purely hydric loading is experimentally studied. The humidification/desiccation cycles are conducted in the ESEM chamber, to investigate the mechanism of the deformation and damage under hydric loading.

In the fourth chapter, the behavior of argillaceous rocks under mechanical loading is investigated. The uniaxial compression tests are conducted on the samples with different humidity states (water contents) to identify the mechanism of deformation and damage of such material under mechanical loading. Moreover, one test under combined hydric and mechanical loadings is performed to investigate the influence of humidity state on the mechanical behavior of such rocks.

The experimental investigations reveal the crucial role of inclusion-matrix interaction on the behavior of argillaceous rocks. Hence, such interaction is investigated by the finite element method and micromechanical modeling in the fifth chapter. The internal stress field, which is crucial for the microcracking study, is studied for different cases. Besides, the overall deformation of argillaceous rocks under hydric loading, due to a free swelling of clay matrix is also investigated.

Bibliography

Abou-Chakra Guéry, A., Cormery, F., Shao, J.F., Kondo, D., 2008. A micromechanical model of elasto-plastic and damage behavior of a cohesive geomaterial. International Journal of Solids and Structure 45 (5), 1406-1429.

Abou-Chakra Guéry, A., Cormery, F., Su, K., Shao, J.F., Kondo, D., 2008. A micromechanical model for the elasto-viscoplastic and damage behavior of a cohesive geomaterial. Physics and Chemistry of the Earth 33, 416-421.

Al-Mukhtar, M., Belanteur, N., Tessier, D., Vanapalli, S.K., 1996. The fabric of a clay soil under controlled mechanical and hydraulic stress states. Applied Clay Science 11, 99-115.

Alonso, E.E., Vaunat, J., Gens, A., 1999. Modelling the mechanical behaviour of expansive clays. Engineering Geology 54, 173-183.

Arifin, Y.F., 2008. Thermo-hydro-mechanical behavior of compacted bentonite-sand mixtures: an experimental study. Thèse Bauhaus-University Weimar, Weimar.

ANDRA, 2005. Référentiel du Site Meuse/Haute-Marne: Tome 2.

Aublivé-Conil N., 2003. Modélisation du comportement mécanique des argilites raides avec prise en compte de l'endommagement : application aux argilites de l'Est, Thèse de doctorat de l'Université de Cergy-Pontoise, Collection Les Rapports ANDRA.

Augier, F., Coumans, W.J., Hugget, A., Kaasschieter, E.F., 2002. On the risk of cracking in clay drying. Chemical Engineering Journal 86, 133-138.

Barbour, S.L., Fredlund, D.G., 1989. Mechanisms of osmotic flow and volume change in clay soils. Canadian Geotechnical Journal 26, 551-562.

Bazant, Z.P., Raftshol, W.J., 1982. Effect of cracking in drying and shrinkage specimens. Cement and Concrete Research 12, 209-226.

Bemer, E., Longuemare, P., Vincké, O., 2004. Poroelastic parameters of Meuse/Haute Marne argillites: effect of loading and saturation states. Applied Clay Science 26, 359-366.

Bishop, A.W., 1959. The principle of effective stress. Teknisk Ukeblad 39, 859-863.

Bisschop, J., Wittel, F.K., 2011. Contraction gradient induced microcracking in hardened cement paste. Cement and Concrete Composites 33, 466-473.

Bisschop, J., van Mier, J.G.M., 2002. Effect of aggregates on drying shrinkage microcracking in cement-based composites. Materials and Structures 35, 453-461.

Bolt, G.H., 1956. Physico-chemical analysis of the compressibility of pure clays. Géotechnique 6 (2), 86-93.

Bobko, C., Ulm, F.-J., 2008. The nano-mechanical morphology of shale. Mechanics of Materials 40, 318-337.

Bornert, M., Valès, F., Gharbi, H., Nguyen Minh, D., 2010. Multiscale full-field strain measurements for micromechanical investigations of the hydromechanical behaviour of clayey rocks. Strain 46, 33-46.

Cariou, S., 2010. Couplage hydro-mécanique et transfert dans l'argilite de Meuse/Haute-Marne : approches expérimentale et multi-échelle. Ecole Nationale des Ponts et des Chaussées, p. 334.

Cariou, S., Duan, Z., Davy, C., Skoczylas, F., Dormieux, L., 2012. Poromechanics of partially saturated COx argillite. Applied Clay Science 56, 36-47.

Cernica, J.N., 1995. Soil Mechanics. John Willey and Sons, New York.

Chiarelli, A.S., Shao, J.F., Hoteit, N., 2003. Modelling of elastic-plastic damage behaviour of a claystone. International Journal of Plasticity 19, 23-45.

Conil, N., Djeran-Maigre, I., Cabrillac, R., Su, K., 2004. Poroplastic damage model for claystones. Applied Clay Science 26, 473-487.

Coussy, O., 2004. Poromechanics. John Wiley & Sons, Ltd.

Coussy, O., 2010. Mechanics and physics of porous solids. John Wiley & Sons, Ltd.

Delage, P., Howat, M.D., Cui, Y.J., 1998. The relationship between suction and swelling properties in a heavily compacted unsaturated clay. Engineering Geology 50, 31-48.

Delville, A., Laszlo, P., 1990. The origin of the swelling of clays by water. Langmuir 6, 1289-1294.

Donohue, M.D., Aranovich, G.L., 1998. Adsorption Hysteresis in Porous Solids. Journal of Colloid and Interface Science 205, 121-130.

Dormieux, L., Lemarchand, E., Coussy, O., 2003. Macroscopic and micromechanical approaches to the modelling of the osmotic swelling in clays. Transport In Porous Media 50, 75-91.

Dormieux, L., Kondo, D., Ulm, F.J., 2006. Microporomechanics. John Wiley & Sons, Ltd.

Erguler, Z.A., Ulusay, R., 2009. Water-induced variations in mechanical properties of clay-bearing rocks. International Journal of Rock Mechanics & Mining Sciences 46, 55-370.

Gaucher, E., Robelin, C., Matray, J.M., Négrel, G., Gros, Y., J.F. Heitz, Vinsot, A., Rebours, H., Cassagnabère, A., Bouchet, A., 2004. ANDRA underground research laboratory: interpretation of the mineralogical and geochemical data acquired in the Callovian-Oxfordian formation by investigative drilling. Physics and Chemistry of the Earth 29, 55-77.

Goltermann, P., 1995. Mechanical predictions of concrete deterioration - Part 2: classification of crack patterns. ACI Materials Journal 92 (1), 58-63.

Gens, A., Alonso, E.E., 1992. A framework for the behavior of unsaturated expansive clays. Canadian Geotechnical Journal 29, 1013-1032.

Hassanizadeh, S.M., Gray, W.J., 1993. Thermodynamic basic of capillary pressure in porous media. Wanter Ressources Research 29 (10), 3389-3405.

Homand, F., Giraud, A., Escoffier, S., Koriche, A., Hoxha, D., 2004. Permeability determination of a deep argillite in saturated and partially saturated conditions. International Journal of Heat and Mass Transfer 47, 3517-3531.

Homand, F., Shao, F., Giraud, A., Auvray, C., Hoxha, D., 2006. Pétrofabrique et propriétés mécaniques des argilites. Comptes Rendus Géosciences 338 (12-13), 882-891.

Hoxha, D., Giraud, A., Homand, F., Auvray, C., 2007. Saturated and unsaturated behaviour modelling of Meuse-Haute/Marne argillite. International Journal of Plasticity 23, 733-766.

Ibrahim, N., 2008. Caractérisation des propriétés mécaniques des géomatériaux par technique de micro indentation. Ph.D. thesis, Université des Sciences et Technologies de Lille.

Jagla, E.A., 2002. Stable propagation of an ordered array of cracks during directional drying. Pysical Review E 65, 046147.

Jenkins, D.R., 2005. Optimal spacing and penetration of cracks in a shrinking slab. Pysical Review E 71, 056117.

Jenkins, D.R., 2009. Determination of crack spacing and penetration due to shrinkage of a solidifying layer. International Journal of Solids and Structure 46, 1078-1084.

Karl K., Turekian, 1968. Oceans, Prentice-Hall. 120p.

Karaborni, S., Smit, B., Heidug, W., van Oort, E., 1996. The swelling of clays: molecular simulations of the hydration of montmorillonite. Science 271, 1102-1104.

Komine, H., Ogata, N., 1994. Experimental study on swelling characteristics of compacted bentonite. Canadian Geotechnical Journal 31, 478-490.

Kowalski, S.J., 2003. Thermomechanics of Drying Processes. Springer.

Laird, D.A., 2006. Influence of layer charge on swelling of smectites. Applied Clay Science 34, 74-87.

Laird, D.A., Shang, C., Thompson, M.L., 1995. Hysteresis in crystalline swelling of smectites. Journal of Colloid and Interface Science 171, 240-245.

Likos, W.J., Lu, N., 2006. Pore-scale analysis of bulk volume change from crystalline interlayer swelling in Na^{+} - and Ca^{2+} - smectite. Clays and Clay Minerals 54 (4), 516-529.

Mainguy, M., Coussy, O., Baroghel-Bouny, V., 2001. Role of air pressure in drying of weakly permeable materials. Journal of Engineering Mechanics 127 (6), 582-592.

Mitchell, J.K., 1993. Fundamentals of soil behaviour. John Wiley and Sons, Inc., New York. 437p.

Montes-H, G., 2002. Etude expérimentale de la sorption d'eau et du gonflement des argiles par microscopie électronique à balayage environnementale (ESEM) et l'analyse digitale d'images. Thèse Université Louis Pasteur Strasbourg, Strasbourg.

Montes-H, G., Duplay, J., Martinez, L., Escoffier, S., Rousset, D., 2004. Structural modifications of Callovo-Oxfordian argillite under hydration/dehydration conditions. Applied Clay Science 25, 187- 194.

Murray, R.S., Quirk, J.P., 1980. Clay-water interaction and the mechanism of soil swelling. Colloids and Surface 1, 17-32.

Ortega, J.A., Ulm, F.-J., Abousleiman, Y., 2007. The effect of the nanogranular nature of shale on their poroelastic behavior. Acta Geotechnica 2, 155-182.

Peron, H., Laloui, L., Hueckel, T., Hu, L., 2009. Desiccation cracking of soils. European Journal of Environmental and Civil Engineering 13, 869-888.

Pham, Q.T., 2006. Effets de la désaturation et de la resaturation sur l'argilite dans les ouvrages souterrains. Ecole Polytechnique, p.175.

Pham, Q.T., Valès, F., Malinsky, L., Nguyen, M.D., Gharbi, H., 2007. Effets of desaturation-resaturation on mudstone. Physics and Chemistry of the Earth 32, 646-655.

Robinet, J.C., 2008. Minéralogie, porosité et diffusion de solutes dans l'argilite du Callovo-Oxfordien de Bure (Meuse/Haute Marne, France) de l'échelle centrimétrique à micrométrique. PhD dissertation, Université de Potiers, p.247.

Robinet, J.C., Sardini, P., Coelho, D., Parneix, J.C., Prêt, D., Sammartino, S., Boller, E., Altmann, S., 2012. Effects of mineral distribution at mesoscopic scale on solute diffusion in a clay-rich rock: Example of the Callovo-Oxfordian mudstone (Bure, France). Water Resources Research 48.

Reynolds, R.C., Jr., R.C. Reynolds, III. 1996. Newmod-for-Windows. The Calculation of One-dimensional X-ray Diffraction Patterns of Mixed-layered Clay Minerals. Published by the authors. 8 Brook Road, Hanover New Hampshire 03755.

Saiyour, N., Hicher, P.Y., Tessier, D., 2000. Microstructural approach and transfer water modelling in highly compacted unsaturated swelling clays. Mechanics of Cohesive-frictional Materials 5, 41-60.

Saiyour, N., Tessier, D., Hicher, P.Y., 2004. Experimental study of swelling in unsaturated compacted clays. Clay Minerals 39, 469-479.

Sammartino, S., 2001. Construction d'un modèle conceptuel d'organisation de la porosité et de la minéralogie dans les argilites du site de Bure. Rapport Andra n°D.RP.0ERM.01.018, France.

Sammartino, S., Bouchet, A., Prêt, D., J.-C., P., Tevissen, E., 2003. Spatial distribution of porosity and minerals in clay rocks from the Callovo-Oxfordian formation (Meuse/Haute-Marne, Eastern France) implications on ionic species diffusion and rock sorption capability. Applied Clay Science 23, 157-166.

Sayers, C.M., 1994. The elastic anisotropy of shales. Journal of Geophysical Research 99, 767-774.

Segad, M., Hanski, S., Olsson, U., Ruokolainen, J., Åkesson, T., Jonsson, B., 2012. Microstructural and swelling properties of Ca and Na montmorillonite: (In situ) observations with cryo-TEM and SAXS. Journal of Pysical Chemistry C 116, 7596-7601.

Shao, J.F., Jia, Y., Kondo, D., Chiarelli, A.S., 2006. A coupled elastoplastic damage model for semi-brittle materials and extension to unsaturated conditions. Mechanics of Materials 38 (3), 218-232.

Shear, D.L., Olsen, H.W.,Welson,K.R., 1992. Effect of desiccation on the hydraulic conductivity versus void ratio relationship for a natural clay. Transportation Research Record 1369, 130-135.

Tessier, D., 1984. Etude expérimental de l'organisation des matériaux argileux : hydratation, gonflement et structuration au cours de la dessiccation et de la réhumidification. Thèse Université Paris VII, Paris.

Tessier, D., Dardaine, M., Beaumont, A., Jaunet, A.M., 1998. Swelling pressure and microstructure of an activated swelling clay with temperature. Clay Minerals 33, 255-267.

Tripathy, S., Subba Rao, K.S., Fredlund, D.G., 2002. Water content - void ratio swell-shrink paths of compacted expansive soils. Canadian Geotechnical Journal 39, 938-959.

Ulm, F.-J., Abousleiman, Y., 2006. The nanogranular nature of shale. Acta Geotechnica 1, 77-88.

Valès, F., 2008. Modes de déformation et d'endommagement de roches argileuses profondes sous sollicitations hydro-mécaniques. Ecole Polytechnique, Palaiseau.

Valès, F., Nguyen Minh, D., Gharbi, H., Rejeb, A., 2004. Experimental study of the influence of the degree of saturation on physical and mechanical properties in Tournemire shale (France). Applied Clay Science 26, 197-207.

Van Olphen, H., 1963. An introduction to clay colloid chemistry - second edition. Wiley-Interscience Publication, New York.

Weinberger, R., 1999. Initiation and growth of cracks during desiccation of stratified muddy sediments. Journal of Structural Geology 21, 379-386.

Wenk, H.R., Voltolini, M., Mazurek, M., Van Loon, L.R., Vinsot, A., 2008. Preferred orientations and anisotropy in shales: Callovo-Oxfordian shale (France) and Opalinus Clay (Switzerland). Clays and Clay Minerals 56, 285-306.

Wersina, P., Curtib, E., Appeloc, C.A.J., 2004. Modelling bentonite-water interactions at high solid/liquid ratios: swelling and diffuse double layer effects. Applied Clay Science 26, 249-257.

Yang, D.S., Bornert, M., Chanchole, S., Wang, L.L., Valli, P., Gatmiri, B., 2011. Experimental investigation of the delayed behavior of unsaturated argillaceous rocks by means of digital image correlation techniques. Applied Clay Science 54 (1), 53-62.

Yang, D.S., Bornert, M., Chanchole, S., Gharbi, H., Valli, P., Gatmiri, B., 2012. Dependence of elastic properties of argillaceous rocks on moisture content investigated with optical full-field strain measurement techniques. International Journal of Rock Mechanics & Mining Sciences 53, 45-55.

Zhang, C.L., Rothfuchs, T., 2004. Experimental study of the hydro-mechanical behaviour of the Callovo-Oxfordian argillite. Applied Clay Science 26, 325-336.

Chapter 2

Experimental method

Contents

2.1 Experimental equipment

In this work, experimental investigation is achieved by the combination of environmental scanning electron microscopy (ESEM) and digital image correlation (DIC) techniques. The hydric (humidification/desiccation) and mechanical (uniaxial compression) loading test and the microscale observation are performed in ESEM. The humidification/desiccation can be achieved through controlling the specimen's temperature (by a Peltier module, see Fig.2.1) and the vapor pressure in the ESEM's chamber. A specific mechanical loading machine (Fig.2.1) has been developed (by D. Caldemaison), allowing uniaxial compression tests in the ESEM chamber at controlled sample's temperature.

The size of the observation zone is typically several hundred micrometers, permitting to distinguish the inclusion-matrix composite microstructure of argillaceous rocks. Beside, local damage phenomena (microcracks at the order of micrometers) can be observed at this observation scale. The recorded high resolution images are then analyzed by DIC techniques, evaluating the local strain distribution of such rocks under hydric and mechanical loadings.

It should be noted that such an observation zone is too small to be a representative volume element (RVE) of these argillaceous rocks under hydric and mechanical loads. They are in particular too small to represente of the fluctuations of the spatial distribution of the mineral components. Unfortunately, the extension of observation zones is limited by the aperture size of the BSE detector used in environmental mode, and a black corner already appears in the top-left of the images (magnification $\times$ 400)recorded during test #2 in section 3.2.2 (Fig.3.6). One solution of this problem could be to choose several continuous observation zones which would constitute a larger studied zone in tests. However, the present study primarily aims at characterizing the local mechanisms of the deformation and damage under hydric and mechanical loads, not yet at giving a detailed statistical quantification of their contribution to the overall strain, which is left for further investigations.

2.1.1 Principle of scanning electron microscopy

Scanning electron microscopy (SEM) is one type of electron microscopy which images a sample by scanning it with a beam of electrons in a raster scan pattern. Its imaging is based on the interaction between the incident electrons and the atoms at and near the sample's surface (Reimer, 1998). Such an interaction produces different types of signals, such as secondary electrons, back-scattered electrons, X-rays and transmitted electrons etc., containing the information about the morphology of the sample surface, compositions and so on. The two most used signals in SEM are secondary electrons (SE) and back-scattered electrons (BSE). Secondary electrons result from the inelastic electron-sample collision, and their energies are weaker than those of incident electrons. The SE mode image contains typically the topography information of the sample surface. Back-scattered electrons are beam electrons that are reflected from the

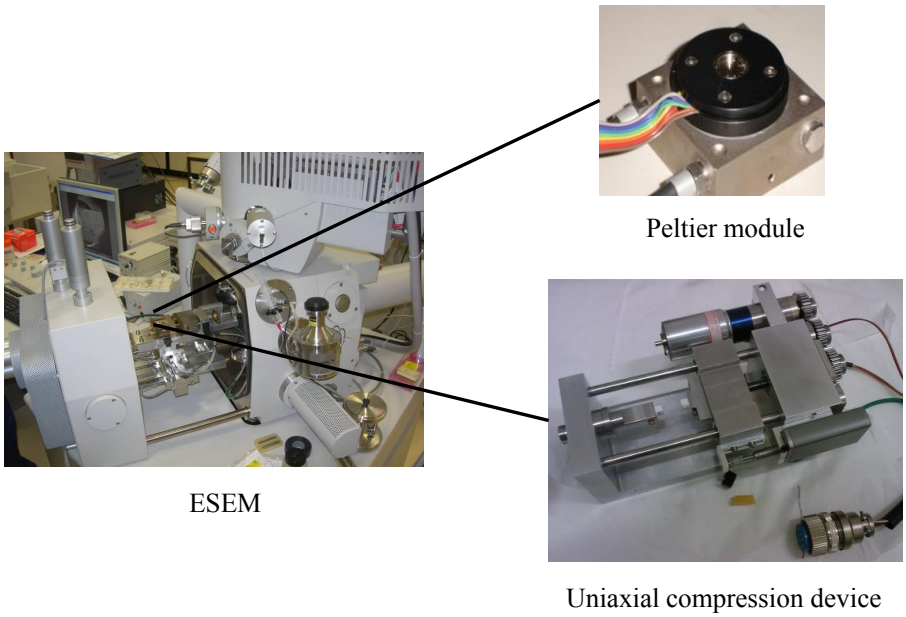

Figure 2.1: Experimental equipment used in this work.

sample by elastic scattering. The intensity of BSE signal is strongly related to the atomic number (Z) of the specimen. Hence, BSE image can provide an information about the distribution of different elements in the sample. A summary of the different detectors usually used in ESEM is shown in Tab.2.1.

Table 2.1: Detector types used in ESEM.

	Secondary electron (SE)	**Back-scattered electron (BSE)**
High vaccum (HV)	Everhart-Thornley (ETD)	Backscattered Electron (BSED)
Low vaccum (LV) $<$ 200 Pa	Large Field (LFD)	Backscattered Electron (BSED)
ESEM $<$ 2600 Pa	Gaseous Secondary Electron (GSED)	Gaseous Analytical (GAD)

In a typical SEM (see Fig.2.2), the electron beam is emitted from an electron gun. The electron beam, having an energy ranging from 0.5 keV to 30 keV, is focused by condenser lenses to a spot about 1 nm to 50 nm in diameter on the sample for the SEM used in this study (FEI Quanta 600) (FEI, 2009). Then, the electron beam passes through pairs of scanning coils or pairs of deflector plates in the electron column, which deflects it in the x and y axes so that it scans in a raster fashion over a rectangular area of the sample surface. Magnification comes from the ratio between the dimension of the raster on specimen's surface and that of the display device. Assuming the pixel size of the display screen is fixed, higher magnification results from

reducing the size of the raster, and vice versa. Therefore, the magnification of SEM is controlled by the current supplied for the x, y scanning coils or the voltage supplied for the (x, y) defector plasters (Brisset et al., 2006). Note this is different from optical and transmission microscopy of which the magnification comes from the power of the objective lens.

When the primary electrons beam arrives at the specimen surface, it interacts with the atoms within a teardrop-shaped volume near the specimen surface. This volume is known as the interaction volume, ranging from less than 100 nm to about 5 μm into the surface. The size of the interaction volume depends on the energy of primary electrons, atomic number of the constitutive atoms of specimen and its density. The energy exchange between incident electrons and the specimen leads to reflection of high-energy electrons by elastic scattering, emission of secondary electrons etc. The SEM image, indeed being a distribution map of the intensity of the signal being emitted from the scanned area of the specimen, is therefore produced.

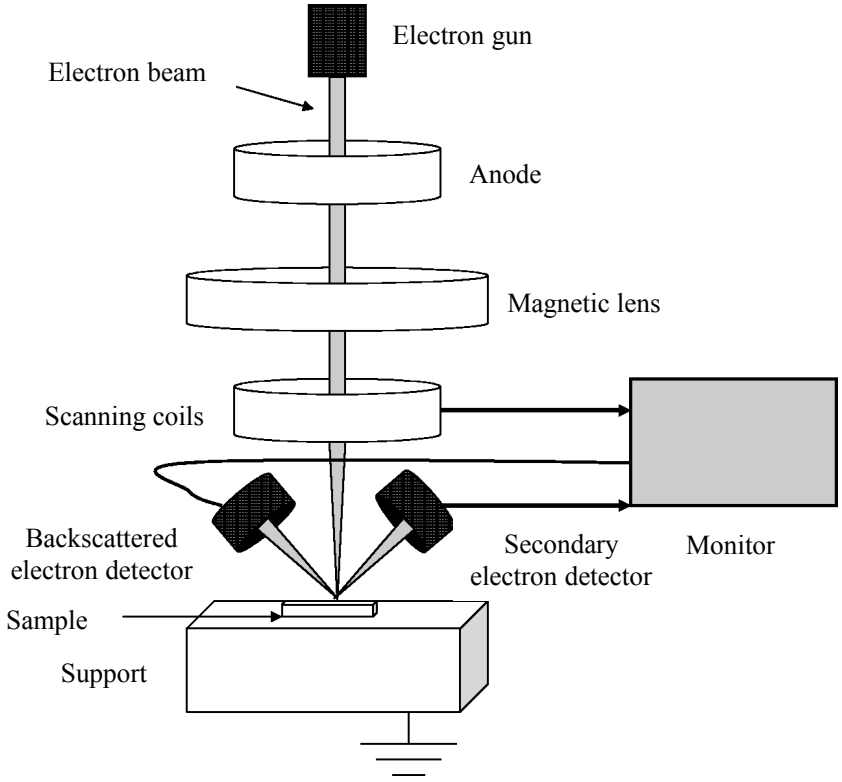

Figure 2.2: Schematic diagram of SEM (Gagnadre et al., 2009).

2.1.2 Environmental scanning electron microscopy

Environmental scanning electron microscopy (ESEM) is a special type of SEM, which has been widely used in the last ten years in material science, particularly in biomechanics. One significant advantage of ESEM, in comparison to conventional SEM, consists in allowing for imaging specimens that are "wet", uncoated, in a controlled humidity environment by adjusting

temperature and pressure.

Indeed, the observation in conventional SEM strictly requires a high vacuum (HV) condition to allow a precise focusing of the incident electrons on the sample and to prevent the emitted electrons (BSE, SE) from interacting with the atmosphere. However, with the ESEM used in this study, the observation of specimens can be carried out in a gaseous environment (up to 2600 Pascals) by two fundamental developments: 1) specialized electron detectors, and 2) a differential pumping system. Due to the presence of vapor, the conventional Everhardt-Thornley detector in standard SEM can't be used for ESEM. Therefore, new types of detectors are developed: gaseous secondary electron detector (GSED) and gaseous analytical detector (GAD) (picking up BSE signals in ESEM mode). In ESEM, a series of pressure limiting apertures (PLAs) are placed along the column, so that a pressure differential is maintained across each PLA. Owing to this differential pumping system, the electron gun can be maintained at high vacuum, yielding the possibility of superior quality imaging, despite the relatively high pressure in the sample chamber. Note that the hole in the center of GSED and GAD serves as the final pressure limiting aperture, and its bore size determines the pressure magnitude attainable in the sample chamber. For example, the pressure in the chamber can reach 2600 Pa for a 500 μm aperture, whereas it can only be 750 Pa if the detector has a 1 mm aperture.

Scattering of the electron beam by gas molecules along the gap (between the final PLA and the sample surface) is a great issue for the observation in ESEM. However, for the typical observation condition (gap length of several millimeter, less than 2600 Pascals), the incident electrons are hardly scattered. A well defined electron "probe" is still incident on the sample, but accompanied by a "skirt" of scattered electrons which can extend over tens of micrometers from the central probe. Not only with the primary electrons, the presence of vapor also leads to the interaction with the emitted signals: they undergo collisions, producing more electrons and ionization of gas molecules (in particular for SE signals). Each ionization generates a daughter electrons, which could themselves ionize other gas molecules furthermore, creating a cascade between sample and detector (shown in Fig.2.3). Finally, the overall ionization effect considerably amplifies the original SE signal. It should be noted that this positive amplification effect (scaling with chamber pressure) is actually counteracted by the negative skirting effect (increasing with chamber pressure as well), hence, an optimal chamber pressure exists from the viewpoint of image quality for a given acquisition condition (kinetic energy and intensity of primary electron beam, working distance etc.). Analogically, there is an optimal working distance for a prescribed chamber pressure (Thiel, 2004). For BSE signals, the signal amplification effect is not evident, and their detection in ESEM is similar to the case of SEM although primary electrons are perturbed by the presenting vapor: reducing WD always leads to an improvement of image quality.

During the observation of insulating specimens, the electrons can't be evacuated so that the negative charge is accumulated at the specimen surface. This would create an electrical

potential tending to deflect the primary electron beam from the scanned point, appearing as an charging artifact on the image. Such a problem of specimen charging is generally eliminated in SEM by depositing a conductive layer on the specimen's surface prior to observation. However, the presence of vapor can prevent such problem in ESEM instead of coating. In fact, the positive charge ions generated by ionization would neutralize the negative charges so that the problem of specimen charging can be eliminated (in Fig.2.3). This is one important advantage of ESEM, which is identical to low vacuum (LV) mode. Moreover, the presence of vapor in ESEM yields another advantage, enabling in-situ hydration in the ESEM chamber, which will be discussed in detail in the following section.

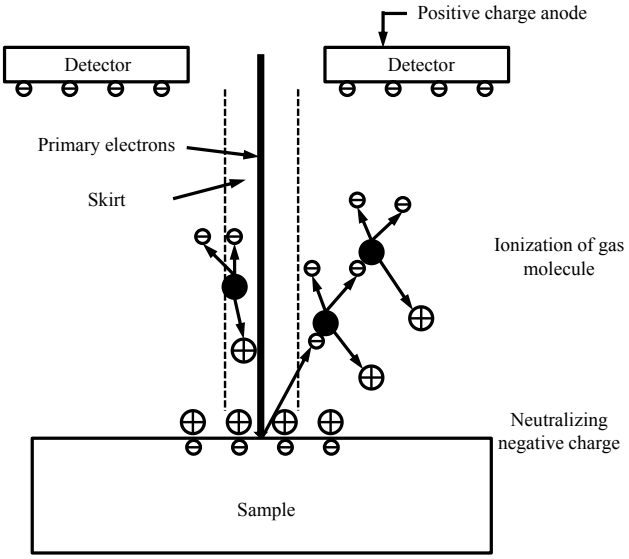

Figure 2.3: Detecting signals in ESEM.

2.1.3 Hydration in ESEM

Relative humidity (RH) is defined by,

$$h_r = \frac{P_v}{P_{vs}(T)} \tag{2.1}$$

in which h_r is relative humidity, P_v is water vapor pressure and $P_{vs}(T)$ saturated water vapor pressure for a given temperature T. This definition indicates that RH is a function of temperature and water vapor pressure. Their relation is graphically represented in Fig.2.4. This essentially defines the principle of controlling the humidity state surrounding the specimen in the ESEM chamber.

The specimen temperature can be controlled by a Peltier module in ESEM. The module used in this study, based on a thermoelectric effect (direct conversion of electric voltage to temperature difference), permits to control the temperature of the specimen placed on it, with

dimensions of a few millimeters, over a range varying from -20°C to 50°C. By means of a purge of the ESEM chamber (discussed more detailed in section 3.1), the initial atmosphere containing dry air is replaced by water vapor and only the latter remains in the specimen chamber at the end of the purge. Therefore, the relative humidity around the specimen can be controlled by the Peltier module governing the temperature of specimen, and by ESEM chamber (total) pressure which is identical to the water vapor pressure surrounding the specimen.

Following the above discussion, three different ways may be followed to apply hydric loads on the specimen (i.e. to humidify or desiccate it): 1) a variation of the ESEM chamber pressure (path 1 in Fig.2.4), 2) a variation of the sample temperature (path 2 in Fig.2.4), 3) a change of the two variables simultaneously. The presence of water vapor degrades in general the image quality as it disturbs not only the incident electrons but also the emitted signals (see discussions in the preceding section). Therefore, for a given RH, it is reasonable to keep the temperature the lowest possible since water vapor pressure decreases with temperature (as shown in Fig.2.4). However, special attention has to be paid to avoid water freezing.

In this study, we choose to vary the pressure of ESEM chamber to change RH (path 1 in Fig.2.4) at a constant temperature of 2°C (the lowest temperature avoiding freezing). This choice is based on the following considerations. First, the variation of temperature can cause thermal expansion or contraction of specimens and induce coupled effects with the swelling or shrinking of the material due to RH variation. Second, the chamber pressure will be always high in every loading step following path 2 while it is smaller except for higher RH following path 1 (in the case of hydration), so the latter will improve the imaging quality which is an essential factor for the accuracy of the strain field evaluation by DIC techniques. Finally, the duration of an experience following path 1 is much shorter than that following path 2, as the variation of chamber pressure is almost instantaneous and produces a homogeneous pressure field around the specimen, while a control of the temperature may be much longer and generate temperature gradients in the specimen, as the Peltier module is of limited power and is only partly in contact with the specimen.

2.1.4 Characterisation of samples microstructure

As presented in section 1.2.1, clay, carbonate and quartz constitute almost 95% mass fraction of the argillaceous rocks of Bure. The investigation of hydric and mechanical behaviors of this material is here focused on the scale of its composite structure, in view of characterizing complex interactions of these three principal components. The spatial distribution of constitutive phases in observation zones is identified by two methods: (1) energy-dispersive X-rays spectroscopy (EDS) and (2) SEM imaging in BSE mode.

By means of EDS and imaging in BSE mode, the three main phases of the material, calcite ($CaCO_3$), quartz (SiO_2), and clay (Al, Si etc.), are analyzed from three chemical elements

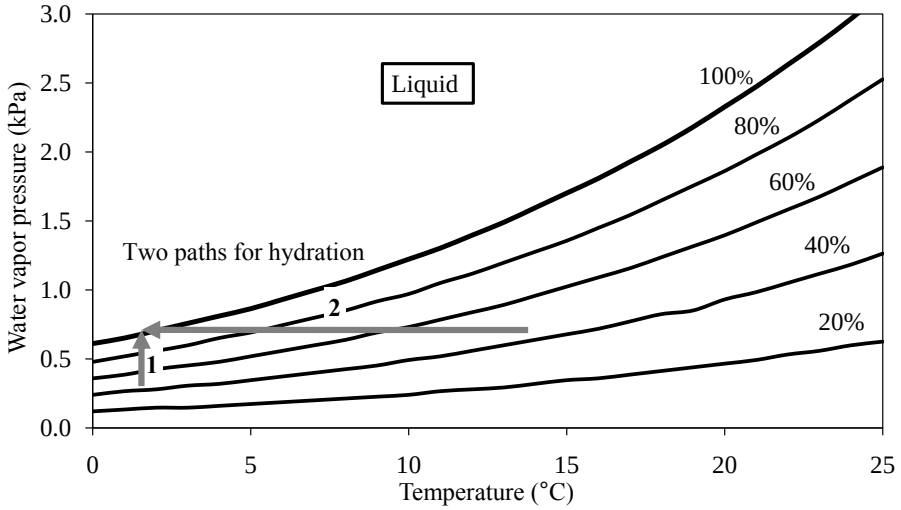

Figure 2.4: Relative humidity curve between 0°C and 25°C (Arrows: two possible paths for hydration).

mapping: the Calcium (Ca) map reflects the calcite distribution, while the map of Al indicates the clay phase. Besides, the brightest parts in the Silicium (Si) map reveal the quartz grains (Sammartino et al., 2003). An example of microstructure characterization by this method is presented in Fig.2.5. The results, at this micro-scale, reveal that there are some grains of calcite and quartz with sizes ranging from a few to dozens of micrometers scattered over a connected clay matrix in the investigated zone.

Note that chemical element analysis has to be carried out, in this study, in a conventional scanning electron microscope (Philips XL 40 equipped with an EDS system from PGT) after the experiment in the ESEM because the latter is not equipped with an EDS device. Besides, a coating by gold, to evacuate the accumulation of electric charges on sample surfaces, is necessary for the EDS analysis as argillaceous rocks are an insulator, whereas samples can be observed directly without coating in the ESEM as explained in 2.1. For the sake of simplicity, an alternative way for characterizing the spatial distribution of phases in argillaceous rocks is directly based on BSE images (Robinet, 2008) which serve also for evaluating deformation by DIC techniques. In fact, the intensity of BSE signals is essentially related to the atomic number of the atom in the interaction volume under electron spots, so that BSE images can provide a qualitative information about the spatial distribution of chemical compositions of the material. For the investigation at the scale of the composite structure, the identification of clay matrix and mineral inclusions (mostly calcite and quartz) can be performed by a criterion based both on the grey level and the contrast homogeneity in BSE images. From Fig.2.5a for example, we can observe that inclusions exhibit a more homogeneous contrast: the brighter particles are calcite, while the darker ones are quartz, as the atomic number of Ca is larger than that of Si. However, the clay matrix itself, with an average grey level similar to that of quartz, exhibits a

complex heterogeneous structure, with a typical length scale near or below a few micrometers, reflecting the particulate structure of clay at this scale. A qualitative identification of the phase distribution by this method is presented in Fig.2.5a (the closed lines in the BSE image), which shows an appropriate correspondence with the EDS analysis.

Note that both ways for chemical element analysis of samples are rough: they can't distinguish the very fine grains because of their limited accuracy and spatial resolution. In this study, only the big grains of carbonate and quartz (with a threshold in area of 10 to 30 μm^2, depending on image magnification) are filtered out in microstructure identifications for the following analysis. Moreover, the intra-phase heterogeneity in the clay matrix is not characterized here. As discussed in section 1.2, the clay matrix itself is also heterogeneous: what will be called the "matrix" in following is indeed a complex mixture of different clay minerals and smaller grains. However, we remind some recent advances in chemical element mapping analysis, which could yield more detailed quantitative petrographic information (Prêt et al., 2010). Based on an improved treatment of multi-elemental maps, the different clay minerals (such as smectite and illite) present in the "matrix" may be characterized.

2.2 Digital image correlation and strain measurement

Digital image correlation method (DIC) has been widely used in the field of experimental mechanics in the last decades (Bornert et al., 2011; Chu et al., 1985; Sutton et al., 2009) and has in particular been adapted to SEM in situ experiments (Doumalin and Bornert, 2000). The improvement of this technique in recent years, aiming at controlling and possibly eliminating various sources of random and systematic errors (Bornert et al., 2009; Schreier et al., 2000; Wang et al., 2009), leads to an appropriate performance for a wide range of its applications. Concerning argillaceous rocks, this method, associated with optical macroscopic and microscopic observations, has been used to investigate their instantaneous mechanical behavior (Bornert et al., 2010; Valès, 2008) and their delayed response (Yang et al., 2011) at some prescribed moisture level, as well as swelling strain due to humidification/desiccation under mechanical load (Yang et al., 2012). In this work, the in-house software CMV developed at LMS (Solid Mechanics Laboratory) and Navier laboratory, implementing the DIC method and various post-processing routines adapted to a micromechanical analysis will be used for the DIC analysis and strain measurement.

2.2.1 Principle of DIC

Generally speaking, DIC enables to measure the in-plane components of displacement field in observation zone with sub-pixel accuracy by searching the same matching-subsets between some reference image and deformed ones. The general operation of DIC is as follows. A subset is

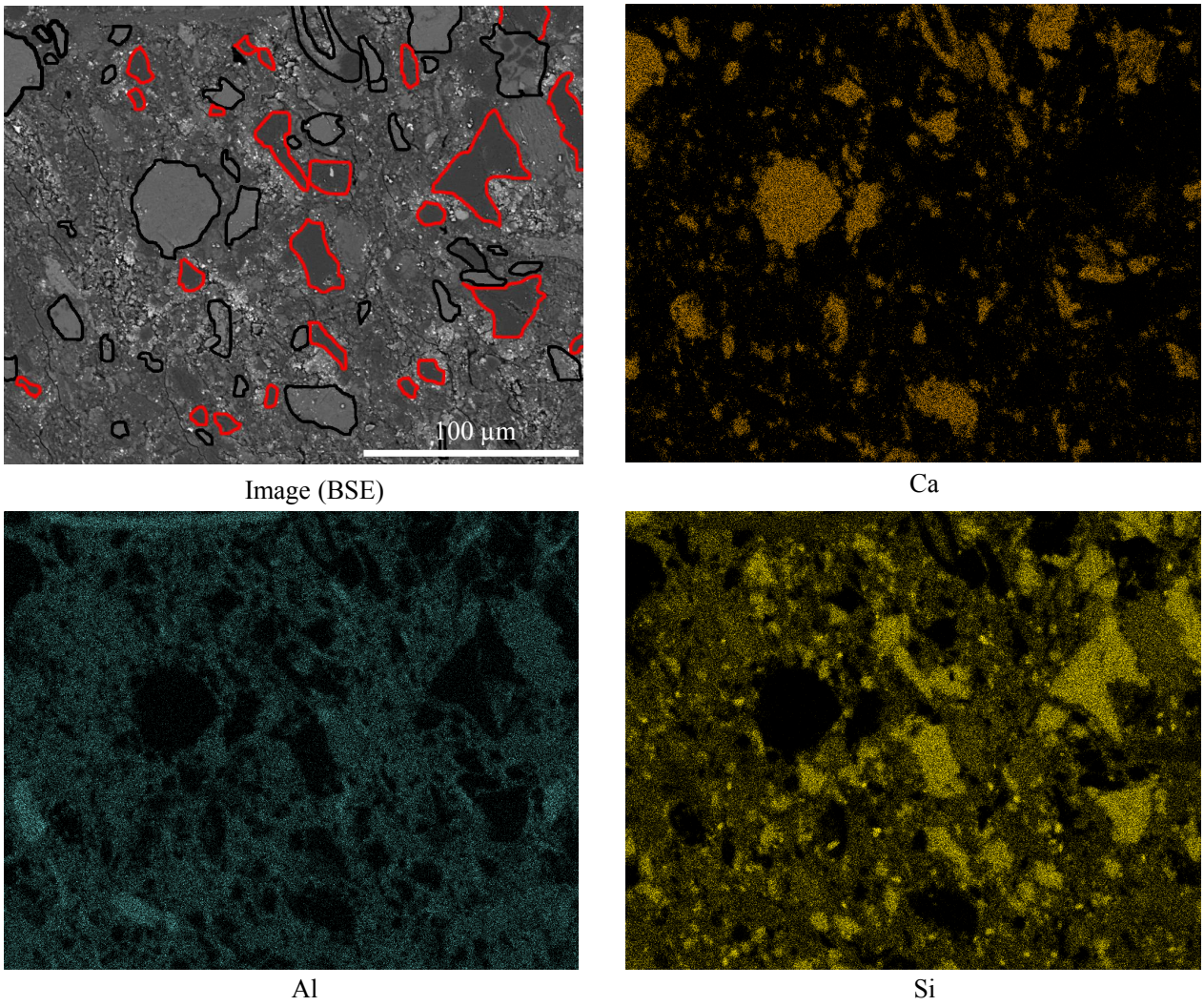

Figure 2.5: Phase distribution in argillaceous rocks identified by energy dispersive X-rays spectroscopy (Working distance: 12 mm, Analysis time: 40 minutes, Current: 8000 counts/s). In the BSE image, the big grains of calcites and quartz can be identified directly by the grey level and the local grey level fluctuations, and their contours are outlined (red: quartz; black: calcite).

selected in a reference image around some chosen positions. Then, the correlation is performed, consisting of searching the most alike subset corresponding to the former in the viewpoint of grey level in a predefined search zone of a deformed image (in Fig.2.6). A parameter, known as "correlation coefficient", quantifies the similarity level of the two subsets. Its minimum, with respect to the parameters charactering the transformation, determines the homologous subset in the deformed image.

Note that DIC is predicated on the principle of grey level conservation, which can be written as:

$$f\left(\underline{X}\right) = c \cdot g\left(\underline{x}\right) + b + g' \tag{2.2}$$

where $f(\underline{X})$ is the grey level of a pixel at position $\underline{X}$ in reference image, while $g(\underline{x})$ is the grey level of the homologous pixel in deformed image (at position $\underline{x}$ after the transformation). The coefficients c and b represent respectively the evolutions of contrast and brightness for the two images acquisition. g' is an additional image noise. In practice, it should be assured that deformation mechanisms don't lead to a modification of the material properties which generate the image contrast.

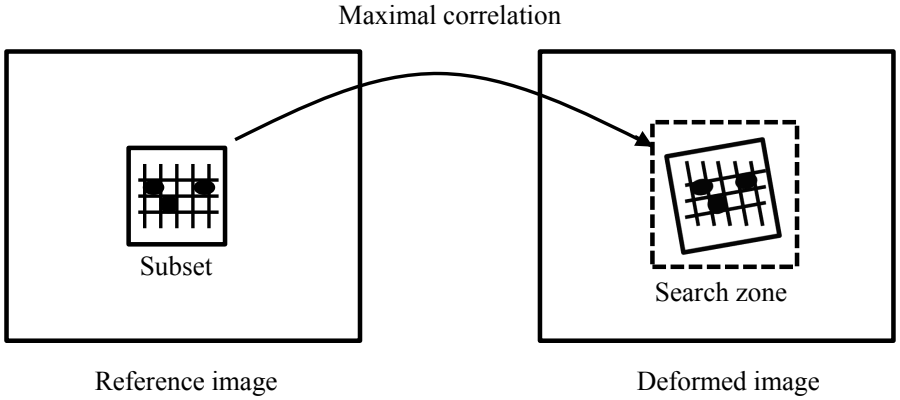

Figure 2.6: Principle of the DIC technique.

Correlation coefficient

Correlation coefficient can be defined in different terms, among which the zero-centered normalized correlation coefficient is an appropriate one for SEM imaging (Doumalin, 2000):

$$C_{ZNCC}(\phi) = 1 - \frac{\sum_{X\in D}^{D}\left[f\left(\underline{X}\right) - \bar{f}\right]\left[g\left(\underline{x}\right) - \bar{g}\right]}{\sqrt{\sum_{X\in D}^{D}\left[f\left(\underline{X}\right) - \bar{f}\right]^2 \sum_{X\in D}^{D}\left[g\left(\underline{x}\right) - \bar{g}\right]}} \quad \text{with, } \underline{x} = \phi\left(\underline{X}\right) \tag{2.3}$$

Here, $f(\underline{X})$ is the grey level at pixel $\underline{X}$ in reference image, while $g(\underline{x})$ is the grey level at pixel $\underline{x}$ in deformed image related to $\underline{X}$ by the tested transformation ϕ. $\bar{f}$ and $\bar{g}$ are means value of the intensity matrices f and g over these subsets, respectively. Note that this correlation coefficient is insensitive to the contrast and brightness evolutions, and this is a remarkable advantage of this coefficient in SEM imaging, for which such evolution can hardly be avoided.

Sub-pixel accuracy

In a digital image, the pixel is the smallest individual element so that the resolution of displacement measurement by DIC method generally can't be below one pixel. Nevertheless,

interpolation is usually used in DIC, yielding sub-pixel accuracy. In general, two interpolation ways are possible: interpolation of grey level and interpolation of correlation coefficient, of which the former has been revealed to lead to a better performance (Doumalin, 2000). For the interpolation of grey level, there are different interpolation types: bi-linear, bi-cubic, bi-quintic etc.

Approximation of material transformation

To calculate the correlation coefficient defined previously, on should know the material transformation ϕ which gives the current position $\underline{x}$ in deformed configuration of the point $\underline{X}$ in reference configuration:

$$\underline{x} = \phi\left(\underline{X}\right) \tag{2.4}$$

It can be rewritten as:

$$\phi\left(\underline{X}\right) = \underline{X} + \underline{u}\left(\underline{X}\right) \tag{2.5}$$

where $\underline{u}$ is the displacement at point $\underline{X}$. The real transformation is normally unknown, particularly it is so delicate to provide an expression for micromechanical investigations in which the deformation is quite complex and totally heterogeneous from point to point. This is why the size of correlation domains is usually chosen to be small. Consider $\underline{X_0}$ is a point in the reference image (normally the center of a correlation domain D), then the transformation of a point $\underline{X}$ in the domain D can be written:

$$\phi\left(\underline{X}\right) = \underline{X} + \underline{u}\left(X_0\right) + \frac{\partial \underline{u}}{\partial \underline{X}}\left(\underline{X_0}\right) \cdot \left(\underline{X} - \underline{X_0}\right) + \frac{1}{2}\left(\underline{X} - \underline{X_0}\right) \cdot \frac{\partial \underline{u}^2}{\partial \underline{X}^2}\left(\underline{X_0}\right) \cdot \left(\underline{X} - \underline{X_0}\right) + ... \tag{2.6}$$

This expression truncated with different orders provides different approximation of transformation ϕ on the correlation domain D. In practice, such an approximation is exclusively performed at the orders of 0 (corresponding to a translation) and of 1 (corresponding to a translation and homogenous deformation). Certainly, one can try the approximation with higher orders to describe more accurately the material transformation. For micromechanical investigations, the relative small size of D, compared to the characteristic length of local deformation phenomena, permit to reasonably assume that the domain is rigid or deforms homogeneously. This is even more true for the case of small deformation.

2.2.2 Strain measurement

The lagrangian transformation ϕ has been defined in equation 2.4, and the gradient of this transformation at $\underline{X}$ is :

$$F\left(\underline{X}\right) = \frac{\partial \phi}{\partial \underline{X}}\left(\underline{X}\right) = \mathrm{I} + \frac{\partial \underline{u}}{\partial \underline{X}}\left(\underline{X}\right) \tag{2.7}$$

where I is the second order identity tensor. The Green-Lagrange strain is defined by:

$$E = \frac{1}{2}\left(F^T \cdot F - \mathrm{I}\right) \tag{2.8}$$

where $\cdot^T$ denotes the transpose of a tensor. For the case of small deformation, typically a few percents of strain and a few degrees of rigid rotation, a linearized expression may be preferred, which is the usual "small strain tensor":

$$\varepsilon = \frac{1}{2}\left(F^T + F\right) - \mathrm{I} \tag{2.9}$$

Discrete evaluation of transformation gradient and deformation

We can find that the transformation gradient is crucial for strain measurement. Nevertheless, its evaluation is usually difficult in practice. Firstly, the displacement field is evaluated by DIC discretely on isolated points (subset center), hence, its derivate can't be known exactly and has to be assessed by some finite difference. Moreover, and more fundamentally, the derivate in equation 2.7 is ill-defined due to the multi-scale nature of the transformation: it leads to very strongly fluctuation of $F(\underline{X})$ with $\underline{X}$ and with the scale of the infinitesimal material vector $d\underline{X}$.

In practice, the theoretical derivative can be replaced by a finite difference with respect to certain gage length ΔL for 1D case and some surface Ω for 2D case. The local transformation gradient at point $\underline{X}$ is thus defined as the average of the infinitesimal gradient over the surface (Allais et al., 1994):

$$F(\underline{X}) \approx \langle F \rangle_\Omega = \frac{1}{|\Omega|}\int_\Omega F dw \tag{2.10}$$

where $|\Omega|$ is the area of Ω. Using Green's theorem, this transformation gradient can be evaluated from the displacement of its boundary (current position $\underline{x}$ and its outgoing normal $\underline{v}$ in reference configuration):

$$F(\underline{X}) = \frac{1}{|\Omega|}\int_{\partial\Omega} \underline{x} \otimes \underline{v} ds \tag{2.11}$$

where $\partial\Omega$ is the boundary of Ω.

In practice, the contour $\partial\Omega$ is chosen as a polygonal path with summits coinciding with measurement points nearby the evaluated position $\underline{X}$ and the transformation is linearly interpolated between two neighbor positions. Various choices of Ω are possible, and some schemes used in CMV are presented in Fig.2.7. Based on these assumptions, the integral (equation 2.11) can be expressed discretely for each in-plane components of $F(\underline{X})$:

$$F_{xx} = \langle F_{xx} \rangle_{\Omega} = \frac{1}{2\,|\Omega|} \sum_{n=1}^{M} x_n \left(Y_{n+1} - Y_{n-1} \right) \tag{2.12}$$

$$F_{xy} = \langle F_{xy} \rangle_{\Omega} = \frac{1}{2\,|\Omega|} \sum_{n=1}^{M} x_n \left(X_{n+1} - X_{n-1} \right) \tag{2.13}$$

$$F_{yx} = \langle F_{yx} \rangle_{\Omega} = \frac{1}{2\,|\Omega|} \sum_{n=1}^{M} y_n \left(Y_{n+1} - Y_{n-1} \right) \tag{2.14}$$

$$F_{yy} = \langle F_{yy} \rangle_{\Omega} = \frac{1}{2\,|\Omega|} \sum_{n=1}^{M} y_n \left(X_{n+1} - X_{n-1} \right) \tag{2.15}$$

where (x_n, y_n) are the coordinates of the n^{th} contour point in the deformed configuration, and (X_n, Y_n) are the coordinates of the n^{th} point in the reference configuration. In addition, the in-plane part of the deformation gradient can be decomposed into an in-plane rotation and a distorsion. The eigenvalues and eigenvectors of the latter lead to the two in-plane eigenvalues of the Green-Lagrange strain tensor ($E1$ and $E2$ with $E2 > E1$) and the angle θ between the principal direction $E2$ and vertical axis of the reference image. The definition of these quantities is presented in Fig.2.8.

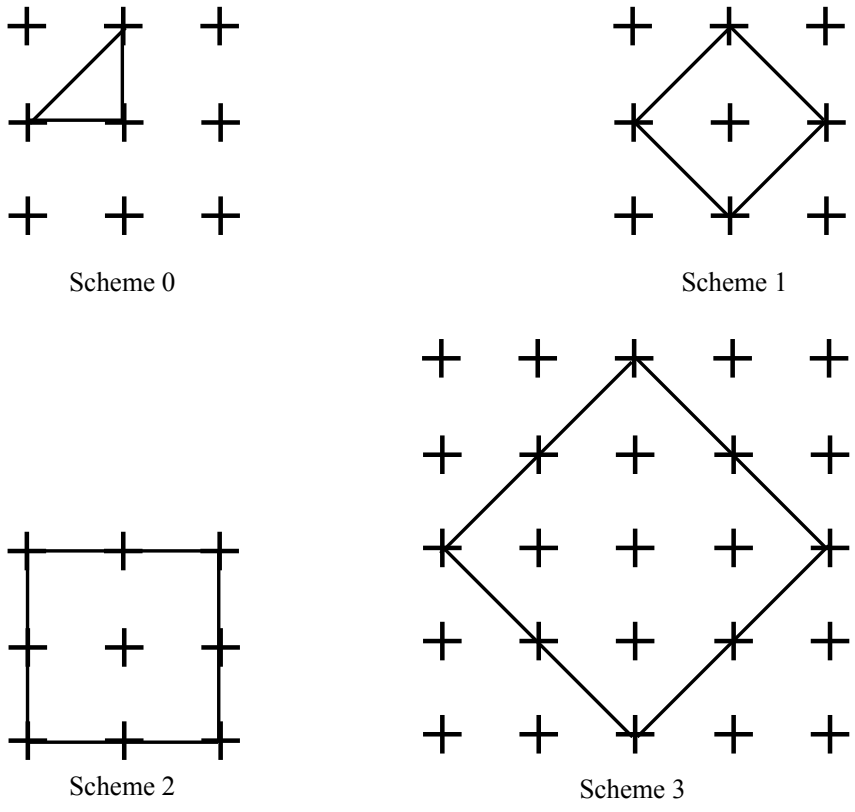

Figure 2.7: Integration schemes for deformation estimation in CMV (Bornert, 1996).

The local transformation and deformation are evaluated approximately from one small region around the considered point. Certainly, these definitions of local transformation gradients and strain tensors can be extended to any surface, based on the same integration principle. Particularly, when Ω is chosen to be the whole region of interest (ROI), the global strain of such region can be evaluated, as shown in Fig.2.8. Similarly, the average strain over a prescribed constituent of the heterogeneous material can be assessed (Allais et al., 1994).

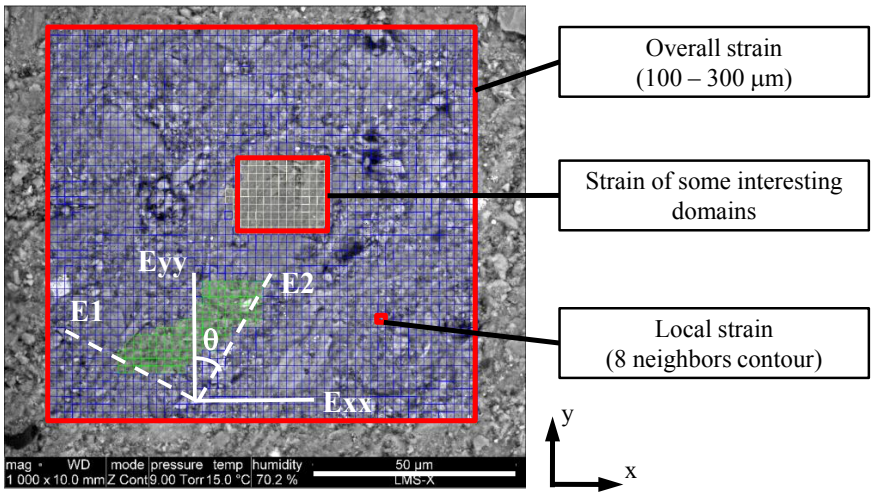

Figure 2.8: Example of discrete measurement positions on an image associated with various averaging domains, some definitions of the local and average strain components and invariants computed with CMV software.

3D issue

It is worth to note that the present evaluation of deformation field, based on a 2D imaging of sample's surface, does not give access to the components of the transformation gradient in the direction perpendicular to the observation plane, so the out-of-plane components of the strain tensor cannot be evaluated (Soppa et al., 1996). Hence, none of the components of the Green-Lagrange strain tensor can be calculated only from in-plane components of F. For the small strain tensor, only its in-plane components can be evaluated. Hence, additional assumptions is required to assess the three missing out-plane components of F. A convenient hypotheses is usually accepted that the normal axis to the observation plane coincides with the principal axis of deformation so that there is no out-plane rotation. With respect to E_{zz}, three options are generally applied: isochoric strain, plane strain , and uniaxial local strain. While the full 3D Green-Lagrange strain tensor is out-of-reach, we nevertheless make use of in-plane mean strain ($E_{is} = E1 + E2$) as a qualitative indicator of the local or averaged volume variation of the studied zone, while equivalent strain ($E_{eq} = 2(E2 - E1)/3$) is an indicator of deviatoric deformation, which would coincide with the actual 3D von Mises equivalent strain if the strain tensor would exhibit rotational invariance with respect to the second principal

direction (associated with E2).

2.2.3 Typical DIC parameters used in this work and corresponding gauge length

In this work, the microscopic observation is typically performed on certain zones with the size of 320 × 276 μm^2, corresponding to image magnification × 400 (some special cases would be specified in the following). Then, the images with high resolution (4096 × 3536) are recorded for DIC analysis. Hence, the physical length represented by a pixel is 78.1 nm. The matching-subset is typically chosen to be 30 × 30 pixels, so about 2.3 μm real physical size. According to this size of matching-subset and that of the integration domain used for calculating deformation (schema 2 in Fig.2.7), the gauge length for local strain measurement is 60 × 60 pixels, i.e. between about 4.6 μm in real space.

2.3 Strain measurement errors and improvement of its performance

DIC applied to SEM images is of interest to evaluate the strain fields at the scale of microstructure and has been widely used for the last ten years in the context of micromechanical investigations of materials (Doumalin, 2000; Héripré et al., 2007). However, its application to argillaceous rocks for our investigations is extremely delicate:

- The associated strain for argillaceous rocks is extremely small in this study. For example, the deformation under hydric loadings is in order of 10^{-3} for a 10%RH change. Such small deformation level places high performance on the strain measurement.
- Comparing to conventional high vacuum condition in SEM, environmental mode in ESEM is an unfavorable condition for observation. In particular, the presence of vapor would degrade the quality of the images recorded in such mode.

Therefore, care should be taken to an appropriate accuracy for the combination of ESEM and DIC techniques. Errors depend on many factors and are more difficult to control than in the context of macroscopic DIC using optical images. In addition to "intrinsic" errors of DIC algorithms induced for instance by shape function mismatch (Bornert et al., 2009) or inaccurate subpixel image restoration by inappropriate grey level interpolations (Wang et al., 2009), there are many potential sources of "extrinsic" errors when using ESEM images, such as scanning instability due to beam drift or fluctuations of digital/analog converters used in the scan generators, undersampling induced by the discrepancy between spot size and pixel size, high image noise levels, magnification fluctuations and other geometric errors due to imperfect

alignment and image distortion (Doumalin, 2000). Some of these errors have been investigated and the procedures to control or correct them have been proposed (Cornille, 2004; Doumalin, 2000). An important study has been performed by Cornille who proposed a procedure to calibrate a SEM and to control its geometric errors. However, such procedure is very time consuming and can hardly be used in practice in the context of in situ mechanical testing (Héripré et al., 2007), essentially because of the long integration time of SEM images: recording of high definition images used in the context of a multiscale analysis often requires several minutes.

The aim of this section is to present simple methods to characterize and quantify three main errors: ESEM image noise, geometric error and systematic error. Then, the optimization and improvement of imaging by ESEM and strain measurement are performed.

2.3.1 SEM image noise

SEM image noise induces errors in displacement evaluation by DIC algorithms which scale linearly with noise levels (Roux and Hild, 2006). Indeed, noise levels in SEM images can reach rather high levels with respect to optical images, acquired with conventional modern CCD cameras, in which noise levels are usually limited to one or two grey levels on a total of 256 levels (8-bits cameras), and can even be smaller on high end cameras. With older SEMs such low levels could hardly be reached (Doumalin, 2000) during a single scan. Image averaging procedures could be adopted to reduce this noise, but image drift can then seriously limit the spatial resolution of images. On more recent SEMs, image noise can be reduced to significantly lower levels thanks to, first, higher electron fluxes in incident beam, especially in SEMs equipped with a field emission gun (FEG) and, second, to improved general efficiencies of detectors.

However, image noise still depends on many factors such as detector mode (secondary -SE- or back-scattered electrons -BSE-, in high or low vacuum conditions, or even in environmental mode), kinetic energy of incident electrons (voltage), intensity of electron beam (controlled by spot size and gun apertures), dwell time, brightness and contrast setups of the detectors and the analog/digital converters, etc. In addition, as contrast in SEM images are essentially the consequence of complex interactions of electrons and matter, noise levels also depend on the material under investigation, and its surface preparation, and might evolve with time because of material evolution. Finally, in low vacuum conditions (pressure in ESEM chamber up to 200 Pa) or under environmental conditions (pressure up to 2600 Pa), interactions of the incident and emitted electrons with the molecules of the surrounding gas play a fundamental role in image -and therefore noise- generation.

Such complex phenomena need to be mastered to optimize parameter settings. Though the skill of an experienced microscopist is essential to obtain good images, it might also be useful to build quantitative models to predict image properties as a function of setting parameters,

for first, a better understanding of the physical processes at the origin of image generation, and second, to optimize parameter settings. This is in particular of interest in the context of mechanical in situ testing, where a compromise between image noise and acquisition time of high definition images needs to be defined.

2.3.1.1 SEM image noise

In optical camera or SEM images, grey levels reflect statistics of discrete and independent events: photons or electrons received by detectors. As such, they carry an intrinsic noise, the standard deviation of which is proportional to the square root of its expectation, as standard statistics show. More precisely, if N is the number of discrete events counted by the detector, $E(N)$ its statistical expectation, then $\sigma_N = \sqrt{E(N)}$ is its standard deviation. Total noise results of the combination of this photon (electron) noise with other sources of noise, such as thermal and read-out noise for optical systems. The relative proportions of each noise source depend on acquisition conditions.

Total noise can be quantified by averaging a large number of images of a fixed device and computing average and standard deviation of recorded grey levels. This can be done globally, for all pixels of an image, or grey level per grey level or even pixel per pixel for a better characterisation of noise.

However, such a procedure may fail for SEM images because their recording is generally slow and suffers from beam drift with time passing and possible evolutions of imaging conditions. A less time-consuming method is proposed and turns out to be sufficient to seek the noise for each grey level (or narrow grey level interval), instead of for each pixel. It is based on the hypothesis that the same grey level for different pixels corresponds to the same amount of electrons detected, which carry the same statistical electron noise. Therefore, the noise investigation can be restricted to two images A and B and to plot the standard deviation of grey levels, which can be evaluted by the difference of the two images $\frac{A-B}{2}$, for all pixels that have the same grey level average $\frac{A+B}{2}$ as a function of the latter. More specifically, the grey level at pixel x can be given the form $A(x) = E(A(x)) + A'(x)$ where $A'(x)$ is the random noise to be characterized. If the two images are acquired with similar conditions, then $E(A(x)) = E(B(x))$ and the difference is $A(x) - B(x) = A'(x) - B'(x)$. Assuming independent and statistically identical noises in the two images, one has simply $\sigma_{A-B} = \sqrt{2}\sigma_A = \sqrt{2}\sigma_B$. With the above assumption, standard deviation can be evaluated from the standard deviation of $A - B$ for all pixels that carry the same average grey level $\frac{A+B}{2}$. In addition, this average can be considered as a good evaluation of the expectation of $E(A(x))$, since usually grey levels fluctuation remain small with respect to their average value. For higher noise levels, or in the case of small images for which the number of pixels carrying the same average grey level might be too small, this analysis might be performed for grey level intervals: the standard deviation of the grey levels for all pixels whose average $\frac{A+B}{2}$ belongs to a given interval is then plotted agains the center of

the interval.

It should be noted that this analysis has to be restricted to pixels for which grey levels are not saturated. Indeed, A and B belong to $[0, A_{\max}]$, one has $-\frac{A+B}{2} \leq \frac{A-B}{2} \leq \frac{A+B}{2}$ and $\frac{A+B}{2} - A_{\max} \leq \frac{A-B}{2} \leq A_{\max} - \frac{A+B}{2}$. So noise levels are only accurately evaluated at pixels for which the difference $A - B$ is strictly inside these intervals. Pixels which do not satisfy these conditions are removed from the analyses. Figure 2.9 illustrates this remark: each blue dot corresponds to a couple $(\frac{A+B}{2}, \frac{A-B}{2})$, while the red line gives standard deviations. The blue cloud is bounded by the green lines corresponding to the above intervals and the red line can not be evaluated for grey level for which the blue cloud attains the green bounds. Another difficulty might be induced by small evolutions of imaging conditions between the recording of image A and B, which might modify grey scales between the two images, or induce a spatial shift of the second image with respect to the first one. Some specific algorithms might then be used to adjust the grey scale of the second image to the first one, and/or to associate corresponding pixels in the two images. For the sake of brevity, these procedures won't be described here.

Photon noise in camera images

In optical camera imaging, grey levels are estimated by conversion of electric charges proportional to the amount of photons which are detected by the photoactive region of the CCD (charge-coupled device). This conversion can be expressed as:

$$S(X,T) = c(T) \times N(X,T) \tag{2.16}$$

where $S(X,T)$ is the grey level of the pixel X for an integration time T, and $c(T)$ is a conversion factor that links $S(X,T)$ to $N(X,T)$, the number of photons received by the detector, which is a random variable. Therefore, camera images carry a statistical photon noise, which can be described by a Poisson process: if $\bar{N}$ photons arrive at a point (for digital image, it is pixel) in a given time T on average, their fluctuation should be around $\sqrt{\bar{N}}$. Therefore, a classical photon noise model presenting optical image noise is:

$$\sigma\big[S(X,T)\big] = \sqrt{c(T) \times E\big[S(X,T)\big]} \tag{2.17}$$

where $\sigma(S(X,T))$ is the standard deviation of the grey level at pixel position X which quantifies its noise level and $E(S(X,T))$ is the statistical expectation of its grey level. In this model, the standard deviation of grey level is the square root of its mean value, and this has been confirmed by the experimental results shown in figure 2.10, obtained from the analysis of two consecutive images recorded with a 12-bits 16 Mpixel camera, whose CCD sensor (Kodak KAI 16000) has a $N_{\max} = 30000$ electrons saturation signal. The noise curve measured with the above described procedure nicely fits the photon noise model, including in terms of numbers of electrons at saturation, as the interpolation of the measured curve corresponds to $N_{\max} = 28556$ electrons. The only discrepancy is observed for low grey levels: the experimental curve does not start

from zero. This is attributed to the other noise sources such as thermal or read-out noise, which are essentially independent on grey level. Under the present acquisition conditions, it is however noted that these other sources of noise can be neglected with respect to photon noise, as illustrated by the difference between the blue (photon noise only) and green (total noise) curves. Remark also that the last point of the curve corresponding to the maximal grey level is false because of the above mentioned saturation effects.

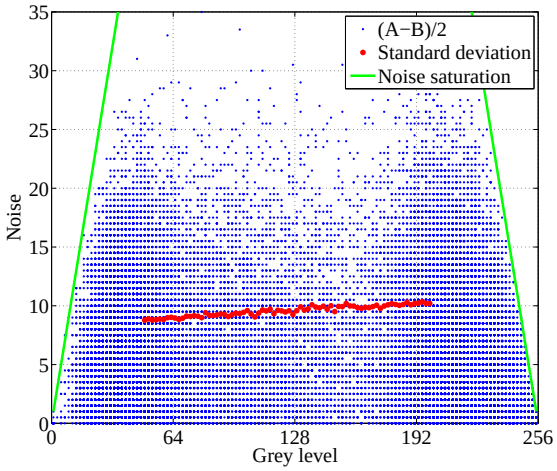

Figure 2.9: Electron noise in a 8-bits SEM image.

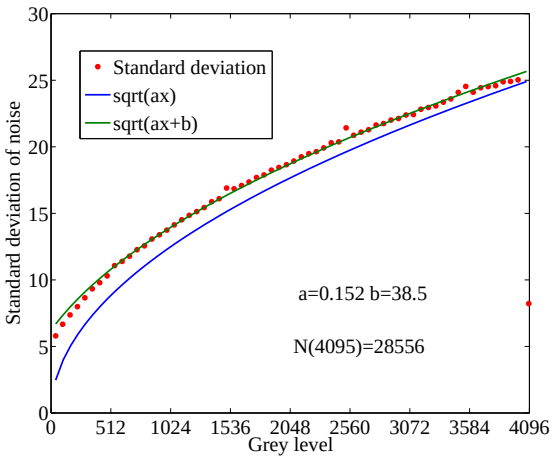

Figure 2.10: Photon noise in a 12-bits camera image.

SEM image noise model

As for camera imaging, SEM images carry the Poisson noise of the electrons (secondary electrons or back-scattered electrons) received by the detector, instead of photons. The noise diagram of Fig.2.9 obtained from a secondary electron mode image in high-vacuum condition shows that the classical photon noise model does not describe the SEM image noise anymore.Unlike camera images, the image contrast and brightness setup can be modified on a wide range with strong consequences on image and noise levels. This can be performed at the level of the detector itself (e.g. by the application of a polarization voltage on the scintillator of SE detector) or at the level of the electronic signal amplifiers. A consequence of this fact is that a zero grey level in an image might not coincide with the absence of electrons on the detector, or more generally that grey levels are no longer directly proportional to electron counts. A new model is thus proposed which extends the classical photon noise model by the addition of a coefficient $b(T)$ which is linked to image brightness setup. Taking into account contrast and brightness setup during SEM imaging, an affine contrast/brightness setup model is applied to describe the conversion from physical signal to digital signal, and equation (2.16) is rewritten as:

$$S(X,T) = c(T) \times \big(N(X,T) - b(T)\big) \tag{2.18}$$

where $N(X,T)$ can also be expressed as:

$$N(X,T) = b(T) + \Delta N(X,T) \tag{2.19}$$

The coefficient $b(T)$ is a constant which is independent of pixel position and $\Delta N(X,T)$ is the fluctuation around $b(T)$. The latter coefficient can be assimilated to the number of electrons received by the detector for a null grey level. Introducing new conversion formula but still assuming that electron counts obey Poisson statistics, SEM image noise model becomes:

$$\sigma\left[S(X,T)\right] = \sqrt{c(T)} \times \sqrt{E\big[S(X,T)\big] + c(T) \times b(T)} \tag{2.20}$$

If we suppose that $\Delta N(X,T) << b(T)$, equation (2.20) can be linearized with respect to $\frac{\Delta E(N(X,T))}{b(T)} = \frac{E(S(X,T))}{c(T)b(T)}$ in the form :

$$\sigma\left[S(X,T)\right] = c(T) \times \sqrt{b(T)} + \frac{E\big[S(X,T)\big]}{2\sqrt{b(T)}} \tag{2.21}$$

For SEM image noise, the relation between standard deviation and mean value of grey level thus reads $\sqrt{ax+b}$ (equation 2.20) or $a'x+b'$ with approximation (2.21). Note that figure 2.9 confirms the coherence with this approximation. By using equations 2.18, 2.20 and 2.21, the amount of electrons received by the detector corresponding to a grey level can be estimated:

$$\text{for the noise model} \quad \sqrt{ax+b} \quad \text{by} \quad N(X,T) = \frac{b}{a^2} + \frac{S(X,T)}{a} \tag{2.22}$$

$$\text{and for the noise model} \quad a'x+b' \quad \text{by} \quad N(X,T) = \frac{1}{(2a')^2} + \frac{S(X,T) \times 2a'}{b'} \tag{2.23}$$

The amount of electrons received by the detector can be used to optimize SEM setting parameters owing to the advantage of this parameter: it represents the intrinsic statistical electron noise, that essentially generates SEM image noise, regardless of contrast and brightness setup. The characterization of image quality by the amount of received electrons shows an appropriate performance for HV and LV modes, as shown in the following section. However, it doesn't work well for environmental mode (perhaps some specific physic phenomena are not incorporated in our proposed model). Hence, SEM image noise will be retained for the optimization of setting parameters for environmental mode.

2.3.1.2 Validation with two different materials

The SEM image model validation is performed for a large number of images recorded with different SEM setting parameters and two different materials: a metallic material, the Ag/Fe

blend (Fig.2.11) and a geological material, the argillaceous rock (Fig.2.12). The choice of these two materials will allow the validation of the model with two different types of images. The Fe/Ag specimen provides highly contrasted images due to the two phases Fe and Ag compared to claystone. Moreover, the images of argillaceous rocks will be taken in low vacuum conditions, that means that there is an influence of SEM chamber pressure on image quality and on the number of detected electrons. For each specimen, a series of images are obtained with different dwell time keeping other parameters constant. SEM images of Fe/Ag blend specimen are taken with standard setting parameters for the metallic material, i.e. with secondary electron detector in high vacuum condition. As for argillaceous rocks, images are taken in low vacuum mode and with back-scattered electron detector. The latter permits to have more contrasted images and low vacuum mode aims at imaging the specimen without any gold sputtering on its surface. For every condition, brightness and contrast are modified so that grey levels spread over the full available range without saturation. The histograms of images are presented in Fig.2.11 and 2.12. It is noted that the peaks of histogram present always the same compositions of material regardless their grey level that can be modified by contrast and brightness setup. For example, the two peaks correspond to Fe and Ag phases in Fig.2.11. This is used to later estimate the amount of electrons corresponding to a certain composition of material.

The noise model is applied to images of these two materials taken with 5 different dwell times (Fig.2.13 and 2.14). Remark that image noise (appear in grey level) decreases with dwell time. This is attributed to the increase of the number of electrons arriving for the same grey level with a longer dwell time. It is interesting to note that noise increases with the amount of electrons (correlated with grey level) for a fixed dwell time, while it decreases with the electron number when dwell time varies (Wang et al., 2010). This is essentially due to the impact of contrast and brightness setup on noise amplitude, which can be explained by the model proposed. For a fixed dwell time, it is easy to note that noise increases with grey level from equation 2.20 and 2.21. Besides, when we change dwell time, it needs usually an adjustment of contrast and brightness to obtain a “wide” histogram, and that would vary the noise amplitude as well. For example, there are $N(t)$ electrons detected corresponding to a contrast $c(t)$ for a pixel, and this number will reach $nN(t)$ for a longer dwell time for the same pixel, therefore the contrast value has to be adjusted to $\frac{c(t)}{n}$ so as to obtain the same grey level (assuming for simplicity there is no brightness adjustment), which will reduce the noise from equation 2.20 and 2.21.

2.3.1.3 Application of model to noise reduction

An important study has been performed by Doumalin (2000), who investigated, by means of real and simulated images, the impact of image noise on displacement measurement accuracy. The results showed an important error due to image noise, as well as an increasing error with noise amplitude. A More recent theoretical analysis confirms this tendency (Roux and Hild,

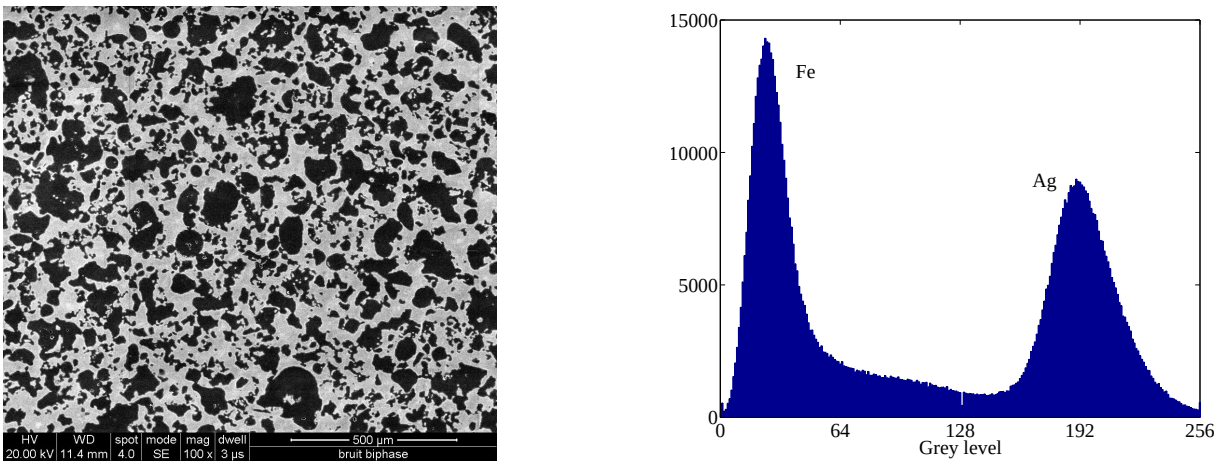

Figure 2.11: SEM image of Fe/Ag blend and its histogram, SE mode, high-vacuum condition, 20kV, spot 6.

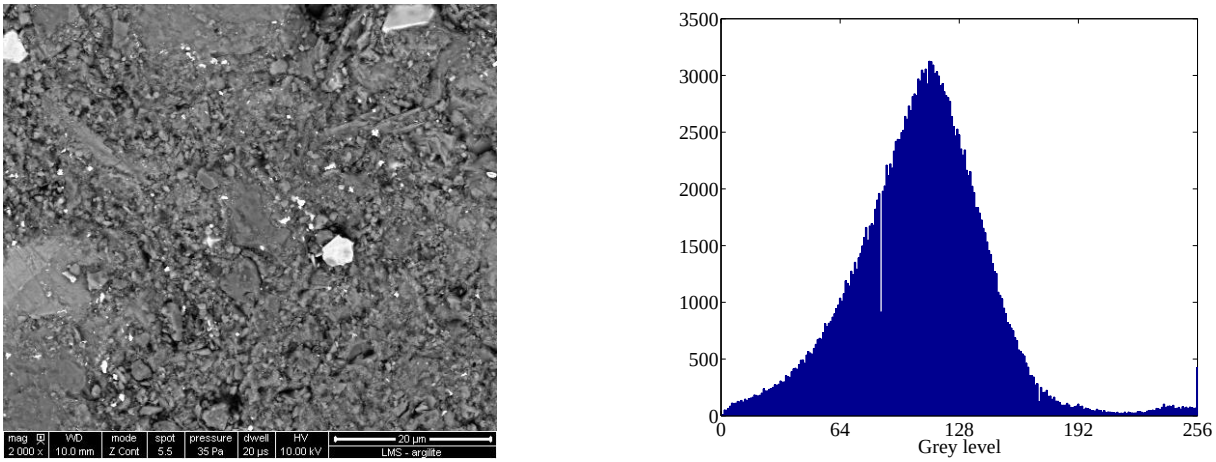

Figure 2.12: SEM image of argillaceous rocks and its histogram, BSE mode, low-vacuum condition (35Pa), 10kV, spot 5.5.

2006). Therefore, it is necessary to reduce image noise for the strain field measurement using DIC and SEM imaging, especially in micromechanical investigations. Since SEM image noise is essentially random, image averaging (integration) has been shown to be an effective method for minimizing the effect of noise (as shown in Fig.2.15): a smaller grey level and more images carry a lower noise level. Moreover, we focus on another approach: optimizing the setting parameters of imaging. The model proposed in the preceeding section is applied to optimize the choice of setting parameters: dwell time, spot size, working distance (WD) and ESEM chamber's pressure in this study.

As shown in the previous section, SEM image noise is essentially due to statistical electron noise. The number of electrons detected by the detector is an intrinsic factor that conditions image noise amplitude. As the study of dwell time impact on noise in 2.3.1.2 has enhanced, noise decreases with the amount of electrons detected for a given grey level. Therefore, the

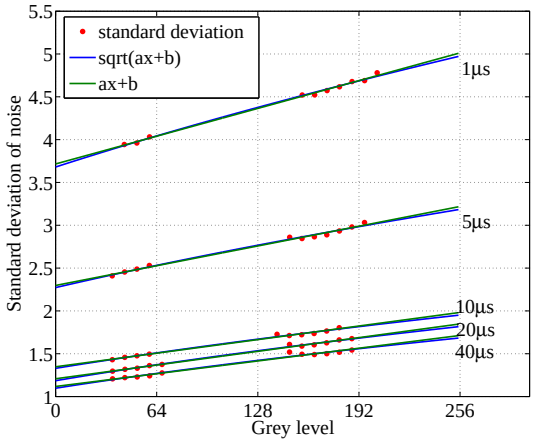

Figure 2.13: Standard deviation of Fe/Ag blend image noises and validation of the noise model.

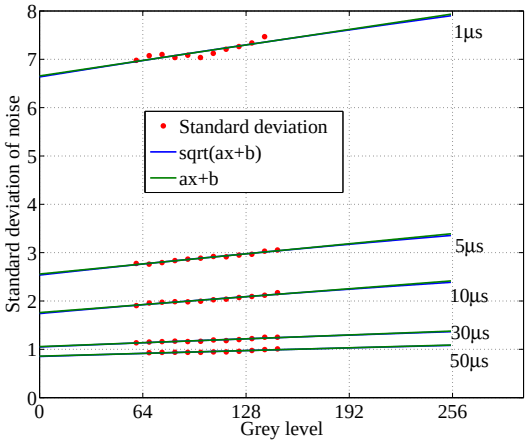

Figure 2.14: Standard deviation of argillaceous rocks image noises and validation of the noise model.

amount of detected electrons, which can be estimated by the model proposed, is used as the parameter representing SEM image noise level. A major advantage of this parameter is that it can eliminate the effects of contrast/brightness setup, which might help to exhibit intrinsic statistical electron noise.

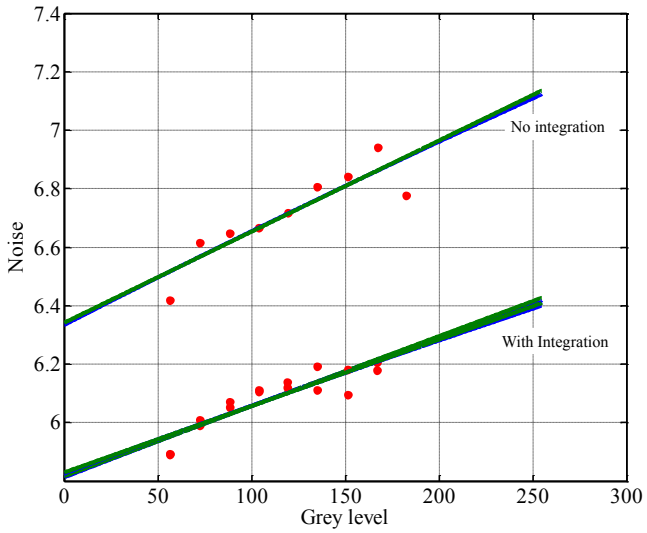

Figure 2.15: Improvement of image quality by integration. Image acquisition condition: BSE mode, 15 keV, ESEM (5.1 Torr = 678 Pa), WD = 10.4 mm, Dwell time = 30 ms/pixel, Spot size = 5.

Evaluation of the amount of electrons captured by the detector

The proposed model can give an interesting information: the amount of electrons that are detected by the detector for a chosen grey level corresponding to one composition of material.

In our study, the amount of the secondary electrons detected corresponding to Fe (the first peak of the grey level histogram) is estimated for the Ag/Fe blend (Fig.2.16), as well as the number of back-scattered electrons detected corresponding to the peak of the claystone histogram (Fig.2.17). It shows that the evolution of the amount of electrons detected varies linearly with respect to dwell time, at least for short dwell times, which demonstrates once more the validity of the new model. Note also that the number of electrons estimated this way are favorably compared with other more direct measurements by Faraday cup.

However, from Fig.2.16, an apparent saturation phenomenon of the detector is observed. This saturation phenomenon is not observed in Fig.2.17 for BSE. The origin of the saturation effect is not clear at this stage. It might be due to an intrinsic saturation of the detector which would be unable to count more electrons than a given threshold, so that SEM image noise would remain almost unchanged regardless the increase of electron number above this threshold. But it might also be attributed to an artifact of our procedure, induced by small image shifts when the sample is scanned with a long dwell-time, generating an apparent noise in the A-B image, not representative of the actual noise. Indeed, all SEM systems exhibit unanticipated image shift during the scanning process. Image shift derives from various sources, such as specimen charging, electromagnetic field fluctuation and environmental factors (e.g., thermal fluctuation, mechanical vibrations) (Sutton et al., 2009). Further investigations are required to discriminate apparent noise due to image shifts from actual random noise.

For low vacuum mode

For low vacuum mode, three main parameters (dwell time, spot size and pressure) are analyzed. From Fig.2.17 and 2.19, a longer dwell time and a larger spot size can remove the background noise in SEM images. This is attributed to the increase of the intensity of the electrons emitted by the interaction between primary electron and specimen. However, it is important to note that a long dwell time is not always favorable: image acquisition time should be as short as possible in the context of *in situ* mechanical testing in order to limit the specimen relaxation for instance, as well as image shift accompanying a long image acquisition time. Compared with high-vacuum conditions, noise level is higher in low vacuum condition for which the gas pressure in the specimen chamber plays an important role. Fig.2.18 shows that noise amplitude increases with pressure, that can be readily attributed to the interaction between gas molecules and electrons.

For environmental mode (ESEM)

Comparing to high vacuum and low vacuum modes, environmental mode (ESEM) is indeed an unfavorable condition for observation: image quality is much degraded by the presence of abundant vapor in ESEM chamber. Hence, special attention has to be paid to optimize the parameters for image acquisition, ensuring an appropriate image noise level for DIC analysis.

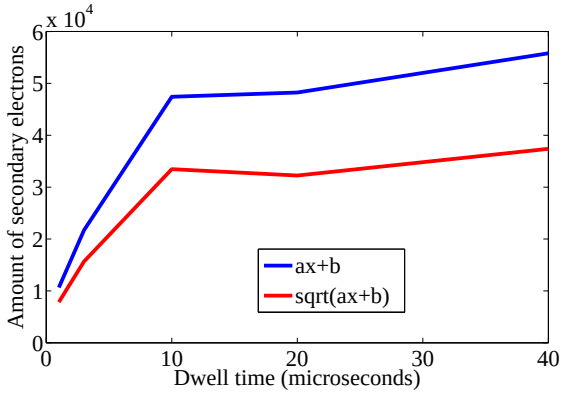

Figure 2.16: Estimation of the amount of SE received by the detector during imaging the Fe/Ag blend (grey level for Fe phase).

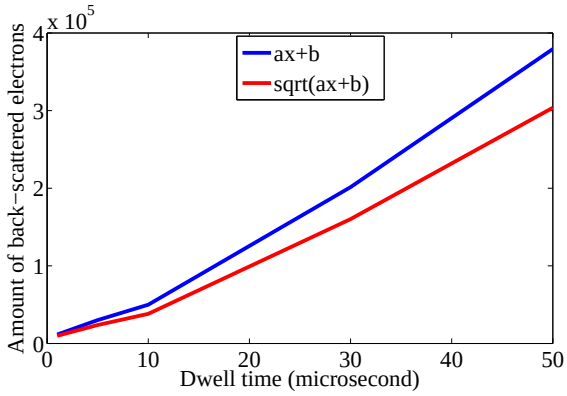

Figure 2.17: Estimation of the amount of BSE received by the detector during imaging arigllaceous rocks (grey level for histogram peak).

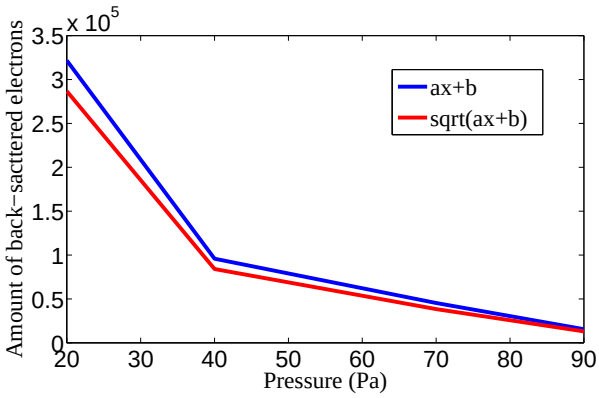

Figure 2.18: Evolution of the amount of electrons received with pressure. Image acquisition conditions: BSE mode, 10 keV, Dwell time = 30μs/pixel, Magnification $\times$2000, Spot size = 5.5

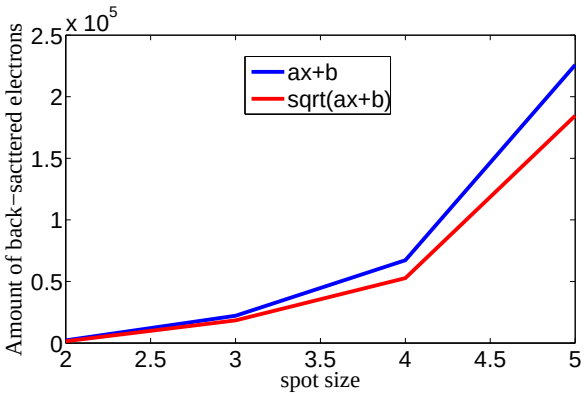

Figure 2.19: Evolution of the amount of electrons received with spot size (SEM units). Image acquisition conditions: BSE mode, 10keV, Dwell time = 30μs/pixel, Magnification $\times$2000, Pressure = 35Pa.

In this work, we focus on four main parameters: diaphragm, dwell time, chamber pressure, and working distance (WD). The evolutions of image noise in function of these parameters are shown in Fig.2.20 - 2.23.

It is shown that ESEM image noise becomes less significant for a big diaphragm (with smaller diaphragm value) and a long dwell time. This is essentially due to the increase of primary electron intensity by these effects. Similarly, the decrease of chamber pressure yields a better image quality since there is less perturbation of the vapor on the primary and emitted electrons. For example, the noise reaches nearly 7 grey levels on a total of 256 levels (8 bits) for 9 Torr ($\times$ 133 Pa/Torr = 1197 Pa) chamber pressure, whereas, it decreases to about 3.5

grey levels when chamber pressure is 1.8 Torrs.

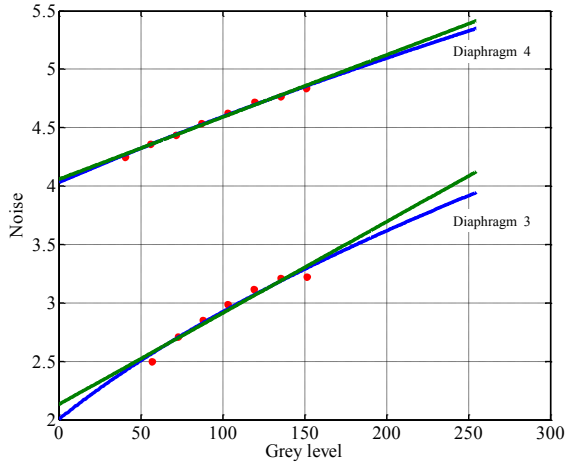

Figure 2.20: Influence of diaphragm on ESEM image noise. Image acquisition conditions: BSE mode, 15 keV, Spot size = 5, ESEM (4.05 Torr = 539 Pa), WD = 10.0 mm, Dwell time = 40 μs/pixel.

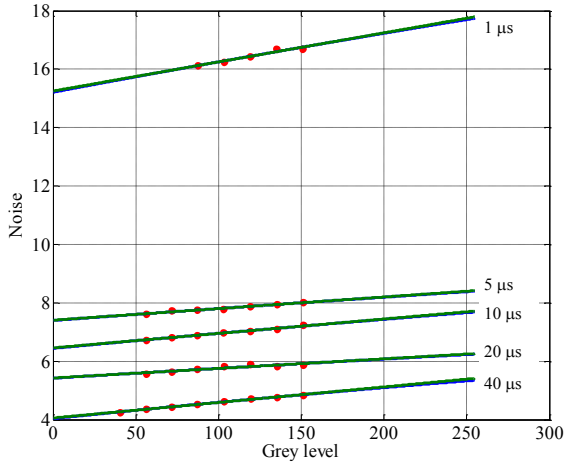

Figure 2.21: Influence of dwell time on ESEM image noise. Image acquisition conditions: BSE mode, 15 keV, Spot size = 5, ESEM (4.05 Torr = 539 Pa), WD = 10.0 mm. Diaphragm = 4.

The evolution of ESEM image noise with WD variation is shown in Fig.2.23, which can be distinguished by two regions: noise decreases when WD decreases from 11.4 mm to 10.4 mm (region 1), nevertheless, it increases again when WD decreases down to 10.1 mm (region 2). This suggests that WD decreasing doesn't always improve image quality, as expected a priori: the decrease of WD would reduce the gap (between the final PLA and sample's surface) so that both primary electrons and emitted signals are less perturbed. This is the principal reason controlling the increase of noise with WD in region 1.

However, the origins of the re-increase of noise with decreasing WD in region 2 are not clear. As discussed in section 2.1, there is an optimal WD for GSED under the combination of skirt effect and ionization amplification, nevertheless, the noise of GAD should increase monotonously with WD under the single skirt effect. We suggest here a possible explanation: geometric effect due to GAD detector's cone. In fact, besides the receiving signal device, GAD detector is also composed of a cone, which serves as the final PLA so that the unfavorable skirt effect can be greatly diminished. Nevertheless, the cone would hinder the detector from gathering signals and only a portion of the emitted BSE (the scattered angle should be bigger than a threshold) can be received by the detector (see Fig.2.24). When WD decreases, the angle threshold increases and the percentage of the emitted BSE received by the detector turns to be smaller. Actually, the effect of WD for GAD in ESEM observation is also a compromise of two effects: decreasing WD would reduce vapor perturbation on primary and emitted electrons, while it leads to less signals being received by the detector due to the geometric effect of the

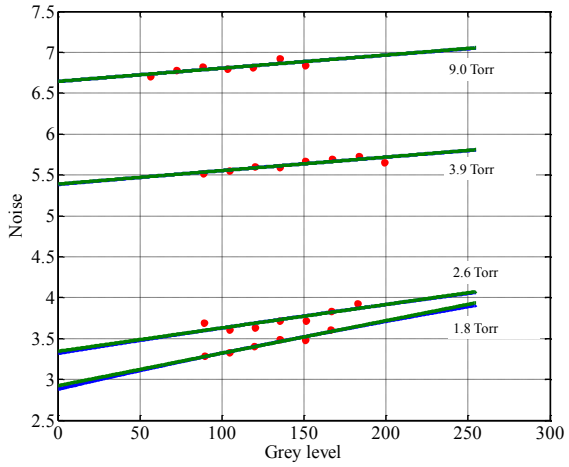

Figure 2.22: Influence of chamber pressure (1 Torr = 133 Pascal) on ESEM image noise. Image acquisition conditions: BSE mode, 15 keV, Spot size = 5, WD = 10.4 mm, Dwell time = 15 μs/pixel.

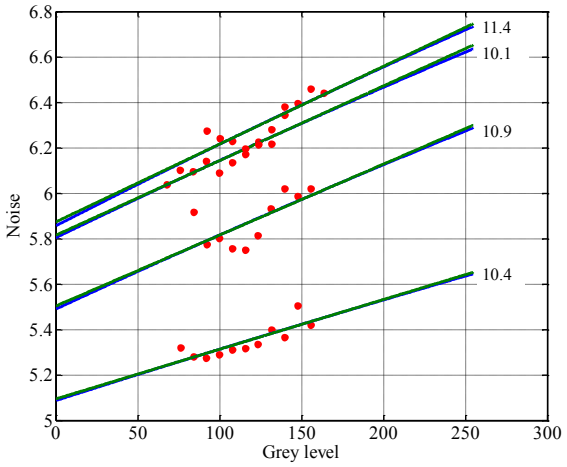

Figure 2.23: Influence of working distance (mm) on ESEM image noise. Image acquisition conditions: BSE mode, 15 keV, Spot size = 5, ESEM (5.1 Torr = 679 Pa), Dwell time = 40 μs/pixel.

cone. Hence, there is a optimal value (10.4 mm for our case) if the other acquisition conditions (primary electron energy, chamber pressure, nature of observed material etc.) are fixed. This is similar to the case of GSED, which are however due to different origins.

It should be noted that the influence of WD remains however small (in the WD range of our test): the noise reduction when WD changes from 11.4 to 10.1 mm is less than 20%. This is probably attributable to a combination of two effects: skirting effect and geometric effect of detector's cone which lead respectively to an increase and a decreasing tendency of image noise with WD.

2.3.2 Geometric error

One of the most important extrinsic error is magnification variation. During the loading of the specimen, the working distance would be modified, and the operator may need to adjust the focus distance. This WD changing would lead to magnification variation, consequently, an apparent deformation emerges even if the sample is undeformed. Such an error due to out-of-plane motions of the sample leads to great issue for optical system, nevertheless, it shouldn't exist a priori for SEM due to its completely special magnification mechanism (discussed in section 2.1.1). Accuracy of magnification is essentially linked to the accuracy of the (x, y) scanning coil, and thus strongly dependent on the SEM technology. Indeed, magnification is much less accurate in older SEMs (see (Doumalin, 2000)) than the more recent ones.

A test evaluating the error by varying WD is performed in this work by the procedure as follows: a series of altitudes Z (the physic position of the stage) is chosen for observing an

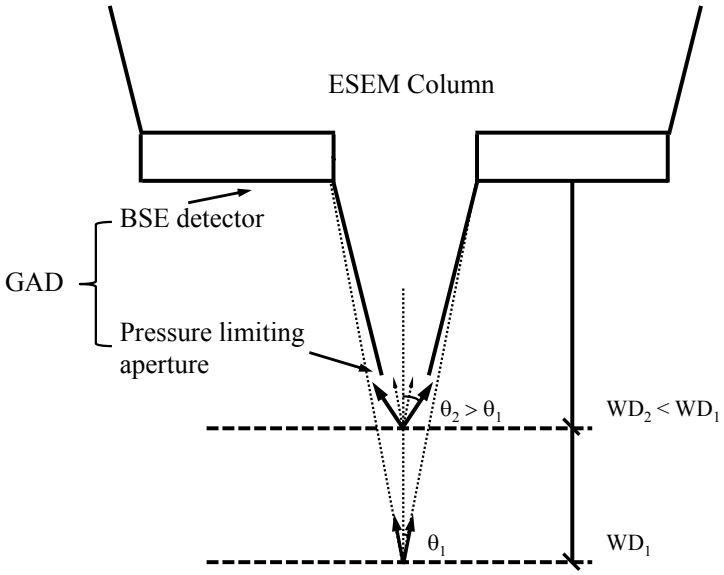

Figure 2.24: Geometric effect of GAD's cone on gathering signals in ESEM.

undeformed specimen; and the focused images (by adjusting WD) for each Z value are recorded and their relative deformations are evaluated by DIC. The image acquisition conditions are: 512 × 471 (resolution), 35 Pa (chamber pressure), 5.5 (spot size), 30 μs/pixel (dwell time). The correlation domain is 30 × 30, and schema 2 is chosen to be the integration schema (refer to Fig.2.7).

The results are shown in Fig.2.25 and 2.26. It should be noted that the apparent scaling deformation evolution with altitude Z in Fig.2.25 is not a conventional magnification variation mentioned above, but related to the effect of secondary magnetic field. In fact, adjusting WD in SEM is achieved by varying magnetic lens' courant, which simultaneously generates a secondary magnetic field. This secondary magnetic field results in an inaccurate WD, and magnification readout. Hence, a Degauss processing should be carried out to decreasing or eliminating the unwanted magnetic field and put all currently used electron lens to a normalized state by removing their hysteretic effects. By means of this Degauss processing with focused image, one can obtain the most accurate magnification and WD readouts and the apparent magnification variation will disappear, as shown in Fig.2.26. The apparent deformation in Fig.2.26 is essentially due to image noise, and the errors related to Degauss processing. The magnification fluctuation is normally smaller than 10^{-3}, which suggests the potential accuracy of global strain measurement.

2.3.3 Systematic error

Systematic error is essentially due to the inaccurate subpixel image reconstruction by imperfect grey level interpolation used in the DIC technique. This error is dependent on the properties of

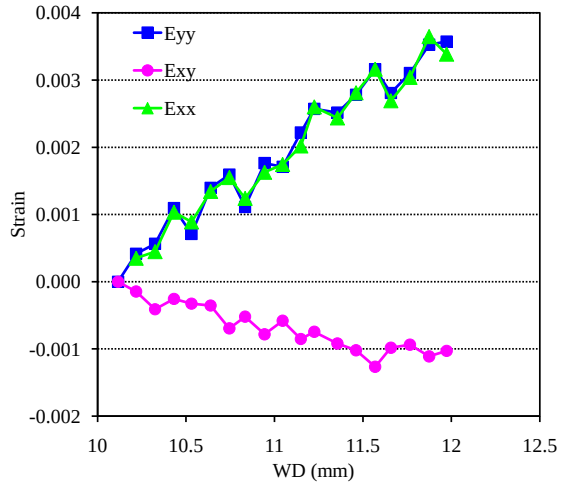

Figure 2.25: Magnification variation in function of the altitude Z (without Degauss).

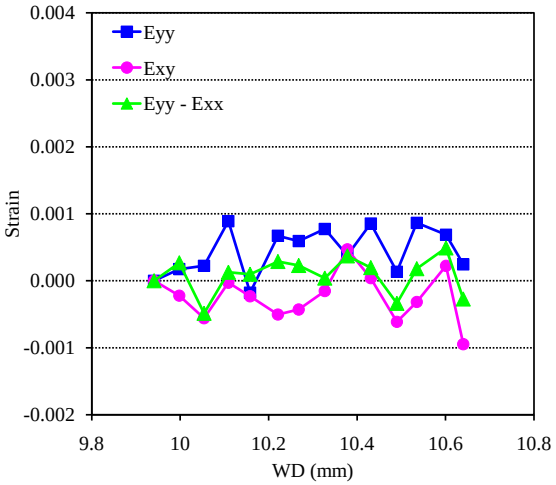

Figure 2.26: Magnification variation in function of the altitude Z (with Degauss).

the interpolators, and the characteristic of the image contrast, which is due to physical properties of both the sample and the imaging device. In DIC analysis, correlation coefficient must be assessed at non-integer locations to obtain subpixel accuracy. Therefore, interpolation must be performed on grey levels and grey level derivatives. The bias between the reconstructed intensity pattern (by interpolation) with the real intensity pattern is the origin of systematic error. When the sub-pixel location is determined by matching a reference image and an interpolated image, such bias due to interpolation is well-defined depending on the subpixel position (Schreier et al., 2000). For example, Wattrisse et al. (2001) found the bias evolution with subpixel position is approximately an inverse sinusoidal function when using bi-cubic spline interpolation. Systematic error, resulting in considerable apparent strain (the slope of the systematic error function), leads to great issue for the usefulness of DIC for strain measurement, particularly in the small deformation cases (such as the deformation of argillaceous rocks involved in this work). A typical illustration of systematic error in strain maps is shown in Fig.2.27, in which some regular vertical and horizontal deformation bands are respectively observed in Exx and Eyy maps.

Following the model proposed by Wang et al. (2009) and using the similar notions, the bias of the displacement measurement by DIC (u_e) is the difference between the measured displacement (u') and the exact motion (u_0):

$$u_e = u' - u_0 \tag{2.24}$$

The bias is null for exact estimation, nevertheless, it is mostly not the case in practice due to image noise (σ) and systematic error.

Concerning systematic error, interpolation bias is the difference between the reconstructed

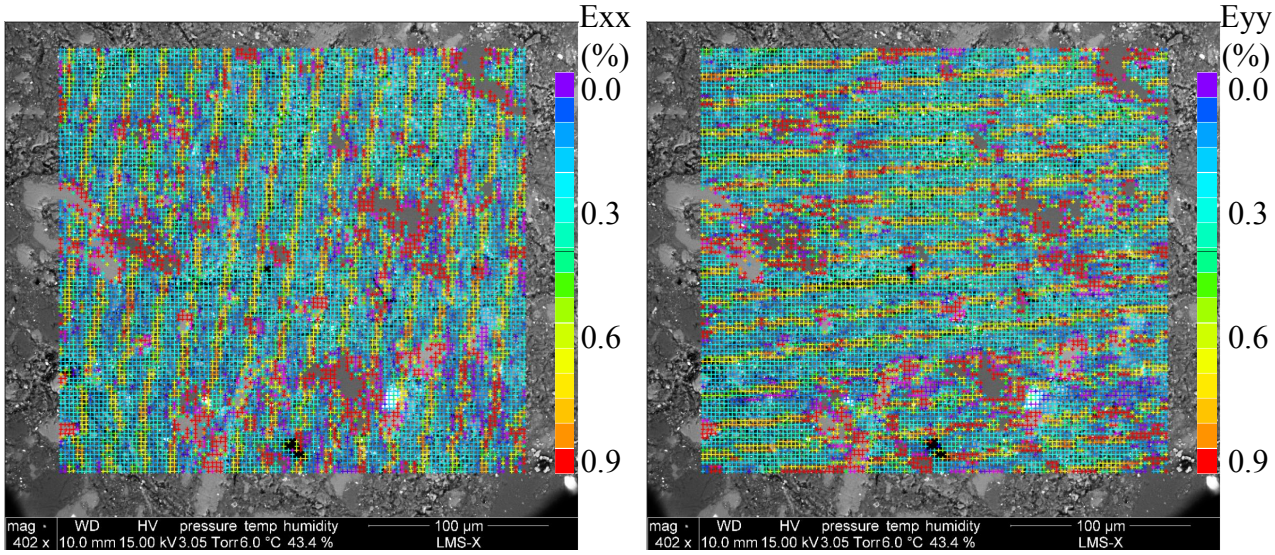

Figure 2.27: One example of systematic error illustrated in strain maps: a) Exx, b) Eyy.

intensity $\left(T\left(\left(\xi_{ij}\right)_0\right)\right)$ in the translated image and the real intensity $\left(I\left(x_{ij}\right)\right)$ in the reference image:

$$h\left(x_{ij}\right) = T\left(\left(\xi_{ij}\right)_0\right) - I\left(x_{ij}\right) \tag{2.25}$$

Note that interpolation bias depends on the fractional part (τ) of the translation.

Considering the coupled effects of image noise and interpolation bias (systematic error), Wang et al. (2009) developed an analytic formula for both the bias (expectation) and variance for DIC analysis, written as:

$$E\left(u_e\right) = -\frac{\sum_{i,j=1}^{N} h\left(x_{ij}\right) \cdot \nabla T\left(\left(\xi_{ij}\right)_0\right)}{\sum_{i,j=1}^{N} \left[\nabla T\left(\left(\xi_{ij}\right)_0\right)\right]^2} + f_{rc}\left(\tau\right) \cdot \frac{N^2\sigma^2}{\sum_{i,j=1}^{N} \left[\nabla T\left(\left(\xi_{ij}\right)_0\right)\right]^2} \tag{2.26}$$

$$Var\left(u_e\right) = -\frac{2\sigma^2}{\sum_{i,j=1}^{N} \left[\nabla T\left(\left(\xi_{ij}\right)_0\right)\right]^2} \tag{2.27}$$

with,

$$f_{rc}\left(\tau\right) = \begin{cases} 1 - 2\tau & \text{for linear interpolation} \\ -1.91\left(\tau - 0.5\right) + 4.06(\tau - 0.5)^3 - 1.67(\tau - 0.5)^5 & \text{for cubic interpolation} \end{cases} \tag{2.28}$$

where N is subset size for DIC analysis, and ∇T (the derivative of intensity pattern) represents contrast. From equations (2.26, 2.27), one can quantify both the bias and covariance for

displacement measurement as a function of 1) interpolation method, 2) subpixel motion, 3) image noise, 4) contrast, and 5) subset size. It is emphasized that systematic error is strongly dependent on image noise (as shown by the second part of the right side in equation 2.26). In general, both the bias and covariance decease with contrast. With respect to subset size, the random error (covariance) would decreases with it, however, its influence on the systematic error is difficult to quantify. The relation between the bias of measured displacement and the interpolation bias is linear. However, both the bias (at least part of it) and covariance dependence on image noise are quadratic, indicating that the reduction of the image noise is so crucial for diminishing the measurement error.

Studying systematic error is mostly achieved using virtual translated speckle image. Dautriat et al. (2011) proposed a method to estimate such error using physically homogeneously transformed image (typically magnification variation). In our work, one reference image ($\times$400) is correlated with another image ($\times$402) to exploit systematic error using the proposed procedure. Note that exploited curves involve both the effects of image noise and interpolation bias. The investigation is performed at 5.1 Torr (678 Pa) ESEM mode, and the other acquisition parameters are chosen by the optimization process to decrease image noise (as discussed in the preceding section): 4096 $\times$ 3669 (resolution), 5 (spot size), 40 μs/pixel (dwell time), 10.4 mm (WD).

The influence of interpolation method and subset size are investigated, shown in Fig.2.28 - 2.29. Bi-linear interpolator seems to be faintly better compared to bi-quintic interpolator. This shows that the interpolation with polynomial of high degree doesn't always improve the reconstruction (Runge's phenomenon), in particular for the high contrasted image of strong heterogeneous material. The effect of subset size on strain measurement error is not evident, indicating its limited effect on the systematic error. One practical method to reduce systematic error is defocusing appropriately the image: it leads to a smoother grey level distribution (contrast) which are easier to be reconstructed more exactly by the interpolation. Such defocus processing is used in our work, nevertheless, it is proved to be not so effective (see Fig.2.30). This is actually related to the high ESEM image noise (about 6 grey level on a total 256 grey level) which plays a predominant role for displacement measurement error (as shown the second term in the right side of equation 2.26). Hence, the effects of interpolation method, subset size, and contrast become secondary and the improvements on them are not evident for reducing errors. However, the error for the image treated by a Gaussian filter (2 pixels) diminishes considerably. This is because the Gaussian filter involves both a smoothing image and a reduction of image noise.

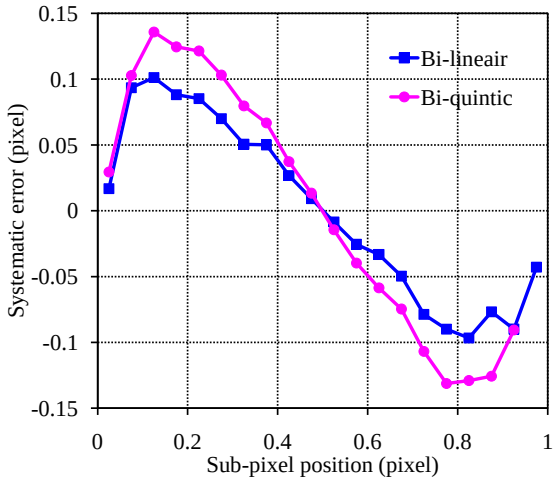

Figure 2.28: Effect of interpolation method on the systematic error.

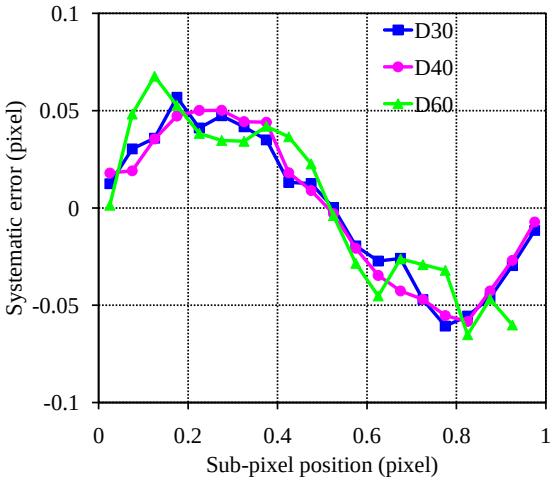

Figure 2.29: Effect of subset size on the systematic error.

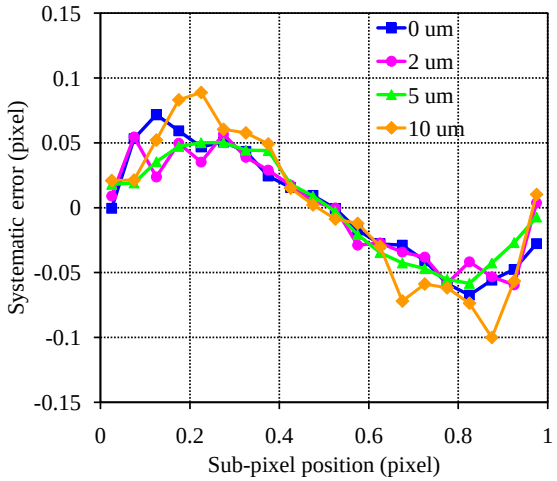

Figure 2.30: Effect of defocus processing on the systematic error.

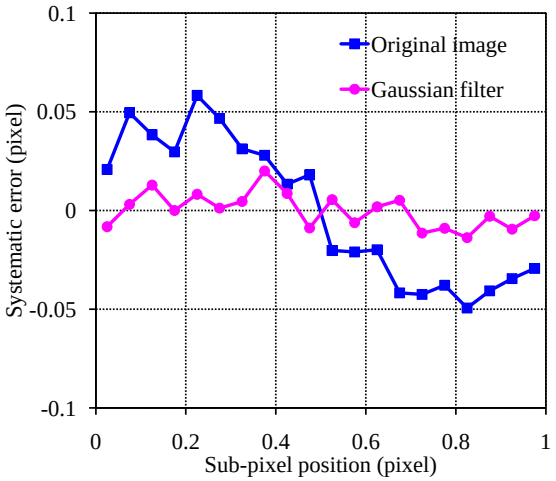

Figure 2.31: Effect of gaussian filter on the systematic error.

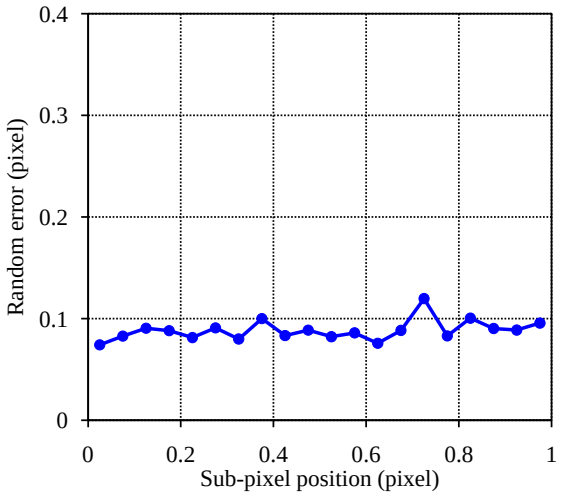

Figure 2.32: Random error of displacement (the case in 2.31 with Gaussian filter).

2.3.4 Strain measurement accuracy for this work

The different types of error related to displacement measurement by DIC analysis have been studied and their depending factors are also discussed in the preceding sections. A good understanding of these errors can help us to perform the optimization process (image acquisition conditions and DIC analysis parameters) and to diminish them. It should be noted that the optimization process is quite difficult since the influence of certain parameters on different errors are totally dissimilar: for example, the increase of subset size could decrease the random error, however, it would increase the shape function error. Hence, characterization of the predominant errors for each case is of crucial importance. For this work, the associated strain level is quite small (typically at the order of 10^{-3}) so that the shape function error is insignificant, and the measurement accuracy is principally limited by the geometric error and systematic error. Moreover, the systematic error is predominantly controlled by the high image noise for the ESEM mode.

Once the error of displacement measurement $\sigma(u_i)$(induced by DIC analysis) is known, the error of strain measurement $\sigma(\varepsilon_{ij})$ can be estimated by the analysis of error propagation:

$$\sigma(\varepsilon_{ij}) \approx \alpha \frac{\sqrt{2}\sigma(u_i)}{\sqrt{N_p} L_j} \tag{2.29}$$

where N_p is number of pairs of independent displacement measurements used for strain measurement, and L_j is an equivalent gauge length along direction j, and α is a coefficient close to 1 (depending on integration schema).

Used equation 2.29, the error of global strain measurement induced by DIC analysis (the image acquisition conditions and the parameters for DIC analysis is shown in section 2.3.3) is estimated to be:

$$\sigma(E) \approx \frac{\sqrt{2} \times 0.02}{\sqrt{16} \times 420} = 2 \times 10^{-5} \tag{2.30}$$

This value is quite small compared to that is shown in Fig.2.26 (about 3×10^{-4}). Note that the latter incorporates the information of all types of errors, including not only the error induced by DIC analysis, but also geometric error etc. Hence, we conclude that the accuracy of global strain is predominantly limited by magnification fluctuations, and it is better than 10^{-3} (about 3×10^{-4}) in this work.

With respect to the accuracy of local strain, it is harder to qualify as it depends on the available natural local contrast which varies from point to point for such heterogeneous argillaceous rocks. However, it can be roughly estimated based on equation 2.29. The random error of displacement measurement is shown in Fig.2.32. Note that it is estimated after optimization process (the case in 2.31 with Gaussian filter). Then, the accuracy of local deformation (rather for the contrasted clay matrix) is:

$$\sigma(\varepsilon) \approx \frac{\sqrt{3} \times 0.1}{4 \times 40} = 1 \times 10^{-3} \tag{2.31}$$

Bibliography

Allais, L., Bornert, M., Bretheau, T., Caldemaison, D., 1994. Experimental characterization of the local strain field in a heterogeneous elastoplastic material. Acta Metallurgica et Materialia 42 (11), 3865-3880.

Bornert, M., 1996. Morphologie microstructurale et comportement mécanique ; caractérisations expérimentales, approches par bornes et estimations autocohérentes généralisées. Ecole Nationale des Ponts et des Chaussées, p. 407.

Bornert, M., Brémand, F., Doumalin, P., Dupré, J.-C., Fazzini, M., Grédiac, M., Hild, F., Mistou, S., Molimard, J., Orteu, J.-J., Robert, L., Surrel, Y., Vacher, P., Wattrisse, B., 2009. Assessment of digital image correlation measurement errors: methodology and results. Experimental Mechanics 49 (3), 353-370.

Bornert, M., Valès, F., Gharbi, H., Nguyen Minh, D., 2010. Multiscale full-field strain measurements for micromechanical investigations of the hydromechanical behaviour of clayey rocks. Strain 46, 33-46.

Bornert, M., Orteu, J.J., Roux S., 2011. Corrélation d'images, Mesures de champs et identification, M. Grédiac et F. Hild Eds., Hermès Science, Chap. 6, 175-208.

Brisset, F., Repoux, M., Ruste, J., Grillon, F., Robaut, F., 2006. Microscopie électronique à balayage et microanalyses. Publication du Groupement National de Microscopie Electronique à Balayage et de microAnalyses, p. 892.

Chu, T., Ranson, W., Sutton, M., Peters, W., 1985. Applications of the digital-image-correlation techniques to experimental mechanics. Experimental Mechanics 25, 232-244.

Cornille, N., 2004. Accurate 3D Shape and Displacement Measurement using a Scanning Electron Microscope. PhD thesis of University of South Carolina & Institute National de Sciences Appliquées Toulouse.

Dautriat, J., Bornert, M., Gland, N., Dimanov, A., Raphanel, J.L., 2011. Localized deformation induced by heterogeneities in porous carbonate analysed by multi-scale digital image correlation. Tectonophysics 503, 100-116.

Doumalin, P., 2000. Microextensomérie locale par corrélation d'images numériques. PhD thesis of Ecole Polytechnique, Palaiseau, p. 260.

Doumalin, P., Bornert, M., 2000. Micromechanical applications of digital image correlation techniques. Proceedings of Interferometry in Speckle Light, Theory and Applications, P. Jacquot and J.M. Fournier Eds., Springer, p. 67-74.

Gagnadre, C., Caron, A., Guézénoc, H., Grohens, Y., 2009. Electron microscopy pictures, mathematical model and approximate solution of the surface potential, Kybernetes 38(5), 780-788.

Héripré, E., Dexet, M., Crépin, J., Gélébart, L., Roos, A., Bornert, M., Caldemaison, D., 2007. International Journal of Plasticity 23, 1512-1539.

Prêt, D., Sammartino, S., Beaufort, D., Meunier, A., Fialin, M., Michot, L., J., 2010a. A new method for quantitative petrography based on image processing of chemical element maps: Part I. Mineral mapping applied to compacted bentonites. American Mineralogist 95, 1379-1388.

Reimer, L., 1998. Scanning electron microscopy: physics of image formation and microanalysis. Springer press.

Robinet, J.C., 2008. Minéralogie, porosité et diffusion de solutes dans l'argilite du Callovo-Oxfordien de Bure (Meuse/Haute Marne, France) de l'échelle centrimétrique à micrométrique. PhD dissertation, Université de Potiers, p. 247.

Roux S, Hild F., 2006. Stress intensity factor measurement from digital image correlation: post-processing and integrated approaches. International Journal of Fracture, 140(1-4): 141-157.

Sammartino, S., Bouchet, A., Prêt, D., J.-C., P., Tevissen, E., 2003. Spatial distribution of porosity and minerals in clay rocks from the Callovo-Oxfordian formation (Meuse/Haute-Marne, Eastern France) implications on ionic species diffusion and rock sorption capability. Applied Clay Science 23, 157-166.

Schreier, H.W., Braasch, J.R., Sutton, M.A., 2000. Systematic errors in digital image correlation caused by intensity interpolation. Optical Engineering 39 (11), 2915-2921.

Soppa, E., Doumalin, P., Binkele, P., Wiesendanger, T., Bornert, M., Schmauder, S., 2001, Experimental and numerical characterisation of "in plane" deformation in two-phase materials, Computational Materials Science (21) 261-275.

Sutton, M.A., Orteu, J.-J., Schreier, H.W., 2009. Image correlation for shape, motion and deformation measurements : basic concepts, theory and applications. Springer press.

The Quanta FEG 250 / 450 / 650 User Operation Manual. 2009. FEI company.

Thiel, B.L., 2004. Master curves for gas amplification in low vacuum and environmental scanning electron microscopy. Ultramicroscopy 99, 35-47.

Valès, F., 2008. Modes de déformation et d'endommagement de roches argileuses profondes sous sollicitations hydro-mécaniques. PhD dissertation, Ecole Polytechnique, Palaiseau.

Wang, L.L., Héripré, E. El Outmani, S., Caldemaison, D., Bornert, M., 2010, A simple experimental procedure to quantify image noise in the context of strain measurements at the microscale using DIC and SEM images. Proceedings of 14th International Conference on Experimental Mechanics, Poitiers, Vol 6, EPJ Web of Conferences, Article Nr. 40008.

Wang, Y.Q., Sutton, M.A., Bruck, H.A., Schreier, H.W., 2009. Quantitative error assessment in pattern matching: effects of intensity pattern noise, interpolation, strain and image contrast on motion measurements. Strain 45 (2), 160-178.

Wattrisse, B., Chrysochoos, A., Muracciole, J. M., Nemoz-Gaillard, M. 2001. Analysis of strain localization during tensile test by digital image correlation. Experimental Mechanics 41, 29-39.

Yang, D.S., Bornert, M., Gharbi, H., Valli, P., Wang, L.L., 2010, Optimized optical setup for DIC in rock mechanics. Proceedings of 14th International Conference on Experimental Mechanics, Poitiers, Vol 6, EPJ Web of Conferences, Article Nr. 22019.

Yang, D.S., Bornert, M., Chanchole, S., Wang, L.L., Valli, P., Gatmiri, B., 2011. Experimental investigation of the delayed behavior of unsaturated argillaceous rocks by means of digital image correlation techniques. Applied Clay Science 54 (1), 53-62.

Yang, D.S., Bornert, M., Chanchole, S., Gharbi, H., Valli, P., Gatmiri, B., 2012. Dependence of elastic properties of argillaceous rocks on moisture content investigated with optical full-field strain measurement techniques. International Journal of Rock Mechanics & Mining Sciences 53, 45-55.

Chapter 3

Microscale experimental investigation under hydric load

Contents

In this chapter, the behavior of argillaceous rocks under purely hydric loadings (humidification or desiccation) is investigated experimentally at macro-scale, based on the combination of high resolution imaging by ESEM and DIC. Several monotonic humidification tests are achieved to investigate the deformation mechanisms of argillaceous rocks under hydric loading. Besides, studying the behavior of such rocks under humidification-desiccation cycle is also preformed so that some irreversible phenomena can be investigated: plastic deformation, microcrackings due to humidification and desiccation. Moreover, different hydric loading rates are applied for these tests, which allows analyzing the depending of the behaviors of the material on the loading rate.

3.1 Equipment and experimental procedure

3.1.1 Sample preparation

The Callovo-Oxfordian argillaceous rocks of Bure are supplied by ANDRA from the EST28031 borehole at 550m depth. Two types of observation planes are chosen in this wrok (see the sketch of the observation plane in Fig. 3.1): plane 1 (perpendicular to the vertical axis), and plane 2 (parallel to the vertical axis). For certain tests, the stratification of the sample (typically plane 2) is marked with painting, which permits to investigate the anisotropic swelling of this stratified material under hydric loads. Samples are prepared in form of slices by saw wire. Cutting is performed gently and carefully to avoid damages induced by the preparation. The thickness of the specimen is less than 1 mm, while its in-plane extension is a few millimeters. The sample's dimensions are measured and formed by caliper, with 10 μm accuracy. The small thickness may shorten the moisture transport process for such weakly permeable material (the intrinsic permeability is in the range 10^{-19} - 10^{-23} m^2). To obtain a smooth surface, specimens are polished by hand with abrasive papers in four stages of decreasing fineness from grade 800 to 4000. Furthermore, special attention is paid to keep both sides of the specimen flat and parallel. Such smooth, flat and parallel surfaces are of critical importance for the ESEM observation: they ensure the images be focused on the whole zone of observation with a constant working distance during imaging.

3.1.2 Experimental procedure

The experimental procedure is as follows. Once the sample (environmental temperature, RH etc.) is placed on the Peltier module and the ESEM chamber is closed, vacuum-pumping, accompanied with purge processing is at first triggered. Purge enables to replace the gas mixture initially present in ESEM chamber by (almost) pure gas (water vapor for humidification/desiccation case). Three parameters should be defined for purge processing: minimum pressure ($P_{\min}$), maximal pressure ($P_{\max}$), and number of cycles (N). For this work, the values

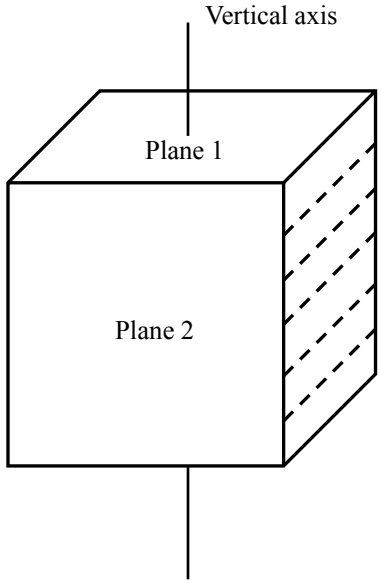

Figure 3.1: Sketch of observation plane (dashed lines indicate the bedding plane of the rock).

of the maximal and minimum pressures should prevent the sample not only to be humidified but also to be desiccated too much. The number of cycles should be chosen, ensuring an appropriate purity of water vapor at the end of purge. The content of sec air (m_a) can be evaluated by the following formula:

$$m_a = {m_a}^i \left(\frac{P_{\min}}{P_{\max}} \right)^N \tag{3.1}$$

where m_a^i is initial content of air sec. For example, it is 99.3% for the atmosphere of 20 °C, 30%RH.

Once purge processing finishes, specimen is cooled down by Peltier module to a low temperature (2°C). Simultaneously an appropriate vapor pressure is prescribed, so as to reach the chosen initial relative humidity. It is worth to note that vacuumizing and cooling the sample can't be transposed: cooling the sample at first would potentially lead to unwanted condensation in ESEM chamber. The advantage of choosing a low temperature is discussed in section 2.1.

When the initial humidity state becomes stable, the specimen is humidified step by step by changing ESEM chamber's pressure maintaining temperature constant. For each step, relative humidity is modified at a fixed speed (in the range 2 - 20 %RH/min for various tests), until a prescribed value is reached, and then the pressure is maintained until moisture transport finishes. The BSE images with high definition ($4096 \times 3536 = 13.8$ MPixels) are recorded every 30 minutes during the pressure maintaining stage (both for the initial and the current RH). Waiting for the absence of detectable evolution of the overall strain ($< 10^{-4}$) in the

observation zone between two images recorded successively and analyzed by DIC, the system is considered to have reached moisture equilibrium and the next step of hydration (or dehydration) can start. Fig. 3.2 illustrates the hydric loading path of test #1, together with the overall strain evolution during the first hydration step. Note that in order to control the noise levels of the ESEM images, the acquisition parameters (beam current, dwell time, spot size...) need to be tuned accurately. We refer to section 2.3.1 for the detailed description of the procedure to quantify noise levels in ESEM images. In addition, specific procedures (Degauss processing with focused image) to control magnification fluctuations are used, in order to limit the bias of strain measurement that they may induce.

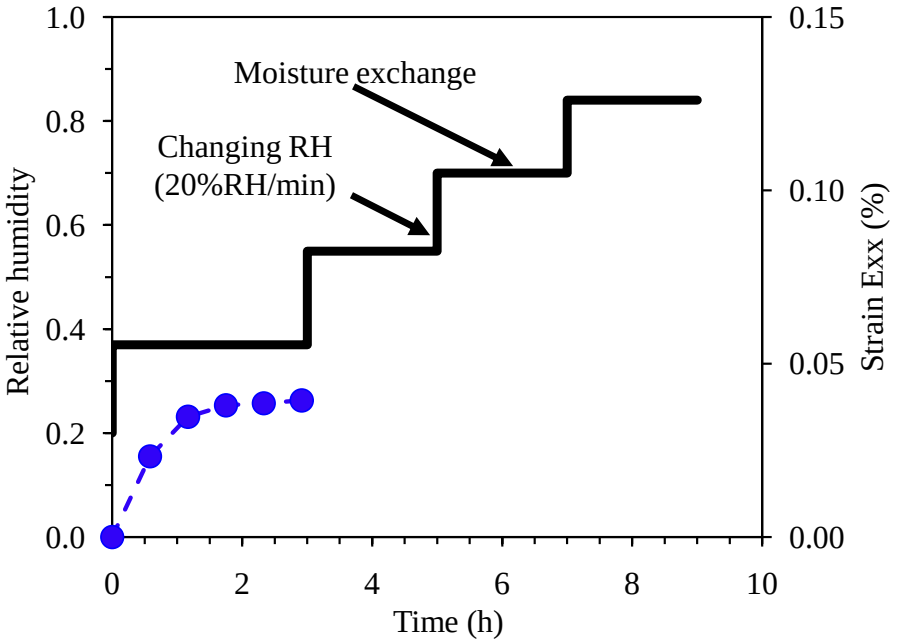

Figure 3.2: Hydric loading path of test #1.

Dozens of tests are carried out to investigate the deformation mechanism of argillaceous rocks with RH changing. The characteristic length of observation zone is several hundred micrometers (100 - 300 μm), allowing to distinguish the three principal components (clay matrix, grains of carbonate and quartz) of such material and so to reveal their interactions under hydric loading. From these observations, the behavior of such material is characterized, of which the mail results are presented by 7 representative tests. These 7 tests can be divided into two parts: under monotonic humidification (section 3.2) and under humidification-desiccation cycle and dessication (section 3.3). For the first part, the heterogenous strain field of argillaceous rocks during humidification is presented in test #1, which enables us to characterize the deformation mechanisms of such materials under hydric loads at the scale of their composite microstructure. Then, the behavior of argillaceous rocks at higher RH, in particular the emergence of some strong nonlinearity in strain-RH curve, is investigated in test #2. In test #3, the observations on the plane 1 and 2 enable to characterize the anisotropic swelling of such material. Such

Table 3.1: Summary of purely hydric loading tests

Test	Hydric loading history	Loading rate	Observation plane
Test #1	20% - 37% - 55% - 70% - 84%	20 %RH/min	Plane 2
Test #2	75% - 82% - 90% - 95% - 99%	2 %RH/min	Plane 2
Test #3	38% - 52%	20 %RH/min	Plane 1 and 2
Test #4	35% - 55% - 75% - 85% - 95% - 99%	5 %RH/min	Plane 1
Test #5	35% - 55% - 75% - 85% - 99%	5 %RH/min	Plane 2
Test #6	66% - 80% - 90% - 66%	20 %RH/min	Plane 2
Test #7	65% - 75% - 85% - 75% - 65% - 18%	5 %RH/min	Plane 2

anisotropic swelling is investigated in more detail by the tests #4 and #5, and its different origins are characterized. Besides the tests under monotonic humidification, the behavior of such material under cyclic hydric loads and the emergence of damage under some circumstances (humidification, desiccation) are also investigated in this work. The microcracking due to humidification is firstly investigated in test #6. In test #7, the irreversible deformations caused by hydric loads are evidenced, as well as the microcracking due to desiccation.

3.2 Behavior under monotonic humidification

3.2.1 Test #1: local deformation modes under moderate hydric loads

The specimen for test #1 is humidified progressively at RHs of 20%, 37%, 55%, 70%, and 84% in ESEM chamber. RH changing is performed with a speed of 20%RH/min. Each humidification step lasts about two hours and the whole test lasts 9 hours (Fig.3.2). One zone (128 × 110.5 μm^2, corresponding to image magnification ×1000) on the specimen surface with a relatively simple morphology (one big grain of calcite 50 μm in size and several small grains of calcite and quartz are scattered in the clay matrix), shown in Fig. 3.3, is chosen as a region of interest (ROI). The strain fields over the observation zone at the equilibrium states (at the end of each step) are determined by the DIC technique and shown in Fig. 3.3. The grains of calcite and quartz with a surface larger than 10 μm^2, identified by means of EDS, are also outlined in these strain maps.

The matching subset is 30 × 30 pixels, corresponding to a 0.94 μm physical size which is appropriate for clay matrix in which the scale of heterogeneity is generally below 1 μm. However, the relatively uniform contrast inside grains of calcite and quartz (especially for the big calcite grain) makes the DIC analysis nore delicate. That is why no measurement are performed at some positions (black dots) and some unphysical fluctuations of local strains,

induced by erroneous pattern matching in some zones inside big grains can be observed. This is however not a critical problems since the analysis is focused on clay mineral which plays a critical role for the behavior of argillaceous rocks under RH changing, whereas the grains of carbonate and quartz are not sensitive to such loads. In addition, average deformation in mineral inclusions can be evaluated from the displacement field only at their boundary, and will not be affected by these errors inside the grains (refer to Allais et al. (1994)).

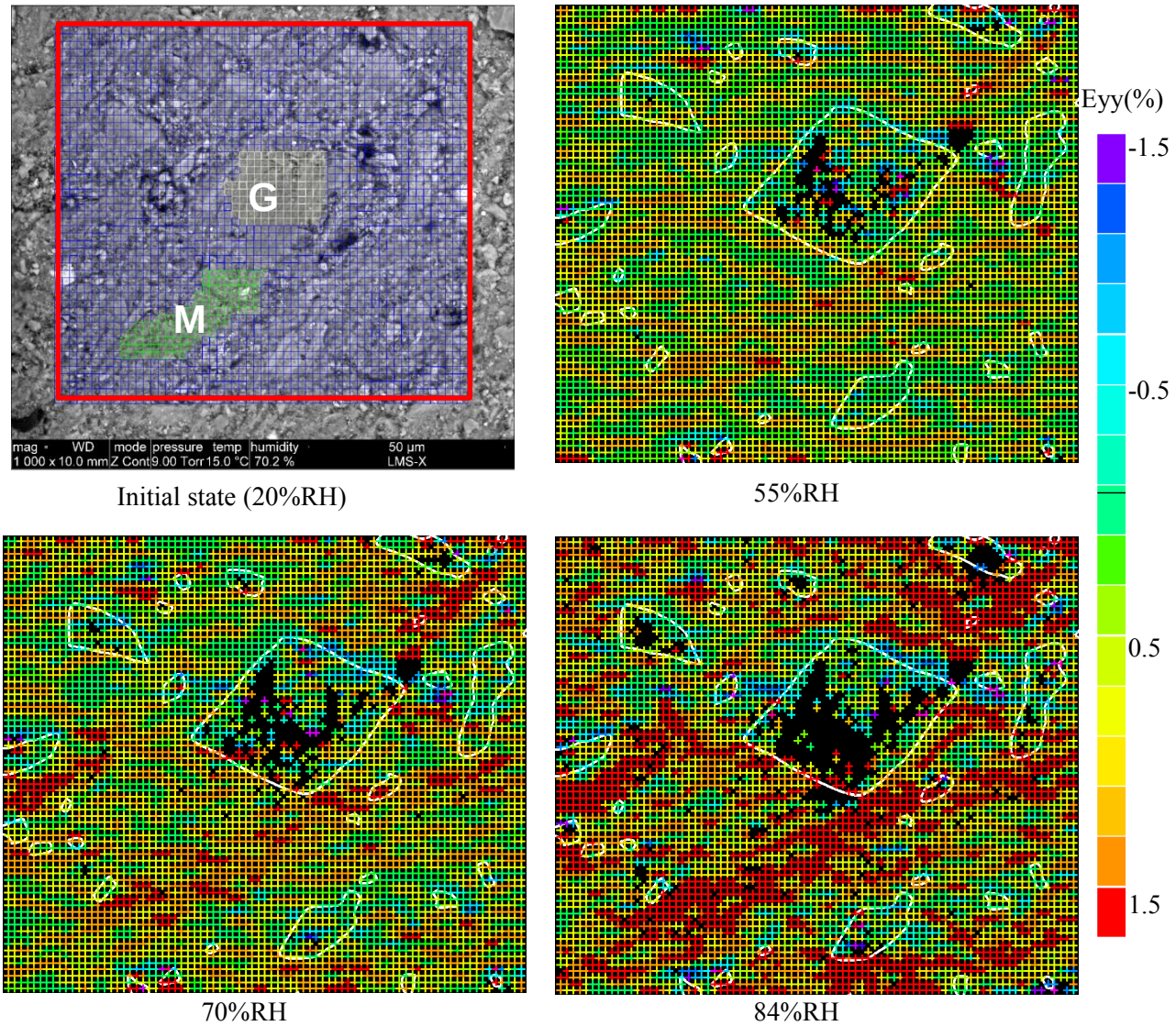

Figure 3.3: Strain field evolution during humidification in test #1. The domain M corresponds to a region in clay matrix while the domain G corresponds to a (or a group of) calcite grain(s). The white lines in the deformation maps represent the contours of some big grains of calcite and quartz. The observation zone is 128 × 111 μm^2 in size, while the investigated area by DIC is 104 × 95 μm^2 (the contour is marked by red lines in top-left image).

Fig.3.3 shows a strongly heterogeneous strain field in argillaceous rocks during humidifica-

tion at this micro-scale. However, this heterogeneity of deformation field shows a very good correspondence with the local phase distribution of the material: the high tensile strains (in red and yellow colors) are mostly located in clay matrix, while the slight strains (in green color) are generally found in the grains of carbonate and quartz. For a more quantitative demonstration of the contrasting deformations related to the local constitutive phases, the average strains of two domains in ROI, one being essentially a grain of calcite (domain G in Fig. 3.3) and the other located in the clay-rich matrix (domain M in Fig. 3.3), are evaluated and their evolutions presented in Fig. 3.4. When the specimen is humidified from 20%RH to 84%RH, the mean strain of the clay-rich domain reaches about 1.9%, but that of calcite grain is only 0.6%. The overall strain of the observation zone is indeed an average of the local deformations of different constituents in the material (1.3%). The contrasting deformation of the different phases of such rocks is essentially related to their dissimilar behaviors when meeting with water: the clay mineral is a water-sensitive material which would swell in a wetter atmosphere, whereas the other constituents, such as calcites and quartz, are not sensitive to water and their volume remains constant regardless RH changing.

Note however that the measured strain in domain G is not null. This observation may be related to mechanical interaction between the swelling clay matrix and the non-swelling grains. In fact, the presence of the non swelling grains would inhibit the swelling of clay minerals so that a local stress field is generated. Such interaction can be considered as the following simple model situation: a non-swelling spherical inclusion perfectly embedded in an infinite matrix submitted to a free swelling (without mechanical stress). The stress generated in the inclusion can be calculated by Eshelby's solution to this problem (Eshelby, 1957). It is proved to be a tension, and accordingly produces an extension of the inclusion. However, the measured extension with a magnitude of 0.6% is too large to be explained by this ideal elastic interaction mechanism, since calcite grain is much stiffer than clay matrix (the Young's modulus of calcite is about 8 times larger than that of clay matrix), therefore, the extension of calcite induced by interaction should be quite small. Another potential explanation of this considerable deformation of the calcite grain might be the fact that this area encompasses also some clay matrix in lower proportion, and that this coarse grain might be composed of several subgrains which may move with respect to each others, so that the effective modulus of domain G would be much lower than that of pure calcite.

The strain field exhibits not only "inter-phase" heterogeneity, but the deformation field is also strongly heterogeneous in the clay matrix itself. Such "intra-phase" heterogeneity can be explained by several mechanisms. First, the "inter-phase" interaction, as discussed above, would prevent clay matrix from swelling in the neighborhood of grains, at the price of the generation of a local stress field. Such influence tends to weaken with the distance from grains, which can generate heterogeneous deformation field in clay matrix, as the result of the combination of hydric and mechanical local loadings. Moreover, the heterogeneity in clay matrix is another

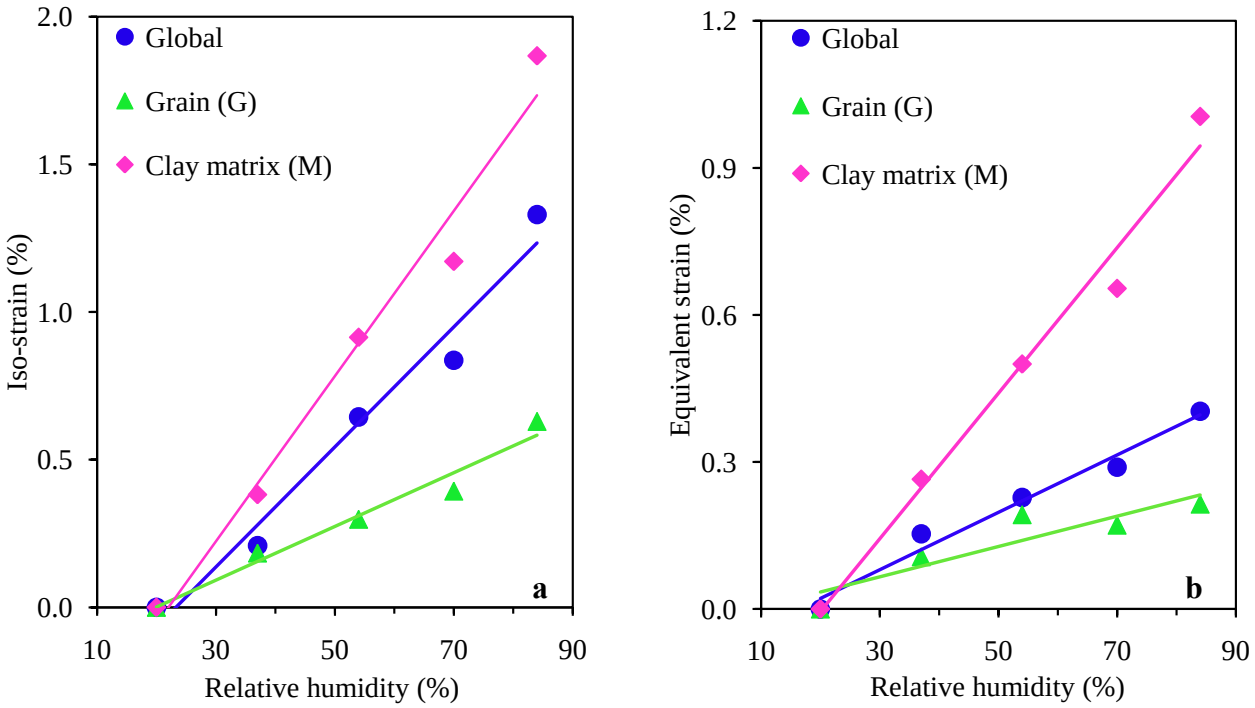

Figure 3.4: Evolution with relative humidity of the average strain over the whole ROI and the domains M and G represented in Fig. 7. a) mean strain b) equivalent strain.

origin of its inhomogeneous deformation field. It can be distinguished by two terms. Firstly, different groups of clays (kaolinite, illite, smectite) of which the swelling properties can be very different may coexist at this local scale, however, their swelling properties are very different: smectite owns a significant swelling capacity while illite and kaolinite hardly swell. Secondly, the various orientations of the swelling clay particles induce swelling strains varying with local orientations, as the clay particles prefer to swell in the direction perpendicular to the orientation of the layers. Note that such incompatible "inter-phase" free swellings also lead to a local stress field, which is superimposed with that induced by inclusion-matrix interaction.

No microcracks are evidenced during test #1. For the investigated RH range, the global and average strains evolve almost linearly with RH (from the plots in Fig. 3.4). This suggests that both the clay swelling mechanisms and the mechanical interactions at the origin of these complex deformation fields can be described, as a first approximation, as linear phenomena. However, they may become nonlinear at higher RH, as observed in test #2 presented in next section.

As a summary, a strongly heterogeneous strain field appears at this micro-scale of the composite structure of the material during humidification. It is the consequence of the contrasted behaviors between clay-rich matrix and non-swelling mineral inclusions, and probably also between various areas in the matrix with different local compositions and texture, as well as of the mechanical interactions between the phases which may generate a local stress field. These

interactions seem to evolve linearly with relative humidity and thus be probably essentially elastic.

3.2.2 Test #2: nonlinear deformation at higher RH

The specimen in test #2 is humidified progressively at 75%, 82%, 90%, 95% and nearly 100% RH (Fig.3.5). Between each hydric loading stage, the speed was controlled at 2%RH/min, i.e. at a much lower rate than 20%RH/min used in test #1. Note such low hydric loading rate enables to humidify the specimen until extremely high RH without introducing obvious microcracking. Two different zones (320 × 276 μm^2, corresponding to image magnification ×400) are chosen to study the swelling of argillaceous rocks: zone 1 with a larger volume fraction of inclusions, and zone 2 with more clay minerals (Fig. 3.6). The coarse grains of carbonate and quartz can be distinguished directly on BSE images and their contours (with surface larger than 30 μm^2) are outlined also for zone 1 in Fig. 3.6.

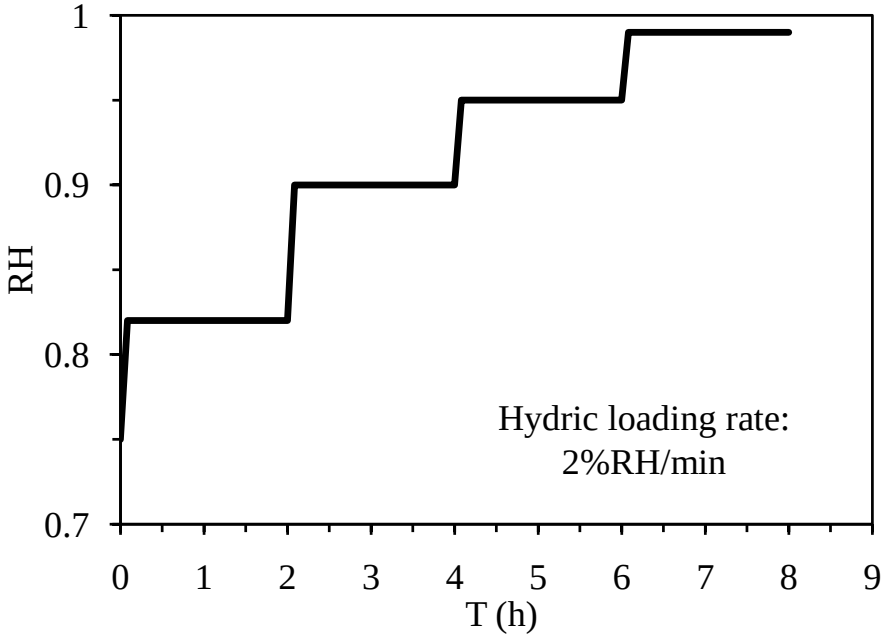

Figure 3.5: Hydric loading path of test #2.

The evolution of the overall strains over the two zones, as well as the direction of the major principal strain θ, are determined by the DIC technique and are reported in Fig.3.6. The results show that the minor principal strain E1 evolves linearly in all RH range, whereas the major principal strain E2 becomes strongly nonlinear after a linear stage. The threshold of nonlinearity is between 95%RH and 99.8%RH in this experiment. The directions of the major principal strain (about 75° clockwise from vertical direction of image) in the two zones remain nearly constant during humidification, even in the nonlinear stage. The strain levels in the two zones are nevertheless different: in the linear stage, the major principal strain E2 of zone 1 is

0.88% when RH varies from 75% to 95%, while it is 1.48% for zone 2. When RH reaches 99.8%: the deformation E2 of zone 1 is 2.92% while that of zone 2 reaches 5.31%.

The difference of deformation in the two zones can be explained by the difference of their mineral content. As clay minerals swell during hydration while the grains of carbonate and quartz do not, the deformation of the zone containing less clay mineral (zone 1) is accordingly smaller than that of the zone containing more clay minerals (zone 2).

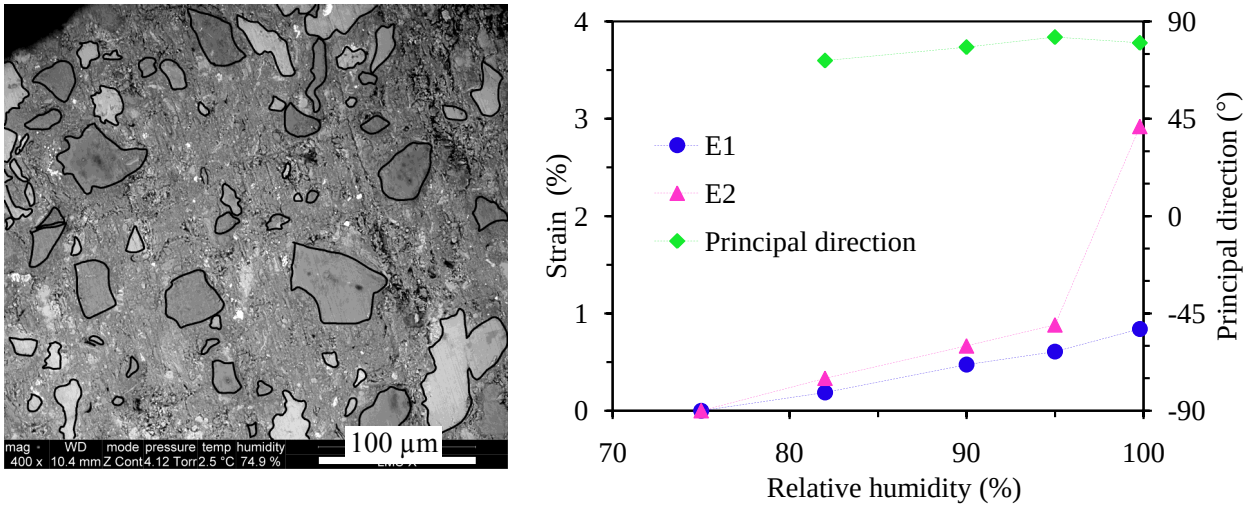

a) Zone 1

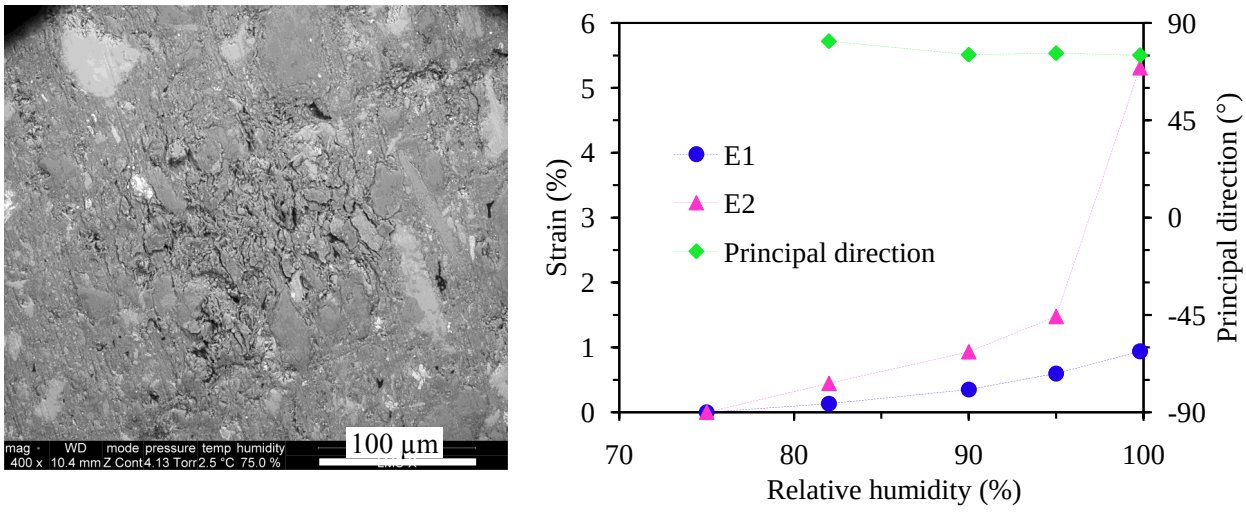

b) Zone 2

Figure 3.6: Micrographs and average deformation of investigated zones in test #2. The black lines in the BSE image of zone 1 represent the contours of some big grains of carbonate and quartz.

Analysis of incremental strain

No obvious microcracking has been observed until the end of test #2, even at this micro-

scale. In zone 2, some microcracks do exist before the beginning of the experiment, but no clear sign of their development during humidification could be evidenced. Hence the nonlinearity observed here cannot be explained by microcracking, which is suggested as the most possible origin for nonlinear swelling. So, what is the mechanism of such nonlinearity in test #2? To answer this question, an incremental analysis of the strain maps in zone 1 is performed: the local deformations are determined by comparing each prescribed step with the previous one, instead of always comparing with the initial stage. Since the nonlinearity is observed for the major principal strain E2, the map of the strain component E_{xx}, of which the direction is close to that of E2 (referring to the definition of deformation quantities in Fig. 2.8 and the major principal direction being $\Theta = 75°$), is chosen to perform the analysis.

The fields of incremental strain component E_{xx} for all steps are determined and plotted in Fig.3.7, together with the contours of big grains of calcite and quartz (referring to Fig.3.6). The strain fields show an evident heterogeneity, of which the origins have already been discussed in previous test #1. Broadly, three colors can be distinguished in strain fields: the blue-green color which represents relatively small tensile strain or even compressive strains, the yellow color representing moderate tensile strain and the red color which represents significant tensile strain. Considering the distribution of components in the material, the blue-green color occurs as expected mostly in the grains of calcite and quartz while the yellow and red colors are generally found in the clay matrix.

For linear steps (Fig.3.7a, b and c), the morphologies of the strain maps are somewhat alike, which means that the deformation distributions are similar for the first three steps of humidification. Furthermore, the deformation magnitudes for the linear steps are also proportional: increasing 7%RH in the two first humidification steps leads to a swelling of 0.8% in the red domains; while the tensile strain of the same domains is about 0.6% in the third step in which the specimen is humidified by 5%RH.

Now consider the deformation field in the last nonlinear step. Surprisingly, a very similar deformation distribution is found again for the last step of humidification (Fig.3.7d). This conservation of deformation distribution in nonlinear stage is very different from the standard behaviors of materials in which the nonlinearity is often accompanied by deformation localization (for instance because of local plasticity) in some area so that the distribution of incremental deformation evolves. In this study, the nonlinearity comes only from deformation magnitude in considerably swelling clay matrix: the red domain swells about 4% for a 4.8%RH variation in the last step, that is to say 0.8% swelling by 1%RH changing, to be compared with less than 0.1% swelling by 1%RH varying in the linear steps.

Since the observation in this work is performed at the scale of the composite microstructure of argillaceous rocks, the heterogeneous strain field is principally associated with the inhomogeneous free swelling accompanied by the mechanical interaction induced by the former. Hence, the similarity of strain maps, at least from a qualitative point of view, suggests that the me-

chanical interactions are somewhat elastic and linear for both the linear and nonlinear steps. The nonlinearity should be principally related to the nonlinear free swelling of clay minerals.

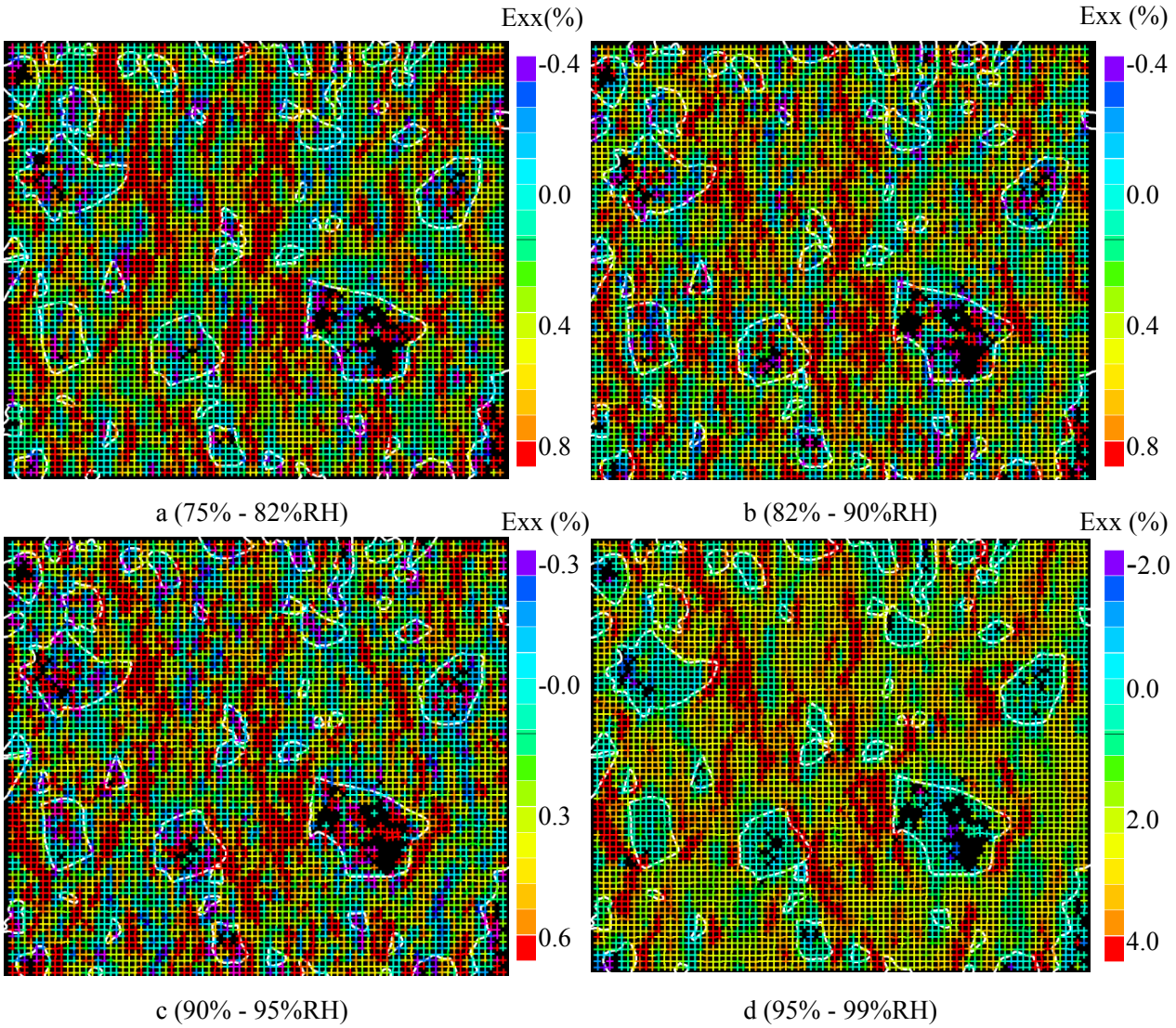

Figure 3.7: Incremental E_{xx} strain maps during hydration in zone 1 of test #2 (the area investigated by DIC is 260 × 238 μm^2 in size).

Incremental strain distribution function

Since the above analysis is rather qualitative, a quantitative analysis, involving in assessing the distribution functions of incremental normalized E_{xx} (local E_{xx} divided by the average value of E_{xx} over the whole ROI) in the two observation zones, is performed and presented in Fig.3.8. It is shown that such distribution functions in zone 2 are relatively sharp and similar in all steps, whereas those in zone 1 are less focused and slightly evolve along the steps, being more focused in the last step from 95% to 99.8%RH.

Referring to strain maps in Fig.3.7, we principally attribute the dissimilarity of distribution

functions in zone 1 to the errors related to DIC analysis, particularly in the zone of grains of calcite and quartz where the contrast is not sufficient for pairing homologue points. Indeed, the matching subset in the present analysis is about 2 μm, which is appropriate for the clay matrix where the scale of heterogeneity is generally below 1 μm. However, such size is too small for the grains in which the contrast is rather homogeneous over zones ranging from a few to several dozens of micrometers in size. Therefore, the DIC does not work well with this size of matching subset in the domains inside grains. This leads to erroneous evaluations of local strain components which over- or under-estimate real strain levels (see the strain fields inside the contour of grains in Fig.3.7) and consequently enlarge strain distribution functions. However, the perturbation of these errors decreases with the magnitude of incremental deformation, as we consider normalized distribution functions and as the amplitude of these errors are essentially independent of strain magnitude. Accordingly, strain distribution function becomes more focused in the last hydrated step (95% - 99.8%RH) for which the overall incremental strain is about 5 times larger than the previous steps. For zone 2, the global incremental deformation is much more significant than zone 1 so that the influence of strain measurement error is less important.

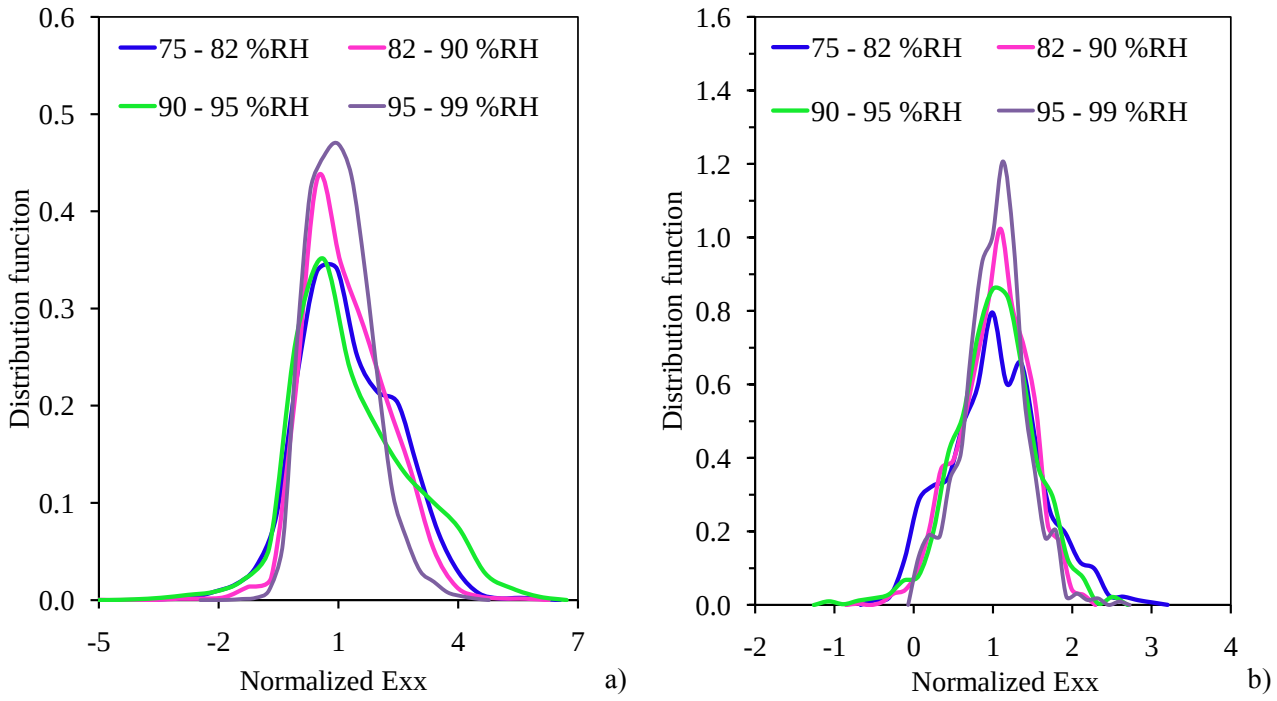

Figure 3.8: Distribution functions of normalized incremental E_{xx} a) zone 1 b) zone 2.

Besides normalized incremental E_{xx}, the distribution functions of θ for the incremental strain are also determined and presented in Fig.3.9. The results show that θ distributions remain similar along all humidification steps, and the altering for the zone 1 can also be explained by the measurement errors as discussed above.

Therefore, we conclude that there is neither any evident change of deformation distribution nor any significant change of local principal directions for the nonlinear step of humidification. This confirms the conclusion derived from the deformation map: the nonlinear deformation of argillaceous rocks with RH under humidification, in test #2 where no micro-cracking has been observed, is primarily related to the nonlinear swelling of clay minerals themselves, which is linked to their physical-chemical properties, rather than to the mechanical interactions between the constitutive phases, which seem to exhibit essentially similar features at all moisture levels.

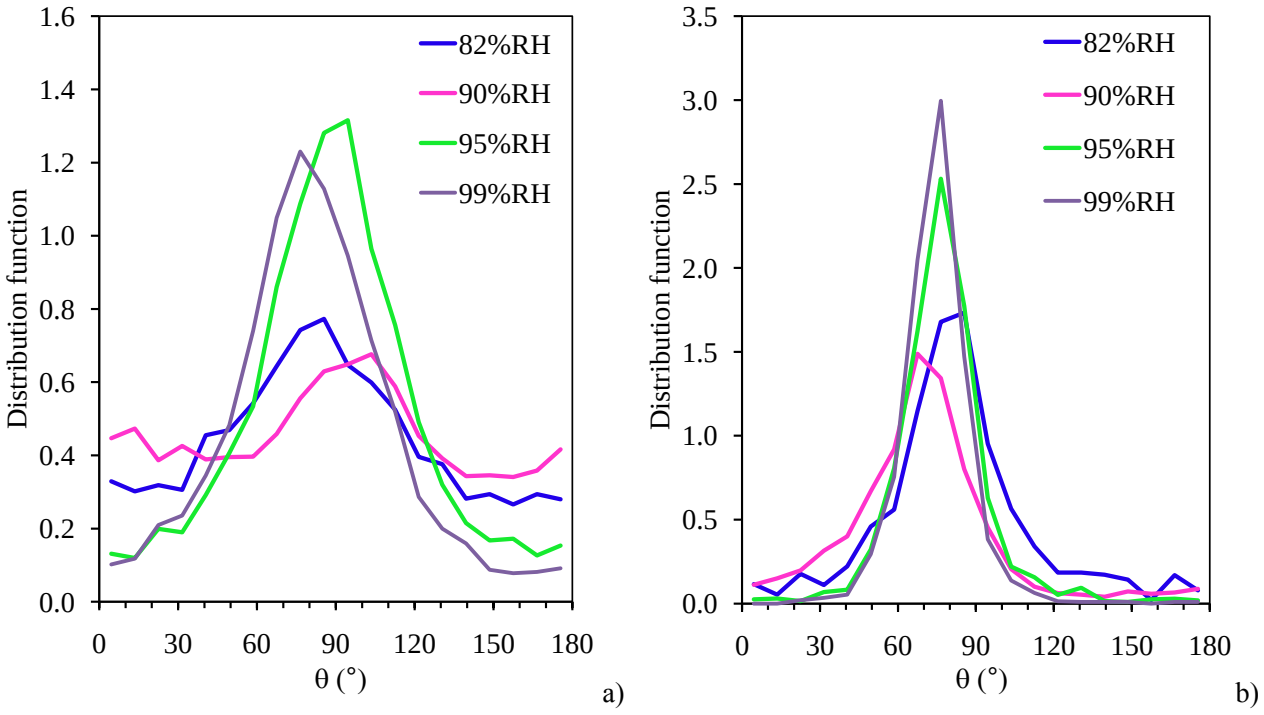

Figure 3.9: Distribution functions of principal directions a) zone 1 b) zone 2.

3.2.3 Test #3: anisotropic deformation under hydric load

In test #3, two specimens are cut from one sample but prepared in different observation planes (plane 1 and 2). Moreover, the bedding direction is marked in plane 2: it coincides with y axis of images. The two specimens are simultaneously subjected to one step humidification 39% - 52%RH with a loading rate of 20%RH/min. Their in-plane strains are evaluated by DIC analysis, shown in Fig.3.10. An anisotropic swelling is found in plane 2, but not in plane 1: E1 and E2 are similar (0.08%) in plane 1, while E2 is 0.17% and E1 is 0.07% in plane 2. Moreover, the direction of E2 is fairly parallel to the bedding direction in plane 2 ($\Theta = 9°$).

The preceding experimental studies at macro-scale reveal the anisotropy of deformation under hydric loads for argillaceous rocks: it is generally more significant in the direction perpendicular to the bedding plane than in the direction parallel to it. This anisotropy is essentially

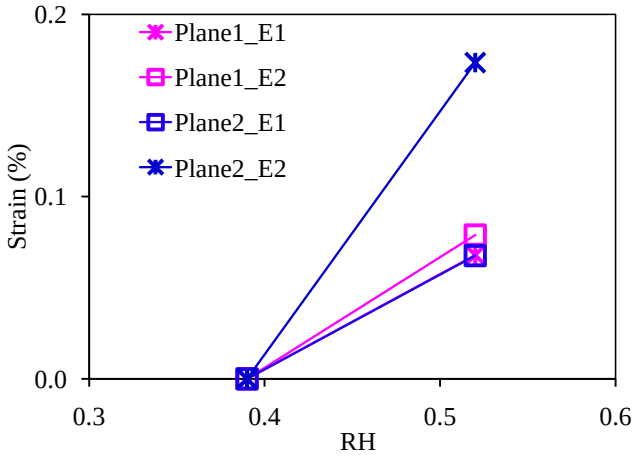

Figure 3.10: Anisotropic deformation of argillaceous rocks under humidification.

related to the preferred orientation of clay particles perpendicular to the bedding direction, which can be in general described by transverse isotropy (Sayers , 1994). The observation in test #3 confirms this anisotropy feature at micro-scale. Other tests of humidification in plane 1 where the bedding plane is recognized (for example test #5) confirm that Θ always coincides with the bedding direction. Hence, the directions of the principal strains can be used to determine the bedding direction in plane 2 when it is unknown for some tests: it coincides with the direction of E2 in case of humidification and the direction of E1 in case of desiccation (desiccation results in contraction so that the strain value is negative).

3.2.4 Test #4: Swelling in plane 1

The sample in test #4 undergoes a staged humidification from 35%RH to a very high relative humidity (99%RH). The hydric loading rate is chosen as 5%RH/min, and the total hydric loading history is shown in Fig.3.11. The observation in test #4 is carried out on the plane parallel to the bedding plane (plane 1). Four zones with size of 256 $\times$ 221 μm^2 (corresponding to image magnification $\times$500) are chosen for DIC analysis, shown in Fig.3.16a - 3.19a.

The overall strains of observation zones are estimated and given in Fig.3.12 - 3.15. In general, the strain curves exhibit a bi-stage swelling: the strain is extremely small at low relative humidity range, whereas it becomes more important at high level. The threshold of this nonlinearity seems to be 75%RH. Averaging the strains in the four zones, the major strain is 0.16% for the first stage (35% - 75% RH = 40%RH), and the material swells 0.93% for the second stage (75% - 99% RH = 24%RH). Besides, the two principal strains are fairly similar in plane 1. The principal directions Θ for the four studied zones are variable: for example, it is about 70° for zone 1, while -45° for zone 2. Nevertheless, they don't evolve obviously with humidification steps for each studied zone. All these results suggest that there is no apparent overall swelling anisotropy in plane 1. Indeed the fluctuations of principal directions Θ and the

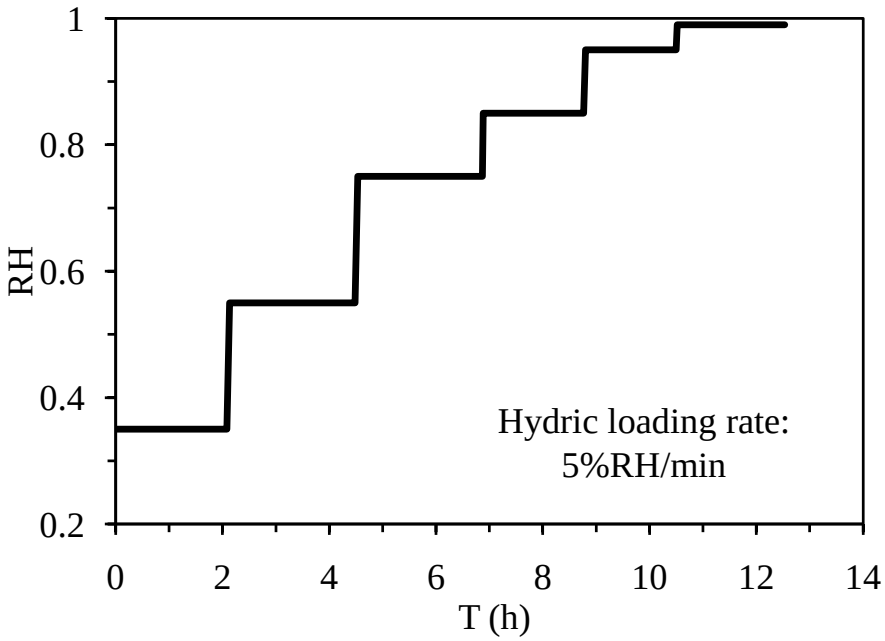

Figure 3.11: Hydric loading path of test #4.

small differences between E1 and E2 are due to the small extension of the observation zones, which are too small to be considered as representative volume elements. The measured average strains are thus sensitive to the local statistical realization of the microstructure.

The local strain fields (ε_2: major swelling component) of the four studied zones are presented in Fig.3.16b - 3.19b. Analogous to the previous observation in section 3.2.2, the strain maps are similar for different humidification steps. Hence, only the total strain (35%RH - 99%RH) maps are presented here, which can be considered to be representative for all the humidification steps. Broadly, the strain maps at such a local-scale are strongly heterogeneous: some violet and blue (low swelling) domains wrapped by yellow and red bands (high swelling) clearly appear. However, these heterogeneous strain fields correlate well to the microstructure: low swelling domains are typically located in inclusions, while high swelling bands are mostly found in the clay matrix. However there are also areas in the clay matrix which do almost not deform. In fact, this indicates a complex interaction phenomenon: the clay matrix tends to swell with increasing RH due to its specific swelling property, but the presence of non-swelling inclusions would inhibit it so that a local stress field would be generated. The heterogeneity inside the clay matrix, such as different clay groups with dissimilar swelling capacities and various clay particle orientations, may also contribute to the local stress field. The total strain is indeed a sum of the free swelling and the strain due to the local stress field.

Concerning high swelling bands in the clay matrix, they are more or less oriented randomly, and there is no obvious preferred orientation of them in the observation zones of plane 1. It is shown that these swelling bands, in some cases, tend to wrap around their neighboring inclusions so that their orientations are strongly controlled by the forms and orientations of

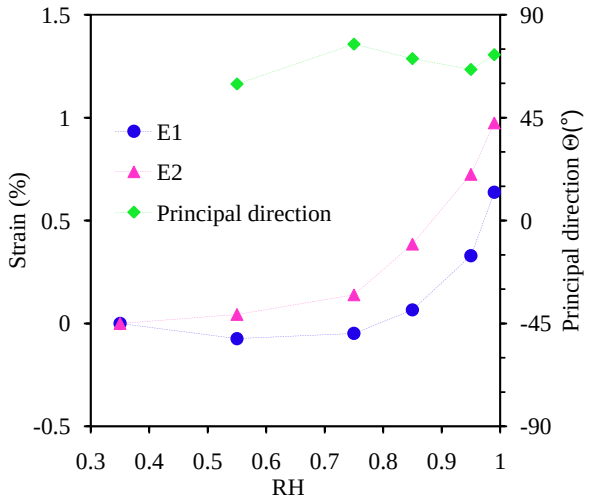

Figure 3.12: Overall strain of zone 1 in test #4.

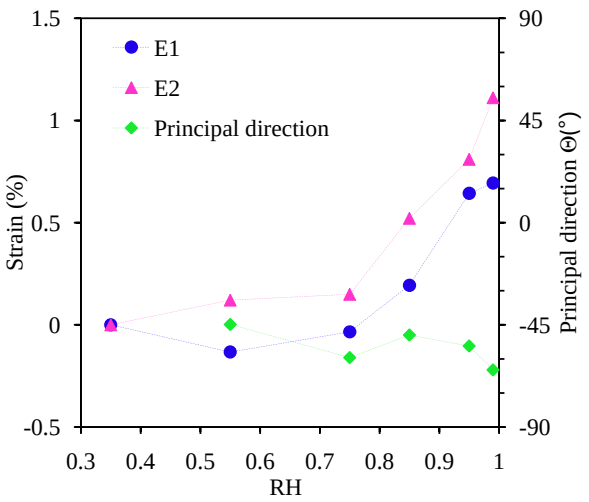

Figure 3.13: Overall strain of zone 2 in test #4.

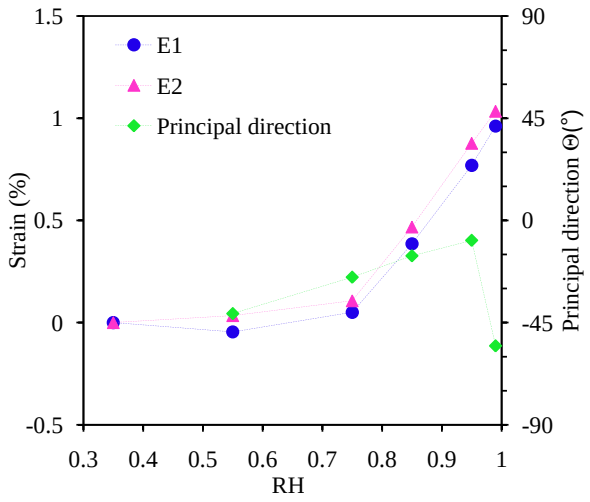

Figure 3.14: Overall strain of zone 3 in test #4.

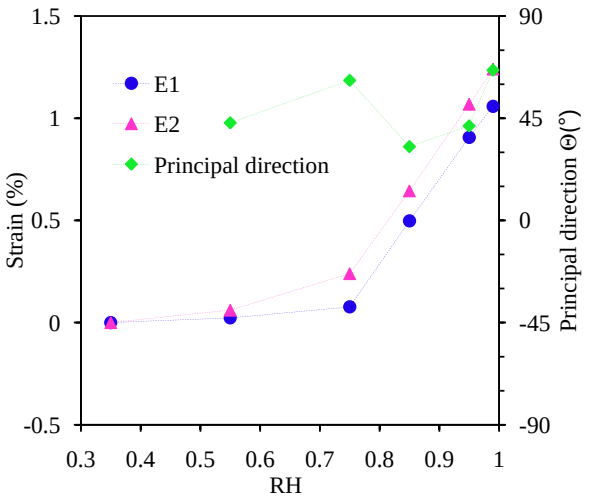

Figure 3.15: Overall strain of zone 4 in test #4.

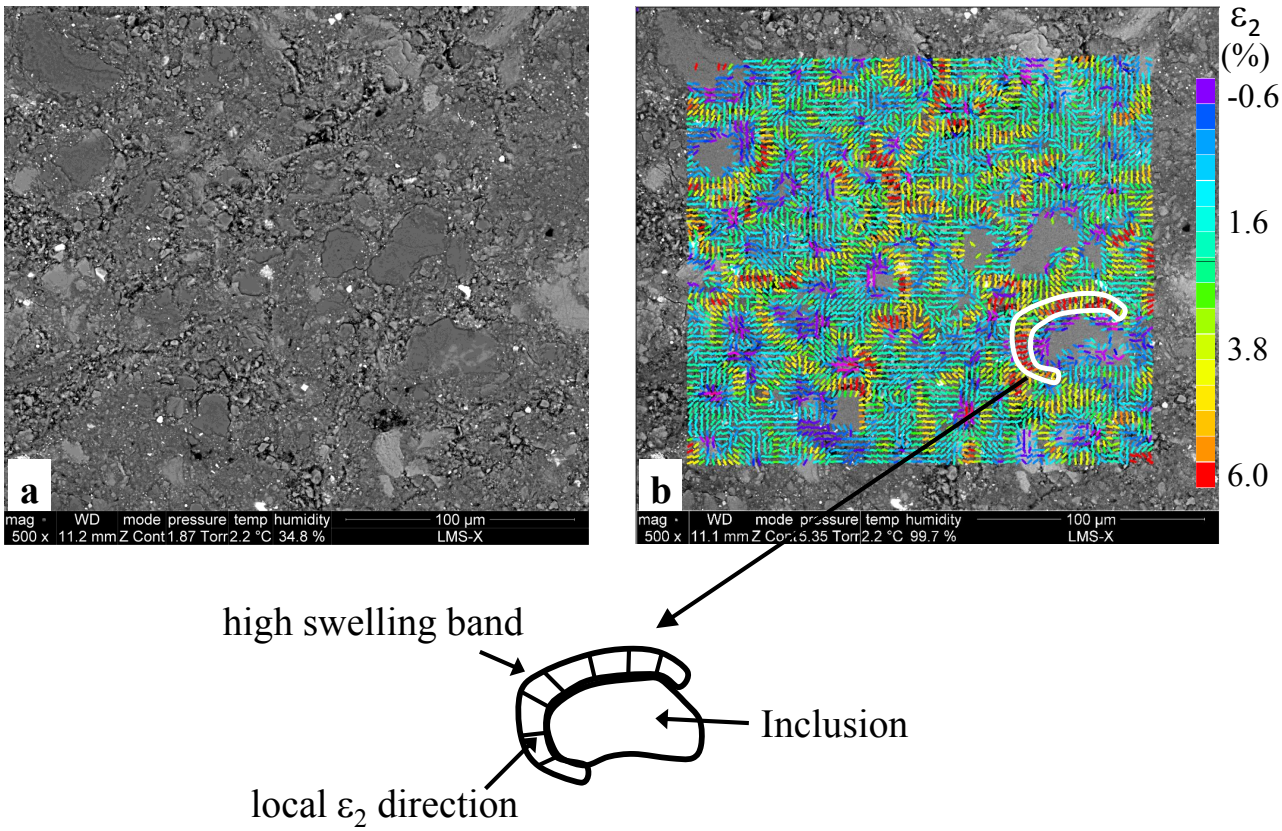

Figure 3.16: BSE image (a) and ε_2 strain map (b) of zone 1 in test #4. An example of a highly strained deformation band oriented along an inclusion boundary is outlines. Besides, local 2 directions inside this band are perpendicular to its orientation, which implies it is associated to a swelling band.

the latter (one example is outlined in Fig.3.16). The symbols used to represent local strains in strain maps are crosses with a major axis indicating the principal direction associated with principal strain ε_2, and measured by local angle θ It is observed that the local ε_2 direction is in general perpendicular to the local orientation of the deformation bands, as illustrated in Fig.3.16. This implies that these deformation bands are indeed extension bands, rather than shear bands, for which the local ε_2 direction would be at 45° with respect to their orientation. The distribution of these local principal directions θ in each ROI is studied by a statistic analysis, and its probability distribution function (pdf) is estimated and shown in Fig.3.20. No preferred direction of local principal strain is observed in plane 1.

When the sample is humidified to extremely high RH, some microcracks appear either in the clay matrix or on inclusions' boundaries. For the latter, it is associated to a split of inclusion-matrix interfaces which leads to high local extension (an example is outlined in Fig.3.18).

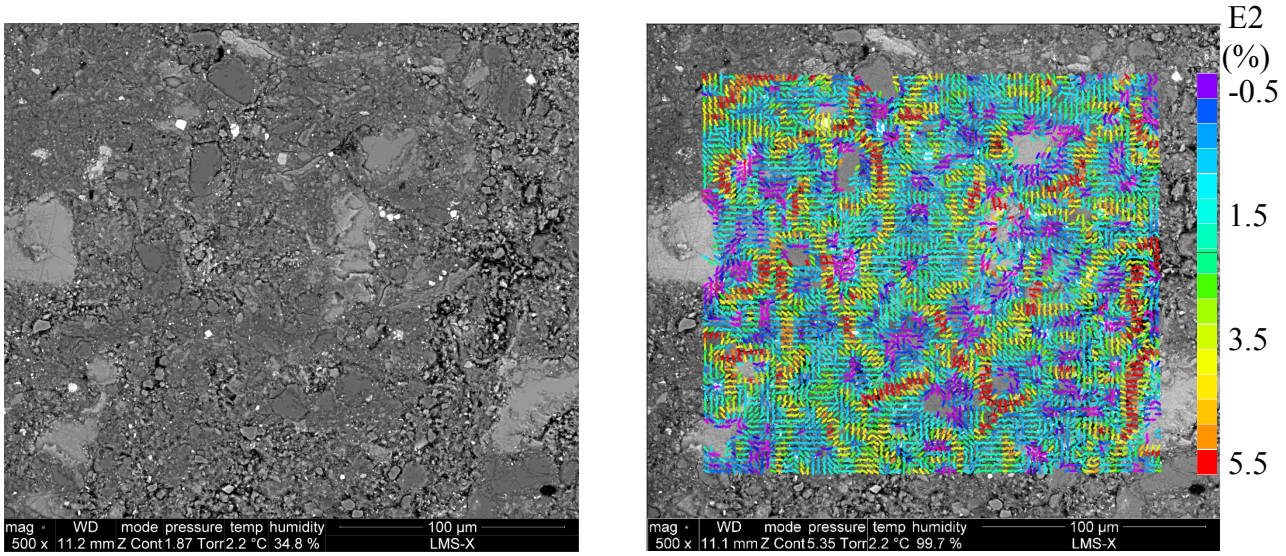

a (BSE image) b (35% - 99%RH)

Figure 3.17: BSE image (a) and ε_2 strain map (b) of zone 2 in test #4.

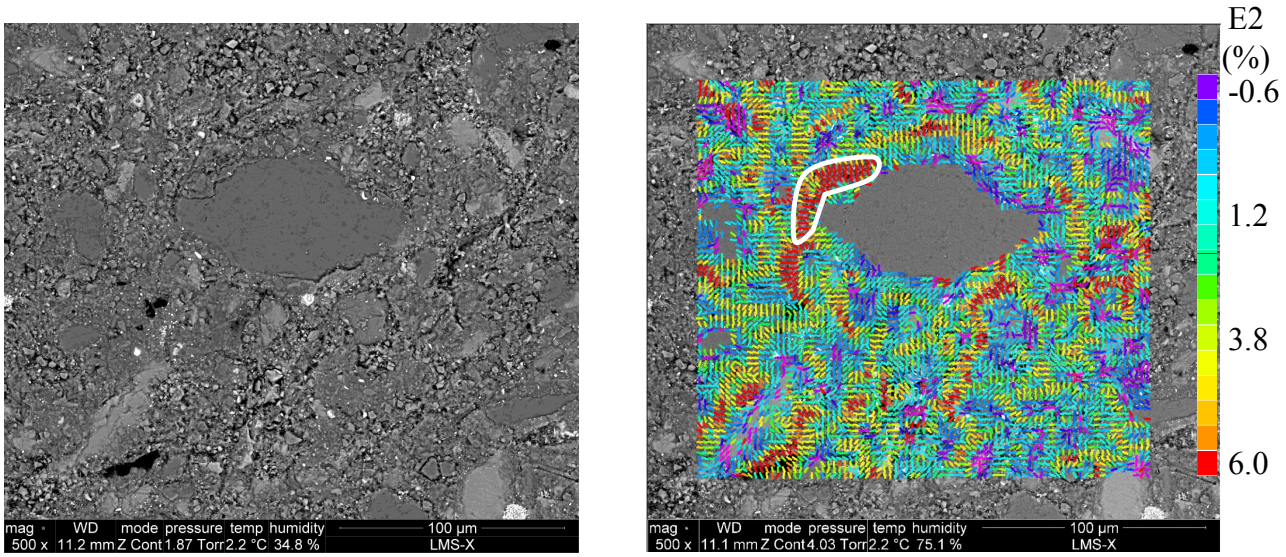

a (BSE image) b (35% - 99%RH)

Figure 3.18: BSE image (a) and ε_2 strain map (b) of zone 3 in test #4. The high extension in the outlined red domain involves in a separation of the interface between one coarse grain of quartz and clay matrix.

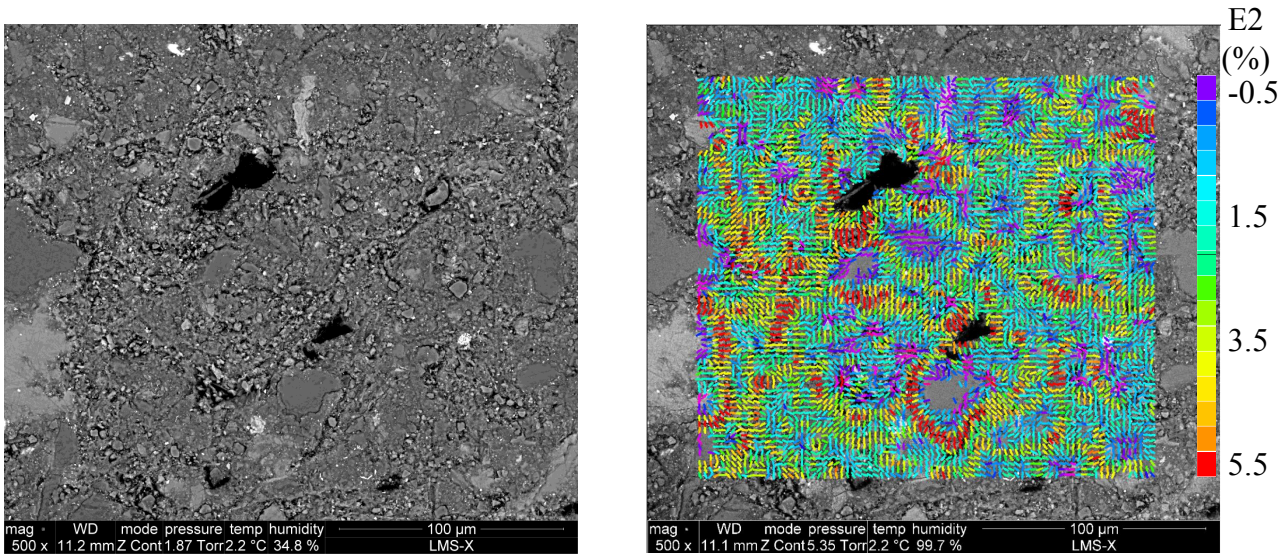

Figure 3.19: BSE image (a) and ε_2 strain map (b) of zone 4 in test #4.

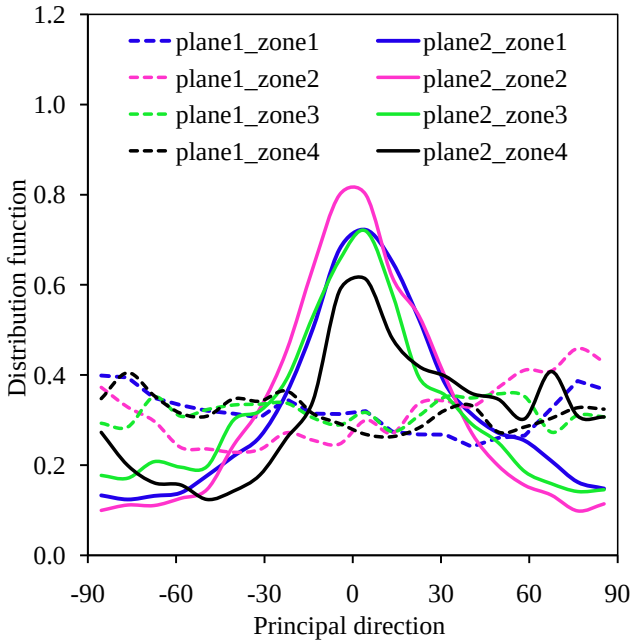

Figure 3.20: θ distribution functions for the zones in test #4 and #5.

3.2.5 Test #5: Swelling in plane 2

The humidification history in test #5 (see Fig.3.21) is similar to test #4, but the observation is concentrated at plane 2. Moreover, the bedding plane is also marked: it coincides with x axis in observation zones. Four zones (256×221 μm^2, corresponding to image magnification $\times 500$), which are representative for specimen's microstructure, are chosen as ROIs. Compared to plane 1, the inclusions in plane 2 are broadly smaller and seem to be more elongated. Note that there

are some pre-existing microcracks observed in plane 2, due to a probable prior damaging before the test. Besides, these pre-existing microcracks are mostly sub-parallel to the bedding plane.

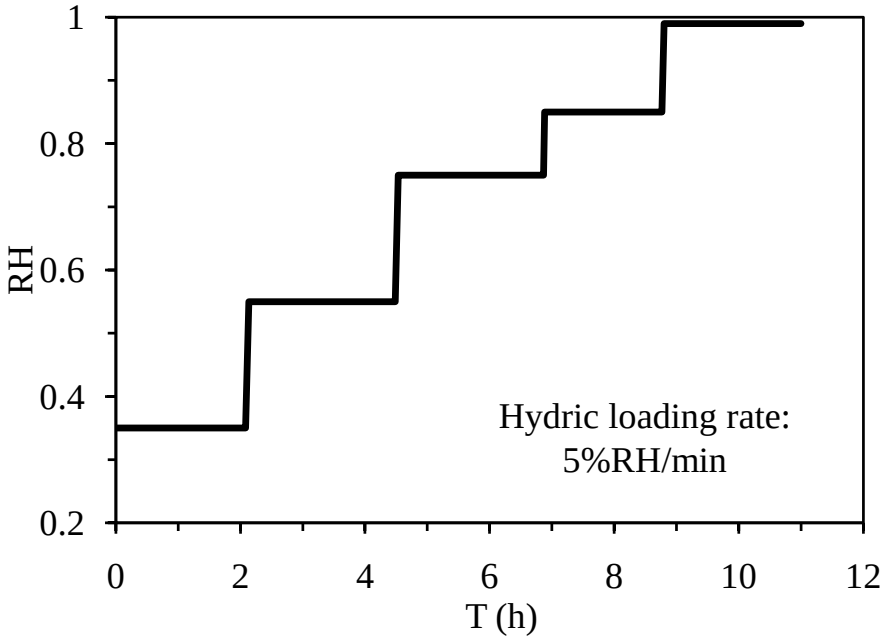

Figure 3.21: Hydric loading path of test #5.

The overall strains of the four ROIs are evaluated and presented in Fig.3.22 - 3.25. Similar to that in plane 1 (test #4), the bi-stage swelling is also evident on the strain curves, and the threshold seems to be between 75%RH and 85%RH. Contrary to isotropic swelling in plane 1, the deformation in plane 2 is noticeably anisotropic: it is more important in the direction perpendicular to the bedding plane (along y axis) than in the direction parallel to the bedding plane (along x axis). Averaging the overall strains of four ROIs, the major strain E2 is 1.12% (from 35%RH to 99%RH) and E1 is 0.32%, so the swelling anisotropy (ratio of E2 to E1) is 3.5. This anisotropic swelling is also confirmed by the measurement of Θ (angle of global E2 direction to vertical axis): it is fairly 0 for all the four observation zones in plane 2. This is different from the values measured for Θ in plane 1, and suggests the existence of a preferred swelling direction (normal to the bedding plane) in plane 2, as already noticed by other authors.

It should be noted that the major strain E2 in plane 2 is comparable with the principal strains in plane 1, despite the two samples with different observation planes were extracted from a same larger core sample. This is in opposition with existing macro-scale results, which have revealed that E2 is much greater than E1 in plane 2 and that the latter is comparable to the principal strains E1 and E2 measured in plane 1. In the present case, one would similarly expect the similar principal strains in plane 1 to be comparable to the lower principal strain along the bedding direction in plane 2. The reason why this is not the case, and more precisely why strains in plane 1 are much larger for similar RH variations, is not clear. A possible reason could be a difference in mineral composition in the considered ROIs, but no significant difference

in particle content is observed between the two tests. Another cause could be related to the introduction of some damage during sample preparation as suggested by the cracks observed in plane 2 but not in plane 1. Under wetting, the swelling of clay matrix would lead to a closing of these pre-existing microcracks. Hence, a considerable proportion of the swelling of clay matrix would be counteracted by this closing so that the overall E2 would be much smaller than on an undamaged material. This would explain a low value of E2 in plane 1, since these cracks are mostly parallel to the bedding plane, but not a low value of E1. A third explanation would be that the thin samples would undergo an additional overall bending because wetting would preferably proceed from the observation plane side, and not from the opposite surface. Swelling would be larger on the upper surface than on the lower one during the transient stages of the test. This may lead to an overall irreversible strain, still present when hydric equilibrium is reached. Such a bending would be bi-directional for plane 1 and uni-directional for plane 2, because of the anisotropy of the material. The detailed analysis of such phenomena is left for further investigations. They should however not modify the directions of the local and global swelling which are discussed here.

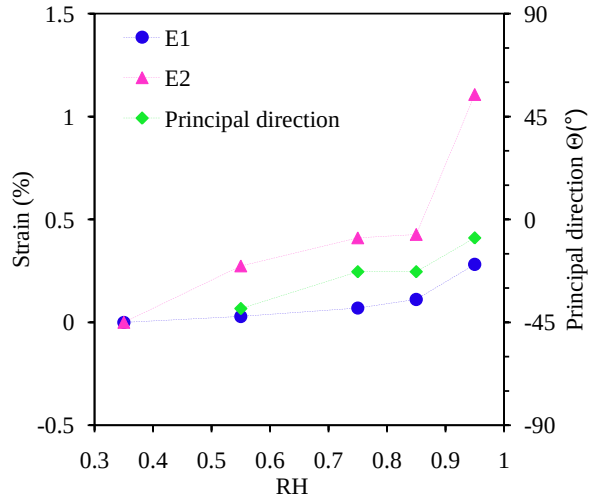

Figure 3.22: Overall strain of zone 1 in test #5.

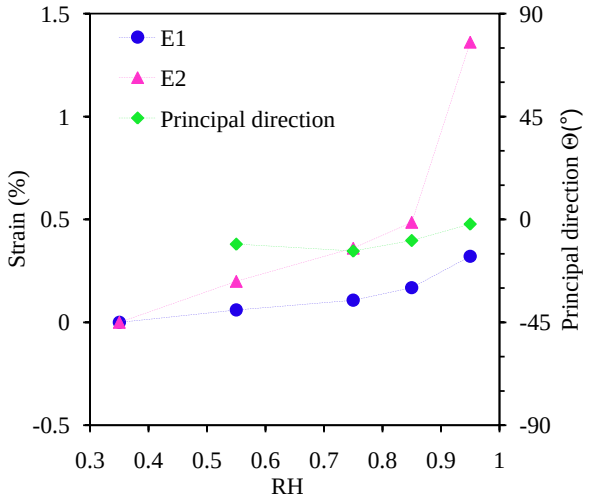

Figure 3.23: Overall strain of zone 2 in test #5.

The major swelling strain maps (35%RH - 99%RH) of the four ROIs in plane 2 are evaluated and presented in Fig.3.26b - 3.29b. Broadly, the sub-horizontal swelling bands (parallel to the bedding plane) are more frequent than other directions. In addition, weakly strained areas, parallel to the bedding plane, seem to alternate with other more intensively strained ones This is particularly true in zone 4 where two horizontal highly strained bands appear in the strain map. This is different from the observations in plane 1 in which no preferred orientation of deformation bands are observed. Moreover, the pdf of the local θ angle (Fig.3.20) is predominantly concentrated between -30° and 30° and exhibits an intense peak at angle 0

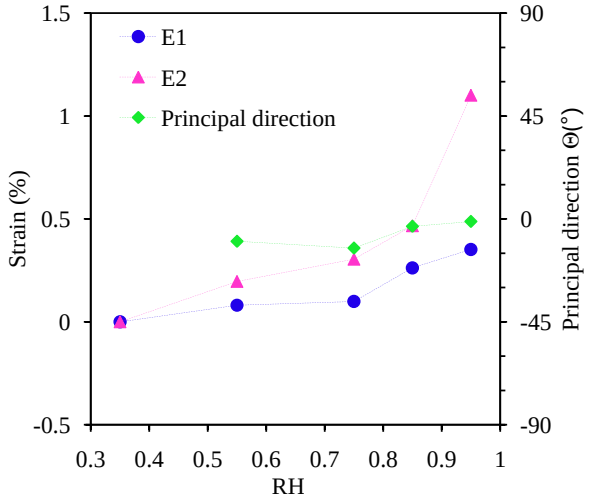

Figure 3.24: Overall strain of zone 3 in test #5.

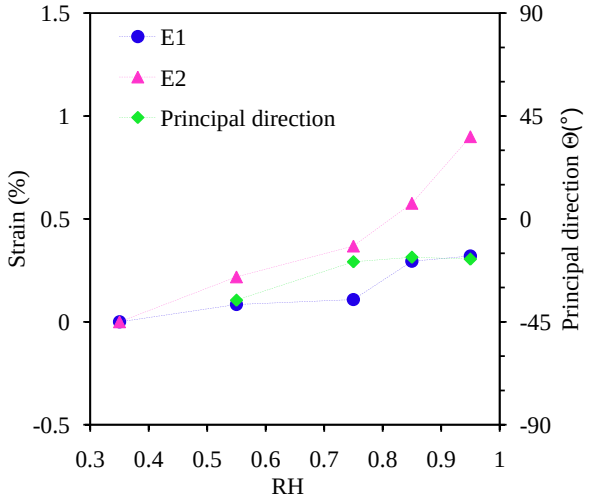

Figure 3.25: Overall strain of zone 4 in test #5.

for all the four ROIs in plane 2. This means that the local major strains ε_2 are predominately oriented sub-vertically (normal to the bedding direction), which coincides with the global Θ.

In summary, there are some dissimilar features between the observations in plane 1 and 2. In plane 1, the overall strain is fairly isotropic. The high swelling bands are randomly oriented in strain maps, as well as the direction of local ε_2. However, anisotropy manifests for the overall strain in plane 2: the overall strain is clearly larger along the direction normal to the bedding plane. Concerning strain maps, the swelling bands oriented sub-parallel to the bedding plane are significantly more frequent. Moreover, a clearly preferred direction normal to the bedding plane is found for the local major strain in plane 2.

3.2.5.1 Discussion: anisotropic swelling of COx argillaceous rock

For the COx argillaceous rock, the anisotropic swelling in plane 2 might be related to several origins: 1) anisotropic swelling and mechanical properties of clay particles, 2) orientation of clay particles, and 3) shape, orientation and distribution of inclusions. The layered microstructure of individual clay particles gives rise to their anisotropy. Swelling of clay particles is an increase of inter-layer and inter-particle spaces, so it is predominant along the direction perpendicular to the orientation of clay particles. Besides, due to their lamellar microstructure, the mechanical property of clay particles is also anisotropic, and can be assumed to be transversely isotropic (Sayers , 1994). Hence, the orientation of clay particles plays a key role for the macroscopic behavior of argillaceous rocks. The other minerals inclusions (mostly carbonate and quartz) are insensitive to water and their mechanical properties can be considered to be more isotropic. However, their form, orientation and distribution might also contribute to the swelling anisotropy because of mechanical inclusion-matrix interactions.

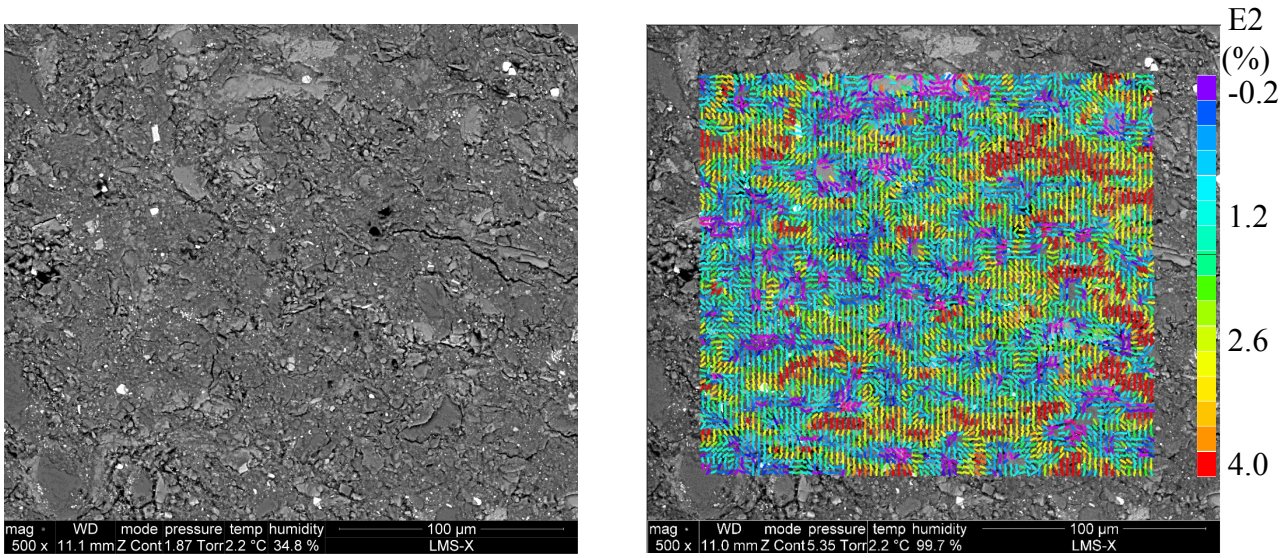

a (BSE image) b (35% - 99%RH)

Figure 3.26: BSE image (a) and ε_2 strain map (b) of zone 1 in test #5.

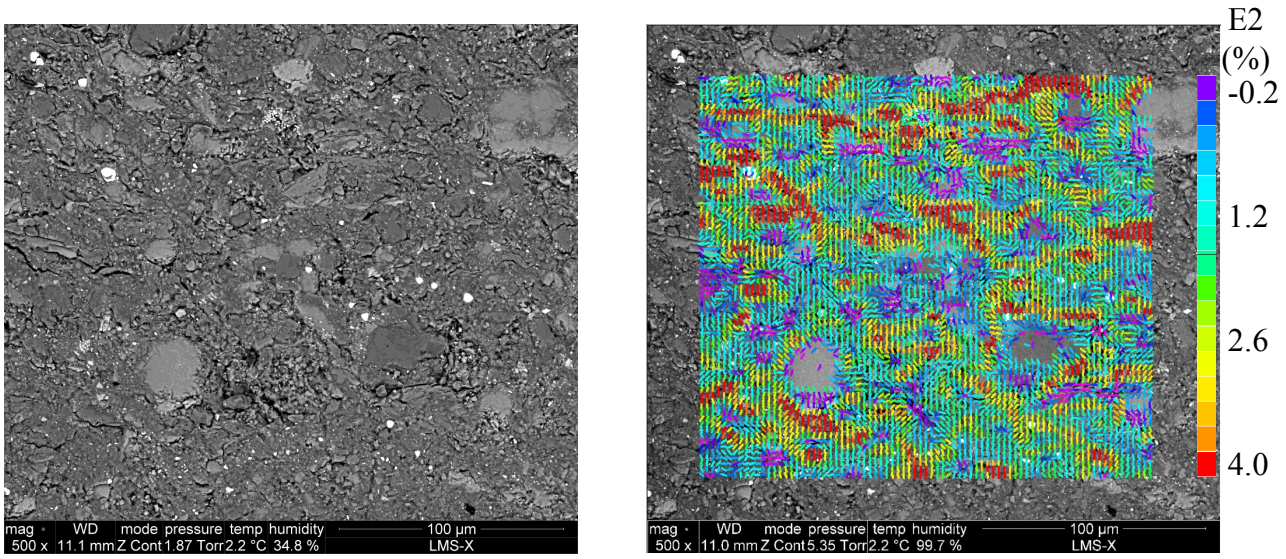

a (BSE image) b (35% - 99%RH)

Figure 3.27: BSE image (a) and ε_2 strain map (b) of zone 2 in test #5.

Preferred orientation of clay particles

Fig.3.20 reveals that local major strains (ε_2) in plane 1 present a preferred direction which is normal to the bedding plane, while those in plane 1 are oriented randomly. In this work, the gauge length of local strain measurements is 5 μm, which is indeed comparable to the typical size of an aggregate of a few clay particles (of the order of 1 μm) with comparable orientation. Hence, the direction of the local major principal strain θ is likely to incorporate an information about the orientation of clay particles: the former might be normal to the layers

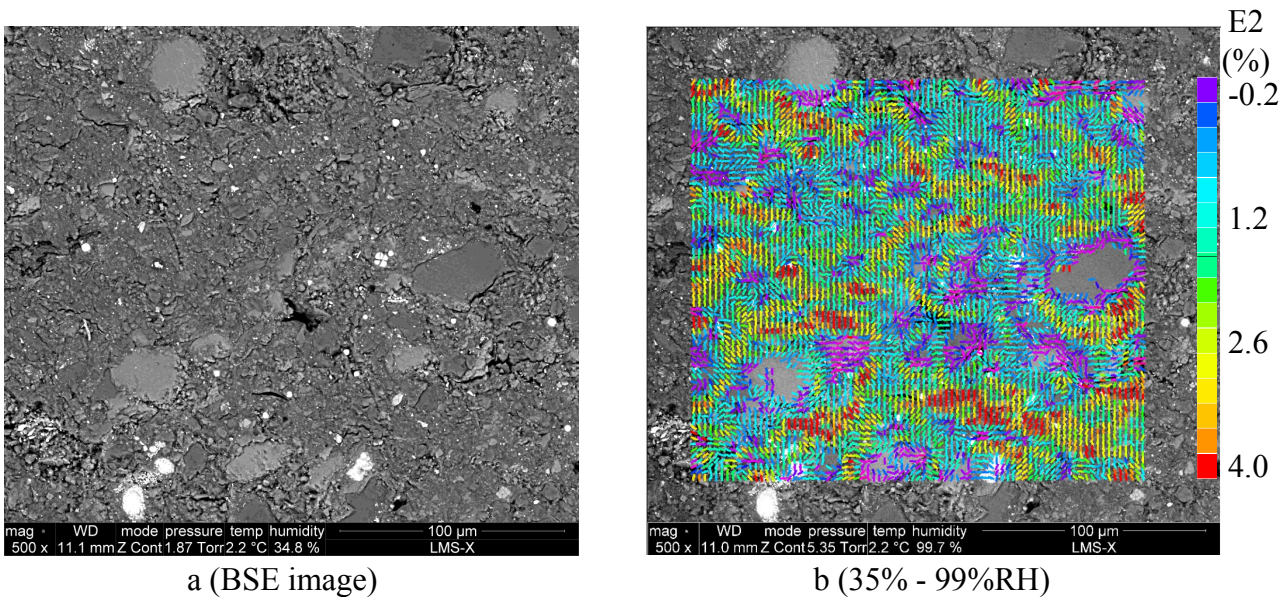

Figure 3.28: BSE image (a) and ε_2 strain map (b) of zone 3 in test #5.

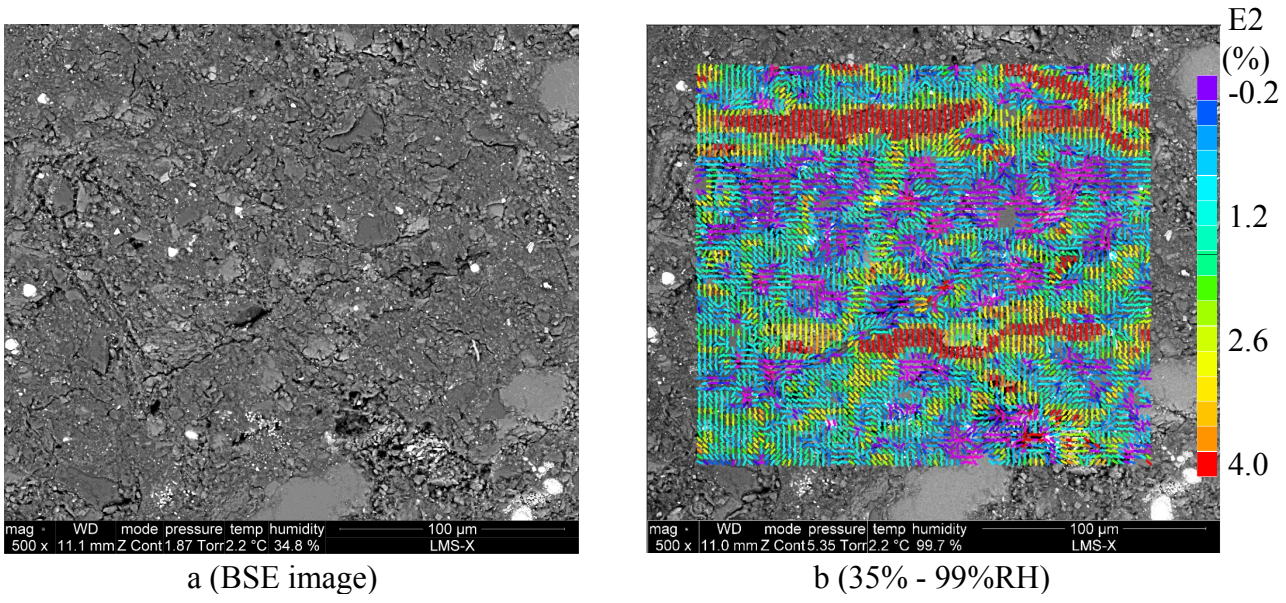

Figure 3.29: BSE image (a) and ε_2 strain map (b) of zone 4 in test #5.

of the latter under a free swelling condition. However, the local strains under wetting in clay rocks are not only linked to the free swelling of clay minerals, but also related to the local stress field due to the microstructural heterogeneity. In particular, the interaction between swelling clay matrix and non-swelling inclusions would lead to the already mentioned local stress field, which also contributes to a part of the total strain. Hence, the total strain, which is measured in this study, is a sum of the two different effects, and its principal direction is controlled by two terms: 1) orientation of clay particle governing the free swelling and the local mechanical properties, and 2) local stress tensor. The latter is generally too complex to be determined.

However, whatever its value, because of the anisotropy of the mechanical properties of clay particles, with probably a much lower stiffness along the direction normal to the layers with respect to other stress directions, it is likely that mechanical strain also exhibits an anisotropy linked to local clay particle orientation. As a consequence, the local strain orientation could be used, as a first approximation, as an indicator of the local orientation of clay particles. This interpretation is at least consistent with the observed distribution of local strain orientation, with no preferred orientation in plane 1 and a pronounced alignment of clay layers parallel to bedding plane.

An additional comment can be made on the local orientation of deformation bands. It has been noticed that local major principal strains are often normal to the bands, as the later are mostly extension bands rather than shear bands. As a consequence, deformation bands are expected to be mostly aligned which the local clay particle layers. This would again be consistent with the fact the deformation bands are mostly parallel to the bedding plane in observation plane 2, and more randomly distributed in plane 1. An additional origin of the preferred orientation of the deformation band is the spatial distribution of the other mineral inclusions, which is essentially random in plane 1, but exhibits some anisotropy in plane 2, in the form of both a preferred orientation of inclusions and a tendency of particles to align with respect to each other along the bedding direction. These particles and alignments are potential obstacles for non horizontal deformation bands, which are thus underpriviledged. These two phenomena explain the overall preferred orientation of deformation bands in observation plane 2 and the absence of preferred orientation in plane 1. The detailed path of the deformation bands is however also determined by the complexity of the local mechanical interactions and the associated stress field, induced by the incompatible swelling deformation of the constituents of the rock. Global expansion bands may thus locally be shear bands no longer parallel to clay particles. The local orientation of these bands is thus less likely to be an indicator of the local particle orientation.

Anisotropic swelling of clay particles

From the arguments developed in previous section, the local preferred orientation of clay particles could be estimated from the orientation of the local strain tensor induced by a swelling experiment. Another interesting question is the quantification of the anisotropy of the local swelling of clay particles. As is it not obvious to separate free swelling strains from mechanical strains due to the local stress field, a direct measurement of this quantity seems to be out of reach. However, it makes sense to quantify the anisotropy of the total strain at the scale of clay particles. This is the purpose of this last section.

To do so, the pdf of the local principal strains (ε_1 and ε_2) have been quantified and are shown in Fig.3.30. Local ε_1 strains vary from -5% to 4% and exhibit a peak at 0 for both observation planes. Local ε_2 strains can attain 10% and the most frequent values are also

comparable in both observation planes: it is 2% for plane 1 and 1.5% for plane 2. In addition, the distribution function in plane 2 is narrower than in plane 1, implying the strain field in plane 2 is less heterogeneous.

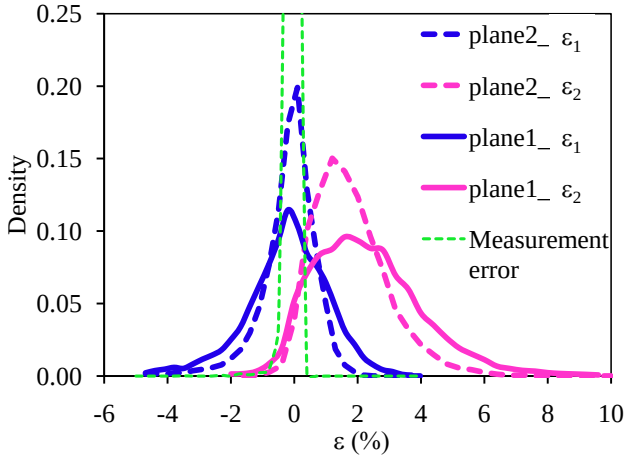

Figure 3.30: Distribution of principal strains in planes 1 and 2.

The distributions of local ε_1 strains exhibit a peak at 0. Considering the measurement error (also shown in Fig.3.30 and evaluated by plotting the pdf of the principal strains obtained when comparing two images without overall deformation), the actual distributions would be narrower (the presence of measurement errors tends to enlarge pdfs), so more concentrated around 0. This means that local swelling strains (of clay particles) are rather unidirectional. Hence, their anisotropy is very pronounced. One may evaluate from these data a lower limit of the maximal anisotropy of local strains from these pdfs. In plane 1, local ε_2 strain may reach 8% and more, while local 1 strain is almost always below 3%, so that the ratio between local principal strains can reach values above 2.7 and probably much more, which may explain the average anisotropy of 3.5 observed on the investigated ROIs on plane 2. Such an anisotropy is much larger than the one observed at macroscopic scale which is at most of the order of 2 (Valès, 2008).

In summary, among the various possible origins of the swelling anisotropy of argillaceous rocks under wetting, it seems that a strong local swelling anisotropy of the clay particles, which are likely to deform almost unidirectionaly, and a preferred orientation of these clay particles parallel to the bedding plane is the most important one. The anisotropy of the shape, orientation and distribution of the other mineral inclusions is observed but is not pronounced. It may contribute to the preferred orientation of deformation bands parallel to the bedding plane but its contribution to the global anisotropy of the swelling seems to be limited.

3.3 Irreversible deformation and microcracking

3.3.1 Test #6: microcracking due to humidification

In test #6, the specimen is humidified from 66%RH by two steps (80%RH, 93%RH) prior to a step desiccation to initial humidity state, with a loading rate of 20%RH/min (Fig.3.31). One zone on specimen's surface, with size of 320 × 276 μm^2, is chosen for observation and strain evaluation by the DIC technique, shown in Fig.3.32a. For the first step (66%RH - 80%RH), humidification results in a heterogeneous strain field, shown in Fig.3.32b. This is essentially associated with the swelling of clay matrix and its interaction with non swelling mineral inclusions (i.e. carbonate, quartz). The overall principal strains on the observation zone are 0.05% for E1 and 0.24% for E2, which evidences anisotropy. The principal direction is -32° from the vertical direction of image clockwise. No microcrack is observed at this micro-scale for the first humidification step.

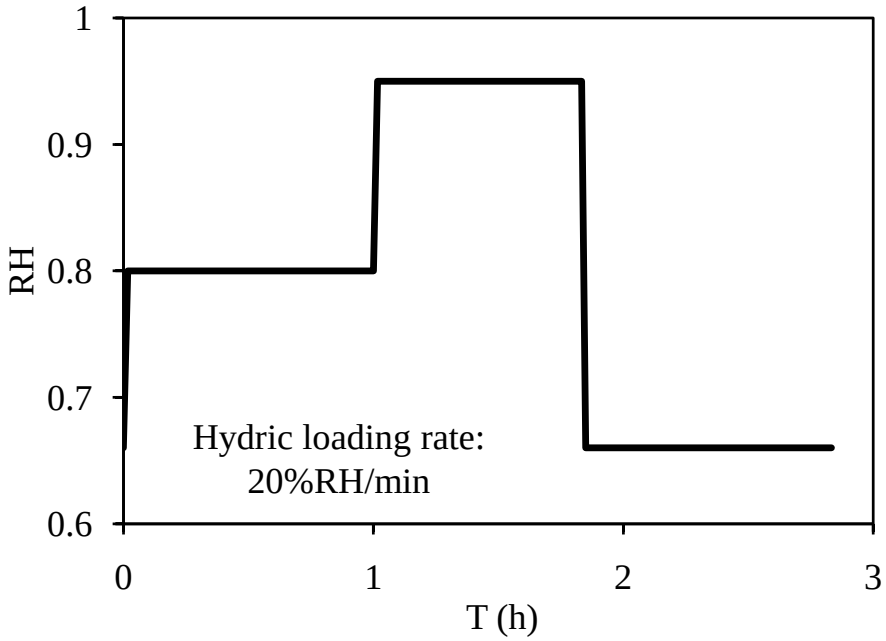

Figure 3.31: Hydric loading path of test #6.

When the specimen is moistened from 80%RH during the second step, a microcracking is triggered suddenly at 93%RH: numerous microcracks emerge at the same moment and spread all over the specimen surface in several seconds. The onset of microcracking occurs at the hydric loading stage, not at the equilibrium stage: 93%RH only corresponds to the humidity state near the specimen surface but there is a moisture gradient inside. Since microcracks propagate very sharply, the humidification is interrupted and RH is turned down to 86% to avoid the failure of specimen in test #6. The second step of humidification leads to greater deformation compared to the first step, while Θ remain similar (-27°). 156 microcracks are found in the observation

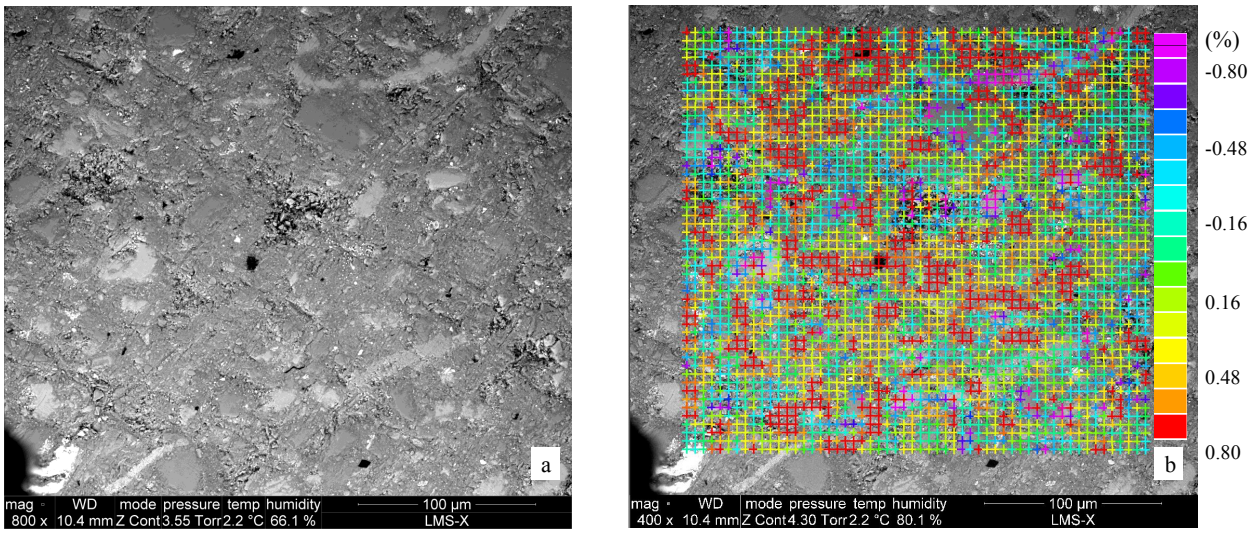

Figure 3.32: Zone of interest in test #3 (a) and the strain field at 80%RH (b).

zone, scattered fairly homogeneously (Fig.3.34). The openings of these microcracks are in the order of 1 μm, and their length are variable with the maximum of 50 μm. This microcracking at such scale can't be observed by unaided-eye: the specimen looks like intact when it is took out from the ESEM chamber at the end of test #6. These microcracks due to humidification are found either at inclusion-matrix interfaces, or in the clay matrix itself. Besides, these microcracks are outlined in red color (Fig.3.35) and a preferred orientation, especially for those in clay matrix, is evidenced. It is 60° from the vertical direction of image clockwise, which is exactly perpendicular to the direction of the major swelling -30°. Nevertheless, the preferred orienation is not evident for the microcracks at the interface, typically extending along the grains boundaries. A systematic observation of the whole specimen surface is also performed, showing similar features of such microcracking (density, size, orientation, localization), which means that the above observations are representative.

After the humidification steps, the specimen is desiccated to the initial state 66%RH. Some microcracks reclose, but the majority remains open with smaller openings (Fig.3.34). The reclosing or not of microcracks seems to be related to their openings: the microcracks with small openings can reclose whereas those with larger openings can't. Note that the average strain is reversible (E2 = 0.02%) or slightly irreversible (E1 = -0.15%) after the humidification-desiccation cycle, even if a residual microcracking is still present at the end.

It is noted that the microcracking due to humidification is strongly controlled by humidification rate. Recall that no obvious microcracking has been observed until 99%RH in test #2 where the specimen is humidified with a moderate hydric loading rate 2%HR/min. However, a significant microcracking already starts when the specimen in test #6 is humidified only to 93%RH with a high loading rate 20%RH.

To get a more detailed understanding of the microcracking due to humidification, the whole

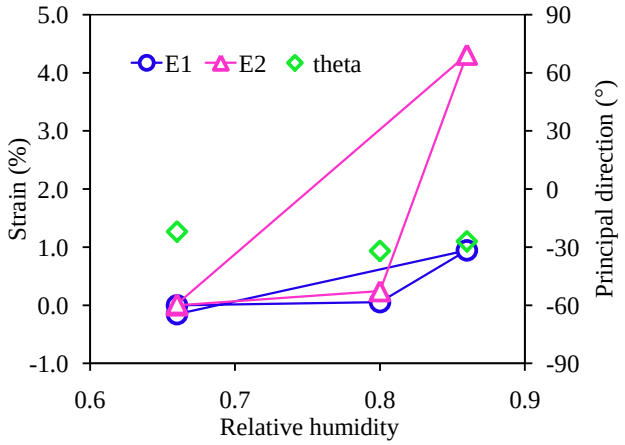

Figure 3.33: Overall strain curve in test #6.

observation zone is divided into two parts: the matching-subsets, where microcracks appear at the second humidification step, are chosen to be the damaged zone, and the rest is chosen to be the undamaged zone (see the definition of the two zones in Fig.3.35). Their deformation evolutions are separately evaluated, presented in Fig.3.36, together with the average strain for the whole observation zone. Some general features and according comments are as follows:

- For 66% - 80%RH step, the deformation in the damaged zone (Eis = 0.46%, Eeq = 0.20%) is more significant than that in undamaged zone (Eis = 0.22%, Eeq = 0.09%). It is noted that there is not yet visible microcracking in this humidification step, which means that the microcracking actually occurs in the more swelling zones.

- For 80% - 86%RH step with an evident microcracking, the deformations of argillaceous rocks are more significant than those in the first step. Note that this nonlinearity exists even in the undamaged zone, which implies that the nonlinear deformation of such rocks at high RH is related not only to the microcracking but also to a nonlinear swelling of clay minerals themselves. This confirms the observation in section 3.2.2.

- After the humidification-desiccation cycle, the deformation in the damaged zone does not return to 0 (Eis = 1.88%), essentially related to the residual microcracks. However, for undamaged zone, contraction (Eis = -0.31%) is observed at the end of hydric cycle. The overall strain (Eis = -0.13%) is indeed an average of the two combined effects: the contraction of the undamaged zone may be counteracted by the expansion of residual microcracks.

The overall deformation is fairly reversible after the humidification-desiccation cycle, even in presence of a residual microcracking: the expansion due to the residual microcracks is counteracted by the contraction of clay minerals. Note that the investigation in this test is performed in

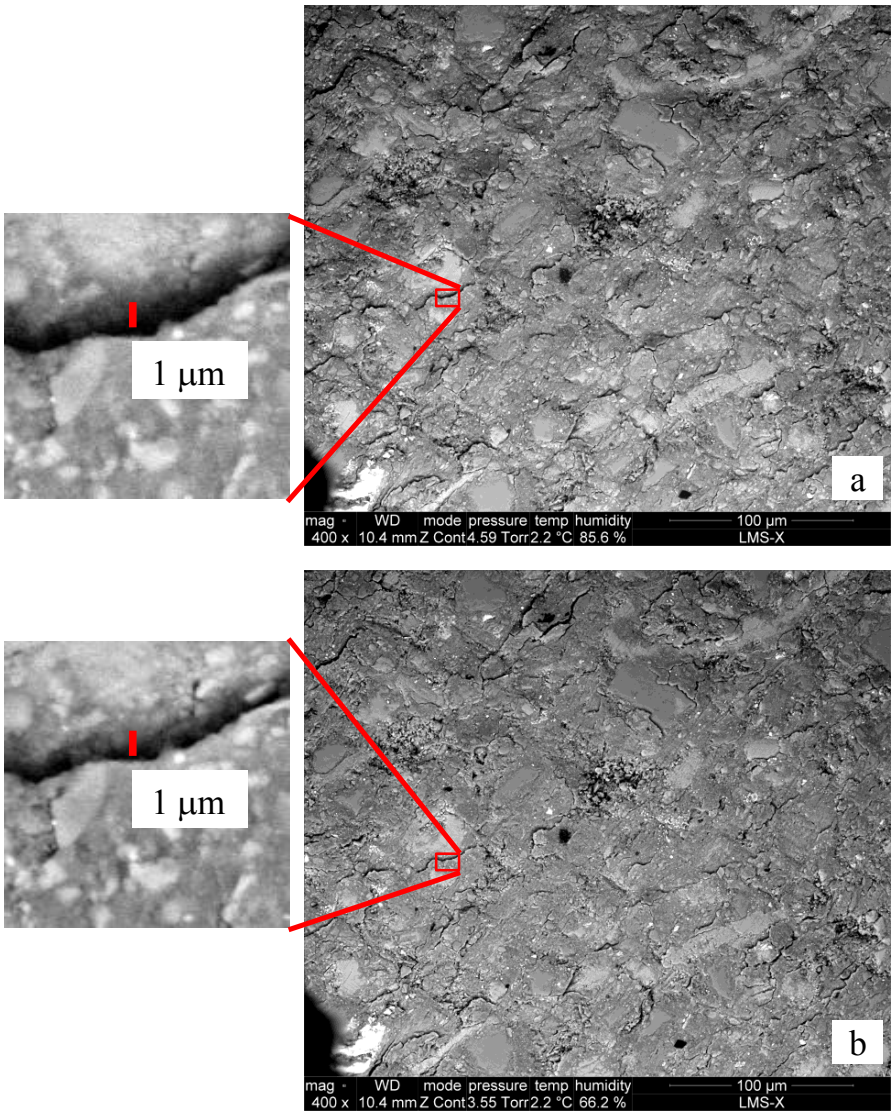

Figure 3.34: Evolution of microcracking due to humidification in test #6: a) 90%RH, b) 66%RH in case of desiccation.

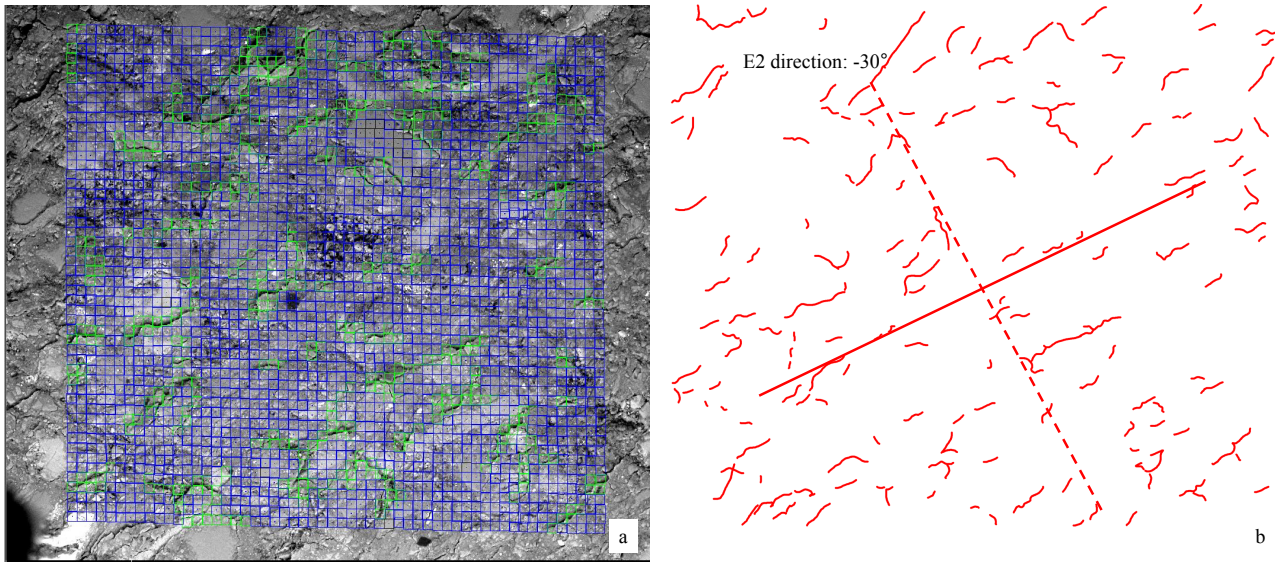

Figure 3.35: Definition of damaged zone (a) and orientation of microcracks due to humidification (b) in test #6.

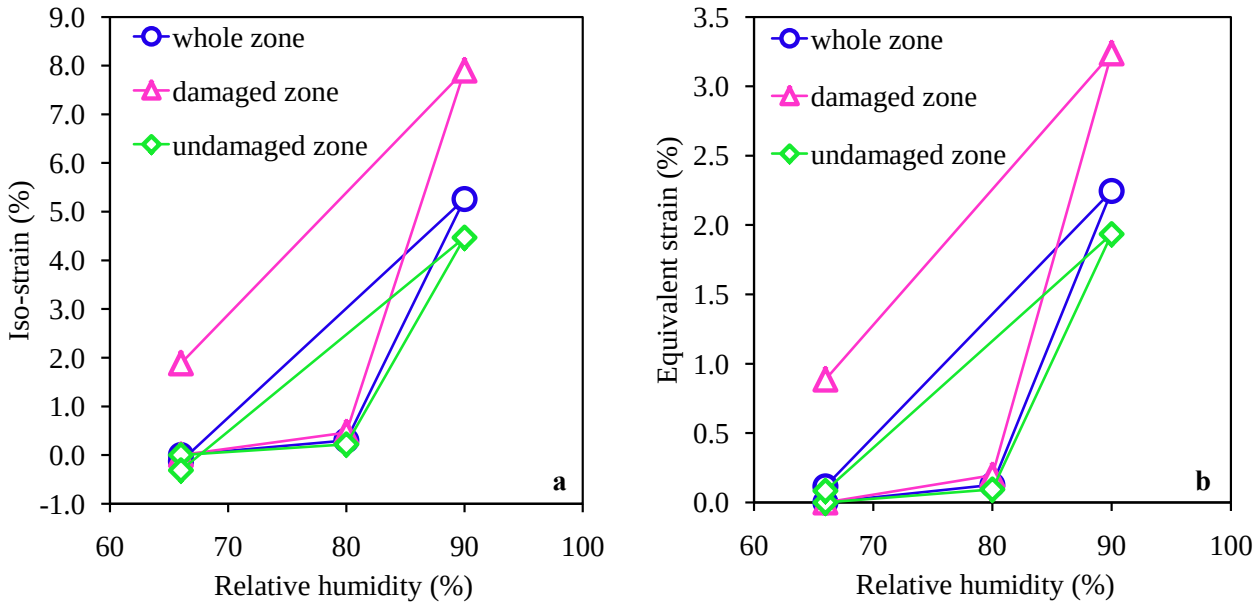

Figure 3.36: Strain curves of the whole observation zone, the damaged zone and the undamaged zone in test #6: a) mean strain, b) equivalent strain.

a clay-rich zone and the observation zone is too small to be an appropriate representative volume element. It is reasonable to deduce that the magnitude of deformation after humidification-desiccation cycle would be even more moderate at macro-scale (the gauge length is in general larger than the size of RVE). The discussion above means that the reversibility of deformation under cyclic hydric loading, which is observed mostly at macro-scale, doesn't implicate at all

that the material returns to its initial state.

3.3.2 Test #7: irreversible deformation and microcracking due to desiccation

Irreversible deformation under hydric loads

The specimen in test #7 is subjected to a humidification-desiccation cycle with a hydric loading speed of 5%RH/min, prior to a desiccation with the speed of 20%RH/min (see the hydric loading history in Fig.3.37). The moderate hydric loading rate for the humidification-desiccation cycle may avoid microcracking as observed in test #6 so that some other irreversible phenomena (for example plastic deformation) can be investigated. The final abrupt desiccation step enables to study the microcracking due to desiccation.

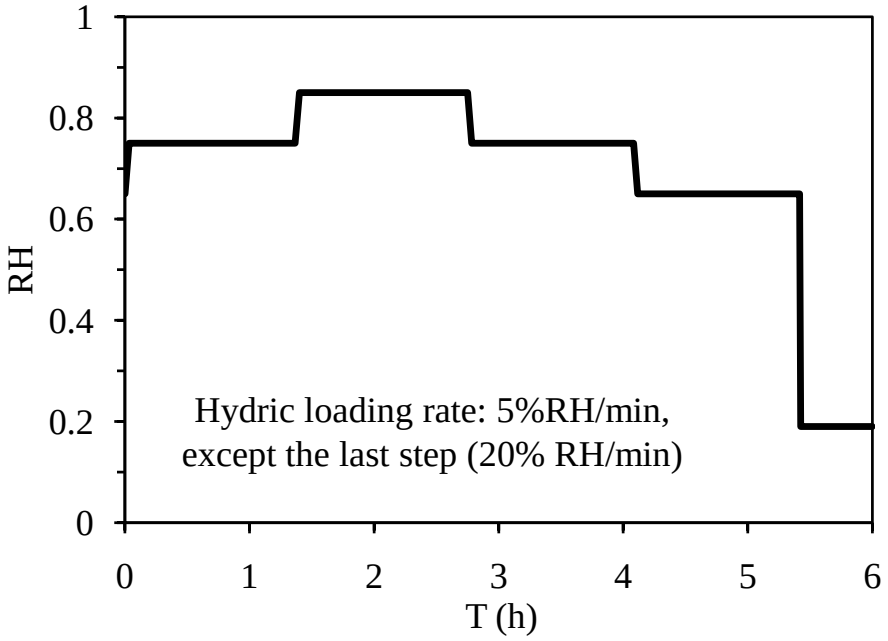

Figure 3.37: Hydric loading path of test #7.

The overall strain curves in observation zone, together with the evolution of Θ are shown in Fig.3.38. During humidification, the strain behavior is similar to test #6: the material exhibits a heterogeneous strain field, and the strain curve becomes nonlinear at high relative humidity. The strain fields at 85%RH are presented in Fig.3.39. Some microcracks due to humidification, traced in red color in Fig.3.41, are found in the clay matrix itself and on the interface between clay matrix and inclusions of carbonate and quartz. But this microcracking is less evident than that in test #6: the density of the microcracks is much smaller (36 in a 256 $\times$ 221 μm^2 observation zone), as well as their openings and extensions. This difference implies that the microcracking due to humidification is strongly related to humidification rate: a fast

RH changing promotes microcracking.

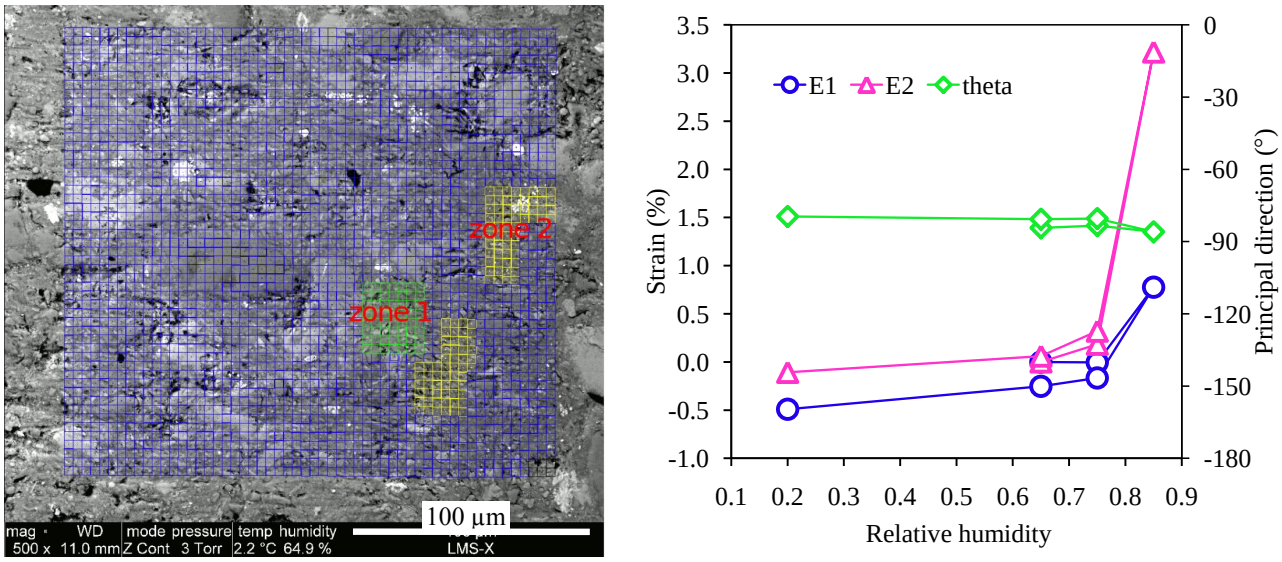

Figure 3.38: Observation zone in test #7 (left) and its overall strain curves (right). Zone 1 and 2 are two interesting domains. Mesh nodes represent discrete measurement positions (center points of matching-subset for DIC technique).

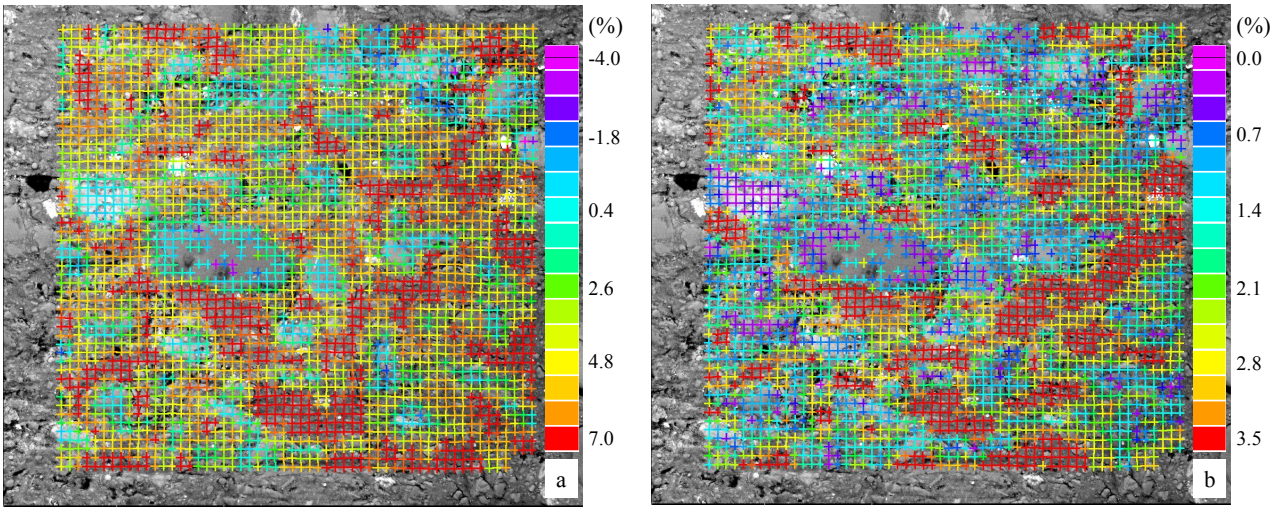

Figure 3.39: Strain field during humidification at 85%RH in test #7: a) mean strain, b) equivalent strain.

When RH returns to initial value 65%, a portion of such type of microcracks recloses while the others remain open. The reclosing or not of the microcracks seems to have no link with their openings, as observed in test #6, as they are all comparable and small in test #7. However, the residual microcracks are probably related to irreversible deformation around them:

they are mostly found in the domain where some irreversible deformations are found after the humidification-desiccation cycle (Fig.3.40). It is noted that some new microcracks, which are actually due to desiccation, are found as well in clay matrix during such steps (they are traced in green color in Fig.3.41b).

Concerning the overall strains of observation zone, they are roughly reversible for E2 and slightly irreversible for E1 (-0.25%). Moreover, some irreversible deformations, mostly in clay matrix, are found in the strain map at the end of hydric loading cycle, as shown in Fig.3.40. The irreversibility is more obvious in the map of equivalent strain where the value can reach more than 3.5%. In the map of mean strain, some contraction occurs in the clay matrix after the humidification-desiccation cycle.

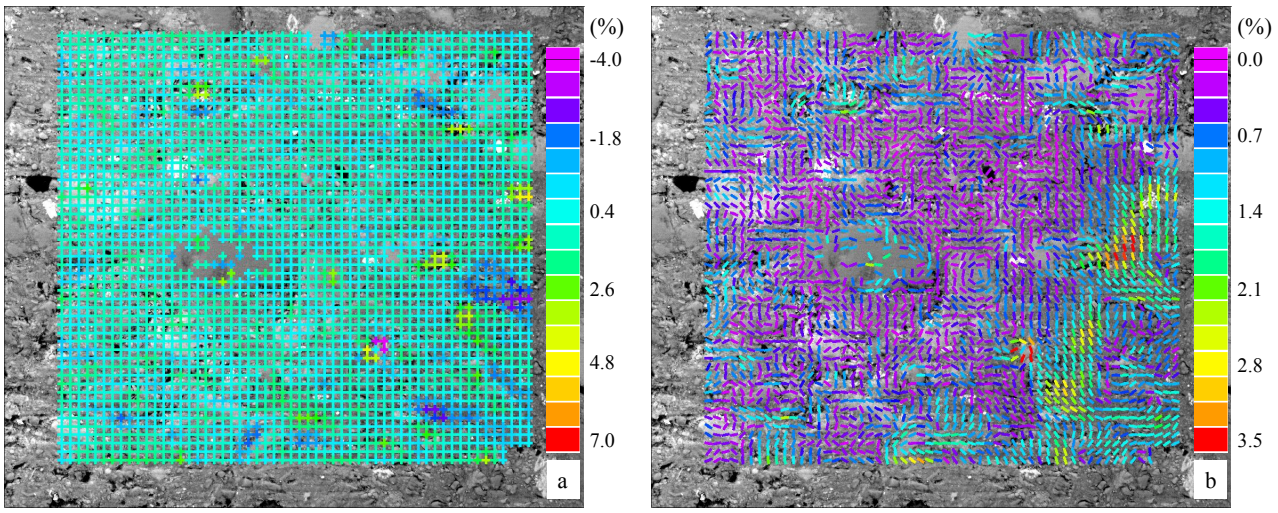

Figure 3.40: Residual deformations at the end of humidification-desiccation cycle (RH=65%) in test #7: a) mean strain, b) equivalent strain.

For a better understanding of the origin of these irreversible deformations, two domains are chosen in clay matrix: the domains with irreversible equivalent deformation are chosen as domain 2, while domain 1 exhibits similar strain level as domain 2 during humidification steps but it is fairly reversible at the end of hydric loading cycle (see the definition of the two domains in Fig.**??**). The deformation evolution of these domains is calculated and presented in Fig.3.42. During humidification, the strain curves (both mean strain and equivalent strain) for the two domains are comparable: the magnitude of equivalent strain for domain 1 (3.7%) is even more significant than domain 2 (3.5%) at 85%RH. After the humidification-desiccation cycle, the mean strain for the two domains comes back to zero, whereas their equivalent strains are quite different. There is a considerable residual equivalent strain (2.2%) for domain 2 whereas the magnitude in domain 1 is much smaller (0.4%).

Such inconsistency may be attributable to the different deformation mechanisms associated in the two domains under hydric loading. Actually, the deformation in zone 1 seems to be

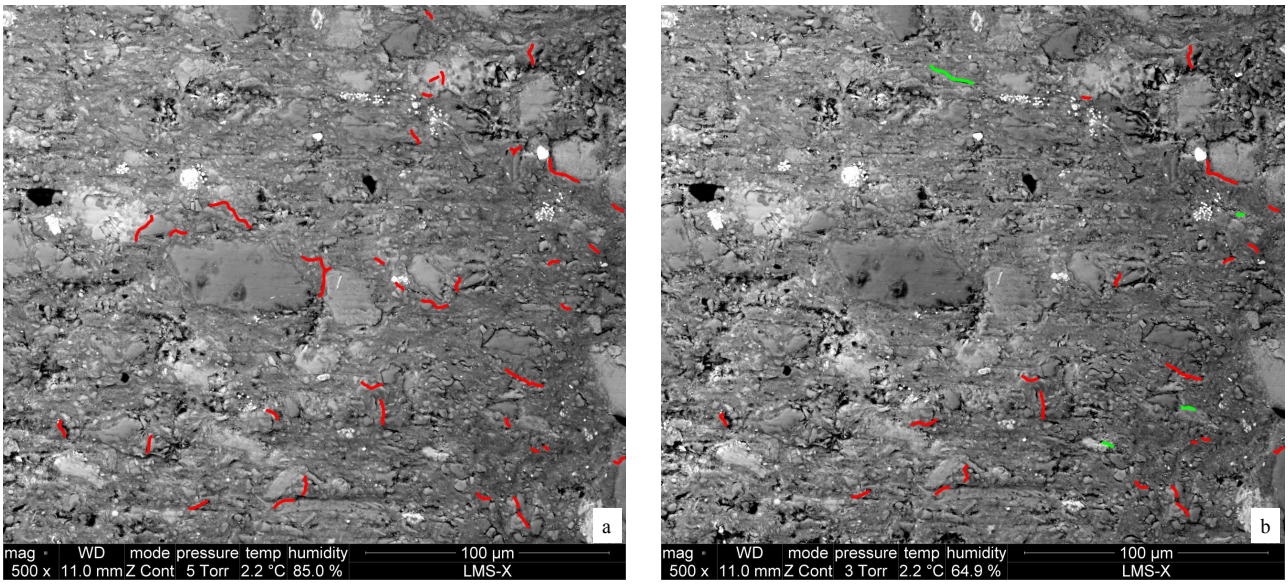

Figure 3.41: Microcracking in test #7: a) 85%RH, b) desiccation to 65%RH (red lines represent residual microcracks due to humidification while green lines represent new microcracks primarily due to desiccation.

predominantly associated with physic-chemical swelling-shrinking of clay minerals itself. This swelling is anisotropic: the strain is more significant in the direction perpendicular to the bedding plane than parallel to it and this could result in a significant equivalent strain. Nevertheless, such physic-chemical swelling is reversible: Montes-H et al. (2001) observed a swelling of clay aggregate with a magnitude reaching 50% but it remains fairly reversible. Therefore, the apparition of irreversible deformation in zone 2 can't be predominantly attributable to this mechanism. However, such irreversible deformation is probably plastic deformation, which is associated to another deformation mechanism of argillaceous rocks under humidification: mechanical stress generated by incompatible free swelling. In fact, argillaceous rock is a heterogeneous material and the behaviors of its components under hydric load are contrasting: the clay matrix swells during humidification while the other mineral inclusions don't. Furthermore, clay matrix is also heterogeneous: smectite owns a strong capacity of swelling, while illite and kaolinite swell hardly. Finally, the anisotropic swelling property of clay particle and its variable orientation in argillaceous rock may intensify this heterogeneity as well. Consequently, the free deformation incompatibility may generate a mechanical stress field, and some plastic deformation can be produced if some local stress exceeds the yield stress of clay matrix.

Microcracking under desiccation

It is noted that three microcracks, different from those due to humidification, have been found in the clay matrix when RH returns to 65% during the humidification-desiccation cycle. They are outlined with green color in Fig.3.41b. After the humidification-desiccation cycle, the

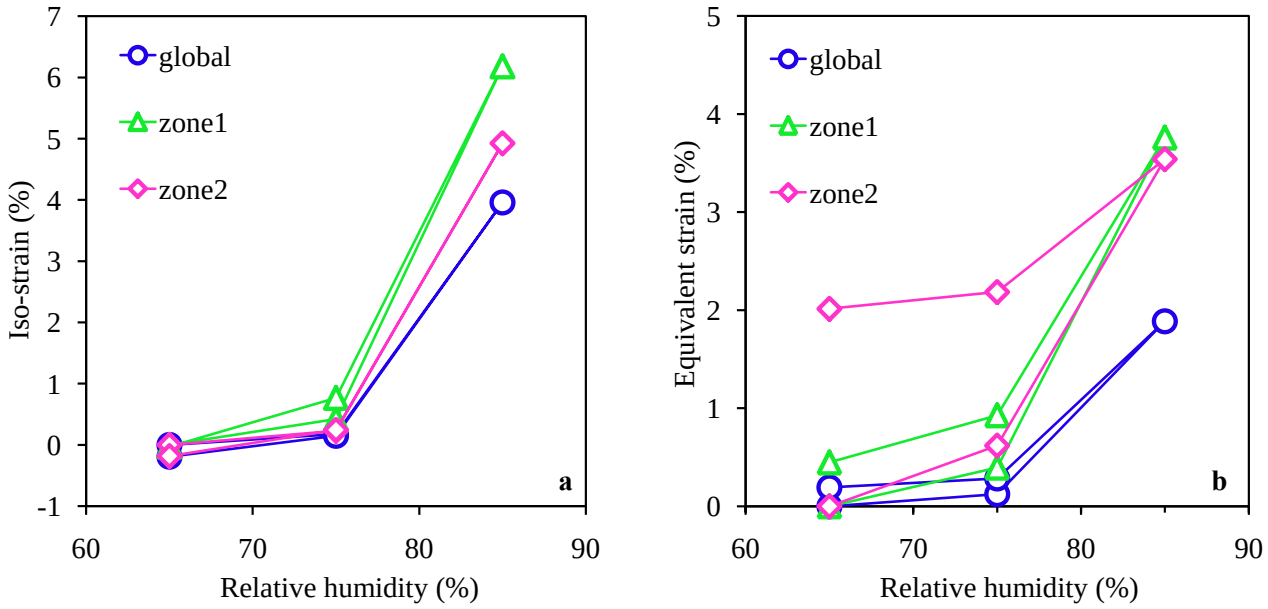

Figure 3.42: Strain curves in different zones in test #7.

specimen continued to be desiccated until 20%RH with a speed of 20%RH/min. This strong and fast desiccation results in an obvious microcracking, shown in Fig.3.43. The microcracks due to desiccation are found mostly in the clay matrix. This is different from the microcracking due to humidification which can be found not only in clay matrix but also mostly on inclusion-matrix interfaces. In addition, these microcracks prefer to propagate in the direction of -80° from vertical direction of image in clockwise, as shown in Fig.3.38. This orientation is actually perpendicular to the direction of E1 (major contraction) which is also consistent with the bedding direction.

3.4 Summary of chapter

In this chapter, the behavior of argillaceous rocks under purely hydric loadings is experimentally investigated by the combination of ESEM and DIC techniques. ESEM observation enables to distinguish the composite microstructure of argillaceous rocks: a continuous clay matrix scattered by the other minerals inclusions (mostly carbonate and quartz). Under purely hydric loading, a heterogeneous strain field but well corresponding to the microstructure of the material is evidenced: clay matrix generally involves in high swelling, while inclusions deforms hardly. According to these observations, deformation mechanisms of argillaceous rocks under hydric loading are characterized: 1) the swelling-shrinking of clay minerals, and 2) the mechanical stress field generated by non-uniform free swelling in such rocks.

The deformation of argillaceous rocks with RH increasing exhibits a strong nonlinearity at

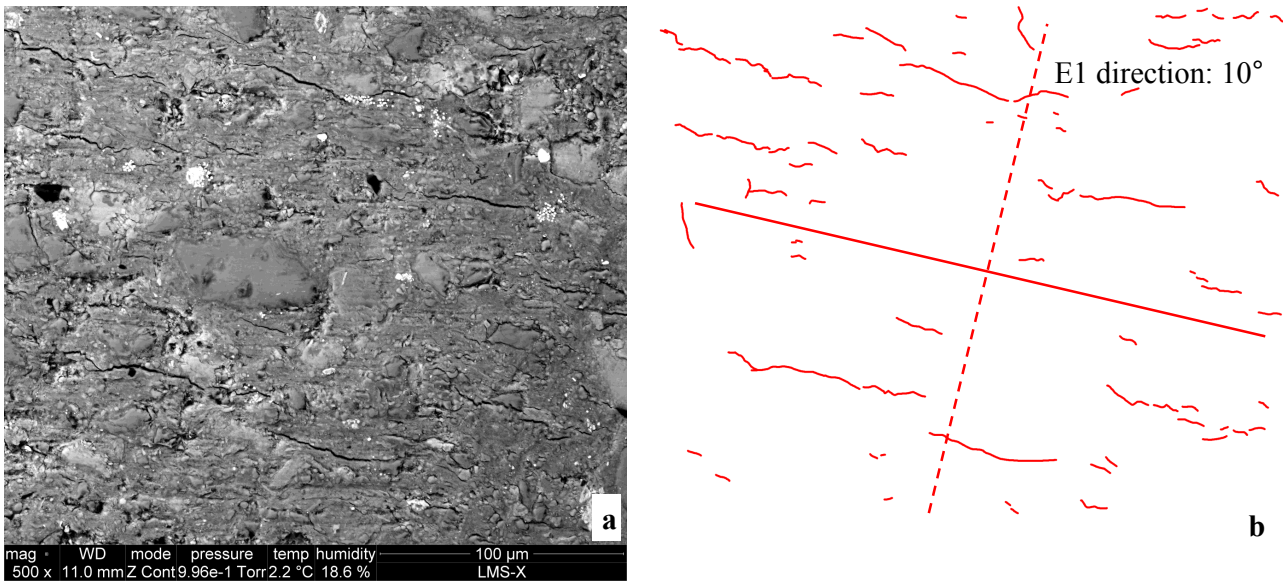

Figure 3.43: Microcracking of argillaceous rocks due to desiccation at 20%HR: a) BSE image, b) orientation of microcracks comparing with the direction of minor principal strain E1.

high relative humidity. It can be attributable to the microcracking due to humidification. But another mechanism is evidenced in this work: the nonlinear swelling of the clay matrix itself.

Under humidification, our investigation reveals an anisotropic deformation of Callovo-Oxfordian argillaceous rocks, as shown by the study at macro-scale: the swelling is more significant in the direction perpendicular to the bedding plane than in the direction parallel to it. And the different origins of this anisotropy is evidenced in this work: 1) anisotropic swelling property of clay particle, 2) micro-textural anisotropy, that consists of existing preferred orientation of clay particle in tested rocks (sub-parallel to the bedding plane), and 3) meso-textural anisotropy, which is strongly controlled by the form and orientation of inclusions. For Callovo-Oxfordian argillaceous rocks, the two scales textural anisotropies are both associated to the bedding process of such sedimentary material, however, it is the micro-textural anisotropy seems to be predominantly contributable to anisotropic swelling.

Besides monotonic humidification test, cyclic hydric loading tests are also achieved, whereby some irreversible phenomena associated to hydric loading is evidenced:

- Some residual deformations (a apparent volumetric contraction and some shear strains) are evidenced during the humidification-desiccation cycle in this work, predominantly being found in clay matrix. The analysis in this work has proved that such residual deformation is strongly associated to internal mechanical stress field, particularly associated to matrix-inclusion interaction: certain plastic deformation would develop when some local magnitude exceeds the elastic limit of material. It is noted that these irreversible deformation are generally concentrated at small domains and sometimes counteracted by

other phenomena so that the global strain (or strained measured at macro-scale) is fairly reversible or slightly irreversible.

- Under humidification, a network of microcracks with an opening of the order of 1 micrometer is found, at high relative humidity, not only in clay matrix but also on inclusion-matrix interfaces. In addition, they prefer to extend in the direction perpendicular to the bedding plane of such stratified rocks. Certainly, the multi-scale heterogeneity of argillaceous rocks is responsible for such microcracking: the internal mechanical stress potentially results in damage.

- Subjected to desiccation, the microcracking with a preferred orientation perpendicular to the stratification was also evidenced in this work, but with different morphology comparing to the humidification case: they are mostly found in clay matrix.

Hydric loading speed has been proved in this work to play also an important role for the behavior of argillaceous rocks. The results have shown that the nonlinearity at high relative humidity during humidification emerges generally earlier when the material is humidified more brutally. Moreover, a high hydric loading speed may also promote the microcracking during humidification, which is another source of nonlinearity, already mentioned in literature.

Bibliography

Allais, L., Bornert, M., Bretheau, T., Caldemaison, D., 1994. Experimental characterization of the local strain field in a heterogeneous elastoplastic material. Acta Metallurgica et Materialia 42 (11), 3865-3880.

Eshelby, J.D., 1957. The determination of the elastic field of an ellipsoidal inclusion and related problems. Proceeding of Royal Society of London. Series A 241, 376-396.

Montes-H, G., Duplay, J., Martinez, L., 2001. Study of bentonite swelling : qualitative and quantitative analysis using ESEM and digital image analysis program. 12th International Clay Conference, Bahia Blanca, Argentina.

Sayers, C.M., 1994. The elastic anisotropy of shales. Journal of Geophysical Research 99, 767-774.

Valès, F., 2008. Modes de déformation et d'endommagement de roches argileuses profondes sous sollicitations hydro-mécaniques. Ecole Polytechnique, Palaiseau.

Chapter 4

Microscale experimental investigation under mechanical load

Contents

In chapter 3, the behavior of argillaceous rocks under purely hydric loading has been experimentally investigated. This chapter addresses the mechanical behavior of such rocks, which is strongly controlled by their humidity state. By means of ESEM and DIC techniques, the evolution of such rocks under combined hydric and mechanical loadings is analyzed at microscale. Using a specifically designed rig, in-situ uniaxial compression tests are conducted in the ESEM chamber, maintaining relative humidity constant. Different humidity states are tested to investigate the unified deformation and damage mechanisms of such rocks and the influence of water content on them.

Moreover, a test under combined hydric and mechanical loadings is performed. For the hydric loading part, the specimen is subjected to a staged humidification (20%RH - 80%RH - 99%RH). For the mechanical loading part, a uniaxial compression test is carried out on the specimen that reaches the moisture equilibrium for each humidity state: A moderate loading-unloading cycle for the first two humidity states (20%RH, 80%RH), accompanied by a mechanical loading until failure for the high humidity state (99%RH). By such a test, deformation mechanisms of argillaceous rocks under hydric and mechanical loads are characterized respectively and can also be correlated together. In addition, the influence of saturation (water content) on the mechanical behavior is studied at local scale.

It should be recalled that such behaviors have been studied by using optical microscopy (Valès, 2008). However, its observation resolution (a physical field of at least 0.7 μm represented by a pixel) is too big to identify the distribution of different constituents in such rocks. In this work, we yield at least one order of observation resolution, which leads to a good characterization of the composite microstructure.

4.1 Equipment and experimental procedure

A specific equipment has been developed at LMS (Mechanical Solids Laboratory, Ecole Polytechnique) by D. Caldemaison and V. de Greef, allowing in-situ combined hydric and mechanical loading experiment in the ESEM chamber. The equipment is composed of two parts: mechanical loading device, and relative humidity controlling system.

Uniaxial compression can be applied on specimens by a displacement-control electromechanical machine of which the loading rate can be controlled (the minimum is lower than 1 μm/s. Displacement measurement is performed by a LVDT (linear variable differential transformer) displacement sensor. Besides, a force sensor is used to monitor the force applied on samples. The measurement limit of the force sensor is 1kN, which corresponds to 35MPa considering the typical cross-section size of specimens (5.5×6 mm^2) used in the test.

Besides mechanical loading, the relative humidity of the specimen surrounding can be controlled in the ESEM chamber, of which the principles and applications have been discussed in detail in the previous chapter. Nevertheless, different from thin specimens (about 1 mm)

normally used in pure hydric loading tests, thick samples have to be prepared for the mechanical loading system in this chapter. Such thick samples lead to crucial issues for RH control, particularly due to the difficulty of cooling them by the Peltier module. In fact, when compared to the size of the ESEM chamber, the Peltier module acts as a point source only controlling sample temperature, not the temperature of the whole ESEM chamber. Consequently, thermal gradient would develop in ESEM chamber which inhibits cooling the specimen. Such effect is not crucial for thin samples which are in contact with the Peltier module. It becomes a great issue for thick ones which are in contact with the testing device. Several systems have been developed to protect samples from the thermal gradient in the ESEM chamber. Firstly, a copper rectangular tube-shaped box is prepared to encompass the sample and to create a local atmosphere with uniform temperature in its neighborhood. Only a small hole (4×3 mm^2) is excavated at the upper side of the box for observation. Besides, a black adhesive made of PVC (Polyvinyl chloride) is attached on the outside surface of the copper box to prevent radiation. In this study, grease is smeared on the interfaces (sample-box, Peltier module-box) to remove the unfavorable effect of their roughness and according increase the thermal resistance of the system. The compression platens are in MACOR, acting also as an efficient thermal insulation, to better control sample's temperature.

The equipment is presented in Fig. 4.1.

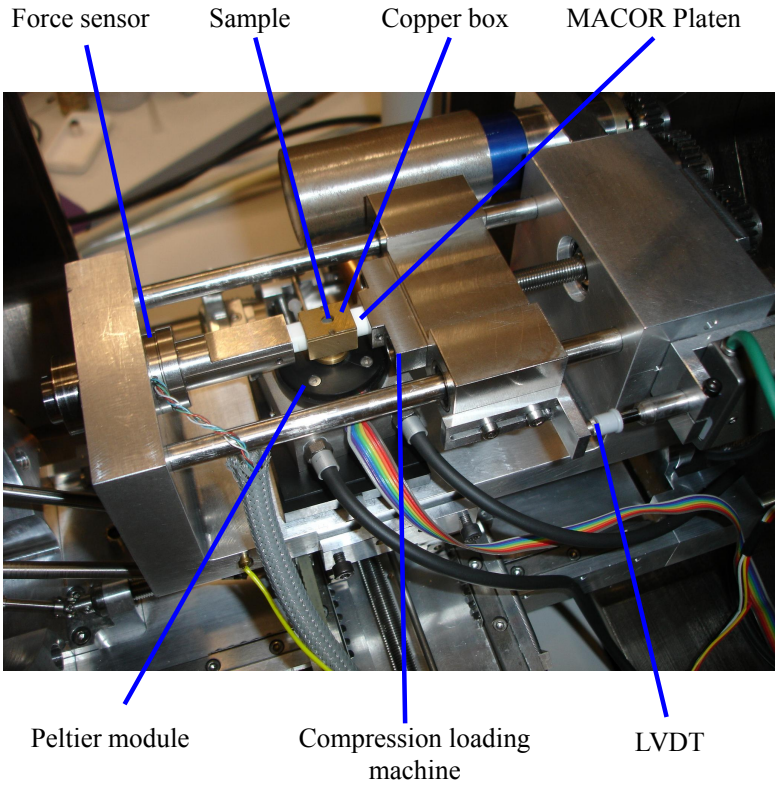

Figure 4.1: Hydric and mechanical loading system in ESEM.

4.1.1 Cooling thick samples in ESEM chamber

In general, temperature control (by the Peltier module) in ESEM is performed on very thin samples and the Peltier module has been developed for such samples. However, thick sample (about 6 × 6 × 12 mm^3) has to be used for mechanical loading in this study, which leads to crucial issue for cooling it. The thermal exchange around samples is controlled by three mechanisms of heat transfer: thermal conduction, thermal convection, and thermal radiation.

When the sample is cooled by the Peltier module, a heat flux q is transferred from the sample (at temperature T_s) to the Peltier module (T_p) by conduction:

$$q_1 = \frac{T_s - T_p}{R} \tag{4.1}$$

where R is the conductance thermal resistance.

However, the sample would simultaneously be heated by its warmer environment (T_{env}) by convection. This can be described by Newton's law:

$$q_2 = Ah\,(T_{env} - T_s) \tag{4.2}$$

where A is the area over which heat is transferred to the surrounding atmosphere (supposed independent of T).

Neglecting radiation, the equilibrium temperature of the sample can be determined by q_1=q_2,

$$T_s = \frac{T_p + ARhT_{env}}{1 + ARh} \tag{4.3}$$

From equation 4.3, sample's temperature is certainly different from that of Peltier module which is monitored by the system. Their difference strongly depends on the performance of the cooling system (such as R), as well as environment conditions (A, T_{env}).

For this reason, a test on temperature is conducted to examine the ability of the system for cooling the sample. The temperatures of three places (see Fig.4.2) are measured by temperature sensor: the Peltier module's surface (point 1), the upper surface of copper box (point 2) and the sample's end (point 3) which is the furthest away from the Peltier module and so the most unfavorable place to be cooled. In atmosphere condition (10^5 MPa, 20°C), their results are shown in Fig.4.3. The temperature of Peltier module's surface isn't identical to the setup value: it is higher for T < 15°C while is lower when T > 15°C. The deviation increases with the distance to the overlapped point (T = 15°C) and can attain 1°C: the temperature of module's surface is 2°C when the setup value is 3°C. As expected, the copper box can't be perfectly cooled to setup value, and the deviation increases when setup value is lower. When the temperature is set as 1°C for example, the temperature at the upper surface can only attain 3.4°C. Concerning the sample, its temperature is even higher than that of copper box.

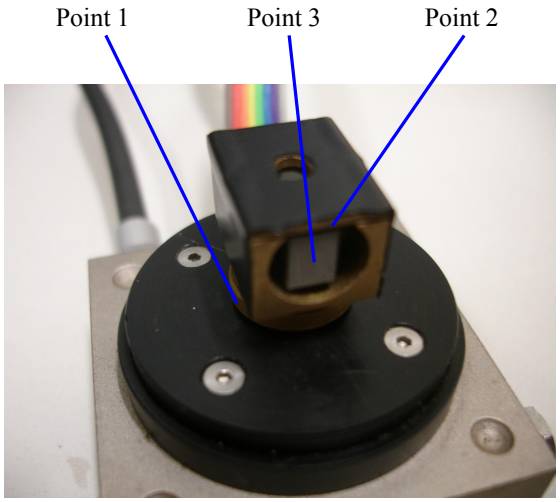

Figure 4.2: Three zones for temperature test.

One cause of these temperature deviations consists in thermal resistances of module-box interface and box-sample contact which would generate temperature difference during thermal conduction (see equation 4.1). One improvement can be performed by smearing grease between the two interfaces: it can augment their contact surface and accordingly increase their thermal resistance. The comparison between the systems with and without grease smearing is performed and shown in Fig.4.3, which reveals the favorable effect of this improvement.

As described in equation 4.2, the sample, cooled by the Peltier module, would absorb some heat flux from its environment by convection. Hence, the ESEM chamber pressure influences the sample temperature. A test is accordingly conducted (shown in Fig.4.4): the atmosphere is pumped to different values (in standard working range), and the corresponding temperatures of a sample of argillaceous rocks are measured. The temperature set being 6°C, sample's temperature increases somewhat linearly with ESEM chamber's pressure. This is natural since more gas would support more heat flux by convection so that it is more difficult to cool the sample. Moreover, heat flux by convection is also controlled by the gas type. In ESEM mode, dry air initially existing in atmosphere would be replaced by water vapor via purge, which ensures that the chamber pressure is identical to the water vapor pressure. For the same chamber pressure, sample temperature would increase when the ESEM chamber is filled with water vapor instead of air (mixture of dry air and water vapor). This is because the convective heat transfer coefficient of pure water vapor is bigger than that of air.

When the sample is cooled in ESEM chamber, its surface reaches its steady value very quickly: only several minutes for normal working condition (see Fig.4.5). The thermal conductivity of Callovo-Oxfordian argillaceous rock is 1.3 - 1.9 W/m/K and its specific heat is 1005 J/kg/K. Hence, the cooling process of such rocks can be considered to be very rapid regarding to the moisture transport process (generally several hours for a sample with 6 mm thickness).

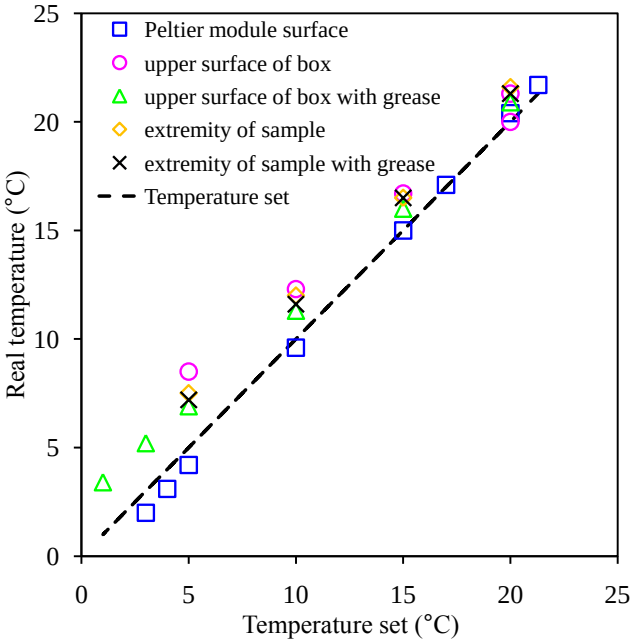

Figure 4.3: Temperature test of relative humidity controlling system.

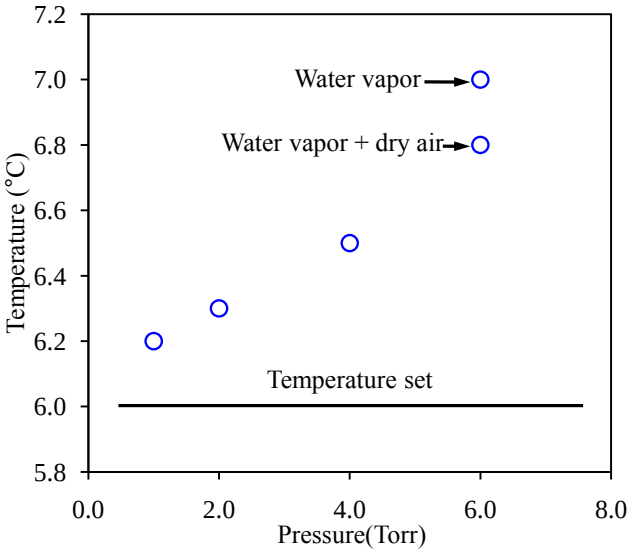

Figure 4.4: The temperature of sample' surface vs. ESEM chamber pressure (1 Torr = 133 Pa).

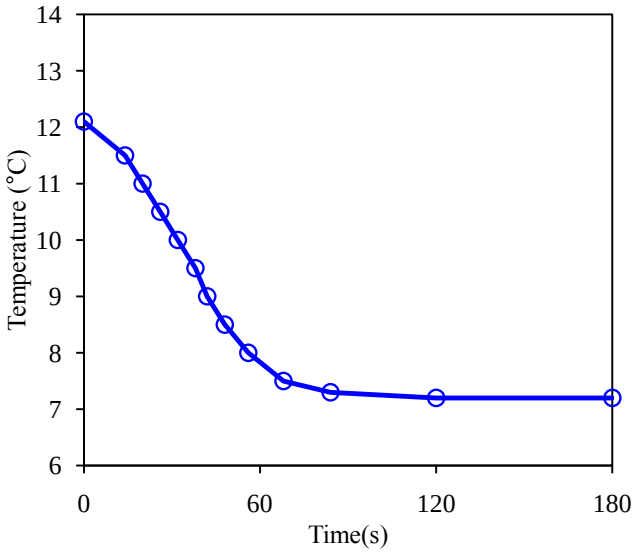

Figure 4.5: Equilibrium time for cooling the sample surface.

Consider that a specimen is expected to be humidified to 85%RH by cooling the sample to 6°C (the conjugate vapor pressure is 6 Torrs). As shown in Fig.4.4, the actual temperature on its surface is 7°C under such condition. Assuming temperature of the sample's bottom is identical to the setup value 6°C (as it is in contact with the Peltier module), a temperature gradient develops inside the specimen. It is simulated by means of $Porofis$, based on a simple model of heat conduction, to give a qualitative idea of the temperature distribution inside the sample (Fig.4.6). Indeed, humidity state is not uniform: it varies between 85%RH and 80%RH ($T = 7$°C, $P_v = 6$ Torrs). Such an analysis provides an idea of the precision for the control of humidity in this study. In general, the system works well for low relative humidity. Nevertheless, the deviation, due to the difficulty to control temperature, becomes more important when high RH, involving low temperature and high vapor pressure, is required. A good example can be demonstrated by the tests #2 and #3 in which the specimens are equilibrated at the same RH of 44%, but by different conjugate temperature and pressure values (see Tab.4.1). Since temperature is higher in test #3, a relatively narrow temperature distribution is attained in the sample, and its water content is bigger than that in test #2.

4.1.2 Sample preparation and experimental procedure

The sample is prepared in cuboid shape (approximate 5.5 × 6.0 × 12.0 mm^3). Such size is suitable to the copper box (6.0 × 6.5 × 13.0 mm^3): the 0.5 mm space is sufficiently small for a better temperature control by the copper box. At the same time, it allows the sample being surrounded by the vapors which would be absorbed by the former during the humidification process. Besides, the similar sizes of the tested samples can avoid size effect on their mechanical behavior, which allows investigating the inherent properties of such rocks. Note that sample

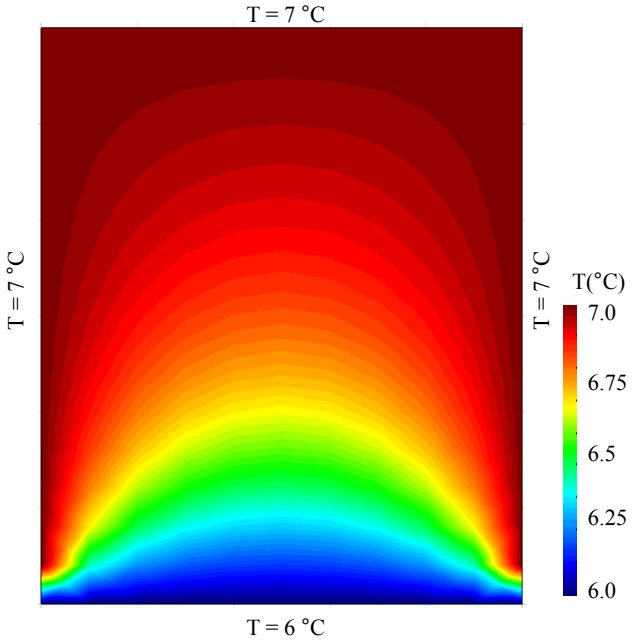

Figure 4.6: Simulation of temperature distribution within sample.

sizes are larger than RVE size as estimated by (Bornert et al., 2010). Special attention is paid to keep both sides of the sample flat and parallel. A tested surface is polished with abrasive papers in four steps with decreasing fineness from grade 800 to 4000. Once the sample is prepared, it is equilibrated in an environmental chamber where the relative humidity is controlled by a saline solution corresponding to the expected value for the test.

It is well known that humidity state is of crucial importance for the mechanical behavior of argillaceous rocks. Broadly, the effect of humidity state consists in two different terms: 1) changing of capillary pressure, 2) variation of water content (w). Both parameters are quantified in this study, to characterize the humidity state of the samples and to investigate its effects on their mechanical behavior. After each test, the sample is immediately weighted once it is taken out of the ESEM chamber to avoid water loss. Then, it is dried in an oven at 200°C for 3 days to assess sample water content. As discussed in the previous section, the actual humidity state of samples is not exactly identical to the RH value monitored by ESEM (based on the temperature measured by the Peltier module): it is generally drier and isn't uniform inside the sample. However, the difference is very limited if especially the related temperature is not too low and the chamber pressure is not too big.

Dozens of tests have been conducted to characterize the local mechanical behavior of argillaceous rocks, of which seven representative tests are reported on in the following to present the main results of these observations. In the first six tests, uniaxial compression tests are conducted on specimens with a constant humidity state all along the test. They cover a wide range of water contents (2.2% - 10.1%) to broadly investigate the mechanical behavior of such rocks and the effect of water content on it. In the seventh test, the specimen is subjected to

Table 4.1: Dimensions and humidity states of the samples.

Test	**Length × Width × Height**	**RH**	**T**	**P**	**W**
	mm	%	°C	Torr(Pa)	%
Test #1	11.76 × 4.98 × 5.27	70	2.0	3.7 (492)	2.2
Test #2	11.04 × 5.83 × 4.39	44	5.0	3.1 (406)	3.1
Test #3	11.20 × 5.50 × 4.61	44	13.5	5.1 (665)	3.8
Test #4	11.81 × 6.07 × 4.41	91	5.5	6.2 (825)	5.4
Test #5	11.00 × 5.93 × 5.34	96	10.0	9.0 (1197)	7.4
Test #6	11.21 × 5.24 × 5.42	99.8	14.0	11.7 (1556)	10.1
Test #7	11.87 × 4.28 × 5.98	21	10.2	2.0 (266)	
		80	7.0	6.0 (798)	
		99	12.8	11.0 (1463)	6.0

Note: temperature presented by the Peltier module might be different from the sample temperature.

a free humidification (20%RH - 80%RH - 99%RH), accompanied with uniaxial compression tests: moderate loading-unloading cycles for the two first low RH states, and a loading until failure for the last high RH step. The sample dimensions and humidity states (RH, w) of the seven tests are summarized in Tab.4.1, together with the temperature and pressure setups in the ESEM.

In this chapter, the direction of macroscopic uniaxial compression always coincides with the vertical (y) axis of ESEM images. In accordance with the previous chapter, the convection of continuum mechanics is applied: extension is considered to be positive while compressive strain is negative. Hence, the direction of local E2 in strain maps is usually normal to the loading direction (see Fig.4.25). However, it should be stressed an exception to this convection in global stress-strain curves, in which the compressive Eyy (along the compression axis) is presented positively whereas the extensive Exx is negative (see Fig.4.9 for example).

4.2 Mechanical behavior at fixed humidity state

4.2.1 At dry state

4.2.1.1 Test #1

In test #1, the specimen is equilibrated in the ESEM chamber under conditions which would be ideally expected to 70%RH. However, the steady water content is 2.2%. Compared to those in other tests, such a water content value seems to be too small for the given humidity state. This can be explained by various origins. Firstly, the temperature and pressure values (2.0 °C

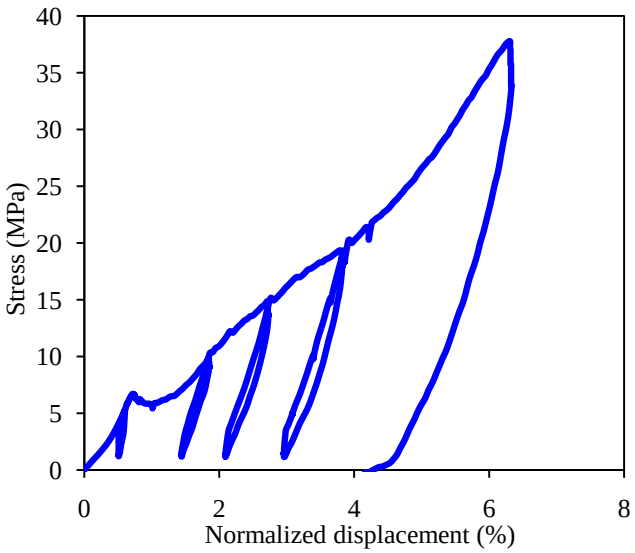

Figure 4.7: Stress vs. normalized displacement (LVDT) in test #1.

and 3.7 Torr) chosen for the given relative humidity is too severe to be attainable. As discussed previously, the sample can't be cooled exactly to setup value, and the difference becomes significant when low temperature is demanded. Consequently, the higher temperature leads to a drier humidity state compared with expected 70%RH for the given vapor pressure 3.7 Torr. Besides, the variety of sample (more inclusions in test #1) may be another origin of low water content. Since mechanical loading is conducted maintaining constant the relative humidity in test #1, capillary pressure plays no role for the evolution of material, and only water content affects its behavior under mechanical loading. Hence, the unknown relative humidity state in test #1 doesn't generate crucial issue. The results here can be considered to correspond to the behavior of a dry sample of argillaceous rocks.

Once the sample is equilibrated with respect to humidity state, uniaxial compression test is conducted on such dry specimen until 35 MPa (corresponding to 1 kN that is the limit of loading system) without failure. Four unloading-reloading loops (5.2 MPa, 9.8 MPa, 14.8 MPa, 18.8 MPa) are introduced to characterize both elastic constants and plastic deformations under different stress states. The curve of stress vs. normalized displacement (displacement measured by LVDT divided by sample's initial length) is presented in Fig.4.7. Four zones (320 $\times$ 276 μm^2, corresponding to image magnification $\times$400) are chosen as ROIs (see Fig.4.8). They are analyzed by the DIC method, which allows estimating local strain fields as well as global strains of ROIs. The gauge length of local strain is 60 $\times$ 60 pixels, i.e. 4.7 μm in real space (refer to section 2.2).

The global strains of the four ROIs are averaged to evaluate the macroscopic overall strain of the specimen. It is noted that the four ROIs cover an area of more than 500 μm in width, which is considered to be the characteristic length of the representative volume element (RVE)

for the deformation of argillaceous rocks under mechanical loading (Bornert et al., 2010). The overall strain of specimen assessed by DIC versus stress is shown in Fig.4.9. Broadly, the stress-strain curve is linear, prior to being nonlinear from about 20 MPa. The elastic properties of the material are estimated by an unloading at 10 MPa: Young modulus is 5.2 GPa, while Poisson's coefficient is 0.06. The unloading loops reveal that the plastic deformation is not evident until 20 MPa. The uniaxial compressive strength for such dry specimen is extremely high: it did not break until the limit of loading system 1 kN, i.e. 35 MPa. Moreover, there is no evident sign of microcracking at the end of loading in test #1.

It is worth noting that the displacement measured by LVDT exhibits irreversibility during loading-unloading cycles, which is different from the results of strain measurement based on DIC analysis. This is mostly attributable to unrecovered evolution of mechanical loading system during loading test, rather to the plastic deformation of the specimen.

Local strain fields of four ROIs are also estimated, of which E1 (major compressive strain) in zone 1 (Fig.4.10) and zone 4 (Fig.4.11) are presented. In general, mechanical loading leads to heterogeneous strain fields at this microscale, however, they are strongly correlated to material's microstructure. Broadly, small local strains (light blue color in Fig.4.10, about 0.4%) are mostly found in inclusions, whereas high deformations (yellow and red color, more than 1.8%) locate generally in clay matrix. Such heterogeneous strain field under mechanical loading can be explained by the contrasting deformability of different phases in such rocks: clay matrix is relatively deformable (its Young modulus is 4 - 20 GPa), whereas the mineral inclusions are much more stiff (for example, the Young modulus of quartz and calcite are respectively 96 GPa and 84 GPa).

Regarding the deformation in clay matrix, some slanted deformation bands appear in the strain map: they are orientated between 45° and 60° to the loading direction. Note that the variable orientation of the deformation bands seems to be associated to the morphology of clay matrix which is strongly controlled by the presence of inclusions. As the previous discussion, argillaceous rocks are made of a continuous clay matrix embedded with some mineral inclusions. In other words, clay matrix would be divided, by the presence of inclusions, into some variably orientated sub-domains. Under mechanical loading, the intense deformation of these sub-domains would be marked in the strain map by some deformation bands with similar orientation. Note that these sub-domains of clay matrix could be orientated in all directions, nevertheless, only 45° - 60° deformation bands are observed here. This implies that the deformation mechanism is probably associated to shear in clay matrix (the maximal shear appear at the direction of 45° to the loading axis under uniaxial compression condition). Besides shear bands, some horizontal bands, which are generally located in the zones that are rich in macropores, are observed in the strain maps. They are essentially related to the compaction of these macropores. Note that the magnitude of these horizontal bands (mostly in red color) is generally more important than shear bands (mostly in yellow color).

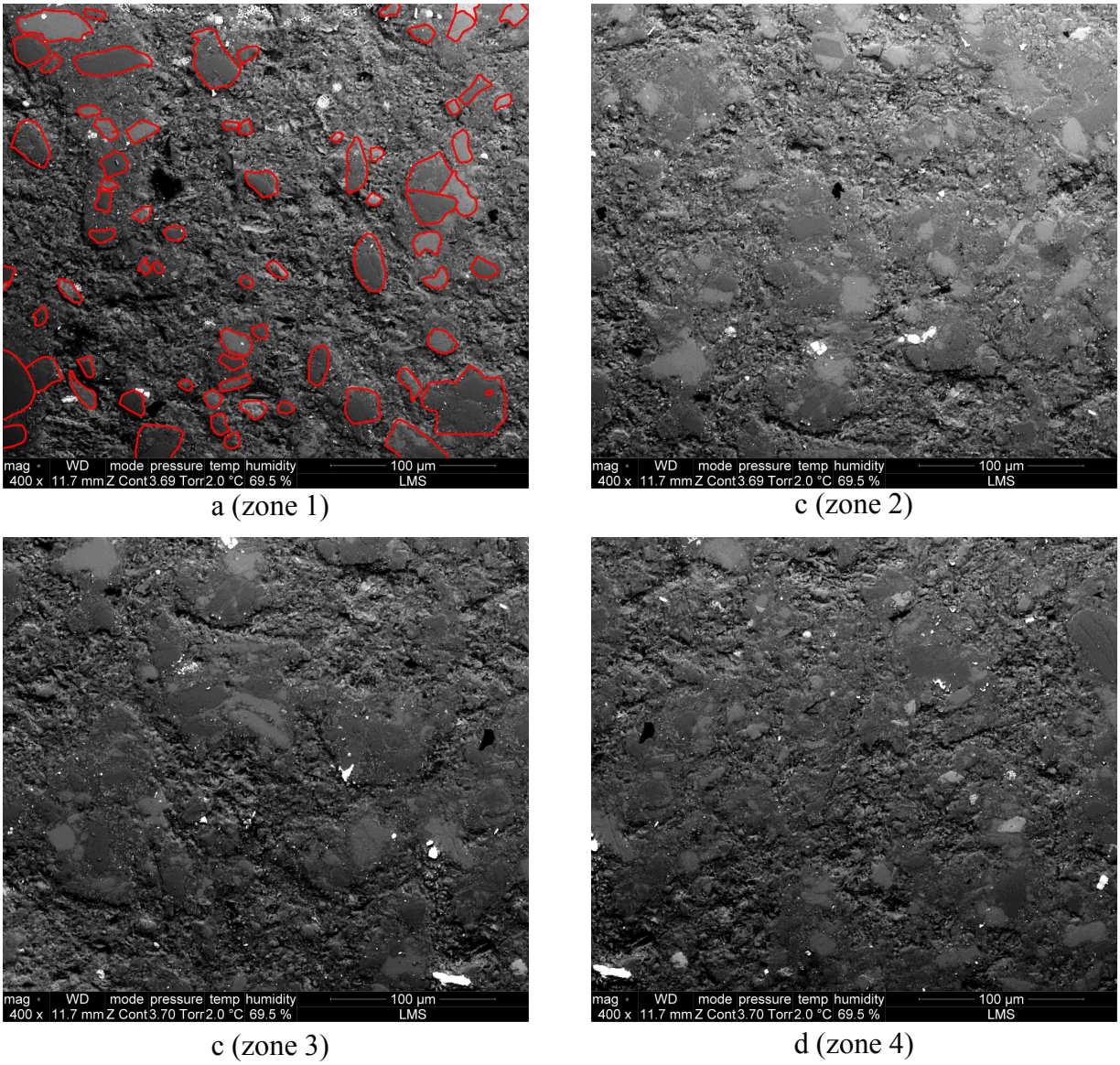

a (zone 1) c (zone 2)

c (zone 3) d (zone 4)

Figure 4.8: Four regions of interest in test #1.

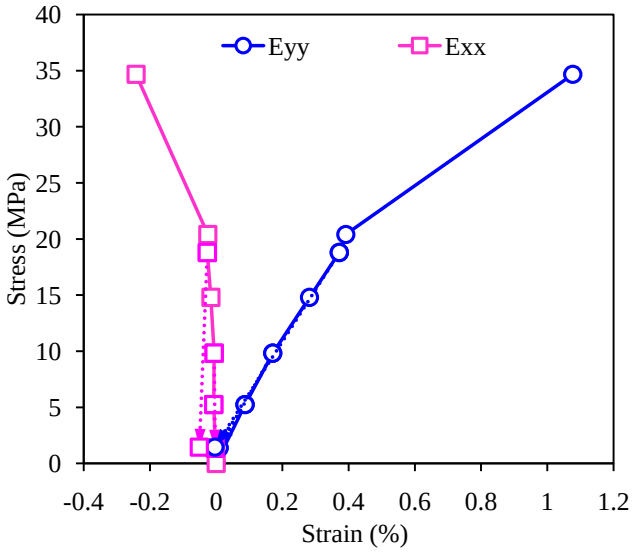

Figure 4.9: Stress-strain curve by DIC measurement in test #1.

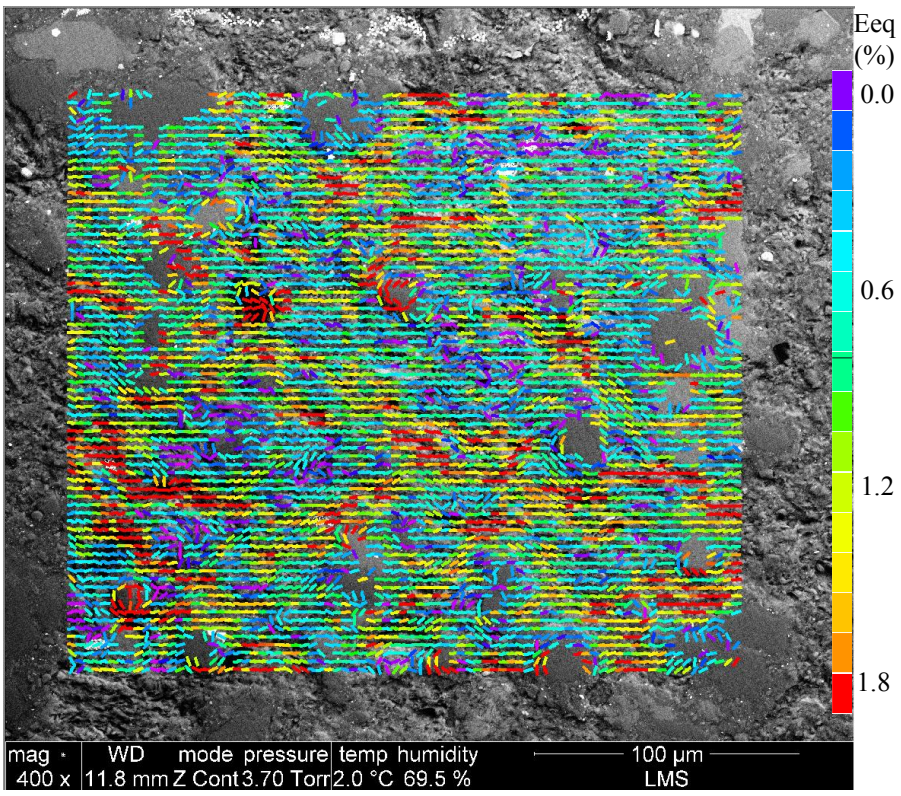

Figure 4.10: Strain map of zone 1 at 35MPa in test #1.

The stress-strain curve becomes nonlinear from about 20 MPa. To investigate the associated mechanisms, the incremental strain fields of zone 4 (0 - 20 MPa, 20- 35 MPa) are determined and compared in Fig.4.11. Broadly, the morphology of the strain field in the nonlinear step (20 - 35 MPa) is similar to that at linear step (0 - 20 MPa). The nonlinearity is merely attributable to non scaling strain magnitude: the strain in great deformed zones is 1.0% (corresponding to red domains in Fig.4.11) for 0 - 20 MPa step, whereas it becomes 1.8% for 20 - 35 MPa step. This phenomenon is confirmed by quantitative analysis on the distribution function of normalized E1 (local E1 divided by the average value E1 of total observation zone). The result, shown in Fig.4.12, reveals that the strain distribution in the nonlinear step is similar to that in the linear step. This means that there is no important deformation localization which is often associated with strain nonlinearity (plasticity). Such conservation of local strain distribution implies that the deformation mechanism in the nonlinear part is probably similar to that in the linear part.

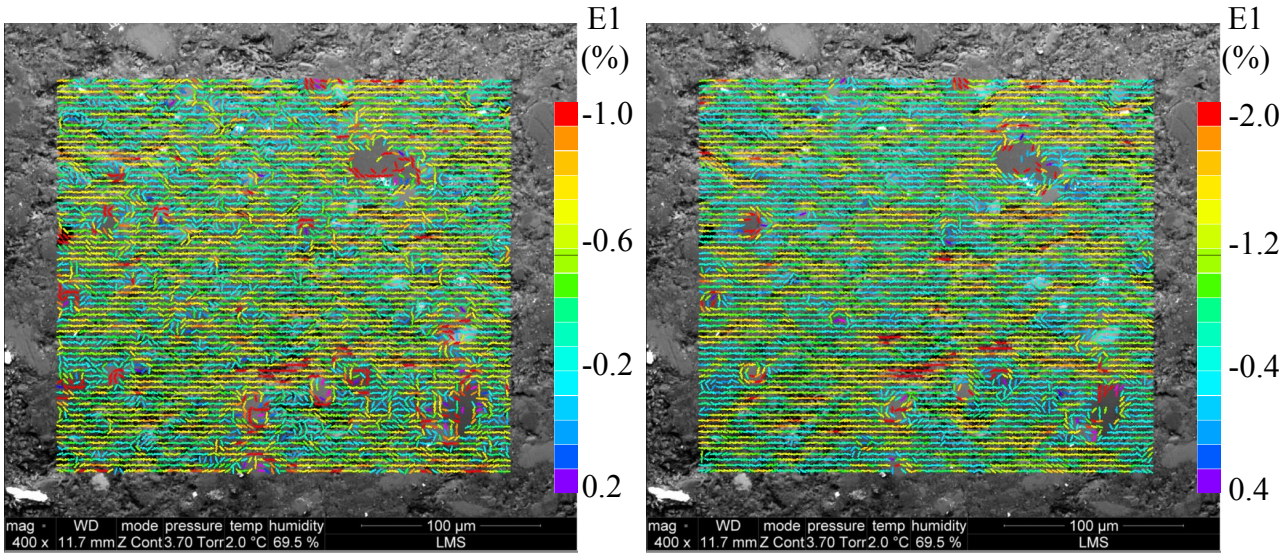

Figure 4.11: Incremental strain maps (E1) of zone 4 in test #1.

4.2.1.2 Test #2

In test #2, a uniaxial compression test is conducted on a specimen equilibrated at 44%RH, with 3.1% water content. The stress curves in function of the normalized displacement estimated by LVDT sensor is shown in (Fig.4.13). Similar to Test #1, the stress-strain curve becomes nonlinear above some value. Nevertheless, the threshold is 16 MPa for test #2, contrasting with 20 MPa for test #1. In addition, a post-failure behavior is evidenced here: the stress curve undergoes two drops after arriving peak stress. It is worth noting that the stress vs. normalized displacement exhibits several pits in its pre-peak part. This is actually associated to

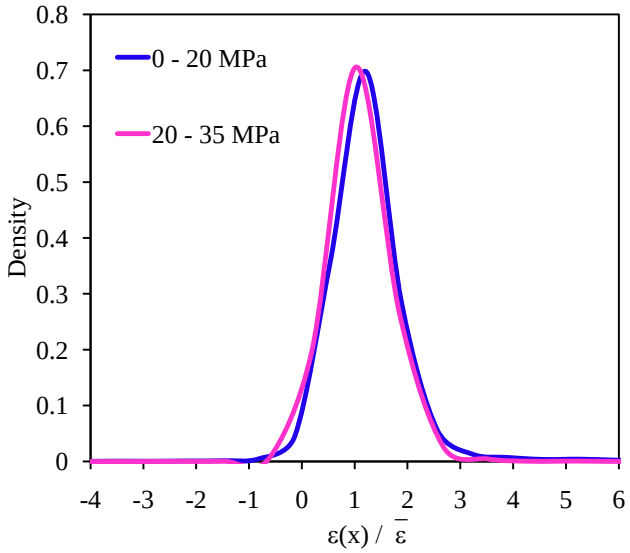

Figure 4.12: Distribution functions of E1 in the linear and the nonlinear steps.

material relaxation during imaging acquisition at certain stress states. Since the loading system is displacement-controlled, there would be relaxation when loading is maintained constant to record images for DIC. The strain measurement by DIC is conducted on two ROIs with a size of 320 $\times$ 276 μm^2 (corresponding to image magnification $\times$400), as shown in Fig.4.15, 4.16. The stress versus the average strain of two ROIs is presented in Fig.4.14. Contrary to test #1, some slight irreversible deformation (0.1%) is already evidenced when the specimen is unloaded from only 7 MPa in test #2.

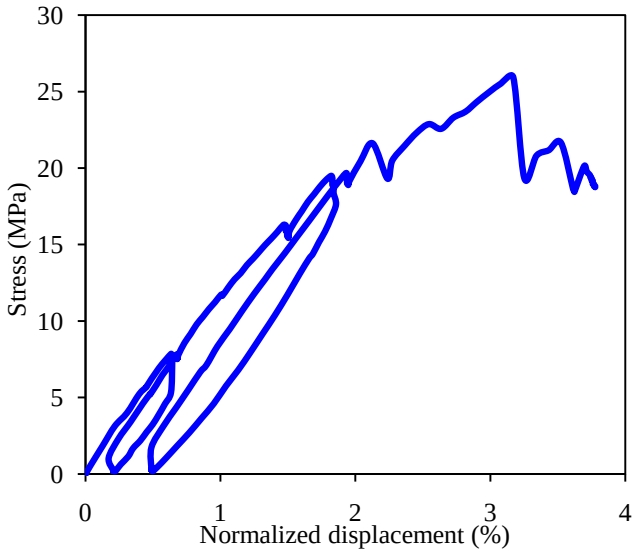

Figure 4.13: Stress vs. normalized displacement (LVDT) in test #2.

The specimen in test #2 breaks at peak stress 26 MPa. At failure, two principal fractures are observed in the whole sample, accompanied by some secondary cracks (see Fig.4.17). The

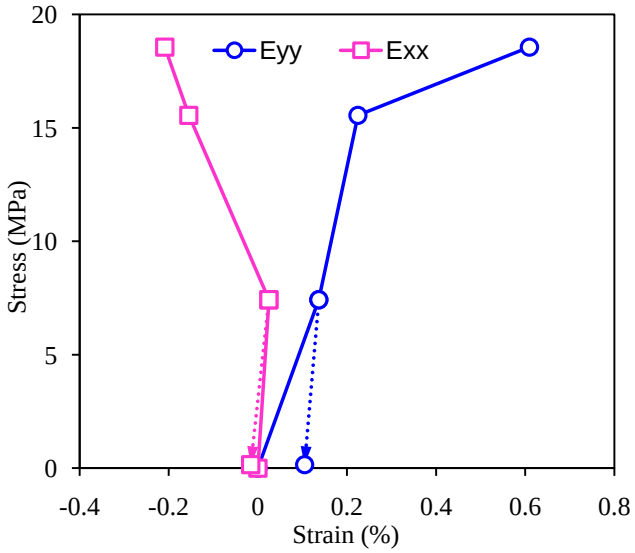

Figure 4.14: Stress-strain curve by DIC measurement in test #2.

two fractures are orientated about 15° to the uniaxial loading direction. Concerning the left principla fracture, echelon-shaped fault geometry is observed. The two end parts (with weak angle to the loading direction) are possible tensile cracks, whereas, the middle part (about 30° to the loading direction) shows in bright color in Fig.4.17, indicating a probable sliding movement between the two sides of the fault. Moreover, one secondary crack is observed near the principal facture.

The right fracture (Fig.4.17) passes through the two ROIs (Fig.4.15, 4.16). Generally, fracture propagates either in clay matrix or along inclusions' boundaries. It is worth to emphasize ROI 2 in which one elongated grain (perhaps mica or chlorite) lies on the propagation path (marked in Fig.4.16). The fracture crosses the grain, orientated sub-normally to the propagation direction, by propagating along its boundary prior to following its primary path. Besides, this grain is greatly shocked, resulting in certain microcracks perpendicular to the principal propagation direction.

Some secondary microcracks, with similar orientations, are also found nearby the fracture (particularly in Fig.4.15). Note that these secondary microcracks are concentrated in one side of the principal fracture (left side in the image). In fact, Moore and Lockner (1995) has demonstrated that such microcrack densities are consistently higher on the dilatational side of the shear than on the compressive side. Hence, the propagation direction can be determined: the fracture is initiated at the sample end and propagates toward the inner part (from the top to the bottom in ESEM image). Referring to the strain field assessed by DIC (the highest stress state for DIC measurement is 18.6 MPa), there is no evident premonitor involved in certain strain localization indicating the ultimate failure.

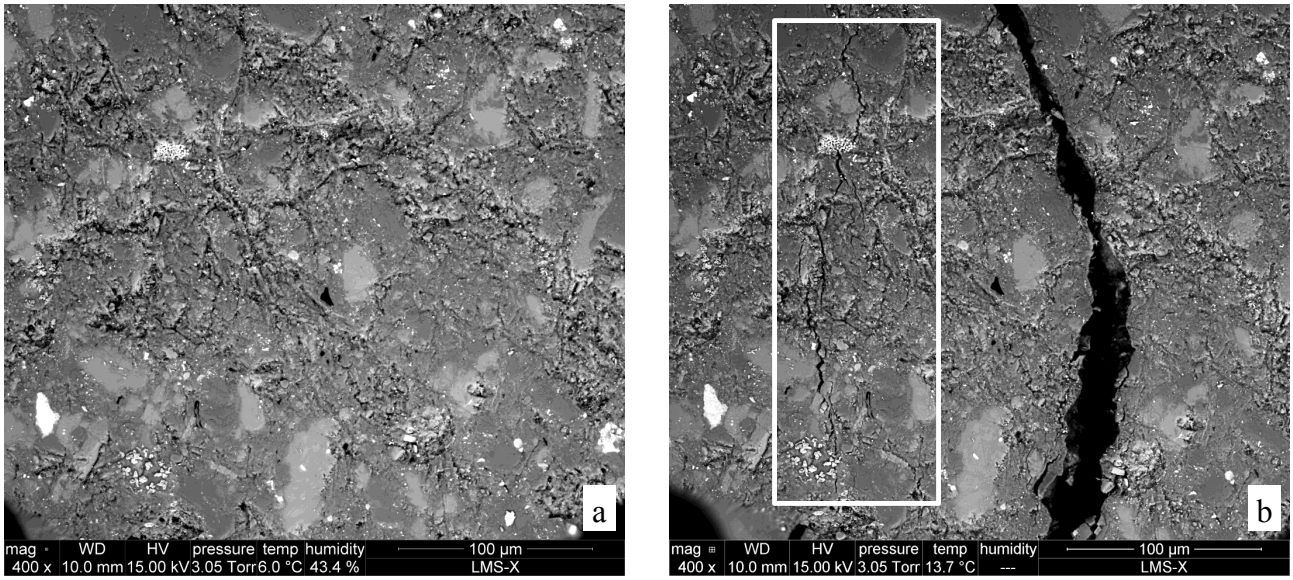

Figure 4.15: ESEM images of zone 1 in test #2: a) initial state, b) failure. Note some microcracks in the left side (the marked zone) of the principal fracture in picture b.

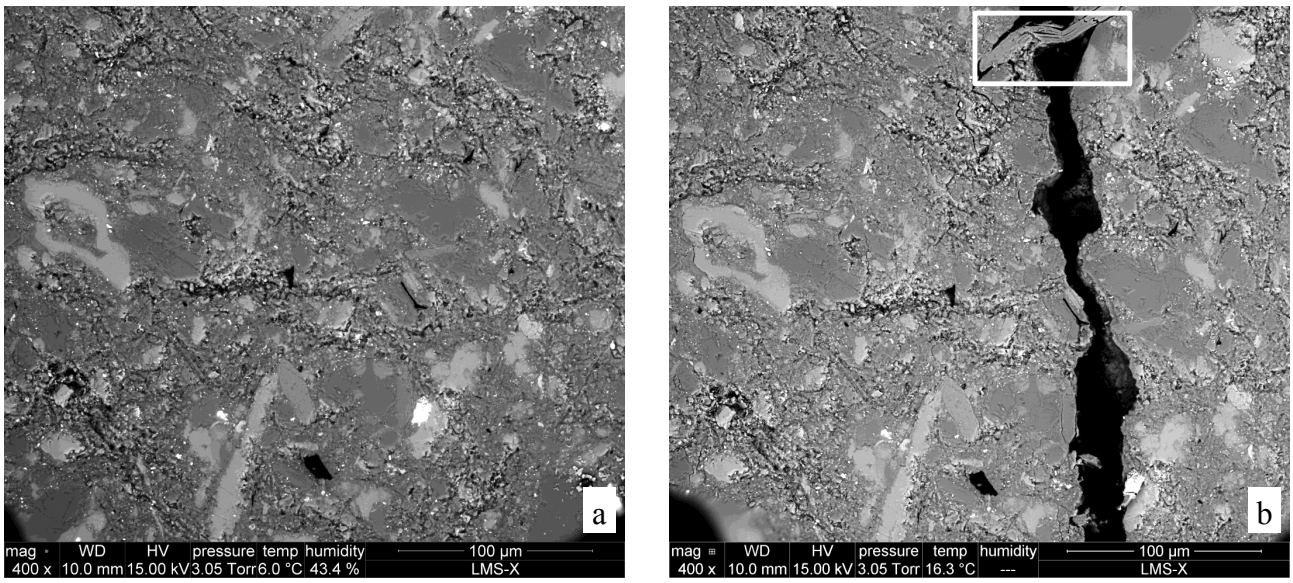

Figure 4.16: ESEM images of zone 2 in test #2: a) initial state, b) failure. Note a grain orientated sub-perpendicular to the propagation direction of the principal fracture.

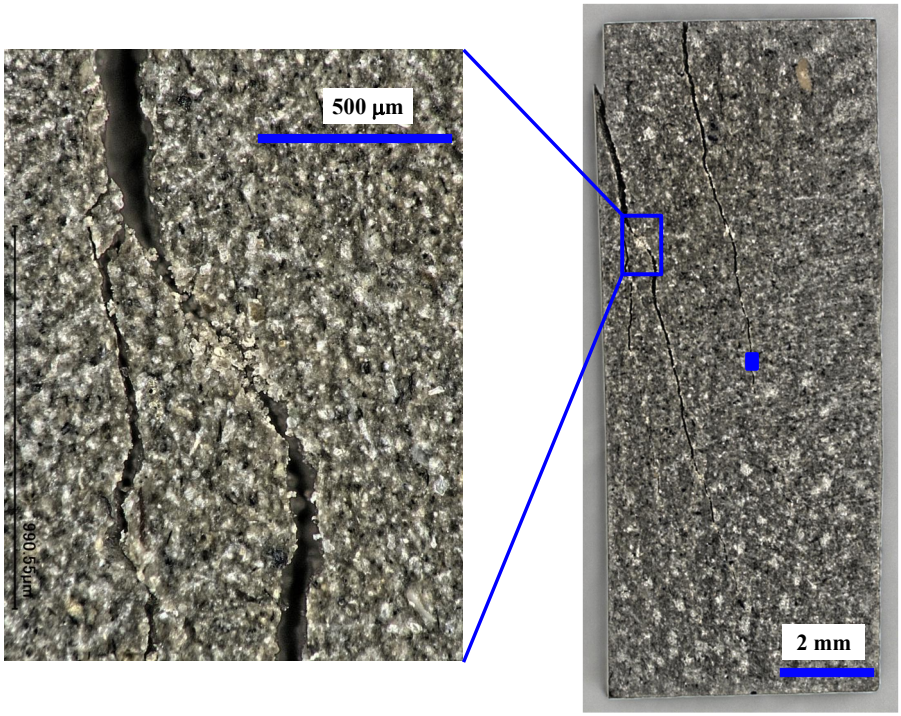

Figure 4.17: Fracture of sample in test #2 observed by optical microscopy. The solid rectangular in the right picture is ROIs 1 and 2. Loading direction coincides with the vertical axis of images.

4.2.1.3 Test #3

The sample in test #3 is equilibrated in a constant 44%RH environment (in the ESEM chamber), prior to a uniaxial compression test. The corresponding water content is 3.8%. The stress vs. normalized displacement curve, qualitatively revealing the macroscopic behavior of tested sample, is shown in Fig.4.18. Three zones with size of 320 $\times$ 276 μm^2 (see Fig.4.19 - 4.21 a) are chosen as ROIs. Three loading stress states (4.4, 9.2 and 17.5 MPa) are chosen for DIC analysis and strain measurement, as well as the unloading states for the two formers. Moreover, the strain measurement at ultimate failure, corresponding to a residual stress 6.7 MPa, is also conducted. The stress vs. overall strains for three zones are shown in see Fig.4.19 - 4.21 b.

From the stress-strain curves, some features are characterized:

- In test #3, a concave upward portion appears at the beginning of the stress-strain curve. Note that this concave upward portion doesn't exist in test #1 and #2. However, this is a typical phenomenon for rock sample under uniaxial compression, of which the origins are well recognized: 1) non-parallel ends of specimen due to imperfect specimen preparation; 2) closing of existing microcracks. Since the strain measurement by DIC is conducted on certain zones in the middle of the sample surface, the first effect can be avoided. Hence, the concave upward portion in test #3 is due to the closing of existing microcracks. That means that the sample of test #3 is pre-damaged before uniaxial compression test.

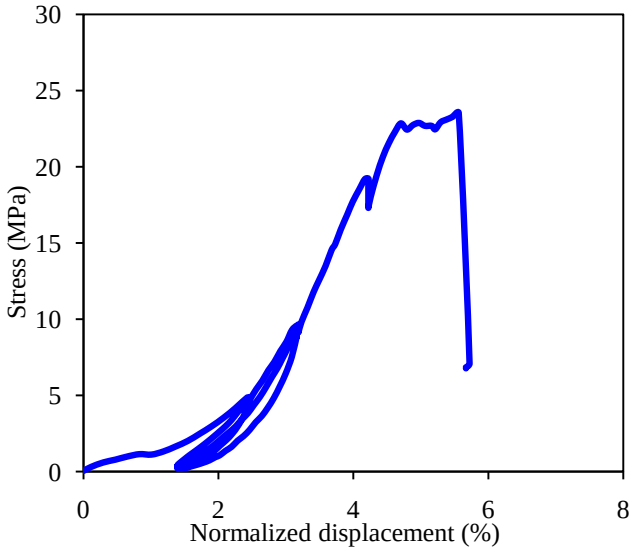

Figure 4.18: Stress vs. normalized displacement (LVDT) in test #3.

Moreover, the irreversible strain already emerging at small stress state 4.4 MPa (see Fig.4.19 - 4.21), is also a proof of pre-existing microcracks.

- After initial concave upward portion, the stress-strain curve is somewhat linear until arriving peak stress 23.6 MPa. It is noted that there is a shelf prior to ultimate failure (Fig.4.18), which implies a possible strong deformation localization. The residual stress is 6.7 MPa.

- Contrary to test #1 and #2 with no or slight irreversible deformation, irreversible deformation is evident in all the three observation zones. It can attain more than 0.5% at 9.2 MPa state.

The equivalent strain field for the three observation zones are shown in Fig.4.22, 4.23, and 4.24. It is emphasized that the local principal strain directions are also marked in these strain field: the major axis coincides with the E2 direction, while the minor axis coincides with the E1 (< E2) direction which is normal to the former (see the illustration in Fig.4.25). Broadly, these strain field exhibit different morphologies which are essentially associated to their various microstructures. Nevertheless, some common features can be characterized. Firstly, due to its relative high stiffness, the inclusion deforms faintly and the overall strain in argillaceous rocks is mostly attributable to deformation of clay matrix. Regarding clay matrix, the strain field is still heterogeneous, and some deformation bands (yellow and red domains in strain maps) can be observed. Broadly, three types can be distinguished for these deformation bands according to their orientations: 1) horizontal bands, 2) vertical bands, and 3) inclined bands. Recall that the uniaxial compression direction coincides with y axis of images. Correlated the orientations of these deformation bands to the somewhat uniform local major strain (E2) direction in them,

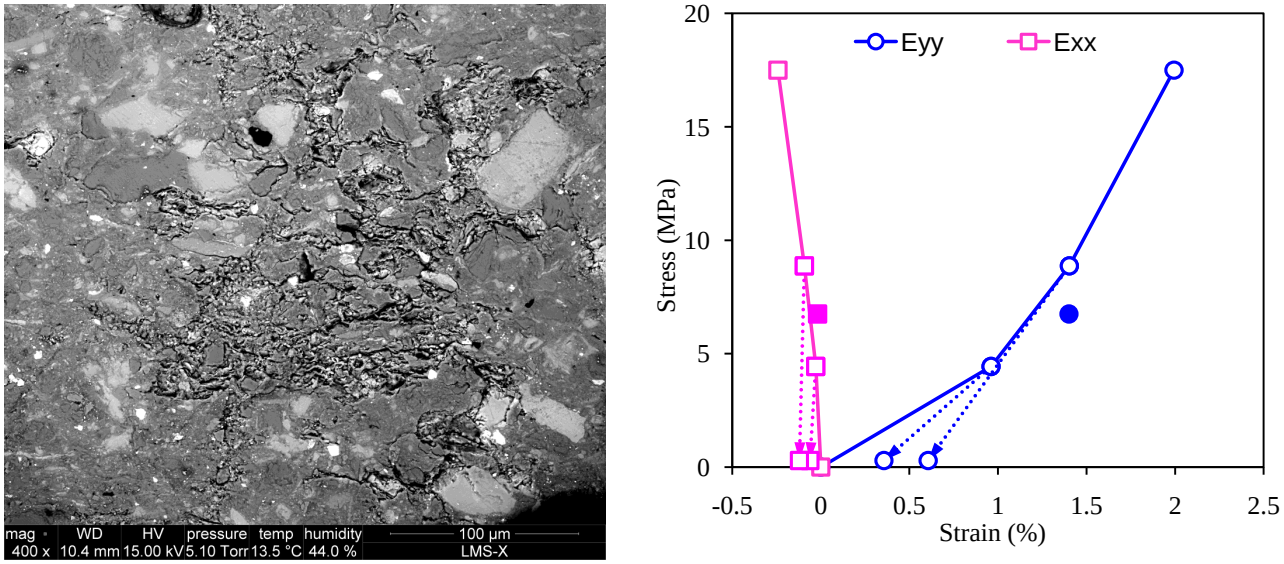

Figure 4.19: Observation zone 1 (left) and its overall strain evolution (right) in test #3. Solid points represent the strain at failure, corresponding to the residual stress level (right).

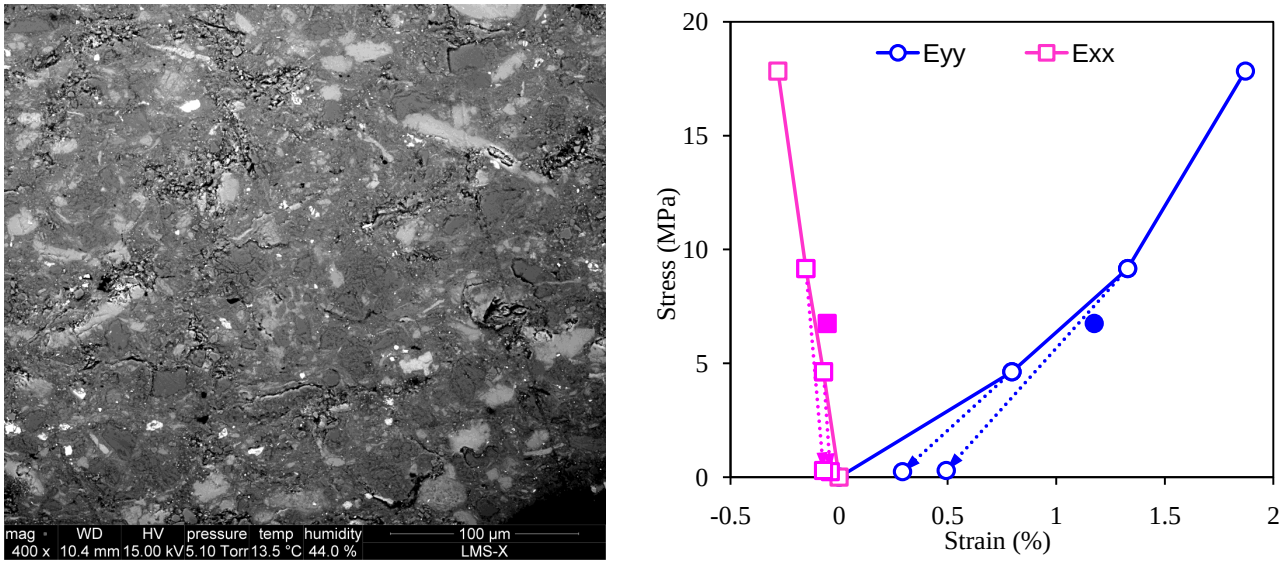

Figure 4.20: Observation zone 2 (left) and its overall strain evolution (right) in test #3. Solid points represent the strain at failure, corresponding to the residual stress level (right).

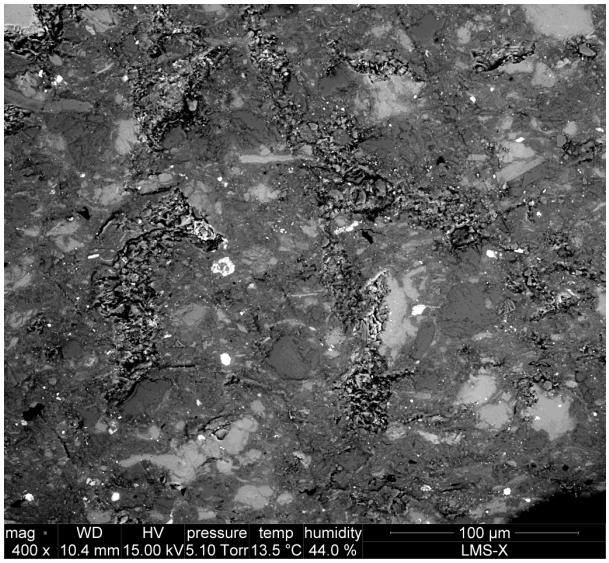

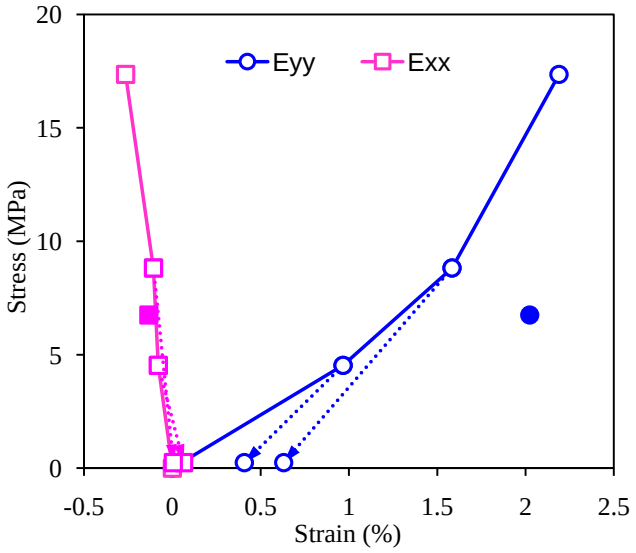

Figure 4.21: Observation zone 3 (left) and its overall strain evolution (right) in test #3. Solid points represent the strain at failure, corresponding to the residual stress level (right).

as illustrated in Fig.4.25, the different deformation mechanisms of these deformation bands can be identified:

- For horizontal bands, the local E2 direction is parallel to their orientations, which implies compaction bands. Indeed, these horizontal bands are generally located at porosity-rich zones or the pre-existing microcracks, and compression leads to compaction and closing of these porous spaces.
- For vertical bands, the local major strain direction is generally perpendicular to their orientations. These extension bands are typically associated to nucleation and growth of microcracks sub-parallel to the loading direction.
- For inclined bands, the angle between their orientations and the local E2 direction in them is not consistent: the latter is generally horizontal, whereas the former is variable between each other. For the case of 45 °, it involves a pure shear deformation. Hence, these inclined bands are principally linked to shear deformation.

It is worth noting that all the above deformation mechanisms occur in clay matrix, or on inclusion boundaries.

Behavior of macropore-rich zone

At this microscale observation, some pore spaces are observed, mostly located at inclusions' boundaries and between clay aggregates in clay matrix. According to porosity classification of argillaceous rocks (see section 1.2), the porosity observed at this scale (with size in order of

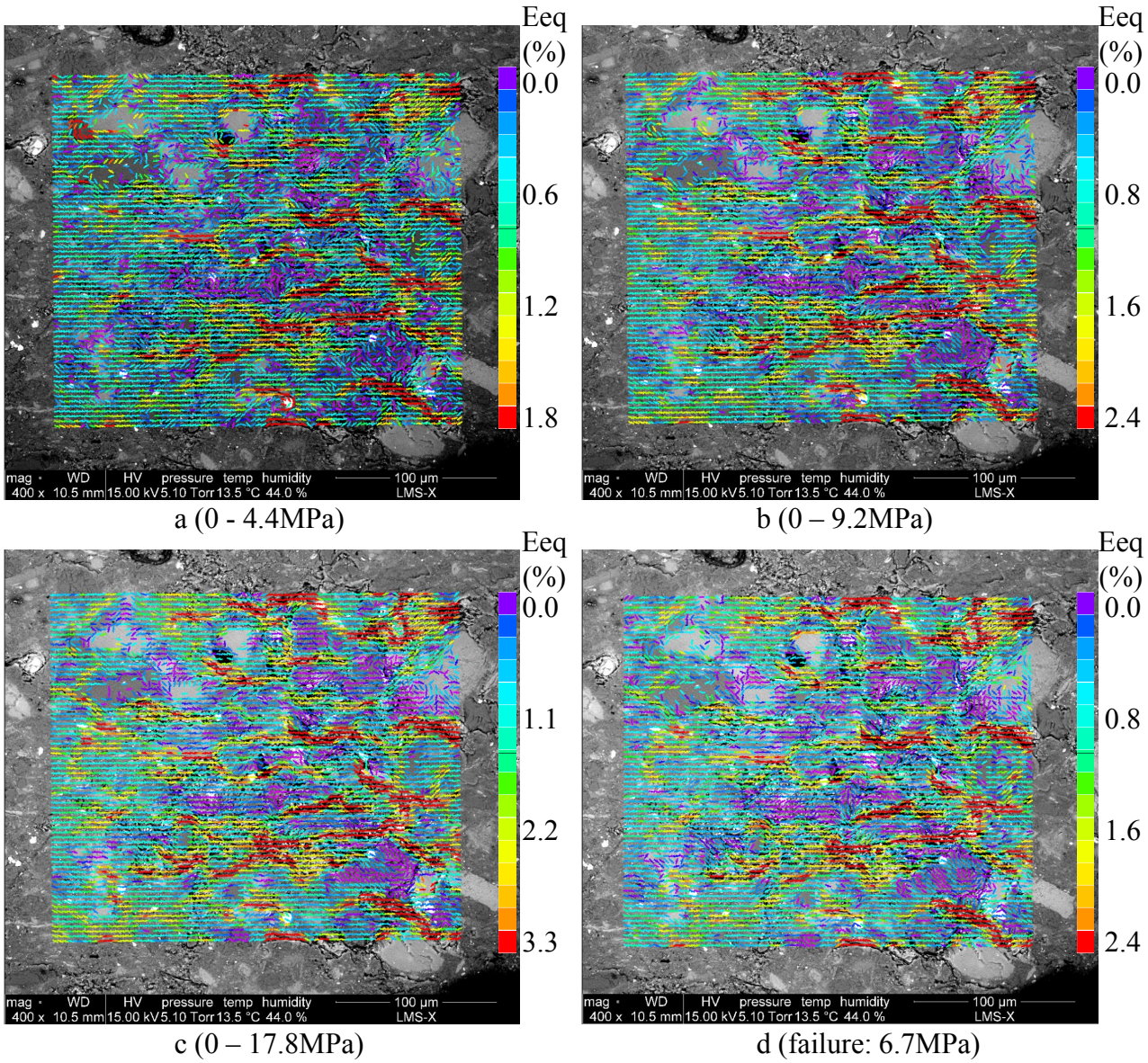

Figure 4.22: Strain fields of zone 1 in test #3 at different stress states. The uniaxial compression direction is vertical in the images.

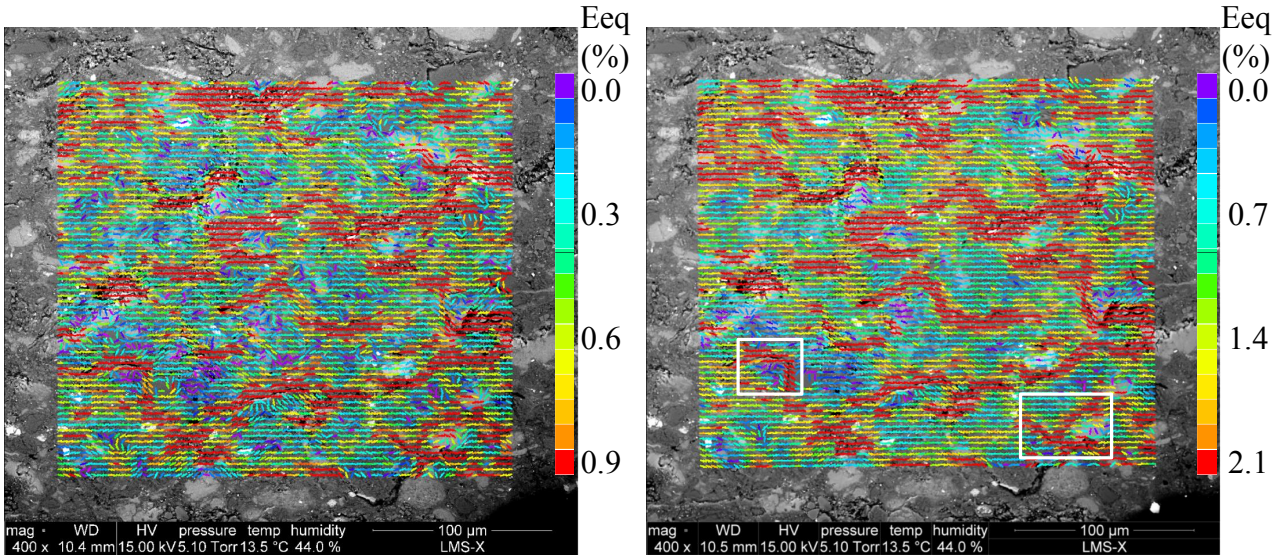

Figure 4.23: Strain fields of zone 2 in test #3 at different stress states. Two rectangles in image b, involving in high strain associated to pre-existing microcracks: (left) opening of vertical microcracks (E2 direction is horizontal, corresponding horizontal extension) and closing of horizontal pre-existing microcracks (E2 direction is horizontal, but corresponding vertical compaction); (right) sliding of slanted pre-existing microcracks.

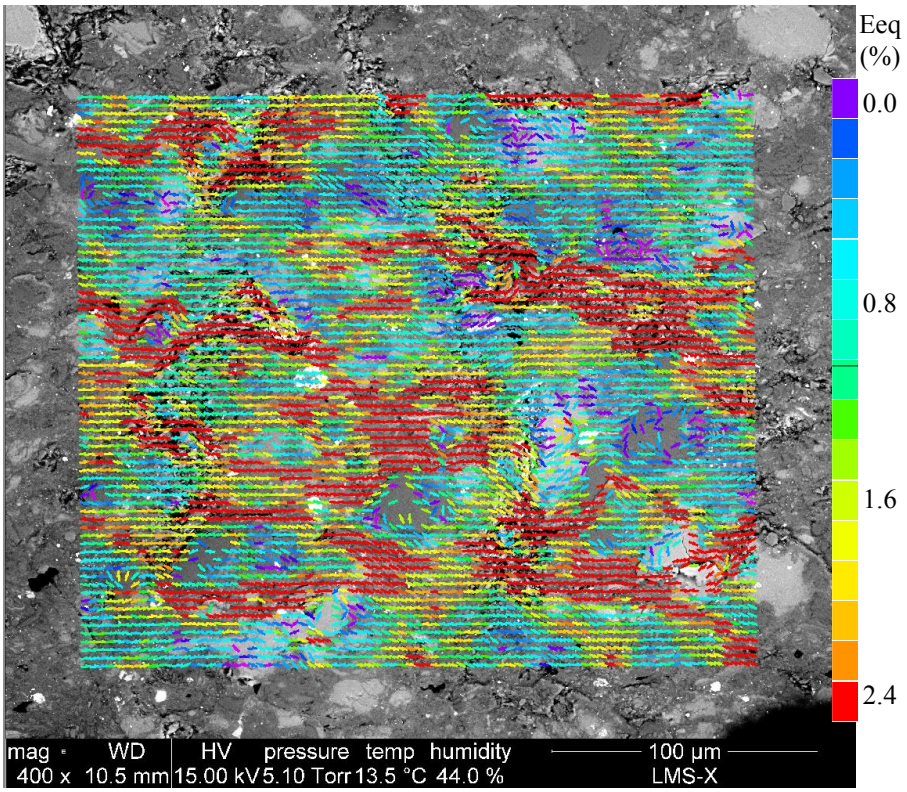

Figure 4.24: Strain field of zone 3 in test #3 (17.4 MPa).

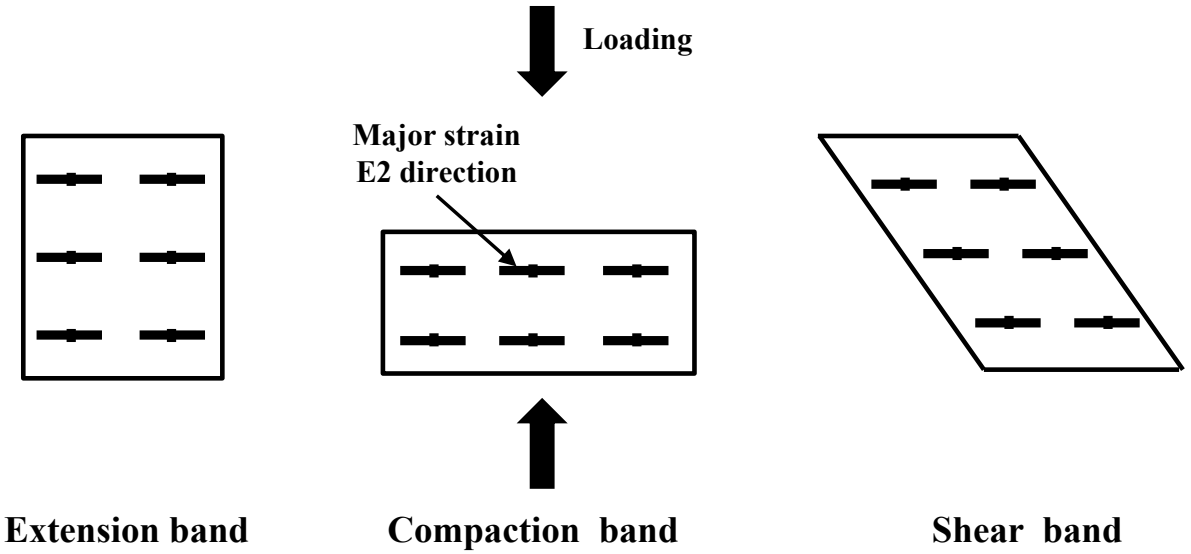

Figure 4.25: Illustration of different deformation bands in local strain maps.

micrometer) is typically inter-aggregate porosity (or macroporosity). Note that these macroporosity also includes pre-existing microcracks that are typically in slit-shape. Strain field estimation reveals that such macropore domains are generally associated to high strains, indicating their crucial role for the deformation of argillaceous rocks under mechanical loading. For a better understanding, macropore domains are selected from observation zone 2 (see Fig.4.26) and their deformation evolutions are calculated and shown in Fig.4.27. It is shown that macropore domain 1 owns much more compressibility in the direction normal to maximal compressive stress: E_{yy} reaches 3.3% at 17.5 MPa, contrasting to 0.6% in intact domain 2 at the same stress level. Moreover, irreversibility is mostly attributable to macropore domain 1: its plastic strain is 0.6% even under a small stress loading (4.4 MPa), whereas, it is just 0.08% for intact domain. Nevertheless, it is interesting to note that the lateral strains for the two domains are somewhat similar, its value in macropore domain at 17.5 MPa (-0.2%) is even a little smaller than that in intact domain (-0.3%). This implies a typical normal compaction of such macropore space. We emphasize that compaction mechanism is generally associated to macropore spaces in argillaceous rocks, rather than in mesopores (inter-particle space) and micropores (intra-particle). Djeran-Maigre et al. (1998) has shown that mechanical compaction has no effect on the evolution of micro and mesopores in clay, since they are controlled by physical-chemical and chemical bonds which owns much higher energy than mechanical loading.

The stress-strain relationship of macropore domain 1 is somewhat nonlinear: its tangent modulus increases with strain. Certainly, this is due to accumulation of plastic deformations, which are evidenced by the unloading steps (in Fig.4.27). Besides, such a nonlinear relationship is also related to the fact that macropores become less compressible with accumulating compressive strain. In fact, the evolution of elastic modulus determined by unloading steps

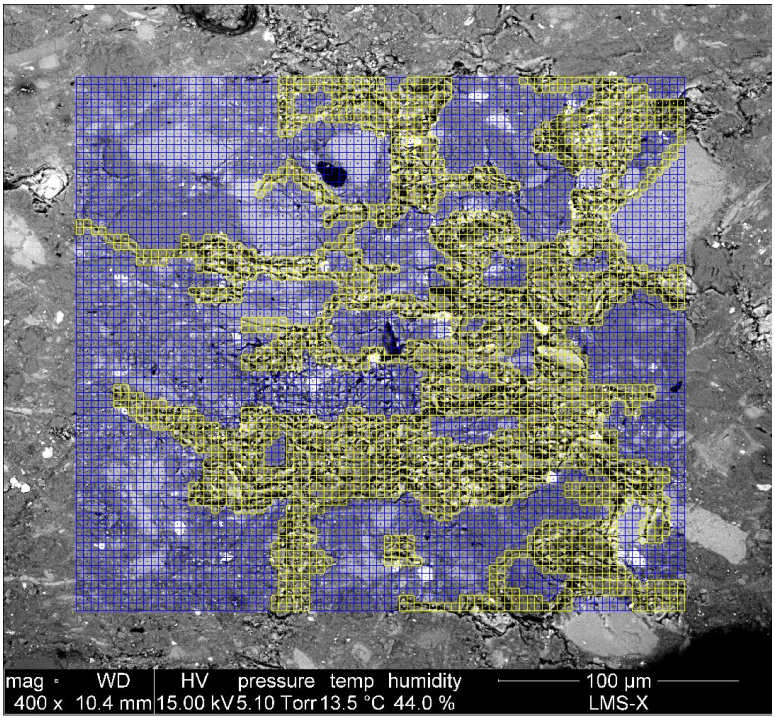

Figure 4.26: Phase definition in zone 1. Yellow color represents macropore-rich domain 1, while blue color represents domain 2.

demonstrates this phenomenon: the modulus for 4.4 MPa step is 4.3 GPa, while it becomes 6.2 GPa for 8.9 MPa. This strain-stiffening phenomenon can be explained by the densification of the macropore spaces: compaction of macropores leads them to a denser texture and their compressibility would decrease consequently.

It is worth noting that the initial concave portion and the plastic strain are also observed in intact domain 2 which is similar with macropore domain 1. Nevertheless, these phenomena are much less evident in domain 2. We think these similarities are essentially due to the existence of macropores in domain 2. Actually, the specimen in test #3 is pre-damaged before mechanical test (see initial ESEM image in Fig.4.19). It is certain that some microcracks and pore spaces, that are too small to be visible at the scale of observation, exist in apparent "intact" domain. We believe that the behavior of test #1, in which neither the concave upward portion nor the plastic deformation is observed at low stress state, is the most likely behavior of intact rocks. Note that "intact" here indicates not only that the sample is initially undamaged, but also that the portion of macroporosity is extremely small in such a dry state. We suggest that the compaction of macropore spaces and closing of pre-existing microcracks are origins of the initial concave upward portion in stress-strain curve. Moreover, the following "apparent linear" portion in stress-strain curve is not elastic at all. Irreversible compaction of macropores would contribute to plastic deformation and strain-stiffen at a wide stress range.

Some microcracks are found at the initial state of mechanical loading in test #3, implying

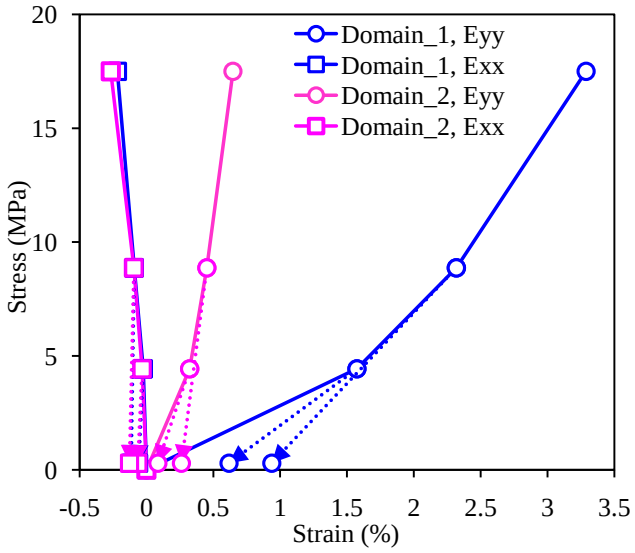

Figure 4.27: Stress-strain curves of two domains in test #3.

the sample is probably pre-damaged. These pre-existing microcracks, located randomly in clay matrix or on inclusions' boundaries, own typical opening in order of 1 μm and variable length ranging from several to dozens of μm. Under uniaxial compression, the behaviors of these pre-existing microcracks are quietly various, nevertheless, their orientation seems to play a crucial role. In general, three types can be distinguished: 1) for the pre-existing microcracks with normal sub-parallel to uniaxial compression direction, they would close under mechanical loading; 2) the pre-existing microcracks with normal perpendicular to maximal compressive stress would continually grow and propagate in tensile-cracking type; 3) the slanted pre-existing microcracks prefer to slide under mechanical loading.

The strain fields at unloading steps are represented in Fig.4.28, which allows characterizing plastic deformation. Broadly, some red horizontal bands (corresponding to residual macropore compaction and closing of pre-existing horizontal microcracks), vertical bands (corresponding to irreversible opening of vertical microcracks), and some inclined bands (corresponding to shear deformation) are observed in these strain maps. Note that the plastic strain field is similar to the loading steps, indicating that they are probably controlled by the same mechanisms.

Under uniaxial compression, some damage phenomena are evidenced at such microscale observation. These damage phenomena generally involve some vertical microcracking, which can be demonstrated by the Exx strain field: some vertical red bands corresponding to high strain level is observed in Fig.4.29. Such microcracking sub-parallel to uniaxial compression (essentially tension splitting) is generally located at inclusion's boundary and in clay matrix. Except for growth of pre-existing vertical microcracks, most of such mode I microcracking is strongly controlled by shear deformation: the microcracks (red domains in 4.29) are mostly located in the high shear strain zones (red domains in 4.23). In addition, some damage are also

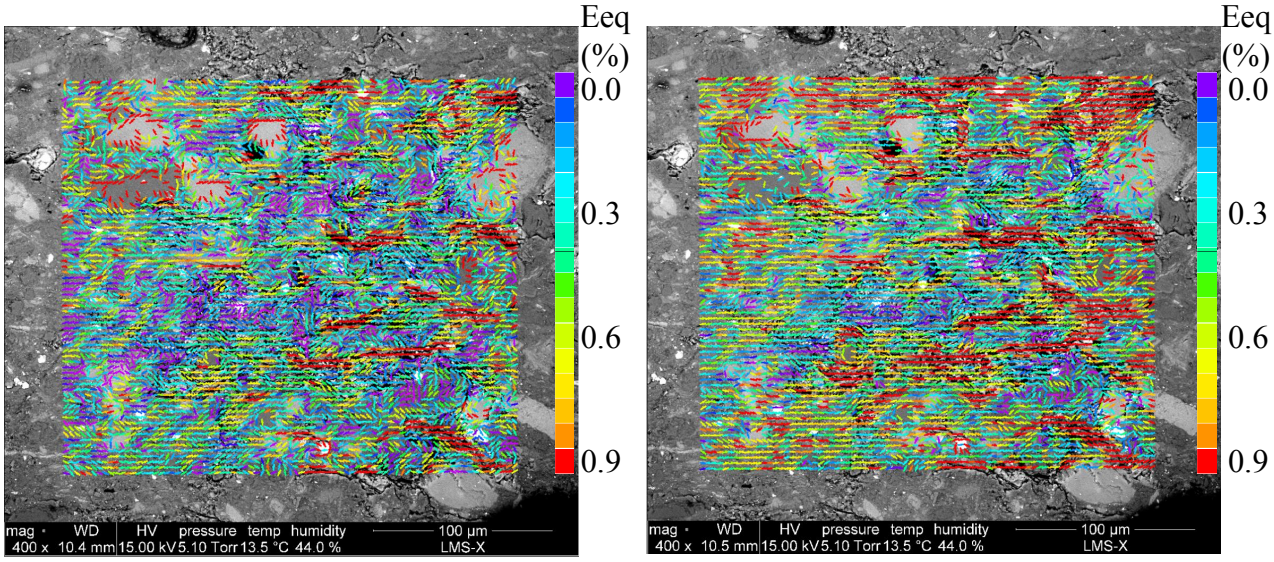

a) Unloading at 4.4.MPa b) Unloading at 8.9MPa

Figure 4.28: Plastic equivalent deformations evolution in zone 1.

observed in mineral inclusions: cleavage is activated by a local stress concentration in some big carbonate grains, as well as breakup of coarse grains, which indicates that the "apparent" coarse grain is probably a group of some sub-grains which may move with respect to each other (Fig.4.31).

Both splitting and faulting fractures are observed in test #3 at failure (see Fig.4.30). The principal fracture leading to sample breaking is one echelon-shape fault: its end portions orientate at 60° with respect to the uniaxial direction, while the middle portion is 45°. Besides, there are two splitting fractures: one emanates from sample's one end; the other is encounter to the principal faulting fracture with an angle of 60°. Moreover, sample spalling is also observed.

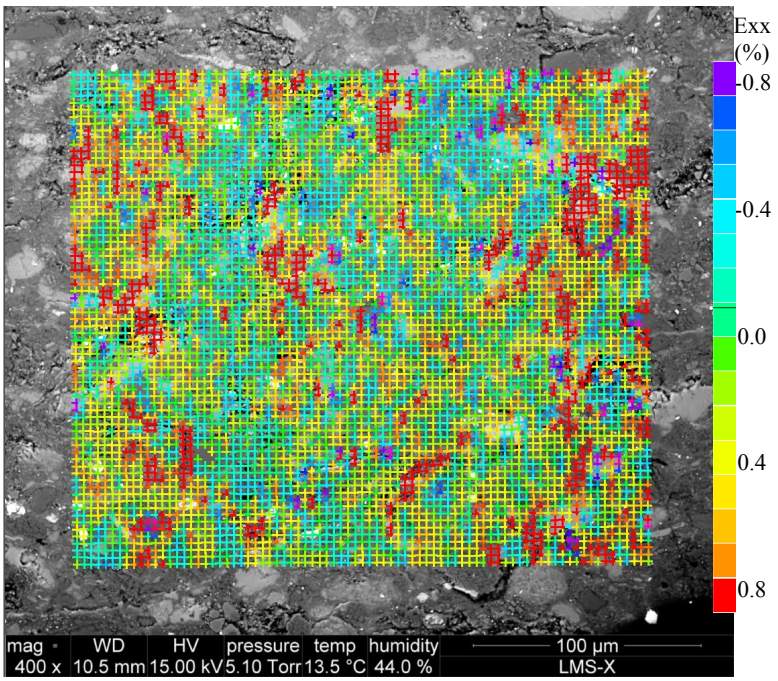

Figure 4.29: Exx strain field of zone 2 at 17.8MPa in test #3.

Figure 4.30: Fracture of sample in test #3 observed by optical microscopy.

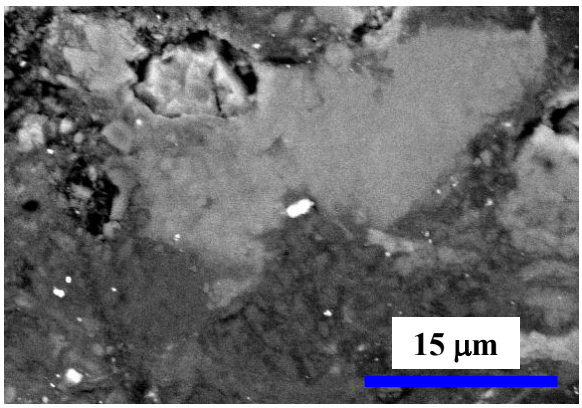

Initial

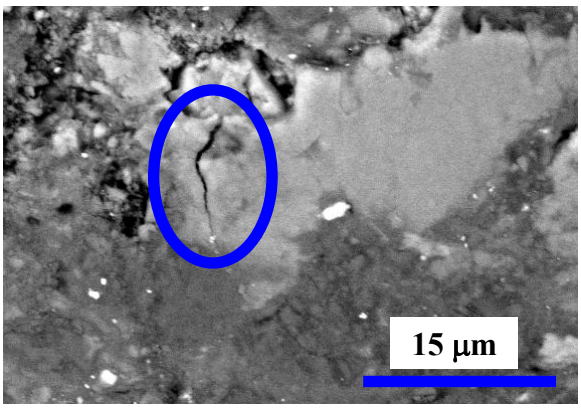

Failure

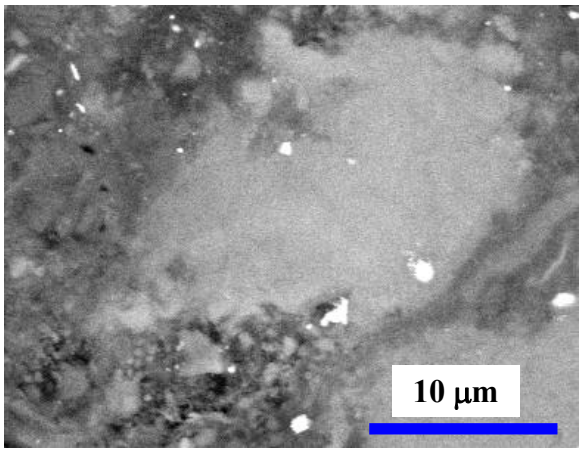

Initial

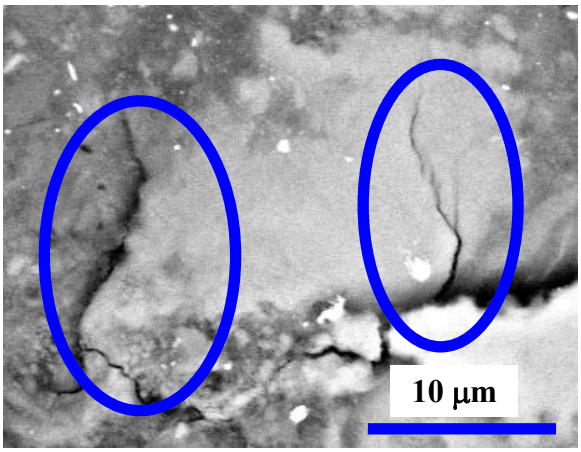

Failure

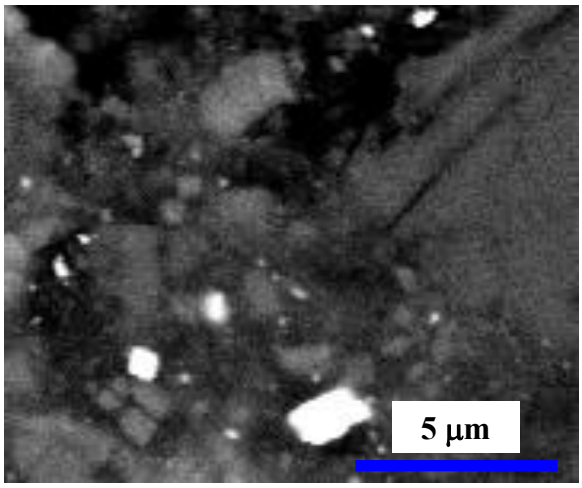

Initial

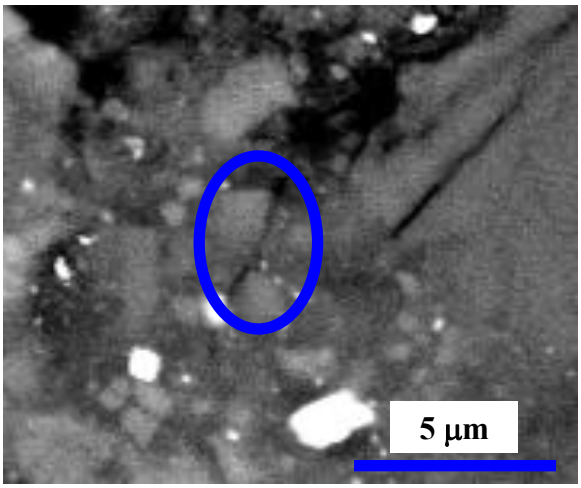

Failure

Figure 4.31: Some damage phenomenon under uniaxial compression. Top: crushing of coarse grain due to a high compression by another inclusion being in contact with it. Middle: crushing of grain, and the peeling of grain from matrix. Bottom: a microcrack emanates from macropore. Note that it is activated by shear deformation.

4.2.2 At moderate wet state

In test #4, the sample's surrounding in the ESEM chamber is maintained at 91%RH. The equilibrated water content is 5.4%. Once the sample is equilibrated in this environment, a uniaxial compression test is conducted until failure. Two zones with size of 320 × 276 μm^2 on the sample's surface are chosen as ROIs. The strain fields of ROIs are estimated by DIC techniques at 6 stress levels from 4.3 MPa to 20.2 MPa. Besides, two unloading loops (from 4.3 and 11.0 MPa) are introduced to estimate plastic deformation. The curves of stress versus normalized displacement measured by LVDT (Fig.4.32), and overall strain of ROIs evaluated by DIC (Fig.4.33 and 4.34) are given.

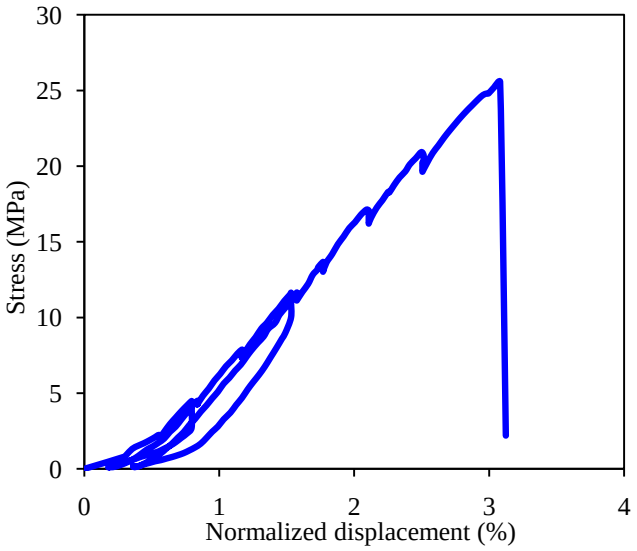

Figure 4.32: Stress vs. normalized displacement (LVDT) in test #4.

Similar to test #3, a primary concave upward portion appears at the beginning of the stress-strain curve, indicating the close of pre-existing microcracks before mechanical loading. After the concave upward portion, the relation between stress and axial strain is quasi-linear. However, the curve of lateral strain becomes nonlinear at high stress state (16.2 MPa). Two unloading loops reveal some plastic deformation, which is more important in observation zone 2: the plastic axial strain reaches 0.3% when unloading from 11.0 MPa, while that for zone 1 is 0.2%. The peak compression of the sample in test #4 is 25.7 MPa, and the residual stress is 2.3 MPa after failure.

The local strain distributions of the two ROIs are also estimated by DIC techniques. Similar to the previous tests, strain fields are similar for the studied stress steps, of which that at 20.2 MPa (maximal stress level among the steps for strain measurement by DIC) is chosen to be representative, shown in Fig.4.35 and 4.36. Regarding the strain field in zone 1, some shear bands (inclined red domains in the strain map) are found in clay matrix, and sometimes intersect with each other. Their orientations are really variable, which seems to be strongly related to

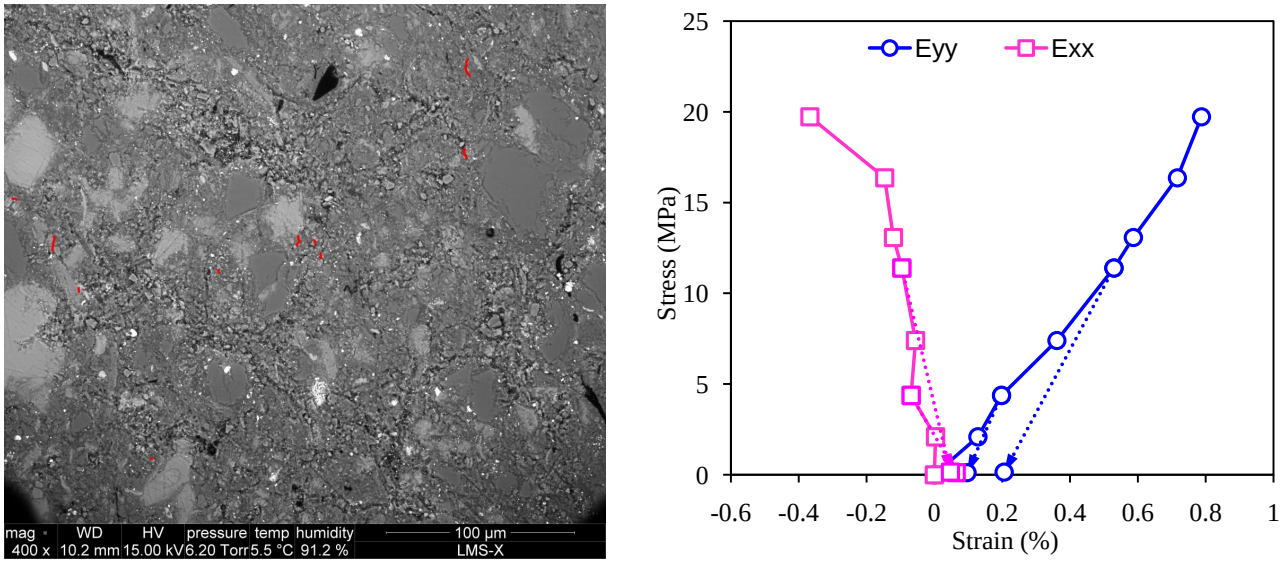

Figure 4.33: Observation zone 1 (left) and its overall strain evolution (right) in test #4. The microcracks at the failure state is traced in red color in the ESEM image (left).

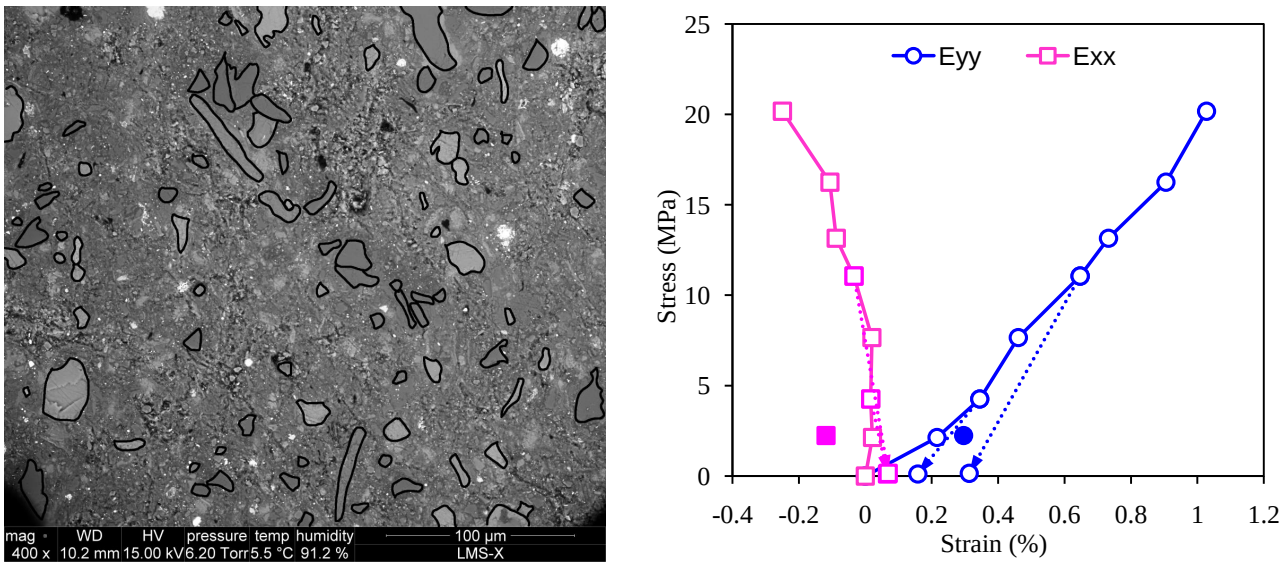

Figure 4.34: Observation zone 2 (left) and its overall strain evolution (right) in test #4. The gross inclusions are outlined in the ESEM image (left). Solid points represent the strain at failure, corresponding to the residual stress level (right).

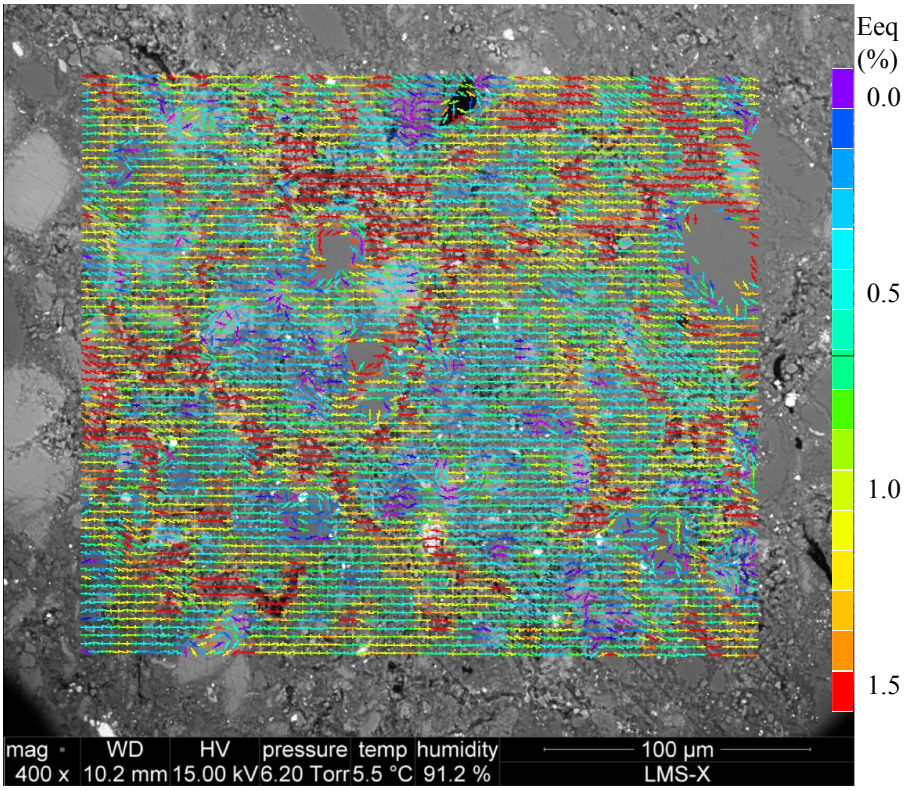

Figure 4.35: Strain field of zone 1 in test #4 (20.2 MPa).

the orientation of inclusions at their vicinities. Some tensile microcracks, with length of several micrometers, are observed during mechanical loading and are traced in red in Fig.4.33. It can be shown that these microcracks are generally found in high shear strain domains, which proves once more the strong association of tensile cracking to shear deformation.

Sliding along inclusion's boundary and induced tensile microcracking

For a better revealing the correlation of heterogeneous strain field to inclusion-matrix composite microstructure, the grains with surface bigger than 10 μm^2 are outlined for zone 2, as shown in Fig.4.34. The correspondence is well evidenced in Fig.4.36: high strain is mostly located in clay matrix, whereas inclusions deform much more faintly. However, it is interesting to note an elongated inclusion orientating about 45° to maximal compressive stress (vertical direction in the image), which involves in high deformation. The microscopic observation reveals that this high deformation is essentially related to a sliding along this long inclusion's boundary which is activated by uniaxial compression. Besides, a vertical microcrack parallel to the direction of maximal compressive stress is observed below the elongated inclusion (see Fig.4.38). Note this tensile microcracking is essentially associated to the sliding of inclusion-matrix interface.

For a better understanding of this sliding system, the deformation evolution of this slender grain and its surrounding (see Fig.4.38) is calculated and presented in Fig.4.37. Regarding the

stress-strain curve, it seems to be the typical behavior that plastic deformation predominantly arises from frictional sliding on microscopic fissures accompanied by further local tensile cracking from fissure tip (Rudnicki and Rice, 1975). At the beginning, shear deformation develops somewhat linearly with stress, with decreasing volume. From 7.7 MPa, the sliding on the inclusion-matrix interface is activated, that results in a decrease of tangent modulus. 7.7 MPa is also a threshold for the volumetric strain, since it turns to dilatation at higher stress from contraction at lower stress. This volume dilatancy is essentially associated to local uplifts in sliding asperities, as well as the subsequent local tensile cracking from fissure tips. The latter has actually been observed, as shown in Fig.4.38. This is why an echelon shaped high strained domain emerges in Fig.4.36. Moreover, such a sliding system is rather irreversible. The plastic strain of such zone is 0.6% at 11.2 MPa while it reaches 1.6% at failure.

Inclusion's boundary is generally a weak interface where sliding is more easily activated due to their relatively low cohesion. Actually, the activation of sliding on the inclusion-matrix interface is controlled by certain factors: inclusion's form and orientation. In general, a slender inclusion, orientated along the direction approaching the maximal shear direction, is easier to be activated to slide along its boundary. The slender inclusion discussed in the previous paragraph is orientated 45° with respect to the loading direction, corresponding to the maximal shear stress under uniaxial compression condition. Hence, it is particularly a favorable system for sliding. This is also why no sliding is observed in other inclusions for the same test. But a simple distribution of deformation bands, likely to be associated with shear deformation, is activated in the clay matrix. Its geometry and spatial localization is controlled by the presence of hard grains.

After failure, the sample is observed by optical microscopy, shown in Fig.4.39. The failure of sample is related to a fault at 55° with respect to the uniaxial compression direction. Besides, a slipping-like fracture is also observed at the top end of the sample, which encounters the principal fracture.

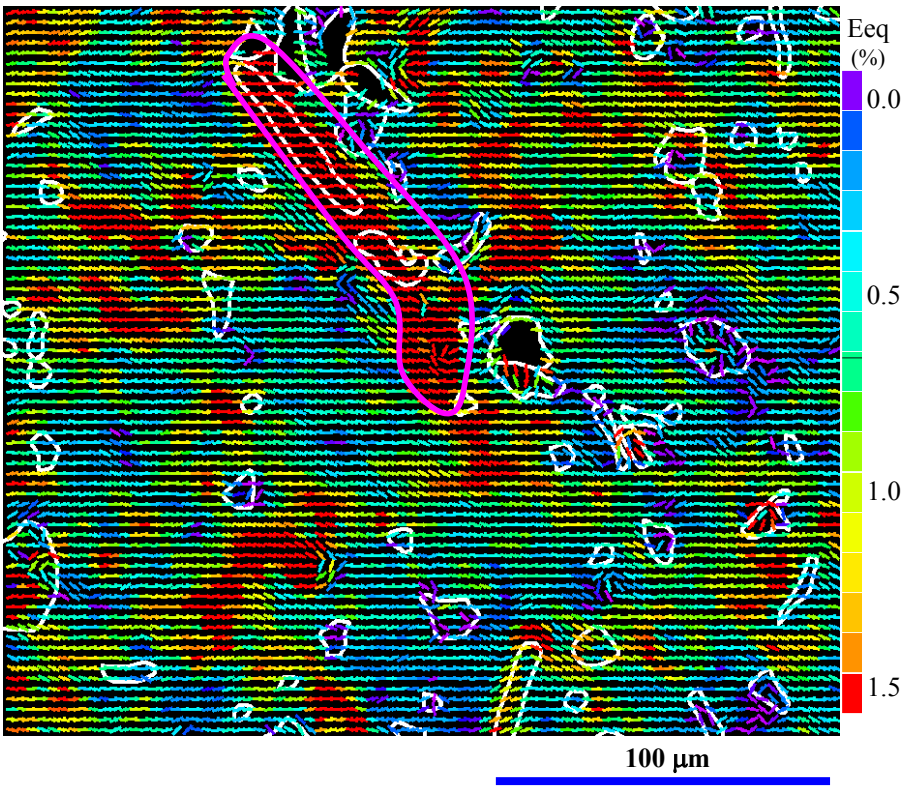

Figure 4.36: Strain field of zone 2 in test #4 (20.2 MPa), in which an echelon shaped high strained domain, associated to a sliding along one slender inclusion's boundary and the subsequent tensile microcracking, is highlighted in pink.

4.2.3 At extremely wet state

4.2.3.1 Test #5

The sample in test #5 is humidified at very high relative humidity (98%) prior to a uniaxial compression test. The equilibrated water content is 7.4%. Three domains with size of 320 × 276 μm^2, (corresponding to image magnification × 400) are chosen as ROIs for DIC analysis, shown in Fig.4.41 - 4.43 a. The strain evolution of the sample is shown by the normalized displacement measured by LVDT (Fig.4.40), and the overall strains of three ROIs (Fig.4.41 - 4.43 b). In this test, the peak stress is 20.9 MPa, while the residual stress after failure is 5.4 MPa.

While the stress-strain curves for the three observation zones are broadly similar, in particular in terms of strain level, some varieties are observed. For zone 1, a concave upward portion appears at the first step of loading, however, this is much less evident for zone 2 and not obvious for zone 3. Subsequently, the stress-strain curves (Eyy: axial strain) are somewhat strain-softening: the tangent modulus decreases with strain. The stress-strain curves for zones 2 and 3 seem to be more linear than for zone 1. However, two unloading paths reveal the loss

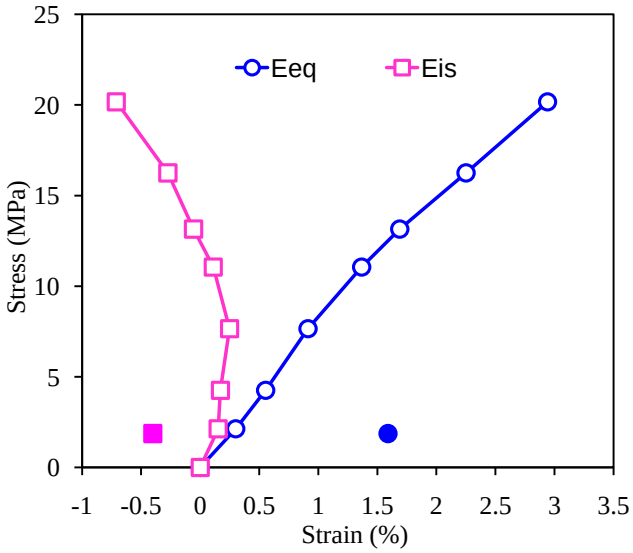

Figure 4.37: Stress-strain curve for the sliding system of slender inclusion. Solid points represent the strain at failure, corresponding to the residual stress level.

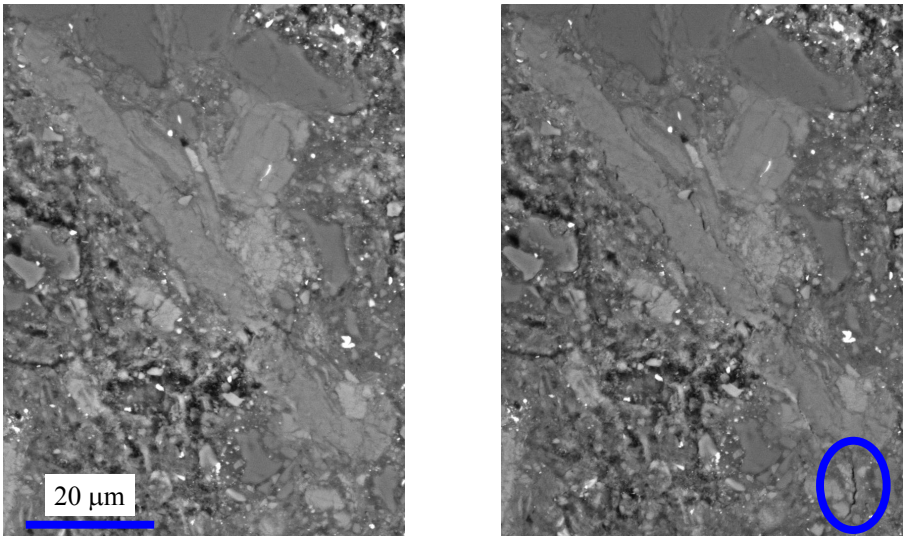

Figure 4.38: Tensile microcracking associated to sliding of inclusion-matrix interface.

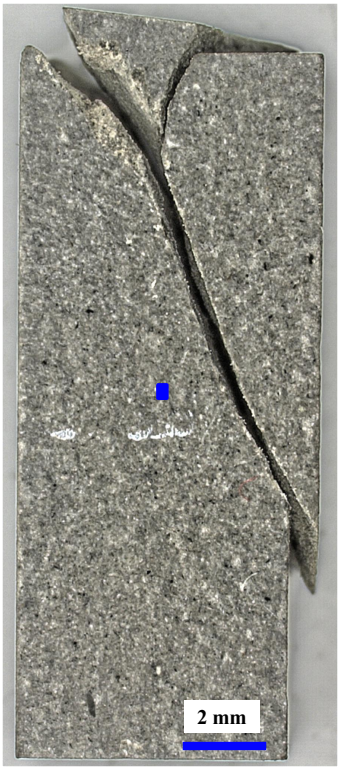

Figure 4.39: Fracture of sample in test #4 observed by optical microscopy. The position of observation zones is marked by a blue rectangle.

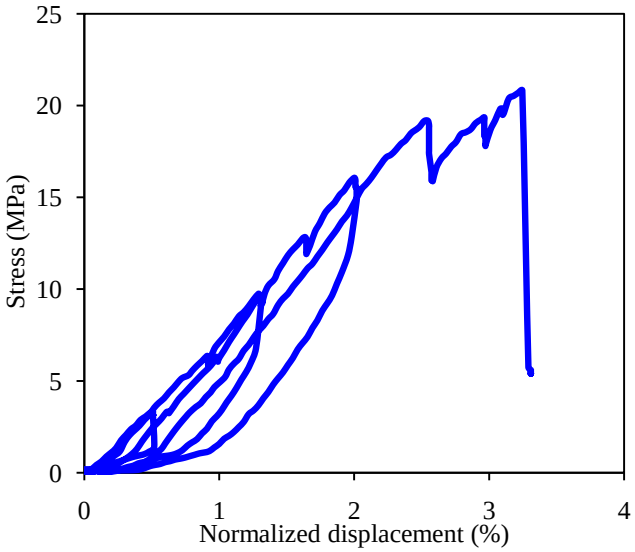

Figure 4.40: Stress vs. normalized displacement (LVDT) in test #5.

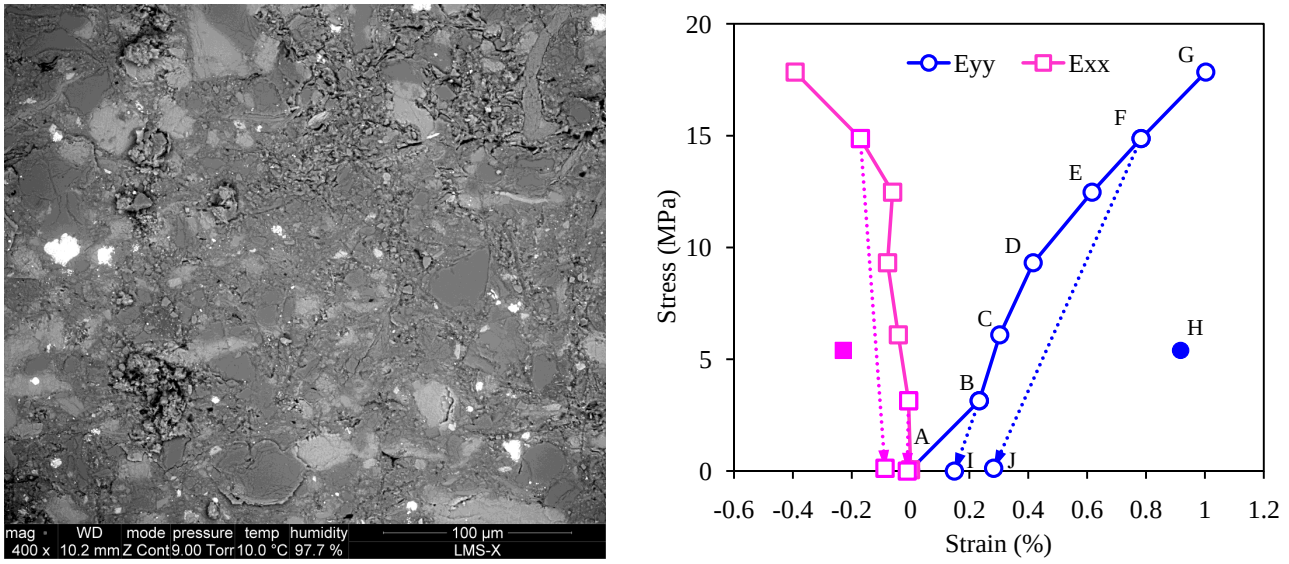

Figure 4.41: Observation zone 1 in test #5 and its overall strain curve. Solid points represent the strain at failure, corresponding to the residual stress level (right).

of Young's modulus when loading goes on in zone 2. Besides, some residual deformations are clearly observed in zones 1 and 2. For zone 3, the plastic deformation is not evident for the two first unloading steps, but it reaches however 0.8% after failure. The strain-softening is more remarkable for the Exx (transverse strain) curve, notably for the two last steps (from 12 MPa). However, it should be noted that the nucleation of vertical microcracks, which are considered as the main mechanism for the nonlinear increase of lateral deformation, is not evident in the three zones from this micro-scale observation.

Behavior of pre-existing cracks

The strain maps of the three observation zones are shown in Fig.4.44 - 4.46. At the first loading step, a horizontal deformation band is observed in zone 1. This is related to the presence of a long pre-existing microcrack (more than 100 μm long), passing horizontally through the clay matrix and some inclusions' boundaries (see the strain map for the first loading step in Fig.4.44). For a better understanding of the behavior of this pre-existing horizontal crack, its deformation is followed (see definition of the sub-domain in Fig.4.47). It is worth noting that the local stress state around the pre-existing crack is unknown due to heterogeneity. However, global stress is used to indicate qualitatively its stress level. It is shown in Fig.4.48 that the deformation for this pre-existing horizontal crack is extremely great (2.2%) for the first loading step, consisting of its closing. Moreover, this deformation is strongly irreversible: it is still 1.5% (i.e. 66% of the total strain) after unloading (see A-I in Fig.4.48). After this closing step, the stress-strain curve for the pre-existing crack zone exhibits somewhat a strain-softening behavior, similar to the global behavior of the material. Note that the plastic deformation in such pre-

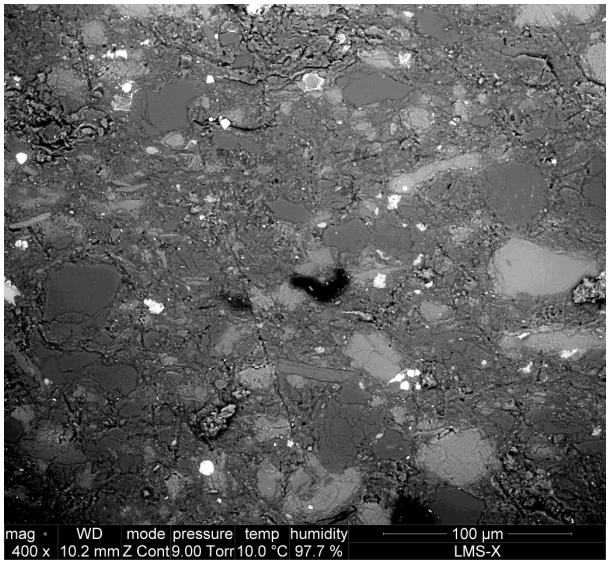

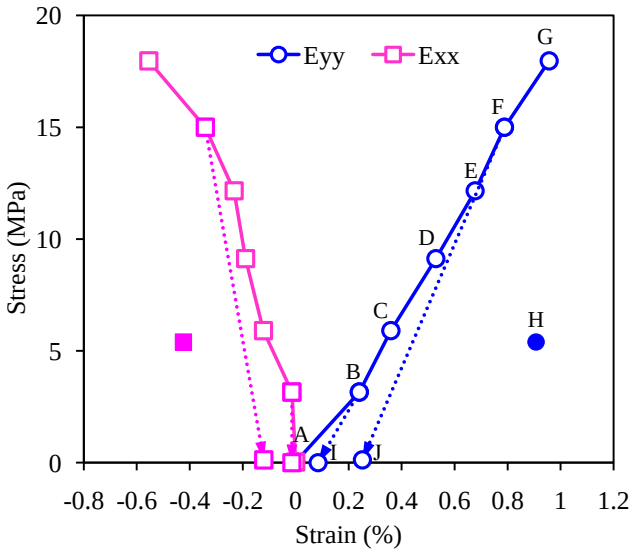

Figure 4.42: Observation zone 2 in test #5 and its overall strain curve. Solid points represent the strain at failure, corresponding to the residual stress level (right).

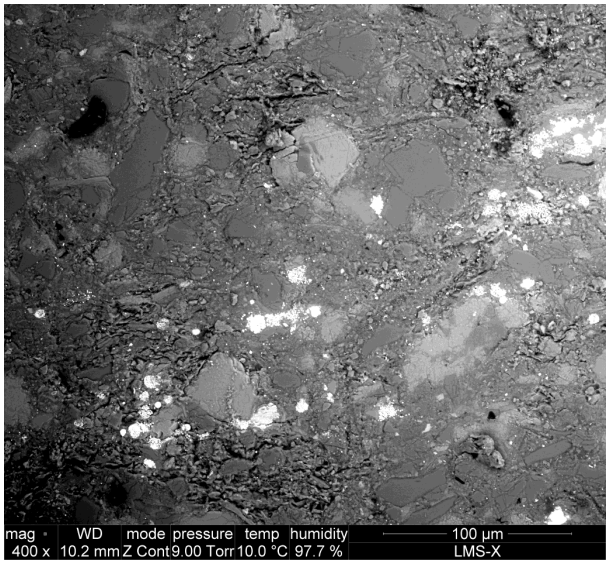

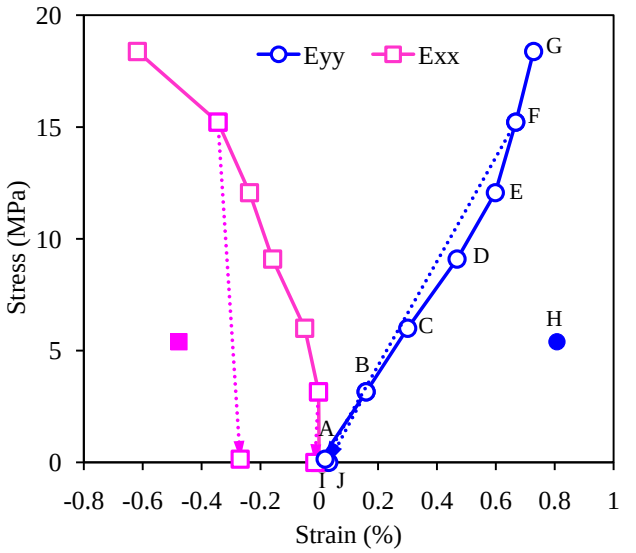

Figure 4.43: Observation zone 3 in test #5 and its overall strain curve. Solid points represent the strain at failure, corresponding to the residual stress level (right).

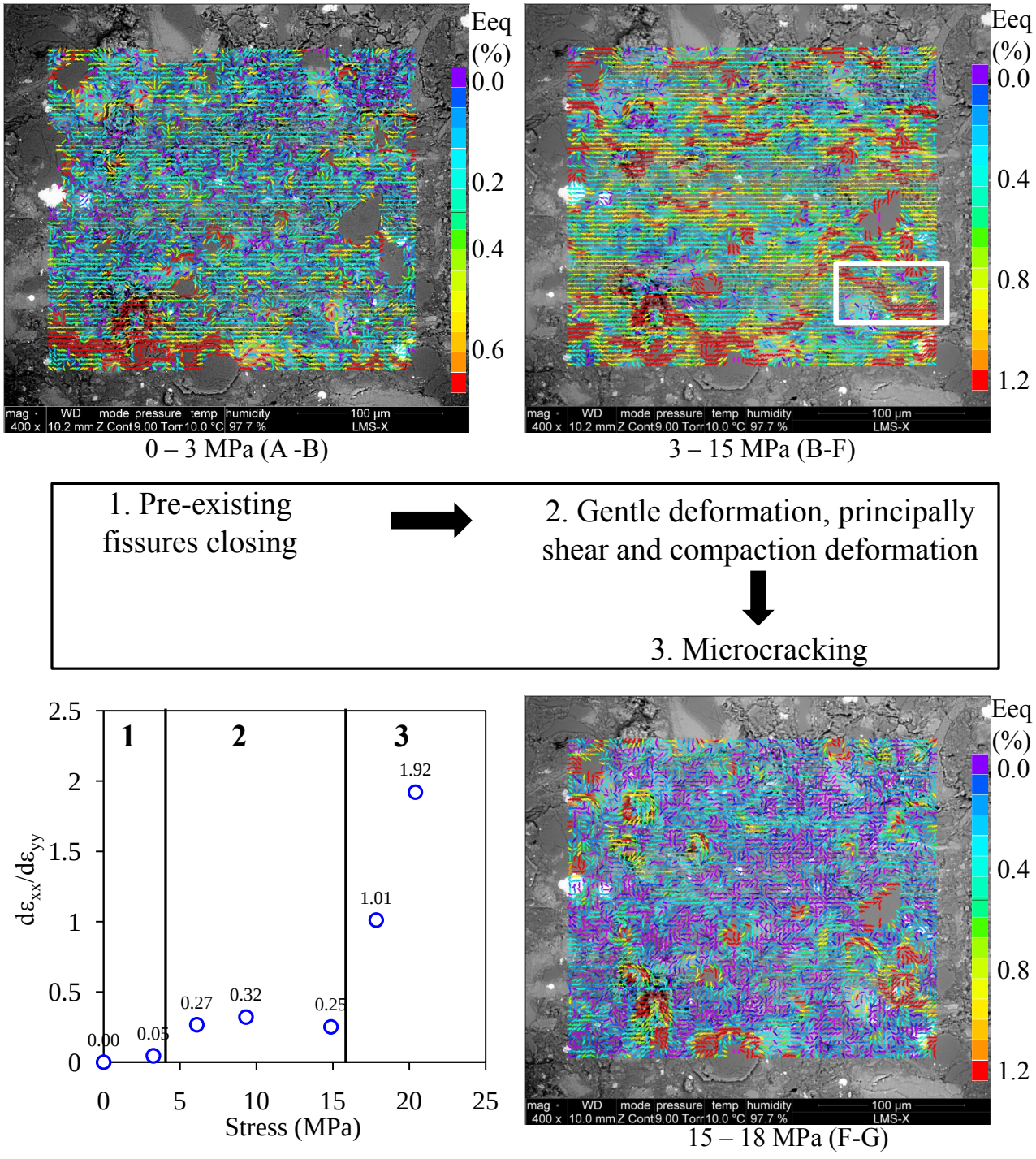

Figure 4.44: Three staged deformation evolutions of zone 1 in test #5. A network of compaction and shear bands are outlined in the strain map (3 - 15 MPa).

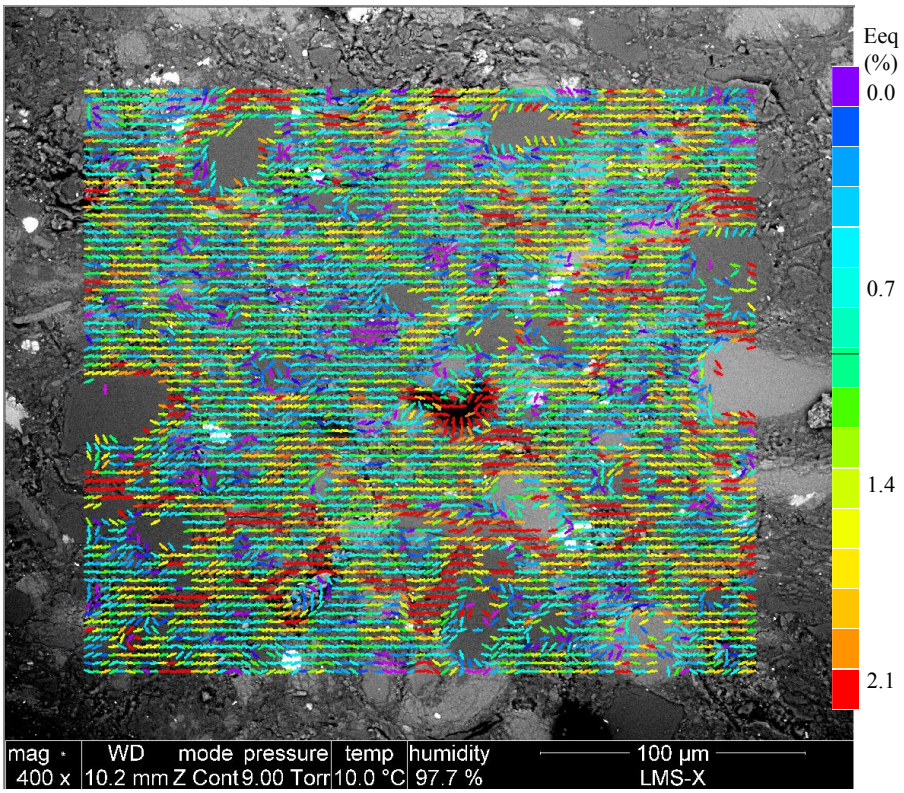

Figure 4.45: Strain map of zone 2 in test #5 (at 18 MPa).

existing cracking zone evolves faintly after the closing step: the incremental plastic deformation is nearly zero from 3 to 15 MPa (see I-J in Fig.4.48). Comparing to overall behavior, such pre-damaged zone is more deformable (Eyy) even after the closing step (nearly two times more than the total zone), whereas, the evolution of strain Exx in this zone is rather similar to in the overall zone.

The behavior of the pre-existing horizontal microcracks is somewhat similar to macropore-rich zones (refer to detailed study in test #3), of which the deformation evolution can be divided into two parts: the first strain-stiffening part, and the second strain-softening part. The strain-stiffening part is essentially related to the densification effect due to compaction of pore spaces, while the strain-softening part at high stress involves in plasticity. Hence, pre-existing microcracking zones and macropores rich zones can be classified as a type of "material", of which the deformation mechanisms are similar. However, it should be noted that pre-existing microcracks are one special type of pore space: its inflexion point (transition from strain-stiffening to strain-softening) is extremely low (less than 3 MPa according to this test), whereas the strain-stiffening part can cover a wide stress range.

It should be noted that there are no obvious pre-existing microcracks observed in the previous tests which have undergone the same sample preparation process but are at lower humidity states. We suggest that these pre-existing microcracks in test #5 are related to humidifica-

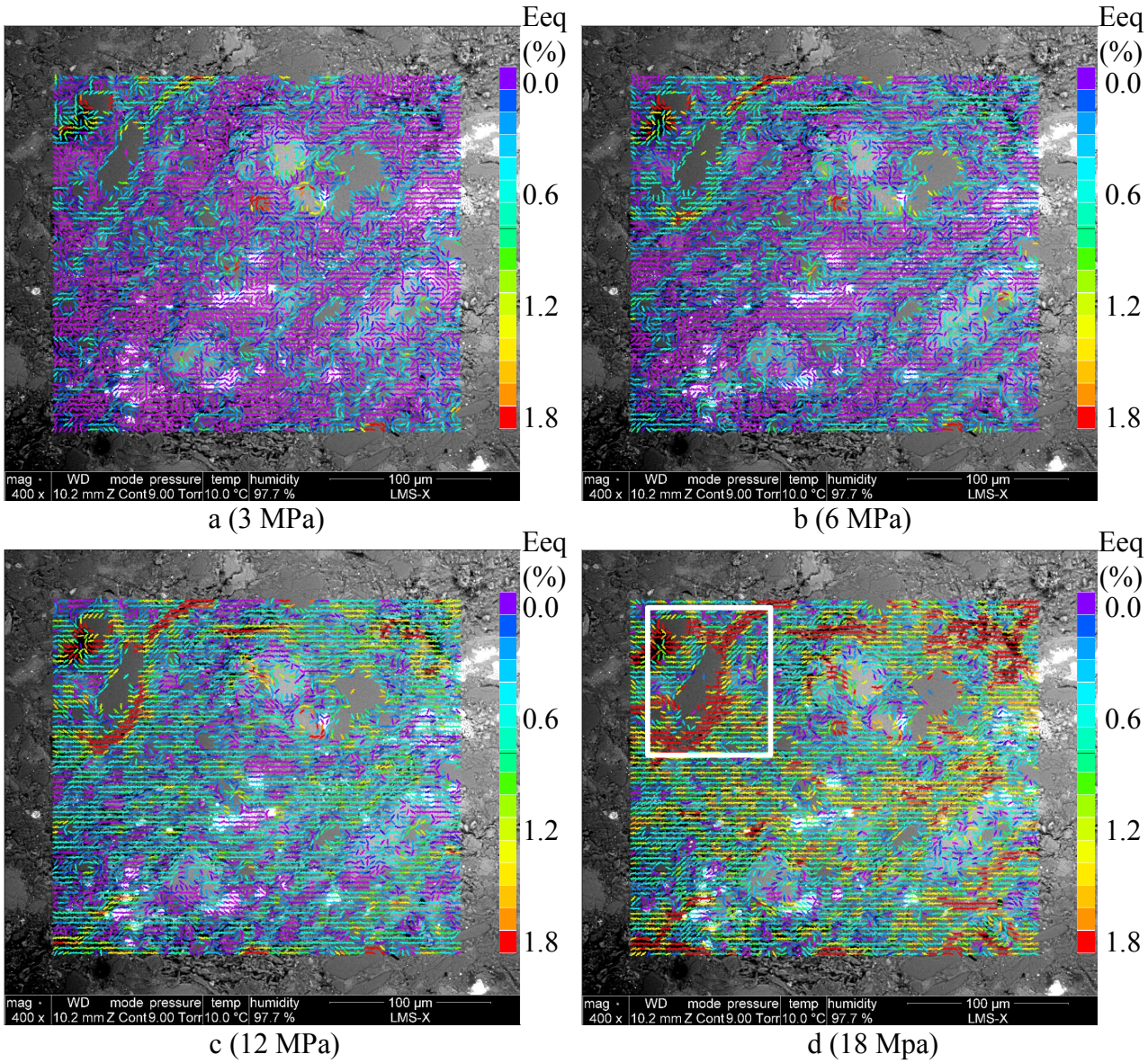

Figure 4.46: Strain map of zone 3 in test #5.A tensile microcracking activated by shear deformation is outlined at the top-left of the observation zone.

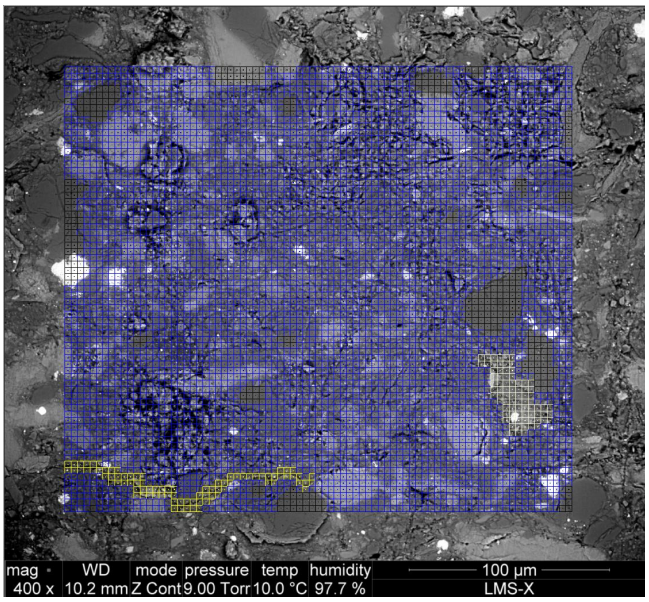

Figure 4.47: Definition of sub-domains in observation zone 1: sub-domain 1 corresponds to a pre-existing fissure (in yellow color), sub-domain 2 corresponds to a connected compaction and shear band (in white color).

tion. In other words, they are microcracks due to humidification, as evidenced and discussed in chapter 3. The microcracking due to humidification would alter the response of the material under mechanical loading, and this is an important factor of the influence of humidity state on the mechanical behavior of such rocks. In the sample of test #5, the pre-existing microcracks are orientated in all directions. As discussed above, horizontal ones would close under low compression. Nevertheless, the others evolve dissimilarly: inclined pre-existing microcracks may slide, and vertical ones could open and propagate further. Actually, the behavior of pre-existing microcracks is strongly controlled by their orientation.

Network of compaction and shear bands and induced microcracking

It is interesting to emphasize a network of compaction and shear bands found in zone 1 (marked in Fig.4.44). Two macropores-rich zones involve two compaction bands under mechanical loading. Between the two compaction bands, a shear band develops which consists of the sliding along a slanted elongated inclusion's boundary. Moreover, this shear band results in two tensile microcracks located below it (see Fig.4.49). Besides, the strain evolution of this interesting domain (the definition of the sub-domain is shown in Fig.4.47) is calculated (Fig.4.50). After a linear portion, the deformation becomes significant from 12 MPa, essentially involving the start-up of sliding and subsequent tensile microcracking.

Three staged strain evolution

The absolute ratio between lateral strain and axial one in show in Fig.4.44, from which a

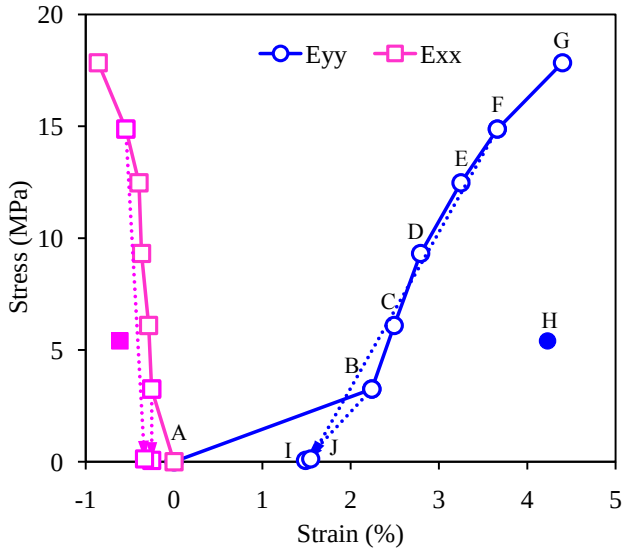

Figure 4.48: Stress-strain curve of the zone surrounding the pre-existing microcrack (sub-domain 1) in zone 1.

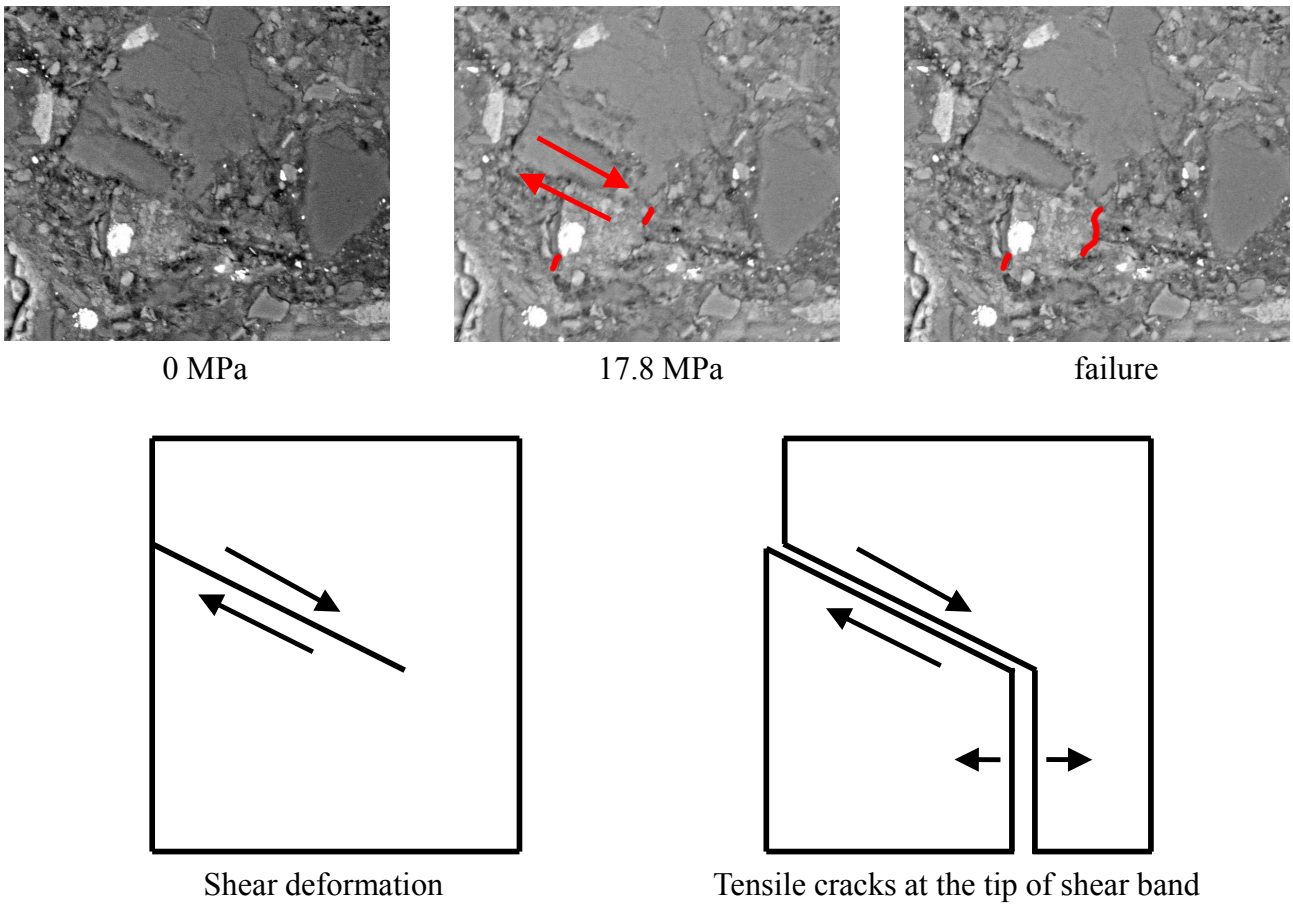

Figure 4.49: Tensile cracks generated at the tip of shear band.

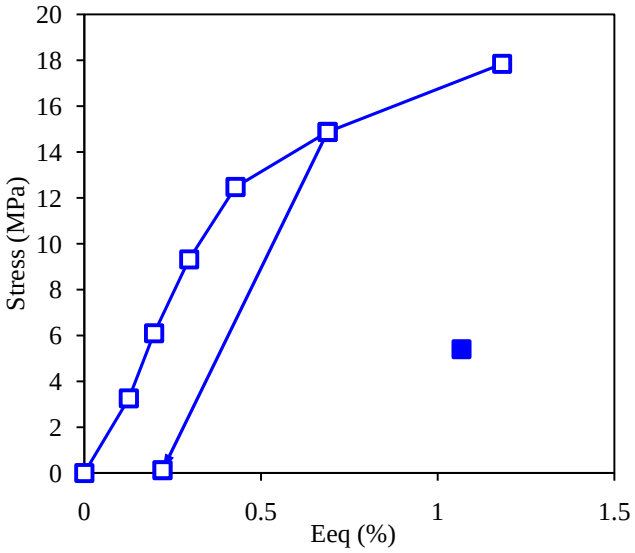

Figure 4.50: Strain evolution of sub-domain 2 in zone 1 of test #5.

three staged strain evolution is well revealed. Indeed, such three staged evolution are associated to different deformation mechanisms, which can be demonstrated by their dissimilar strain fields. The ratio for the first stage (0 - 4 MPa) is extremely low and is associated to closing of pre-existing cracks. For the second stage, the ratio is about 0.3, approximately in the typical range of Poisson's coefficient of argillaceous rocks. The deformation mechanisms for this stage typically consist of an elastic response of such rocks, accompanied by some compaction and shear bands contributing to plastic deformation. After the second stage, the ratio increases sharply, principally due to the great increase of lateral deformation. Such nonlinearity of Exx is principally related to the transverse microcracking process. It is worth noting the moderate shear bands emerging in the second stage are not evident in the third stage: deformation is more concentrated in certain isolated domains. This means that, in the third stage, besides the other deformation mechanisms, microcracking is principally contributable to the total deformation of the material. Besides, the developing of microcracks would also unload their neighborhood.

The elastic (see F-J in Fig.4.41) and plastic portions (see J-I in Fig.4.41) for 15 MPa in zone 1 are calculated, and their strain maps are shown in Fig.4.51. Note that plastic deformation is calculated with respect to the first unloading point from 3 MPa to exclude the effect of the closing of pre-existing cracks. It is shown that most of the shear bands at such stress state are elastic. It is emphasized that the some plastic deformations are found in macropore rich zone (at the upper part of image), whereas the elastic deformation in this zone is nearly null. This is principally related to the irreversible compaction of macropores.

The strain maps of zones 2 and 3 are shown in Fig.4.45. Similar deformation mechanisms are found, as in zone 1. It is worth to emphasized a network of two shear bands in the top-left part of zone 3 (in Fig.4.46). Two shear bands separately develop at low stress state, while

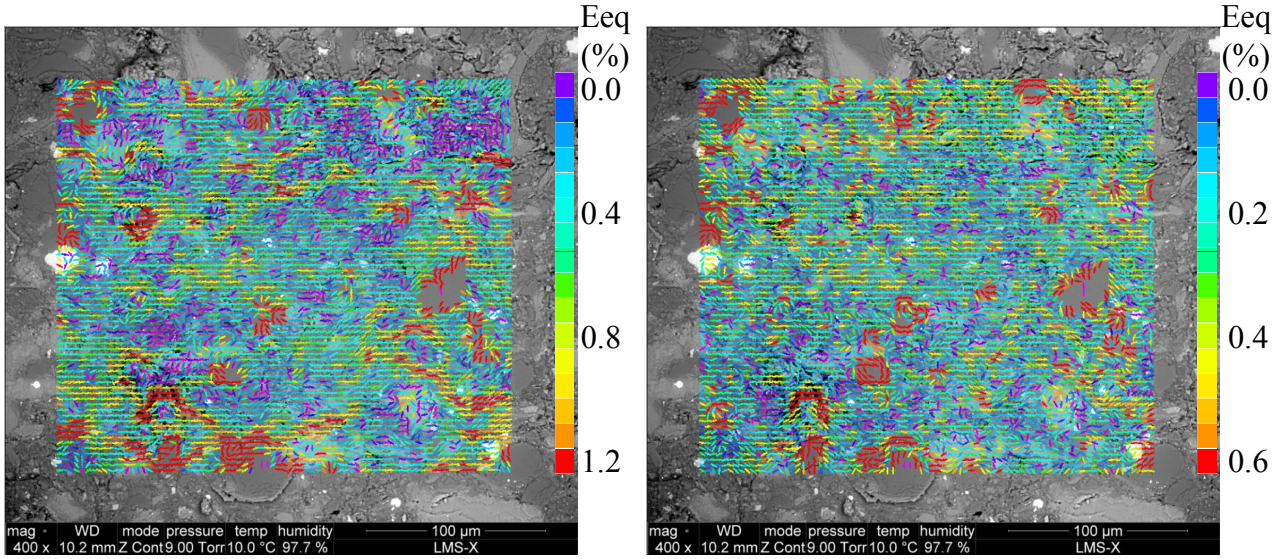

Figure 4.51: The elastic and plastic portions for 15 MPa state in observation zone 1 of test #5.

they are subsequently connected by a vertical tensile microcrack consisting of separation of an inclusion-matrix interface.

4.2.3.2 Test #6

The sample in test #6 is hydric equilibrated in ESEM chamber at 98%RH, and its water content is 10.1%. Uniaxial compression test is conducted on the sample until failure at 16.3 MPa. The residual stress after failure is 4.5 MPa. Two unloading loops (4.0, 9.3 MPa) are introduced for estimating elastic constants as well as characterizing irreversible deformation. The curve of stress vs. normalized displacement is shown in Fig.4.52. Four zones on the sample's surface are chosen as ROIs for DIC analysis, and their overall strains evolutions are calculated and shown in Fig.4.53 - 4.56.

The stress-strain curve in test #6 exhibits a somewhat S-shaped form in its pre-peak part, which can be divided into two portions: the beginning strain stiffening portion, and the following strain softening portion. The first portion involves an increase of tangent modulus with strain accumulation. Moreover, two unloading steps show that elastic modulus also increases with strain, which means that stress stiffening effect is essentially associated to the loss of material's compressibility with strain. Besides, the strain stiffening portion also involves considerable plastic deformation: it is approximately 0.4% for 9.3 MPa. For the second portion, the tangent modulus decreases with strain. This strain softening portion is related to some irreversible phenomena (such as plasticity and damage) of such rocks. It is interesting to note that the residual strain after failure is quite significant. For observation zone 1, it (1.7%, corresponding to residual stress 4.5 MPa) is even more important than that for the 11.5 MPa loading step

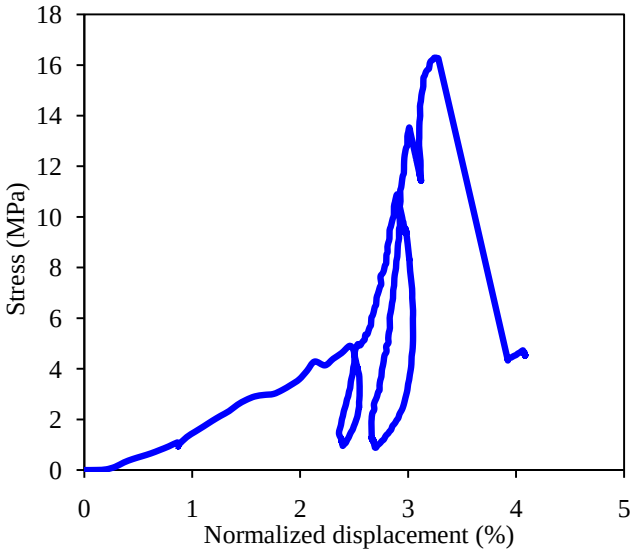

Figure 4.52: Stress vs. normalized displacement (LVDT) in test #6.

(1.2%). Such large residual strain implies a significant accumulation of plastic deformation before the failure of the material.

The strain fields of four observation zones are estimated by DIC, among which those of zone 1 (Fig.4.57 and 4.58)and of zone 3 (Fig.4.59) are presented. Similar to the observations in the previous tests, certain common deformation mechanisms of argillaceous rocks under uniaxial compression condition can be summarized: 1) compaction of macropores and pre-existing microcracks perpendicular to the compression direction; 2) shear deformation developed in clay matrix and sliding of some activated inclusion-matrix interfaces, 3) opening of microcracks sub parallel to the compression axis. Such various mechanisms lead to some horizontal, inclined and vertical deformation bands in strain maps.

Regarding their locations, two types of inclined shear bands can also be distinguished: 1) in clay matrix; 2) in the zone around some elongated inclusions' boundaries. The shear bands developed in clay matrix, mostly shown in yellow color (corresponding to a moderate strain level), are orientated generally in the direction about 60° with respect to the compression axis. They are principally related to the shear deformation developed in the clay matrix. The second type of shear bands, typically found at the vicinity of some inclined slender inclusions, involves in a higher strain level (normally in red color in strain maps) compared to those in the clay matrix. They are generally associated to sliding of inclusion-matrix interfaces. Contrary to the similar orientated shear bands in the clay matrix, the shear bands developed on inclusion-matrix interfaces are variably orientated: they are strongly controlled by the form and orientation of inclusions.

It is worth noting that the mechanisms mentioned above are rather pre-peak behaviors. More precisely, they are related to the behavior prior to the inception of macroscopic deforma-

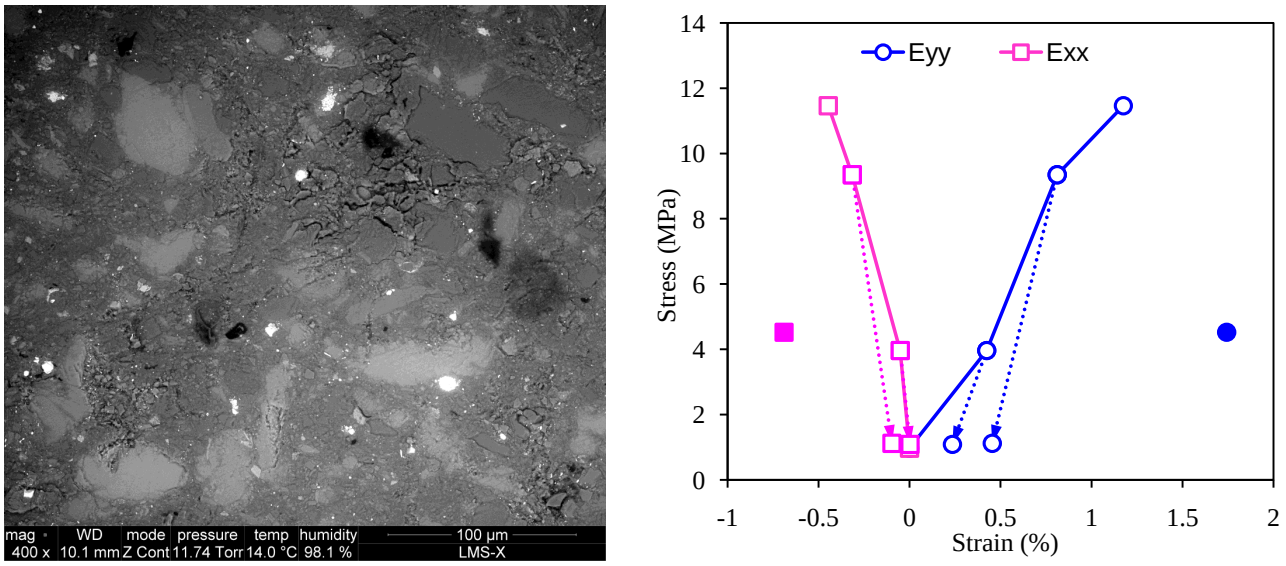

Figure 4.53: Observation zone 1 (left) and its overall strain evolution (right) in test #6.

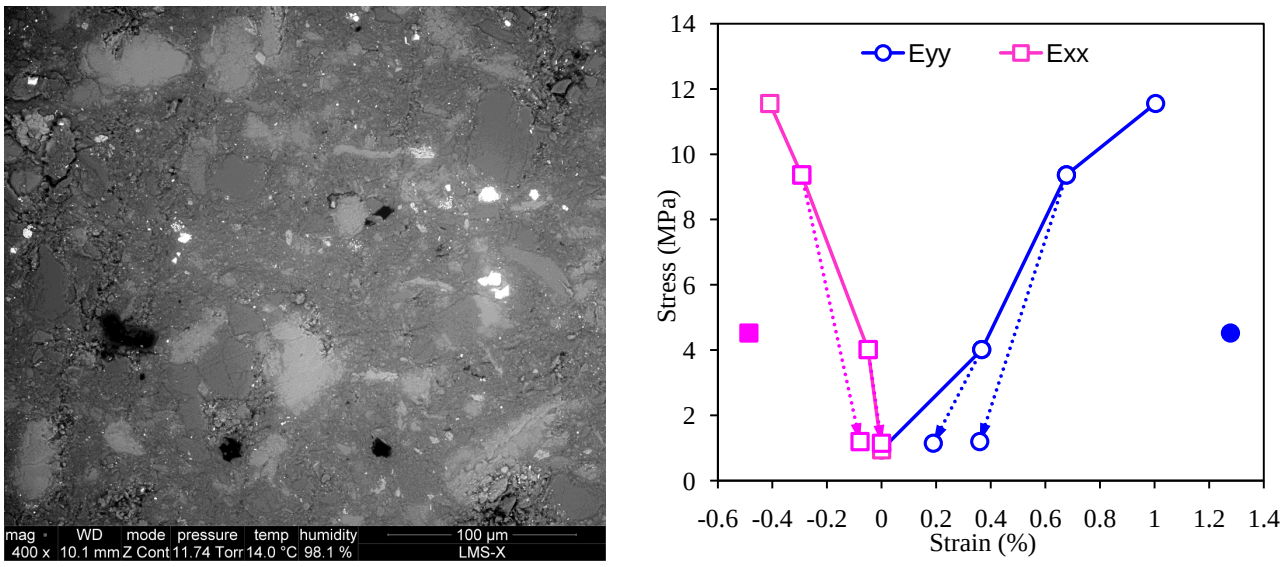

Figure 4.54: Observation zone 2 (left) and its overall strain evolution (right) in test #6.

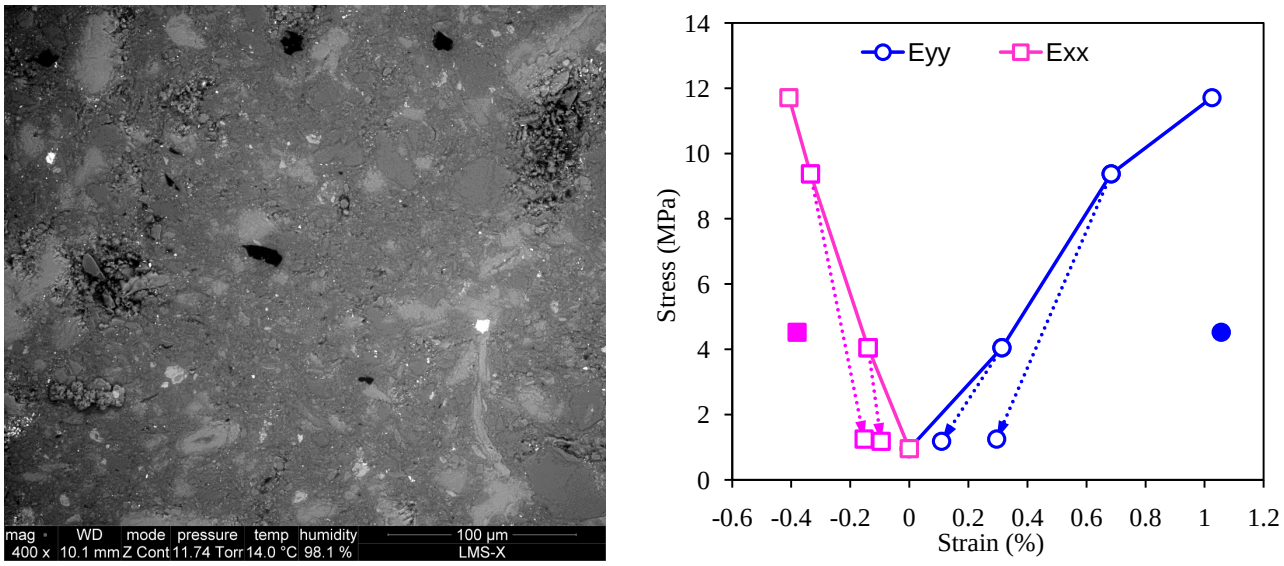

Figure 4.55: Observation zone 3 (left) and its overall strain evolution (right) in test #6.

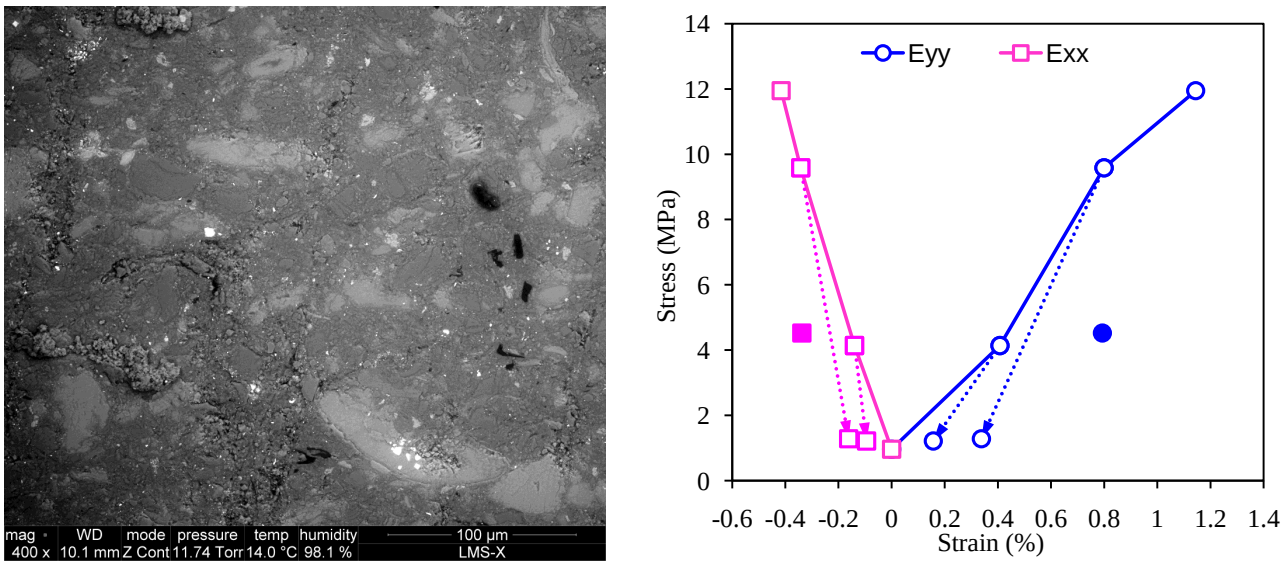

Figure 4.56: Observation zone 4 (left) and its overall strain evolution (right) in test #6.

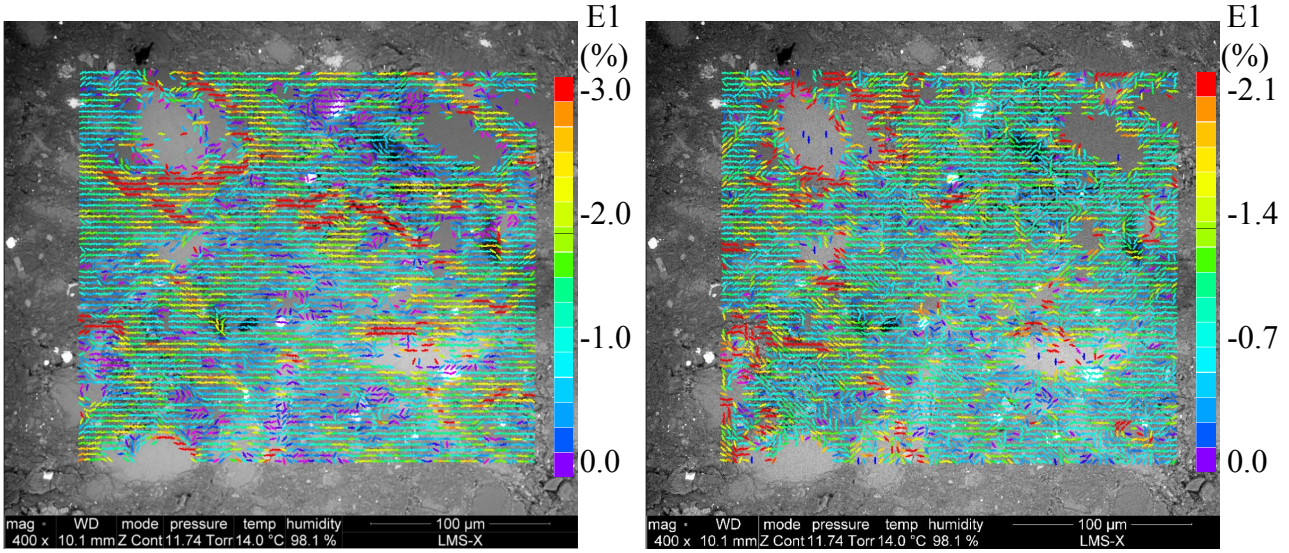

Figure 4.57: E1 strain fields of zone 1 in test #6. Left: at the pre-peak loading stage, right: at the failure.

tion localizations that result in the ultimate failure of material (Rudnicki and Rice, 1975). It is well recognized that macroscopic deformation localization generally starts near or after peak stress (Lenoir et al., 2007; Tang et al., 2000). However, some compaction and shear bands, principally due to the heterogeneity of material, are already evidenced in the pre-peak loading stage. We call them microscopic deformation localization here. The pre-localization regions already involve in some nonlinear phenomena (such as plasticity and microcracking). Nevertheless, they are controlled by similar evolution mechanisms: that is why the strain fields are always similar in the pre-peak loading stage. When mechanical loading exceeds certain threshold, some other mechanisms (for example macroscopic deformation localization) would be activated. The two deformation bands are linked to different mechanisms: microscopic deformation bands are essentially due to the material heterogeneity, while macroscopic deformation bands are related to the instability (Bésuelle, 2001; Rudnicki, 2002).

To investigate the post-peak behavior of such material, the relative strain fields between residual stress state and 11.5 MPa (the maximal stress state before failure) in observation zone 1 are estimated and presented in Fig.4.57 and 4.58 b, allowing to exclude the contribution of deformation mechanisms associated to the pre-localization loading stage and merely characterize the post-peak behavior of the material. Compared to the strain fields at pre-peak region, compaction of macropores and opening and developing of vertical microcracks still contribute to deformation. However, shear bands existing in the pre-localization loading stage disappear in the post-peak stage. The failure of material links to some macroscopic localized phenomena (macroscopic compaction and shear bands, fracturing) in the viewpoint of the scale of sample. However, the observation zones in this test seem to be beyond such zones.

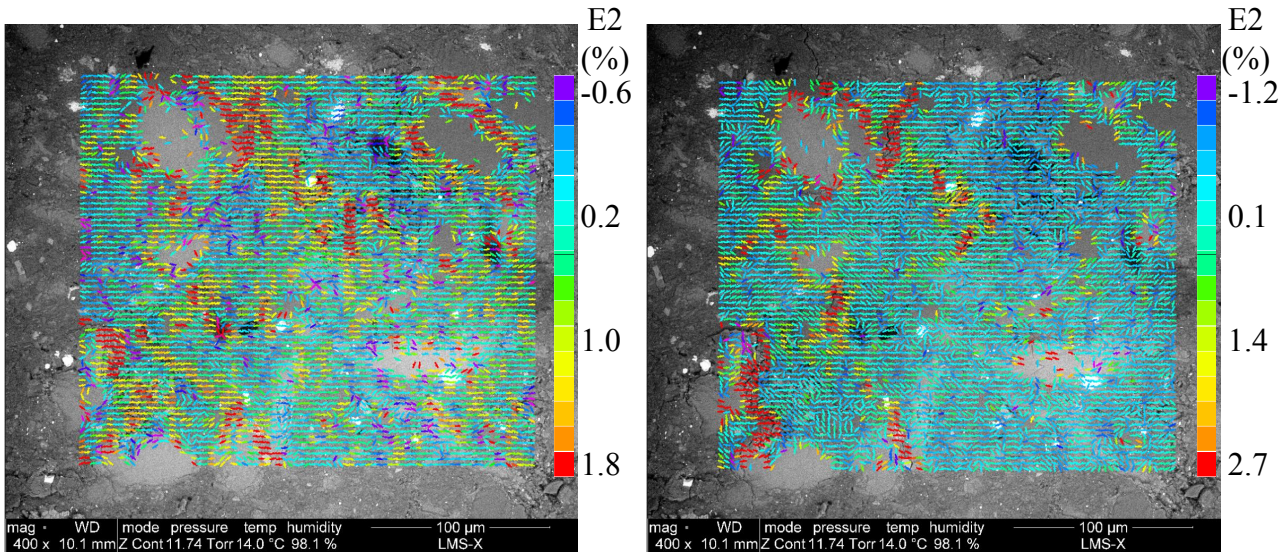

Figure 4.58: E2 strain fields of zone 1 in test #6. Left: at the pre-peak loading stage, right: at the failure.

It is interesting to focus on an elongated inclusion owing a shape made of two parts with a 60° angle kink (see Fig.4.60). Under moderate stress of 9.4 MPa, the bottom inclined part starts to slip on the interface, but the top vertical part doesn't. It is until more than 11.7 MPa when the top part of inclusion begins to be separated from the clay matrix and slipping is activated. This is indeed a good example to characterize the slipping system on inclusion-matrix interfaces. As the bottom part is orientated about 30° to the axial compression while the orientation of the top part is parallel to it, it is natural that shear stress is more important at the bottom part and slipping can be activated at smaller stress level. Therefore, one can conclude that slipping on inclusion-matrix interfaces is strongly controlled by the shape and orientation of inclusions. Assuming slipping on interface obeys Mohr-Coulomb's law, the most dangerous orientation of inclusion is $\pi/4 + \varphi/2$ (φ is the friction angle of interface) to uniaxial compression axis.

The strain fields of E1 and E2 in zone 3 after failure are presented in Fig.4.61. Note that their morphologies are very different: E2 strain field exhibits some horizontal deformation bands associated to high compressive strain), whereas, certain vertical bands consisting of high extensional strain emerge in E1 strain map. Actually, the two strain maps reveal different deformation mechanisms respectively. For horizontal bands in the E2 map, high compressive strains are related to uni-dimensional compaction of macropores. However, for vertical bands in the E1 strain field, high extensional strains are associated to opening of microcracks sub parallel to the compression axis. There are also some high strain bands overlapped in the two strain field of E1 and E2. They are generally linked to great shear deformation: shear developed in clay matrix and slipping of inclusion-matrix interfaces.

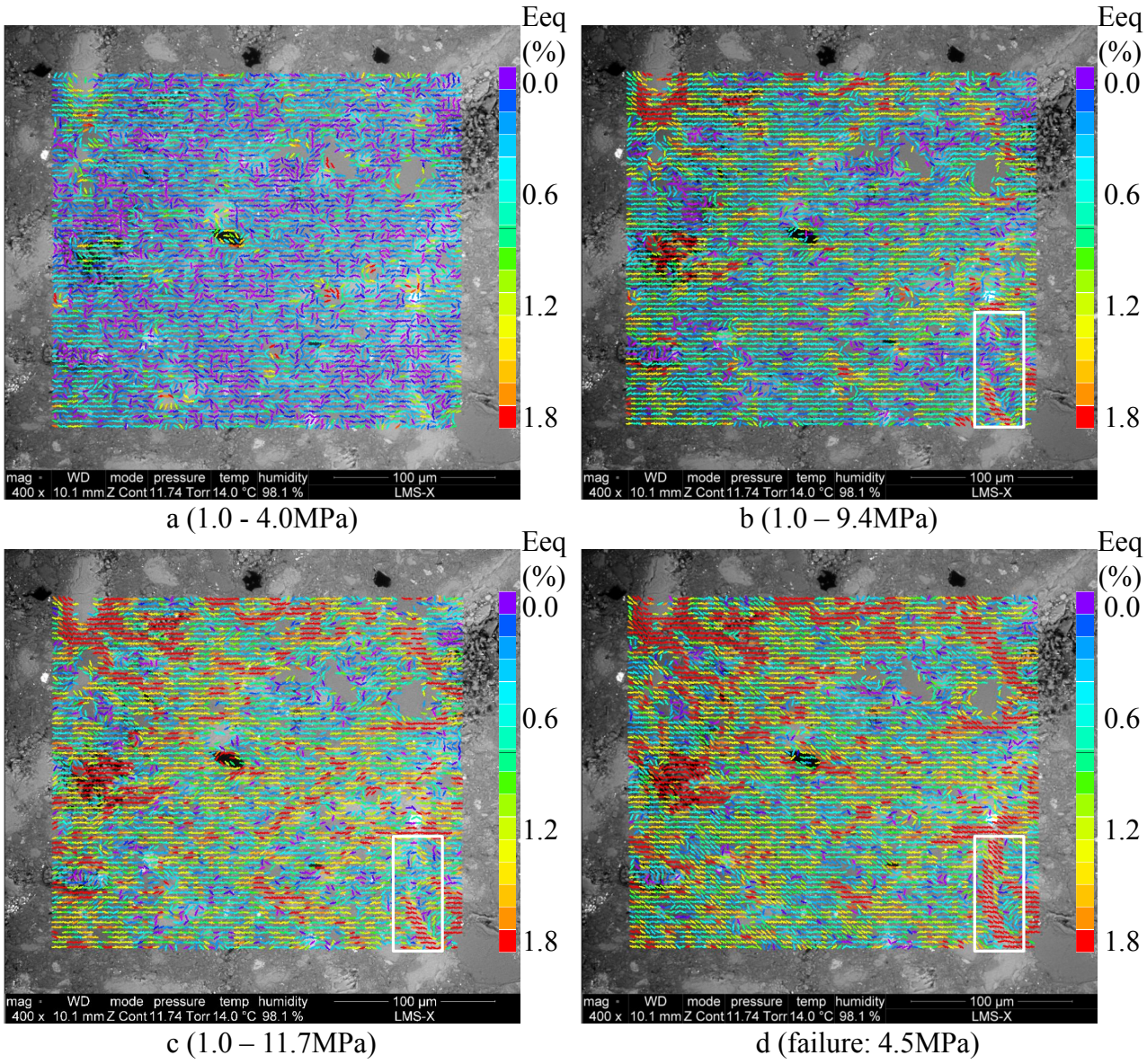

Figure 4.59: Strain field evolution of zone 3 in test #6. The rectangular frame, containing one elongated inclusion, will be zoomed on in Fig.4.60.

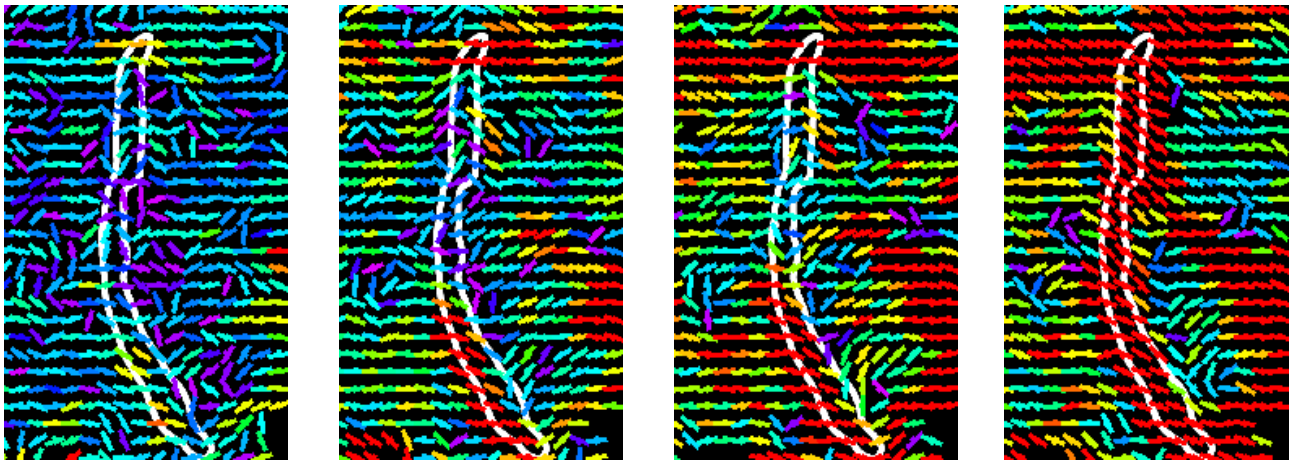

Figure 4.60: Sliding of a slanted slender inclusion boundary. The contour of inclusion is outlined in white line.

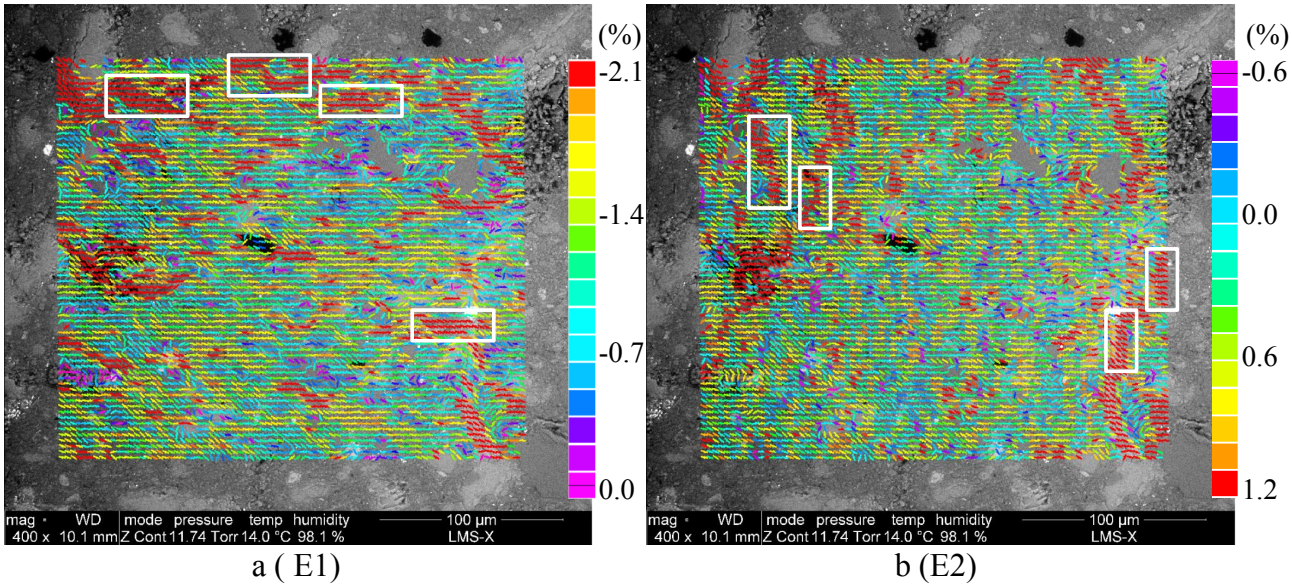

Figure 4.61: The strain field of zone 3 after failure.

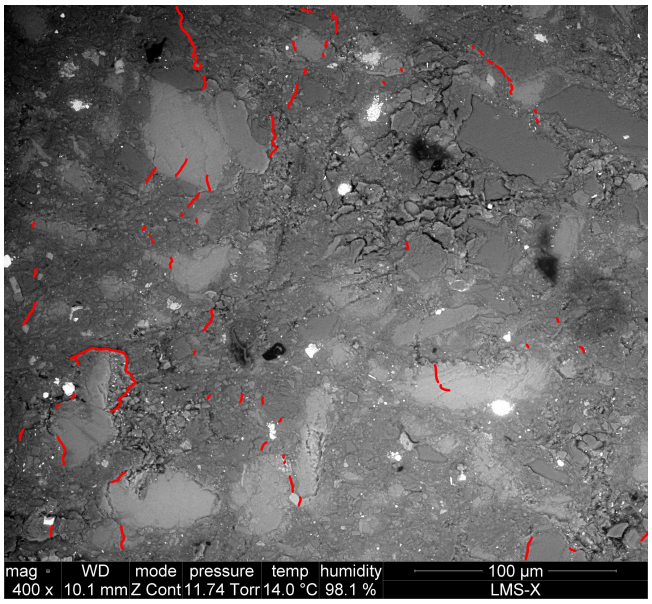

Figure 4.62: Microcracking (traced in red color) in zone 1 after failure.

After failure, numerous microcracks are observed in the observation zones (see Fig.4.62). Certainly, some slanted microcracks associated to shear deformation are observed. Nevertheless, most microcracks are sub-parallel to the compression axis. Regarding their locations, microcracks are mostly found on inclusion-matrix interfaces, as well as some in clay matrix. Similar to the preceding tests, there are still several microcracks developed in some grains, which are essentially related to crushing of them. Several types can be distinguished for vertical microcracking regarding their locations: 1) separation of interface between inclusion and matrix, 2) tensile microcracking in clay matrix, 3) breakup of one gross grain into several smaller ones.

Vertical microcracks are essentially activated by two mechanisms: 1) some microcracks own strong links to shear deformation. One typical case is the local cracking from shear fissure tip in the tension quadrant. Such type of microcracking is normally found in high shear deformation zone. 2) Some vertical cracks are activated by the local tension under uniaxial compression conditions (see Fig.4.63). They are typically initiated at pre-existing faults (for example inclusion boundary). Moreover, their propagations are strongly controlled by the presence of inclusions: they prefer to go through interfaces (inclusion-matrix, inclusion-inclusion): that is why some microcracks exhibit zigzag shapes.

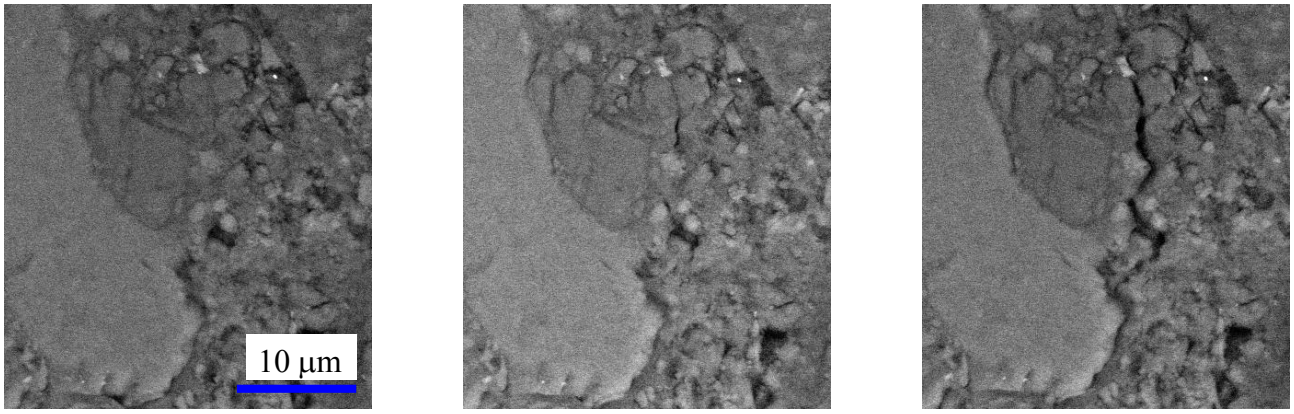

Figure 4.63: Nucleation and propagation of a vertical tensile microcrack in observation zone 1 of test #6.

4.3 Behavior under combined hydric and mechanical loads

In the previous 6 tests, the uniaxial compression is conducted on samples in a constant RH environment. In test #7, the behavior of argillaceous rocks under coupled hydric and mechanical loadings is investigated. The hydric and mechanical loading path is shown in Fig.4.64. For the hydric loading part, the specimen is at fist equilibrated in the ESEM chamber at a dry state of 21%RH as initial state. Then, the specimen is subjected to a two-step humidification: 80%RH and 99%RH. No external mechanical loading is applied on the specimen during the humidification process, which allows a free swelling. Once the specimen is stable for each humidity state, the uniaxial compression test is conducted. A 20 MPa loading-unloading cycle is performed for 21%RH, while a 10 MPa loading-unloading loop is introduced for 80%RH. Since the specimen is generally rigid for dry state, 20 MPa loading allows sufficient deformation for a reliable performance when applying DIC techniques. Nevertheless, 20 MPa is too large for 80%RH where the specimen would suffer from some nonlinear phenomena (plasticity, damage). Therefore, 10 MPa loading is chosen for 80%RH to characterize the elastic behavior of the material, which can be compared with the two other humidity states. For the last humidity state at 99%RH, uniaxial compression is conducted until failure. Three zones with size of 320 $\times$ 276 μm^2 are chosen as ROIs, shown in Fig.4.65 - 4.67.

4.3.1 Hydric behavior under humidification

For the three observation zones, the swelling strains are estimated by DIC at the steady state of each humidification step. Their strain-RH curves are shown in Fig.4.68, as well as their

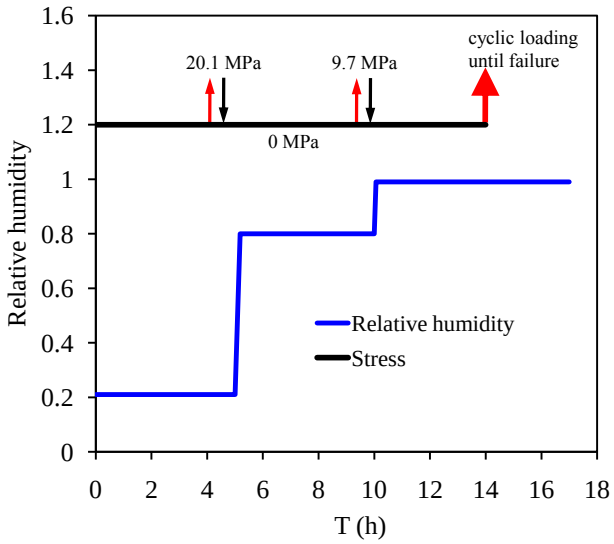

Figure 4.64: Hydric and mechanical loading path in test # 7.

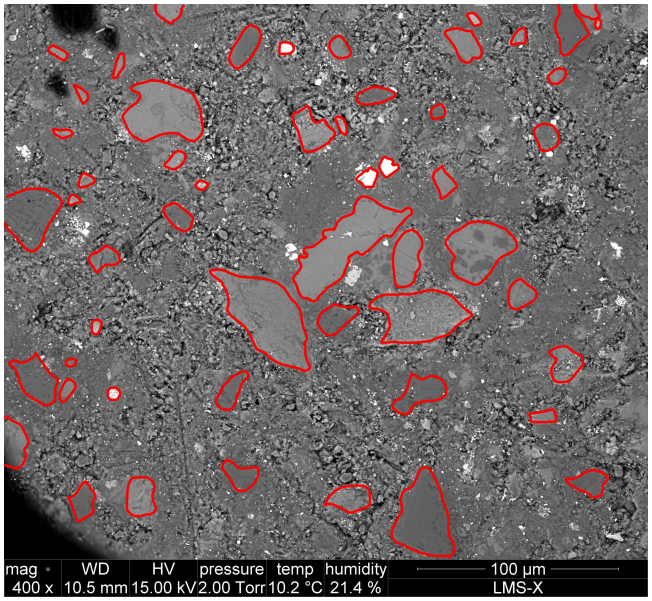

Figure 4.65: BSE image of observation zone 1 in test #7. The gross inclusions are outlined in red curves.

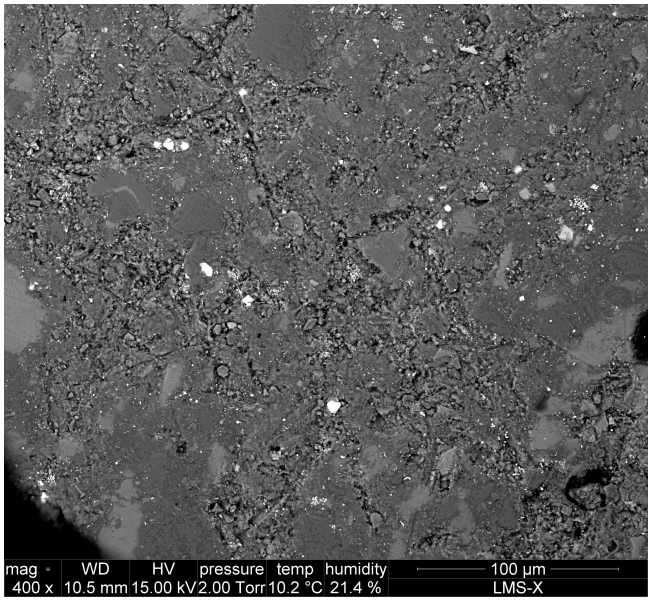

Figure 4.66: BSE image of observation zone 2 in test #7.

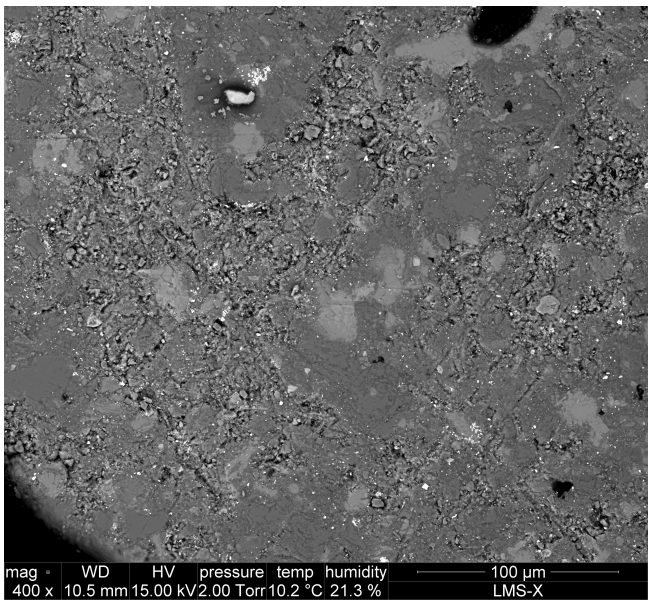

Figure 4.67: BSE image of observation zone 3 in test #7.

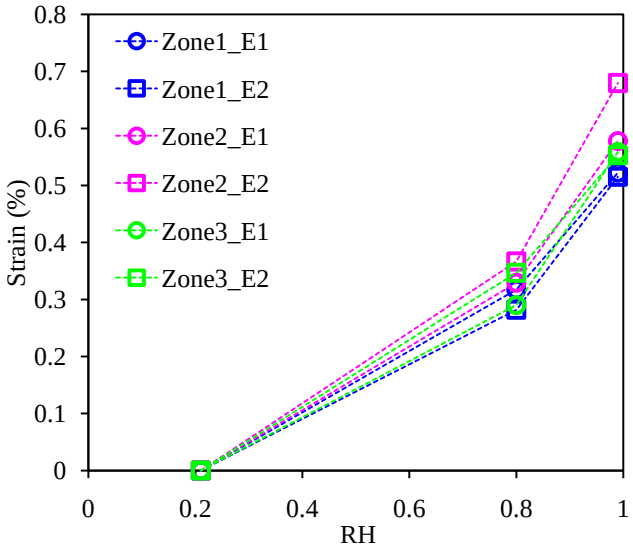

Figure 4.68: Strain-RH curves of three observation zones.

local strain (E2: major principal strain) fields (Fig.4.69 - 4.71). Similar to the observation in chapter 3, some features are observed once more here: heterogeneous swelling field which well correspond to the microstructure, nonlinear swelling at high RH and so on. The mechanisms of these features have been discussed in the previous chapter, and so don't be repeated here. However, some dissimilar phenomena should be emphasized. Firstly, the swelling magnitude in this study is seemly so small: the maximal swelling (zone 2) is merely 0.7% for 21% - 99% RH, which is much less than the results of the preceding chapter. It is reasonable to suspect that the sample is not totally humidified to the prescribed RH value, since the control of thick sample can be a crucial issue for a humidification process in ESEM (see section 4.1). However, the final steady water content 6.6% seems to be somewhat normal for 99%RH. We think the small swelling of the sample is probably because the sample is not yet equilibrated as expected when the mechanical loading begins. In fact, the relative permeability is very small at extremely high RH level (Pham, 2006) so that the moisture transport still operates after 4h, which seems however to be enough for the moderate RH range. The sample still absorbs water during the mechanical loading test. However, it seems to become stable at the end of test, as the final water content looks like normal. Besides the small swelling, no obvious anisotropy of swelling is evidenced in this study, even the observation is conducted on the plane 2 in which an anisotropic swelling is always observed in the preceding results. The explanation of this isotropic swelling is not clear. It might because the sample is not yet equilibrated with respect to humidity state. Besides, the loading machine might also inhibit the swelling in the y direction, so its value is much smaller than that in the case of free swelling in chapter 3.

Broadly, a network of high swelling bands (red and yellow colors) is observed in the strain fields due to humidification, and they enclose some domains with low strains (violet and blue

colors). In fact, such heterogeneous swelling field is well correlated to the composite microstructure of argillaceous rocks: inclusions deform so faintly, whereas their surrounding clay matrix mostly involves in significant swelling. Some negative strain (contraction) is also observed in strain maps, notably in macropore domains. This is essentially a problem of micro-macro porosity interaction: swelling of clay particle can invade the space of neighboring macropores and contraction deformation is consequently found in the latter zone.

As discussed in section 3.2, local E2 direction in the clay matrix can be considered as an indicator of the normal to the orientation of clay particle in this study. This qualitative estimation is essentially based on the anisotropic swelling property of clay particle: the swelling is indeed an increase of inter-layer spacing and inter-particle spacing, so it is predominately in the direction perpendicular to the orientation of clay particle, i.e. along its thickness direction. The high swelling bands in local strain maps own generally 1 - 4 subsets thickness (corresponding to 3 - 12 μm physic size). This is relatively bigger than the typical thickness of a clay particle (dozens or hundreds of nanometers). Therefore, we suggest that high strain bands are rather a set of clay particles with sub-parallel orientations.

It is well known that the presence of inclusions strongly affects the orientation of clay particles: clay platelets tend to drape the inclusions (Hornby et al., 1994). Such influences are more obvious for the grains of quartz than for those of carbonate. This is essentially related to the sedimentation process of argillaceous rocks: clay minerals and grains of quartz sedimentate simultaneously, prior to grains of carbonate invading the macropores. One example is outlined in Fig.4.71: E2 direction is always normal to the inclusion contour. It should be noted that such a predominant swelling normal to the inclusion boundary is not only related to the orientation of clay particles, but also due to the mechanical interaction: the inhibition of inclusion on the free swelling would lead to the local stress normal to its boundary. However, such a mechanical interaction doesn't play a predominant role, compared to the free swelling. For example, considering a 10 MPa local stress (reasonable from the study in chapter 5), the induced mechanical strain is only 10^{-3} (the Young's modulus is chosen as 10 GPa) in elastic context. This is much smaller than the magnitude of free swelling (typically at the order of 10^{-2}). Therefore, the total swelling deformation is predominantly attributable to the free swelling, and the local principal direction (E1) can be considered as a qualitative indicator of the orientation of clay particles.

4.3.2 Mechanical behavior

Once the specimen is equilibrated in the ESEM chamber for each humidity state, uniaxial compression test is conducted to characterize its mechanical behaviors. The specimen is subjected to a moderate loading-unloading cycle for both first humidity states: 20.1 MPa for 21%RH and 9.7 MPa for 80%RH. At 99%RH humidity state, the specimen is subjected to uniaxial

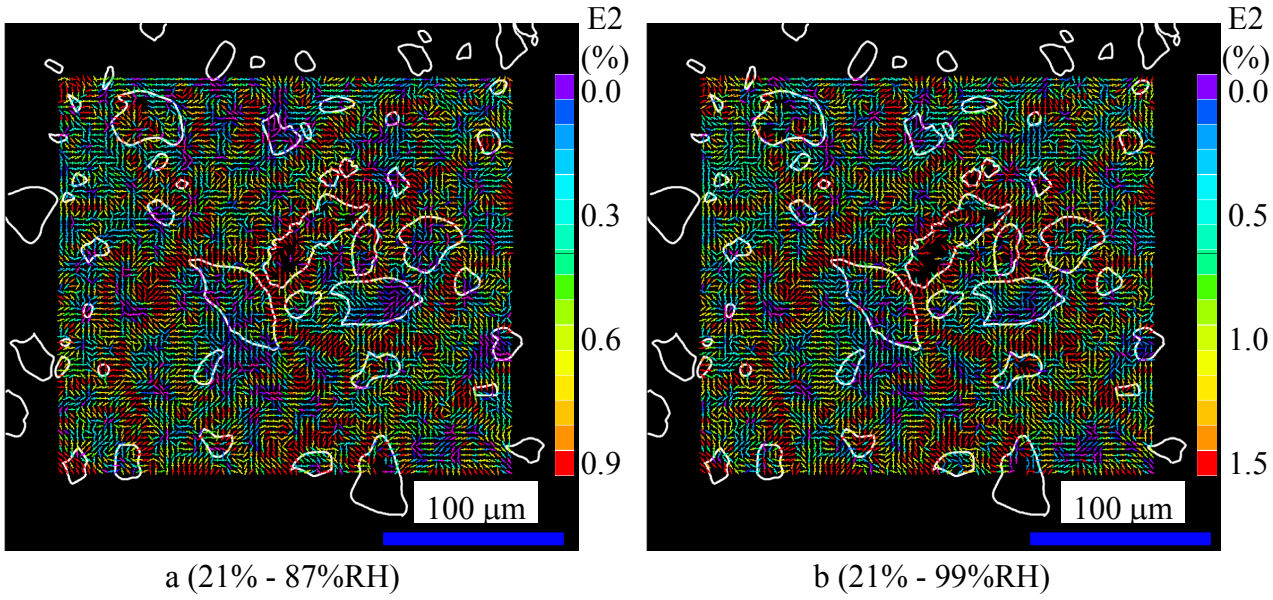

a (21% - 87%RH) b (21% - 99%RH)

Figure 4.69: Strain field of observation zone 1 under hydric loading.

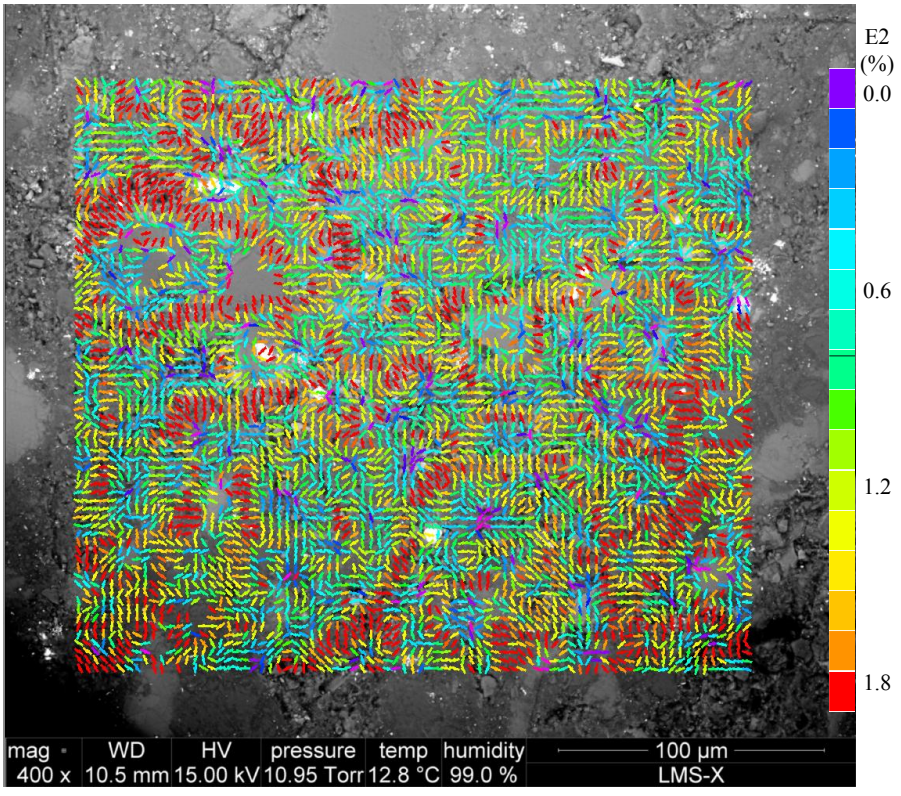

Figure 4.70: Strain field of observation zone 2 under hydric loading (21% - 99%RH).

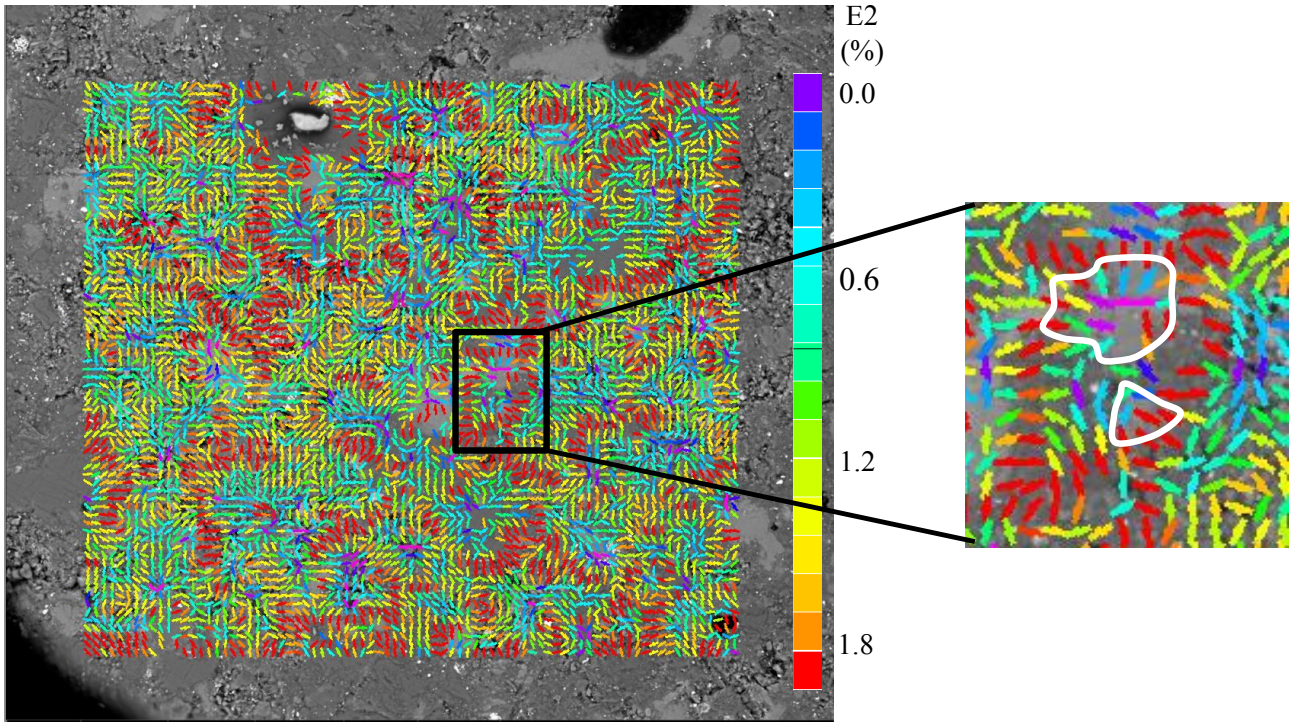

Figure 4.71: Strain field of observation zone 3 under hydric loading (21% - 99%RH).

compression until failure at 23.6 MPa. Moreover, two unloading loops (9, 14 MPa) are introduced to determine its elastic moduli, as well as residual strains. The stress versus normalized displacement (measured by LVDT) is shown in Fig.4.72.

The relationships between stress and overall strains of three observation zones are estimated by DIC techniques and shown in Fig.4.73 - 4.75. For 21%RH state, the stress-strain curve is linear, with a large slope, when the specimen is loaded until 20 MPa. Moreover, such deformation is somewhat reversible: no apparent plastic deformation is observed after unloading stage. For the 80%RH humidity state, the stress-strain curve is less steep than at 21%RH, implying a loss of Young's module at 80%RH. The plastic deformation at 10 MPa is still very small at 80%RH (the biggest of the three observation zones is 0.04%). It is however more evident compared to 20 MPa loading at 21%RH state. When the specimen is humidified to 99%RH, the stress-strain curve reveals some features which are different from the two other drier states:

- The specimen at 99%RH is more deformable than drier states. This is attributable to two terms. First, plastic deformation emerges earlier and is more significant at the 99%RH state: it reaches 0.1% for 9 MPa loading, contrasting with no observable plastic deformation for higher stress level at drier states. Besides, the Young's modulus decreases for high RH (see more gradual unloading loop for higher humidity states).

- An upward concave portion appears at the beginning of stress-strain curve for 99%RH

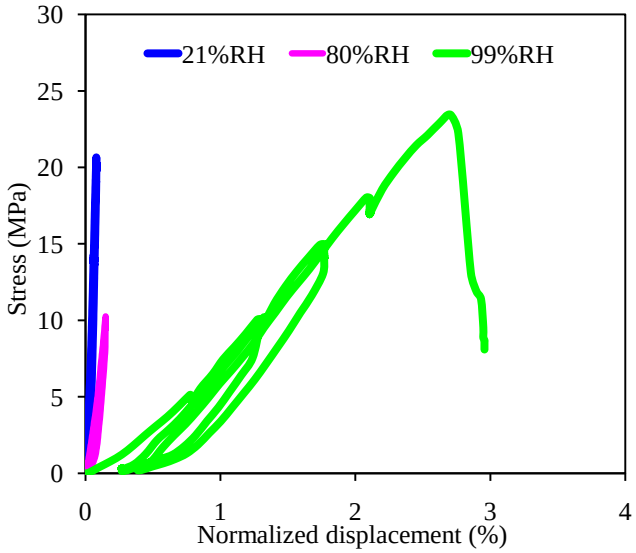

Figure 4.72: Stress-strain curve measured by LVDT in test #7.

humidity state, whereas it doesn't exist for drier states. The two loading steps for 21%RH state reveal a linear relation between stress and strain. For 80%RH state, the existence of an upward concave portion or not is uncertain since only one loading step is conducted. For 99%RH state, the upward concave portion is evidenced in zone 2 and 3, but not in zone 1.

The strain maps of three ROIs for different humidity states are presented in Fig.4.73 - 4.75. In general, local high strains are mostly found in the clay matrix, rather than in the inclusions. It is associated to the contrasting mechanical properties of clay matrix and inclusion. The inclusion owns generally much more stiffness than clay matrix, consequently it deforms more moderately than the latter. Note that certain significant strains are also found in inclusions, notably in some gross grains of carbonate. These grains are indeed a set of sub-grains and they would slide between each other under mechanical loading, which is responsible for the high strains in such inclusions. Concerning the intense deformation, the same deformation mechanisms, as revealed in the previous tests, are recognized: 1) compaction of macropores and closing of pre-existing horizontal microcracks (horizontal band), 2) shear deformation in clay matrix or sliding of inclusion-matrix interfaces (inclined bands); 3) opening of vertical microcracks (vertical bands). Recall that uniaxial compression is vertical.

For 14 MPa stress state, the elastic portion (D-G in Fig.4.75) and plastic portion (G-A in Fig.4.75) for observation zone 3 are calculated and their strain maps are shown in Fig.4.76. Broadly, the strain fields for the two portions are similar, implying that both elastic and plastic deformations probably evolve in the same way. Plastic deformation arises from the clay matrix itself.

The role of humidity state on mechanical behavior

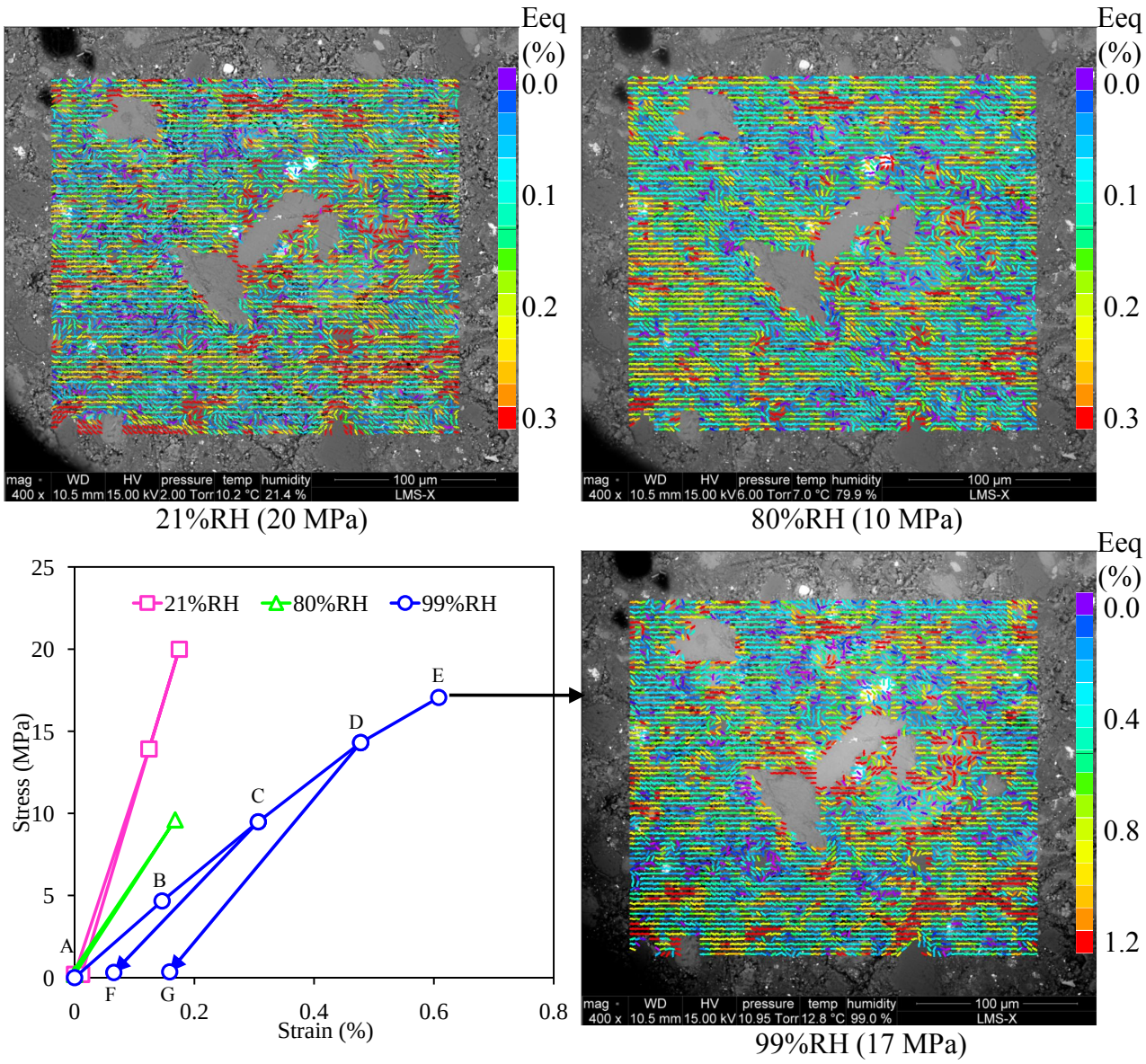

Figure 4.73: Stress-strain curve and strain fields of zone 1 in test #7 measured by DIC.

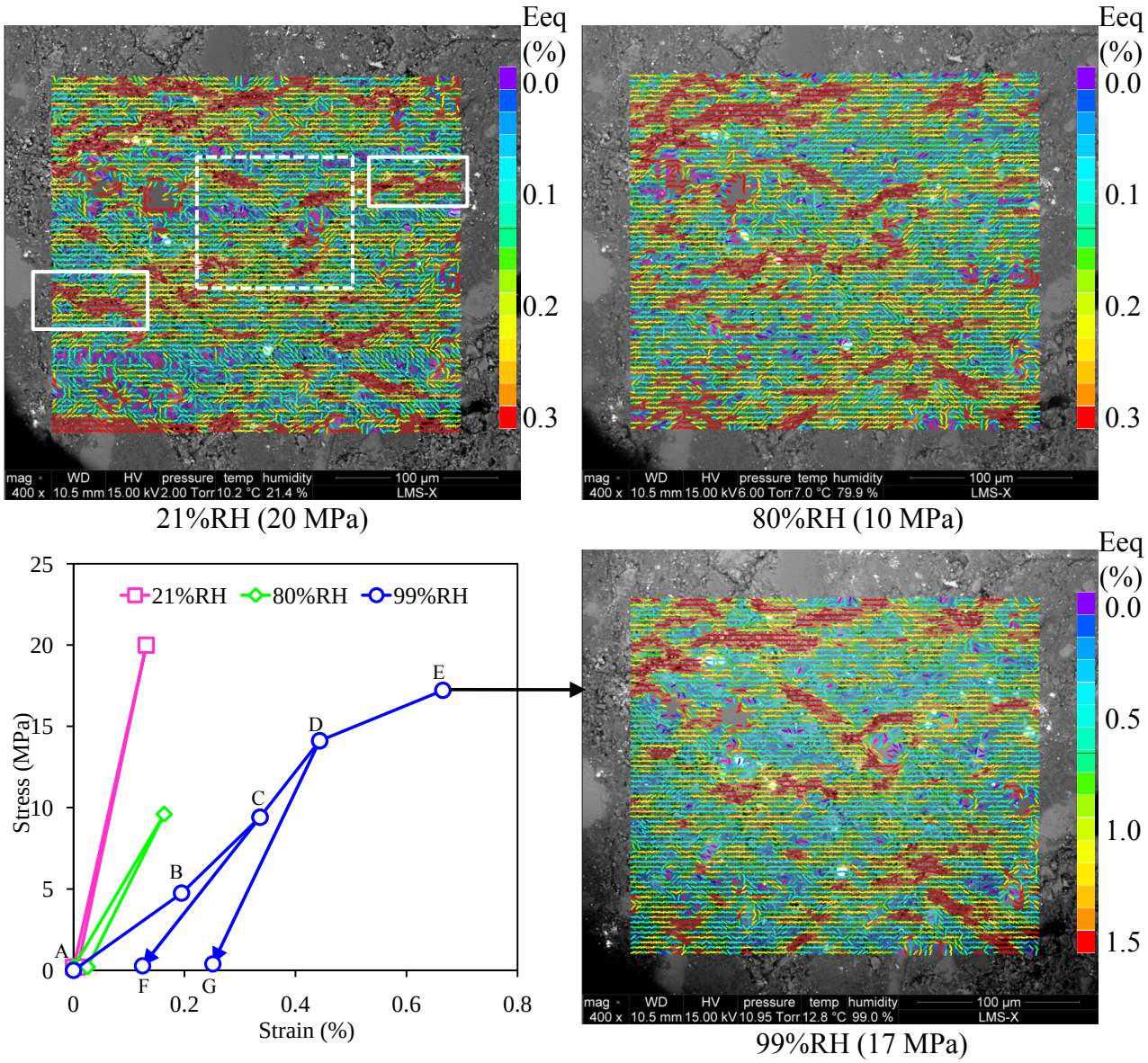

Figure 4.74: Stress-strain curve and strain fields of zone 2 in test #7 measured by DIC. Dashed rectangle would be zoomed on in Fig.4.77.

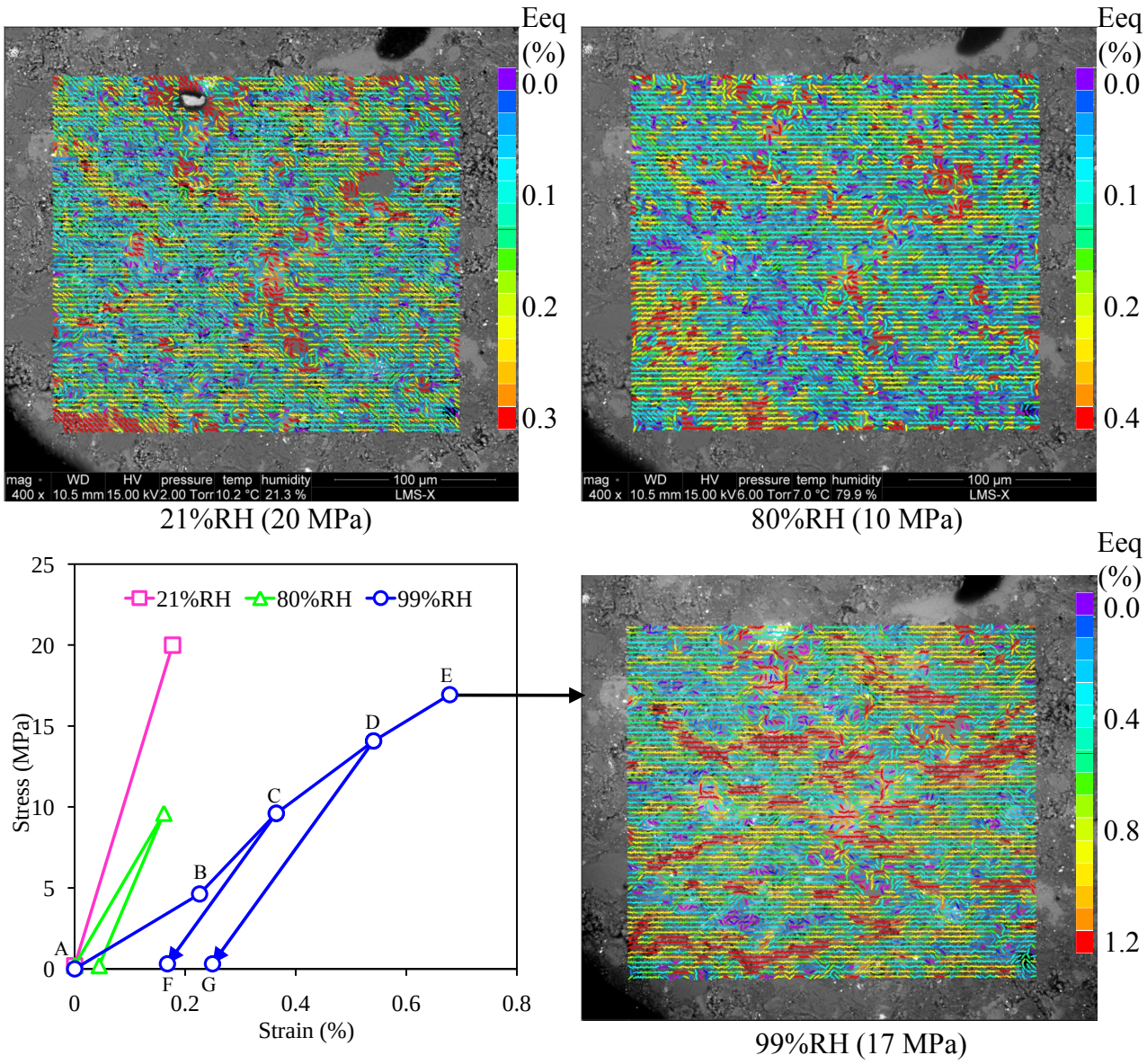

Figure 4.75: Stress-strain curve and strain fields of zone 3 in test #7 measured by DIC.

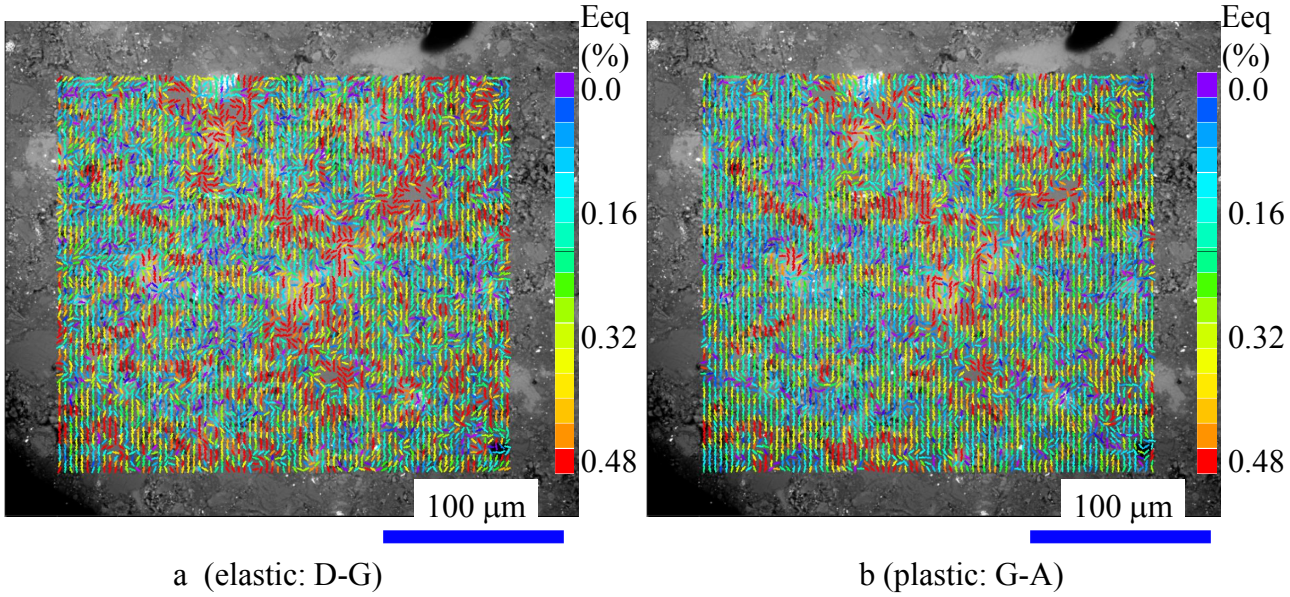

Figure 4.76: Elastic and plastic deformations of zone 3 under 14 MPa loading.

The local strain level corresponding to the same color in strain maps is set to be proportional with the magnitude of overall strain. For example, red color represents 0.3% local strain for an overall strain 0.13% (as the case of 20 MPa loading at 21%RH in zone 2); it would correspond to 1.5% for an overall strain of 0.65%. By means of such scaling representations, the strain fields for different humidity states can be compared, and some features can be characterized:

- The strain fields are somewhat similar for different humidity states. The intense strains are located at the same places.

- In general, the strain field for 21%RH consists of some isolated deformation bands (most are compaction bands). Less numerous but more intense deformation bands, in particular some inclined (shear) bands, are observed in higher RH states. To a better understanding of this phenomenon, it is interesting to emphasize one domain in observation zone 3 (see Fig.4.77). At 21%RH, some isolated deformation bands (one shear band, and three compaction bands) are found in this domain. These isolated bands are linked up into two intersected gross shear bands for 80%RH and 99%RH states. Note that the overall strains for 21%RH and 80%RH are comparable, but the strain maps are dissimilar: the connection of isolated deformation bands still exists in 80%RH. This means that coalescence of deformation bands is essentially related to a changing deformation mechanism because of humidity variation, rather to a simple plastifying process for the same mechanism. Concerning the deformation in junction domains, they involve generally shear deformation. Hence, one can derive that coalescence of deformation bands for high relative humidity, is essentially related to the loss of shear modulus due to humidification. Such loss of

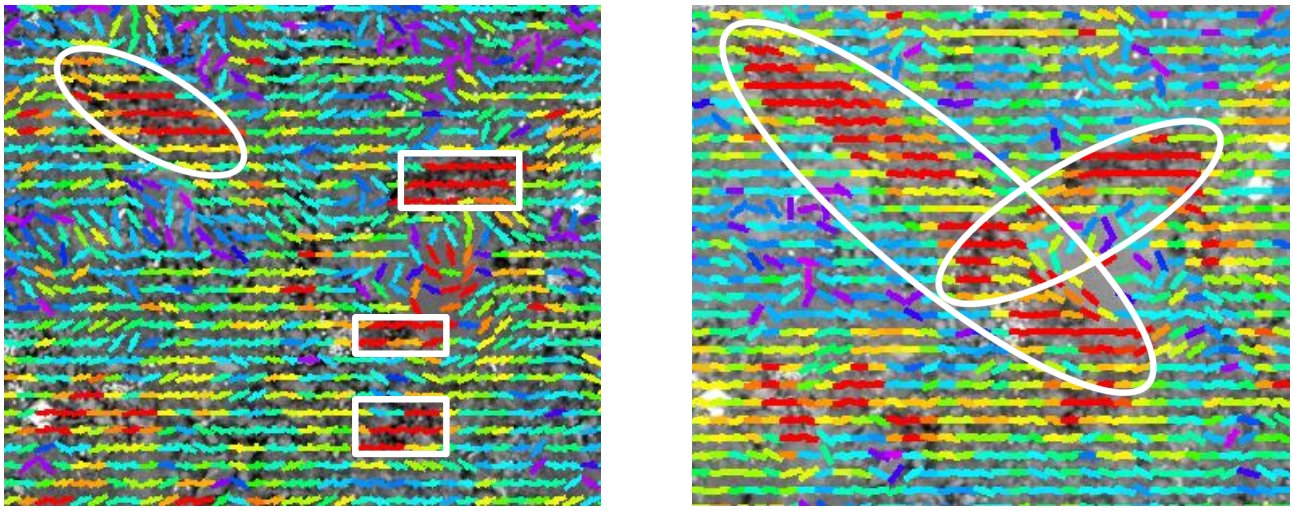

21%RH 99%RH

Figure 4.77: Transition of deformation mechanism for different humidity states (the domain is outlined by dash lines in Fig.4.74).

shear modulus due to humidification can also be proved by the fact that the range of shear bands' orientations varies with RH. For 21%RH state, some inclined (shear) bands already appear with typical orientation close to 60° to the loading direction. Under higher RH, these shear bands extend under uniaxial loading, and their orientation could turn to be further closer to the loading direction: the shear bands orientated at 30° to the loading direction can be found at 99%RH in this study.

- It is worth noting that some compaction bands (see the two solid rectangles in Fig.4.74) that appear for 21%RH disappear gradually at high humidity states. This is essentially related to irreversible compaction of macropores or closing of pre-existing horizontal microcracks. For the first uniaxial loading at drier state, a considerable portion of these compaction bands are not be recoverable after unloading. Therefore, the second mechanical loading at higher RH state would be conducted on a relatively denser texture so that the associated deformation becomes less significant (due to strain stiffening in macropore zone). Note that these local irreversible phenomena are not observable at macro-scale: the overall strain for 21%RH looks elastic. Besides, it is emphasized that such compaction bands are typically located in macropores rich zones owning a somewhat losse texture. Their swelling under humidification (see Fig.4.70) is extremely small, even negative, of which the explanation (micro-macro interaction) has been provided previously.

Correlation between hydric and mechanical behaviors

The strain maps under hydric and mechanical loadings are compared (see Fig.4.78), to

correlate hydric and mechanical behaviors of argillaceous rocks. Broadly, the deformation fields under hydric and mechanical loads are greatly different. However, some features can be obtained. It is shown that shear bands under mechanical loading are also subjected to large swelling under humidification (mostly inclined red bands in strain maps of humidification). It exists some domains with high swelling (mostly horizontal and vertical red bands in strain maps of humidification) don't deform so much under mechanical loading. As discussed before, the swelling maps for humidification can roughly reveal local orientations of clay particles in ROIs: it is generally parallel to the direction of swelling bands, i.e. normal to major strain direction. Referencing such information, one can recognize that no correlating behaviors under hydric and mechanical loadings are related to dissimilar responses of different orientated clay particles: some inclined orientated clay particles are favorable to be deformed under shear stress (greatest at 45° to the uniaxial compression axis), whereas, the others (typical horizontal and vertical orientated ones) is less deformable.

Indeed, clay particle has a 2D lamellar structure composed of several to thousands of layers. Due to its lamellar structure, clay particle is indeed anisotropic not only for its swelling property, but also for the mechanical behavior. As shown in Tab.1.3, the Young's modulus is less important in normal-to-orientation direction e_3 ($E_1 > E_3$), while the sliding between the layers is easier to be activated compared to other shear modes ($G_{13} < G_{12}$). Hence, the response of randomly oriented clay particles is variable even under the same stress condition. For example, the clay particle oriented at 45° to the uniaxial compression axis is favorable for shear deformation: the weakest shear modulus meets with the greatest shear stress.

Note that there are also some domains that don't swell so much during humidification, but exhibit considerable deformation (typical horizontal bands) in the mechanical strain map (at 21%RH). They are generally attributable to compaction of macropores space. However, under humidification, the swelling in these macropore rich domains is not evident. This is essentially related to interaction between micro and macropores: the swelling consists in an increase of interlayer space (micropore) and inter-particle (mesopore). It would invade the space of macropores and the total volume change is consequently moderate.

The specimen's failure in test #7 is observed by optical microscopy, shown in Fig.4.79. A 3D network of faults (both in- and out- plan of observation) is observed. Besides, the secondary fractures due to splitting and spallation are considerable. Note that the density of these secondary fractures is much more intense here than in drier samples of the previous tests.

4.4 Summary of chapter

The hydromechanical behavior of argillaceous rocks is investigated in this chapter by six uniaxial compression tests under different maintained constant humidity states, of which the main macroscopic mechanical properties deduced from the average response of the investigated ROIs

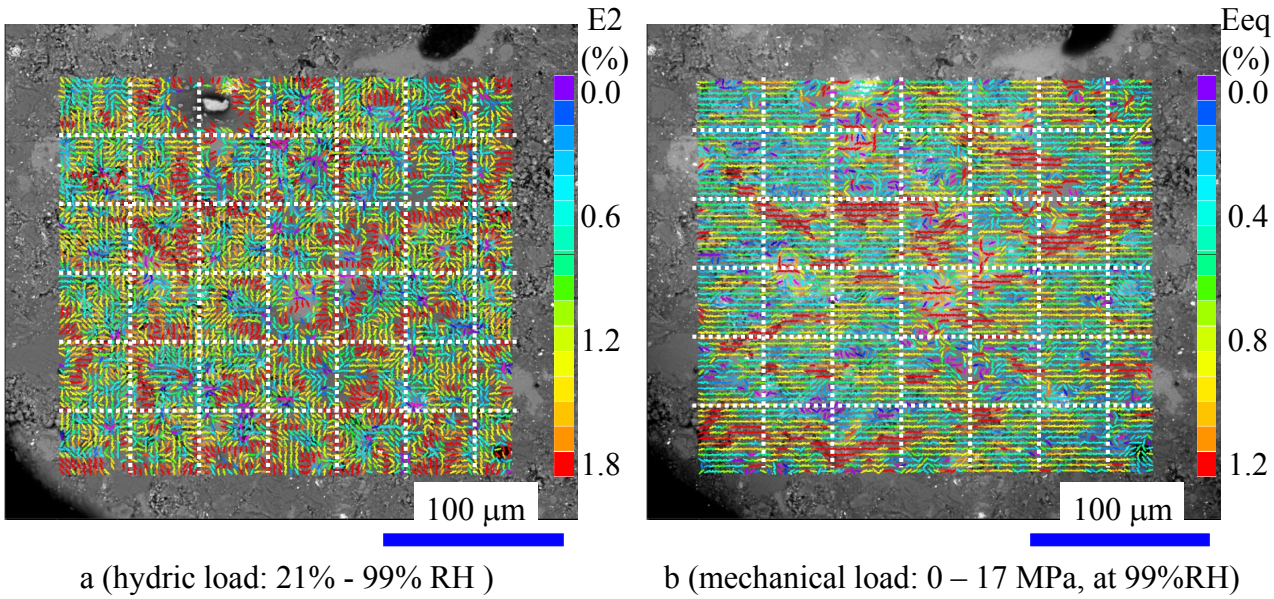

Figure 4.78: Comparing strain maps (zone 3) for hydric and mechanical loadings.

are summarized in Tab.4.2. In general, a heterogeneous strain field has been evidenced at the scale of the inclusion-matrix composite structure of such rocks, which is well correlated to the microstructure: clay matrix generally deforms significantly under mechanical loading, while other mineral inclusions deform faintly. Typically, three deformation bands can be distinguished in strain maps according to their orientation (note uniaxial compression is applied vertically): 1) horizontal bands, which generally involve in compaction of macropore-rich zones and closing of some pre-existing horizontal microcracks; 2) inclined bands consisting of some shear deformation in clay matrix and sliding of inclusion-matrix interfaces; 3) vertical bands, which are principally associated to nucleation and developing of vertical microcracks.

Table 4.2: Summary of the main mechanical behavior of the specimens in different tests.

Test	**W**	**RH**	**Young's modulus**	**Poisson's ratio**	**Peak stress**
	%	%	GPa		MPa
Test #1	2.2	70	5.2 (10 MPa)	0.06	> 38
Test #2	3.1	44	5.4 (7 MPa)	0.1	26.0
Test #3	3.8	44	1.0 (9 MPa)	0.1	23.6
Test #4	5.4	91	3.2 (11 MPa)	0.3	25.7
Test #5	7.4	96	2.7 (15 MPa)	0.08	20.9
Test #6	10.1	99	2.1 (9 MPa)	0.24	16.3

Note: Elastic constants are determined by unloading paths from certain stress levels (given in the bracket after Young's modulus).

These deformation mechanisms are also principally responsible for nonlinear behaviors of

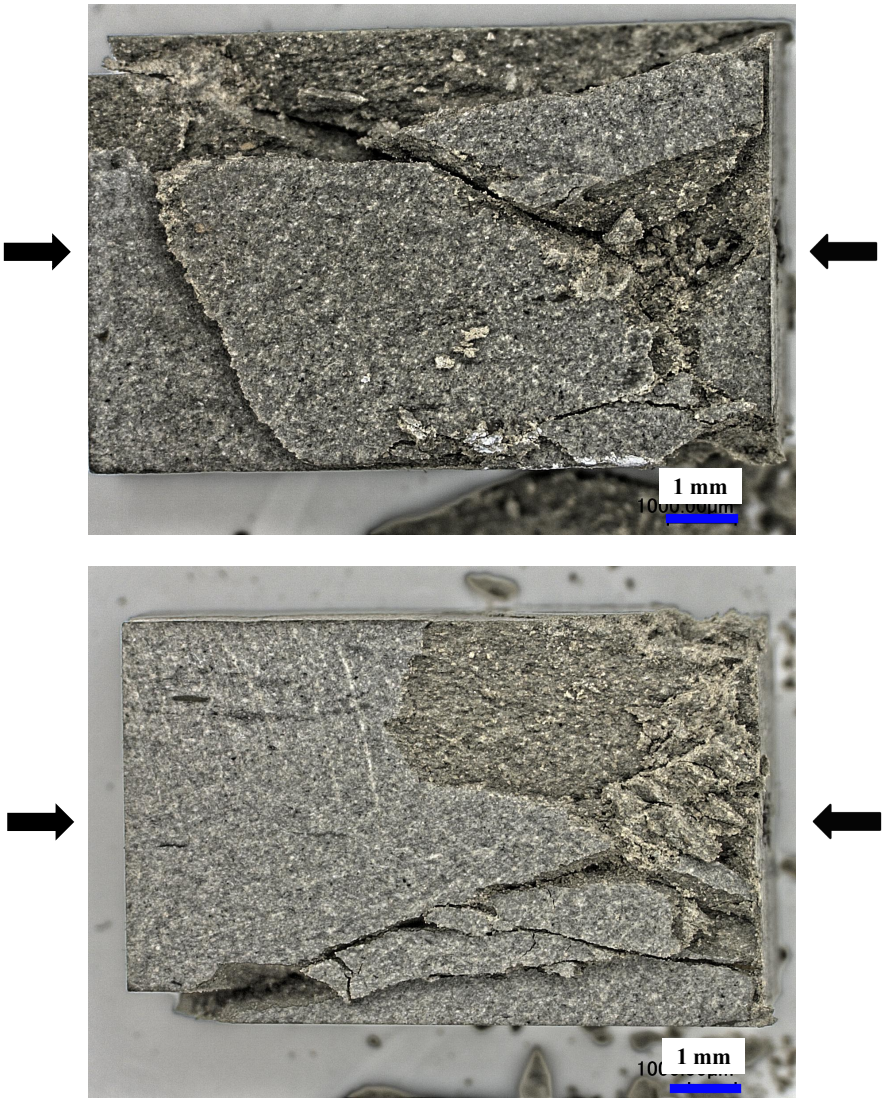

Figure 4.79: Fracture of sample in test #7 observed by optical microscopy. The arrows indicate uniaxial compression direction.

such rocks, such as plasticity and damage. Damage is mostly activated in certain modes: 1) vertical microcracking either in clay matrix, or in coarse inclusions; 2) inclined microcracking mostly consisting of sliding along inclusions' boundaries. Most of vertical microcracks are activated by shear deformation, while the others seem to be tensile microcracks, which prefer to be initiated at the boundary of inclusion. The inclined microcracking has been shown to strongly depend on the form and orientation of inclusions. In general, an elongated inclusion with orientation approaching to the maximal shear stress is a favorable place for the activation of sliding.

The sample in the tests may be pre-damaged. Under uniaxial compression, the behavior of pre-existing microcracks is strongly associated to their orientation: horizontal microcracks

would close under small compression, inclined ones may slip, and vertical pre-existing microcracks could grow further. Note that the behavior of horizontal pre-existing microcracks is similar to macropore-rich zones. Typically, a bi-staged stress-strain relationship has been found for these zones: 1) a strain-stiffening stage at the beginning, consisting of a densification effect due to compaction of macropores or closing of pre-existing cracks; 2) a subsequent strain-softening stage, involving in some nonlinear phenomena such as plasticity and new damage. The strain-stiffening of macropores and pre-existing microcracks, is responsible for the concave upward portion usually appearing at the beginning of the stress-strain curve of such rocks. For pre-existing microcracks, its inflexion point (transition from strain-stiffening to strain-softening) is extremely low. This is different from macropore-rich zone in which the strain-stiffening part can cover a wide stress range.

Since uniaxial compression tests are conducted on different humidity states, the influence of humidity state on mechanical behavior of argillaceous rocks can also be discussed. A comparison between a extreme dry case (test #1) and a extreme wet one (test #6) is shown in Fig.4.80. In general, the stress-strain curve of such rocks becomes softer for wetter sample. This is related to not only a loss of elastic modulus with RH, but also plastic deformation appearing earlier and more greatly under more humid state. Besides, the initial concave upward portion of stress-strain curve, usually found for humid samples, would disappear for extremely dry samples. This is essentially associated to the reduction of macropores and pre-existing microcracks under low RH states. The peak stress for humid samples is generally lower than that for dry samples. Moreover, microcracking is more intense before failure for wet samples. Concerning local strain maps, both compaction and shear bands appear whatever the humidity state. It is emphasized that some shear bands have been observed even at extremely dry state, but they are somewhat reversible. At wet state, shear bands become more diffuse compared to those at dry state. Sliding along the inclusion boundaries seems to be activated more easily at wet state. This may be related not only to a decrease of effective stress, but also to a loss of the cohesion of inclusion-matrix interface. Besides, more vertical bands are observed at wet state, which are related to opening of some pre-existing microcracks parallel to the loading direction. In fact, these pre-existing microcracks are essentially related to damage phenomena due to humidification.

The influence of humidity state has been further studied on one sample which undergoes combined hydric and mechanical loadings (test #7). When the sample is humidified, a transition of several isolated compaction bands to an assembly of them connected by shear bands has been evidenced in strain maps, which implies that humidification weakens the shear modulus of clay matrix. Moreover, test #7 also reveals some consistencies between the deformation under hydric loading and that under mechanical loading, which is essentially related to the microstructure of material. Actually, the clay particles, owning different orientations which can be revealed by the swelling map under humidification, have been shown to deform dissimilarly under uniaxial compression: shear bands are mostly found on clay particles with inclined ori-

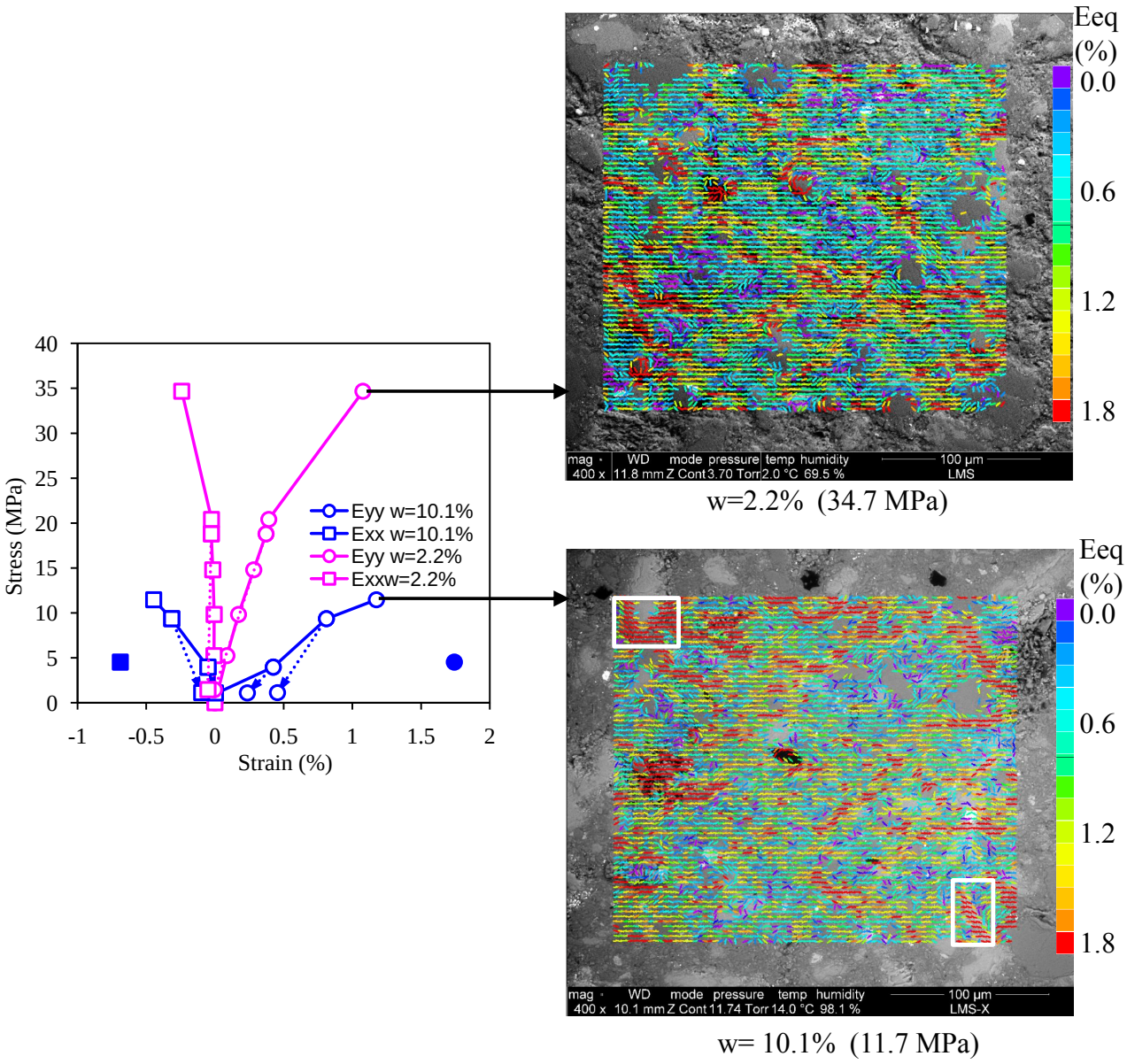

Figure 4.80: Influence of water content on mechanical behavior of argillaceous rocks. Two examples of sliding along the inclusion boundaries are outlined.

entation, whereas, those orientating horizontally and vertically don't deform so much. This reveals the anisotropic behavior of clay particles. It should be noted that the mechanical inclusion-matrix interaction also plays a crucial role.

Bibliography

Bésuelle P., 2001, Compacting and dilating shear bands in porous rock: Theoretical and experimental conditions. Journal of Geophysical Research 106, 13435-13442.

Bornert, M., Valès, F., Gharbi, H., Nguyen Minh, D., 2010. Multiscale full-field strain measurements for micromechanical investigations of the hydromechanical behaviour of clayey rocks. Strain 46, 33-46.

Djéran-Maigre, I., Tessier, D., Grunberger, D., Velde, B., Vasseur, G., 1998. Evolution of microstructures and macroscopic properties of some clays during experimental compaction. Marine and Petroleum Geology 15, 109-128.

Hornby, B.E., Schwartz, L.M., Hudson, J.A., 1994. Anisotropic effective-medium o the elastic properties of shales. Geophysics 59(10), 1570-1583.

Lenoir N., Bornert M., Desrues J., Bésuelle P., Viggiani G., 2007, Volumetric digital image correlation applied to X-ray microtomography images from triaxial compression tests on argillaceous rock, Strain, Vol. 43, pp. 193-205.

Moore, D.E., Lockner, D.A., 1995. The role of microcracking in shear-fracture propagation in granite. Journal of Strucrural Geology 17 (1), 95-114.

Pham, Q.T., 2006. Effets de la désaturation et de la resaturation sur l'argilite dans les ouvrages souterrains. Ecole Polytechnique, p.175.

Rudnicki, J.W., 2002. Conditions for compaction and shear bands in a transversely isotropic material. International Journal of Solids and Structures 39, 3741-3756.

Rudnicki, J.W., Rice, J.R., 1975. Conditions for the localization of deformation in pressure-sensitive dilatant materials. Journal of the Mechanics and Physics of Solids 23, 371-394.

Tang, C.A., Liu, H., Lee, P.K.K., Tsui, Y., Tham, L.G., 2000. Numerical studies of the influence of microstructure on rock failure in uniaxial compression - Part I: effect of heterogeneity. International Journal of Rock Mechanics and Mining Sciences 37, 555-569.

Valès, F., 2008. Modes de déformation et d'endommagement de roches argileuses profondes sous sollicitations hydro-mécaniques. Ecole Polytechnique, Palaiseau.

Chapter 5

Modeling of inclusion-matrix interaction under hydric load

Contents

The experimental observation in the previous two chapters has revealed the crucial role of inclusion-matrix interactions for the behavior of argillaceous rocks under both hydric and mechanical loadings. These interactions are believed to be strongly responsible for damage phenomena under hydric loading (both humidification and desiccation cases), which has evidenced not only in our study but also in the others. Microcrackings under hydric loadings are essentially associated to the specific swelling/shrinking properties of clay minerals, and different types of restraint. The restraint can generally be distinguished by two groups: external restraint and internal restraint. External restraint is related to external mechanical loading and substrate-restraint effect. Actually, internal restraint also consists of two terms: 1) inclusion-matrix interaction, 2) self-restraint. Argillaceous rocks are a heterogeneous material, essentially made of a continuous clay matrix scattered by other mineral inclusions (mostly carbonate and quartz). Under humidification (desiccation), the water-sensitive clay matrix trends to swell (shrink) due to its specific physic-chemical properties, however, it would be inhibited by the no-swelling (shrinking) inclusions. Such inclusion-matrix interaction results in local stress in the specimen. The magnitude of stress induced by this mechanism is controlled by the swelling capacity of clay matrix, the morphology, and the mechanical properties of inclusions and matrix (Bisschop et al., 2002; Mihai and Jefferson, 2011). Secondly, a moisture gradient develops inside the specimen during humidification (desiccation) process which results in non-uniform swelling (shrinking). This is commonly called self-restraint, which is also contributable to internal stress field, resulting in potential cracking (Jagla, 2002; Jenkins, 2005, 2009; Timm et al., 2003). Such moisture gradient induced stress is maximal at the beginning of humidification (desiccation) process, and vanishes gradually when moisture transport goes on. The self-restraint is governed by specimen's dimension, as well as hydric loading rate.

In this chapter, the internal restraint (without external restraint) of argillaceous rocks under humidification (desiccation) is investigated. Argillaceous rocks are considered as a matrix-inclusion composite, while clay matrix would swell (shrink) freely (without mechanical stress) when relative humidity varies. This chapter is composed of three parts. The first part addresses the mathematical formulation of internal restraints. The local governing equation of argillaceous rocks under humidification/desiccation is derived, as well as a simplified model of humidification (desiccation) process which is necessary for the study of self-restraint. The secondary part is focused on the internal stress field generated by the two terms of internal restraint. Concerning inclusion-matrix interaction, different cases are considered: one inclusion in infinite swelling matrix, the influence of neighboring inclusions, and the effect of free surface. Besides, moisture gradient induced stress during transient stage is also studied. The third part addresses the overall deformation of argillaceous rock under hydric loading, due to a free swelling of clay matrix. A micromechanical modeling based on classic Eshelby's problem is conducted. Besides, the modelings by finite element method, based on periodic microstructure as well as real microstructure, are also performed.

5.1 Behavior under humidification/desiccation

5.1.1 Governing equations under hydric load

As revealed by the previous chapters, the behavior of argillaceous rocks under humidification/desiccation is indeed a coupled problem of physical-chemistry and mechanics. Firstly, clay mineral would undergo a changing of volume due to RH variation. This type of deformation is indeed a physic-chemical response, can be considered as a free strain in the context of mechanics. Secondary, the presence of non-swelling mineral inclusions would inhibit the swelling/shrinking of clay matrix and consequently produces a mechanical stress field inside the rocks.

Three mechanisms of deformation and damage of argillaceous rocks under hydric loads can be distinguished:

- Swelling-shrinking of clay mineral as a function of the chemical potential of water (i.e. RH).
- Mechanical stress induced by inclusion-matrix interaction.
- Stress generated during transient moisture transport process, during which local humidity states are heterogeneous so that incompatible swelling or shrinking strains are generated.

Based on the above considerations, the equations governing local behavior of argillaceous rocks may reasonably be written in the following simple hydric-elastic form:

$$\underline{\underline{\sigma}}(\underline{x}) = \underline{\underline{\underline{\underline{C}}}}(\underline{x}) : \left(\underline{\underline{\varepsilon}}(\underline{x}) - \underline{\underline{\varepsilon}}^{F}(\underline{x})\right) \tag{5.1}$$

where $\underline{\underline{\sigma}}(\underline{x})$ and $\underline{\underline{\varepsilon}}(\underline{x})$ are the local stress and strain at position $\underline{x}$, respectively. The mechanical interactions are governed by the heterogeneous tensor of elastic stiffness $\underline{\underline{\underline{\underline{C}}}}(\underline{x})$, and the incompatibility of free strains $\underline{\underline{\varepsilon}}^{F}$ because of the two last mechanisms mentioned above.

Argillaceous rocks are multi-scale heterogeneous materials. Generally, it can be considered as inclusion-matrix composite which results in inter-phase heterogeneity, nevertheless, intra-phase heterogeneity exists as well. For example, there are various clay groups (smectite, illite and kaolinite) and distributed clay particle orientation in clay matrix. Since this study concerns inclusion-matrix interaction, intra-phase heterogeneity is neglected here. Therefore, the local tensor of elastic stiffness can be written as:

$$\underline{\underline{\underline{\underline{C}}}}(\underline{x}) = \begin{cases} \underline{\underline{\underline{\underline{C}}}}^{M} & \text{in clay matrix} \\ \underline{\underline{\underline{\underline{C}}}}^{I} & \text{in inclusion} \end{cases} \tag{5.2}$$

Similarly, the local free strain can be written as:

$$\underline{\underline{\varepsilon}}^F(\underline{x}) = \begin{cases} \underline{\underline{\varepsilon}}^h & \text{in clay matrix} \\ 0 & \text{in inclusion} \end{cases} \tag{5.3}$$

Equation 5.3 indicates that local free strain is merely found in clay matrix associated to its physic-chemical swelling $\underline{\underline{\varepsilon}}^h$. Swelling mechanisms are intensively discussed in section 1.3. In general, swelling of clay matrix can be considered as a function of relative humidity, which can be written as:

$$\frac{d\varepsilon^h}{dh_r} = H \tag{5.4}$$

where h_r is the relative humidity. H is swelling coefficient of clay matrix, which is a parameter describing the swelling capacity of clay minerals. It is worth to note that ε^h - RH relationship is actually nonlinear so as H is RH-dependent: it is small at low RH, whereas it becomes significant at high RH (the threshold is around 80%RH for Callovo-Oxfordian argillaceous rocks). Since clay particle swells predominantly in the direction normally to its orientation, H is also anisotropic: swelling is generally more significant in the direction perpendicular to the stratification which is consistent with the preferred orientation of clay particle. Nevertheless, H is assumed to be constant and isotropic for simplicity in this study.

5.1.2 Moisture transport model during humidification/desiccation

The humidification (desiccation) of porous medium consists in bi-phases movement: vapor diffusion which obeys Fick's law, as well as liquid water transport which can be described by Darcy's law. Moreover, phase transition (condensation or evaporation) occurs simultaneously in pours medium due to capillary effect. Broadly, humidification (desiccation) process is generally achieved by two mechanisms (detailed discussion in section 1.4): 1) one process of vapor diffusion followed by a water condensation (evaporation) inside the specimen, 2) one process of liquid water transportation from (towards) the boundary of specimen where vapor condensates (water evaporates). For argillaceous rocks (intrinsic permeability $K < 10^{-19}$), the moisture transport in such weakly permeable materials is conducted mainly in its liquid form, that to say the second mechanism (see the discussion in detail in section 1.4). That means that the effect of the vapor diffusion and the condensation within the sample can be ignored. For such case, a simplified diffusion equation can be used to govern the humidification process:

$$\phi \frac{\partial S_l}{\partial t} + div\left(D_l grad S_l\right) = 0 \tag{5.5}$$

with,

$$D_l = P_c'\left(S_l\right) K_l = P_c'\left(S_l\right) \frac{K k_{rl}\left(S_l\right)}{\eta_l}$$

where ϕ, η_l denote respectively porosity and dynamic viscosity of water. K is intrinsic permeability of porous medium independent of saturation, while k_{rl} is relative permeability which is a function of saturation of porous medium. For Callovo-Oxfordian argillaceous rocks, it is expressed by the formula proposed by Bovet et al. (1995):

$$K_{rl} = (S_l)^n \tag{5.6}$$

where $n = 3$ for the saturation case, while $n = 3.5$ for the desaturation case.

Recall capillary pressure P_c is defined as the difference between gas pressure and water pressure ($P_c = P_g - P_w$). The relation between capillary pressure and degree of saturation is described by isothermal water retention curve. Based on laboratory experimental data, a representative approximation based on Vauclin-Vachaud relation has been chosen for the isothermal water retention curve of Callovo-Oxfordian argillaceous rocks (ANDRA, 2005):

$$S_l = \frac{100a}{a + (100P_c)^b} \tag{5.7}$$

where $a = 2842$, $b = 0.906$ when P_c is expressed in MPa, and S_l varies between 0 and 1.

Supposed gas pressure remains constantly equal to the atmosphere pressure (P_{atm}), capillary pressure can be linked to relative humidity by the famous Kelvin's law:

$$\rho_l \frac{RT}{M_v} \ln(h_r) = P_c \tag{5.8}$$

where M_v, R, T respectively stand for molar mass of water, ideal gas constant, and temperature. ρ_l is mass density of water.

Finally, the parameters describing specimen's humidity state (RH, P_c, S_l) is linked. If one parameter is known, the two others can be evaluated by Kelvin's law and isothermal water retention curve.

In the following, a humidification with 10%RH increase (80% - 90%RH) is considered. The investigation of internal stress field is conducted in the context of elasticity. Hence, the stress field for the case of desiccation is identical if only the sign has to been changed. The swelling coefficient of clay matrix is chosen as $10^{-2}/(100\%\text{RH})$, which is order compatible with experimental data in chapter 3. For simplicity, the swelling of clay matrix is supposed to be isotropic. The matrix and inclusion are considered as homogeneous isotropic elastic materials, of which the mechanical constants are chosen from data collected by ANDRA and listed in Tab.5.1.

Table 5.1: Reference values for the key parameter of Callovo-Oxfordian argillaceous rocks.

Notation	Parameter	Value
E_m	Young's modulus of matrix	10 GPa
ν_m	Poisson's ratio of matrix	0.2
E_i	Young's modulus of inclusion	80 GPa
ν_i	Poisson's ratio of inclusion	0.2
H	Swelling coefficient of clay matrix	10^{-2}/(100%RH)
K	Intrinsic permeability	10^{-20} m^2
η_l	Dynamic viscosity of water	10^{-3} Pa.s
ρ_l	Volumetric mass of water	1000 kg.m^{-3}
M	Molar mass of vapor	$1.8\times10^{-}2$ kg.mol^{-1}
R	Ideal gas constant	8.31 J.K^{-1}.mol^{-1}
T	Temperature	293.8 K

5.2 Internal stress field under humidification/desiccation

5.2.1 A circular inclusion embedded in an infinite matrix with free swelling

5.2.1.1 Analytical solution

Consider an elastic cylinder (inclusion) embedded in an infinite homogeneous isotropic elastic medium (clay matrix) which undergoes a uniform isotropic free swelling. It is assumed that the thickness of inclusion and matrix in the z-direction is much smaller than in-plane dimensions, hence plane stress condition manifests itself (Fig.5.1). The cylindrical coordinates are used here. Due to symmetry and plane stress condition, all stress and strain components are only r-dependent; therefore, the governing equations are:

1) Equilibrium equation:

$$\frac{d\sigma_{rr}}{dr} + \frac{\sigma_{rr} - \sigma_{\theta\theta}}{r} = 0 \tag{5.9}$$

where σ_{rr}, $\sigma_{\theta\theta}$ denote radial stress and tangential stress respectively, while r denotes radial coordinate.

2) Strain-displacement relation:

$$\varepsilon_{rr} = \frac{du}{dr}, \quad \varepsilon_{\theta\theta} = \frac{u}{r} \tag{5.10}$$

where ε_{rr}, $\varepsilon_{\theta\theta}$ denote radial strain and tangential strain, while u is radical displacement only depending on r.

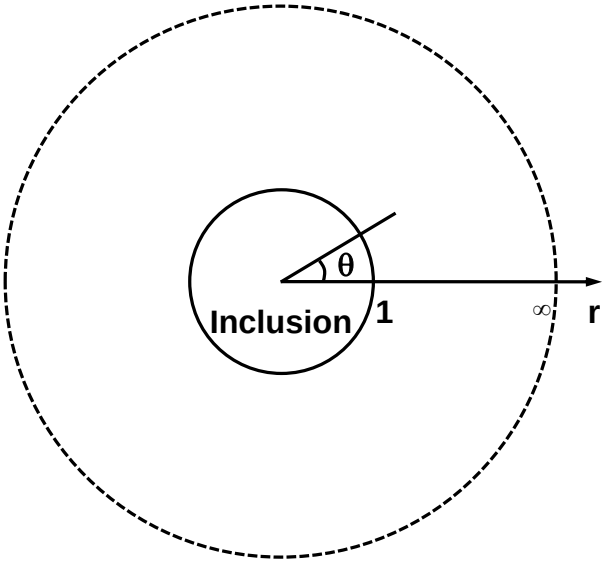

Figure 5.1: Schema of an inclusion in an infinite matrix.

3) Constitutive equation

For the inclusion:

$$\begin{aligned}\varepsilon_{rr} &= \frac{1}{E_i}\left(\sigma_{rr} - \nu_i\sigma_{\theta\theta}\right)\\ \varepsilon_{\theta\theta} &= \frac{1}{E_i}\left(\sigma_{\theta\theta} - \nu_i\sigma_{rr}\right)\\ \varepsilon_{zz} &= \frac{-\nu_i}{E_i}\left(\sigma_{\theta\theta} + \sigma_{rr}\right)\end{aligned} \tag{5.11}$$

For the matrix with free deformation:

$$\begin{aligned}\varepsilon_{rr} &= \frac{1}{E_m}\left(\sigma_{rr} - \nu_m\sigma_{\theta\theta}\right) + \varepsilon^h\\ \varepsilon_{\theta\theta} &= \frac{1}{E_m}\left(\sigma_{\theta\theta} - \nu_m\sigma_{rr}\right) + \varepsilon^h\\ \varepsilon_{zz} &= \frac{-\nu_m}{E_m}\left(\sigma_{\theta\theta} + \sigma_{rr}\right) + \varepsilon^h\end{aligned} \tag{5.12}$$

where E, ν denote Young's modulus and Poisson's ratio respectively, and the subscripts i and m represent inclusion and matrix. Note that the constitutive equations are based on the hypothesis of plane stress condition: vertical stress would be null ($\sigma_{zz} = 0$).

The combination of above equations gives:

$$\frac{d^2u}{dr^2} + \frac{1}{r}\frac{du}{dr} - \frac{u}{r^2} = 0 \tag{5.13}$$

Note it is valid not only for the inclusion, but also for the matrix. Its general solution is:

$$u = Ar + \frac{B}{r} \tag{5.14}$$

where A and B are two constants which can be determined by boundary conditions. For inclusion, $B = 0$ as $u(0) = 0$ due to symmetry. Therefore, the strain and stress are uniform in the inclusion, which can be expressed as:

$$\begin{aligned} \varepsilon_{rr} &= \varepsilon_{\theta\theta} = A_i \\ \sigma_{rr} &= \frac{E_i}{1-\nu_i} A_i \end{aligned} \tag{5.15}$$

The strain and stress in the matrix,

$$\begin{aligned} \varepsilon_{rr} = A_m - \frac{B_m}{r^2}, \quad \varepsilon_{\theta\theta} = A_m + \frac{B_m}{r^2} \\ \frac{1-{\nu_m}^2}{E_m}\sigma_{rr} = (1+\nu_m)\left(A_m - \varepsilon^h\right) - (1-\nu_m)\frac{B_m}{r^2} \end{aligned} \tag{5.16}$$

Since the stress at infinity should be null $\sigma_{rr}(\infty) = 0$, then

$$A_m = \varepsilon^h$$

Considering the displacement at inclusion-matrix interface is continuous, we derive

$$A_i = \varepsilon^h + \frac{B_m}{R^2}$$

B_m can be determined by the continuity of normal stress at inclusion-matrix interface:

$$B_m = \frac{-R^2\varepsilon^h}{1 + (1-\nu_i)E_m/(1+\nu_m)E_i}$$

Finally, the uniform stress in the inclusion is:

$$\sigma_{rr}(R) = \frac{\varepsilon^h}{(1-\nu_i)\,E_i + (1+\nu_m)/E_m} \tag{5.17}$$

The strain and stress distributions, plotted in Fig.5.2, reveal that the presence of non-swelling inclusion leads to a uniform hydrostatic tension in the inclusion (7.7 MPa). The stress in the matrix is maximal at the interface: it is tensile radially and compressive in tangential direction. Their values decrease in order of r^{-2} with distance from the interface. For the strain, it is homogeneous in the inclusion and equal to 0.08×10^{-3}. The radial strain of matrix at inclusion's boundary is 2.3×10^{-3}, which is more important than the free deformation (1×10^{-3}).

For a better understanding, inclusion-matrix interaction can be considered with the help of a set of imaginary cutting, straining and welding operation, shown in Fig.5.3. In initial state, the inclusion (circle) and matrix (circular ring) well adhere with each other. Secondary, cut around the inclusion and remove it from the matrix. Allow a non constraint swelling of the matrix to take place. Note that such swelling results in an increase of the inner diameter of the circular ring. Finally, put the inclusion back in the matrix and rejoin it across the cut. The adhesion of

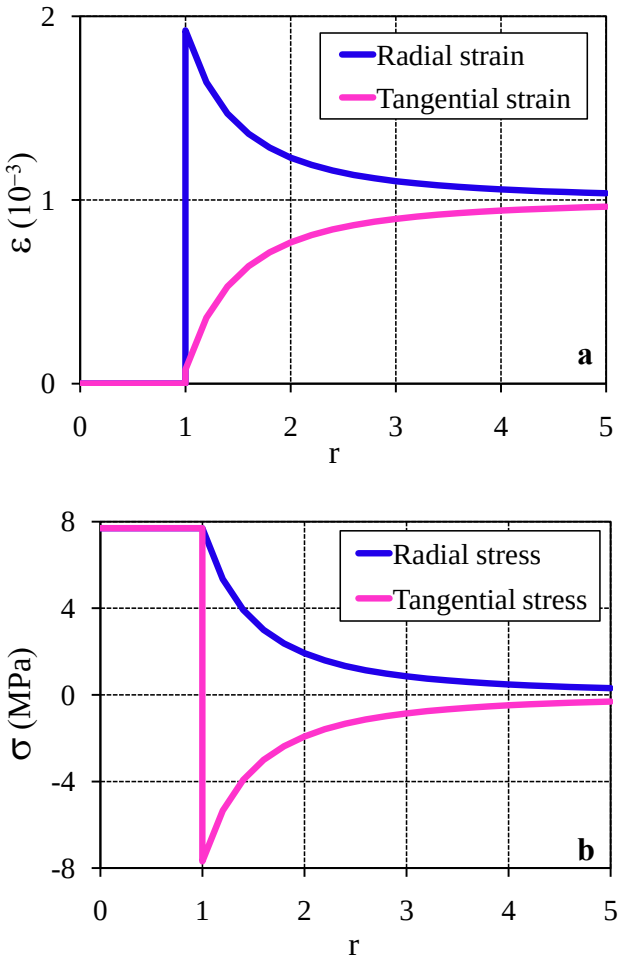

Figure 5.2: Local strain (a) and stress (b) due to matrix's swelling (inclusion's radius is 1).

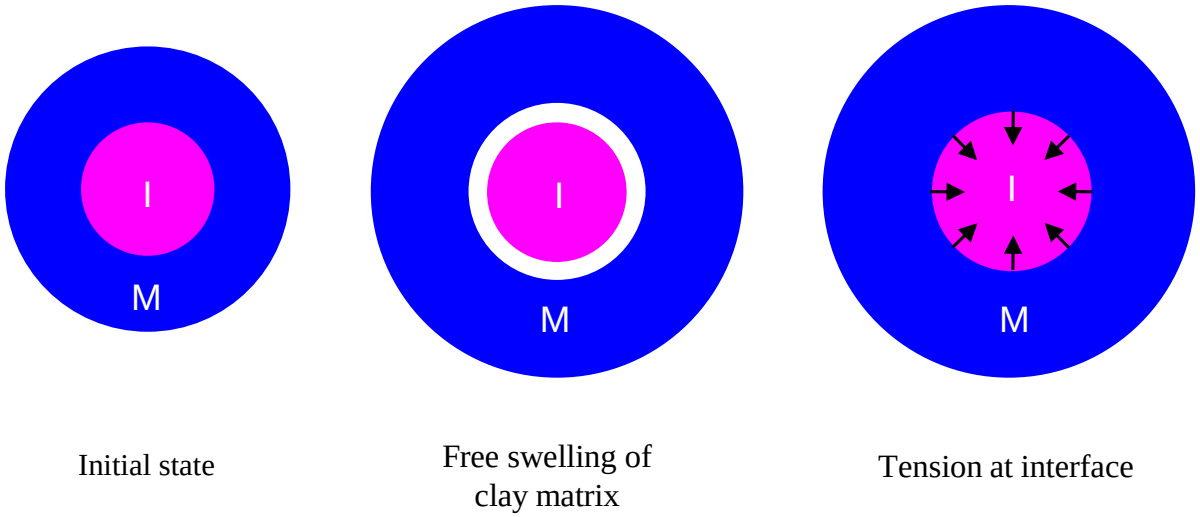

Figure 5.3: Schema of inclusion-matrix interaction due to matrix's swelling.

non-swelling inclusion hinders the growing of the hole in the matrix and consequently results in a tension at the interface.

5.2.1.2 Microcrack patterns under humidification/desiccation

The above analysis reveals that the free swelling (or shrinking) of clay matrix results in an internal stress field in the inclusion and its surrounding. The evaluation of local stress distribution has a great interest for damage study. The tensile strength of Callovo-Oxfordian argillaceous rocks is about 2.7 MPa, while their compressive strength is 21 MPa (ANDRA, 2005). Note that these reference values, obtained by uniaxial compression tests and Brazilian tension tests, actually reveal the macroscopic mechanical behavior of argillaceous rocks. However, the microcracking here is associated to three phases: inclusion, clay matrix and inclusion-matrix interface, of which the mechanical behaviors are actually contrasting. In general, the inclusion (carbonate, quartz) is relatively stiff and owns high resistance. For example, the tensile strength of quartz is 48 MPa while its compressive strength can attain 1.1 GPa. Hence, damage occurs more likely in clay matrix, or at inclusion-matrix interfaces. Unfortunately, the mechanical resistances for the two parts are extremely lacking. Therefore, only qualitative analysis on potential dangerous positions and likely crack patterns is concentrated in the following.

For the case of humidification, one isolated ellipsoidal inclusion is subjected to uniform hydrostatic tension, while the stress in clay matrix would be in tension radially and in compression tangentially, and their extents will decrease in order of r^{-2} with the distance to inclusion's center. No shear stress will be generated in this analysis due to rotational symmetry. Besides in the inclusion, the maximum tensile stress is located at the interface lying in radical direction.

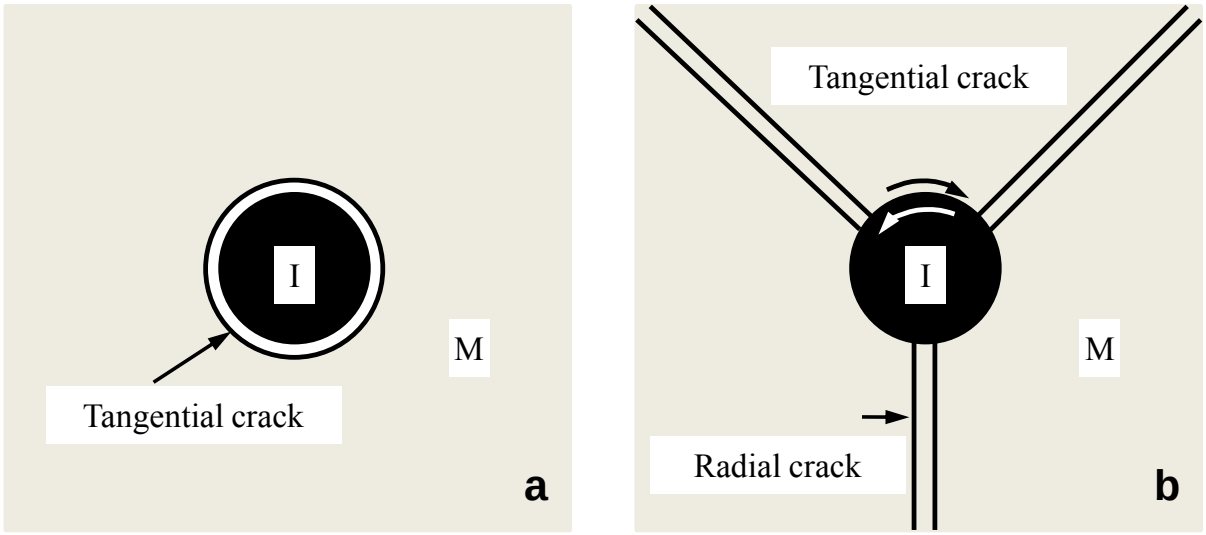

Figure 5.4: Potential crack patterns in case of a) swelling matrix, b) shrinking matrix.

If its value exceeds the inclusion-matrix bond strength, a separation of the inclusion from the clay matrix would occur (Fig.5.4). Note that if the tensile strength of clay matrix is even lower than the inclusion-matrix cohesion, a tensile failure would occur in the immediate vicinity of the interface. The crack pattern is similar to the previous one, only now the sphere would be covered by a thin layer of clay.

For the case of desiccation, the stress distribution is similar to the case of humidification, but with opposite sign. The shrinking of clay matrix results in uniform hydrostatic compression in the inclusion, while the stress in clay matrix will be in compression radially, and in tension tangentially. The tensile tangential stress potentially creates microcracking in the clay matrix near the inclusion-matrix interface, where the extent of stress is highest. Tensile cracks would radiate from the interface into the clay matrix. Consequently, shear stress is generated along the interface and its extent would attain a maximum near the radial cracks. This can result in shear microcracks at the boundary of inclusion.

As a resume, the free swelling (or shrinking) of clay matrix creates local stress in the inclusion as well in the clay matrix surrounding the former, which is a potential source of damage. The maximum is always located at the inclusion-matrix interface, no matter humidification or desiccation. However, the possible microcrack patterns are dissimilar in the two cases: the microcracking due to desiccation should be manifested by several radial cracks, together with thin tangential shear cracks along all or part of the interface, whereas, humidification probably results in tensile failure along inclusion-matrix interface.

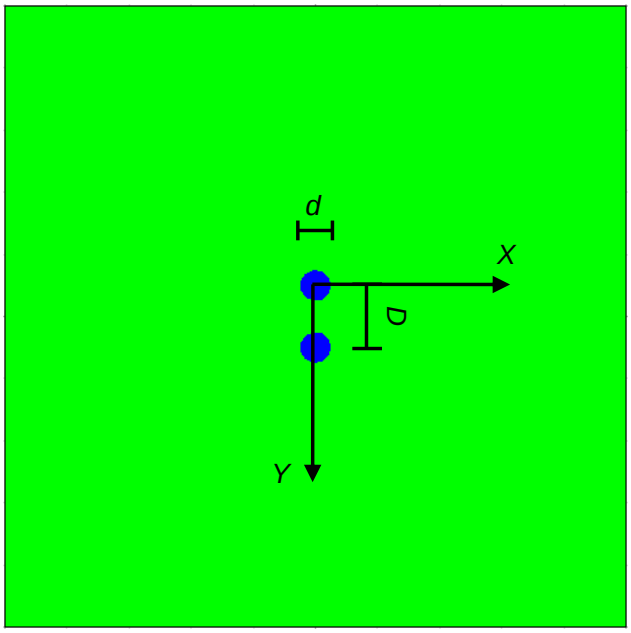

Figure 5.5: Geometry of the specimen with two inclusions.

5.2.2 Two inclusions embedded in an infinite swelling matrix

The previous modeling concerns one inclusion in an infinite matrix, however, there are numerous inclusions scattered randomly in clay matrix for argillaceous rocks. The strain and stress of one inclusion would consequently be perturbed by its neighborhood. In general, two types of interaction for such complex morphology exist: inclusion-matrix interaction, and interaction between inclusions. To take into account the two types of interaction, a case of two inclusions embedded in an infinite swelling matrix is modeled. Contrary to the preceding problem owning analytical solution, the problem of two inclusions has to be solved by finite element method. The software *Porofis* (Pouya, 2011) is applied for the calculation. Two circular inclusions with uniform diameter ($d = 0.5$) in a matrix with free strain (10^{-3}) are modeled in plane stress condition. The size of matrix (20 times the diameter of inclusion) is chosen large enough to represent the field condition as infinite boundary. Since the interaction is strongly controlled by the distance between two inclusions, various D values (distance between the centers of two inclusions) are studied. The distribution of principal stress (σ_1, σ_3) for the case $D = 1.2d$ are presented in Fig.5.5. The stress maps, shown in Fig.5.6, manifest that the stress field around one inclusion is strongly perturbed by the presence of the neighboring inclusion, especially in the front side of the inclusion and the matrix between two inclusions. In the inclusion, the homogeneous stress field becomes heterogeneous and their extent is more important: the maximum values for principal stresses (σ_1, σ_3) are respectively 20.4 MPa and 8.2 MPa, comparing to 7.7 MPa for the case of one inclusion. Such maximal tension locates at the front side of the inclusion, and it decreases gradually to the rear side.

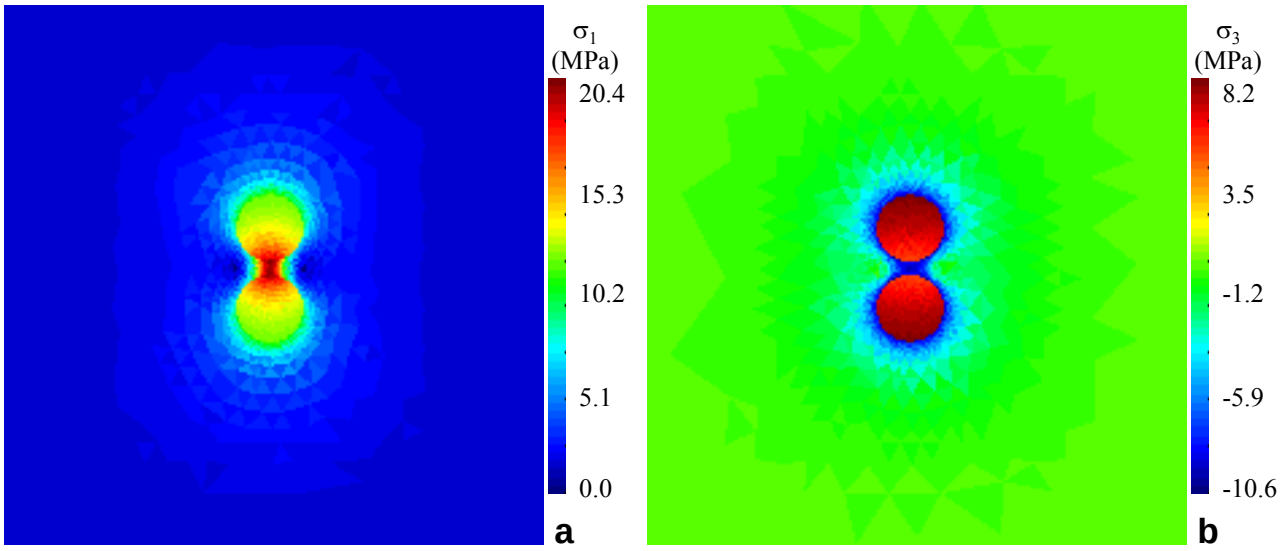

Figure 5.6: Stress maps for the case of two inclusions in free swelling matrix.

The σ_{yy} profiles along y axis (see Fig.5.5), for the various distances between two inclusions, are presented in Fig.5.7. When the two inclusions are faraway (for example $D = 4d$), the stress field in the inclusion is homogenous, which is similar to the case of single inclusion. This means that there is no interaction between inclusions. When the neighboring inclusion gets closer, the stress field would be disturbed: the stress field would be amplified by the presence of the neighboring one. This amplification is more important in front side: it can attain 20.4 MPa when $D = 1.2d$, which is nearly 3 times that for the single inclusion case (7.7 MPa).

5.2.3 Inclusion at free surface during moisture transport process

The preceding analysis always concerns internal stress fields generated by a given homogeneous swelling/shrinking of clay matrix. This actually corresponds to the steady stage of humidification/desiccation process, nevertheless, the role of transient stage isn't taken into account. In fact, the inhomogeneous moisture content during transient stage leads to non-uniform swelling/shrinking in the specimen. These incompatible free strains also contribute to the internal stress field, which is commonly called as "self-restraint". That is why the damage of argillaceous rock due to humidification/desiccation strongly depends on hydric loading rate. Self-restraint, combined with inclusion-matrix interaction, results in the total internal stress field which controls the microcracking of specimen under humidification/desiccation. In this section, these two types of restrain effect would be considered together.

The experimental study on the behavior of argillaceous rocks (such as strain measurement, damage and fracture observation) is mostly conducted at specimen's surface, which consists of a free surface for the studied zone. The free surface certainly modifies the response of material and would also be considered in this modeling.

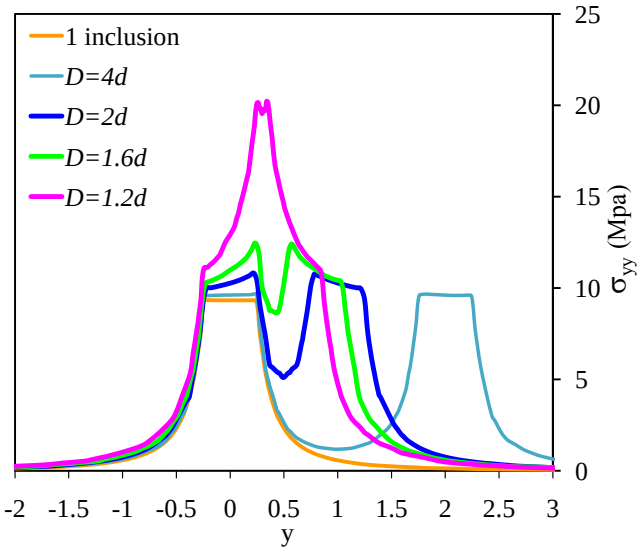

Figure 5.7: Local stress distribution near the two inclusions.

Consider a semi-sphere inclusion with diameter of 0.5 mm scattered on the free surface of one clay formation. The thickness of the specimen is 3 mm while the sizes in two other dimensions are infinite. Such specimen, with initial saturation $S_l^0 = 0.66$ ($\mathrm{RH}_0 = 80\%$), undergoes a humidification due to an increase of atmosphere RH to 90% ($S_l^1 = 0.80$). No external mechanical loading is applied on the specimen. Such problem exhibits axial symmetry, hence the cylindrical coordinates are used. The configuration of the specimen and boundary conditions are presented in Fig.5.8. z is symmetry axis and the free surface is on the r axis. The size in r direction (6 times inclusion's radius) is enough large to represent the field condition as infinite boundary.

For the problem of the inclusion-matrix interaction during humidification process, the modeling is divided into two parts: 1) moisture transport process, 2) estimation of internal stress due to incompatible free swelling of clay matrix and inclusion-matrix interaction. The humidification process is firstly modeled to determine the evolution of the local saturation field within the specimen. Then, the local free swelling of clay matrix can be estimated, and the internal stress field within the specimen is calculated. It is noted that such local stress would alter the microstructure of specimen (deformation), which leads to the variation of permeability. Nevertheless, this coupled effect is ignored in this modeling for simplicity.

5.2.3.1 Humidification process

With the help of the simplified moisture transport model (equation 5.5), the humidification process of argillaceous rocks is modeled by *Porofis*. It is reasonably assumed that the clay matrix is permeable, whereas the inclusion is impermeable. The specimen is initially at saturation state $S_l^0 = 0.66$, and an instantaneous increase of relative humidity RH = 90% is applied on the free surface of specimen. The saturation fields for four different moments are presented

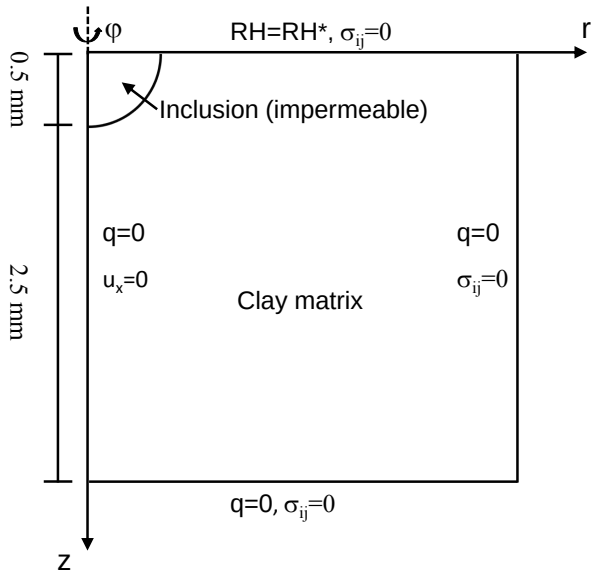

Figure 5.8: Geometry of the specimen and boundary conditions.

in Fig.5.9, which manifests a quasi-1D humidification process in the specimen. The humid moisture penetrates gradually from the top of specimen to the bottom side. The penetration front is somewhat horizontally, unless it is disturbed by the impermeable inclusion.

5.2.3.2 The internal stress field

Once the saturation distribution inside the specimen for a given moment has been assessed, the local free swelling of clay matrix can be evaluated by equation 5.3. The corresponding stress and strain fields can be calculated by *Porofis* in the context of elasticity. No external mechanical loading is applied in this modeling and the boundary condition for the mechanical simulation is described in Fig.5.8. The local stress for two representative stage of humidification is represented here: at the beginning (10s), and the steady state. For each stage, the stress distribution of the inclusion and the matrix (Fig.5.10 and 5.13), as well as that at the inclusion-matrix interface (Fig.5.12), are calculated and presented. Regarding the inclusion-matrix interface, the normal stress and the shear stress are drawn from the inclusion bottom (point 1) to the free surface (point 2). The related definitions for the interface are presented in Fig.5.11.

Remind the formula of normal and shear stress applied on the inclusion at its boundary:

$$\begin{aligned} \sigma_n &= \sigma_{rr}\sin^2\theta + \sigma_{zz}\cos^2\theta + \sigma_{rz}\cos\theta\sin\theta \\ \tau &= (\sigma_{zz} - \sigma_{rr})\cos\theta\sin\theta + \sigma_{rz}\left(\sin^2\theta - \cos^2\theta\right) \end{aligned} \tag{5.18}$$

At transient stage

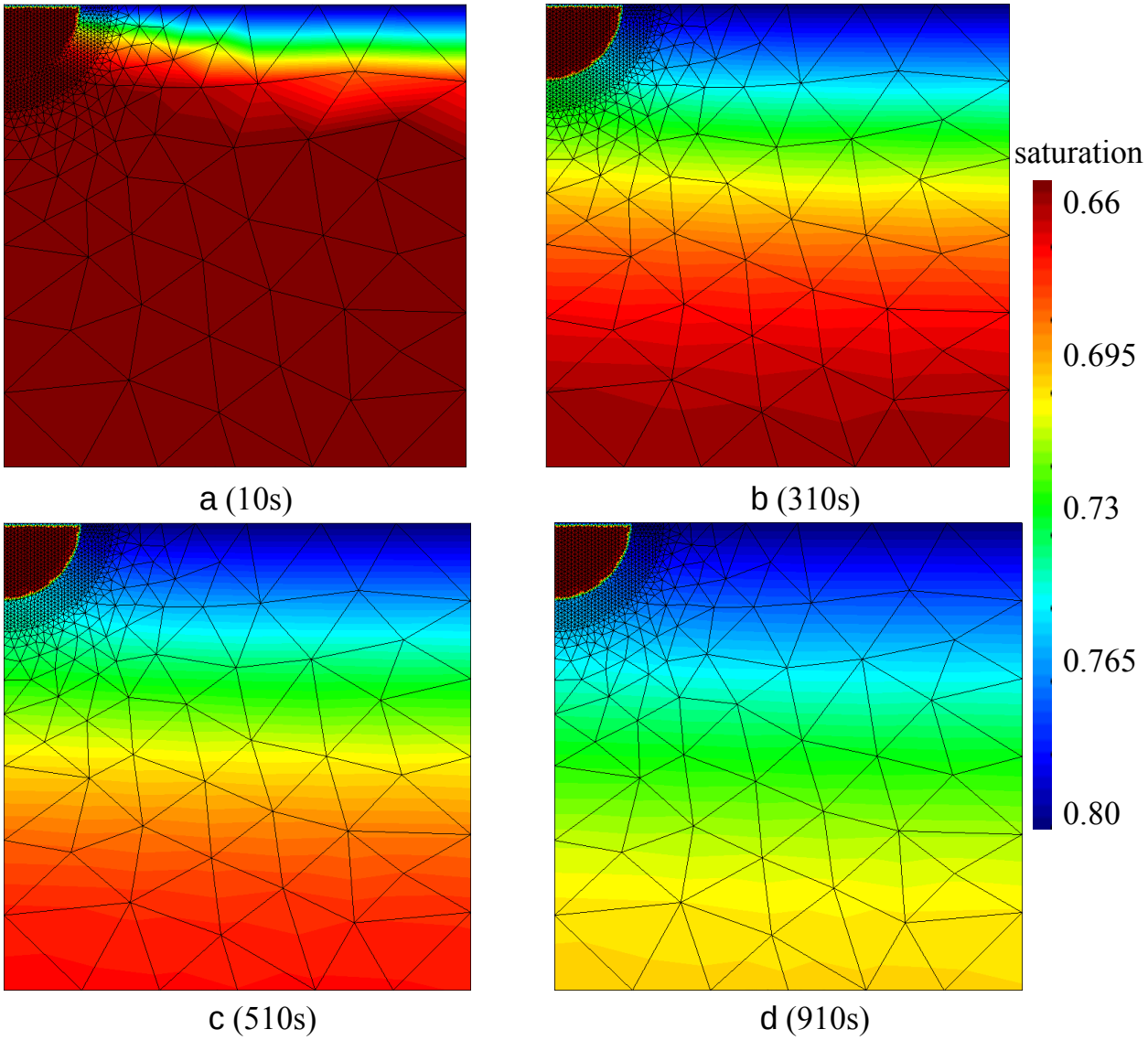

Figure 5.9: Evolution of saturation within the specimen.

At 10s, the free swelling of clay matrix only occurs at the vicinity of free surface (Fig.5.9a). Concerning the local stress, compression is manifested at the surface zone of clay matrix near the inclusion (see Fig.5.10). The maximum attains more than 9MPa at inclusion's boundary. The stress in the inclusion is mostly tensile (about 4.5 MPa), unless the free surface zone is compressive (more than 9 MPa). From point 1, the normal stress is null along the interface, however, it becomes compressive when approaching the free surface, and increases steeply to its maximum at point 2. The evolution of shear stress at interface is similar: it varies moderately around 0, prior to reaching the maximum at point 2 which tends to pull out of the inclusion form the free surface. Whatever, the inclusion-matrix interface at the free surface is a dangerous zone: it is subjected high compression as well as great shear stress which tends to pull the inclusion out of the surface (see the definition of shear stress in Fig.5.11).

It should be noted that point 2 is a singular point: the free stress condition at surface requires its shear stress being null ($\sigma_{rz} = \sigma_{zr} = 0$), however, the material heterogeneities results in a s shear at the inclusion-matrix interface. In fact, when dissimilar materials are joined together, localized stress singularities would be found around the points where the materials meet (like point 2). In such case, the stress and strain value tends to infinite approaching the singular point. Nevertheless, the simulation based on finite element method always provides finite value. This is because finite element method assesses the stress and strain at integration point inside element, whereas, singular point is always mesh node which is at element's edge. Hence, stress evaluation is never performed at singular point and infinite value isn't found to determine the singularity. The magnitude of such finite stress at singular point would be intensified by refining the mesh around it. The order of stress singularity at the free edge of the interface of bonded dissimilar materials depends on wedge angles and materials properties (Sator and Becker, 2012; Tadanobu et al., 1999).

As humidification process goes on, the profile of the normal stress at the inclusion-matrix interface wholly shifts upwards: it becomes mostly tensile and increase gradually over time, whereas the compression near point 2 decreases also. The shear stress at interface broadly increases from the bottom (point 1) to the surface (point 2). The point 2 is always the highest stress location, however, its risk decreases when time goes on.

At steady stage

At steady stage, the normal stress is 6.6 MPa at point 1 (the inclusion's bottom, $\theta = 0°$), it increases gently until its maximum 9.9 MPa at $\theta = 78°$, prior to a sharp decrease to 0.6 MPa at point 2 (the inclusion's boundary at free surface $\theta = 90°$). The tension magnitude at the interface is comparable to the case of one inclusion (7.7 MPa), nevertheless, one remarkable difference for the case of inclusion at free surface consists in the appearance of high shear stress. The shear stress is null at point 1, which can be explained by symmetry. It increases linearly to the maximum 6.8 MPa, prior to a steep fall to 4.7 MPa at point 2. It is worth to note again

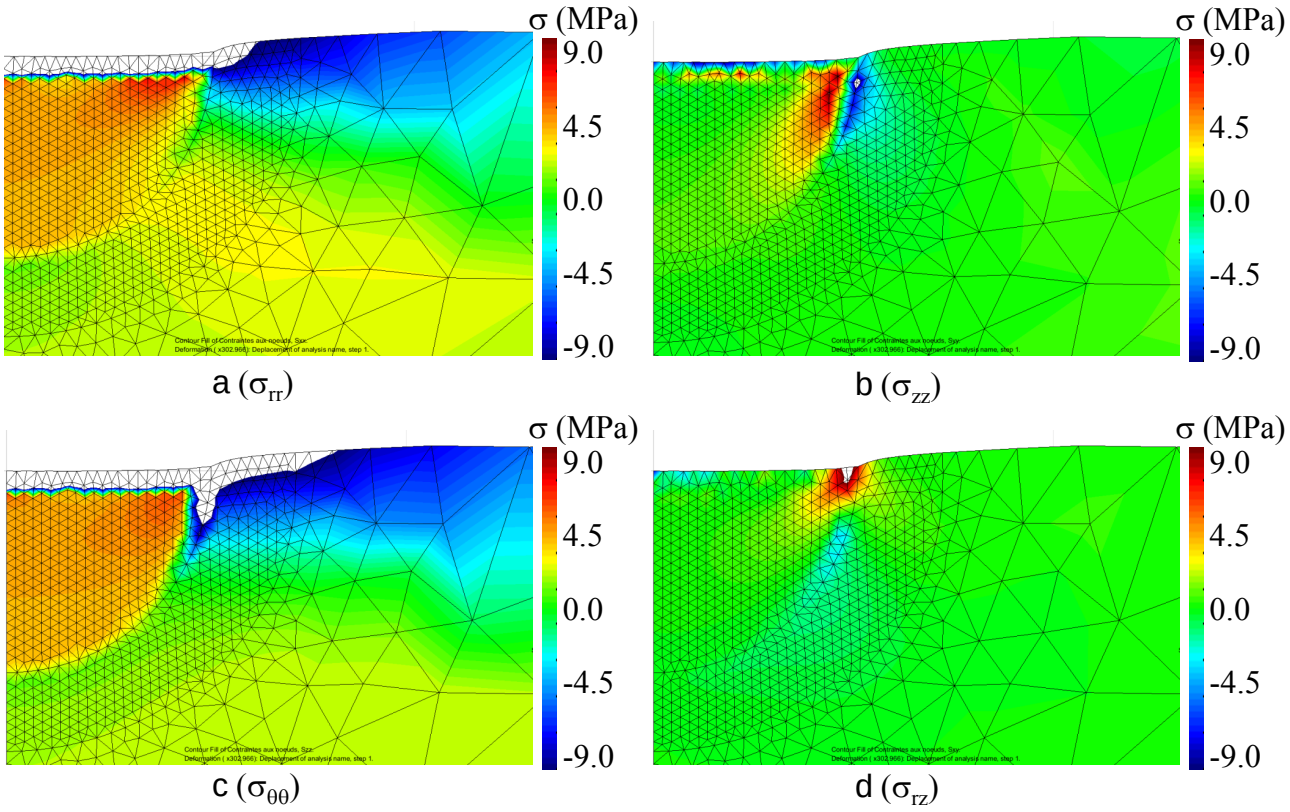

Figure 5.10: Stress fields at 10s. It is worth to note that the extreme stress value near inclusion's free surface, due to singularity, is not considered: no color is shown is such zone. This scale setting adjustment allows presenting more evidently the internal stress field around the inclusion.

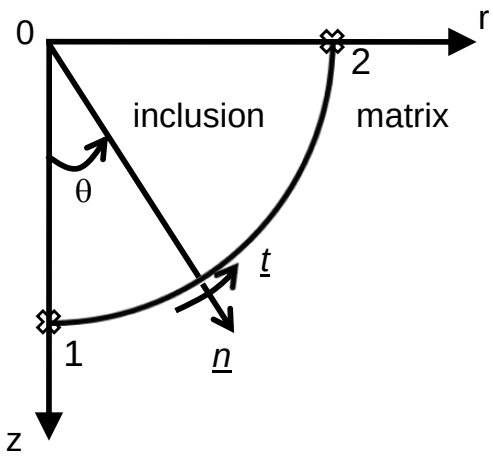

Figure 5.11: Coordinate system around the inclusion.

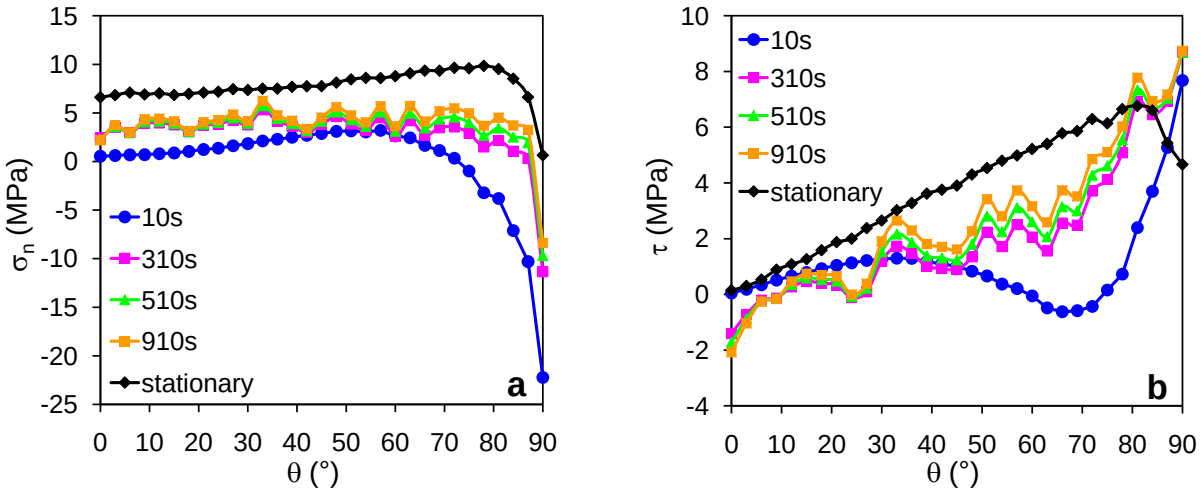

Figure 5.12: Stress evolution along inclusion-matrix interface.

that the point 2 is a singular point: the shear stress σ_{rz} should attain its maximum at right vicinity of point 2, whereas, the free surface requires $\sigma_{zr} = 0$ at exact point 2. The value 4.7 MPa is an approximate evaluation by the finite element numerical simulation. Virtually, the maximal shear stress, deduced by the extension of the linear evolution, would be about 7.7 MPa at right vicinity of point 2, and it falls abruptly to 0 at point 2. In a similar case, the normal stress attains its maximum in the proximity of point 2. Comparing to one inclusion in an infinite swelling matrix with a hydrostatic tension 7.7 MPa, the inclusion at free surface is very different: the tension of inclusion boundary at bottom is somewhat smaller (6.6 MPa), whereas, it is greater at the free surface (about 9.9 MPa). Moreover, there is also a shear stress (7.7 MPa) at the inclusion's boundary close to the free surface: matrix's swelling would pull out of the inclusion. Similar to transient stage, the inclusion's boundary near free surface is always a dangerous place: it undergoes high shear as wells as tension. It is noted that the shear stress at vicinity of point 2 during transient stage and steady state are comparable, however the normal stress is compressive at transient stage while it is tensile at steady state. That means the steady state is the worst stage near point 2 in case of humidification, whereas the initial transient stage (t = 0) is the worst stage in case of desiccation.

The stress fields at steady state are presented in Fig.5.13. Broadly, the radial stress in the inclusion varies principally with depth, whereas, it doesn't evidently evolve horizontally. From the stress map σ_{rr}, the maximal tension is found close to the bottom of inclusion (point 1), the value being 19.7 MPa. It decreases gradually up to the free surface (its evolution is shown in Fig.5.13). This tension with great extent potentially results in vertical cleavage inside the inclusion. Concerning the matrix near the inclusion, it is compressive around the bottom of inclusion, while it becomes tensile near the free surface with the maximum 8.6 MPa. Axial stress is concentrated along the inclusion-matrix interface: it is tensile in the inclusion while it

is compressive in the matrix. The maximal is shown to be near point 2. The evolution of local stress along z-axis, as wells as line L' (see Fig.5.13a), are drawn in Fig.5.14. In contrary to the uniform hydraulic tension 7.7 MPa for the case of one inclusion, the tension in the inclusion is no more uniform and is more significant: it is 16.0 MPa at the interface on line L' and 19.7 MPa at the bottom (point 1). In the matrix, the local stress distribution is comparable with that for the case of one inclusion, except for the high tension at the interface on line L'.

The characterization of high stressed zone is evidenced by the major principal stress map, shown in Fig.5.15. The high stressed zones in the inclusion and matrix are all located at the inclusion's boundary a little below point 2: its value is 24 MPa in the inclusion and is 12 MPa in the matrix. These high tensions potentially lead to tensile microcracking in the material. It should be noted that microcracking is also possible to occur in the matrix although its value is smaller than that in the inclusion, as the tensile strength of the clay matrix is normally much smaller than that of the inclusion.

5.2.3.3 Self-restraint at the transient stage of humidification (without inclusion)

The previous analysis has shown that the highest stress level is broadly reached at steady stage, except for the zone near point 2. The stress in this zone is subjected to a sign change during the transient moisture transport stage: it is highly compressive at the beginning, whereas it becomes slight tension at steady state. Actually, this phenomenon is attributable to self-restraint effect: the moisture gradient during moisture transport process leads to a local stress field within the specimen. Naturally, the self-constraint effect is combined with inclusion-matrix interaction (as in this case). To better understand the contribution of self-restraint effect, the domain of inclusion is considered as a gap (stiffness being null) to exclude inclusion' effect: the matrix could deform freely without inclusion-matrix interaction. The stress field for 10s step is recalculated and presented in Fig.5.16. Choosing 10s step is because the self-restraint is most significant at this moment: the moisture gradient is maximal at the beginning of hydric loading and would gradually vanish when moisture transport goes on (see saturation gradient in Fig.5.9).

The moisture gradient at 10s is shown in Fig.5.9, which represents also the swelling gradient of clay matrix. At 10s, high compression is shown in the surface zone of clay matrix near the inclusion's boundary (the magnitude can attain 12 MPa), while a moderate tension field with maximum 3 MPa occurs at the lower part of clay matrix. It is worth to note that the r-displacement of point 2 is negative (-0.18×10^{-3}) at 10s, whereas it is positive (0.5) at steady stage.

To a better understanding of this negative displacement, consider a simple case: a rectangular specimen undergoes a one-side humidification from top to bottom. At the beginning of humidification, the upper part of specimen is firstly humidified, whereas the humid moisture hasn't arrived at the bottom part. Consequently, the top surface zone swells, however, it is

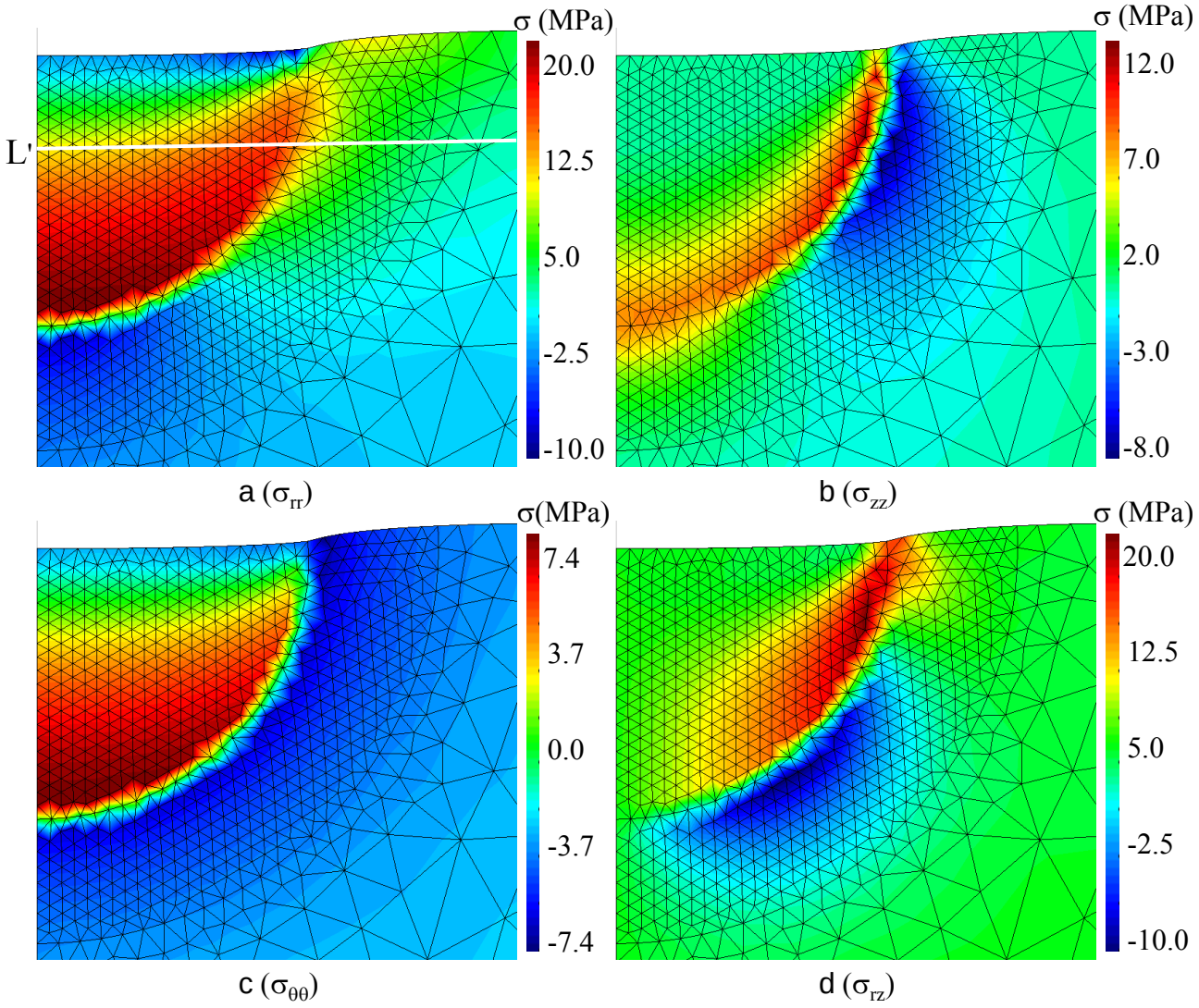

Figure 5.13: Stress fields at steady stage.

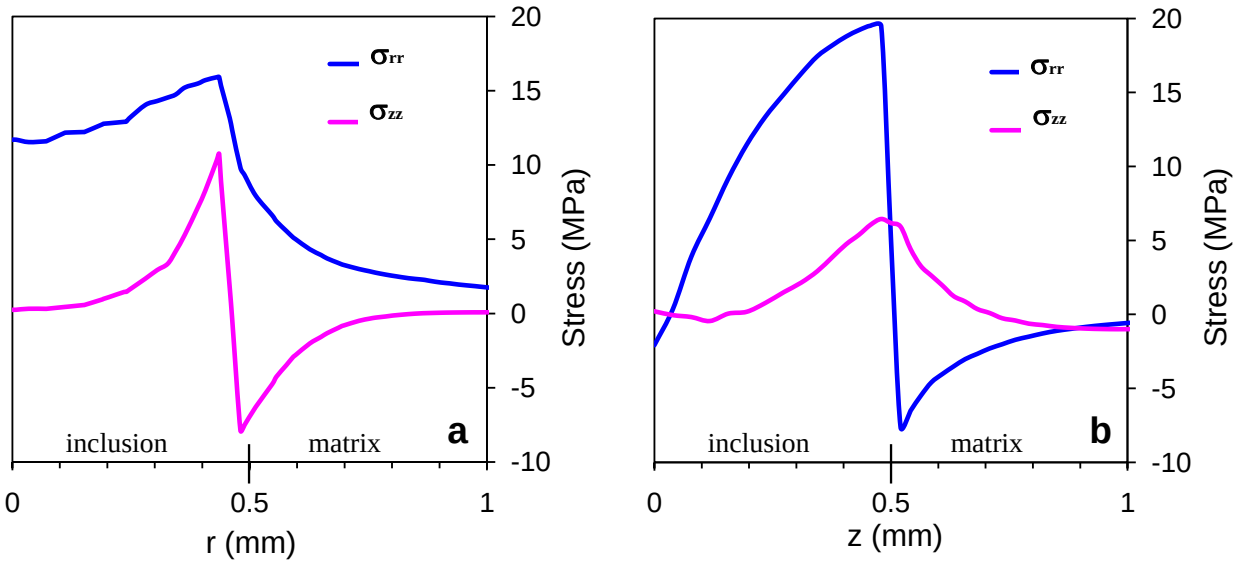

Figure 5.14: Profile of the stress at steady state along 1) line 1', 2) Z-axis.

restrained by the non-swelling bottom part. Such self-restraint effect results in compression at the top part while tension at the bottom part (see Fig.5.17). Similarly, the swelling of top surface zone would lead the point 2 (the corner of the two free surfaces) to move negatively in r-direction and upwards in z-direction. As moisture transport goes on and the free swelling becomes more homogeneous inside the specimen, such stress gradually decreases and finally vanishes at steady state. That is why the compression at the neighboring zone of point 2 decreases with time. It is worth to note that such self-restraint induced stress at hydric loading surface is compressive for the swelling (humidification) case, whereas it is tensile for the shrinking (desiccation) case.

Compared to the case without inclusion, the stress field at 10s is more intense with the presence of inclusion. The maximal compression is 6.0 MPa without inclusion (near the arc free surface as shown in Fig.5.18), whereas the stress at the same point can attain 9.0 MPa and the maximum is 32 MPa (at the point2) with inclusion. Actually, the non-swelling inclusion would hinder the displacement of point 2 due to free swelling (toward to the inclusion for the humidification case and apart from the inclusion for the desiccation case). And this would intensify the extent of the stress due to self-restraint: not only the compression for the case of humidification, but also the tension for the case of desiccation. The point 2 and its neighborhood is indeed a dangerous place under hydric loading. The self-restraint effect is most significant at the wetting surface where the moisture gradient is most important. The inclusion-matrix interaction is most intense at the interface and decays with distance.

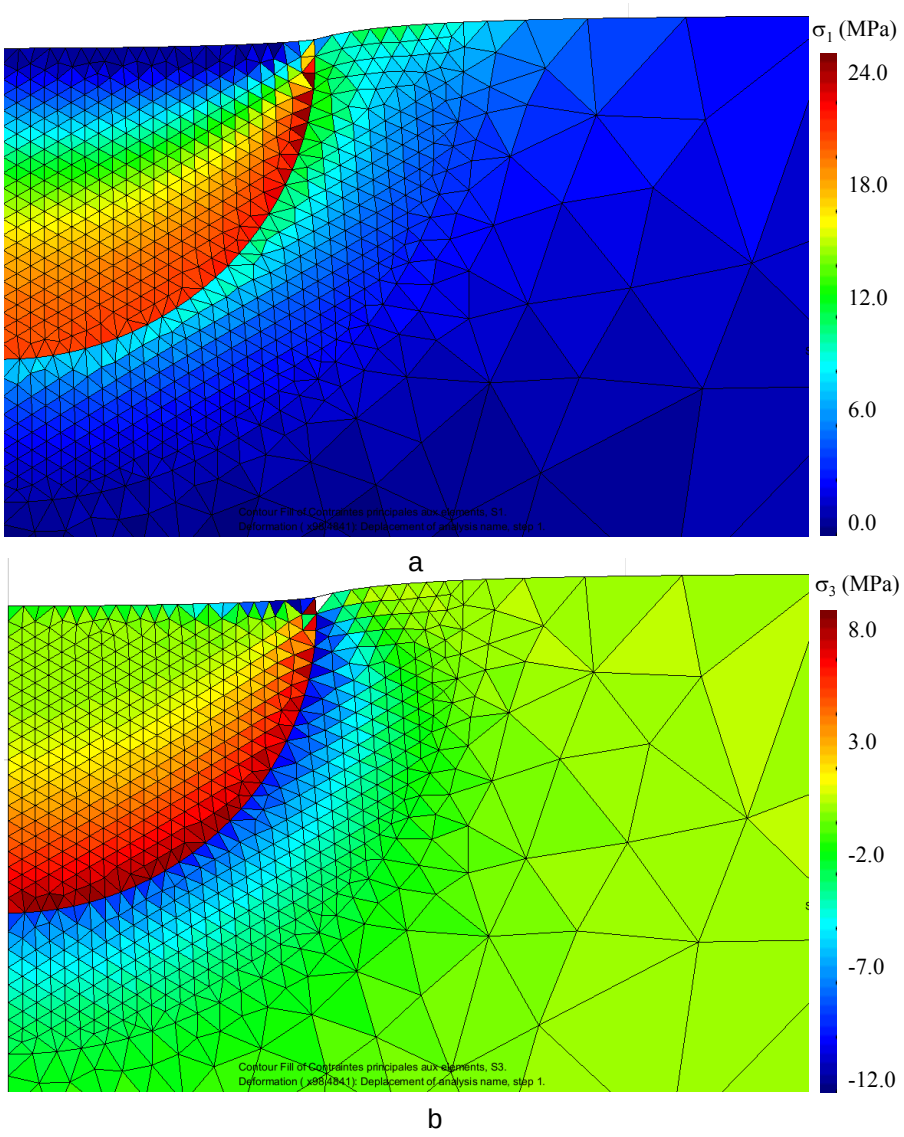

Figure 5.15: Principal stresses at steady stage a) σ_1, b) σ_3.

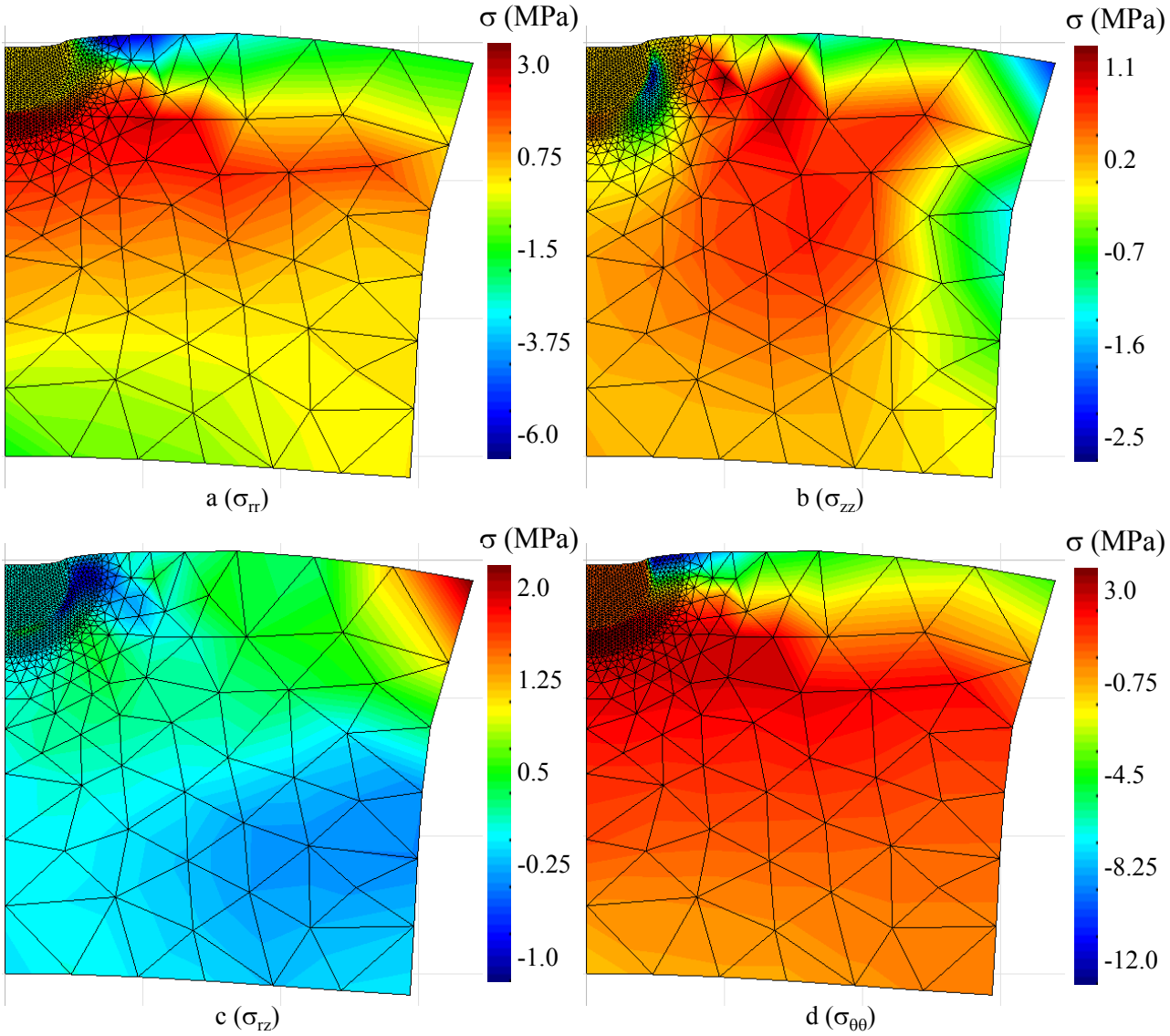

Figure 5.16: Stress fields at 10s (without inclusion).

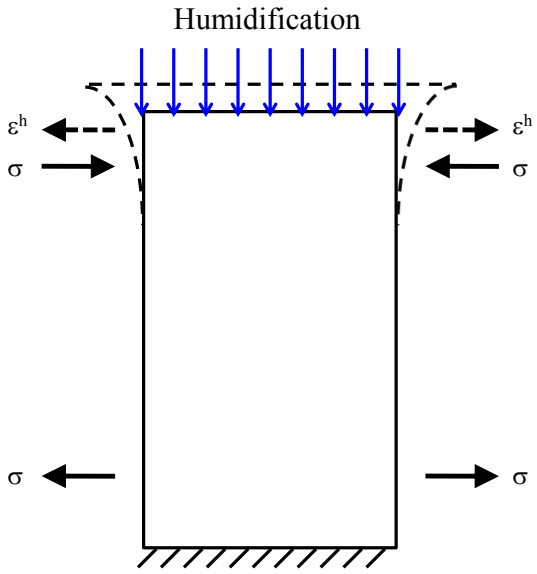

Figure 5.17: Schema of self-restraint during humidification.

5.2.3.4 The role of hydric loading rate

As discussed in the previous section, the internal stress field inside argillaceous rocks during humidification process is attributable to two terms: self-restraint and inclusion-matrix interaction. For self-restraint effect, hydric loading rate plays an important role by which the moisture gradient developed inside the specimen is strongly controlled. Therefore, a series of hydric loading rates, 0.003%RH/min, 1%RH/min, 10%RH/min and instantaneous hydric loading (see Fig.A.8), is considered in this study to investigate the influence of hydric loading rate. The saturation distribution at 10s after the finishing of hydric loading is estimated. This means: 3610s for 0.003%RH/min, 610s for 1%RH/min case, 70s for 10%RH/min, and 10s for instantaneous hydric loading. Their saturation distributions, as well as the saturation gradient within the specimen, are presented in Fig.5.20. Generally, the saturation gradient at the beginning of humidification increases with hydric loading rate.

The comparison of stress is concentrated at point 2, where the local stress is obviously attributable to self-restrain effect. Its evolution at the beginning of humidification is plotted in Fig.5.21. When RH begins to change, the stress at point 2 increases linearly and attains its maximum once hydric loading is achieved. Then the normal stress gradually decreases whereas its shear stress remains constant. The stress at point 2 for the moment of 10s after the end of hydric loading is drawn versus hydric loading rate: it is 18 MPa in case of 1%RH/min, while it attains 32MPa in case of instantaneous hydric loading (as shown in Fig.5.22). This difference is actually attributable to the variation of saturation gradient for different hydric loading rates: it becomes steeper when the hydric loading increases (as shown in Fig.5.20d) and the stress due to self-restraint becomes more important consequently.

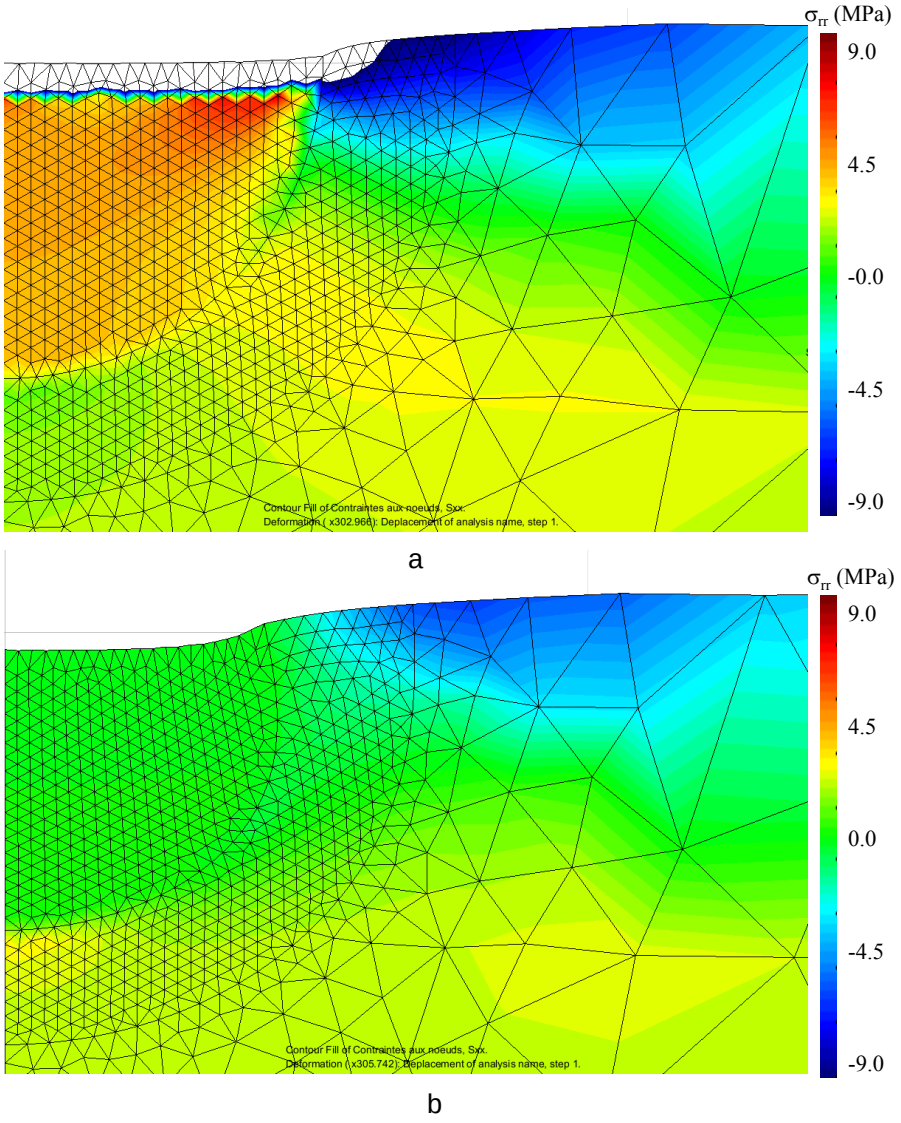

Figure 5.18: Radial stress filed in the case of a) with inclusion, b) without inclusion.

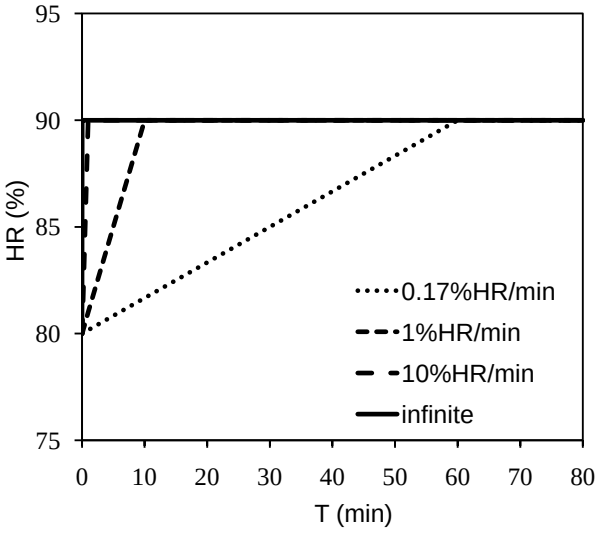

Figure 5.19: Different hydric loading rates.

5.3 Overall deformation under humidification/desiccation

When RH varies, the clay matrix of argillaceous rocks would undergo a volume changing due to its specific physic-chemical property. Due to the presence of non-swelling inclusions, local stress will be present and consequently results in mechanical strains both in inclusions and in clay matrix. Finally, the total strain of argillaceous rocks under hydric loading is a sum of free deformation and mechanical deformation, of which the magnitude depends on several factors: the free strain of clay matrix, inclusion fraction (f_I) and the mechanical properties of clay matrix and inclusion.

In this section, the total deformation of argillaceous rocks due to the swelling of clay matrix is firstly investigated by a micromechanics approach. Then, the modelings of periodic microstructure and real microstructure are conducted to valid the proposed formulation.

5.3.1 Homogenization

5.3.1.1 Eshelby's problem

Considering one domain I (inclusion) in an infinite homogeneous elastic media Ω which is subjected to a uniform free deformation (i.e. hydric swelling and thermal expansion), what is the elastic field in the inclusion and its surrounding (matrix)? The general equations of above problem can be written as:

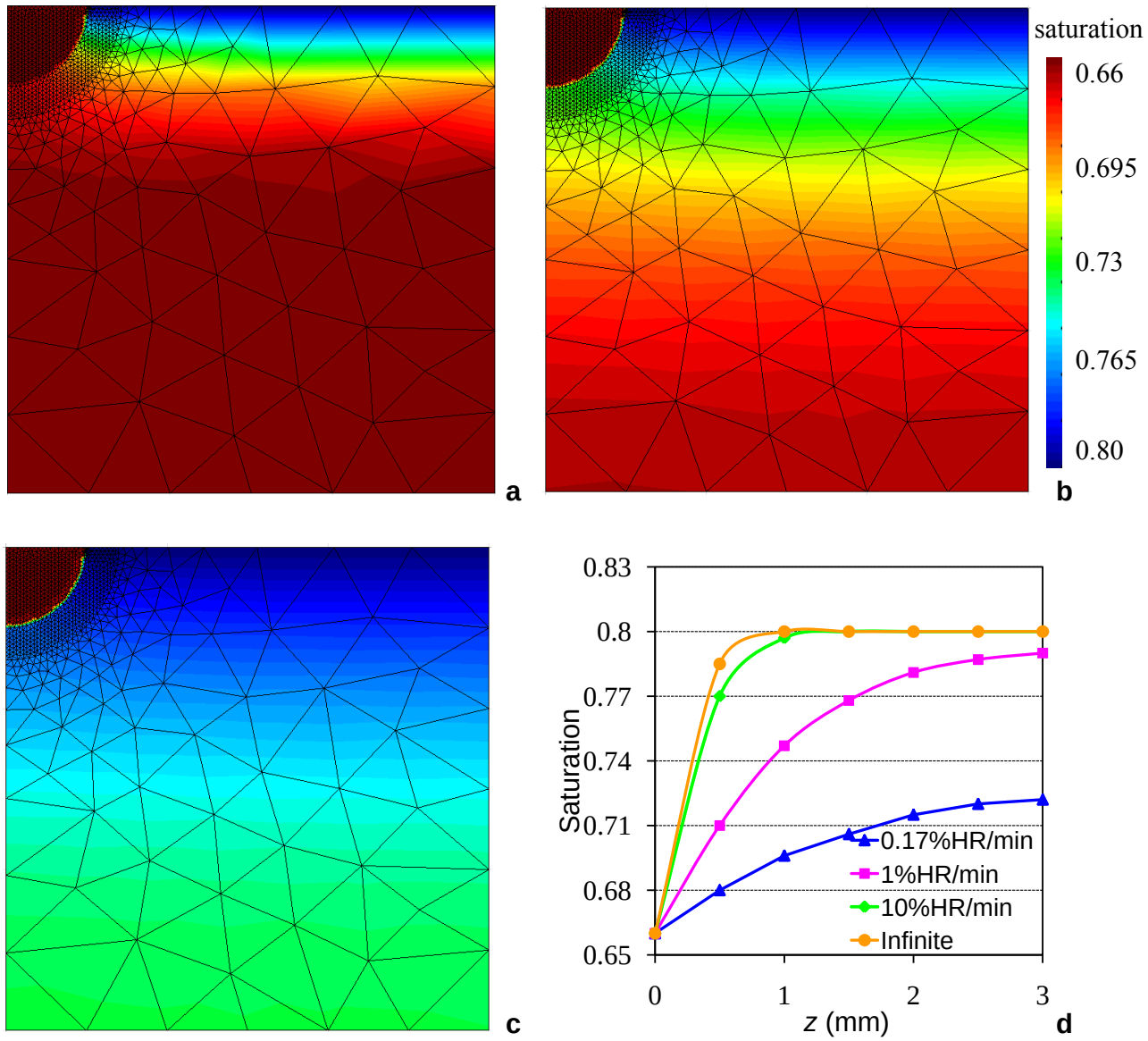

Figure 5.20: Saturation distribution in specimen at 10s after the end of hydric loading: a) 70s for the case of 10%RH/min, b) 610s for the case of 1%RH/min, c) 3610s for the case of 0.17%RH/min, d) far away from inclusion ($r = 3$), the saturation gradients from top ($z = 0$) to bottom ($z = 3$mm) of specimen for different hydric loading rates.

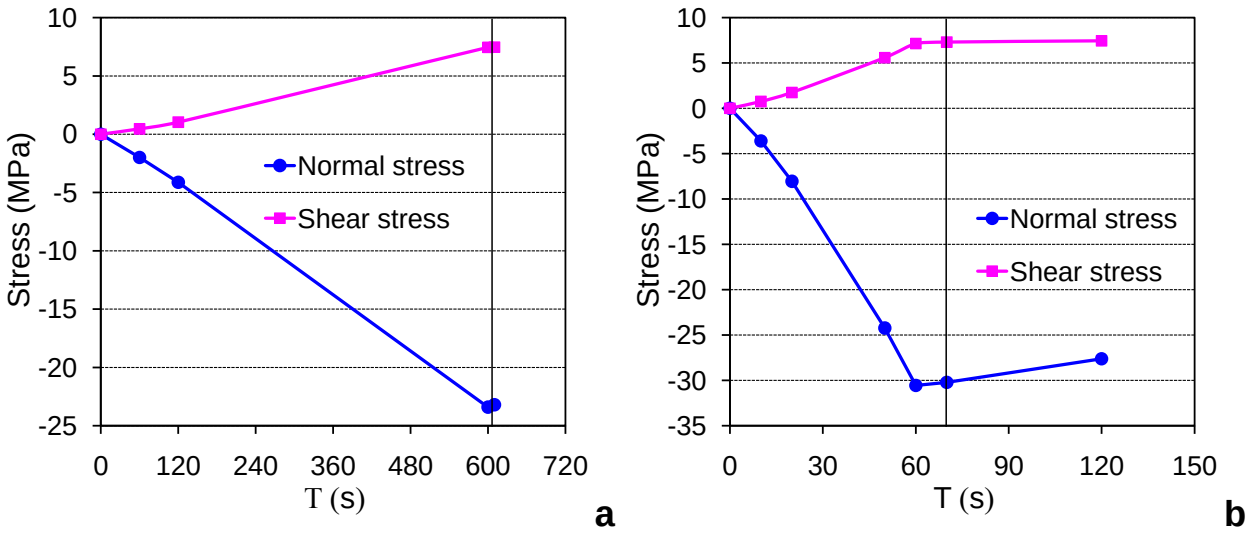

Figure 5.21: Stress evolution at point 2 during the hydric loading: a) in case of 1%RH/min, b) in case of 10%RH/min.

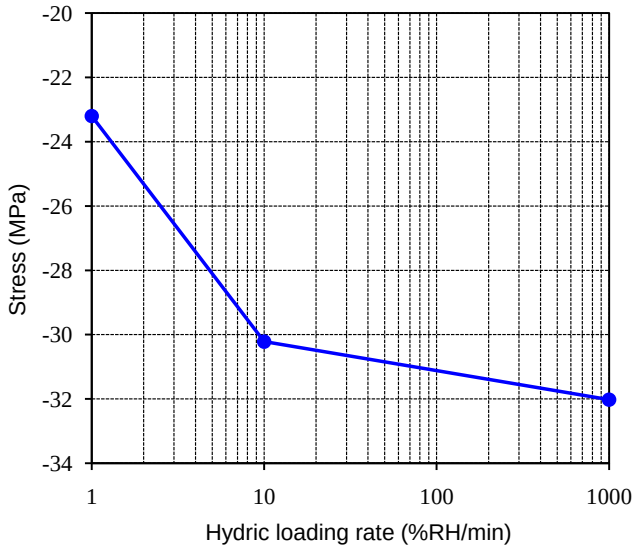

Figure 5.22: Normal stress of point 2 at 10s after the end of hydric loading vs. hydric loading rate.

$$\begin{cases} \nabla \cdot \underline{\underline{\sigma}}(\underline{x}) = 0 \\ \underline{\underline{\varepsilon}}(\underline{x}) = \dfrac{1}{2}\left(\nabla \underline{u}(\underline{x}) + \nabla^T \underline{u}(\underline{x})\right) \\ \underline{\underline{\sigma}}(\underline{x}) = \underline{\underline{\underline{\underline{C}}}}^0 : \left(\underline{\underline{\varepsilon}}(\underline{x}) - \underline{\underline{\varepsilon}}^h\right) = \underline{\underline{\underline{\underline{C}}}}^0 : \underline{\underline{\varepsilon}}(\underline{x}) + \underline{\underline{\tau}} & \text{in } I \\ \underline{\underline{\sigma}}(\underline{x}) = \underline{\underline{\underline{\underline{C}}}}^0 : \underline{\underline{\varepsilon}}(\underline{x}) & \text{in } \Omega - I \\ \underline{u}(\infty) = 0 \end{cases} \tag{5.19}$$

where σ, ε and u respectively denote stress, strain and displacement. C^0 is stiffness tensor. Note that the problem of free swelling deformation ε^h in the inclusion can as well be considered as a problem of eigenstress τ in it, which can be expressed as:

$$\underline{\underline{\tau}} = -\underline{\underline{\underline{\underline{C}}}}^0 : \underline{\underline{\varepsilon}}^h \tag{5.20}$$

If the inclusion is in form of ellipse, Eshelby (1957) proved in his famous papers that the strain and stress field would be uniform in the inclusion and their analytic solutions are given as well:

$$\underline{\underline{\varepsilon}}^I = \underline{\underline{\underline{\underline{S_I}}}}^0 : \underline{\underline{\varepsilon}}^h = -\underline{\underline{\underline{\underline{P_I}}}}^0 : \underline{\underline{\tau}} \tag{5.21}$$

where S_I^0 is Eshelby's tensor, and P_I^0 is Hill's tensor. They depend on C^0 and the form of inclusion. Note that Hill's tensor is generally symmetric, whereas Eshelby's tensor is not. In the case of isotropic with the inclusion in form of sphere, their expressions are:

$$\underline{\underline{\underline{\underline{S_I}}}}^0 = \alpha^0 \underline{\underline{\underline{\underline{J}}}} + \beta^0 \underline{\underline{\underline{\underline{K}}}} \tag{5.22a}$$

$$\underline{\underline{\underline{\underline{P_I}}}}^0 = \frac{\alpha^0}{3k^0} \underline{\underline{\underline{\underline{J}}}} + \frac{\beta^0}{2\mu^0} \underline{\underline{\underline{\underline{K}}}} \tag{5.22b}$$

with

$$\alpha^0 = \frac{3k^0}{3k^0 + 4\mu^0}, \quad \beta^0 = \frac{6\left(k^0 + 2\mu^0\right)}{5\left(3k^0 + 4\mu^0\right)}$$

The fourth order unite tensors are defined as:

$$\underline{\underline{\underline{\underline{I}}}} = \underline{\underline{\underline{\underline{J}}}} + \underline{\underline{\underline{\underline{K}}}}, \quad I_{ijkl} = \frac{1}{2}\left(\delta_{ik}\delta_{jl} + \delta_{il}\delta_{jk}\right), \quad J_{ijkl} = \frac{1}{3}\delta_{ij}\delta_{kl} \tag{5.23}$$

5.3.1.2 Problem of heterogeneous inclusion

Contrary to the classic Eshelby's problem, the elastic modulus of the matrix and the inclusion are not identical for argillaceous rocks. Besides, free deformation occurs in the matrix. Therefore, the general equations of argillaceous rocks under hydric loading, due to a free swelling of clay matrix, can be written as:

$$\begin{cases} \nabla \cdot \underline{\underline{\sigma}}(\underline{x}) = 0 \\ \underline{\underline{\varepsilon}}(\underline{x}) = \dfrac{1}{2}\left(\nabla \underline{u}(\underline{x}) + \nabla^T \underline{u}(\underline{x})\right) \\ \underline{\underline{\sigma}}(\underline{x}) = \underline{\underline{\underline{\underline{C}}}}^I : \underline{\underline{\varepsilon}}(\underline{x}) & \text{in } I \\ \underline{\underline{\sigma}}(\underline{x}) = \underline{\underline{\underline{\underline{C}}}}^M : \left(\underline{\underline{\varepsilon}}(\underline{x}) - \underline{\underline{\varepsilon}}^h\right) & \text{in } \Omega - I \\ \underline{u}(\infty) = 0 \end{cases} \tag{5.24}$$

where C^I and C^M denote repectively the stiffness tensor of inclusion and clay matrix.

We introduce a variable:

$$\underline{\underline{\tilde{\varepsilon}}}\,(\underline{x}) = \underline{\underline{\varepsilon}}\,(\underline{x}) - \underline{\underline{\varepsilon}}^h \tag{5.25}$$

Then the equations can be rewritten:

$$\begin{cases} \nabla \cdot \underline{\underline{\sigma}}(\underline{x}) = 0 \\ \underline{\underline{\varepsilon}}(\underline{x}) = \dfrac{1}{2}\left(\nabla \underline{u}(\underline{x}) + \nabla^T \underline{u}(\underline{x})\right) \\ \underline{\underline{\sigma}}(\underline{x}) = \underline{\underline{\underline{\underline{C}}}}^M : \underline{\underline{\varepsilon}}(\underline{x}) + \underline{\underline{\tau}} = \left(\underline{\underline{\underline{\underline{C}}}}^I - \underline{\underline{\underline{\underline{C}}}}^M\right) : \underline{\underline{\tilde{\varepsilon}}}\,(\underline{x}) + \underline{\underline{\underline{\underline{C}}}}^I : \underline{\underline{\varepsilon}}^h & \text{in } I \\ \underline{\underline{\sigma}}(\underline{x}) = \underline{\underline{\underline{\underline{C}}}}^M : \underline{\underline{\tilde{\varepsilon}}}(\underline{x}) & \text{in } \Omega - I \\ \underline{u}(\infty) = 0 \end{cases} \tag{5.26}$$

This problem is identical to Eshelby's problem, if we consider:

$$\underline{\underline{\tau}} = \left(\underline{\underline{\underline{\underline{C}}}}^I - \underline{\underline{\underline{\underline{C}}}}^M\right) : \underline{\underline{\tilde{\varepsilon}}}\,(\underline{x}) + \underline{\underline{\underline{\underline{C}}}}^I : \underline{\underline{\varepsilon}}^h$$

Therefore, the deformation of inclusion is:

$$\underline{\underline{\tilde{\varepsilon}}}^I = -\underline{\underline{\underline{\underline{P_I}}}}^0 : \underline{\underline{\tau}} = -\underline{\underline{\underline{\underline{P_I}}}}^0 : \left[\left(\underline{\underline{\underline{\underline{C}}}}^I - \underline{\underline{\underline{\underline{C}}}}^M\right) : \underline{\underline{\tilde{\varepsilon}}}\,(\underline{x}) + \underline{\underline{\underline{\underline{C}}}}^I : \underline{\underline{\varepsilon}}^h\right] \tag{5.27}$$

Hill's influence tensor is defined as:

$$\underline{\underline{\underline{\underline{C}}}}^* = \left(\underline{\underline{\underline{\underline{P_I}}}}^0\right)^{-1} - \underline{\underline{\underline{\underline{C}}}}^M \tag{5.28}$$

Substituting Hill's influence tensor and equation (5.26) into equation (5.27), we finally obtain:

$$\left(\underline{\underline{\underline{\underline{C}}}}^* + \underline{\underline{\underline{\underline{C}}}}^I\right) : \underline{\underline{\varepsilon}}^I = \underline{\underline{\underline{\underline{C}}}}^* : \underline{\underline{\varepsilon}}^h \tag{5.29}$$

or,

$$\underline{\underline{\sigma}}^I = \left(\underline{\underline{\underline{\underline{S}}}}^* + \underline{\underline{\underline{\underline{S}}}}^I\right)^{-1} : \underline{\underline{\varepsilon}}^h \tag{5.30}$$

5.3.1.3 Total strain of argillaceous rocks due to the swelling of clay matrix

By definition, macroscopic (total) stress and strain for a "representative volume element" (RVE) is written as:

$$\left\langle \underline{\underline{\sigma}} \right\rangle = f_I \left\langle \underline{\underline{\sigma}} \right\rangle^I + (1 - f_I) \left\langle \underline{\underline{\sigma}} \right\rangle^M \tag{5.31a}$$

$$\left\langle \underline{\underline{\varepsilon}} \right\rangle = f_I \left\langle \underline{\underline{\varepsilon}} \right\rangle^I + (1 - f_I) \left\langle \underline{\underline{\varepsilon}} \right\rangle^M \tag{5.31b}$$

where $\langle . \rangle$ denotes the mean value of certain quantity. The subscripts I and M represent respectively inclusion and matrix.

The constitute equation for the inclusion, and the matrix (with free strain ε^F) can be expressed as:

$$\left\langle \underline{\underline{\varepsilon}} \right\rangle^I = \underline{\underline{\underline{\underline{S}}}}^I : \left\langle \underline{\underline{\sigma}} \right\rangle^I \tag{5.32a}$$

$$\left\langle \underline{\underline{\varepsilon}} \right\rangle^M = \underline{\underline{\underline{\underline{S}}}}^M : \left\langle \underline{\underline{\sigma}} \right\rangle^M + \underline{\underline{\varepsilon}}^F \tag{5.32b}$$

where the fourth order tensor S denotes compliance tensor of each phase. For the case of free swelling (without external stress), we deduce:

$$f_I \left\langle \underline{\underline{\sigma}} \right\rangle^I = -(1 - f_I) \left\langle \underline{\underline{\sigma}} \right\rangle^M \tag{5.33}$$

Substituting equation (5.32) and (5.33) into (5.31), we obtain:

$$\left\langle \underline{\underline{\varepsilon}} \right\rangle = f_I \left(S^I - S^M :\right) \left\langle \underline{\underline{\sigma}} \right\rangle^I + (1 - f_I)\, \underline{\underline{\varepsilon}}^h \tag{5.34}$$

The total strain can be evaluated by the above equation once the average stress (or strain) of inclusion is known. In general, it consists of two terms: inclusion-matrix interaction, and interaction between neighboring inclusions. If the volume fraction of inclusion f_I is so small that the inclusions are far away with each other, the secondary term can be ignored. That to say, the average stress (strain) of inclusions is identical to the case of one inclusion in an infinite swelling matrix. This method is often called as high dilution model. Substituting equation (5.30) to equation (5.34), we finally obtain:

$$\left\langle \underline{\underline{\varepsilon}} \right\rangle = (1 - c f_I)\, \underline{\underline{\varepsilon}}^h \tag{5.35}$$

with,

$$c = 1 - \left(\underline{\underline{\underline{\underline{S}}}}^I - \underline{\underline{\underline{\underline{S}}}}^M\right) : \left(\underline{\underline{\underline{\underline{S}}}}^* + \underline{\underline{\underline{\underline{S}}}}^I\right)^{-1} : \underline{\underline{I}} \tag{5.36}$$

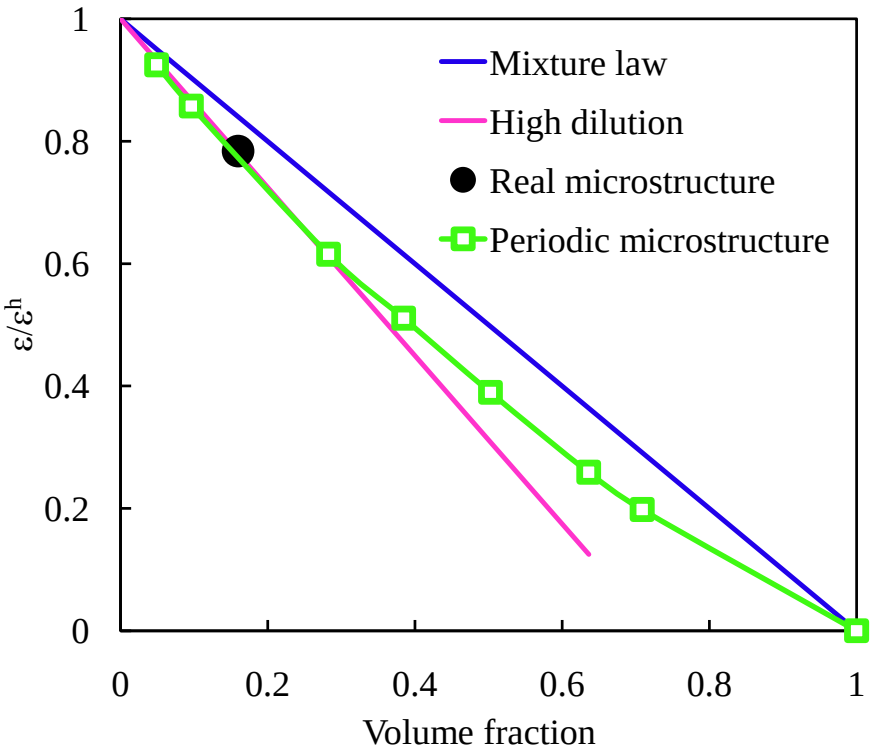

Figure 5.23: Total strain versus the volume fraction of inclusion.

It is noted that $c = 1$ corresponds to a mixture law where no interaction is taken into account. Considering the mechanical behaviors of each components (Tab.5.1), c is 1.366 for this modeling. The ratio between the total strain and the free swelling of clay matrix versus the volume fraction of inclusion estimated by high dilute model is shown in Fig.5.23.

5.3.2 Simulation based on periodic microstructure

The total deformation of argillaceous rocks due to matrix's swelling is also investigated by finite element method *Porofis*. It is assumed that the specimen undergoes plane strain deformation, due to 10%RH increase. A periodic inclusion-matrix composite microstructure is constructed for the study. With an unchanged total surface of specimen, a serial of inclusion's rayon is chosen to represent different volume fraction of inclusion (from 5% to 79%). The geometry of specimen and its meshing for the case of 20% is shown in Fig.5.24. The total deformation for each f_I value is calculated and plotted at Fig.5.23. It is shown that the high dilution method gives a good prediction of total deformation until the volume fraction of inclusion attains 40%. Note that f_I for argillaceous rocks is also in this range. This means that the simple high dilution model is applicable to describe the total deformation of such rocks under hydric loading.

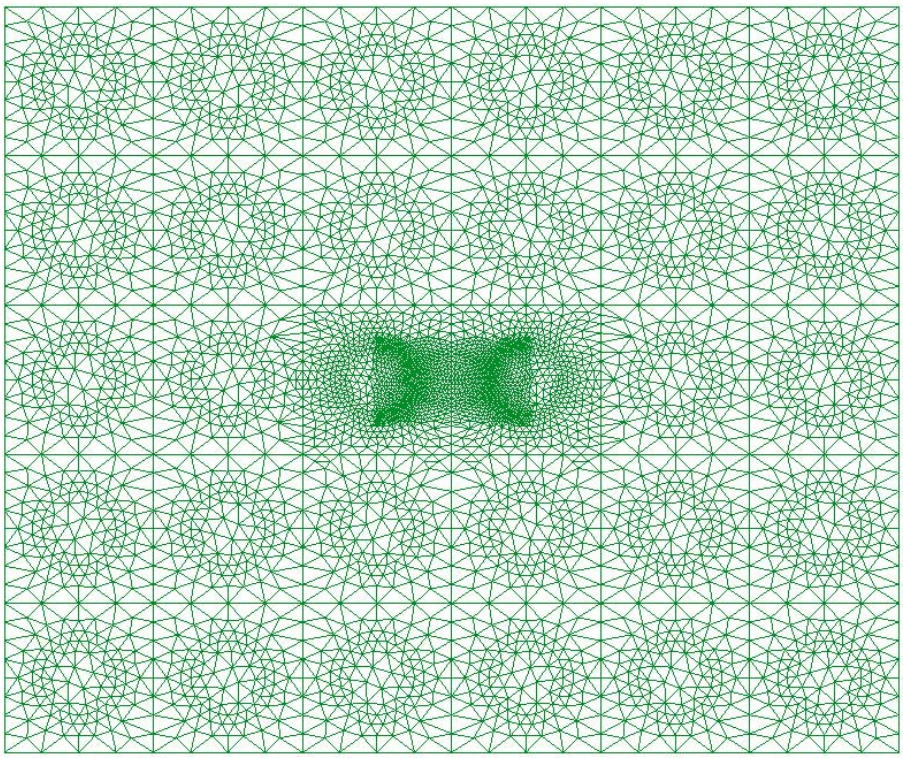

Figure 5.24: Meshing of periodic inclusion-matrix composite.

5.3.3 Simulation based on real microstructure

By means of scanning electron microscope (SEM), the composite microstructure of argillaceous rocks can be roughly recognized. Based on the observation zone 1 in test #2 of chapter 3 (see Fig.3.6), a fairly "real" microstructure of argillaceous rocks is reconstructed and simulated by *Porofis*, to investigate the total deformation induced by a free swelling of matrix ($10^{-2}/(100\%\text{RH}) \times 10\%\text{RH} = 10^{-3}$) and inclusion-matrix interaction. It should be noted that only big inclusions (with surface larger than 50 μm^2) are taken into account, as the rest portion of inclusions with smaller size can't be detected at this scale of observation and consequently is considered as a part of clay matrix in this work. However, we think this yields no issue for representing the real microstructure: in fact, from equation 1.33, we could find that the big inclusions (> 50 μm^2) occupy more than 90% of the total volume of inclusions (see Fig.5.25). The total deformation is calculated and its ratio to free strain is plotted at Fig.5.26. It is shown that it also coincides with the prediction of high dilution model.

5.3.4 Influence of the elastic constant of clay matrix

For the simulation, the elastic modulus of different components in argillaceous rocks can be found in the literature. The elastic constant for carbonate and quartz is well determined and their average value weighted by their volume fraction is chosen as a unique value for the

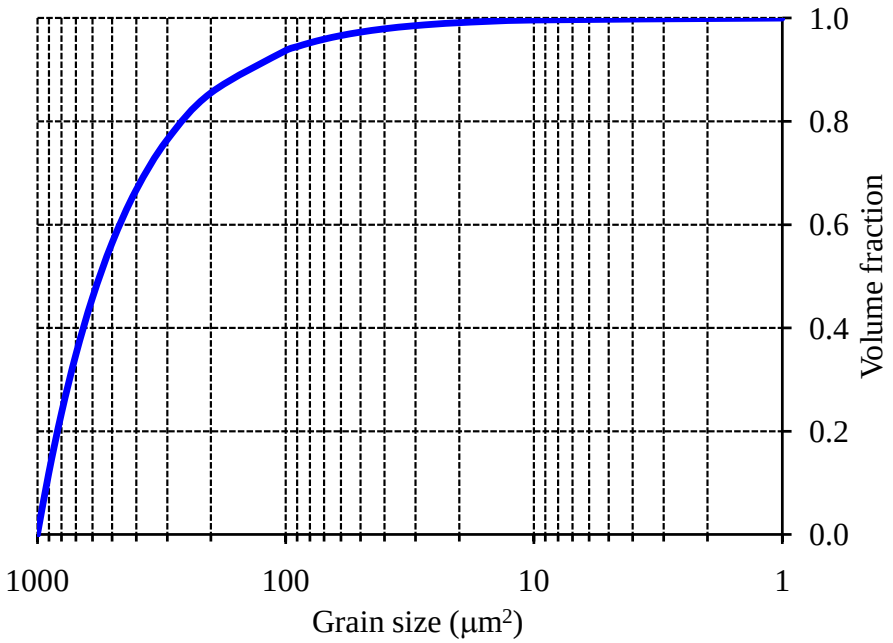

Figure 5.25: Grain size versus volume fraction.

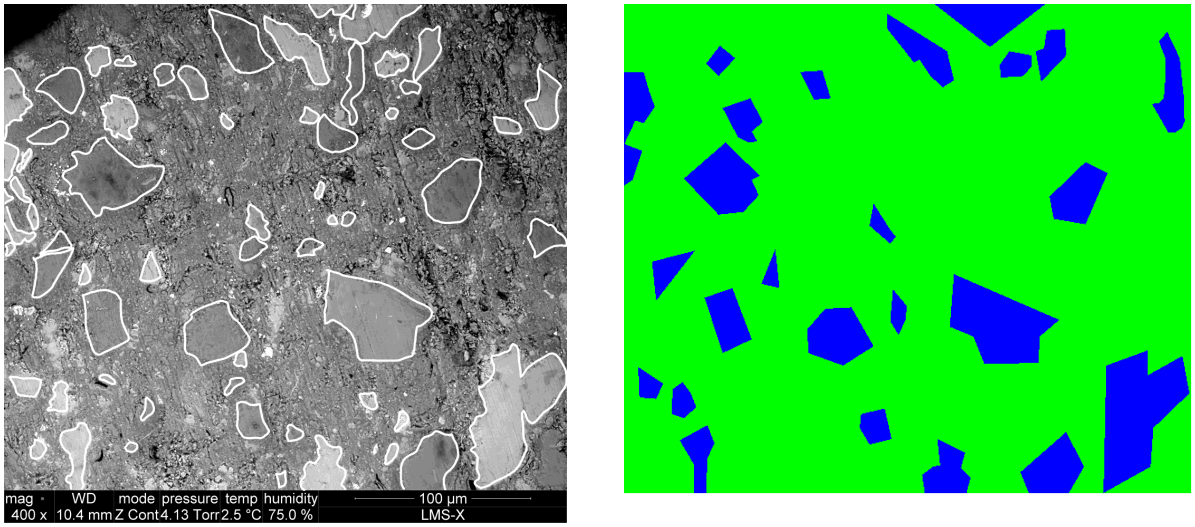

Figure 5.26: Modeling of a real microstructure: a) ESEM image of argillaceous rocks (the inclusions' contours are outlined in whit; b) modeling of microstructure (the green part represents the clay matrix, while the blue part represents the inclusion.

inclusion. However, the elastic modulus for clay matrix is actually variable, which is strongly controlled by its microstructure: orientation of clay particle, and density etc. Moreover, they are variable in function of its humid state: it is believed that the swelling of clay matrix during humidification would result in a loss of its elastic stiffness. That is why its value is often given by a range, for example 4 - 20 GPa in ANDRA rapport. A series of Young's modulus are chosen for clay matrix in the simulation to investigate its effect. The results (see Fig.5.27) show that the total deformation decreases with the Young's modulus of clay matrix. Accordingly, the coefficient c in the model increase with Young's modulus of clay matrix.

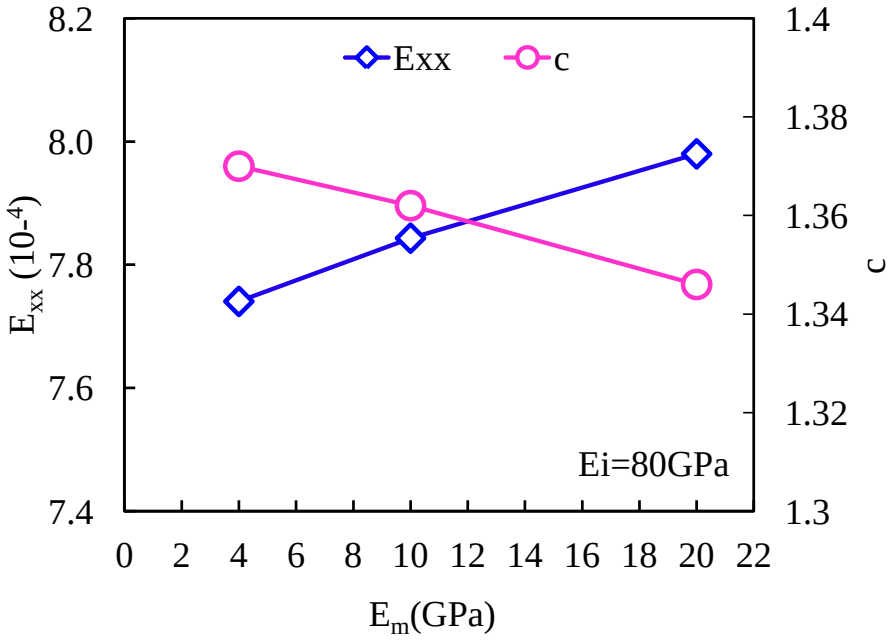

Figure 5.27: Influence of Young's modulus of clay matrix on the total strain and coefficient c.

5.4 Summary of chapter

In this chapter, the internal stress induced by self-restraint and inclusion-matrix interaction is investigated by analytical and numerical methods. For self-restraint, moisture gradient results in tensile stress at the desiccation (shrinking) surface, but compressive stress at the humidification (swelling) surface. Such moisture gradient induced stress reaches its maximum once hydric loading is achieved, prior to decreasing when moisture transport goes on. The tensile stress for desiccation case could lead to microcracking perpendicular to the drying surface, which is a common phenomenon for a wide range of shrinking materials (Jagla, 2002; Jenkins, 2005). The stress induced by self-restraint strongly depends on hydric loading rate, by which the moisture gradient is controlled. In general, the maximal stress increases with hydric loading rate.

For argillaceous rocks, the inclusion-matrix interaction results in tensile stress in the in-

clusion for humidification case (swelling clay matrix) and compressive stress for desiccation case (shrinking clay matrix). The radial tensile stress in humidification case possibly leads to interface separation or tangential microcracking in the matrix, whereas the tangential tensile stress in desiccation case potentially results in radial microcracking in the matrix. Besides, the presence of neighboring inclusions would perturb and intensify the internal stress field, and this amplification increases when the neighboring inclusion gets closer. It is worth to note that the effect of inclusion is different for transient state and steady state. For humidification case, for example, the presence of inclusion would amplify the compression induced by moisture gradient at transient stage, whereas, it leads to tension at steady stage.

The free surface effect on internal stress field has also been studied for a case of a single inclusion scattered at the free surface of clay matrix. The highest stress zone is found to be located on the inclusion-matrix interface a little below the free surface. For humidification, it undergoes high tension combined with a high shear pulling the inclusion out of the matrix. Generally, the high stress state is found at the steady state unless the stress of the inclusion-matrix interface near the free surface undergoes a sign changing: it is compressive at the beginning of humidification process mainly due to self-restraint and it decreases when moisture transport goes on. This demonstrates that self-restraint effect and inclusion-matrix interaction should be taken into account with together for the analysis of cracking and damage of arigllaceous rocks under hydric loading.

Besides the studies on the internal stress field, the total strain of argillaceous rocks under hydric loading is investigated. The high dilute model in micromechanics is proposed to resolve this problem, and it is valided by comparing with the modeling of periodic microstructure and real microstructure by finite element method.

Bibliography

ANDRA, 2005. Référentiel du Site Meuse/Haute-Marne: Tome 2.

Bisschop, J., van Mier, J.G.M., 2002. Effect of aggregates on drying shrinkage microcracking in cement-based composites. Materials and Structures 35, 453-461.

Bovet, D., Jouannna, P., Recordon, E., Saix, C. 1995. Experimental studies, Modern issues in Non-saturated soils. Gens A, Jouanna P, ScRHefler B. Eds, 159-21, Springer-Verlag.

Eshelby, J.D., 1957. The determination of the elastic field of an ellipsoidal inclusion and related problems. Proceeding of Royal Society of London. Series A 241, 376-396.

Jagla, E.A., 2002. Stable propagation of an ordered array of cracks during directional drying. Pysical Review E 65, 046147.

Jenkins, D.R., 2005. Optimal spacing and penetration of cracks in a sRHinking slab. Pysical Review E 71, 056117.

Jenkins, D.R., 2009. Determination of crack spacing and penetration due to sRHinkage of a solidifying layer. International Journal of Solids and Structure 46, 1078-1084.

Maleki, K., Pouya, A. 2010. Numerical simulation of damage-Permeability relationship in brittle geomaterials, Computers and Geotechnics. 37:619-628.

Mihai, I.C., Jefferson, A.D., 2011. A material model for cementitious composite materials with an exterior point Eshelby microcrack initiation criterion. International Journal of Solids and Structure 48, 3312-3325.

Pouya 2011: Porofis, Finite Element software for porous cracked media, Navier Laboratory.

Sator, C., Becker, W., 2012. Closed-form solutions for stress singularities at plane bi- and trimaterial junctions. Archive of Applied Mechanics 82, 643-658.

Tadanobu, I., Masaki, H., Shojiro, O., 1999. Disappearance conditions of thermal stress singularities based on stress intensity in two and three-phase bonded structures. International Journal of Fracture 96, 179-201.

Timm, D.H., Guzina, B.B., Voller, V.R., 2003. Prediction of thermal crack spacing. International Journal of Solids and Structure 40, 125-142.

Chapter 6

Discussion on hydromechanical behavior of argillaceous rocks

Contents

The combination of ESEM and DIC has been applied to investigate the behavior of argillaceous rocks under hydric (chapter 3) and mechanical (chapter 4) loadings at the scale of the composite microstructure. In addition, the internal stress field developed within such rocks under humidification/desiccation has been studied by modeling and numerical simulation in chapter 5 and appendix A. Based on these experimental investigations and modelings, the micromechanisms of strain and damage under hydric and mechanical loadings will be discussed and summarized in this chapter.

6.1 Behavior under hydric loading

6.1.1 Deformation mechanisms

The observation at micro-scale (chapter 3) in this work has revealed a heterogeneous deformation field when argillaceous rocks undergo a humidification/desiccation. Besides, such a heterogeneous deformation field is well correlated to their microstructure: the grains of carbonate and quartz do not swell so much, whereas the clay matrix swells significantly. These observations provide strong evidences that the behavior of argillaceous rocks under hydric loading is always a coupled problem of physics/chemistry and mechanics: it results from combined effects of a physic-chemical response of clay minerals (ε^h) under hydration/dehydration and a mechanical response (ε^m) produced by the complex interactions between different constituents, which are associated with the generation of a local stress field. The global deformation of such rocks under humidification/desiccation is the sum of these two responses:

$$\varepsilon = \varepsilon^h + \varepsilon^m \tag{6.1}$$

Three mechanisms of deformation and damage under hydric load can be distinguished:

- Physic-chemical swelling-shrinking of clay minerals as a function of the chemical potential of water (i.e. RH);
- Mechanical interactions between different constituents of such rocks induced by their incompatible free deformations under hydric load;
- Stress generated within the transient moisture transport process, during which local humidity states are heterogeneous leading to incompatible swelling/shrinking strains.

6.1.1.1 Physic-chemical swelling of clay minerals

Clay minerals play a predominant role for the behavior of argillaceous rocks under hydric loading: they significantly swell or shrink when RH varies. Such swelling property of clay minerals is predominantly due to their specific physic-chemical properties, besides the effect

of capillary pressure change as other standard porous solids. The change of the total volume of clay minerals consists, at the scale of clay particle, in a distancing of interlayer spacing (crystalline swelling) and inter-particle spacing (double-layer swelling), together with a change of the number of inter-particle pores (breakup of clay particle): increasing RH produces in general a decrease of the average number of layers per clay particle and accordingly an increase of the number of inter-particle pores (see the detailed discussion in section 1.3). Based on the above discussions, it is natural to deduce that the local swelling of clay particle is not isotropic: it is predominant along the direction perpendicular to the stacking of layers. Hence, the orientation of clay particles plays a crucial role for swelling.

6.1.1.2 Mechanical deformation due to heterogeneity

Argillaceous rocks exhibit a multi-scale heterogeneity, which would lead to an inhomogeneous free swelling inside the material under hydric loading. In general, three terms are responsible for this multi-scale heterogeneity of free swelling:

- At the scale of inclusion-matrix composite, clay matrix significantly swells when RH increases while inclusions (most carbonate and quartz) are not sensitive to water and so don't swell at all.
- Within the clay matrix, there are various groups of clay minerals of which the swelling properties are diverse: smectite swells greatly whereas illite and kaolinite swell hardly.
- The various orientations of clay particles also contribute to the heterogeneous free swelling.

The incompatibility of free swelling due to these inter-phase and intra-phase heterogeneities would generate a mechanical internal stress field which is the second deformation mechanism of the material under hydric loading.

The inclusion-matrix interaction, due to a free swelling of clay matrix, has been investigated by a modeling study in chapter 5. It is shown that the presence of non-swelling inclusions would inhibit the free swelling of matrix, and the mechanical response might be more important than the free swelling response (refer to Fig.5.2 where $\varepsilon^m/\varepsilon^h = 1.3$ at inclusion-matrix interface). The total strain of such composite is smaller than that predicted by a simple mixture law (the free swelling multiplied by the fraction of matrix), which is a good signature of such interaction (Fig.5.23). In addition, the role of such interaction would be more important when the mechanical stiffness of inclusion and matrix become more contrasted (see Fig.5.27).

It should be noted that the mechanical stress field is related not only to inclusion-matrix interaction, but also to the heterogeneity inside the clay matrix. In fact, the observation in this work has evidenced that the local swelling field in the clay matrix is also heterogeneous (refer to the swelling maps in chapter 3), which reveals such an intra-phase heterogeneity inside the clay matrix: different groups of clay minerals (smectite, illite, kaolinite etc.) which own contrasting

swelling properties, variable orientation of clay particle and so on. This would lead to a complex interaction inside the clay matrix, even without the presence of inclusions. We emphasize one important phenomenon related to such intra-phase heterogeneity: micro-macro interaction. In fact, the physic-chemical swelling of clay minerals is indeed the motor of swelling. However, macroscopic swelling is not only associated with this physic-chemical swelling, but also with a structure rearrangement activated by the former (see detailed discussion in section 1.3.3).

6.1.1.3 Self-restraint effect

When moisture transport takes place between specimens and their surroundings, a moisture gradient develops inside the material during the transient stage, causing differential swelling /shrinking. This deformation incompatibility also leads to a mechanical stress field which is the origin of the third deformation mechanism. It is worth noting that the moisture gradient might exist at the scale of the sample in which it can be generated between the surface and the core of the sample (Fig.A.4). It may also act at the smaller scale of the microstructure in which transport is heterogeneous as a consequence of contrasting transport properties of different phases of material (for example in Fig.5.9).

This mechanism is also investigated by modeling in chapter 5 and Appendix A. It is shown that self-restraint results in a compressive (tensile) stress at the outer-part of specimens and a tensile (compressive) stress at the inner-part during humidification (desiccation) process. Such stresses attain their maximums at the end of hydric loading (variation of the relative humidity of environment) or a little later, and vanish gradually when moisture transport goes on (see Fig.A.5 - A.7). Hence, this third mechanism does not induce any observable effect in the final equilibrium state in elastic condition, whereas it may play an important role if plasticity or damage is generated during such transient stage. In particular, during desiccation, the tensile stress developed parallel to the drying surface may cause microcracks perpendicular to this surface.

Effect of hydric loading rate

From the experimental observations in this work, the microcracking due to humidification/desiccation is usually activated during the hydric loading stage, which implies a crucial role of this third mechanism on the microcracking. Hydric loading rate plays a key role for self-restraint effect, which has in fact been revealed by this work: for a sample (with 1 millimeter thickness, and several millimeters extension) undergone a humidification, there is no obvious microcracking until 99%RH under 2%RH/min hydric loading (test #2 in chapter 3), whereas it is already abundant at 90%RH for the case of 20%RH/min (test #6 in chapter 3). The effect of hydric loading rate, as well as specimen size, have been investigated by the modeling study: the magnitude of the self-restraint stress increases with the two factors (Fig.5.22 and A.15 - A.17).

Combination of inclusion-matrix interaction and self-restraint effect

The self-restraint stress leads to a local stress field inside samples, and the presence of rigid inclusions would amplify it (as shown in Fig.5.18 of section 5.2). Moreover, inclusions are also responsible for inclusion-matrix interaction. It is emphasized that the two effects are inverse from the modeling study in this work. For the case of desiccation, the self-restraint effect would generate significant tensile stress near the drying surface, which would be intensified by the inclusion. However, the interaction between the inclusion and the shrinking clay matrix would result in compressive stress near the inclusion-matrix interface (see section 5.2.1). Finally, the total local stress is indeed a sum of the two terms. Therefore, the combination of inclusion-matrix interaction and self-restraint effect should be accounted for (Fig.6.1).

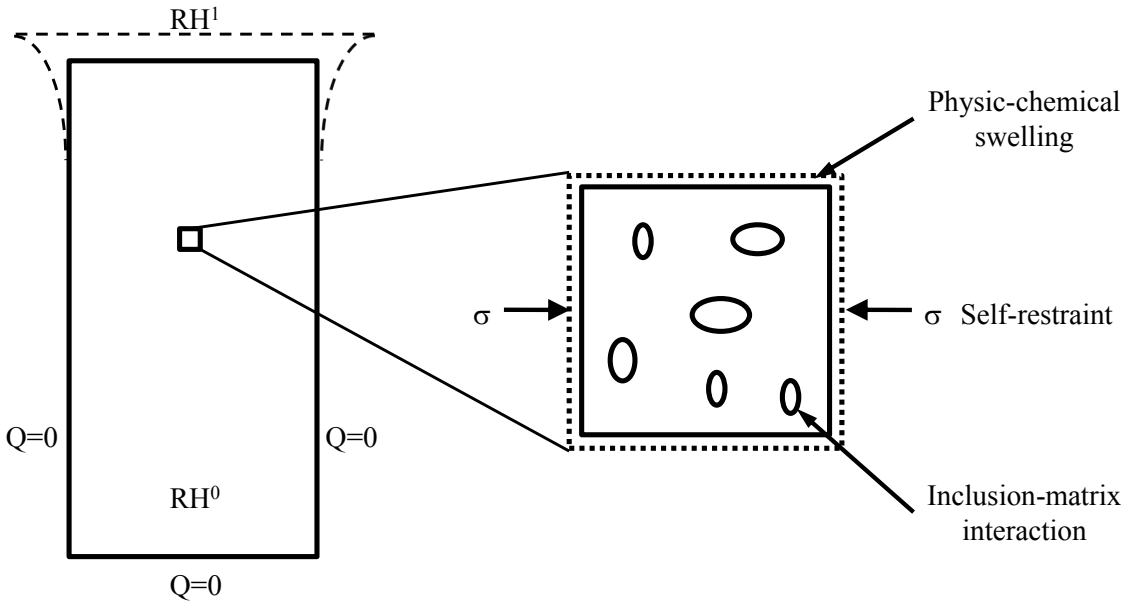

Figure 6.1: Combination of inclusion-matrix interaction and self-restraint effect.

Let us recall that, although the evolution of local swelling strains inside the clay matrix with RH is strongly nonlinear, our tests have revealed that the spatial distribution of the local strain fields do almost not evolve: they evolve only in intensity. This is true as long as the humidification is sufficiently slow (see test #2 of chapter 3). In such a case, the equations governing the local behavior may reasonably well be written in the following simple hydric-elastic form:

$$\sigma(x) = g(\mathrm{RH}) \cdot C^0(x)(\varepsilon(x) - f(\mathrm{RH}) \cdot \varepsilon^h(x)) \tag{6.2}$$

where $\sigma(x)$ and $\varepsilon(x)$ are the local stress and strain at position x in the microstructure, respectively. The mechanical interactions are governed by the heterogeneous tensor of elastic moduli

$C(x)$, and the swelling strains ε^h are non null only in the matrix. $g(\text{RH})$ accounts for the effect of humidity state on the mechanical properties of the material (see section 6.3), and $f(\text{RH})$ considers the nonlinear swelling of clay, which would be discussed in the following.

6.1.2 Anisotropic swelling

Under humidification, argillaceous rocks exhibit an anisotropic deformation: they swell predominantly along the direction perpendicular to the bedding plane (test #3 and #5 of chapter 3). Such anisotropy has not been observed in the bedding plane (test #3 and #4 of chapter 3). From the viewpoint of micromechanics, anisotropy is generally related to the anisotropy of properties of individual constituents or to texture. For the three main phases of argillaceous rocks, carbonate and quartz don't swell and their elastic properties can be reasonably considered to be isotropic. However, the hydric and mechanical behaviors of clay particle are anisotropic: they are strongly controlled by the orientation of clay particles. Concerning texture anisotropy, several terms can be distinguished for argillaceous rocks: 1) form, orientation and distribution of inclusions, 2) orientation of clay particles.

Based on the observation in this work as well as the existing results from literatures, the texture anisotropy of inclusions is not strongly manifested for Callovo-Oxfordian argillaceous rocks. From our observations (see Fig.3.20), it is demonstrated that the anisotropic swelling is essentially related to a preferred orientation of clay particles which coincides with the bedding plane. The orientation of clay particles is controlled by certain factors: 1) bedding process, 2) form and distribution of inclusions (as clay particle trends to wrap the neighboring inclusion). It should be noted that the preferred orientation of clay particles is less pronounced than in other argillaceous rocks (refer to Fig.1.9).

Therefore, we suggest that, for Callovo-Oxfordian argillaceous rocks, the contribution of anisotropic form and distribution of inclusions is limited. Anisotropic deformation is predominantly related to the bedding process by which the 2D clay particles tend to get orientated parallel to the bedding plane.

6.1.3 Behavior under humidification

6.1.3.1 Nonlinear deformation at high RH

From our observation, argillaceous rocks exhibit a nonlinear swelling during humidification: it is moderate and somewhat linear at low RH but becomes important for high RH. The threshold of this nonlinearity for Callovo-Oxfordian argillaceous rocks is about 80%RH from this work, which coincides with the results at macro-scale (Valès, 2008). Besides, there seems to be another threshold of nonlinearity at about 95%RH, as revealed in test #2 of chapter 3 (75%RH - 99%RH humidification). The nonlinearity still exists when the deformation evolution is plotted versus

suction (or capillary pressure).

The deformation of porous solids under humidification/desiccation can generally be described by the theory of poromechanics. In fact, the swelling of argillaceous rocks at the beginning linear part (< 80%RH) is certainly in this case. As shown in appendix A, a moderate humidification experience (47%RH - 56%RH) can be well reproduced by a poroelasticity model. The good prediction of poroelasticity suggests that the swelling in moderate RH range seems to be predominantly controlled by variation of capillary pressure, which is the key phenomenon addressed in standard poromechanics theory. However, at high RH range, the swelling is quite significant, so that it can't be only explained by the loss of elastic stiffness at high humidity state. Hence, the significant swelling at high RH can't only be attributable to variation of capillary pressure, and there are some other mechanisms.

One potential origin of the significant swelling is the microcracking due to humidification, as discussed in section 1.5. In fact, this is demonstrated in this work (test #6 of chapter 3). However, we have demonstrated, in test #2 of chapter 3, that microcracking is not the only mechanism. The nonlinear swelling can also be attributable to the nonlinear swelling of the clay matrix itself at high relative humidity (particularly the physic-chemical swelling).

Nonlinear swelling of clay minerals

Let us go back to the three mechanisms of physic-chemical swelling of clay minerals: crystalline swelling, double-layer swelling, and breakup of one big clay particle into smaller ones. In fact, double-layer swelling exhibits a nonlinearity (see Fig.1.14). Considering porosity distribution in Callovo-Oxfordian argillaceous rocks (mesoporosity occupies 86% of the total porosity), we can deduce that the nonlinearity exhibited in double-layer swelling is appreciably responsible for the nonlinear swelling of such rocks. In addition, the third swelling mechanism (breakup of clay particles) is not triggered at moderate RH range, whereas it becomes significant at high RH level as elementary layers are sufficiently separated. This could also increase the nonlinearity of swelling.

In general, 95%RH can be considered as the upper limit of the two-layer hydration state for both clays. Note that 95%RH is also the second threshold of nonlinearity revealed in this work. This may suggest that the extremely significant swelling starting from 95%RH is probably related to a transition from 2 to 3 layers of crystalline swelling.

Nonlinear swelling of argillaceous rocks

From above discussions, the two main mechanisms of nonlinear swelling (as a function of RH) can be identified: 1) nonlinear physic-chemical swelling of clay minerals; 2) nonlinear behavior of such rocks (in particular microcracking due to humidification). The effect of capillary pressure is responsible for the nonlinearity when strain is plotted as a function of RH (due to the nonlinear relationship between RH and capillary pressure in Kelvin's law), but its contri-

bution to nonlinearity would vanish when strain is plotted as a function of capillary pressure in the context of poroelasticity. Moreover, the plastic deformation induced by inclusion-matrix mechanical interaction would be also contributable to the nonlinear swelling of argillaceous rocks. However, it is not abundant from the observations of this work: plastic deformations are located at some isolated small domains so that the overall deformation is somewhat reversible after a humidification-desiccation cycle (refer to test #6 of chapter 3). Hence, we think that the contribution of inclusion-matrix mechanical interaction to the nonlinearity of swelling is very limited.

Two-staged swelling of argillaceous rocks

To summarize, a two-staged swelling of argillaceous rocks can be recognized:

Under humidification within the moderate RH regime ($< 80\%$RH), the deformation of the material is moderate and somewhat linear. In this stage, the effect of capillary pressure seems to plays a predominant role for the deformation. The contribution of physic-chemical swelling of clay minerals is very limited. Within such RH regime, the deformation can be described by the standard poroelasticity model.

For the humidification at high RH level ($> 80\%$RH), a significant fraction of the deformation seems to be due to the physic-chemical swelling of clay minerals. Capillary pressure effect still operates, but its contribution becomes less important. This stage can also be divided into two sub-stages. 80% - 95% perhaps involves a transition from 1 to 2 layers of crystalline swelling, while a transition from 2 to 3 layers would occur from 95%RH. These transitions would be accompanied by a breakup of big clay particles, which would reinforce the nonlinearity.

Two (or three) staged swelling is merely a rough estimation of the contributions of different swelling mechanisms. In a following work, a more sophisticated microscopic model may be elaborated. In fact, the porous space in argillaceous rocks owns a wide range of size distribution, and they are governed by different bonds and related to different swelling mechanisms (refer to section 1.3). In the modeling, such information should be accounted for (for example, a tri-porosities model), so that the contribution of different mechanisms (at least capillary pressure, crystalline swelling and double-layer swelling) can be investigated quantitatively. Furthermore, the structural rearrangement due to the swelling, such as the double structure concept (see section 1.3.3), might also be incorporated in the model.

6.1.3.2 Microcracking due to humidification

As discussed in the preceding section, the nonlinear swelling of argillaceous rocks might be related to the microcracking due to humidification (particularly at extremely high RH). It is activated during the hydric loading stage (variation of the environment RH), and it is strongly controlled by the humidification rate. In general, the microcracks due to humidification are located not only in the clay matrix, but also at grain boundaries. Moreover, we have evidenced

that these microcracks own a preferred orientation under free swelling condition (without external mechanical loading): parallel to the bedding plane.

From preceding discussions, the local stress due to the heterogeneity as well as the self-restraint effect might be a mechanism of the microcracking at inclusion-matrix interface due to humidification. In addition, we argue that such microcracking is also related to the physic-chemical swelling of clay minerals itself, principally to the breakup of clay particles during humidification. When increase of interlayer spacing due to crystalline swelling reaches a critical value (i.e. hydration with four layers of water), the inter-layer forces may undergo a complete reversal from being attractive to being repulsive and one large clay particle would break into several smaller ones. We argue that such transition from interlayer space to inter-particle space is probably responsible for the initiation of microcracking in the clay matrix under humidification.

6.1.4 Behavior under desiccation: microcracking due to desiccation

Besides microcracking due to humidification, our observations have found that microcracking can also operate during desiccation. Similar to the microcracking due to humidification, the microcracking due to desiccation is activated during the hydric loading stage and the desiccation rate also plays a key role. However, the locations of the microcracking due to desiccation are different from the case of humidification: it is mostly found in the clay matrix. Such disparity implies that they are controlled by different mechanisms for the two cases.

Obviously, the local stress is certainly responsible for both types of microcracking. Besides this common mechanism, there are also other special ones for each case. In fact, the microcracking due to desiccation can belong to the problem of shrinkage cracking which has been extensively investigated (see the discussion in section 1.5). The shrinkage cracking is essentially due to the tensile stress caused by various restraints which can be generally classified into two types: external restraint (such as restraining substrate) and internal restraint (essentially the non-uniform shrinkage of the specimen). For our tests in which specimens were deposed directly on the platform of Peltier module so that there is no external confinement (refer to section 4.1), the microcracking is only due to the self-restraint effect. During the transient desiccation regime, a moisture gradient develops across the drying direction which accordingly leads to a contraction gradient inside the specimen. This results in a restraint by inner parts of shrinking element where the moisture loss is slower. Such contraction gradient causes microcracks perpendicular to the drying surface when the tensile stress is enough important: a microcrack nucleates on the drying surface of the specimen where tensile stress is maximal and it subsequently propagates along the drying direction.

Due to the dimension of specimens (thickness less than 1 millimeter and several millimeters for in-plane extension) and the lower side of specimen being in contact with the Peltier module

(moisture exchange from this side can be considered impossible), the desiccation test in our investigation can be considered as one-dimensional (along the thickness), one side (from upper side of specimen) desiccation problem and the plane of observation coincides with the desiccation surface. The observation of specimen' surface evidenced a network of microcracking due to desiccation with a preferred orientation parallel to bedding plane, contrasting with a polygonal pattern on desiccation surface as discussed in the existing literature. This difference is actually related to the anisotropic deformation of argillaceous rocks due to stratification. Argillaceous rocks prefer to deform in the direction perpendicular to the bedding plane, which results in the maximal tensile stress also occurring in this direction.

The influence of desiccation rate has been evidenced in this work: for the typical thickness of specimens, the moderate rate for the first two steps of desiccation (10%RH decrease with a hydric loading rate of 5%RH/min) hardly results in microcracking, but a notable microcracking occurs under higher rate of desiccation for the last step (45%RH decrease with a loading rate of 20%RH/min). The influence of hydric loading rate and specimen thickness has been investigated in chapter 5 and appendix A. The stress induced by self-restraint effect (the risk of microcracking) would increase with both factors. Hence, there is a critical specimen thickness and a critical desiccation rate below which contraction gradient is too small to generate significant tensile stress causing microcracking. Moreover, such a risk of microcracking would increase with the presence of inclusions, since the latter will intensify the stress field produced by moisture gradient (as discussed in the first section of this chapter). It should be noted that the present simulation work is really a qualitative investigation. In the further, a more sophisticated simulation (for example, accounting for a more realistic microstructure and boundary conditions) can be conducted. And the results can be compared with the experimental results to realize a quantitative analysis of the material: for example, an identification of the tensile strength from recognizing the critical hydric loading rate by experimental studies.

Since the observation is only performed on the surface of the specimen, the depth of such microcracking due to desiccation is unknown and so the theoretical prediction of crack spacing and depth doubling process can't be evidenced. In the following work, the micro-tomography might be used, which yields the possibility of a 3D reconstruction of the network of microcracks after desiccation/humidification. However, the spatial resolution of micro-tomography is worse than ESEM. Hence, the combination of ESEM and micro-tomography is also promising: determination of strain field on the sample surface by ESEM, combined by a real 3D identification of microstructure by micro-tomography.

6.1.5 Discussion on the microcrackings due to humidification/desiccation from simulation results

From the observations in this work, the microcracks due to humidification are located not only in the clay matrix, but also on the grain boundaries. The latter implies that such a microcracking perhaps links to the inclusion-matrix interaction which leads to a maximal stress at grain boundaries and decreases gradually with distance. For the steady regime, the simulation work in chapter 5 has revealed that stress at the inclusion-matrix interface would be tensile for a swelling clay matrix (humidification), while it is compressive for desiccation. The microcracking is always observed during the hydric loading stages, implying an important role of self-restraint effect. However, for the transient regime, the effect of inclusions is totally different from that for the stationary regime: the presence of inclusions would intensify the tensile (compressive) stress for the case of desiccation (humidification). Hence, we can deduce that the risk of microcracking at inclusion-matrix interface might be greatest at the beginning of desiccation. However, the experimental results show that there is no microcracking at grain boundaries for the case of desiccation, whereas it exists for the case of humidification!

Experimental observations in this work are conducted on the sample surface, which involves a free surface. Based on such an experimental condition, an inclusion at free surface during moisture transport process is modeled (section 5.2.3). The results reveal a high shear at the inclusion-matrix interface: for humidification, it tends to pull the inclusion out of the matrix (see Fig.5.12). Hence, for the experimental condition in this work, it might be the shear stress which plays a predominant role for the microcracking at the inclusion-matrix interface, rather than the tensile stress. This is demonstrated by the experimental observation in which a relief is always observed after the microcracking. However, why is there no microcracking at the inclusion-matrix interface during desiccation, since the shear stress would develop whatever desiccation or humidification? We suggest that the tensile strength of clay matrix is perhaps smaller than the shear strength of the inclusion-matrix interface. Hence, in the case of desiccation, the tensile stress due to self-restraint would lead to a microcracking in the clay matrix more easily. And this microcracking will results in a stress release so that there is no microcracking at the inclusion-matrix interface. As discussed before, under desiccation, the tensile stress due to the self-restraint at grain boundaries would be counteracted by the compressive stress due to inclusion-matrix interaction. The combination of the two inverse effects may results in the maximal tensile stress not being at grain boundaries, which might also explain the absence of microcracking at the inclusion-matrix interface during desiccation.

6.1.6 Irreversible deformation under hydric loading

Besides the microcracking, the results in this work have evidenced some irreversible deformations under hydric loading, mostly being found in clay matrix. In general, these irreversible

deformations can be distinguished into two types: 1) the plastic deformation of clay matrix caused by the mechanical stress, 2) the irreversible deformation associated with structural alteration of clay minerals during hydration-dehydration cycles.

Test #6 of chapter 3, in which two domains of clay matrix show similar swelling behavior during humidification but exhibit quite disparate irreversible deformation magnitudes, evidences the first mechanism. As discussed in the preceding section, a local stress field would be generated due to the incompatibility of free swelling in argillaceous rocks. When some local stresses exceed the elastic limit, plastic deformation would be produced. Since the yield stress of clay matrix is in general much smaller than those of grains of carbonate and quartz, plasticity is principally activated in the clay matrix.

When RH changes, some swelling phenomena would occur in the porous spaces of argillaceous rocks: interlayer space, inter-particle space etc. Moreover, these physic-chemical swellings as a function of RH (microscopic strain), would result in a structural rearrangement (macroscopic strain). This is why the sum of microscopic strain is not identical to the bulk volume change of the material. The upscaling of physic-chemical response, principally interaction of micro-macro pores, should be taken into account for the swelling behavior of argillaceous rocks. The principle of double structure concept is discussed in detail in section 1.3. In general, physic-chemical swelling depends exclusively on RH, thus it can be considered to be reversible. Indeed, this has been demonstrated by Montes-H (2002) who observed a nonlinear, significant swelling of smectite aggregates (50%) but with slight irreversibility. The strain due to structure rearrangement is certainly elastoplastic: it may be irreversible in both cases of humidification and desiccation. And the difference of these irreversible deformations would exhibit a residual deformation after a humidification-desiccation cycle.

Structural rearrangement can be incorporated into the mechanical strain in equation 6.2, since the mechanical stress is not only due to the inclusion-matrix interaction but also because of the heterogeneity within the clay matrix. However, we still distinguish the two terms here: plastic deformation is generally responsible for some irreversible shear strain (without irreversible volumetric strain), whereas the residual volumetric strain (a contraction revealed in this work) is principally due to the structural arrangement.

These irreversible deformations are actually local phenomena: they are located at some quite small domains of the material. Moreover, the nonlinear phenomena are interacted sometimes: for example, the residual contraction could be counteracted by the residual expansion induced by irreversible microcracking (as shown in test #5 of chapter 3). All these local irreversible phenomena may finally result in an apparent reversible deformation or a slight irreversible deformation at macro-scale after a humidification-desiccation cycle. Therefore, a reversible deformation after a hydric loading cycle, as shown by most of the existing results, doesn't imply that the material returns to its initial state. Moreover, the microcracking revealed in test #6 of chapter 3 is so small (with openings at the order of 1 micrometer) that the sample

seems to remain intact even after the test. However, their further propagation and coarsening might produce fatal problems for the long-term storage.

Finally, it should be noted that a reversible macroscopic strain, accompanied by some local irreversible phenomena, is indeed a fatigue problem. Unfortunately, only a hydric loading cycle has been conducted in this work. For the following work, more humidification-desiccation cycles should be accomplished to investigate the evolution of these nonlinear phenomena, which is crucial for the long-term storage.

6.1.7 Influence of inclusions on orientation of clay particles

The local strain gauge length in this work is several micrometers, which is comparable to the typical size of clay particle. Hence, the direction of local major principal strain can be considered as a qualitative indicator of orientation of clay particles (see discussion in test #4 and #5 in chapter 3). Accordingly, the orientation of clay particles in observation zones can be qualitatively studied, as shown in Fig.3.20, and it seems to be sometimes controlled by the inclusion at its neighborhood. In fact, to drape the inclusion, the clay platelets tend to get orientated along its boundary: the particle orientations are generally horizontal on the top and bottom sides, while they are vertical and inclined on the lateral sides. Under humidification, the principal swelling directions are different due to these variable orientations. They are vertical on the top and bottom sides, and horizontal on the lateral sides, which has been revealed by the experimental results (refer to Fig.4.71). It should be noted that such principal swelling direction distribution is not only related to the clay particle orientation, but also due to inclusion-matrix mechanical interaction: the induced strain owns a similar principal direction as mentioned above.

6.2 Behavior under mechanical loading

6.2.1 Deformation mechanisms

Based on the observation in chapter 4, the deformation mechanisms of argillaceous rocks under mechanical loading have been identified at the scale of their composite microstructure. In general, a heterogeneous strain field is generated under mechanical loading, but it is well correlated to the microstructure of such rocks: the clay matrix deforms more than the inclusions. This is essentially related to the contrasting modulus of the two phases: the inclusion is more rigid than the clay matrix. However, the inclusions play of crucial importance role for the behavior of such rocks under mechanical loading. Firstly, their boundaries are favorable places for damage, involving not only the tensile vertical microcracking but also the inclined microcracks activated by shear deformation (see Fig.4.36 for example). Secondly, the presence of inclusions strongly

affects the orientation of clay particle surrounding them: the clay particles tend to wrap the inclusion so their orientations are controlled by the inclusions' shapes and orientations, as discussed in the preceding section. Due to the anisotropy, the orientation of the clay particle is decisive for its mechanical response (refer to Tab.1.3).

The strain field in the clay matrix is also heterogeneous, due to the inclusion-matrix interaction and the intra-phase heterogeneity in the clay matrix. Typically, three deformation bands (intensive deformation domains) can be distinguished according to their orientations: 1) horizontal band, 2) inclined band, and 3) vertical band (refer to Fig.4.23 for example). Note that the uniaxial compression direction is vertical for this discussion. From this classification, the general deformation mechanisms have been identified in this work, and can be summarized as following:

- The horizontal bands are generally found in the macropore-rich zones or some pre-existing horizontal microcracks. The deformation of such band involves the compaction of the former and the closing of the latter. Note that the macropores here correspond to the inter-aggregate (inclusion-matrix and between clay aggregates) pore spaces in the argillaceous rocks. In fact, the mesopore (inter-particle) and the micropore (inter-layer) seem to be hardly affected by the mechanical loading, since they are controlled by stronger physical and chemical bounds.

- The inclined bands are principally related to shear deformation. According to their locations, two sub-types can be recognized. Firstly, the shear band can be associated with shear deformation developed in the clay matrix. It is emphasized that such shear deformation is strongly controlled by the orientations of clay particles (refer to Fig.4.78 of test #7 in chapter 4). Since the sliding between the elementary layers is easier to be activated compared to other shear deformation ways, the high shear deformation is normally in the case when the orientation of clay particle approaches the direction of greatest shear component of the stress tensor. Besides, the shear bands sometimes consist in sliding, typically on the inclusion boundaries. Normally, this friction problem can be described by Coulomb's law. Hence, the inclusion's shape and orientation is of crucial importance: the elongated inclusion orientated close to the critical angle is more favorable for activating the sliding (see Fig.4.38 of test #3 and Fig.4.60 of test #6 in chapter 4).

- The vertical bands are typically associated to the vertical tensile microcracking, which is located mostly at the inclusions' boundaries or in the clay matrix (refer to Fig.4.62). Note some vertical microcracks are found in the "gross" inclusions which are actually assemblies of sub-grains (see Fig.4.31). The vertical microcracking is strongly related to the shear deformation. The tensile microcrack generated at the tip of one shear band is one typical case (Fig.4.49).

It is worth noting that these deformation bands are sometimes connected, implying a strong interaction and coupling between them. For example, the networks of compaction and shear bands (Fig.4.44 for example), as well as the tensile microcracking activated by the shear deformation or the sliding (Fig.4.46 for example), are both evidenced in this study.

6.2.2 Role of macropores and pre-existing microcracks

Argillaceous rocks of Callovo-Oxfordian are indeed a porous medium: their reference porosity is 18%, while for the macropores it is 1.8%. Besides, pre-existing microcracks can be found in such rocks frequently, notably for the high humidity state (microcracking due to humidification). These empty spaces are important for the deformation of the material. From the observation in this work, the behavior of pre-existing microcracks under mechanical loading is strongly influenced by their orientations. Consider the loading direction is vertical. In general, the horizontal microcracks would close under loading, whereas the vertical ones tend to open and propagate. For the slanted microcracks, the mechanical loading probably leads to the sliding between their two lips (see discussion in test #6 of chapter 4). The macropore-rich zones generally form compaction bands under mechanical loading. The high deformation associated to the pre-existing microcracks and macropore-rich zones is predominately contributable to certain macroscopic behavior of argillaceous rocks: the concave upward portion at the beginning of loading, as well as the plastic deformation appearing even at low stress level. The plastic deformation at low stress level should be distinguished with that developed at high stress level (before the failure of the material): the former involves the irreversible compaction of pore spaces, while the latter consists in the plastifying process (for example the activation of sliding system) and the microcracking.

The pre-existing microcracks and macropores are both empty space. Hence, they can be considered as one material of which the mechanical behavior is similar. In particular, one initial strain-stiffening portion can be characterized for these two zones. The mechanical loading results in the compaction of such vide spaces and consequently a densification process: the deformation modulus would increase with the strain accumulation. Note that a considerable part of such deformation is irreversible, and this is one reason for appearance of the plastic deformation at low stress level. Moreover, we consider the pre-existing microcracks as one special empty space: it closes entirely at very low stress. Hence, the inflexion point (the finishing of strain-stiffening part) is extremely low and generally no more plastic deformation is generated afterward (Fig.4.48). However, the strain-stiffening portion can cover a wide stress range for macropore-rich zones (Fig.4.27).

In rock mechanics, the typical stress-strain is generally divided into four regions: 1) a concave upward portion involving in the closing of pre-existing microcracks, 2) a nearly linear portion, 3) a non-linear portion with decreasing slope, and 4) the post-failure portion after

the peak stress (Hundson and Harrison, 1997). From the observations on argillaceous rocks, the initial concave upward appears usually, except for one extremely dry case in test #1 of chapter 4. However, the second linear portion doesn't appear for argillaceous rocks. Although the apparent linear portion is also observed in some tests, the unloading is this region reveals always the increase of Young's modulus and plastic deformation evolution due to the compaction of the macropores. Hence, we propose that the secondary region can be incorporated into the first region for the porous rocks (such as argillaceous rocks) where the collapse of porosity is one decisive mechanism for the deformation during this state. Hence, the stress-strain relation should be rewritten in a non-linear poroplasticity form:

$$\underline{\underline{\sigma}} = \underline{\underline{\underline{\underline{C}}}}\,(\varphi) : \left(\underline{\underline{\varepsilon}} - \underline{\underline{\varepsilon}}^{p}\right) - \underline{\underline{\underline{B}}}\,(\varphi)\, P_c \tag{6.3a}$$

$$\varphi - \varphi_0 = \underline{\underline{\underline{B}}}\,(\varphi) : \underline{\underline{\varepsilon}} + \frac{P_c}{M\,(\varphi)} \tag{6.3b}$$

where P_c is the capillary pressure. ε^p is the plastic strain. C, b and M are respectively stiffness tensor, Biot's coefficient and Biot's modulus of the material. They all depend on porosity (φ). Qualitatively, when porosity increases, the stiffness decreases (Fig.1.36), while the Biot's coefficient increases (Fig.1.37).

6.2.3 Damage mechanisms

Under mechanical loading, some damage phenomena are evidenced at micro-scale in this work. In general, some vertical and inclined microcracks can be generated. The vertical microcracks are typically located in the clay matrix, at the inclusions' boundaries, and inside the gross inclusions (refer to Fig.4.62 for example). Note that a great quantity of such vertical microcracks is related to shear deformation. The tensile microcracking at the tip of shear band is one common phenomenon. There are also some microcracks are generated by the local concentration of tensile stress, notably for the pre-existing vertical microcracks and on the inclusion contacts. For the inclined microcracks, they are mostly related to the sliding on the inclusions' boundaries. This is strongly influenced by the inclusion's shape and orientation. Typically, the inclined elongated inclusion is favorable to activate the sliding. The inclusion's boundary plays a key role for the damage due to its weak cohesion. The microcracks prefer to propagate along their boundaries even with some deviations (see Fig.4.15 - 4.16).

The failure of the material is generally related to fault, as shown in the tests of chapter 4. Note that the faults are not always straight, they are sometimes echelon-shapes (see Fig.4.30 for example). Besides, some vertical fractures due to splitting are often observed, of which some are connected to the main fault.

6.3 Influence of humidity state on the mechanical behavior

The mechanical behaviors of argillaceous rocks with different maintained humidity states have been investigated by the first six tests of chapter 4, and the main macroscopic mechanical properties are summarized in Tab.4.2 and in Fig.4.80. Besides, the mechanical behavior of a unique sample with three RHs has been studied in test #7 of chapter 4. From these observations, some features regarding the influence of humidity states (water contents) on the mechanical behavior of argillaceous rocks can be derived:

- For the pre-peak behavior, the deformability of such rocks increases with the humidity state. This phenomenon actually involves two terms. Firstly, at higher humidity state, the plastic deformation is activated at lower stress state and its magnitude is more significant. For example, no irreversible phenomena appear until 20 MPa for the case of 2.2% water content (test #1 of chapter 4), while plastic strain can reach 0.2% even under 4 MPa loading for the case of 10.1% water content in test #6 of chapter 4. Secondly, the elastic Young's modulus becomes smaller when the rocks are more humid. Besides the greater deformability, a concave upward portion emerges at the beginning of the stress-strain curve for the humid specimen, whereas this portion disappears for the dry state (for example 2.2% water content in test #1 of chapter 4). Regarding local strain maps, some shear bands have been observed even at extremely dry state, but they are somewhat reversible. At wet state, shear bands become more diffuse compared to those at dry state. Sliding along the inclusion boundaries seems to be activated more easily at wet state. Besides, more vertical bands are observed at wet state, which are related to opening of some pre-existing microcracks parallel to the loading direction (Fig.4.80).

- When the specimens of argillaceous rocks become more humid, we observed that their failure mode seems to undergo a brittle-to-ductile transition. For the dry specimen, the stress-strain curve is quasi-linear for a great portion before its failure. For the high humidity state, the linear portion is very limited and a considerable strain-softening portion is observed before the failure. Besides, the peak stress is very high for the dry specimen. For example, the peak stress for 2.2% water content (test #1 of chapter 4) is more than 38 MPa, whereas that for 10.1% water content (test #6 of chapter 4) is merely 16.3 MPa. Regarding the failure mechanism, the fractures of specimen are rather related to splitting: they orientate in a direction very close to the loading direction. However, the faulting becomes predominant for the failure of humid specimen. It is worth noting that the secondary fracture and microcracking are more intense for the high humidity state: the specimen in test #7 of chapter 4 (7.0% water content) is really crushed, while

only two fractures accompanied by one secondary crack are observed for the test #2 of chapter 4 (3.1% water content).

It is well recognized that water pressure plays a crucial role for the mechanical behavior of porous solids, as investigated in the context of poromechanics. This can be extended to the effect of relative humidity (or suction) for the unsaturated case. Typically, the variation of suction due to humidification/desiccation would alter effective stress and the deformation of porous material is variable for the same total stress. However, this can't be applied to explain our tests where the uniaxial compression test is conducted on the specimen at different but constant humidity states: suction doesn't vary during the mechanical test. Actually, the contrasting mechanical behaviors of argillaceous rocks in our tests are essentially related to the evolution of the material due to the history of loading, in particular altering the microstructure due to its specific swelling property.

In general, the influence of argillaceous rocks swelling on their mechanical behaviors can be summarized in several terms:

- At high humidity state, the swelling leads to an increase of the porosity of argillaceous rocks which is a crucial parameter for their deformation. Actually, the different swelling mechanisms involves an increase of porous spaces at multi-scales: crystalline swelling consists of an increase of inter-layer space, double-layer swelling results in separation of inter-particle space, and the breakup of clay particle leads to a transition from inter-layer space to inter-particle space. Note that the swelling here involves also the effect of capillary pressure (normally on the macropore for argillaceous rocks), as discussed in the standard porosmechanics. As discussed in previous section, porosity plays a crucial role for the deformation of porous solids which can be broadly divided into two terms: compaction of pores, as well as deformation of solid phase. The pore space is much more deformable than the solid phase. Besides, compaction of the porous space is nonlinear (strain-stiffening before certain threshold) and irreversible (plastic deformation). Due to the swelling in humidification case, the contribution of pore compaction becomes predominant, and some of its features exhibit more evidently at the macroscopic behavior of such rocks: the decrease of Young's modulus, the appearance of initial concave upward portion, and the emergence of plastic deformation at low stress.

- The swelling would modify some mechanical properties of argillaceous rocks, in particular that of the clay matrix. Note that the increase of porosity is also one type of such evolution, but this is not the whole. Actually, the interpolation of 1 to 4 water layers between elementary clay layers (crystalline swelling) would make the sliding between them much easier. Consequently, the shear modulus becomes lower at high humidity state and so much more shear bands are developed. This is why the isolated compaction bands at

dry state would be connected and coalesced into some shear deformation bands at high humidity state, as shown in test #7 of chapter 4. Besides the decrease of shear modulus, humidification would decrease not only the cohesion inside the clay matrix, but also the adherence at inclusion-matrix interfaces. Note that this decrease at high relative humidity state is partially due to decrease of suction, which is favorable for the adherence at some interfaces. Hence, the sliding systems are much more abundant for the humid state.

- The microcracking due to humidification is also responsible for the evolution of the mechanical behavior of argillaceous rocks. In fact, the microcracking is not obvious at low relative humidity, whereas its density becomes considerable at high relative humidity. The closing of these microcracks under mechanical loading is contributable to the increasing of material's deformability and the concave upward portion at the beginning of the stress-strain relation. It is worth noting such microcracks can be considered as one special type of porosity in some context, as discussed in the previous section. Hence, its effect can be incorporated into the effect of porosity increasing.

- Finally, the heterogeneity would amplify at the high humidity state. Actually, the Young's modulus of the clay matrix is much smaller than that of the inclusions. Due to the increasing of porosity, the clay matrix becomes softer and the contrast with the water-insensitive inclusion would be more significant. Moreover, the microcracking due to humidification, which can be considered as faults in the view point of mechanics, is also contributable to the increase of heterogeneity index. Such heterogeneity amplifying would intensify the local internal stress field (predominantly due to inclusion-matrix interaction) under mechanical loading. In fact, this is a crucial issue for all heterogeneous materials. For the effect of heterogeneity, Tang et al. (2000) has investigated this problem under uniaxial compression condition by numerical studies. The material properties (strength and elastic modulus) for elements are randomly distributed throughout the specimen, assumed to obey Weibull's distribution. A series of rocks with different heterogeneity indexes are studied, and a typical result is shown in Fig.6.2. In general, the amplifying of heterogeneity would lead to a ductile behavior wiht a smaller peak stress (corresponding also to a smaller peak strain) at the failure. These phenomena are well correlated to our observations.

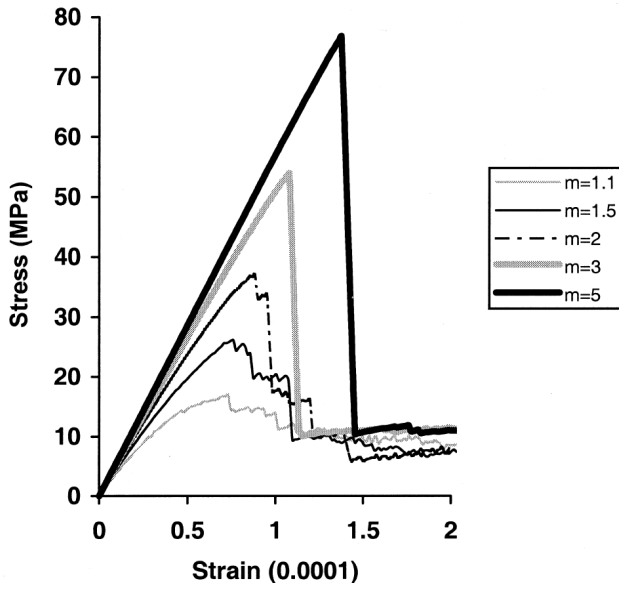

Figure 6.2: Influence of heterogeneity on the mechanical behavior of rocks (Tang et al., 2000a). m is heterogeneity index, and a larger value implies a less heterogeneous material.

Bibliography

Hundson, J.A., Harrison, J.P., 1997. Engineering rock mechanics.

Montes-H, G., 2002. Etude expérimentale de la sorption d'eau et du gonflement des argiles par microscopie électronique à balayage environnementale (ESEM) et l'analyse digitale d'images. Thèse Université Louis Pasteur Strasbourg, Strasbourg.

Tang, C.A., Liu, H., Lee, P.K.K., Tsui, Y., Tham, L.G., 2000. Numerical studies of the influence of microstructure on rock failure in uniaxial compression - Part I: effect of heterogeneity. International Journal of Rock Mechanics and Mining Sciences 37, 555-569.

Valès, F., 2008. Modes de déformation et d'endommagement de roches argileuses profondes sous sollicitations hydro-mécaniques. Ecole Polytechnique, Palaiseau.

Chapter 7

Conclusions

Argillaceous rocks are chosen as possible host rocks in the context of underground storage of radioactive nuclear waste. During their service life, such rocks may undergo various environmental aggressions. One important term of these environmental loads is the humidity change of the surroundings, for example the desiccation due to the ventilation during the stage of tunnel excavation. These changes of humidity, leading to moisture transport processes, would alter the hydromechanical (such as elastic properties, rupture mode, and permeability etc.) and physic-chemical properties of such rocks. Indeed, a good characterization of the hydromechanical behavior of argillaceous rocks is crucial for the long-term storage safety assessment.

Numerous models have been proposed to describe the hydromechanical behavior of argillaceous rocks. In the viewpoint of long-term stability assessment, physically based micromechanical models at relevant scales are still required for establishing reliable constitutive relations. Such models always require experimental investigations at appropriate scales, to identify the relevant micro-mechanisms involved and to validate their predictions at all scales. However, these identifications are generally very delicate, since argillaceous rocks are indeed a multi-scale heterogeneous material, ranging from the nanometric scale of clay layers to the kilometric scale of the geological formation. Measurement of mechanical properties and response at multi-scale is still a challenging work, despite numerous recent developments. One important characteristic scale of heterogeneity of argillaceous rocks is related to their composite microstructure, at which such material can be described as a composite made of a continuous clay matrix with a scatter of some other mineral inclusions. Actually, the inclusion-matrix interactions under hydric and mechanical loads lead to a complex coupled macroscopic behaviors and are a potential source of damage.

In the purpose of experimental investigations on argillaceous rocks at micro-scale:

- We have pioneered the application of Digital Image Correlation techniques (DIC) on Environmental Scanning Electron Microscopy (ESEM), whereby humidification/desiccation of samples can be conducted and the involved evolution can be observed at micro-scale.

- Besides humidification/desiccation, an original loading apparatus matching to ESEM has been developed, which allows in-situ combined hydric and mechanical loading test in the ESEM chamber.

- The size of tested samples is typically several millimeters, and observation zones are chosen to be several hundred micrometers in width. This guarantees observation results to be representative. At the same time, the physical size for a pixel is dozens of nanometers, which could reveal the composite microstructure of such rocks. Then, high resolution images recorded by ESEM are analyzed by DIC techniques, evaluating the evolution of local strain fields.

- Because of unfavorable condition for observation (due to the presence of vapor) and

extremely small involved strains, the strain measurement accuracy is a key issue for this work. Based on a careful study on the different sources of strain measurement errors, we have performed several optimizations and improvements to finally obtain a relevant accuracy for the measurement (accuracy for global strain measurement: 10^{-4}, and accuracy for local strain measurement: 10^{-3}).

Compared to the previous existing micro-scale investigations (the strain measurement gauge is at least 50 μm), we have finally yielded at least one order of spatial resolution for the observation (the strain measurement gauge is typically less than 5 μm). Based on this significant progress, we succeed in experimental investigations at the scale of the real composite microstructure of such rocks.

Dozens of humidification/desiccation tests has been investigated, and some phenomena have been evidenced:

- A strong heterogeneous strain field has been evidenced at the micro-scale. Based on these observations, we have characterized the different deformation mechanisms of such rocks: 1) physic-chemical swelling of clay minerals, and a local mechanical stress field due to 2) complex hydromechanical interactions between different constituents, 3) self-restraint effect. The self-restraint effect is strongly sensitive to the humidification/desiccation rate.

- The strain of argillaceous rocks due to humidification exhibits anisotropy: it is predominantly along the direction normal to the bedding plane. Based on the observations in this work, we have revealed that this anisotropic swelling is predominantly related to a preferred orientation of clay particles, which can be evaluated from the anisotropy of the local swelling.

- The swelling of argillaceous rocks is generally moderate at low RH range, whereas it becomes much significant at high RH level. From previous studies, such a nonlinear swelling might be linked to the microcracking due to humidification, which has also been proved in this work. However, based on a gentle humidification test (with small hydric loading rate), we have found that this nonlinearity can be related to a nonlinear swelling of the clay mineral itself, controlled by different local mechanisms depending on RH. Hence, a two-staged swelling concept has been proposed.

- Our observations have revealed that some irreversible deformations can be produced during hydric loading cycles, as well as some microcracks. The microcracking due to humidification is located not only in the clay matrix but also at inclusion-matrix interfaces, while the microcracking due to desiccation is mostly activated in the clay matrix. This localization difference implies that these two types of microcrackings may be related to different micro-mechanisms. The former is probably linked to the physic-chemical swelling of clay

minerals, in particular the breakup of clay particles due to hydration, while the latter is principally due to the self-restraint effect. However, the local mechanical stress due to the heterogeneity and to the self-restraint effect is a common origin for both. These irreversible phenomena, in particular the microcrackings, are strongly affected by the hydric loading rate, so the self-restraint effect. It is noted that these irreversible phenomena are localized and sometimes counteract each other so that the apparent overall deformation is fairly reversible.

Based on the experimental observations, the inclusion-matrix interaction, as well as the self-restraint effect, have been furthermore investigated. The material is modeled as a composite made of non-swelling elastic inclusions embedded in an elastic swelling clay matrix. Analytical and numerical models have given access to evaluations of induced local stress fields and the final overall deformation.

- Various idealized situations have been considered: an isolated inclusion embedded in an infinite matrix, a pair of inclusions with various separation distances as well as an inclusion near a free surface. The inclusion-matrix interaction would generate a local stress field which is maximal near the interface and gradually decreases with distance. In addition, such a local stress field would be affected by the presence of the neighboring inclusions and the free surface.

- Besides the inclusion-matrix interaction, the self-restraint effect is also responsible for the local stress field. The self-restraint induced stress attains its maximum at the ending of hydric loading (variation of the environment RH finishes) and vanishes gradually when the humidification/desiccation process goes on. In addition, its magnitude increases with the hydric loading rate and the specimen size.

- An analytical micromechanical model based on Eshelby's solution has been proposed to predict the overall deformation under hydric load, as well as the induced stress field. In addition, 2D finite element computations, based on a periodic microstructure as well as a realistic microstructure derived from SEM observations, are performed. Results are discussed in relation with experimental observations.

Besides, tests of argillaceous rocks under combined hydric and mechanical loads have been conducted, and the main observation results can be summarized:

- Under mechanical loading, three types of deformation bands have been evidenced in this work. Based on the correlation between orientation of these deformation bands and somewhat uniform local major strain (E2) direction in them, the mechanisms of these deformation bands can be identified: 1) the band normal to the compression direction is

related to compaction of macropores and pre-existing microcracks, 2) the band parallel to the loading direction is associated to microcracking, and 3) inclined band is linked to shear deformation. Besides, these deformation mechanisms are usually interacting: for example, several compaction bands may lead to a shear band connecting them. In addition, large shear strain could activate microcracking at the tip of shear bands.

- The conventional mechanical tests on argillaceous rocks normally exhibit a linear strain-stress relationship at the beginning. However, this linear portion already involves considerable plastic deformation. The investigations in this work have demonstrated that the emergence of plastic deformation at low strain level is essentially linked to the irreversible compaction of macropores and pre-existing microcracks which is an important deformation mechanism of such a porous rock.

- It is shown, from this work, that the mechanical behavior of argillaceous rocks are strongly controlled by their water content (or humidity state), and the origins of this influence have been studied by our micro-scale observations. A high humidity state would result in a swelling of the material (growth of porous spaces), which leads to more and bigger compaction bands. In addition, increased water content would decrease the shear modulus (for example, hydration might make easier the slip between clay layers), so shear bands are in particular prone to appear at high RH states. Finally, the microcracking due to swelling at high RH may also affect the mechanical behavior of such rocks. These are the main origins of the softening of material at high RH state.

- A combined test during which both hydric and mechanical loads are subsequently applied on a same sample is performed. The localizations of deformation induced by both types of loads are very different. However, we have found some correlations between the two maps, which reveal the role of microstructure (such as orientation of clay particles) on the hydromechanical behavior of such rocks. When the sample is humidified, a transition of several isolated compaction bands to an assembly of them connected by shear bands has been evidenced in strain maps, which implies that humidification weakens the shear modulus of clay matrix.

In the viewpoint of experimental investigations on hydromechanical behavior of argillaceous rocks at micro-scale, some improvements may be proposed for a further investigation:

- In this work, we have evidenced some nonlinear behaviors under a humidification/desiccation cycle, despite a somewhat reversible deformation observed at macro-scale. This is indeed a fatigue problem. In a following work, more hydric and mechanical loading cycles should be performed to study the evolution of the nonlinear phenomena: for example, propagation of microcracks under cyclic loading. This is a key issue for the long-term storage stability assessment.

- The inclusion-matrix composite microstructure can be characterized in the present work. However, the inter-phase heterogeneity is not known enough, since the clay matrix itself is also inhomogeneous: what is be called the "matrix" in the present work is indeed a complex mixture of different clay minerals and smaller grains. More detailed quantitative microstructure information, in particular the intra-phase heterogeneity, is still required. For example, we remind some recent advances in chemical element mapping analysis (Prêt et al., 2010), whereby the different clay minerals (such as smectite and illite) present in the "matrix" can be characterized.

- The present work involves a 2D observation on the surface of specimens. However, the behavior of such material is a 3D problem. The micro-tomography is a possible solution of this issue. In particular, a 3D reconstruction of the network of microcracks generated by mechanical and hydric loads would be of great interest. However, the spatial resolution of current micro-tomography system is far not so good as ESEM system. Hence, the combination of ESEM and micro-tomography is also a promising tool: determination of strain field on the sample surface by ESEM, combined with a real 3D identification of microstructure by micro-tomography, and a post-morten characterization of the network of cracks.

- Simulations on the evolution of argillaceous rocks under hydric loading has been performed in this work. However, simulations on that under mechanical loading, furthermore under combined hydric and mechanical loads, are still required. Moreover, a better identification of phase distributions in such rocks (as discussed in the two preceding perspectives) would yield the possibility to reconstruct more "real" microstructures in the modeling. This is also of great interest.

Appendix A

Modeling of self-restraint induced stress during humidification process

The moisture gradient develops across the specimen during humidification/desiccation process and results in non-uniform deformation. Consequently, the outer-part of specimen which is humidified/desiccated more rapidly would be constrained by the inner-part. Such effect, commonly called "self-restraint", leads to internal stress fields by which the microcracking is possibly activated. The self-restraint effect is investigated here, and its several controlling factors are considered: hydric loading rate and specimen's size.

This apprendix is composed of three parts. In first part, the mathematical model for the moisture gradient induced stress during humidification/desiccation process is proposed, consisting in two distinct problems: the moisture transport and the hydromechanical behavior of argillaceous rocks. In second part, the proposed model is applied for a humidification experiment, to be compared with the experimental results and be validated. Finally, two important controlling factors for self-restraint induced stress are investigated: hydric loading rate and specimen's size.

A.1 Theory

The humidification/desiccation process of argillaceous rocks consists in two distinct problems: the moisture transport with phase transition (capillary condensation) as well as the deformation induced by the former which can be studied using mechanics of porous solids. Moreover, the two distinct problems are actually coupled: the moisture change induced deformation, resulting in modifying the porous space of material, would influence in return the permeability of material.

A.1.1 Moisture transport model

The humidification/desiccation in porous medium is a process of two-phase flow with phase transition. For gas phase which is a vapor-air mixture, the vapor is transported not only by molecular diffusion but also by advection as the mixture pressure is varied by the former. The former is governed by Fick's law while the latter is governed by Darcy's law. For liquid phase, the water liquid is transported by advection, governed by Darcy's law. At the same time, vapor-liquid phase transition occurs within the porous media, which can be described by Clapeyron's relation assuming that the liquid and vapor remain in permanently thermodynamic equilibrium.

Argillaceous rocks are weakly permeable (intrinsic permeability $K < 10^{-19}\mathrm{m}^2$). For such porous medium, the Darcean advection can be neglected in regard to the molecular diffusion, so the mixture pressure effect can be ignored ($P_c = -P_l$). In addition, Coussy has proved that the two-phase flow for such material is time scale separated, leading to a two-step moisture transport process: the vapor diffusion is predominant in the firstly step, while the subsequent step involves mainly the water liquid transport through Darcean advection. Besides, the contribution of vapor diffusion to the variation of water content is negligible. Therefore, the hu-

midification/desiccation of argillaceous rocks is mainly achieved by the water liquid movement, and the effect of gas phase can be neglected.

The water transport in porous media is governed by Darcy's law:

$$w_l = -\rho_l k_l \nabla P_l \tag{A.1}$$

with

$$k_l = \frac{K k_{rl}\left(S_l\right)}{\eta_l}$$

where k_l is the permeability of water. w_l ,P_l and ρ_l denote respectively the water flux, pressure and density. K is the intrinsic permeability of porous media independent of saturating phases and saturation, while the relative permeability k_{rl} depends on degree of saturation.

A.1.2 Poroelasticity

Argillaceous rocks are considered as porous solid, so its mechanical behavior can be described by poroelasticity. It is assumed that air pressure remains constant during humidification process and is equal to atmosphere pressure, the isotropic poroelasticity is written as:

$$\sigma_{ij} = \lambda \mathrm{tr}\left(\varepsilon_{ij}\right)\delta_{ij} + 2\mu\varepsilon_{ij} - bP_l\delta_{ij} \tag{A.2a}$$

$$\frac{dm_l}{\rho_l} = b\mathrm{tr}\left(\varepsilon_{ij}\right) + \frac{P_l}{M} \tag{A.2b}$$

where λ is Lame's coefficient and μ is shear modulus. $\mathrm{tr}(\varepsilon_{ij})$ represents volumetric strain. The parameters b and M denote respectively Biot's coefficient and Biot's modulus. From equation (A.2b), one can find that the variation of water content depends on two factors: 1) volume changing of porous space due to the deformation, 2) variation of water pressure.

A.2 Humidification experiment and modeling

A.2.1 Humidification experiment of argillaceous rocks

The humidification experiment is conducted on one cylindrical sample of argillaceous rocks (diameter: 36mm, height: 36 mm). At initial stage, the sample, undergoing constant z-axis force (equal to 0.1 MPa) applied by a loading machine platen, is steady in an environmental chamber where relative humidity is controlled at 47%RH. At one moment, relative humidity in the chamber is varied to 56%RH. However, the z-axial mechanical force is maintained during humidification process. The strain gauge was plastered on sample's surface to monitor the evolution of axial strain. The evolution of axial strain and relative humidity in environmental chamber is shown in Fig.A.3.

A.2.2 Modeling

The proposed model is used in this study to reproduce the experiment, and be validated by this way. A schema of the humidification experiment is shown in Fig.A.1. The simulation can be divided into two terms. Firstly, the simplified moisture transport model is used to assess the evolution of water pressure field within the specimen. The changing of water pressure field results in deformation, which is calculated by poroelasticity model in the second part.

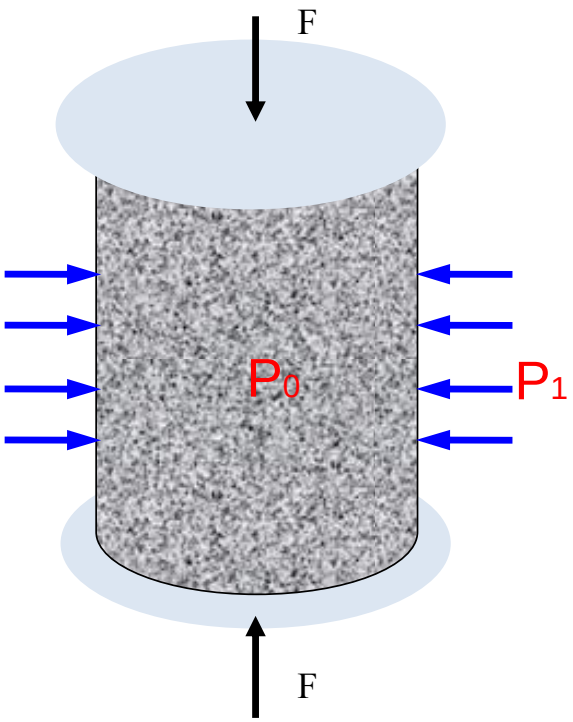

Figure A.1: Schema of humidification experiment.

Since the sample is cylindrical, it is natural to use the cylindrical coordinate system for the following analysis. By reason of symmetry, all the quantities in this simulation are θ-independent, leading to a 2D problem as shown in Fig.A.2. Moreover, only one half of specimen is considered due to z-axis symmetry. For moisture transport, the loading machine platen would prevent the two extremities of the specimen from moisture exchange and results in 1D humidification process (along radial direction). Water pressure is only r-dependent. For poromechanical response, considering the two extremities of sample being in contact with the loading machine platen, it is reasonable to consider the displacements in the z direction are r-independent. It is assumed that the radial displacement is uniform in the z direction. Finally, the displacement is written as:

$$\underline{u} = \begin{pmatrix} u_r(r) \\ 0 \\ u_z(z) \end{pmatrix} \tag{A.3}$$

And the initial and boundary conditions are: Initial conditions:

$$\sigma_{ij} = 0, \quad P_l = P_l^0 \tag{A.4}$$

Boundary conditions:

$$r = 0: \qquad u_r = 0, \qquad \frac{\partial P_l}{\partial r} = 0 \tag{A.5a}$$

$$r = R: \qquad \sigma_{rr} = 0, \qquad \begin{cases} \dfrac{\partial P_l}{\partial t} = \dfrac{P_l^1 - P_l^0}{T} & t < T \\ \dfrac{\partial P_l}{\partial t} = 0 & t \geq T \end{cases} \tag{A.5b}$$

ε_{zz} is uniform within the specimen and $\int_0^{2\pi}\int_0^R \sigma_{zz} r dr d\theta = F$.

It is noted that the hydric loading rate is considered in this study by introducing the hydric loading time T: the hydric loading is applied linearly during a period T, prior to be maintained constant after T.

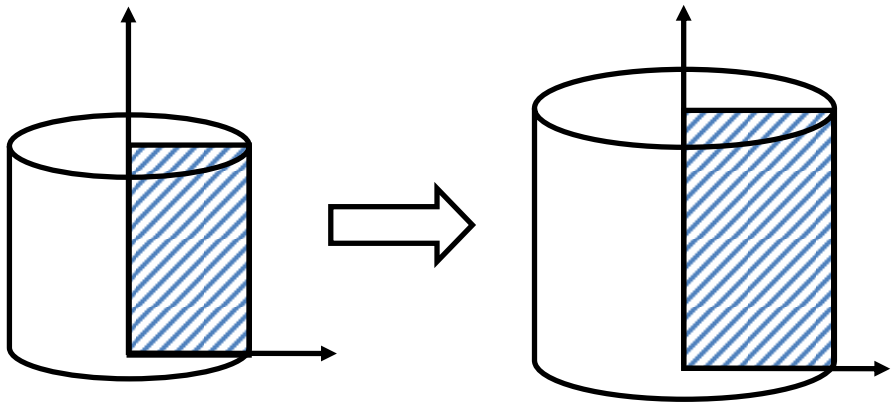

Figure A.2: Transformation configuration of the specimen under humidification.

Hydromechanical behavior

Then, the strain is written in cylindrical coordinate:

$$\begin{pmatrix} \varepsilon_{rr}(r) & 0 & 0 \\ 0 & \varepsilon_{\theta\theta}(r) & 0 \\ 0 & 0 & \varepsilon_{zz}(z) \end{pmatrix} = \begin{pmatrix} \dfrac{du_r}{dr} & 0 & 0 \\ 0 & \dfrac{u_r}{r} & 0 \\ 0 & 0 & \dfrac{du_z}{dz} \end{pmatrix} \tag{A.6}$$

Equilibrium equation for this problem is:

$$\begin{cases} \dfrac{\partial \sigma_{rr}}{\partial r} + \dfrac{\sigma_{rr} - \sigma_{\theta\theta}}{r} = 0 \\ \dfrac{\partial \sigma_{zz}}{\partial z} = 0 \end{cases} \tag{A.7}$$

Substituting equation A.2 and A.6 into A.7, one obtains:

$$\begin{cases} (\lambda + 2\mu)\left(\dfrac{\partial^2 u_r}{\partial r^2} + \dfrac{1}{r}\dfrac{\partial u}{\partial r} - \dfrac{u_r}{r^2}\right) = \dfrac{\partial}{\partial r}(bP_l) \\ \dfrac{\partial u_z}{\partial z} = 0 \end{cases} \tag{A.8}$$

One introduces a parameter v, defined by:

$$v = \frac{1}{r}\frac{\partial (ru)}{\partial r} \tag{A.9}$$

It is noted that $v = \varepsilon_{rr} + \varepsilon_{\theta\theta}$. It is assumed Biot's coefficient is constant, equation A.8 becomes

$$(\lambda + 2\mu)\frac{\partial v}{\partial r} = b\frac{\partial P_l}{\partial r} \tag{A.10}$$

Therefore,

$$v = \frac{b}{\lambda + 2\mu}P_l + A \tag{A.11}$$

A is a constant which can be determined by boundary conditions. Then, the volumetric strain can be written as:

$$\mathrm{tr}(\varepsilon_{ij}) = v + \varepsilon_{zz} = \frac{bP_l}{\lambda + 2\mu} + C \tag{A.12}$$

with,

$$C = A + \varepsilon_{zz}$$

Estimation of A

The general solution of u_r is:

$$u_r = \frac{b}{(\lambda+2\mu)r}\int_0^r p_l(\xi)\xi d\xi + \frac{Ar}{2} + \frac{B}{r} \tag{A.13}$$

Therefore,

$$\varepsilon_{rr} = \frac{bP_l}{(\lambda+2\mu)} - \frac{b}{(\lambda+2\mu)r^2}\int_0^r P_l(\xi)\xi d\xi + \frac{A}{2} \tag{A.14a}$$

$$\varepsilon_{\theta\theta} = \frac{b}{(\lambda+2\mu)r^2}\int_0^r P_l(\xi)\xi d\xi + \frac{A}{2} \tag{A.14b}$$

Since ε_{zz} is uniform under constant force ($\int_0^{2\pi}\int_0^R \sigma_{zz} r dr d\theta = F$),

$$\varepsilon_{zz} = \frac{1}{\pi R^2(\lambda+2\mu)}\left(F + \frac{4\pi\mu b}{\lambda+2\mu}\int_0^R P_l r dr - \pi R^2\lambda A\right) \tag{A.15}$$

Since $u_r(0) = 0$, constant B should be null. Besides, constant A can be determined by $\sigma_{rr}(R) = 0$:

$$A = \frac{1}{\mu(3\lambda+2\mu)}\left(\frac{2\mu(2\mu-\lambda)b}{(\lambda+2\mu)R^2}\int_0^R P_l r dr - \frac{\lambda F}{\pi R^2}\right) \tag{A.16}$$

The volumetric strain is written as:

$$\mathrm{tr}(\varepsilon_{ij}) = \frac{1}{(\lambda+2\mu)}\left(bP_l + \frac{8\mu b}{(3\lambda+2\mu)R^2}\int_0^R P_l r dr + \frac{(\lambda+2\mu)F}{(3\lambda+2\mu)\pi R^2}\right) \tag{A.17}$$

Moisture transport in porous media

Neglecting vapor-liquid phase transition, the mass conservation of water is expressed as:

$$\frac{\partial m_l}{\partial t} = -\nabla\cdot w_l \tag{A.18}$$

where m_l is water content of porous media.

Combining equation 6.2, A.2b and A.18, the govern equation of moisture transport can be described in form of P_l:

$$\frac{\partial}{\partial t}\left(\frac{P_l}{M}\right) + \frac{\partial}{\partial t}\left(b\mathrm{tr}\left(\varepsilon_{ij}\right)\right) = \nabla\cdot\left(k_l\nabla P_l\right) \tag{A.19}$$

Combining equation A.8 and A.19, one obtains:

$$\left(\frac{1}{M} + \frac{b^2}{\lambda+2\mu}\right)\frac{\partial P_l}{\partial t} + \frac{8\mu b^2}{(\lambda+2\mu)(3\lambda+2\mu)R^2}\int_0^R \frac{\partial P_l}{\partial t} r\mathrm{d}r = \nabla\cdot\left(k_l\nabla P_l\right) \tag{A.20}$$

The two sides of above equation is performed by the operation $\int_0^R(\cdot)\, r\mathrm{d}r$, one can find that

$$\int_0^R\left(\frac{\partial\left(P_l r\right)}{\partial t}\right)dr = \frac{k_l R}{L}\frac{\partial P_l}{\partial r}\bigg|_R \tag{A.21}$$

with,

$$L = \frac{b^2}{\lambda + 2\mu} + \frac{1}{M} + \frac{4\mu b^2}{(\lambda + 2\mu)(3\lambda + 2\mu)}$$

Hence, equation A.20 can finally be written as:

$$G\frac{\partial P_l}{\partial t} = \nabla \cdot (k_l \nabla P_l) - H\frac{\partial P_l}{\partial r}\bigg|_R \tag{A.22}$$

with,

$$G = \frac{1}{M} + \frac{b^2}{\lambda + 2\mu} \tag{A.23a}$$

$$H = \frac{8\mu b}{(\lambda + 2\mu)(3\lambda + 2\mu)R} \cdot \frac{k_l}{L} \tag{A.23b}$$

This is the governing equation for humidification process. In this model, the effect of gas phase is neglected which is reasonable for weakly permeable argillaceous rocks. Such model takes into account the coupled hydromechanical effect for such porous medium.

A.3 Simulation results and discussion

The proposed moisture transport model (equation A.22) is solved using finite difference method. Then, the axial strain is calculated to compare with experiment results. The stress quantities are also assessed for further study on microcracking risk. As discussed previously, the humidification experiment can be considered as a 1D process. From the numerical point of view, the spatial derivatives in the moisture transport equation are discretized according to the finite difference approximation. A 50-grid block mesh is used for the specimen with length of 18 mm. In addition, the Euler discretization with an implicit approximation is applied for the time derivatives, allowing a better stability of the scheme. The reference group of Callovo-Oxfordian argillaceous rocks properties are chosen from the data collected by ANDRA (ANDRA, 2005), and some key values of parameters involved in the simulation are reported in Tab.A.1.

A.3.1 Strain evolution

The evolution of axial strain is calculated, for the comparison with experimental result. It is worth to note that the relative humidity in the environmental chamber is variable. It jumped from 47%RH to 58%RH in less than 1 hour, prior to fluctuating around the steady value 56%RH in the following 10 days. For simplicity, the humidification process (47% - 56%RH) is simulated without considering the fluctuation. It is shown that the proposed model succeeds to reproduce the experimental results. At the steady stage of humidification, the axial strain is 0.09%. It increases rapidly at the beginning: its value is nearly 0.06% (about 64% of the steady strain)

Table A.1: The values of the main parameters of Callovo-Oxfordian argillaceous rocks.

Notation	Parameter	Value
E	Young's modulus	5.5 GPa
ν	Poisson's coefficient	0.15
b	Biot coefficient	0.3
M	Biot modulus	4.9 GPa
K	Intrinsic permeability	5×10^{-22} m^2
η_l	Dynamic viscosity of water	1.00×10^{-3}Pa $\cdot$ s
ρ	Volumetric mass of water	1000 kg $\cdot$ m^{-3}
M_v	Molar mass of vapor	1.8×10^{-2} kg $\cdot$ mol^{-1}
R	Ideal gas constant	8.31 J $\cdot$ K^{-1} $\cdot$ mol^{-1}
T	Temperature	293.8 K

at the end of first day. At the end of five days, the axial strain attains 98% of the steady strain: the humidification process can be considered to finish at this time. The evolution of moisture profile is calculated and shown in Fig.A.4. It is note that water pressure is chosen as humidity state variable in the simulation, nevertheless, the moisture profile is presented by degree of saturation which is more commonly used. Their relation can be provided by water retention curve. For Callovo-Oxfordian argillaceous rocks, it can be expressed by Van Genutchen relation:

$$S_l = \left(1 + \left(\frac{P_c}{P_{cr}}\right)^b\right)^c \tag{A.24}$$

with P_{cr} = 22 MPa, b = 0.95, c = -0.38 for humidification case.

It is shown that only the surface zone is humidified at the beginning of humidification, not yet the inner part. A strong moisture gradient develops at the surface zone. Subsequently, the humid moisture penetrates gradually from the surface toward the inside part: the moisture profile becomes smoother. At 10 days, the humidification process is almost finished, and the moisture gradient vanishes totally at this stage.

A.3.2 Internal stress

As shown in Fig.A.4, the moisture gradient is developed during humidification process. Due to such non-uniform moisture, the incompatible deformation is developed, leading to local stress inside the specimen even without external mechanical loading. Such phenomenon is commonly called self-restraint effect. The evolution of these internal stresses, shown in Fig.A.5 - A.7, reveals that the maximal magnitude of these stresses is found at the beginning of humidification process, corresponding to the most important moisture gradient developed. Then, it decrease gradually when moisture transport goes on, and totally vanishes at steady stage where the

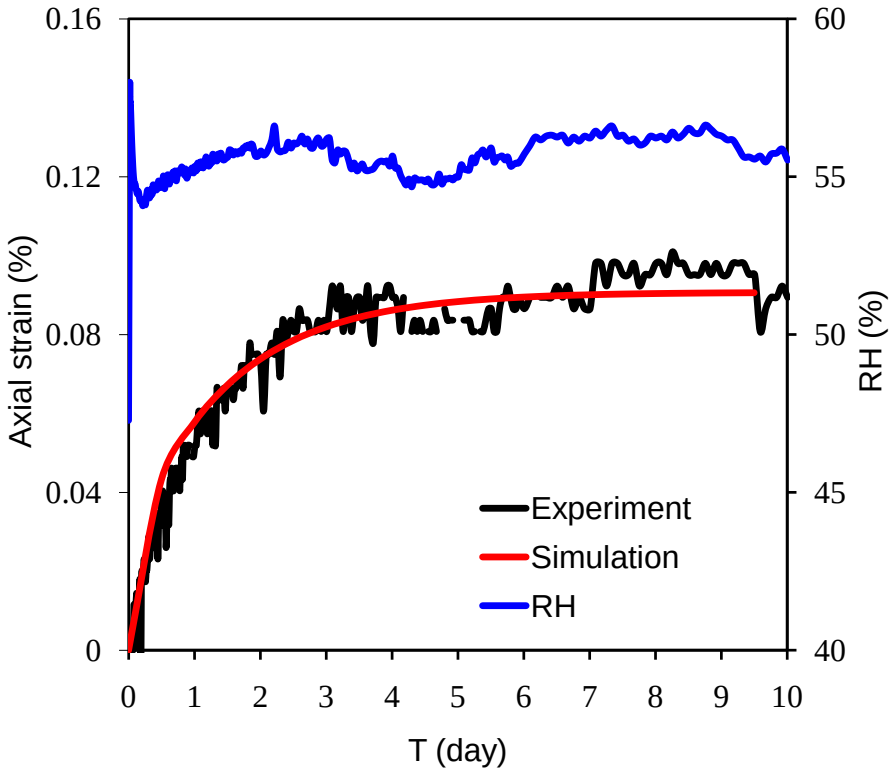

Figure A.3: Experimental and predicted evolution of axial strain during humidification.

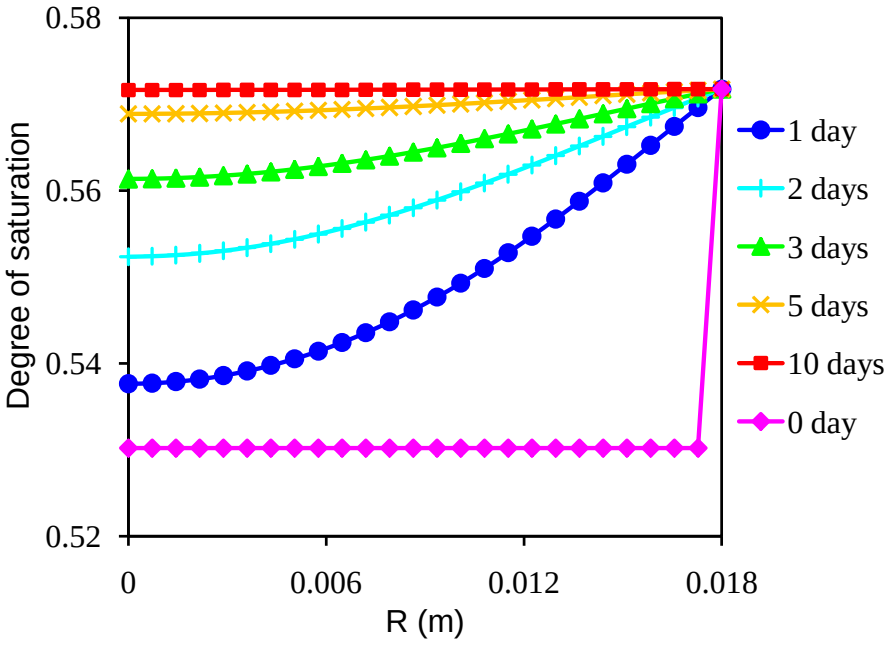

Figure A.4: Saturation profiles within the specimen at different times.

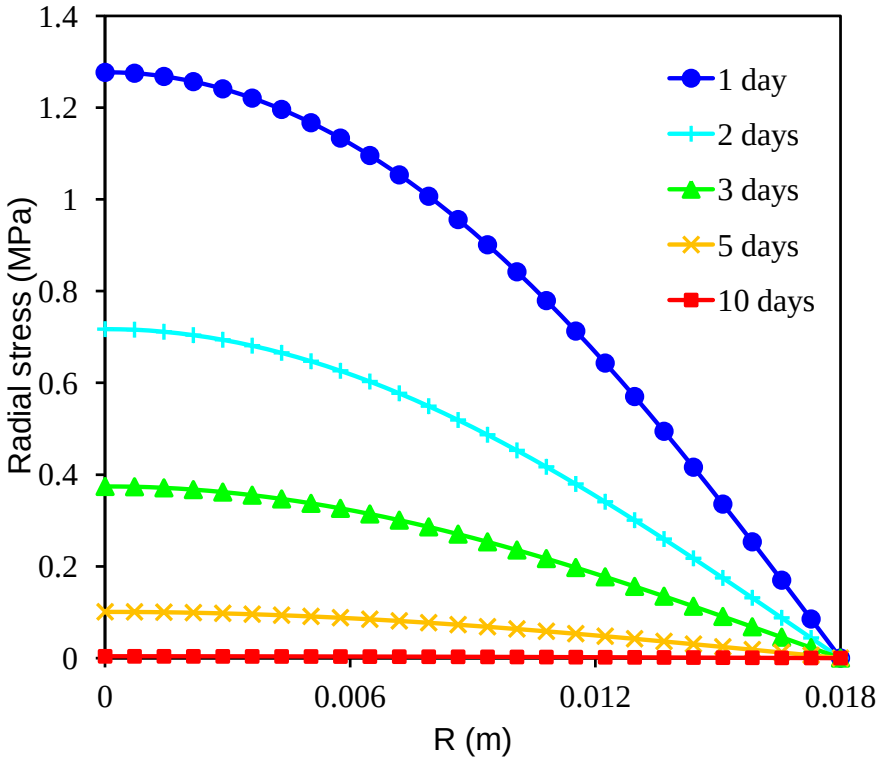

Figure A.5: Local radial stress σ_{rr} within the specimen during humidification process.

moisture becomes uniform. The radical stress is null at the surface as required by boundary condition, and it is tensile inside the specimen of which the maximum is 1.3 MPa at the center of the specimen. The tangential and axial stresses are compressive at the inner part of the specimen, whereas they are tensile at the outer part. Nevertheless, their integration with surface is null since there is no external loading. The changing of stress sign occurs at 10mm for tangential stress, and 12.4 mm for axial stress.

A.3.3 Effect of hydric loading rate

It is natural to realize that hydric loading rate plays a critical role for internal stress induced by self-restraint since the moisture gradient is strongly controlled by it. The effect of hydric loading rate is considered in this study. The hydric loading paths are shown in Fig.A.8, as well as their related axial strain evolution in Fig.A.9. If humidification process can be considered to finish when axial strain attains 98% of the steady level, it needs 5 days for infinite loading rate, 5.5 days for 0.4%RH/h, and 7.5 days for 0.1%RH/h. The fastness of moisture penetration with hydric loading rate can also revealed by moisture profile evolution, shown in Fig.A.10 (for the case of 0.4%RH/h).

The evolution of internal stress profile for the case of 0.4%RH/h is presented in Fig.A.11 - A.13. The maximal tensile radial stress at the center of the specimen is 1.15 MPa, a litter

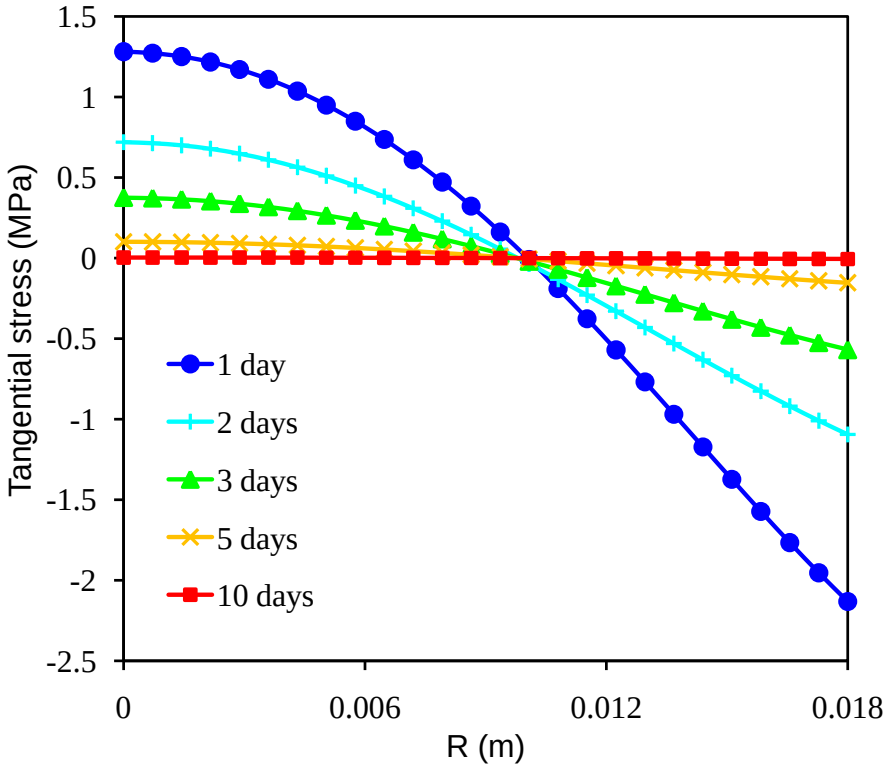

Figure A.6: Local tangential stress $\sigma_{\theta\theta}$ within the specimen during humidification process.

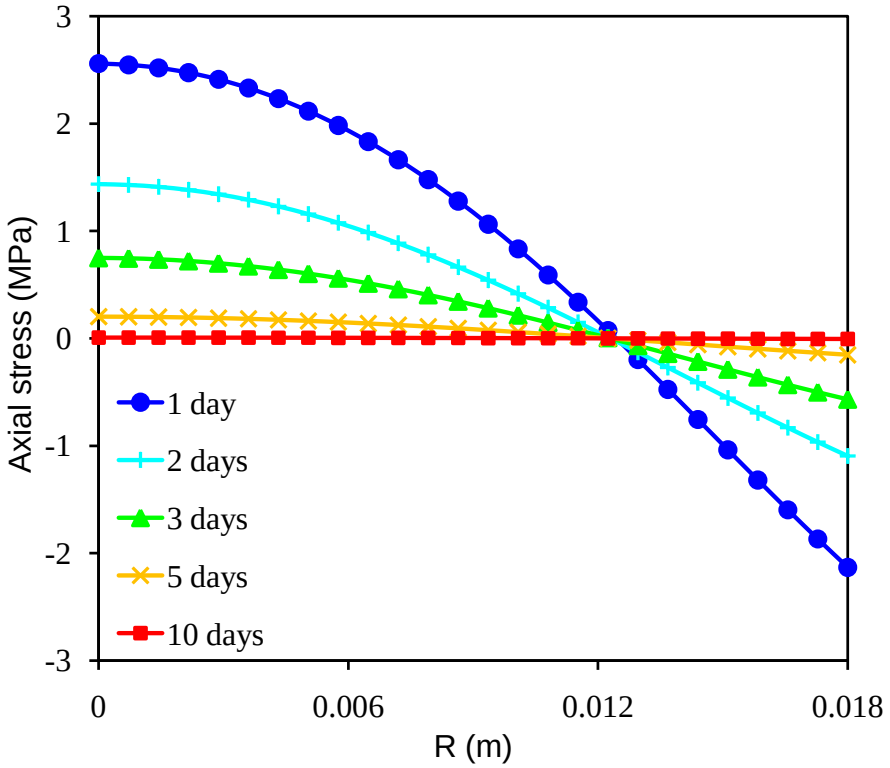

Figure A.7: Local axial stress σ_{zz} within the specimen during humidification process.

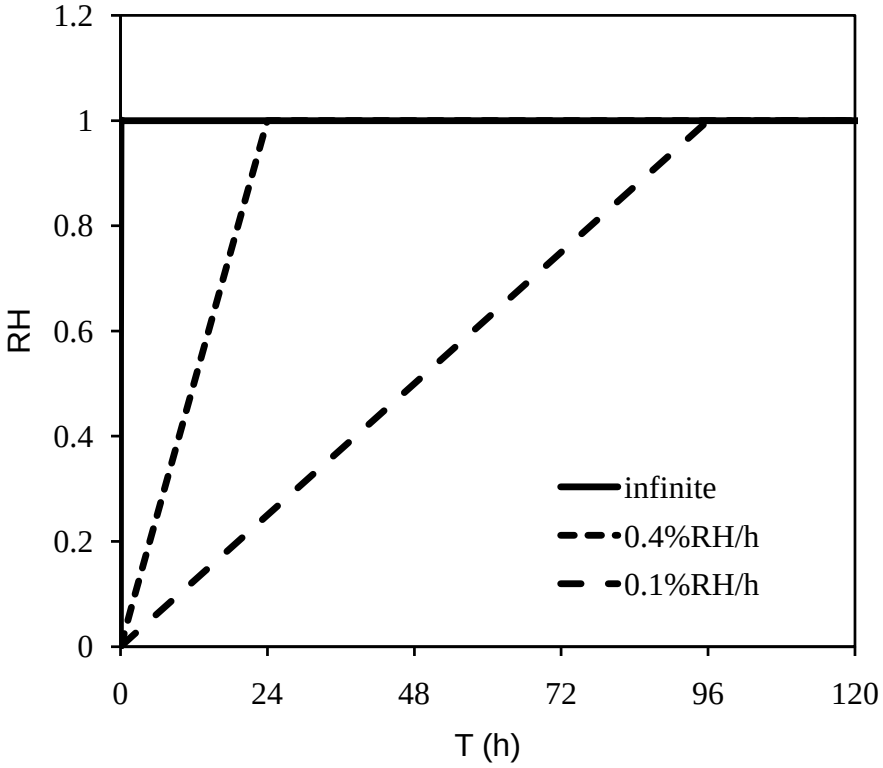

Figure A.8: Different hydric loading ways.

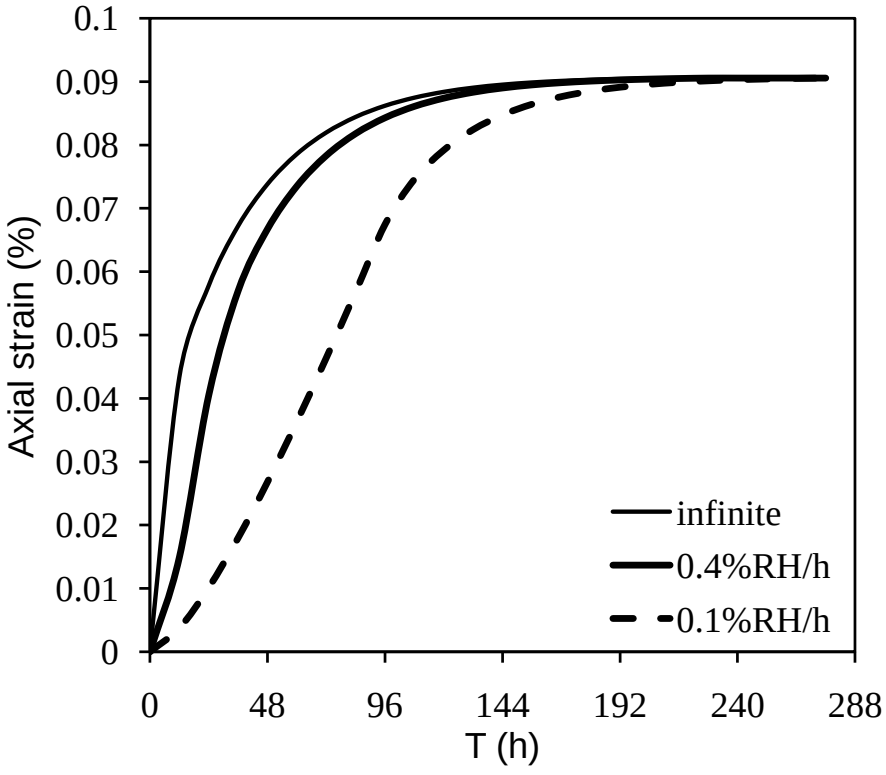

Figure A.9: Axial strain evolution for different hydric loading rates.

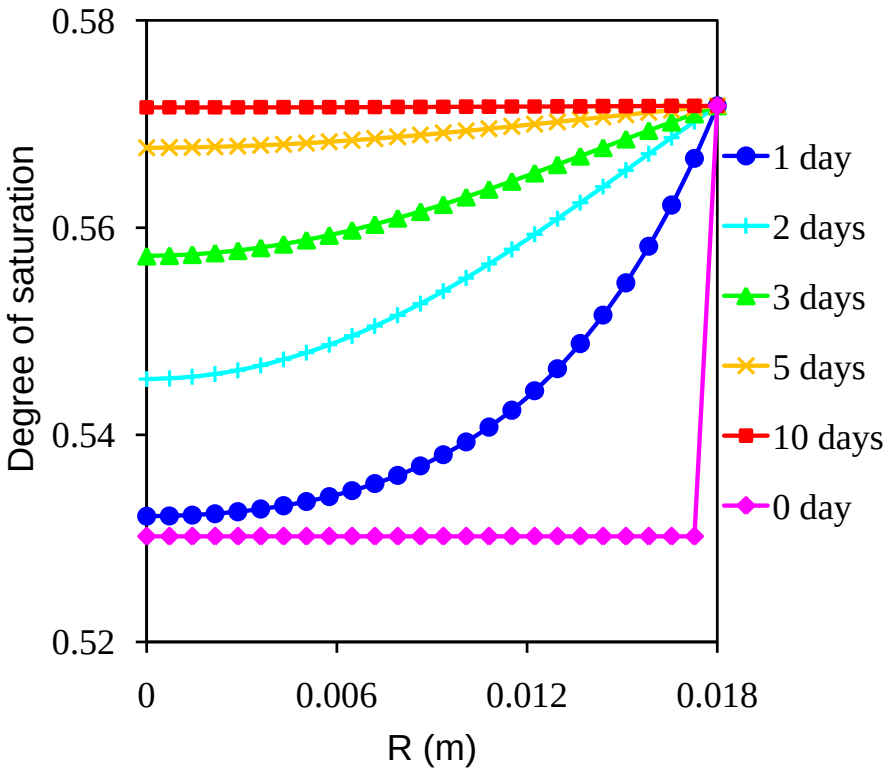

Figure A.10: Evolution of moisture profile in the case of 0.4%RH/h.

smaller than that 1.28 MPa for the case of infinite hydric loading rate. This is also the case for tangential and axial stress at the center of the specimen. It is natural to understand that smaller hydric loading rate, leading to gentler moisture gradient, would result in smaller internal stress. However, for the stress at the surface, their values at 1 day in the case of 0.4%RH/h is greater than that in the case of instantaneous hydric loading. This is because that the stress value on specimen's surface at 1 day is maximal for the case of 0.4%RH/h (T = 24 h), whereas it is not the case for infinite hydric loading rate. This can be proved by the stress evolution with time, shown in Fig.A.14. Considering the maximal tensile and compressive stress, the radial stress at center of the specimen and the axial stress at the surface are investigated. For the axial stress at surface σ_{zz}(R), its maximal stress level is attained once hydric loading is finished: it is 0 h for instantaneous hydric loading case (T = 0), while it is 24 h for the case of 0.4%RH/h (T = 24 h). However, for the radial stress at center $\sigma_{rr}(0)$, its maximum occurs after hydric loading is finished: it is 16.2 h for instantaneous hydric loading case (T = 0), while it is 31.0 h for the case of 0.4%RH/h (T = 24 h). This is why the stress value on surface at 1 day is greater in the case of 0.4%RH/h than in the case of infinite loading rate. Nevertheless, the maximal stress level increases with hydric loading rate. This conclusion can be proved by the curve of maximal stress vs. hydric loading rate, shown in Fig.A.15. The infinite loading rate is considered as 10000%RH/h. For the radial stress at center, the maximum value increases linearly with hydric loading rate until 1%HR/h, prior to being constant 1.4 MPa for more rapid

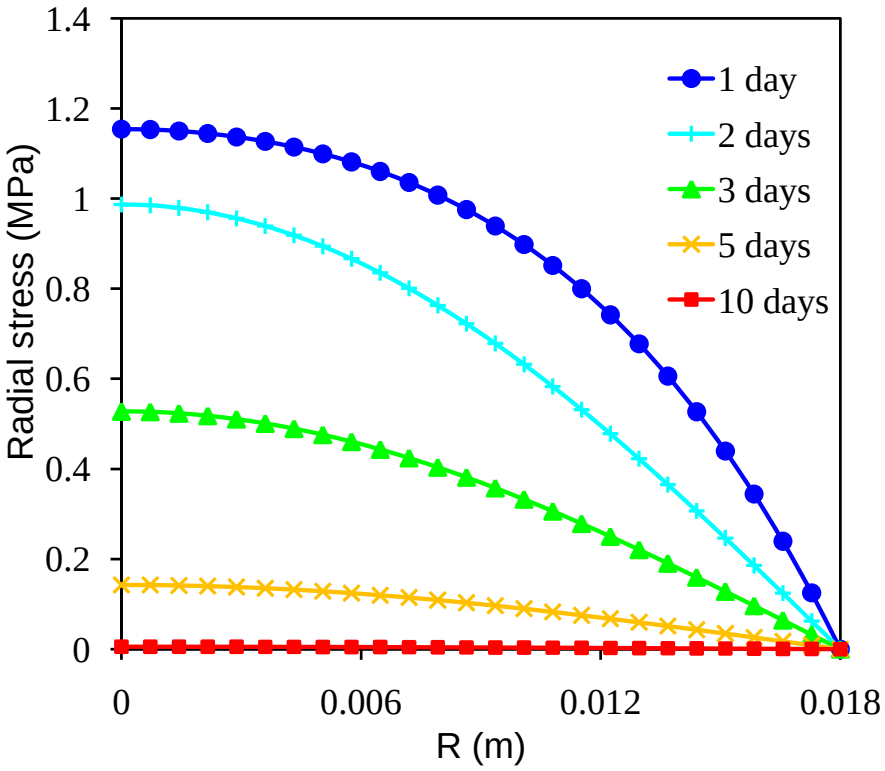

Figure A.11: Evolution of radial stress profile in the case of 0.4%RH/h.

hydric loading. For the axial stress at surface, its evolution with respect to hydric loading rate is somewhat concave before approaching its asymptotic value 5.5 MPa. Considering the tensile strength of Callovo-Oxfordian is 2.7 MPa, there is no risk of cracking for humidification since the maximal tension is 1.4 MPa (radial stress at center) even for instantaneous hydric loading. However, for desiccation, cracks due to tangential and axial tensile stress at surface would appear perpendicular to the drying surface if hydric loading rate exceeds 0.3%RH/h.

A.3.4 Effect of specimen's size

Besides hydric loading rate, the moisture gradient is also controlled by specimen's size. The effect of specimen's size is considered for instantaneous hydric loading in this study, shown in Fig.A.16 and Fig.A.17. The maximal radial stress at center increases smoothly and linearly with specimen's length. For maximal axial stress at surface, its relation with specimen's length is concave.

A.4 Summary

The moisture gradient induced stress during humidification/desiccation process is investigated, which has critical importance for the microcracking analysis. The proposed model includes

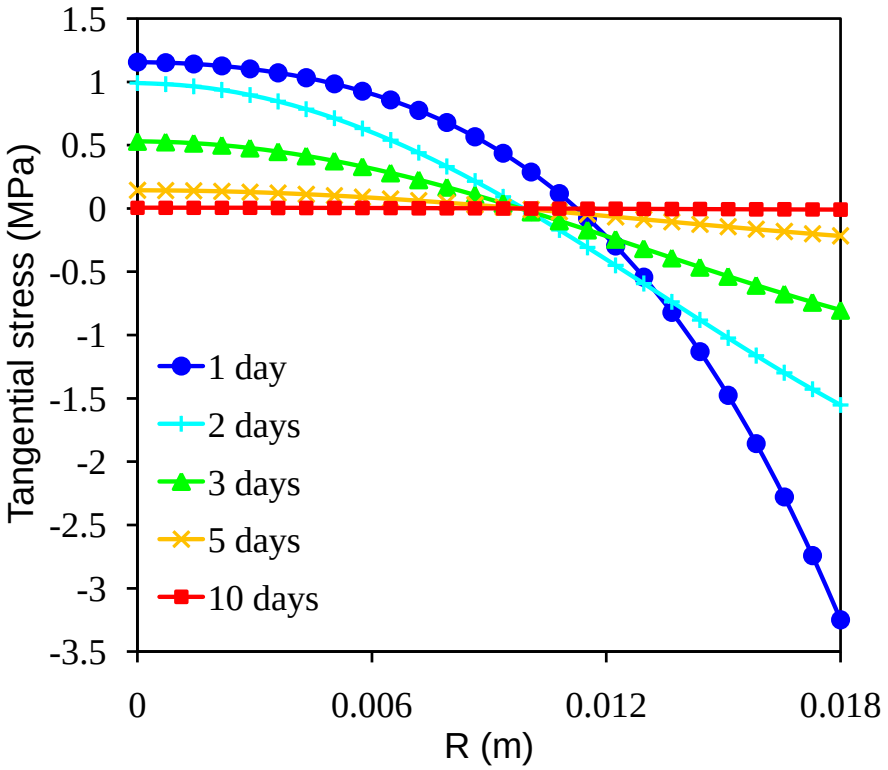

Figure A.12: Evolution of tangential stress profile in the case of 0.4%RH/h.

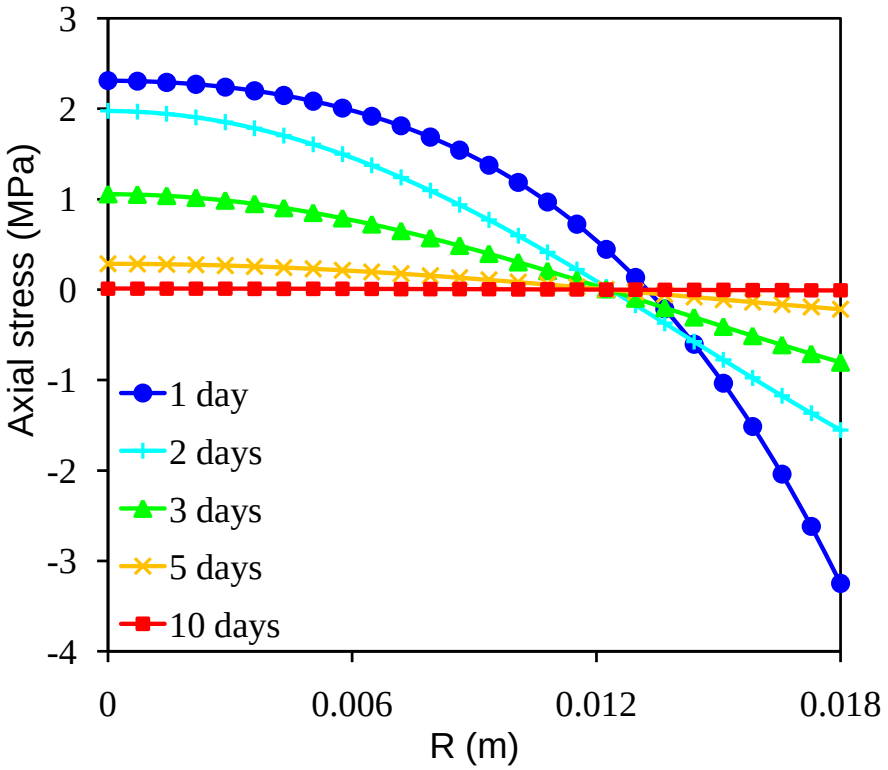

Figure A.13: Evolution of axial stress profile in the case of 0.4%RH/h.

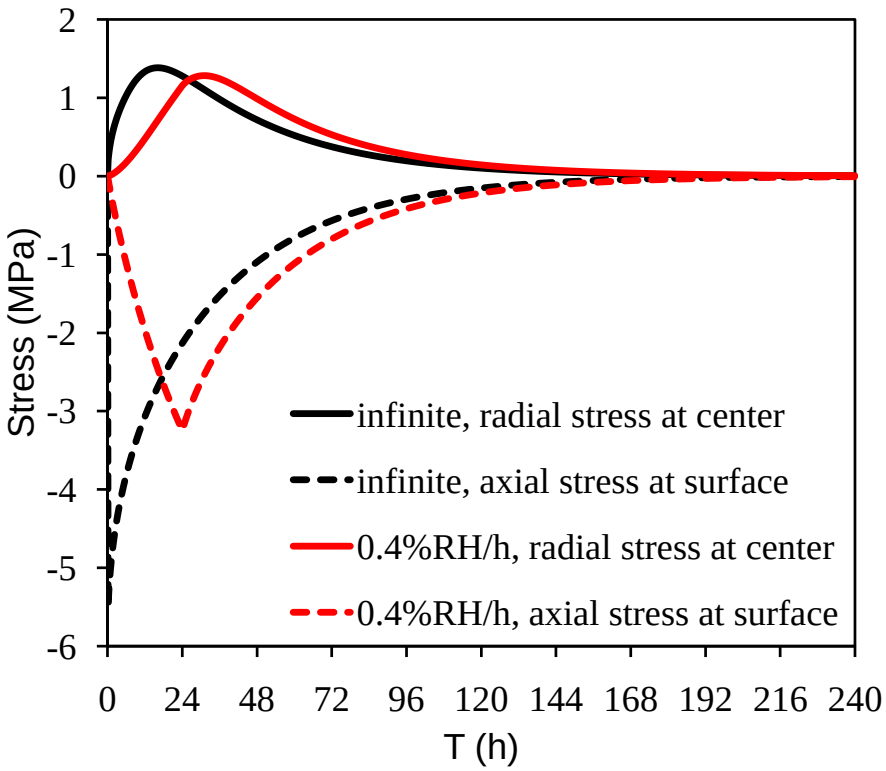

Figure A.14: Stress evolution with time for different hydric loading rate.

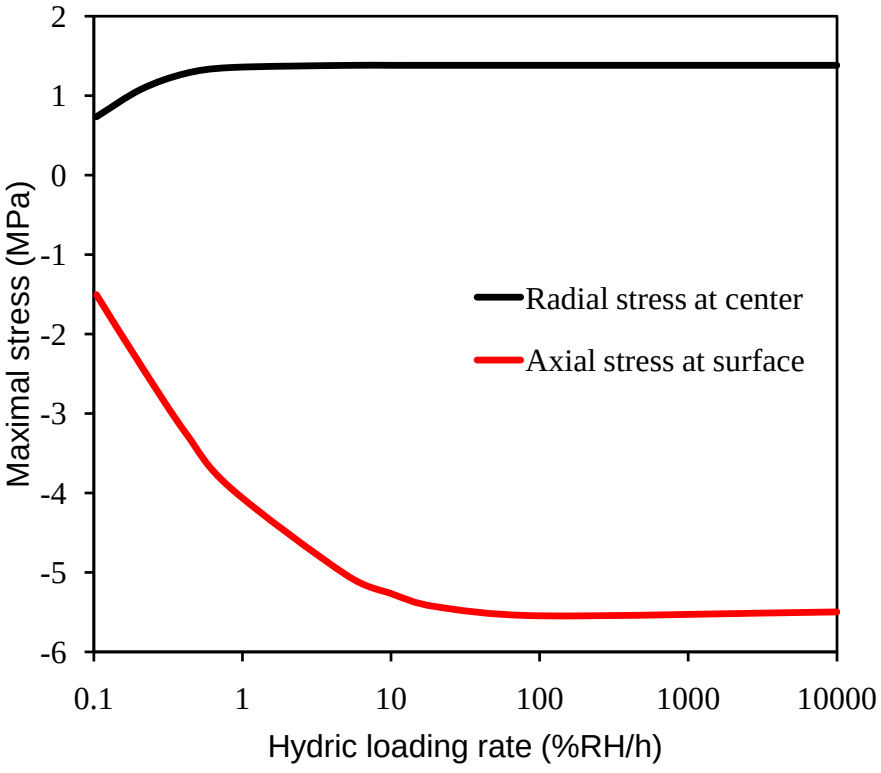

Figure A.15: Maximal stress vs. hydric loading rate.

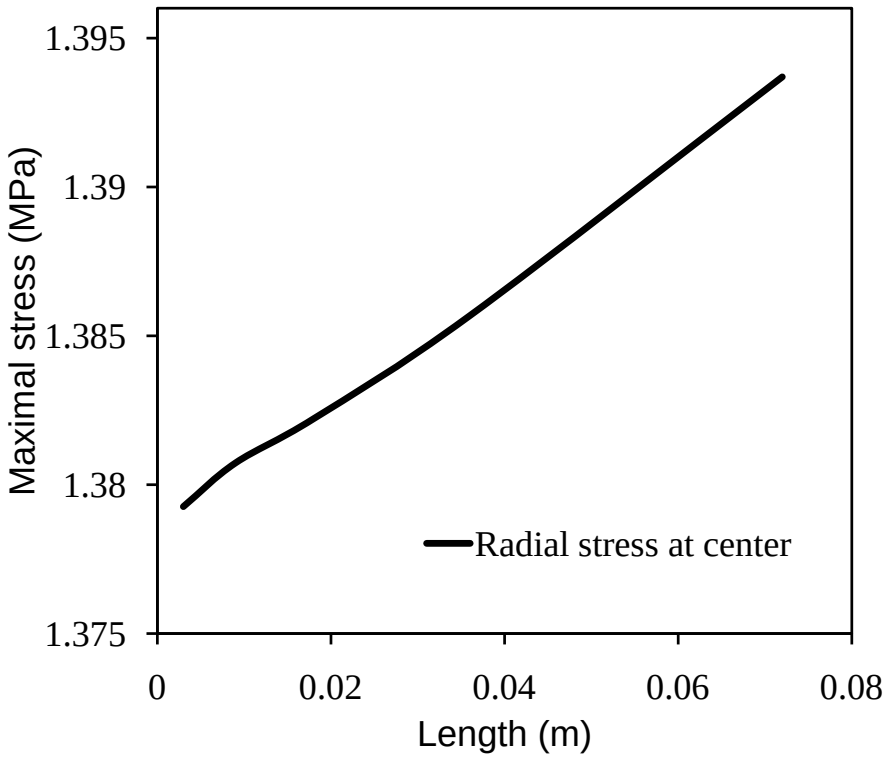

Figure A.16: Maximal radial stress at center vs. specimen's length.

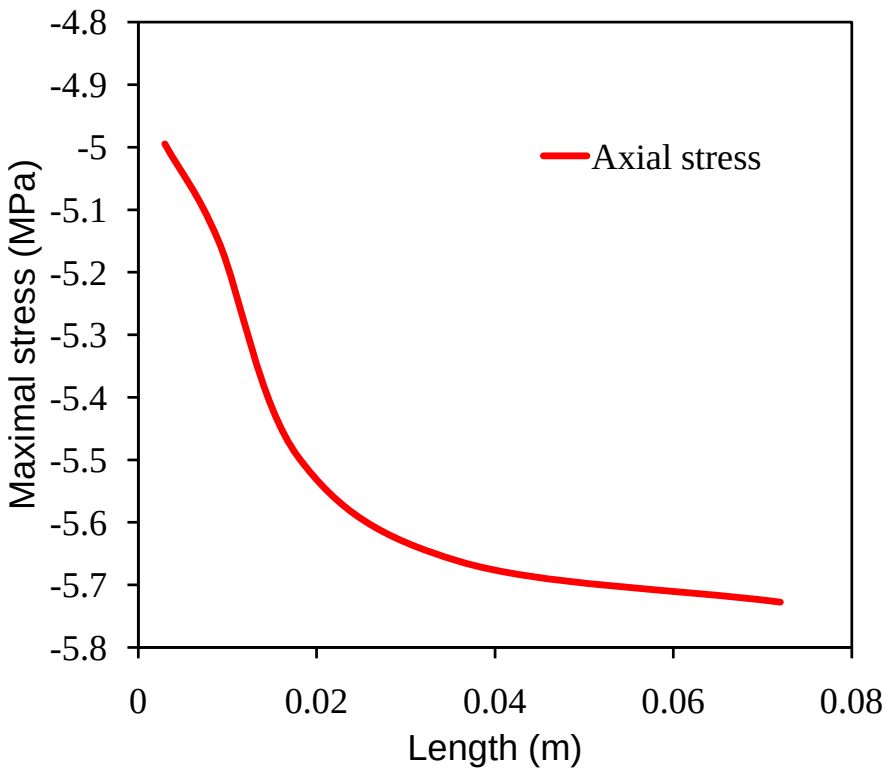

Figure A.17: Maximal axial stress at surface vs. specimen's length.

two parts: moisture transport in porous medium and poroelasticity. Since argillaceous rocks are weakly permeable, the effect of gas phase is neglected in this study: Darcy's law is used as moisture transport model, and poroelasticity assuming constant gas pressure is applied to describe the hydromechanical behavior. The validation of the propose model is given, based on simulating a humidification experiment and comparing with experimental results.

The self-restraint leads to compressive (tensile) stress at the outer-part of specimen and tensile (compressive) stress at the inner-part during humidification (desiccation) process. Such stress attains its maximum rightly at the ending of hydric loading or a little later, and vanishes gradually when moisture transport goes on. Besides, the magnitude of stress induced by moisture gradient increases with hydric loading rate and specimen's size.

Appendix B

Experimental investigation of the free swelling of crushed argillite

The free swelling capacity of the constitutive clay minerals is a key parameter, not only for the analysis of damage but also for the micromechanical modelling of the total deformation of such rocks under wetting or drying conditions. Quantitative experimental data on free swelling at local scale are still missing, since most of the existing investigations are performed at macro-scale at which free swelling is always coupled with mechanical deformation. We propose here a new methodology to quantify free swelling at micrometric scale. To do so, the argillite is first pulverized fine enough to remove local stress. The free swelling of the obtained powder particles essentially made of individual clay aggregates is then investigated by the combination of environmental scanning electron microscopy (ESEM) and digital image correlation (DIC) techniques.

B.1 Sample preparation and experimental methods

Callovo-Oxfordian argillite samples were crushed in laboratory by a grinder for 24 hours in standard laboratory conditions, without controlling RH. The powder was sieved with a screen opening of 100 micrometers.

It should be noted that the ESEM images merely ownare essentially 2D information projections of the surface of the grains, so thate neither out-of-plane components of the displacement field areis out-of-reach quantified here, nor displacement inside the grains. and they are neglected here. Hence, the real actual volume change is impossible tocannot be determinedquantified exactly. However, the so-called iso-strain (E1+E2) is applied used as a qualitative indicator of volumetric deformation. The selected ROIs are located on top of the aggregates so that artefacts in strain measurements due to possible global rotations of the grains are limited, and that only grains which do not undergo such rotations, as indicated by the evolution of their contrast in the periphery of the grains, are considered for the analysis.

The general experimental procedure is as follows. The powder of crushed argillite was put directly on the Peltier module and underwent a multi-step swelling/drying in the ESEM chamber. The micro-scale observation and DIC analysis were performed on dozens of clay aggregates. It is emphasized that only isolated ones (as shown in Fig.B.2) were chosen to avoid confinement effects and to ensure a free swelling. Between each wetting/drying step, relative humidity was varied up to the new prescribed value at a moderate rate (1-7%RH/min) to prevent the violent break-up of samples, which would be induced by too strong local gradients of water content in the grains during the transient stage. This permits also to avoid condensation of water vapour on the Peltier module. Then, RH was maintained constant waiting for hydric equilibrium of aggregates. ESEM images were recorded every two minutes for strain measurement. Once the average deformation increment between two successively recorded images became extremely small ($< 10^{-4}$), the aggregates were considered to have attained their steady states and the subsequent wetting/drying step was triggered. The equilibrating period was generallylasted in

general less than 20 minutes, as shown in the illustrative example in Fig.B.1.

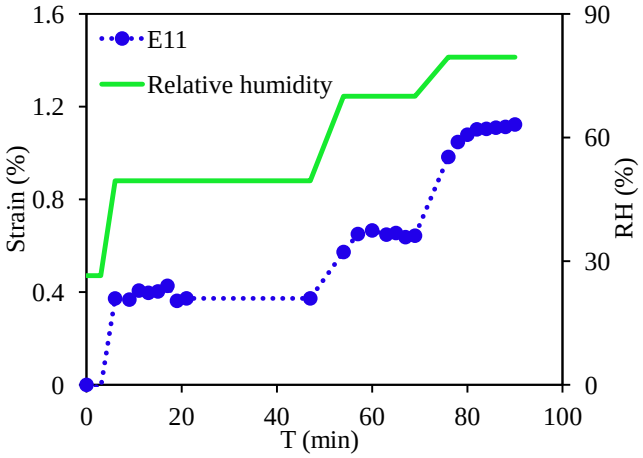

Figure B.1: Example of wetting history and deformation evolution with time.

B.2 Results and discussions

Monotonic swelling tests were performed on samples 1 to 6 with RH ranging from about 25% to 80%, while sample 7 underwent a wetting-drying cycle, as illustrated in Fig.B.4. In crushed argillite, the mesoscopic confinement due to non-swelling inclusions is eliminated. It should however be noted that the individual grains or "aggregates", with typical size ranging from 20 to 50 μm, are indeed assemblies of clay particles with various orientations and inter-particle pores, so that the swelling field still exhibits fluctuations at the scale of a few micrometers, as shown in Fig.B.2. The average strains over the considered ROIs (typically 10 to 20 μm in size) measured here as a function of RH should therefore be considered as the free swelling strain at the scale of clay aggregates, not of individual clay particles. A zoom of sample 7 is shown in Fig.B.3. In general, the ESEM image seems smoother after wetting. This is associated with the absorption of water on particles surfaces. Moreover, some menisci, associated with capillary effect, are observed in some inter-particle pore space.

Fig.B.4a is a plot of steady iso-strain as a function of RH during the wetting process for samples 1 to 6. Broadly, the deformation due to wetting is several percent at the highest increment in RH but a strong heterogeneity is observed: a maximum of 3.5% was recorded for sample 6, while the minimum was 0.8% for sample 5. The observed heterogeneity can be explained by the anisotropy of local swelling induced by a preferential orientation of clay particles on the aggregates. Assuming an axial-symmetric behaviour with 2 of the 3 eigenstrains equal to a minimum swelling Emin and the third equal to the maximum E_{max}, measurements of 2D iso-strains would then range from $2E_{min}$ to E_{min}+E_{max}, depending on the orientation of the observed aggregates. In addition, the non-uniformity of measured strains may be related to the

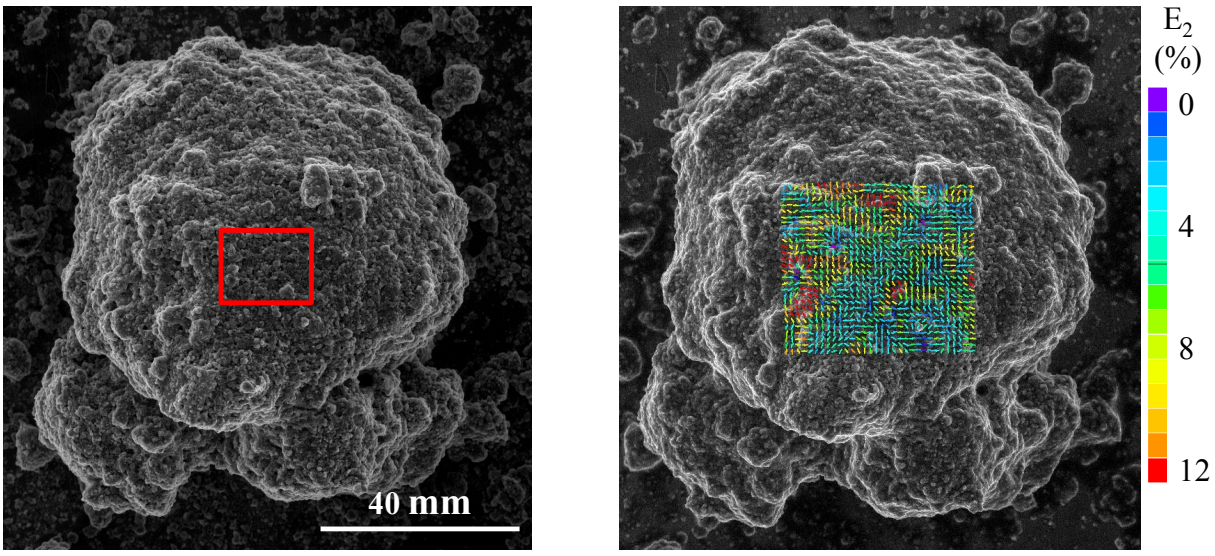

a (27%RH) **b** (85%RH)

Figure B.2: ESEM image of sample 7 in reference configuration at 27%RH (a) and its swelling strain field at 85%RH (b). In the left image, the domain outlined in red is zoomed in Fig.B.3.

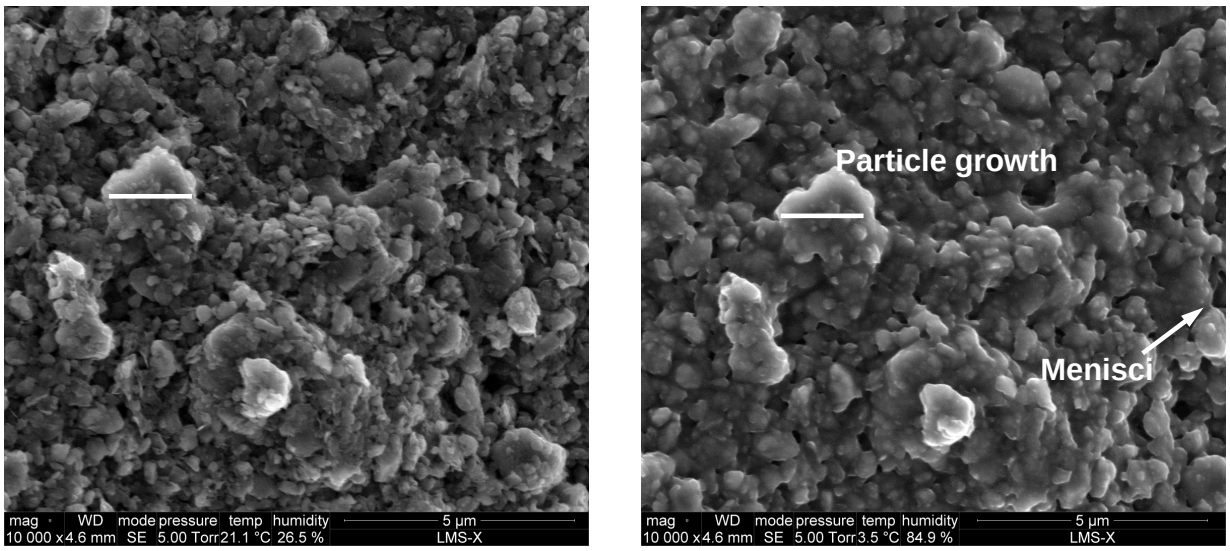

a (27 %RH) **b** (85 %RH)

Figure B.3: Hydration of clay aggregate observed by ESEM (sample 7).

different types of clay minerals owning variable swelling capacities: for example, smectite can swell greatly whereas illite and kaolinite deform hardly during wetting processes. The measured results suggest that $E_{min} =$ 0.4% and Emax = 3.1%, i.e. 3D local volume change would be about 4%. These values are all much less than the swelling magnitude of 15% recorded by Montes (2003) for MX80 bentonite aggregates subjected to a similar RH increase.

Based on numerical simulations in Chapter 5, we have estimated a ratio of overall free

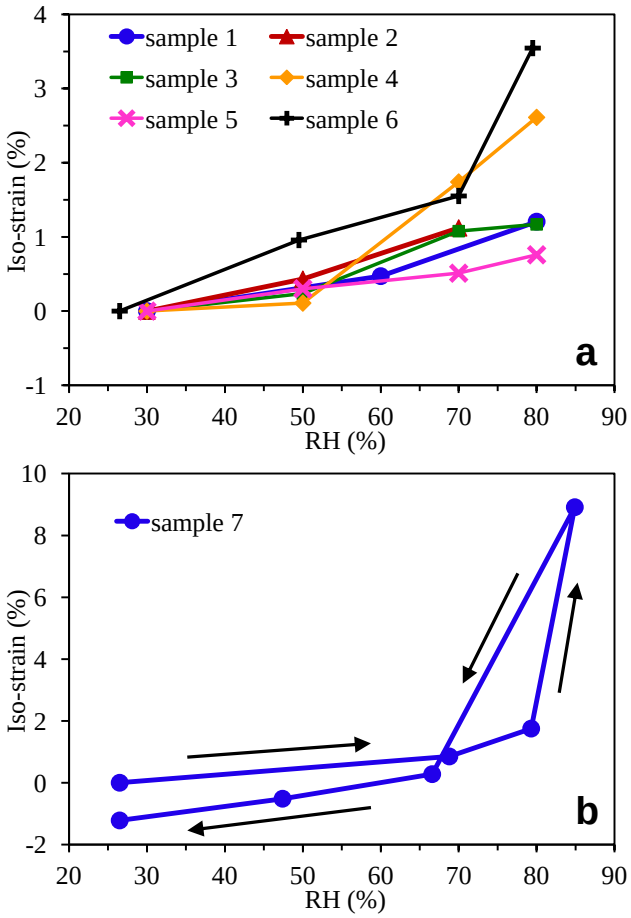

Figure B.4: Steady-state iso-strains measured during monotonic swelling (a) and swelling-drying cycle (b).

strain to free clay swelling of 0.45-0.7 for the volume fraction of inclusions varying from 40% to 20% (refer to Fig.5.23). Such relations allow us to compare our local measurements to overall swelling measurements of argillite for similar RH variations. For instance, Pham (2007) has recorded a volume strain of 1.7% for a swelling from 33%RH to 76%RH, while Yang (2012) found it to be 0.5% for a 36%RH to 79%RH increase. Orders of magnitude are very similar, with limited discrepancies being likely to be related to the variability of microstructure and over-simplifications in the above preliminary models. These results underline that the free swelling capacity of clay minerals in the COx argillite is rather limited, which is consistent with the abundance in these rocks of I/S inter-stratifies, in which illite hardly swells.

The evolution of swelling as a function of RH is somewhat linear at low RH range: it is the case until 80%RH for samples 1-5, while this holds true at least up to 70%RH for samples 6 and 7. For higher RH (80% for sample 6 and 85% for sample 7), the deformation increases significantly. As discussed in Chapter 3, by means of incremental analysis of strain maps, we have found that the nonlinear swelling of clay minerals is a mechanism of the significant deformation of argillaceous rocks at high RH. The present observation confirms this conclusion,

both in terms of the existence of this nonlinearity and of the threshold at which it occurs (about RH= 80%).

Finally, it is also interesting to stress out an irreversible contraction observed after the wetting-drying cycle (about 1.5% volume strain, see Fig.B.4). This phenomenon also verifies the observation in the tests 6 and 7 of Chapter 3. Its interpretation is so far unclear, and additional investigations would be required to confirm it.

Analyse expérimentale et modélisation micromécanique de la déformation et de l'endommagement des argilites sous chargement hydrique et mécanique combinés

Résumé

Ce mémoire présente l'étude expérimentale et la modélisation à l'échelle microscopique du comportement hydromécanique des argilites, roche hôte potentielle pour le stockage souterrain des déchets radioactifs. Le champ de déformation est mesuré par microscopie électronique à balayage environnementale et corrélation d'images numériques. En premier lieu, on étudie le cas du chargement hydrique pur. Le champ de déformation obtenu est très hétérogène, et montre une anisotropie. La non-linéarité de déformation pour HR élevée est le résultat combiné d'une fissuration et d'un gonflement non-linéaire de la phase argileuse dû à des mécanismes différents selon humidité relative (HR). On constate une déformation irréversible lors d'un cycle hydrique, ainsi qu'un réseau de microfissures localisées dans la phase argileuse ou aux interfaces grain-matrice. Ensuite, on étudie le cas du chargement combiné hydrique et mécanique dans le MEBE. Trois types de bandes de déformation apparaissent au cours du chargement mécanique : horizontales (compaction), verticales (fissuration), et inclinées (cisaillement). Les bandes de cisaillement apparaissent plus tôt à HR plus élevée. Finalement, le matériau sous chargement hydrique est modélisé comme un composite constitué par de inclusions non gonflantes au sein d'une matrice gonflante. On calcule d'abord le champ de contrainte interne dû aux interactions inclusion-matrice ainsi qu'au gradient d'humidité, et ensuite la déformation globale. On en dérive un modèle micromécanique du type du problème d'Eshelby. De plus, des modélisations 2D aux éléments finis sont effectuées.

Mots-Clés: Argilite, Comportement hydro-mécanique, Microscopie électronique à balayage environnementale, Corrélation d'images numériques, Micromécanique

Micromechanical experimental investigation and modelling of strain and damage of argillaceous rocks under combined hydric and mechanical loads

Abstract

The hydromechanical behavior of argillaceous rocks, which are possible host rocks for underground radioactive nuclear waste storage, is investigated by means of micromechanical experimental investigations and modellings. Strain fields at the micrometric scale of the composite structure of this rock, are measured by the combination of environmental scanning electron microscopy, in situ testing and digital image correlation techniques. The evolution of argillaceous rocks under pure hydric loading is first investigated. The strain field is strongly heterogeneous and manifests anisotropy. The observed nonlinear deformation at high relative humidity (RH) is related not only to damage, but also to the nonlinear swelling of the clay mineral itself, controlled by different local mechanisms depending on RH. Irreversible deformations are observed during hydric cycles, as well as a network of microcracks located in the bulk of the clay matrix and/or at the inclusion-matrix interface. Second, the local deformation field of the material under combined hydric and mechanical loadings is quantified. Three types of deformation bands are evidenced under mechanical loading, either normal to stress direction (compaction), parallel (microcracking) or inclined (shear). Moreover, they are strongly controlled by the water content of the material: shear bands are in particular prone to appear at high RH states. In view of understanding the mechanical interactions a local scale, the material is modeled as a composite made of non-swelling elastic inclusions embedded in an elastic swelling clay matrix. The internal stress field induced by swelling strain incompatibilities between inclusions and matrix, as well as the overall deformation, is numerically computed at equilibrium but also during the transient stage associated with a moisture gradient. An analytical micromechanical model based on Eshelby's solution is proposed. In addition, 2D finite element computations are performed. Results are discussed in relation with experimental observations.

Keywords: Argillaceous rock, Hydromechanical behavior, Environmental scanning electron microscopy, Digital image correlation, Micromechanics